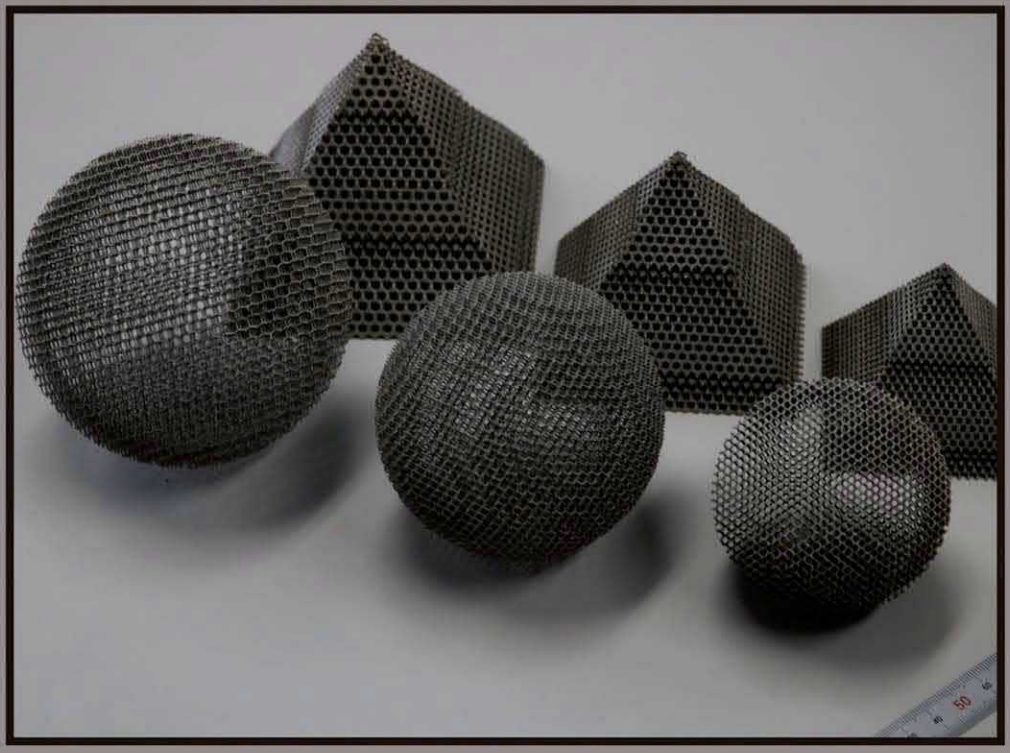
WOODHEAD PUBLISHING SERIES IN BIOMATERIALS



METALS FOR BIOMEDICAL DEVICES

SECOND EDITION

Edited by
MITSUO NIINOMI

ELSEVIER

Metals for Biomedical Devices

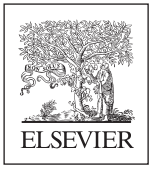
Woodhead Publishing Series in Biomaterials

Metals for Biomedical Devices

Second Edition

Edited by

Mitsuo Niinomi





An imprint of Elsevier

Woodhead Publishing is an imprint of Elsevier
The Officers' Mess Business Centre, Royston Road, Duxford, CB22 4QH, United Kingdom
50 Hampshire Street, 5th Floor, Cambridge, MA 02139, United States
The Boulevard, Langford Lane, Kidlington, OX5 1GB, United Kingdom

© 2019 Elsevier Ltd. All rights reserved.

No part of this publication may be reproduced or transmitted in any form or by any means, electronic or mechanical, including photocopying, recording, or any information storage and retrieval system, without permission in writing from the publisher. Details on how to seek permission, further information about the Publisher's permissions policies and our arrangements with organizations such as the Copyright Clearance Center and the Copyright Licensing Agency, can be found at our website: www.elsevier.com/permissions.

This book and the individual contributions contained in it are protected under copyright by the Publisher (other than as may be noted herein).

Notices

Knowledge and best practice in this field are constantly changing. As new research and experience broaden our understanding, changes in research methods, professional practices, or medical treatment may become necessary.

Practitioners and researchers must always rely on their own experience and knowledge in evaluating and using any information, methods, compounds, or experiments described herein. In using such information or methods they should be mindful of their own safety and the safety of others, including parties for whom they have a professional responsibility.

To the fullest extent of the law, neither the Publisher nor the authors, contributors, or editors, assume any liability for any injury and/or damage to persons or property as a matter of products liability, negligence or otherwise, or from any use or operation of any methods, products, instructions, or ideas contained in the material herein.

Library of Congress Cataloging-in-Publication Data
A catalog record for this book is available from the Library of Congress

British Library Cataloguing-in-Publication Data
A catalogue record for this book is available from the British Library

ISBN: 978-0-08-102666-3

For information on all Woodhead publications visit our website at https://www.elsevier.com/books-and-journals

Publisher: Matthew Deans
Acquisition Editor: Christina Gifford
Editorial Project Manager: Emma Hayes
Production Project Manager: Joy Christel Neumarin Honest Thangiah
Cover Designer: Greg Harris

Typeset by SPi Global, India



Contributors

Amirhesam Amerinatanzi Dynamic and Smart Systems Laboratory, Mechanical Industrial and Manufacturing Engineering Department, The University of Toledo, Toledo, OH, United States

Margam Chandrasekaran Wise Consultants and Services Pte Ltd, Singapore, Singapore

Bohan Cheng The University of Tokyo, Tokyo, Japan

C. Cui Hebei University of Technology, Tianjin, China

Amir Dehghanghadikolaei School of Mechanical, Industrial and Manufacturing Engineering, Oregon State University, Corvallis, OR, United States

Mohammad Elahinia Dynamic and Smart Systems Laboratory, Mechanical Industrial and Manufacturing Engineering Department, The University of Toledo, Toledo, OH, United States

U. Gbureck University of Würzburg, Würzburg, Germany

T. Hanawa Department of Metallic Biomaterials, Institute of Biomaterials and Bioengineering, Tokyo Medical and Dental University, Tokyo, Japan

Hiroyuki Hasebe Department of Orthopedic Surgery, National Hospital Organization Hokkaido Medical Center, Sapporo, Japan

Hendra Hermawan Department of Mining, Metallurgical and Materials Engineering and CHU de Québec research center, Laval University, Quebec City, QC, Canada

Sachiko Hiromoto National Institute for Materials Science, Tsukuba, Ibaraki, Japan

Hamdy Ibrahim Mechanical Engineering Department, The University of Tennessee at Chattanooga, Chattanooga, TN, United States

Kazuhiko Ishihara The University of Tokyo, Tokyo, Japan

Manabu Ito Department of Orthopedic Surgery, National Hospital Organization Hokkaido Medical Center, Sapporo, Japan

Ahmadreza Jahadakbar Dynamic and Smart Systems Laboratory, Mechanical Industrial and Manufacturing Engineering Department, The University of Toledo, Toledo, OH, United States

Toshihiro Kasuga Division of Advanced Ceramics, Nagoya Institute of Technology, Nagoya, Japan

S. Lerouge Ecole de Technologie Supérieure (ETS), Montreal, QC, Canada

Sergio Loffredo Department of Mining, Laboratory for Biomaterials and Bioengineering, CRC-I, Metallurgical and Materials Engineering and CHU de Québec research center, Laval University, Quebec City, QC, Canada; Department of Mechanical Engineering, Politecnico di Milano, Milan, Italy

Mohammad Javad Mahtabi Dynamic and Smart Systems Laboratory, Mechanical Industrial and Manufacturing Engineering Department, The University of Toledo, Toledo, OH; Department of Mechanical Engineering, University of Tennessee at Chattanooga, Chattanooga, TN, United States

Diego Mantovani Department of Mining, Laboratory for Biomaterials and Bioengineering, CRC-I, Metallurgical and Materials Engineering and CHU de Québec research center, Laval University, Quebec City, QC, Canada

Norio Maruyama Collaboration Planning Office, National Institute for Materials Science, Tsukuba-shi, Japan

T. Matsushita Chubu University, Kasugai, Japan

C. Moseke Mittelhessen University of Applied Sciences, Giessen, Germany

Takayoshi Nakano Graduate School of Engineering, Osaka University, Osaka, Japan

Mohammadreza Namatollahi Dynamic and Smart Systems Laboratory, Mechanical Industrial and Manufacturing Engineering Department, The University of Toledo, Toledo, OH, United States

T. Narushima Department of Materials Processing, Tohoku University, Sendai, Japan

Mitsuo Niinomi Tohoku University, Sendai; Osaka University, Osaka; Nagoya University, Nagoya; Meijo University, Nagoya, Japan

Hideaki Nishikawa Research Center for Structural Materials, National Institute for Materials Science, Tsukuba-shi, Japan

Yoshimitsu Okazaki National Institute of Advanced Industrial Science and Technology, Tsukuba, Japan

H. Takahashi Teijin-Nakashima Medical Corp., Okayama, Japan

Maurizio Vedani Department of Mechanical Engineering, Politecnico di Milano, Milan, Italy

Y. Yan University of Leeds, Leeds, United Kingdom

Introduction

Metallic materials are used as structural materials for medical devices in the fields of orthopedic surgery, blood circulatory system, and dentistry. Approximately 70%–80% of the structural materials employed in implants are metallic materials. The elderly population (over 65 years old) is rapidly increasing (by approximately 2%–3% per year) all over the world, as shown in Fig. I.1 (Cabinet Office, Government of Japan, 2018). In particular, the elderly population in Japan is currently over 21% and has been since 2010. A society with the elderly population over 21% is called a super aged society. Italy and Germany also have a super aged societies. Therefore, the number of elderly people with failed tissues needing replacement with artificial instrumentation made of metallic biomaterials is also growing.

Metallic biomaterials are roughly grouped into the following categories: stainless steels (mainly SUS 316L stainless steel); cobalt (Co)—chromium (Cr)—molybdenum (Mo) alloys; titanium (Ti; pure titanium) and its alloys; mainly pure titanium and Ti-6mass% aluminum (Al)-4mass% vanadium (V); and precious metal alloys (gold (Au) based, silver (Ag) based, or platinum (Pt) based alloys). The implant materials used for fabricating artificial hip joints, other artificial joints, bone plates, screws, and artificial tooth roots are mainly stainless steel, Co-Cr-Mo alloys, titanium, and titanium alloys. Precious metal alloys are mainly used as dental materials, for fabricating dental products such as dentures, crowns, inlays, and bridges. In the early days of using metallic materials as biomaterials, general structural metallic materials were used. Now, we are seeing a large number of metallic materials composed of nontoxic and allergy-free elements and exhibiting excellent mechanical biocompatibility being proposed or under development.

The metallic materials used in biomaterials, namely metallic biomaterials, do not possess bio-functionalities such as bone conductivity, bioactivity, and blood compatibility. Hence, surface modification of metallic biomaterials using bioactive ceramics, such as hydroxyapatite and biopolymers, is required.

The integration and harmonization of metals, ceramics, and polymers is very important for developing metal-based bio-functional biomaterials; these integrated materials are called biometals. The harmonization of metals, ceramics, and polymers also leads to the harmonization of metallic biomaterials and living tissues. If these sorts of metallic biomaterials are established, then metallic biomaterials will become the new scaffold used for artificial organs.

Further, advanced processing methods, such as powder metallurgy processing and modified conventional net shape fabrication processing are important in fabricating metallic medical devices. Understanding the clinical applications of metallic medical devices is very important in developing the metallic biomaterial and medical implants.

Metals for Biomedical Devices (second edition) has been fully updated and builds upon the success of its first edition, discussing the latest techniques in metal processing methods and the behavior of this important material.

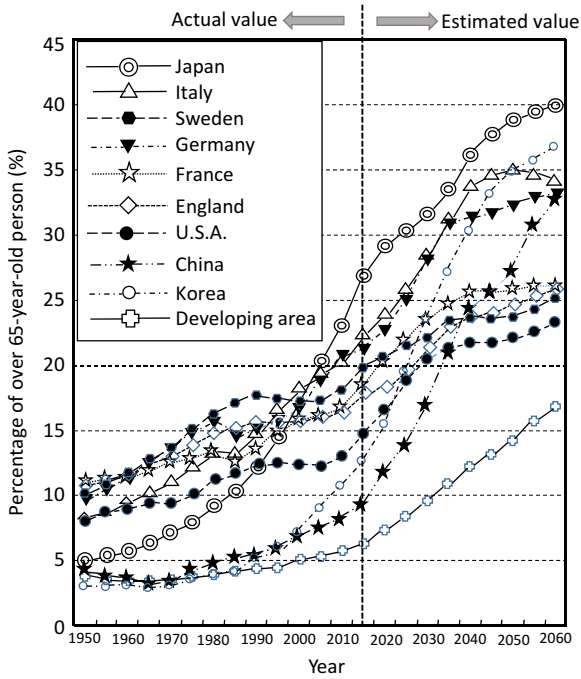


Fig. I.1 Change and estimation of elderly (over 65 years old) population (%) of selected countries.

This book has four parts. Part one is the general introduction and it reviews the current status and selection of metals for biomedical devices. Part two discusses mechanical behavior, degradation, and testing of metals biomedical devices with specific chapters on corrosion, wear testing, and biocompatibility of biomaterials. Part three covers the processing of metals for biomedical applications with chapters on forging metals and alloys, surface treatment, coatings and sterilization, and a new chapter discussing the use of additive manufacturing in the production of medical devices, as well as new material on the metal injection molding (MIM) and casting processes. Part four presents the specific applications of metals for biomedical applications and discusses clinical applications of metals such as cardiovascular, orthopedic, and new generation biomaterials.

Every chapter in this book is contributed to by distinguished experts in the biomaterials field. The editor (M.N. Mitsuo Niinomi) is grateful to all the authors for their outstanding efforts. The editor is also grateful to the staff of Elsevier publishing company, in particular, to Ms. Emma Hayes, editorial project manager, for their help and encouragement in publishing this book.

References

Cabinet Office, Government of Japan, 2018. White Paper on Aging Society. http://www8.cao.go.jp/kourei/whitepaper/w-2017/zenbun/29pdf_index.html.

Part One

General introduction

Overview of metals and applications

1

T. Hanawa
Department of Metallic Biomaterials, Institute of Biomaterials and Bioengineering, Tokyo Medical and Dental University, Tokyo, Japan

1.1 Introduction

The use of metals as raw materials has a long history and it can be said that materials science and engineering have been based on research into metals. However, metals are sometimes thought of as "unfavorite materials" for biomaterials because of memories of the environmental and human damage caused by heavy metals. Since an improvement in the safety of metals for medical use is vital, strenuous efforts have been made to improve corrosion resistance and mechanical durability. In addition, metals are typically artificial materials and have no biofunctions, which makes them fairly unattractive as biomaterials. However, this viewpoint is short-sighted and is caused by misunderstandings. On the other hand, the fast technological evolution of ceramics and polymers has made it possible to apply these materials to medical devices over the last four decades. In particular, because of their excellent biocompatibility and biofunctions, ceramics and polymers are expected to show excellent properties for use as biomaterials; in fact, many devices made from metals have been replaced by others made from ceramics and polymers. In spite of this fact, over 70% of implant devices are still made from metals and this percentage remains unchanged because of their high toughness and durability. Therefore, current metallic biomaterials cannot be replaced with ceramics or polymers at present. In addition, research into their use in regenerative medicine will not be completed for at least another few decades. In other words, artificial materials such as metals will continue to be used as biomaterials in the future.

This chapter looks at the utilization and types of metals used in medicine and dentistry. The properties and problems or the advantages and disadvantages of metals used for medical devices are then explained. In addition, new alloys are introduced that are currently being researched and developed.

1.2 General properties required for metals in medical devices

1.2.1 Biological environment

The biological environment that influences the durability of metals is summarized in Fig. 1.1. The concentrations of chloride ions in serum and interstitial fluid are 113 and 117 mEq L^{-1}, respectively, which is 1/3 of the concentration in brine and a seriously

Metals for Biomedical Devices. https://doi.org/10.1016/B978-0-08-102666-3.00001-8
© 2019 Elsevier Ltd. All rights reserved.

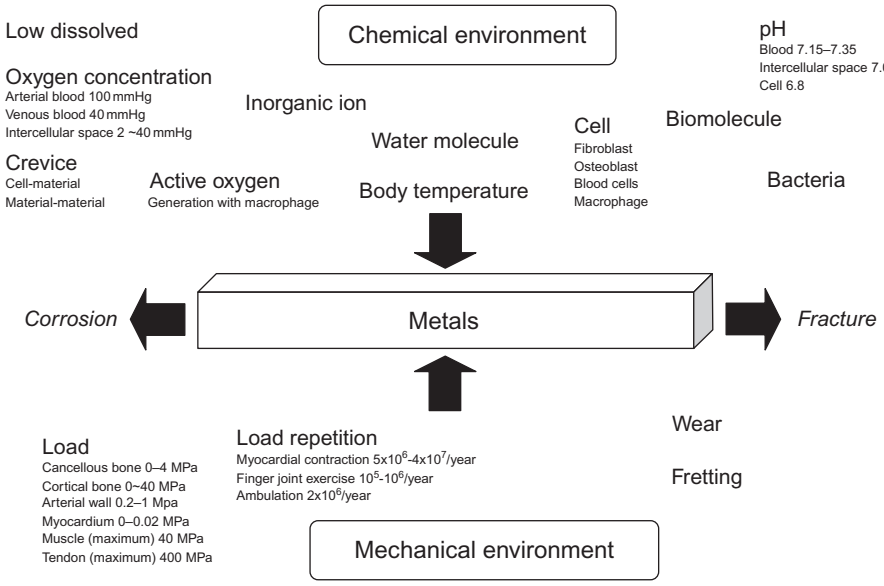


Fig. 1.1 Biological environments against metals implanted into the human body.

corrosive environment for metallic materials (Fig. 1.1). Body fluids contain various amino acids and proteins that influence metallic corrosion (Merritt and Brown, 1998; Williams et al., 1988; Hanawa et al., 2004) because they are electrolytes. In addition, the concentration of dissolved oxygen in venous blood is 1/4 of that of air and in intercellular spaces is 1/80–1/4 of that of air (Black, 1984), which accelerates the corrosion of metallic materials. The changes in the pH of body fluids are small because the fluids are buffered solutions and the pH usually remains between 7.0 and 7.35 (Black, 1984). The pH of the hard tissue into which a material is implanted decreases to approximately 5.2 and then recovers to 7.4 within 2 weeks (Hench and Ethridge, 1975). However, the local pH may change according to the dissociation of protein in the body fluid and the isoelectric point of protein (usually 5–7). The pH in an oral cavity may decrease to about 2 if carbonated drinks and some foods are ingested. The cell and bacteria is also a kind of charging body that may influence the corrosion of metallic materials.

Materials implanted in the human body are intermittently stressed with loads due to weight and activity (Fig. 1.1). In particular, materials in the lower extremities are intermittently loaded with stressors several times heavier than the body weight. In addition, loading is repeated a great number of times. Such loads are applied in the chemical environment described above.

Under these conditions, material properties such as toughness, rigidity, elasticity, wettability, bioinertness, bioactivity, biodegradability, X-ray imaging, and so on, are required according to their purpose. Since biomaterials are in contact with living

tissues, they need to be absolutely safe for the human body. Moreover, it must be possible to sterilize biomaterials. Needless to say, durability in the human body is also important. In particular, corrosion resistance is required in metals.

1.2.2 Properties required for metals in medicine and dentistry

Materials are categorized as metals, ceramics, and polymers (Fig. 1.2). Metallic materials generally have a multi-crystal body consisting of metal bonds. For example, metal oxides, metal salts, metal complexes, etc., contain metal elements, however, since these compounds consist of ionic bonds or covalent bonds, their properties are completely different from those of metals consisting of metal bonds. Therefore, in the field of materials engineering, ceramics and metals are clearly distinguished, despite the fact that both of them are categorized as inorganic compounds. Each material has its own advantages and disadvantages and applications are determined according to their properties.

Metals have been utilized for dental restoration and bone fixation for the past 2500 years and have a long history as biomaterials. The properties of metals derive from their metal bonds and their advantages as biomaterials are as follows:

(a) Large fracture toughness due to large strength and large ductility
(b) Large plasticity and workability
(c) Suitable balance between elasticity and stiffness
(d) Large electroconductivity.

Metals and alloys are widely used as biomedical materials and are indispensable in the medical field. The advantages of metals compared with ceramics and polymers are their great strength and resistance to fracture. In particular, toughness, elasticity, rigidity, and electrical conductivity are essential properties required of metals used in medical devices. The metals used for such devices are listed in Table 1.1. Conventionally, metals have been essential for orthopedic implants, bone fixators, artificial joints, external fixators, etc., because they can substitute for the function of hard tissues in orthopedics. Stents and stent grafts are placed in blood vessels for dilatation. Therefore, these devices require elasticity or plasticity for expansion and rigidity for maintaining dilatation. In dentistry, metals are used for restorations, orthodontic wire, and dental implants. The most important property of biomaterials is safety. Therefore, corrosion-resistant materials such as stainless steel, cobalt (Co)-chromium (Cr) alloys,

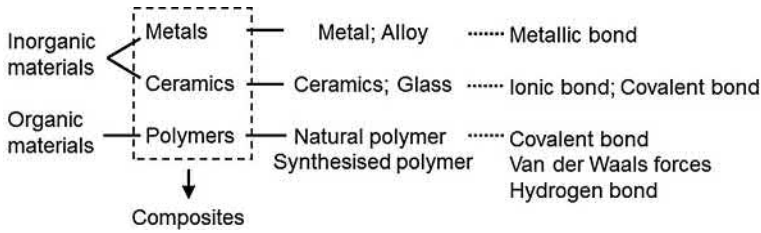


Fig. 1.2 Category of materials and their chemical bonding.

Table 1.1 Metals used for medical devices

Clinical division	Medical device	Material
Orthopedic surgery	Spina fixation	Ti; Ti-6Al-4V; Ti-6Al-7Nb; 316L stainless steel
	Bone fixation (bone plate, screw, wire, bone nail, mini-plate, etc.)	Ti; Ti-6Al-4V; Ti-6Al-7Nb; 316L stainless steel
	Artificial joint; bone head	Ti-6Al-4V; Ti-6Al-7Nb; Co-Cr-Mo, Zr-Nb
	Spina spacer	Ti-6Al-4V; Ti-6Al-7Nb; 316L stainless steel
Cardiovascular medicine and surgery	Implant-type artificial heart (housing)	Ti
	Pace maker (case)	Ti; Ti-6Al-4V
	(electric wire)	Ni-Co
	(electrode)	Ti; Pt-Ir
	(terminal)	Ti; 316L stainless steel; Pt
	Artificial valve (frame)	Ti-6Al-4V
	Stent	Co-Ni-Cr-Mo; Co-Cr-Ni-W; 316L stainless steel; Ti-N; Ta; Co-Cr
	Guide-wire	Co-Ni-Cr-Mo; 316L stainless steel; Ti-Ni;
	Embolization wire	Pt
	Clip	Ti-6Al-4V; Co-Ni-Cr-Mo; 630 stainless steel
Otorhinology	Artificial inner year (electrode)	Pt
	Artificial eardrum	316L stainless steel
Dentistry	Filling	Au foil; Ag-Sn(-Cu) amalgam
	Inlay, crown; bridge; clasp; post; denture base	Au-Cu-Ag; Au-Cu-Ag-Pt-Pd; Ti; Ti-6Al-7Nb; Co-Cr-Mo; 304 stainless steel; 316L stainless steel
	Thermosetting resin facing crown; porcelain-fused-to-metal	Au-Pt-Pd; Ni-Cr
	Solder	Au-Cu-Ag; Au-Pt-Pd
	Dental implant	Ti; Ti-6Al-4V; Ti-6Al-7Nb; Au
	Orthodontic wire	Ti-Ni; Ti-Mo; Co-Ni-Cr-Mo; 316L stainless steel
	Magnetic attachment	Sm-C; Nd-Fe-B; Pt-Fe-Nb; 444stainless steel; 447J1 stainless steel; 316L stainless steel
	Treatment device (bar, scaler, periodontal probe, dental tweezers, raspatory, etc.)	304 Stainless steel
General surgery	Needle of syringe	304 Stainless steel
	Scalpel	420J1 stainless steel
	Cathetel	Ni-Ti; 304 stainless steel; 316L stainless steel; Co-Ni-Cr-Mo; Au; Pt-In
	Suture stapler	630 stainless steel

commercially pure titanium (CP Ti), and Ti alloys are used. Noble-metal-based alloys, such as gold (Au) alloys and silver (Ag) alloys, are also used in dentistry.

Safety to the human body is essential in biomaterials; therefore, no toxic material is used for biomaterials. Metals implanted in tissues do not show any toxicity unless there is metal ion dissolution from corrosion and/or the generation of debris from wear. Therefore, corrosion resistance is absolutely essential for metals in biomedical use, necessitating the use of noble or corrosion-resistant metals and alloys for medicine and dentistry. Of the noble metals and alloys, Au markers are used for the imaging of stents, platinum (Pt) is used for embolization wires, and Au alloys and Ag alloys for dental restoratives. Of the base metals and alloys, stainless steels, Co-Cr alloys, Ti and Ti alloys, whose corrosion resistance is maintained by a passive film of surface oxide, are used for implant materials. In addition, wear resistance is required to reduce the generation of wear debris. Co-Cr-molybdenum (Mo) alloys have good wear resistance and are used for sliding parts of artificial joints. A comparison of the various properties of metals used for implants is summarized in Table 1.2. The relation between elongation to fracture and tensile strength of a variety of metallic biomaterials is shown in Fig. 1.3. The positions of the component elements of metals in biomedical use on the periodic element table are shown in Fig. 1.4.

1.3 Stainless steels

1.3.1 Definition and category

"Stainless steel" is defined as an iron (Fe)-based alloy containing over 10.5 mass%Cr and total amount of elements other than Fe is not over 50 mass%. Stainless steel is not corroded under an oxygen-containing atmosphere, but is locally corroded and sometimes forms pits in chloride solutions such as body fluids. Nickel (Ni), Mo, copper (Cu), Ti, niobium (Nb), nitrogen (N), etc., are added to stainless steels to improve their corrosion resistance, heat resistance, strength, and workability. The metallurgical structure, strength, and corrosion resistance of stainless steels depend on the concentrations of Ni and Cr. Stainless steels are basically categorized as ferritic (Fe-Cr system), martensitic (Fe-Cr system), and austenitic (Fe-Cr-Ni system), according to their crystal phase. Austenitic-type stainless steels have outstanding corrosion resistance, but do not have great strength. Therefore, austenitic stainless steels are strengthened by working and heat treatment and hardened with the addition of N. The addition of Mo improves their corrosion resistance, because their passive film becomes more stable. The categories of popular stainless steel series are summarized in Fig. 1.5, according to their development history. In AISI numbering, the 200 series represents the Fe-Cr-Ni-manganese (Mn) alloy system, the 300 series represents the Fe-Cr-Ni alloy system, the 400 series represents the Fe-Cr system, and the 600 series represents precipitation hardening type. The stainless steels used for the stems of artificial hip joints and bone fixators have been replaced by Ti alloys. However, stainless steel is still used for internal bone fixators that are retrieved after healing, and sternal wire and bone fixation wire, because of its excellent torsion property and elongation. Some

Table 1.2 Comparison of properties of metals for implant

Materials		Mechanical property	Workability			Corrosion resistance
		Tesile strength	Wear resistance	Plasticity	Machinability	Pitting
Stainless steel	Type316L	Good	Excellent	Excellent	Excellent	Excellent
Co-Cr-Mo alloy	Cast	Good	Good	Poor	Poor	Good
	Annealed	Excellent	Good	Good	Good	Fair
Ti; Ti alloy	CP Ti	Excellent	Excellent	Fair	Fair	Excellent
	Ti-6Al-4V	Excellent	Excellent	Fair	Excellent	Excellent

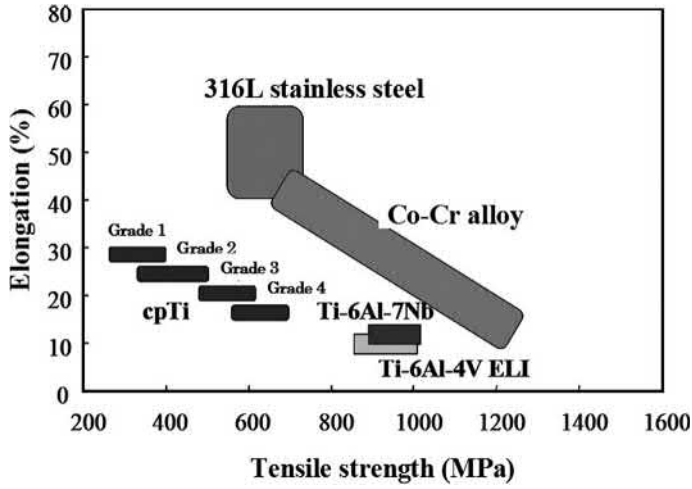


Fig. 1.3 Relation between elongation to fracture and tensile strength of conventional metals.

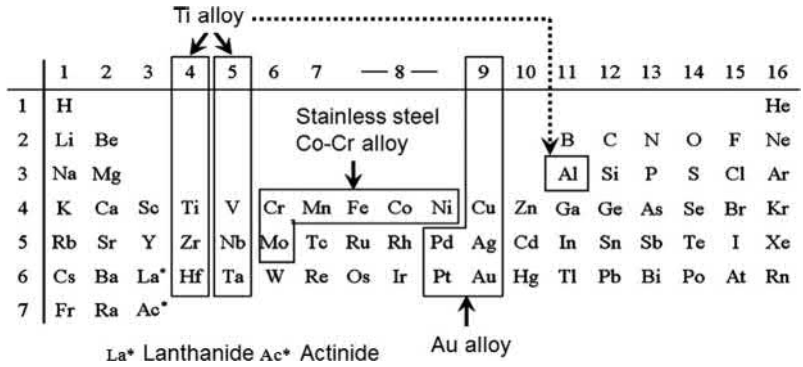


Fig. 1.4 Position of elements constituting alloys in periodic table.

stents are made from austenitic stainless steel. Stainless steels are also used for treatment and operating equipment and instruments. Type 304 stainless steel is used for medical equipment such as scalpels, forceps, dental tweezers, etc. Type 630 stainless steel is used for suture stapler.

1.3.2 Type 316L stainless steel

The design of type 316L stainless steel is based on type 302 stainless steel. Its corrosion resistance is improved by adding 2.0–3.0 mass% of Mo, increasing Ni from 8.0–10.0 mass% to 12.0–15.0 mass%, and reducing carbon (C) to <0.030%. "L" means "low C content." The presence of Mo as an alloying element in stainless steel

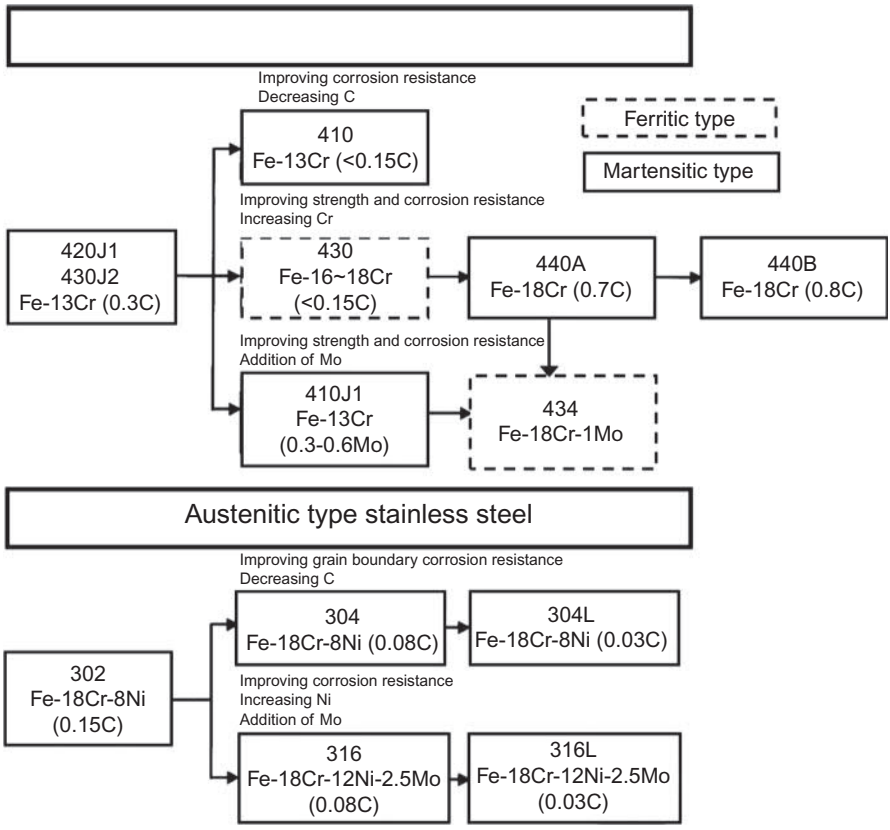


Fig. 1.5 Concept of design of predominant stainless steels.

reduces both the number and the size of nucleations and metastable pits. This is because bonds in the oxide film are strengthened and active sites caused by the formation of molybdates or of molybdenum oxyhyroxides are eliminated (Ilevbare and Burstein, 2001). The composition and mechanical properties of this alloy are summarized in Table 1.3.

In the case of type 316L stainless steel, solution treatment is carried out, followed by rapid cooling (such as water cooling), after the products have been heated to 1010–1150°C. This form of heat treatment causes dissolution of precipitates during the manufacturing process, as well as the release of strains which were induced during rolling. The release of strain energy causes recrystallization of the structures. Metallic biomaterials must possess essential prerequisite properties such as corrosion resistance, strength, toughness, and ductility. As discussed above, these properties can be achieved through chemical composition, heat treatment, and working such as forging and rolling.

The surface oxide film on type 316L steel polished mechanically in deionized water consists of oxide species of Fe, Cr, Ni, Mo, and Mn, and its thickness is about

Table 1.3 Composition and mechanical property of 316L type stainless steel solution treated and annealed

C	P	S	Si	Mn	Cr	Ni	Mo	Fe
<0.03	<0.045	<0.03	<1.0	<2.00	16.0–18.0	12.0–15.0	2.0–3.0	Bal.
Tensile strength (MPa)			Proof strength (MPa)			Elongation (%)		
>480			>175			>40		

3–4 nm (Hanawa et al., 2002). The surface film contains a large amount of OH^-—the oxide which is hydrated or oxyhydroxidized. In pins and wires made from 316L austenitic stainless steel retrieved from the human body, calcium and phosphorus were present in the surface oxide. Calcium phosphate was formed for specimens immersed in Hanks' solution and in a cell culture medium, as well as incubated with culture cells. Sulfate is adsorbed by the surface oxide film and reduced to sulfite in the cell culture medium and with the cultured cells. The surface oxide changes into iron and chromium oxides with a small amount of molybdenum oxide after releasing Ni.

1.3.3 Ni-free austenitic stainless steel

Ni is a high-risk element from the viewpoint of allergic problems. Thus, Ni-free austenitic stainless steel is required. Schaeffler's phase diagram can be used for the development of high-performance austenitic stainless steels (see Fig. 1.6). The y-axis corresponds to the Ni-equivalent for the elements which stabilize the austenitic microstructure; the x-axis corresponds to the Cr-equivalent for the elements which stabilize the ferritic microstructure.

Nitrogen (N), which is one of the austenitizing elements, is an important alloying element for austenitic stainless steels in terms of corrosion resistance and strength (Ornhagen et al., 1996). N dissolved in austenitic stainless steel acts to increase its strength and improve its resistance to pitting corrosion and crevice corrosion in solutions containing chloride ions. The mechanisms have been summarized as follows (Baba et al., 2002):

(1) N is dissolved in solid solution and produces NH_4^+, hence depressing oxidation inside a pit;
(2) Concentrated N at the passive film/alloy surface stabilizes the film and prevents the attack from anions (Cl^-);

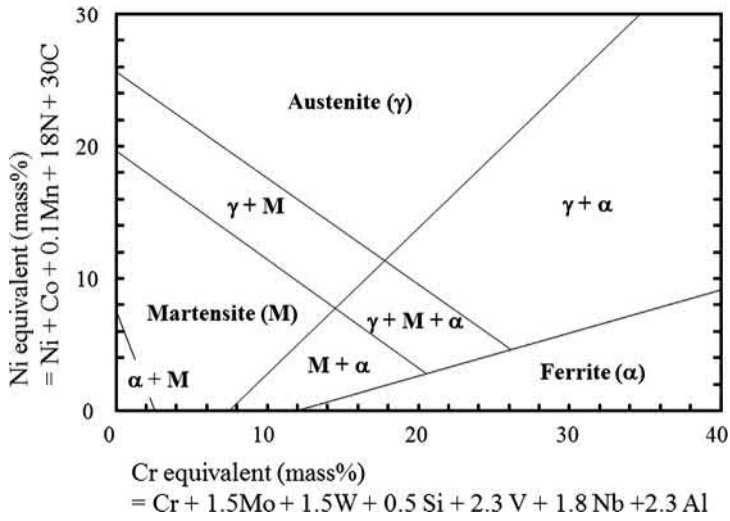


Fig. 1.6 Schaeffler's phase diagram.

(3) Nitrate ions are produced to improve resistance to pitting corrosion;
(4) N addition stabilizes the austenitic phase; and.
(5) N blocks kink and controls the increase of electric current for pit production.

Therefore, austenitic high-nitrogen stainless steels containing over 0.3mass%N are used.

Nickel-free austenitic stainless steel, having a high concentration of N and Mn instead of Ni and displaying high strength and corrosion resistance, has been developed (Sumita et al., 2004). Fe-(19–23)Cr-(21–24)Mn-(0.5–1.5)Mo-(0.85–1.1)N (BioDur 108) in the United States (Gebau and Brown, 2001), Fe–18Cr–18Mn–2Mo–0.9N in Germany (Menzel et al., 1996), and Fe-(15–18)Cr-(10 – 12)Mn-(3–6)Mo-0.9N in Switzerland (Uggowitzer et al., 1996) have been developed for medical use. These alloys are fabricated with an electro-slug remelting process where N is absorbed into the alloy during melting under a high-pressure N atmosphere. A new manufacturing process, where N is absorbed into ferritic stainless steel after forming at 1200°C, has also been developed (Kuroda et al., 2003).

1.4 Cobalt-based alloys

1.4.1 Properties of Co-based alloys

Co-Cr alloys were originally developed for aircraft engines and heat-resistant materials.Co-Cr alloys show excellent mechanical properties such as strength and toughness, castability, corrosion resistance, and wear resistance. Their corrosion resistance is better than that of stainless steel; their wear resistance is better than that of stainless steel and Ti alloys; but their plasticity and workability are lower than those of stainless steel and Ti alloys. They were initially used for cast alloys because working them was difficult.

Co-Cr alloys establish the status of metallic biomaterials as summarized in Table 1.1, because of their excellent strength, corrosion resistance, and wear resistance. A variety of Co-Cr alloys are standardized to satisfy required properties with alloy composition and thermomechanical treatment. Co-Cr-Mo alloys containing C are used as cast, because they show excellent wear resistance and the difficulty of working due to the hardness. The workability of Co-Cr-Mo alloys is improved by decreasing C content. Wrought Co-Cr-Mo alloys whose strength and elastic modulus increase with thermomechanical treatment are used as wire and plate. Specification and composition of typical Co-based alloys are summarized in Table 1.4.

In the field of orthopedics, a cast Co-Cr-Mo alloy as “Vitallium” (ASTM F75) with a main phase of ε as hcp is used for artificial knee joint and artificial hip joint especially head. The precipitation of Cr- and Mo-rich carbides due to large content of C contributes to large strength and wear resistance of the alloy. ASTM F79 Co-Cr-Mo alloy with γ phase as fcc is hot worked to produce the F75 with fine grains. The tensile strength and yield strength of the F99 alloy are twice those of F75 alloy. To improve workability of Co-Cr-Mo alloy, ASTM F90 as “HS25” or “L-605” used for orthopedic wire is

Table 1.4 Composition, specification, brand name, and composition of major co-based alloys

Alloy system	ASTM specification	General bland name	Composition (mass%)
Co-Cr-Mo	F75	Vitallium HS21	27.0–30.0 Cr, 5.0–7.0 Mo <0.5 Ni, < 0.75 Fe, <0.35C, <1.0 Mn, <1.0 Si, <0.25N
Co-Cr-W-Ni	F90	HS25	19.0–21.0 Cr, 14.0–16.0 W, 9.0–11.0 Ni 0.05–0.15C, 1.0–2.0 Mn <3.0 Fe, <0.4 Si
Co-Ni-Cr-Mo-Ti	F562	MP35N	33.0–37.0 Ni, 19.0–21.0 Cr, 9.0–10.5 Mo, <1.0 Ti, <1.0 Fe, <0.15 Mn, <0.15 Si, <0.025C
Co-Cr-Ni-Mo-Fe	F1058 grade1	Elgiloy	39.0–41.0 Co, 19.0–21.0 Cr, 14.0–16.0 Ni, 6.0–8.0 Mo, 1.5–2.5 Mn, <1.20 Si, <0.15C, <0.1 Be, Balance Fe

developed by decreasing C content and adding tungsten (W) and Ni that shows 44% workability and the strength after working is more than twice that of F75 alloy.

In cardiovascular surgery, ASTM F562 Co-Ni-Cr-Mo alloy as "MP35N" is used for stent whose strength, elasticity, and corrosion resistance are excellent and the tensile strength is over 1600 MPa. This alloy as well as ASTM F90 alloy have large elastic modulus which is advantageous to use as stent. On the other hand, ASTM F1058 Co-Cr-Ni-Mo-Fe alloy as "Elgiloy" is used for artificial heart spring and aneurysm clip. It is possible for this alloy to work for wire and foil and to strengthen by aging, while elastic modulus of this alloy is lower than that of other Co-Cr alloys.

In dentistry, Co-Cr-Mo alloy is used for the removal of partial denture, crown, and bridge. ISO-22674 requires dental alloy to be over an elongation of 2%, a yield strength of 500 MPa, and an elastic modulus of 150 GPa. Gallium (Ga), W, Nb, ruthenium (Ru), etc., are added to Co-Cr-Mo alloy for porcelain-fused-to-metal to improve workability and castability, especially Mo works as solution strengthening element and decreases coefficient of thermal expansion. Elgiloy is used for orthodontic arch wire due to the large elastic limit and feasibility of heat treatment and bonding.

The application of Co-based alloys is categorized according to plastic workability: cast and wrought. Wrought alloys are further categorized to rod, plate and sheet, and wire, due to difficulty in plastic processing. Plastic workability of Co-based alloy is governed by the stacking fault energy (SFE) (Allain et al., 2004) that are categorized into three groups: alloys with large SFE such as ASTM F90 Co-Cr-Ni-W alloy, alloys with medium SFE such as ASTM F562 Co-Ni-Cr-Mo alloy, and small SFE such as ASTM F75, F799, and F1537 Co-Cr-Mo alloy.

The surface oxide film of a Co-Cr-Mo alloy is characterized as containing oxides of cobalt and chromium without Mo, and the film on another Co-Cr-Mo alloy, polished mechanically in deionized water, consists of oxide species of Co, Cr, and Mo, and has a thickness of about 2–3 nm (Hanawa et al., 2001). This surface film contains a large amount of OH^-—the oxide which is hydrated or oxyhydroxidized. Co was dissolved

in a Co-Cr-Mo alloy during immersion in Hanks' solution and in a cell culture medium, as well as during incubation in a cell culture (Hanawa et al., 2001). After dissolution, the surface oxide consisted of chromium oxide (Cr^{3+}) which contained molybdenum oxide (Mo^{4+}, Mo^{5+}, and Mo^{6+}). Calcium phosphate was also formed on the top surface.

The surface oxide film on Co-Ni-Cr-Mo alloy (MP35N) consists of oxides of Cr, Co, Ni, and Mo containing a large amount of OH^-. During immersion in Hanks' solution, Co and Ni dissolve from the oxide and the composition changed as Cr^{3+} oxide containing a small amount of Co, Ni, and Mo oxides. Calcium phosphate is formed on the oxide. Also in Co-Cr-Mo alloy, preferential dissolution of Co and calcium phosphate formation occur (Nagai et al., 2012).

1.4.2 Ni-free Co-Cr alloys

The allergy problem of Ni mentioned above is also a problem in Co-Cr alloys. Thus, Ni-free Co-Cr alloys are required. The Co-Cr-Mo alloy contains a small amount of Ni and this may preferentially dissolve under wear conditions. However, since the plastic workability of the Co-Cr-Mo alloy decreases in the absence of Ni, it is necessary to add strength and ductility to the Ni-free Co-Cr-Mo alloy by grain refinement. An Ni-free Co-(16–29)Cr-6Mo alloy with a grain size controlled by various forging ratios has been developed (Kurosu et al., 2007; Lee et al., 2007), which is named "COBARION." This alloy series are used for allergy-free accessories.

1.5 Titanium-based alloys

Ti and Ti alloys were developed for aerospace materials and have also been used for medical and dental implants, because they show good corrosion resistance and great specific strength. Their Young's modulus is about half of that of stainless steel and Co-Cr alloys and this low Young's modulus makes them the preferred material for use in bone fixators. Ti materials form stable titanium oxide films on their surface, with the result that their corrosion resistance is better than that of stainless steel and Co-Cr alloys. Ti and most of the Ti alloys show high corrosion resistance and are safe for use in the human body; moreover, they exhibit good tissue compatibility, especially for hard tissue. On the other hand, Ti and Ti alloys are not suitable for bone fixation wires and sternal wires that require ligatures because of their low torsion strength (torque) and torsion angle to fracture.

1.5.1 Properties of Ti

Ti is an extremely active element, causing a low standard electrode potential of -1.63 V vs NHE in the reaction, $Ti \rightarrow Ti^{2+} + 2e^-$. This activity is the basis of the chemical properties of Ti, such as the difficulty in smelting it, high corrosion resistance, and safety in the human body (Fig. 1.7). The corrosion resistance of Ti is very high, in spite of the high activity of the titanium element, because Ti immediately reacts with water molecules in aqueous solutions and moisture in the air, and forms

a very thin Ti oxide film on its surface. This oxide film is immediately repaired even when it is ruptured by scratching, and thus the reaction of Ti with the external environment is inhibited, causing the apparent inactivity of Ti. This property directly contributes to its corrosion resistance and its safety.

Pure Ti is composed of hcp crystals (α phase) at ambient temperatures, but is composed of bcc crystals (β phase) over 882°C. Real pure Ti does not exist, because Ti easily dissolves oxygen (O), C, and N and contains them as impurities. Ti containing these impurities is described as CP Ti. CP Ti is classified into four grades, according to its impurity content and the resulting mechanical properties (Table 1.5). The higher

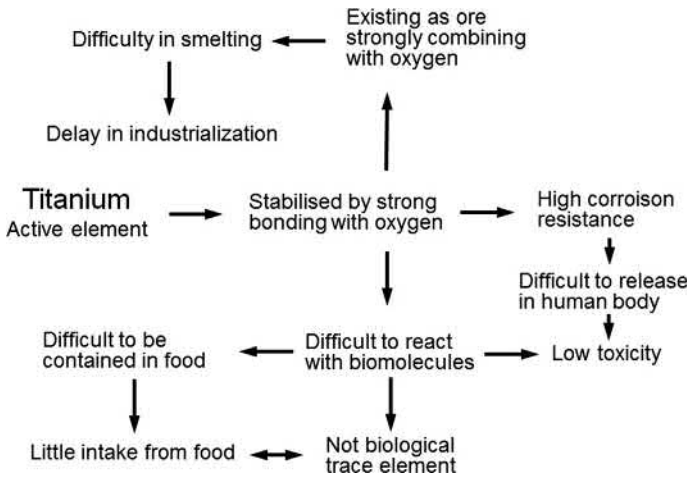


Fig. 1.7 Properties of titanium induced by thermodynamical activity of titanium.

Table 1.5 Compositions and mechanical properties of commercially pure titanium (CP Ti)

Element	Grade 1	Grade 2	Grade 3	Grade 4
	Composition (mass%)			
Fe	<0.15	<0.2	<0.25	<0.3
O	<0.18	<0.25	<0.35	<0.45
N	<0.03	<0.03	<0.05	<0.05
H	<0.0125	<0.0125	<0.0125	<0.0125
C	<0.1	<0.1	<0.1	<0.1
Ti	Balance	Balance	Balance	Balance
	Mechanical property			
Tensile strength (MPa)	275–412	343–510	481–618	>550
0.2% Proof strength (MPa)	170	275	380	>440
Elongation (%)	>27	>23	>18	>15
Young's modulus (GPa)	114			

the grade number, the higher the impurity, tensile strength, and offset yield stress and the lower the elongation (Fig. 1.8). In other words, CP Ti is a type of alloy, by the definition of an alloy and the general effects of alloying. CP Ti is used for maxillofacial prosthetic plates, sternal wire, dental implants, dental restoratives, and dental denture bases. Sometimes, CP Ti containing more impurities than grade 4 displays almost the same strength as Ti alloys, and since the tensile strength greatly increases with cold working, bone screws that are exposed to a large load are sometimes made of CP Ti.

The surface oxide film on Ti consists mainly of amorphous or low-crystalline and nonstoichiometric TiO_2, and can withstand chloride ions. Since a considerable portion of oxidized titanium remains as Ti^{2+} and Ti^{3+} in the surface film, the oxidation process can only be fully completed on the uppermost part of the surface film. When titanium that has been surgically implanted into the human jaw is characterized using an Auger electron spectroscopy (AES), its surface oxide film reveals constituents of calcium (Ca), phosphorus (P), and sulfur (S) (Sundgren et al., 1986; Espostito et al., 1999).

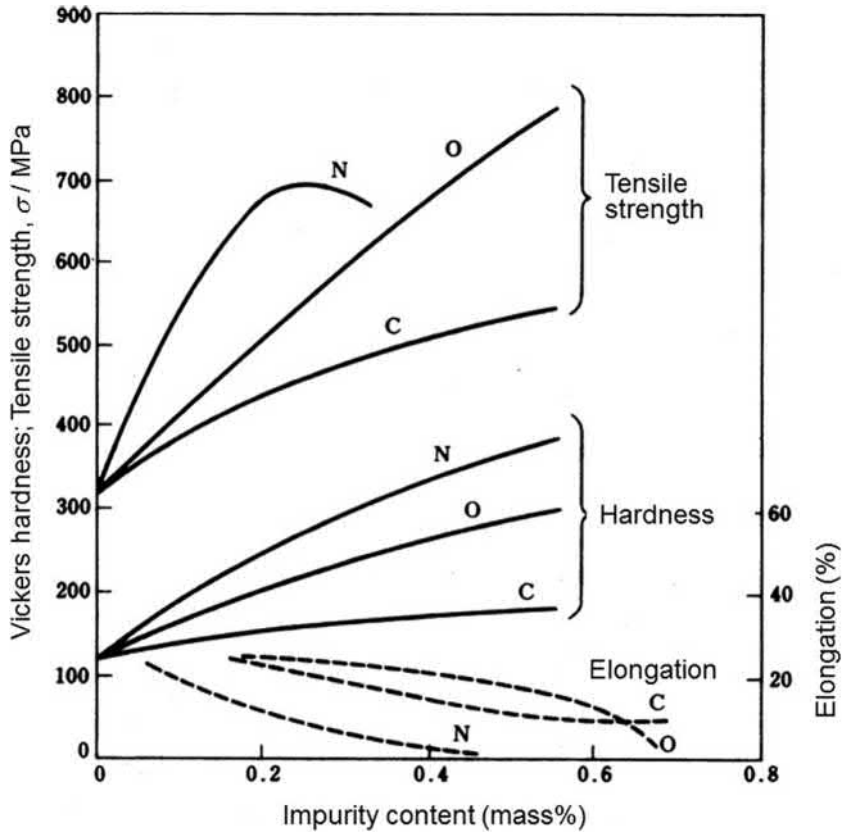


Fig. 1.8 Changes in tensile strength, hardness, and elongation of titanium with impurities.

Immersion of titanium and its alloys in Hanks' solution and other solutions (Hanawa and Ota, 1992; Healy and Ducheyne, 1992) causes the formation of calcium phosphate on their surfaces. Extrapolating from this, it can be assumed that bone formation is faster on titanium implanted in hard tissue simply because the surface oxide film is Ti oxide.

1.5.2 Ti alloys

Ti alloys at ambient temperatures are categorized as α-type, α + β-type, and β-type alloys, according to the quantities and types of their alloying elements. Many kinds of alloys have been developed (Table 1.6) but the Ti-6 aluminum (Al)-4 vanadium (V) alloy, an α + β-type alloy, is the most conventional one for medical use. This alloy show good workability, heat treatment ability, and weldability, as well as corrosion resistance, strength, and biocompatibility. The extra low interstitial (ELI) grade alloy, containing only small amounts of interstitial impurities,O, C, N, and hydrogen (H), is used for biomaterials. The Ti-6Al-4V ELI alloy shows great toughness, because the impurities decrease the fatigue strength with the notch effect. The ELI alloy is used for bone fixation plates, screws, bone nails, and the stems of artificial hip joints. Ti-6Al-4V alloy has an extremely large (0.2%) offset yield strength of 895 MPa, which is much larger than that of stainless steel and Co-Cr-Mo alloys, making plastic deformation difficult even under a large load.

The Ti-6Al-7Nb alloy (Semlitsch et al., 1985) has been developed as a replacement for the Ti-6Al-4V alloy, mainly used in Europe, because the V shows cytotoxicity, although there are no reports of accidents when using Ti-6Al-4V alloy implants. The Ti-6Al-7Nb alloy has been created by substituting V with Nb of the same atomic concentration. Its corrosion resistance and safety are greater than those of Ti-6Al-4V. Elsewhere, the Ti-6Al-2.5Fe alloy is developed in Europe and Ti-6Al-2Nb-1 tantalum (Ta)-0.8Mo alloy is developed in Japan (Anon, 1994). These are α + β-type alloys. Ti-13zirconium (Zr)-13Ta alloy (nearly β) has been developed in United States.

Table 1.6 Specificated titanium alloys

Composition (mass%)	Type	UNS	ASTM	ISO
Ti-5Al-2.5Fe	α+β	–	–	ISO 5832-10
Ti-6Al-4V	α+β	R56400	F1108 (Cast) F1472 (Wrought)	ISO 5832-3
Ti-6Al-4V ELI	α+β	R56401	F136 (Wrought)	ISO 5832-3
Ti-6Al-7Nb	α+β	R56700	F1295	ISO 5832-11
Ti-3Al-2.5V	α+β		F2146	
Ti-6Al-2Nb-1Ta-0.8Mo	α+β	R56210	F136	ISO 5832-14
Ti-13Nb-13Zr	Near β	R58130	F1713	–
Ti-15Mo	β	R58150	F2066	–
Ti-12Mo-6Zr-2Fe	β	R58120	F1813	–
Ti-15Mo-5Zr-3Al	β		F136	ISO 5832-14

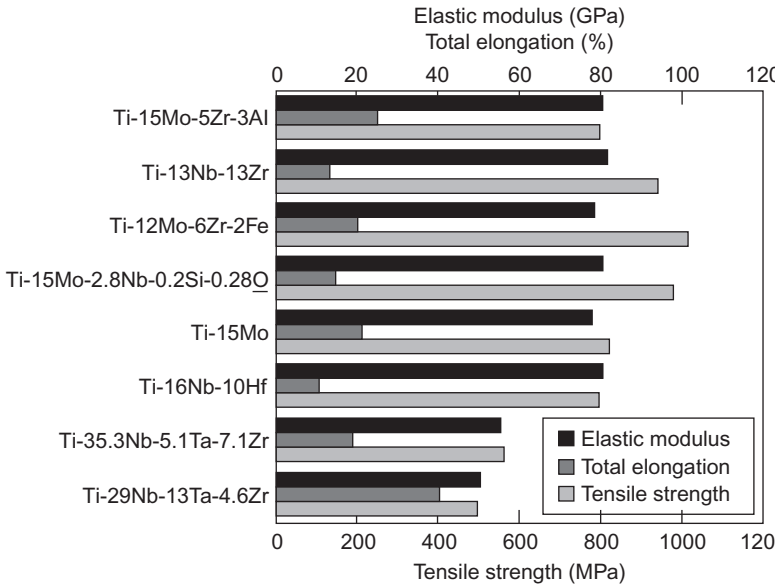


Fig. 1.9 Mechanical properties of β-type titanium alloys.

On the other hand, Young's modulus could decrease to about 60 GPa in a β-type alloy. Various β-type alloys, Ti-12Mo-6Zr-2Fe alloys (Wang et al., 1993), T-15Mo (Zardiackas et al., 1996), and Ti-15Mo-2.8Nb-0.2silicon (Si)-0.28O alloy (Fanning, 1996) have been developed in the United States and Ti-15Mo-5 Zr-3Al alloy (Matsuda et al., 1997; Maehara et al., 2002) and Ti-15Zr-4Nb-Ta alloy are developed in Japan. The mechanical properties of β-type alloys are shown in Fig. 1.9.

Ti alloys consisting of elements with low toxicity have been developed. The basic design of the alloys is the substitution of V and Al with Nb, Ta, Zr, and hafnium (Hf), which are in groups 4 and 5 of the periodic table (Fig. 1.4). On the other hand, the requirement for a low Young's modulus to prevent stress shielding in bone fixation is fulfilled by a β-type alloy; for this reason, Ti-29Nb-13Ta-4.6Zr has been developed as a β-type alloy (Kuroda et al., 1988). This alloy is transformed to the β phase by heat treatment and forging, and shows the smallest Young's modulus among β-type alloys. Elsewhere, the Ti-Nb-tin (Sn) alloy system is in the process of development (Ozaki et al., 2004) (Fig. 1.9).

1.6 Shape memory and superelastic alloys

Ni-Ti alloys consisting of equal atomic amounts of Ni and Ti (49–51 mol%Ni) show unique mechanical properties such as shape memory, superelasticity, and dumping. With the shape memory effect, the original shape can be recovered after deformation by heating; with superelasticity, any apparent plastic deformation can be returned to the original shape by releasing the load. Because of these unique properties, the Ni-Ti

alloy is used for guide wires, stents, orthodontic arch wires, and endodontic reamers and files.

The range of composition for the Ni-Ti alloy displaying these properties is very narrow, nearly a 1:1 atomic ratio. This Ni-Ti alloy has a optimal transformation temperature as a biomaterial, and an austenitic phase (A phase) at a higher temperature and a martensitic phase (M phase) at a lower temperature with a heat-elastic martensitic phase. As shown in Fig. 1.10A, when the temperature of the alloy is decreased from the A phase, the martensitic transformation begins at M_s (1) and all phases transform to the M phase at M_f (2). On the other hand, when the temperature is increased from the M phase, austenitic transformation begins at A_f (3) and all phases transform to the A phase at A_f (4). From the viewpoint of the crystal structure, as shown in Fig. 1.10B, when the alloy in the A phase is cooled under M_s, the phase transforms to the M phase; however, the apparent morphology is not changed, although the crystal lattice is somewhat strained. When external stress is loaded onto the crystal, the

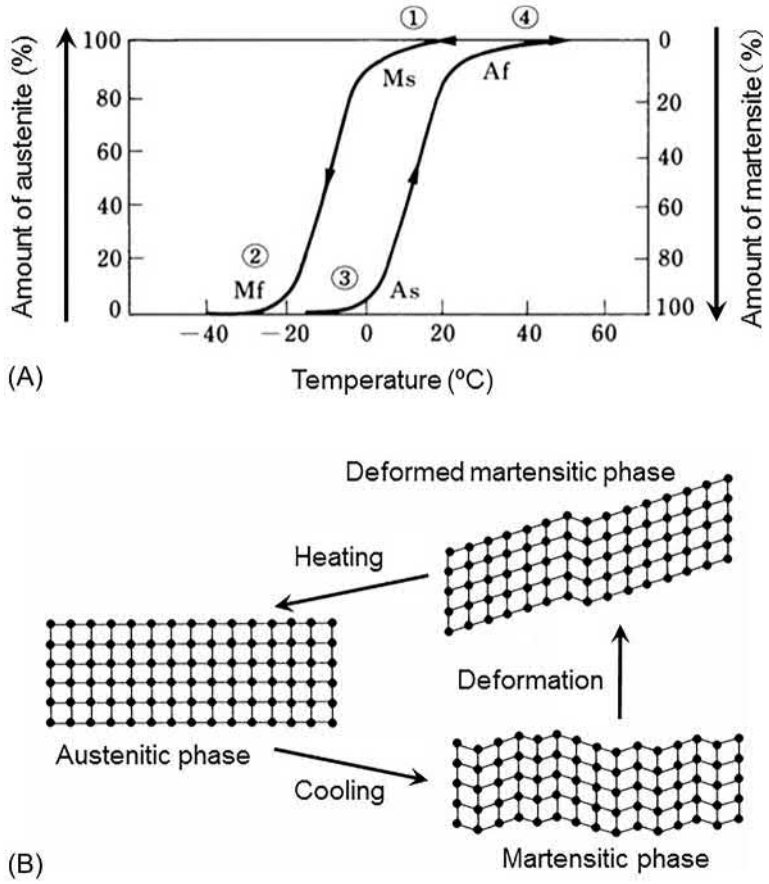


Fig. 1.10 Transformation of Ni-Ti alloy and mechanism of shape memory effect.

crystal deforms by the formation of a twin, not by slip, and the relative configuration of the atoms is not changed. Therefore, when the temperature is again increased, the crystal returns to the original crystal structure and original morphology. The twin compensates for 8% of the deformation in tensile strain; slip will occur above this strain and it is then impossible to recover the original morphology. This transformation is caused by the change in temperature. However, superelasticity is caused by stress, not by a change in temperature, and is known as a stress-induced transformation. The transformation between the A phase and the M phase is caused by stress: the A phase transforms to the M phase by stress and the M phase transforms to the A phase by the release of stress. The characteristics of the Ni-Ti alloy change according to the transformation temperature and the service temperature, with the transformation temperature being influenced by composition, impurity, and heat history.

The safety level of the Ni-Ti alloy is lower than that of Ti, but is the same as that of stainless steels and Co-Cr alloys, because the Ni-Ti alloy is covered by a surface oxide film, consisting mainly of titanium oxide and nickel hydroxide. However, the Ni-Ti alloy contains about 50 mol%Ni and its use in medicine is limited from the viewpoint of safety. In the case of stent graft, Ni-Ti alloy sometimes shows crevice and/or pitting corrosion in the human body (Heintz et al., 2001). In addition, the fatigue mechanism of Ni-Ti alloy is still unknown to use as stents and endodontic files.

Therefore, there is a great demand for Ni-free shape memory and superelastic alloys. Ti-Sn-Nb (Takahashi et al., 2002), Ti-Nb-Al (Hosoda et al., 2003), Ti-Mo-Ga (Kim et al., 2004a), Ti-Mo-Sn (Maeshima and Nishida, 2004), Ti-Nb-O (Kim et al., 2004b), Ti-Nb-Zr (Kim et al., 2005), and Ti–Zr–Nb–Sn (Pavón et al., 2015) alloy systems are reported to have a good shape memory effect and superelasticity, while the recovery strain and superelastic deformation stress of these alloys are still smaller than those of the Ni-Ti alloy. It is possible to improve the shape memory effect and superelasticity by changing the transformation temperature, martensite-induced stress transformation, and critical slip stress due to alloy composition and working heat treatment.

1.7 Noble metals and alloys

Au alloys and Ag alloys are used for dental restoratives such as inlays, crowns, bridges, and clasps. Dental casting Au alloys are the Au-Ag-Cu system alloys, which have high corrosion resistance, high ductility, good castability, and cast fitness. Au alloys are categorized into four types, according to their Au content and mechanical properties (Tables 1.7 and 1.8). A type 1 alloy contains the most Au and is used for simple inlays; the type 2 alloy is used for complex inlays and crowns; the type 3 alloy is used for crowns and bridges; and type 4 alloy is used for denture bases, clasps, and bridges that require strength. Type 3 and 4 alloys could be hardened by heat treatment. zinc (Zn) is added to them as a deoxidizer.

Cross-sectional illustration of porcelain-fused-to-metal is shown in Fig. 1.11A. The composition of Au alloys used for porcelain-fused-to-metal repairs to teeth is listed in Table 1.9. This alloy has a high melting temperature, because the porcelain is sintered

Table 1.7 Standardized dental casting gold alloys

Type	Heat treatment	Vickers hardness (HV)	Proof strength (MPa)	Elongation (%)
1	Softened	50–90	>80	>18
2	Softened	90–120	>180	>12
3	Softened	120–150	>240	>12
4	Softened	>150	>300	>10
	Hardened	>220	>450	>2

Table 1.8 Composition ranges of dental casting gold alloys

Type	Composition (mass%)					
	Au	Ag	Cu	Pd	Pt	Zn
1	80.2–95.8	2.4–12.0	1.6–6.2	0–3.6	0–1.0	0–1.2
2	73.0–83.0	6.9–14.5	5.8–10.5	0–5.6	0–4.2	0–1.4
3	71.0–79.8	5.2–13.4	7.1–12.6	0–6.5	0–7.5	0–2.0
4	62.4–71.9	8.0–17.4	8.6–15.4	0–10.1	0.2–8.2	0–2.7

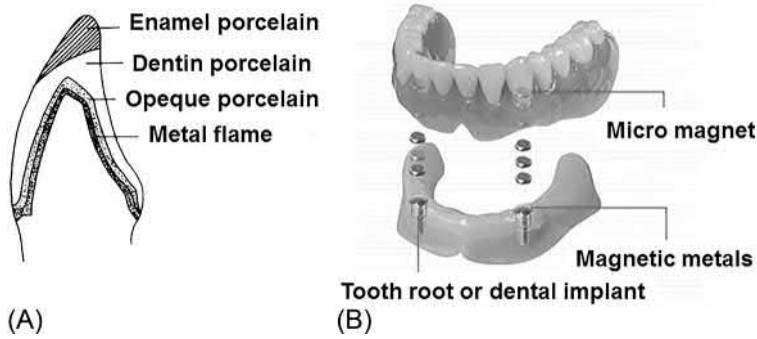


Fig. 1.11 Cross-sectional illustration of porcelain-fused-to-metal (A) and magnetic attachment system (B).

Table 1.9 Representative composition of gold alloy for porcelain-fused-to-metal (mass%)

Au	Pt	Pd	Ag	Others
85	8	4	1	2

during casting. In and Sn are also added to increase the bonding strength with the porcelain. This alloy system contains no Cu and only a small amount of Ag, because these elements stain the alloy after porcelain sintering.

In the case of bridges connecting several teeth, the cast parts are soldered together. Dental solders have a basic composition of Au-Cu-Ag with 58%–84% Au, and Zn and Sn are added to lower the melting point. Solder for porcelain-fused-to-metal contains Pt and palladium (Pd) to raise the melting point, inhibiting deformation during sintering of the porcelain.

1.8 Permanent magnetic alloys

Permanent magnetic alloys are utilized for magnetic attachments in dental restoratives as shown in Fig. 1.11B (Takada and Okuno, 2005). Samarium (Sm)-Co and neodium (Nd)-Fe-boron (B) alloys are used as magnetic materials and type 444 stainless steel and type 447J1 stainless steel are used as keepers in dental attachments. It is difficult to simultaneously fulfill the qualities of strong magnetism, high corrosion resistance, and miniaturization.

1.9 Biodegradable alloys

Corrosion resistance of metallic biomaterials consisting of passive or noble metals and alloys is usually high to acquire their safety to the human body and durability. Therefore, metals and alloys remains semipermanently in the human body. Common metals used for stents are not biodegradable but remain in the vessel semipermanently. Biodegradation is also required of materials used for bone fixators such as plates, screws, and nails. To eliminate a material after service, it is sometimes preferable to use biodegradable materials; however, only polymeric and ceramic biodegradable materials are currently available. Magnesium (Mg) alloys, pure Fe, and Zn alloys are candidates of biodegradable metals at present. Category and progress of biodegradable metals are reviewed (Li et al., 2014; Zheng et al., 2014).

1.9.1 Magnesium alloy

The key to manufacturing Mg-based alloys that are suitable as biodegradable orthopedic implants is adjusting their degradation rates and mechanical integrity in the physiological environment. Biodegradable Mg alloys have been widely investigated in the field of biomaterials because they can be gradually dissolved and absorbed by the human body. The use of Mg alloys as biodegradable metals for stents and bone fixators is expected. Mg has the least density of all commercially utilized metals. Pure Mg cannot be utilized as a structural material due to its low strength; therefore, at least one of the following is added to form the alloy: Al, Zn, Mn, Zr, or rare-earth metals. The addition of rare-earth metals improves castability and pressure resistance, but the strength at ambient temperature is low. Clinical trials of stents consisting of Mg alloys (WE30) are underway in Europe (Peeters et al., 2005; Erbel et al., 2007).

Mg alloys used as stents in Germany contain Al, yttrium (Y), cerium (Ce), neodymium (Nd), and/or rare-earth metals. Controlling degradation and corrosion of Mg in the human body is difficult due to its extreme activity. In addition, hydrogen evolution occurs when it dissolves. Control of the degradation rate, so that it is safe for the human body, is a key factor for enabling the utilization of Mg alloys for medical devices.

The history of biodegradable Mg alloy is well reviewed (Witte, 2010) and corrosion and biocompatibility is summarized (Virtanen, 2011). Mg alloys are expected to be applied in biomedical fields as biodegradable metals because Mg is a bioessential element even though it is corrosive in an aqueous environment. Mg is dissolved using the following reaction:

$$Mg + 2H_2O \rightarrow Mg^{2+} + 2OH^- + H_2 \uparrow .$$

Because the control of degradation, that is, corrosion, of Mg in the human body is difficult due to the extreme activity of Mg, alloying is absolutely necessary to control the corrosion rate. In addition, hydrogen evolution occurs when Mg is dissolved and a gas cavity is formed during the implantation of Mg alloys (Witte et al., 2005). The control of the corrosion rate for safety in devices to be used in the human body is a key factor in the utilization of Mg alloys for medical devices. Efforts to achieve this purpose are currently underway (Heublein et al., 2003).

It has been found that bare Mg implants suffer from rapid corrosion. Therefore, surface coating is applied to improve the corrosion resistance and biocompatibility of Mg alloys. Electrodeposition of hydroxyapatite (HAp) on Mg alloys has been studied (Wen et al., 2009; Guan et al., 2012; Kannan and Wallipa, 2013). Ca compounds are also coated on Mg alloys (Wang et al., 2014). A composite coating of HAp and stearic acid is developed on the substrate surface from the modification of HAp coating by stearic acid (Zhang et al., 2012). The composite coating could provide effective protection and enhance the corrosion resistance of the Mg alloy.

1.9.2 Iron and zinc alloys

Pure Fe is one of other candidates of biodegradable metal (Peuster et al., 2006; Mueller et al., 2006; Hermawan et al., 2008). Degradation rate of pure ion in physiological media is very low, so the acceleration of the degradation rate is main subject to utilize pure ion for medical implants. Fe-Mn-Pd alloy is designed to accelerate degradation rate (Schinhammer et al., 2010).

Zinc alloys are also studied as biodegradable metal and many compositions are proposed (Levy et al., 2017).

1.10 Zirconium alloys

Zr alloys are conventionally used for protection tube of nuclear fuel rod in nuclear plants due to their low neutron absorption cross section. Zr-Sn-Fe-Ni-Cr alloy (Zercalloy2), Zr-Sn-Fe-Cr alloy (Zercalloy 4), and Zr-Sn-Nb-Fe-Cr alloy are used. On the other hand, Zr is used for an alloying component of Ti alloys.

The first application of Zr-based alloy, Zr-2.5Nb alloy, to medical device is to solve a problem on sliding wear of artificial joint. Wear debris of ultrahigh-molecular-weight polyethylene (UHMWPE) against Co-Cr-Mo alloy in UHMWPE-metal combination induces osteolysis. In metal-metal combination, metal ions are released which may be an origin of toxicity. Yttria-stablized zirconia (YSZ) is one of the solution to decrease wear debris. However, YSZ sometimes fractures during service though it shows excellent wear resistance. Therefore, zirconia is coated on Zr-2.5Nb alloy by thermal oxidation to obtain both wear resistance and fracture toughness simultaneously (Long et al., 1998; Spector et al., 2001). Oxinium is the brand name of the material that is applied to artificial knee and hip joints.

Magnetic resonance imaging (MRI) is used as an important diagnostic tool for the whole body. However, images of organs and tissue are disturbed around metallic implants and artifacts occur in intense magnetic field of MRI instruments because magnetic susceptibility of conventional metallic biomaterials is much larger than surrounding living tissues. Therefore, metals show a low magnetic susceptibility and antimagnetic materials are required for medical devices. Among various pure metals, Zr possesses low magnetic susceptibility compared to Ti, Co, and Fe alloys. Zr-Nb and Zr-Mo alloys exhibit low magnetic susceptibility, high strength, and corrosion resistance (Nomura et al., 2009; Suyalatu et al., 2010, 2011; Kondo et al., 2011, 2013). The magnetic susceptibilities of Zr alloys are almost one-third of that of Ti-6Al-4V and one-seventh of Co-Cr alloy.

1.11 Niobium and tantalum

Nb and Ta are widely used as component elements for making Ti alloys. Porous Ta is used as a filling material for bone defects and bone-contacting parts in artificial joints (Bobyn et al., 1999, 2004). Ta is also used for skull implants and X-ray image markers for stents. Ta is ductile and produces good X-ray imaging, because of the heavy metal. Ta is easily oxidized and passivated. Ta_2O_5, as a passive film, is very stable and difficult to corrode in a biological environment. Nb and Ta also shows low magnetic susceptibility.

References

Allain, S., Chateau, J.P., Bouaziz, O., Migot, S., Guelton, N., 2004. Correlations between the calculated stacking fault energy and the plasticity mechanisms in Fe–Mn–C alloys. Mater. Sci. Eng. A 387–389, 158–162.

Anon, 1994. Materials properties handbook: titanium alloys. In: Boyer, R., Welsch, G., Collings, E.W. (Eds.), Materials Properties Handbook. ASM International, pp. 321–336.

Baba, H., Kodama, T., Katada, Y., 2002. Role of nitrogen on the corrosion behavior of austenitic stainless steels. Corros. Sci. 44, 2393–2407.

Black, J., 1984. Biological Performance of Materials. Plenum, New York.

Bobyn, J.D., Stackpool, G.L., Hacking, S.A., Tanzer, M., Krygier, J.J., 1999. Characteristics of bone ingrowth and interface mechanics of a new porous tantalum biomaterial. J Bone Joint Surg 81B, 907–914.

Bobyn, J.D., Poggie, R.A., Krygier, J.J., Lewallen, D.G., Hanssen, A.D., Lewis, R.J., Unger, A.S., O'Keefe, T.J., Christie, M.J., Nasser, S., Wood, J.E., Stulberg, S.D., Tanzer, M., 2004. Clinical validation of a structural porous tantalum biomaterial for adult reconstruction. J. Bone Joint Surg 86A, 123–129.

Erbel, R., Di Mario, C., Bartunek, J., Bonnier, J., de Bruyne, B., Eberli, F.R., Erne, P., Haude, M., Heublein, B., Horrigan, M., Ilsley, C., Bose, D., Koolen, J., Luscher, T.F., Weissman, N., Waksman, R., 2007. Temporary scaffolding of coronary arteries with bioabsorbable magnesium stents: a prospective, non-randomised multicentre trial. Lancet 369, 1869–1875.

Espostito, M., Lausmaa, J., Hirsch, J.M., Thomsen, P., 1999. Suface analysis of failed oral titanium implants. J Biomed Mater Res Appl Biomater 48, 559–568.

Fanning, J.C., 1996. Properties and processing of a new metasatable beta titanium alloy for surgical implant applications. In: Blenkinsop, P.A., Evans, W.J., Flower, H. (Eds.), Titanium '95: Science and Technology. The University Press, Cambridge, pp. 1800–1807.

Gebau, R.C., Brown, R.S., 2001. Biomedical implant alloy. Adv Mater Process 159, 46–48.

Guan, R.G., Johnson, I., Cui, T., Zhao, T., Zhao, Z.Y., Li, X., Liu, H., 2012. Electrodeposition of hydroxyapatite coating on Mg-4.0Zn-1.0Ca-0.6Zr alloy and in vitro evaluation of degradation, hemolysis, and cytotoxicity. J Biomed Mater Res Part A 100A, 999–1015.

Hanawa, T., Ota, T., 1992. Characterization of surface film formed on titanium in electrolyte. Appl. Surf. Sci. 55, 269–276.

Hanawa, T., Hiromoto, S., Asami, K., 2001. Characterization of the surface oxide film of a Co-Cr-Mo alloy after being located in quasi-biological environments using XPS. Appl. Surf. Sci. 183, 68–75.

Hanawa, T., Hiromoto, S., Yamamoto, A., Kuroda, D., Asami, K., 2002. XPS characterization of the surface oxide film of 316L stainless samples that were located in quasi-biological environments. Mater. Trans. 43, 3088–3092.

Hanawa, T., Kohyama, Y., Hiromoto, S., Yamamoto, A., 2004. Effects of biological factors on the repassivation current of titanium. Mater. Trans. 45, 1635–1639.

Healy, K.E., Ducheyne, P., 1992. The mechanisms of passive dissolution of titanium in a model physiological environment. J. Biomed. Mater. Res. 26, 319–338.

Heintz, C., Riepe, G., Birken, L., Kaiser, E., Chakfe, N., Morlock, M., Delling, G., Imig, H., 2001. Corroded nitinol wires in explanted aortic endografts: an important mechanism of failure? J. Endovasc. Ther. 8, 248–253.

Hench, L.L., Ethridge, E.C., 1975. Biomaterials—The interfacial problem. Adv Biomed Eng 5, 35–150.

Hermawan, H., Alamdari, H., Mantovani, D., Dube, D., 2008. Iron-manganese: new class of metallic degradable biomaterials prepared by powder metallurgy. Powder Metall 51, 38–45.

Heublein, B., Rohde, R., Kaese, V., Niemeyer, M., Hartung, W., Haverich, A., 2003. Biocorrosion of magnesium alloys: a new principle in cardiovascular implant technology? Heart 89, 651–656.

Hosoda, H., Fukui, Y., Inamura, T., Wakashima, K., Miyazaki, S., Inoue, K., 2003. Mechanical properties of Ti-base shape memory alloys. Mater. Sci. Forum (426–4), 3121–3125.

Ilevbare, G.O., Burstein, G.T., 2001. The role of alloyed molybdenum in the inhibition of pitting corrosion in stainless steels. Corros. Sci. 43, 485–513.

Kannan, M.B., Wallipa, O., 2013. Potentiostatic pulse-deposition of calcium phosphate on magnesium alloy for temporary implant applications—an in vitro corrosion study. Mater. Sci. Eng. C C33, 675–679.

Kim, H.Y., Ohmatsu, Y., Kim, J.I., Hosoda, H., Miyazaki, S., 2004a. Mechanical properties and shape memory behavior of Ti-Mo-Ga alloys. Mater. Trans. 45, 1090–1095.

Kim, J.I., Kim, H.Y., Hosoda, H., Miyazaki, S., 2004b. Shape memory behavior of Ti-22Nb-(0.5–2.0)O(at%) biomedical alloys. Mater. Trans. 45, 852–857.

Kim, J.I., Kim, H.Y., Inamura, T., Hosoda, H., Miyazaki, S., 2005. Shape memory characteristics of Ti-22Nb-(2–8)Zr(at.%) biomedical alloys. Mater. Sci. Eng. A A403, 334–339.

Kondo, R., Suyalatu, T.Y., Doi, H., Nomura, N., Hanawa, T., 2011. Microstructure and mechanical properties of Pt-added and Pd-added Zr-20Nb alloys and their metal release in 1 mass % lactic acid solution. Mater. Sci. Eng. C 900–905, C31.

Kondo, R., Shimizu, R., Nomura, N., Doi, H., Suyalatu, T.Y., Mitsuishi, K., Shimojo, M., Noda, K., Hanawa, T., 2013. Effect of cold rolling on the magnetic susceptibility of the Zr-14Nb alloy. Acta Biomater. 9, 5795–5801.

Kuroda D, Niinomi M, Morinaga M, Kato Y and T. Yashiro T (1988), Design and mechanical properties of new b type titanium alloys for implant materials, Mater. Sci. Eng. A A243, 244–249.

Kuroda, D., Hanawa, D., Hibaru, T., Kuroda, S., Kobayashi, M., Kobayashi, T., 2003. New manufacturing process of nickel-free stainless steel with nitrogen absorption treatment. Mater. Trans. 44, 414–420.

Kurosu, S., Nomura, N., Chiba, A., 2007. Microstructure and mechanical properties of Co-29Cr-Wo alloy aged at 1023K. Mater. Trans. 48, 1517–1522.

Lee, S.H., Nomura, N., Chiba, A., 2007. Effect of Fe addition on microstructures and mechanical properties of Ni- and C-free Co-Cr-Mo alloys. Mater. Trans. 48, 2207–2211.

Levy, G.K., Goldman, J., Aghion, E., 2017. The prospects of zinc as a structural material for biodegradable implants—a review paper. Metals 7, 402.

Li, H., Zheng, Y., Qin, L., 2014. Progress of biodegradable metals. Prog Nat Sci Mater Int 24, 414–422.

Long, M., Riester, L., Hunter, G., 1998. Nano-hardness measurements of oxidized Zr-2.5Nb and various orthopaedic materials. Trans Soc Biomater 21, 528.

Maehara, K., Doi, K., Matsushita, T., 2002. Application of vanadium free titanium alloys to artificial hip joints. Mater. Trans. 43, 2936–2942.

Maeshima, T., Nishida, M., 2004. Shape memory properties of biomedical Ti-Mo-Ag and Ti-Mo-Sn alloys. Mater. Trans. 45, 1096–1100.

Matsuda, Y., Nakamura, T., Ido, K., Oka, M., Okumura, H., Matsushita, T., 1997. Femoral component made of Ti-15Mo-5Zr-3Al alloy in total hip arthroplasty. J. Orthop. Sci. 2, 166–170.

Menzel, J., Kirschner, W., Stein, G., 1996. High nitrogen containing Ni-free austenitic steels for medical applications. ISIJ Int 36, 893–900.

Merritt, K., Brown, S.A., 1998. Effect of proteins and pH on fretting corrosion and metal ion release. J. Biomed. Mater. Res. 22, 111–120.

Mueller, P.P., May, T., Perz, A., Hauser, H., Peuster, M., 2006. Control of smooth muscle cell proliferation by ferrouos iron. Biomaterials 27, 2193–2200.

Nagai, A., Tsutsumi, Y., Suzuki, Y., Katayama, K., Hanawa, T., Yamashita, K., 2012. Characterization of air-formed surface oxide film on a Co-Ni-Cr-Mo alloy (MP35N) and its change in Hanks' solution. Appl. Surf. Sci. 258, 5490–5498.

Nomura, N., Tanaka, Y., Suyalatu, K.R., Doi, H., Tsutsumi, Y., Hanawa, T., 2009. Effects of phase constitution of Zr-Nb alloys on their magnetic susceptibilities. Mater. Trans. 50, 2466–2472.

Ornhagen, C., Nilsson, J.O., Vannevik, H., 1996. Characterization of a nitrogen-rich austenitic stainless steel used for osteosynthesis devices. J. Biomed. Mater. Res. 31, 97–103.

Ozaki, T., Matsumoto, H., Watanabe, S., Hanada, S., 2004. Beta Ti alloys with low Young's modulus. Mater. Trans. 45, 2776–2779.

Pavón, L.L., Kim, H.Y., Hosoda, H., Miyazaki, S., 2015. Effect of Nb content and heat treatment temperature on superelastic properties of Ti–24Zr–(8–12)Nb–2Sn alloys. Scr. Mater. 95, 46–49.

Peeters, P., Bosiers, M., Verbist, J., Deloose, K., Heublein, B., 2005. Preliminary results after application of absorbable metal stents in patients with critical limbischemica. J. Endovasc. Ther. 12, 1–5.

Peuster, M., Hesse, C., Schloo, T., Fink, C., von Schnakenburg, C., 2006. Long-term biocompatibility of a corrodible peripheral iron stent in the porcine descending aorta. Biomaterials 27, 4955–4962.

Schinhammer, M., Hänzi, A.C., Löffler, J.F., Uggowitzer, P.J., 2010. Design strategy for Biodegradable Fe-Based alloys for medical applications'. Acta Biomater. 6, 1705–1713.

Semlitsch, M., Staub, F., Weber, H., 1985. Titanium-aluminum-niobium alloy, development for biocompatible, high strength surgical implants. Biomed. Tech. 30, 334–339.

Spector, M., Ries, M.D., Bourne, R.B., Sauer, W.S., Long, M., Hunter, G., 2001. Wear performance of ultra-high molecular weight polyethylene on oxidized zirconium total knee femoral components. J Bone Joint Surg 83A, 80–86.

Sumita, M., Hanawa, T., Teoh, S.H., 2004. Development of nitrogen-containing nickel-free austenitic stainless steels for metallic biomaterials—review. Mater. Sci. Eng. A C24, 753–760.

Sundgren, J.E., Bodo, P., Lundstrom, I., 1986. Auger electron spectroscopic studies of the interface between human tissue and implants of titanium and stainless steel. J. Colloid Interface Sci. 110, 9–20.

Suyalatu, N.N., Oya, K., Tanaka, Y., Kondo, R., Doi, H., Tsutsumi, Y., Hanawa, T., 2010. Microstructure and magnetic susceptibility of as-cast Mo alloys. Acta Biomater. 6, 1033–1088.

Suyalatu, K.R., Tsutsumi, Y., Doi, H., Nomura, N., Hanawa, T., 2011. Effects of phase constitution on magnetic susceptibility and mechanical properties of Zr-rich Zr.Mo alloys. Acta Biomater. 7, 4259–4266.

Takada, Y., Okuno, O., 2005. Effect of heat history on the corrosion of ferritic stainless steels used for dental magnetic attachments. Dent. Mater. J. 24, 391–397.

Takahashi, E., Sakurai, T., Watanabe, S., Masahashi, N., Hanada, S., 2002. Effect of heat treatment and Sn content on superelasticity in biocompatible TiNbSn alloys. Mater. Trans. 43, 2978–2983.

Uggowitzer, P.J., Magdowski, R., Speidel, M.O., 1996. Nickel free high nitrogen austenitic steels. ISIJ Int 36, 893–900.

Virtanen, S., 2011. Biodegradable Mg and Mg alloys: corrosion and biocompatibility. Mater Sci Eng B 176, 1600–1608.

Wang, K., Gustavson, L., Dumbleton, J., 1993. Low modulus, high strength, biocompatible titanium alloy for medical implants. In: Froes, F.H., Caplan, H.L. (Eds.), Titanium'92: Science and Technology. TMS, Warrenda, pp. 2697–2704.

Wang, H., Zhu, S., Wang, L., Feng, Y., Ma, X., Guan, S., 2014. Corrosion protection of mesoporous bioactive glass coating on biodegradable magnesium. Appl. Surf. Sci. 307, 92–100.

Wen, C., Guan, S., Peng, L., Ren, C., Wang, X., Hu, Z., 2009. Characterization and degradation behavior of AZ31 alloy surface modified by bone-like hydroxyapatite for implant applications. Appl. Surf. Sci. 255, 6433–6438.

Williams, R.L., Brown, S.A., Merritt, K., 1988. Electrochemical studies on the influence of proteins on the corrosion of implant alloys. Biomaterials 9, 181–186.

Witte, F., 2010. The history of biodegradable magnesium implants: a review. Acta Biomater. 6, 1680–1692.

Witte, F., Kaese, V., Haferkamp, H., Switzer, E., Meyer-Lindenberg, A., Wirth, C.J., Windhagen, H., 2005. In vivo corrosion of four magnesium alloys and the associated bone response. Biomaterials 26, 3557–3563.

Zardiackas, L.D., Mitchell, D.W., Disegi, J.A., 1996. Characterization of Ti-15Mo beta titanium alloy for orthopaedic implant applications. In: Browns, S.A., Lemons, J.E. (Eds.), Medical Applications of Titanium and Its Alloys. West Conshohoken, PA, ASTM, pp. 60–75.

Zhang, X., Li, Q., Li, L., Zhang, P., Wang, Z., Chen, F., 2012. Fabrication of hydroxyapatite/stearic acid composite coating and corrosion behavior of coated magnesium alloy. Mater. Lett. 88, 76–78.

Zheng, Y.F., Gu, X.N., Witte, F., 2014. Biodegradable metals. Mater Sci Eng R 77, 1–34.

Selection of metals for biomedical devices

2

Yoshimitsu Okazaki
National Institute of Advanced Industrial Science and Technology, Tsukuba, Japan

2.1 Introduction

Many types of metallic biomaterial have been widely used in implants to replace failed bone tissues, namely, bone screws, bone plates, compression hip screws (CHSs), intramedullary fixations, short femoral nails, artificial hip joints, artificial knee joints, spinal instruments, and dental implants. Orthopedic implants require biomechanical and biochemical compatibility as well as biological safety. Therefore, many types of metallic orthopedic device, which are manufactured from metallic materials with excellent mechanical properties and structural stability, are used worldwide in the orthopedic field. To determine biomechanical and biochemical properties as well as biological safety, various mechanical, chemical, and biological tests are conducted as part of device development. This chapter will provide the test methods for characterizing potential materials for metallic orthopedic devices such as osteosynthesis devices and artificial joints. Recent mechanical, chemical, and biological test results of new biocompatible materials will be introduced along with the development of new orthopedic devices.

2.2 Standardized implantable metals

Stainless steel, cobalt (Co)-chromium (Cr)-molybdenum (Mo) alloys, commercially pure titanium (C.P. Ti), and Ti alloys are widely used in orthopedic surgery. Many types of these alloys have been standardized on the basis of international and national standards, namely, International Organization for Standardization (ISO), Japanese Industrial Standard (JIS), and American Society for Testing and Materials (ASTM). As well as the alloy specifications, the main corrosion test methods and corrosion testing solutions for metals used for orthopedic implants have also been standardized as guidelines (Table 2.1) (ISO 5832-1, 2016; ISO 5832-2, 2018; ISO 5832-3, 2016; ISO 5832-4, 2014; ISO 5832-9, 2007; ISO 5832-11, 2014; ISO 5832-12, 2007; ISO 5832-14, 2007; JIS T 7401-4, 2009; ISO 16428, 2005; JIS T 0302, 2000; JIS T 0304, 2002). The relationship between the metallic material and fatigue is illustrated in Fig. 2.1, which is useful for selecting metallic materials. The corrosion resistance and biocompatibility of stainless steel can be improved by increasing the amount of each of the elements added to the steel, such as Cr and Mo. In addition, fatigue strength

Metals for Biomedical Devices. https://doi.org/10.1016/B978-0-08-102666-3.00002-X
© 2019 Elsevier Ltd. All rights reserved.

Table 2.1 Implantable metals and the testing methods specified in ISO and JIS

ISO 5832-1	Wrought 18Cr-14Ni-2Mn-2.5Mo stainless steel
ISO 5832-9	Wrought high-N 21Cr-10Ni-3Mn-2.5Mo stainless steel
ISO 5832-4	Co-28Cr-6Mo casting alloy
ISO 5832-12	Wrought Co-28Cr-6Mo alloy
ISO 5832-2	Unalloyed titanium
ISO 5832-3	Wrought Ti-6Al-4V alloy
ISO 5832-11	Wrought Ti-6Al-7Nb alloy
ISO 5832-14	Wrought Ti-15Mo-5Zr-3Al alloy
JIS T 7401-4	Wrought Ti-15Zr-4Nb-4Ta alloy
ISO 16428	Test solutions and environmental conditions for static and dynamic corrosion tests on implantable materials and medical devices
JIS T 0302	Testing method for corrosion resistance of metallic biomaterials by anodic polarization measurement
JIS T 0304	Testing method for metal release from metallic biomaterials

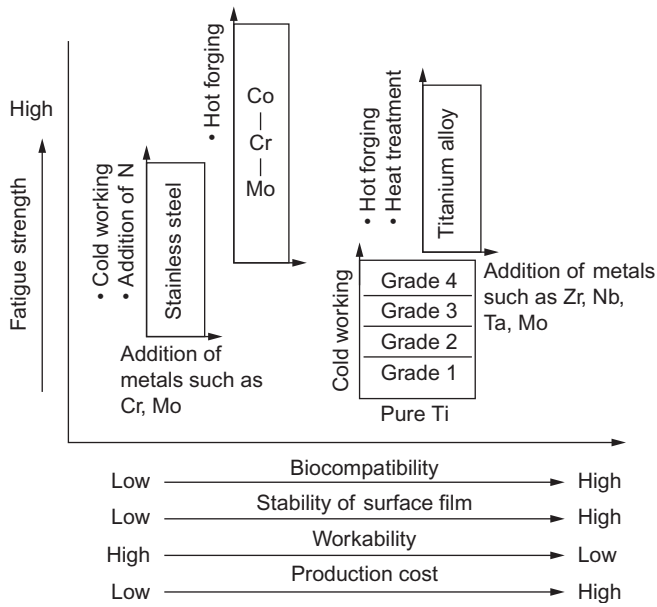


Fig. 2.1 Relationship between metallic material and fatigue strength.

can be increased to a level equivalent to that of Ti alloy by adding nitrogen (N) and 20% cold working. The fatigue strength of an industrial Ti material can be increased by increasing the amounts of trace elements such as oxygen (O) and iron (Fe), whereas the fatigue strength of grade 4 C.P. Ti can be made close to that of Ti alloys by 20% cold working. Ti alloys have higher corrosion resistance and biocompatibility than C.P. Ti through the addition of Mo, zirconium (Zr), niobium (Nb), tantalum (Ta), and so forth. In addition, the fatigue strength of materials can be substantially increased by changing the conditions of heat treatment and the hot forging process.

Table 2.2 Main metallic materials used in orthopaedic implants

	Device	Used material
Osteosynthesis	• Bone plate	• Commercially pure Ti, Ti alloy
	• Bone screw	• Ti alloy, Stainless steel
	• Compression hip screw	• Ti alloy
	• Short femoral nail	• Stainless steel, Ti alloy
	• Intramedullary nail	• Stainless steel, Ti alloy
Hip joint	• Cemented stem	• Hot-forged Co-28Cr-6Mo, Cold-worked stainless steel
	• Cementless stem	• Ti alloy
Knee joint	• Femoral component	• Co-28Cr-6Mo casting
	• Tibial plate	• Ti alloy

The main applications of these alloys in orthopedic surgery are shown in Table 2.2. Stainless steel, C.P. Ti, and Ti alloys are widely used in osteosynthesis devices, while Co-28Cr-6Mo alloy is used in artificial-joint-bearing parts. Artificial hip joints, consisting of two types of stem and immobilizing bone with or without cement, are widely used in many countries. However, for the cement-type hip stem, the amount of Ti alloy used has tended to decrease recently (Thomas et al., 2004). This is due to concerns about the corrosion caused by micromotion between the stem and the cement mantle (formed by cement inserted into bone), particularly when a less stiff Ti alloy is used for the artificial hip stem. In contrast, Co-28Cr-6Mo alloy and high-N stainless steel, with high strength and stiffness, have become the most popular cement-type hip stem materials. On the other hand, for the cementless hip stem, the use of a Ti alloy with high biocompatibility has become popular. Fig. 2.2 shows typical optical micrographs and transmission electron microscopy (TEM) images of wrought Co-28Cr-6Mo alloy and cold-worked high-N stainless steel used for cement-type hip stems. In the TEM images of the hot-forged Co-28Cr-6Mo alloy, much finer face-centered-cubic (fcc) γ-structures are observed. For high-carbon Co-28Cr-6Mo alloys, $M_{23}C_6$ carbide precipitates in the γ matrix (Okazaki, 2008a). In the cold-worked high-N stainless steel, CrNbN precipitation can be observed in the fine austenitic (γ) phase in Fig. 2.2D (Okazaki, 2008b).

2.3 Biocompatibility of various metals

The relationship between the cytocompatibility and polarization resistance of various pure metals is summarized in Fig. 2.3 (Steinemann, 1980; Steinemann, 1999; Okazaki et al., 1993; Okazaki et al., 1998). Cr toxicity appears to be closely related to the Cr valence state, unlike toxic elements such as Co, nickel (Ni), and vanadium (V). Co

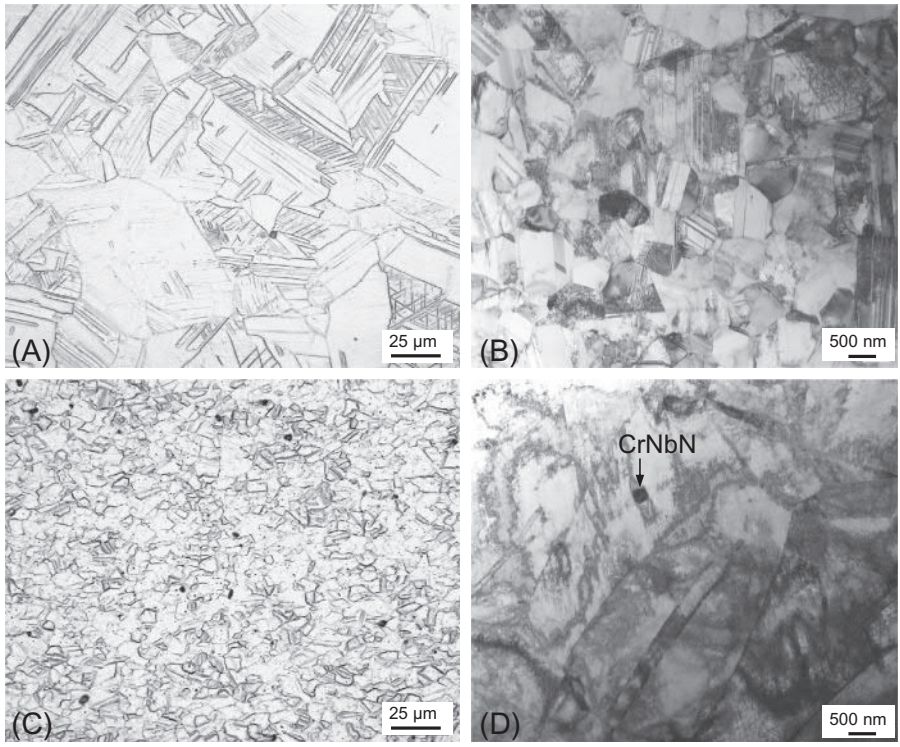


Fig. 2.2 Optical micrographs (A, C) and TEM images (B, D) of hot-forged Co-28Cr-6Mo alloy (A, B) and cold-worked high-N stainless steel (C, D).

toxicity is strongly dose-related. It has been reported that Zr, Nb, and Ta exhibit excellent corrosion resistance and biocompatibility, all of which belong to the loose connective vascularized (vital) group with regard to the tissue reaction. Among the 70 metals in the periodic table of elements, only Ti and Zr show excellent cytocompatibility with both soft-tissue-derived mouse fibroblast cells and bone-derived mouse osteoblast cells. Adding a small amount of alternative metal elements improves the quality of the alloy. However, the addition of too much Nb and Ta to Ti alloy may increase the manufacturing cost. In particular, the fabrication of an alloy that has >5 mass% Ta content requires a special melting apparatus; conventional vacuum arc melting is not applicable.

2.4 Cytotoxicity of metal ions

Stainless steel and Co-Cr-Mo and Ti-6aluminum (Al)-4V alloys are most often used in various orthopedic implants. In particular, the use of Ti-6Al-4V alloy has been increasing. However, there are several clinical reports on the in vivo effect of

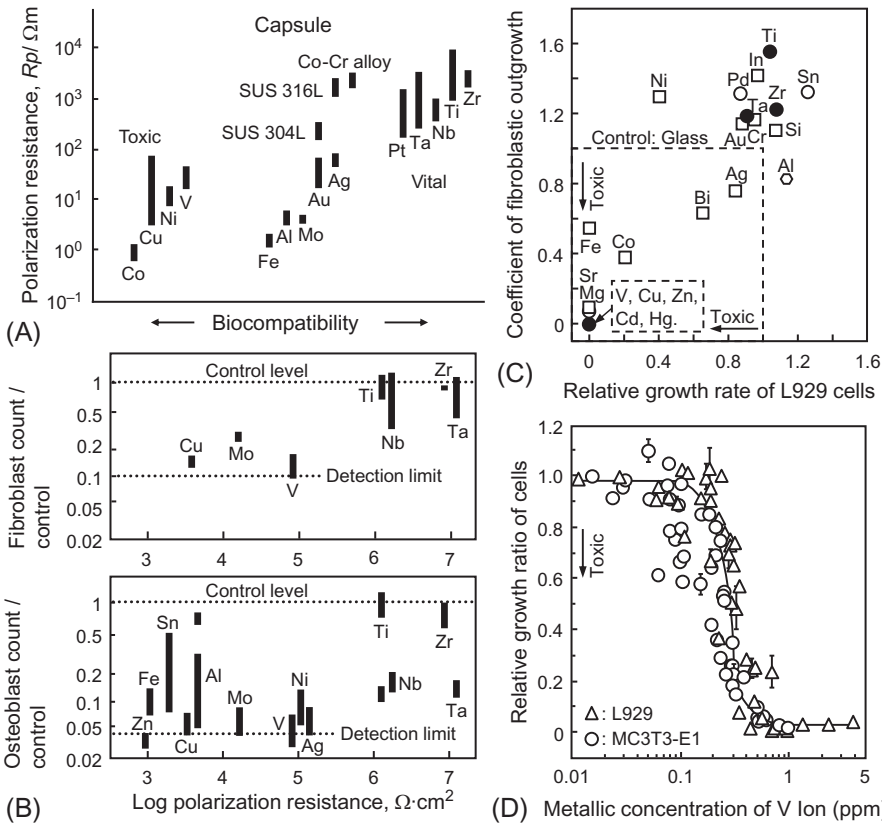


Fig. 2.3 Relationship between the polarization resistance and biocompatibility of various pure metals and alloys (A, B). Cytotoxicity of various pure metals (C) and for different V ion concentrations (D).

metal ions released from orthopedic implants. For instance, clinical concern about the toxicity of V ions has been reported (Okazaki and Gotoh, 2013). Recently, the toxicity of Co ions from metal-on-metal artificial hip joints has attracted attention (Okazaki and Gotoh, 2013). In addition, there have been reports on tumors called aseptic lymphocytic vasculitis-associated lesions (ALVALs) (Okazaki and Gotoh, 2013). Fig. 2.4 shows the effects of the concentration of various metal ions on the relative growth ratios of mouse fibroblast L929 and osteoblastic MC3T3-E1. When the relative growth ratio is 1 or less, cytotoxicity increases. V and Al ions strongly inhibit the growth of both L929 and MC3T3-E1 cells compared with lead (Pb), copper (Cu), Ni, Co, zinc (Zn), and Mo, causing a significant decrease in the relative growth ratio at a concentration of 0.1 ppm or above. In contrast, the relative growth ratio for Mo gradually decreases from a reasonably high concentration. Fig. 2.5 shows the effects of lipopolysaccharide (LPS) (positive control), V, and Ni concentrations in a medium

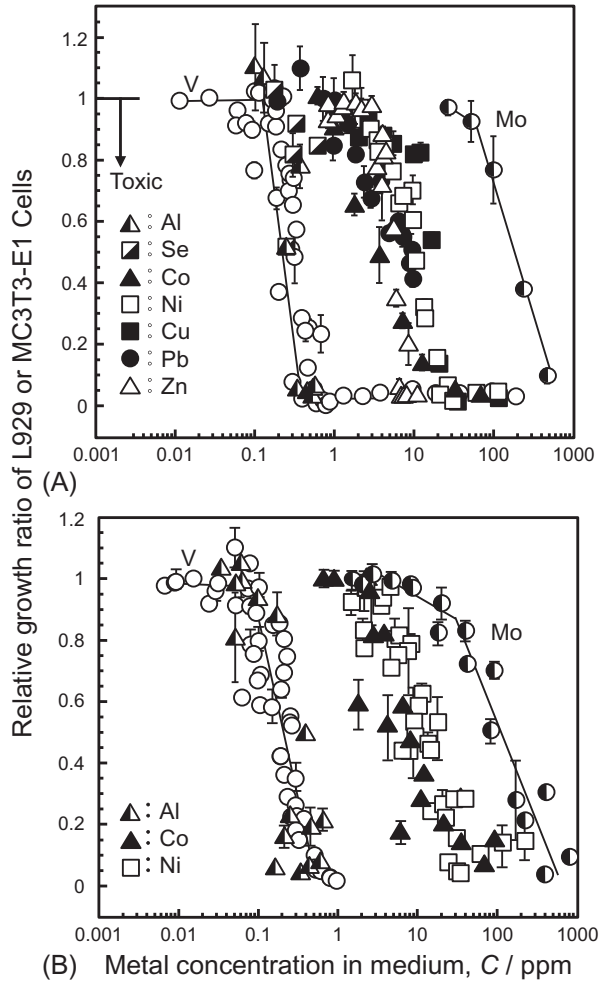


Fig. 2.4 Effects of metal concentration in medium on relative growth ratios (cytotoxicity) of (A) L929 and (B) MC3T3-E1 cells.

on the relative growth ratio of macrophage-like J774.1 cells. The relative growth ratios on days 3 and 4 are similar. When the LPS concentration in the medium is 0.01 ppm, the relative growth ratios are 0.3 at 3 days and 0.2 at 4 days, which are lower than those in the medium containing V ions. The cytotoxicity among materials is compared with the 50% inhibitory concentration (IC_{50}). The relative growth ratio at approximately 0.05 ppm V decreases from 1. For V, IC_{80} (20% inhibitory concentration) is 0.5 ppm and IC_{50} is 0.8 ppm. On the other hand, for Ni, IC_{80} is 1.5 ppm and IC_{50} is 3 ppm. The toxicity of V ions is approximately 10-fold that of Ni ions. The rate of increase of the concentration of nitric oxide (NO) released with the activation of the mouse-macrophage-like J774.1 cells starts to increase at a concentration of V ions 10 times lower than that of Ni ions (Okazaki and Gotoh, 2013).

Fig. 2.6 shows a schematic illustration of the incorporation of metal ions into cells. Metal ions are incorporated through various ion channels and combine with proteins

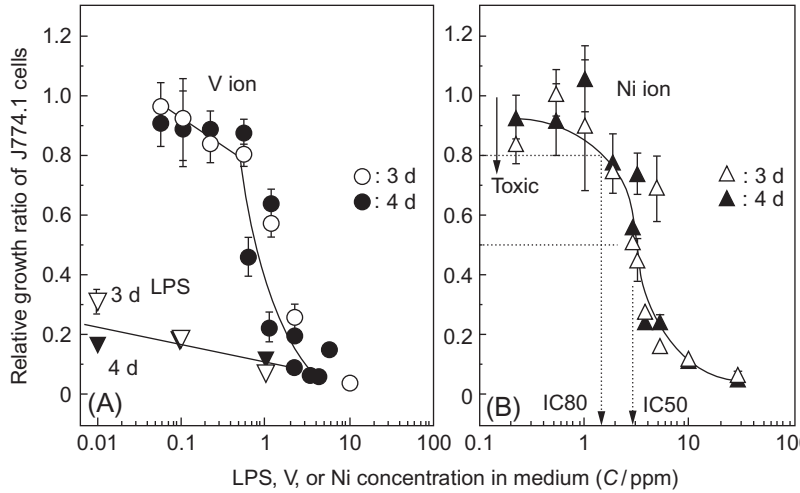


Fig. 2.5 Effects of (A) V and (B) Ni ion concentrations (ppm: μg/mL) in medium on relative growth ratio of J774.1 cells after incubation for 3 or 4 days.

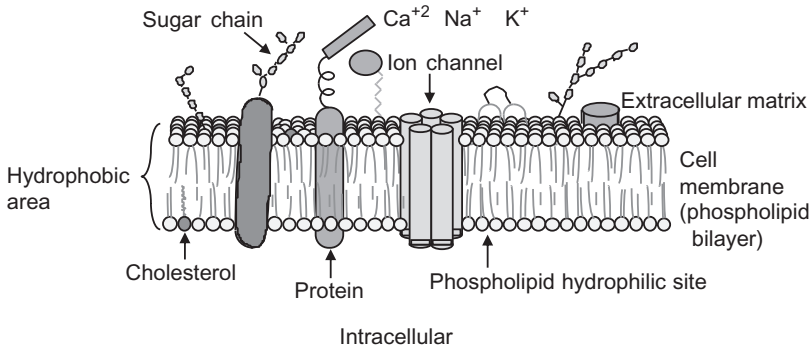


Fig. 2.6 Schematic illustration of incorporation of metal ions into cells.

and amino acids (Okazaki and Gotoh, 2013). To interpret the mechanism of cytotoxicity expression, the amounts of V and other metal ions incorporated into L929 and MC3T3-E1 cells are investigated using an inductively coupled plasma–mass spectrometry (ICP-MS) system (Okazaki and Gotoh, 2013). Fig. 2.7 shows the effects of the incubation time on the mean quantity of metal [(femtogram (fg), 10^{-15} g] incorporated into L929 and MC3T3-E1 cells. Fig. 2.7A shows that L929 cells incorporate Mo and V ions and then discharge them with increasing incubation time. The quantity of incorporated Ni ions slowly increases with increasing incubation time. Fig. 2.7B shows that MC3T3-E1 cells, similarly to L929 cells, incorporate Mo, Pb, and V ions (>1 ppm) and then discharge them. When the V concentration is changed

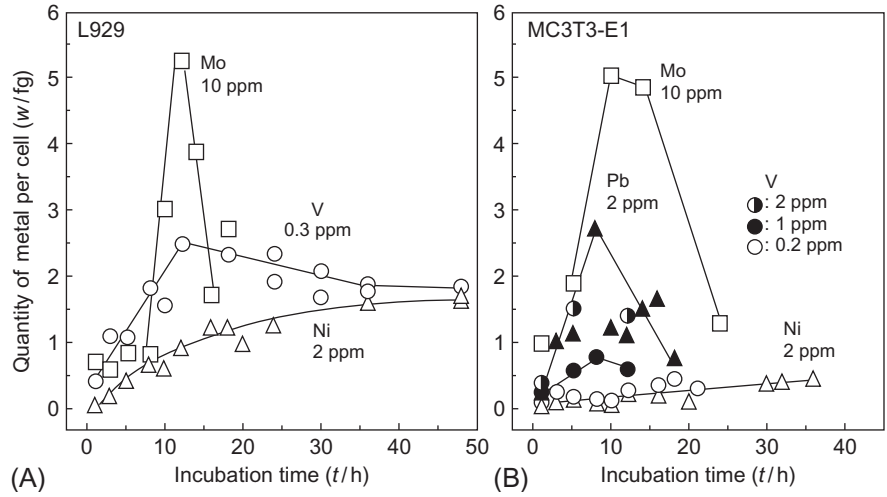


Fig. 2.7 Relationship between length of time of incubation in medium (incubation time) containing metal ions and quantity of metal per cell. (A) L929 cells and (B) MC3T3-E1 cells.

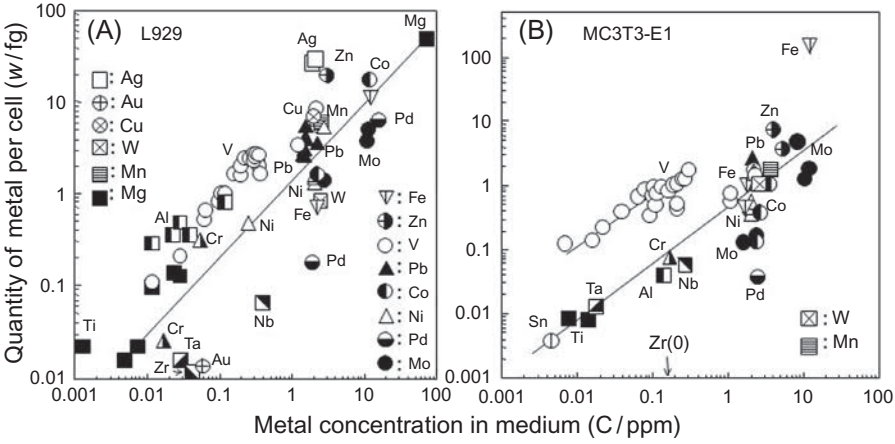


Fig. 2.8 Relationship between metal concentration in medium and quantity of metal per cell. (A) L929 cells and (B) MC3T3-E1 cells.

to 0.2, 1, and 2 ppm, the quantity of incorporated V increases. On the other hand, MC3T3-E1 cells incorporate a smaller quantity of Ni (2 ppm) than L929 cells. Fig. 2.8 shows the relationship between the concentration of various metals in the cell culture medium and the mean quantity of incorporated metal ions. It is clear that, in both L929 and MC3T3-E1 cells, the quantities of metal ions incorporated into the

cells increase with increasing metal concentration in the medium, depending on the metal ion type. Lower quantities of Ti, Zr, gold (Au), Ta, Nb, and Cr are released into the medium and also incorporated in the cells. Higher quantities of Fe, tungsten (W), Mo, palladium (Pd), Ni, Co, Mn, and magnesium (Mg) are incorporated. Moreover, V, Pb, Cu, Zn, and silver (Ag) are incorporated in the highest quantities. As shown in Fig. 2.8B, higher quantities of V, Fe, Pb, and Zn are incorporated into the MC3T3-E1 cells. In particular, the quantity of V incorporated into the MC3T3-E1 cells is considerably higher than those of other metals. Thus, it is suggested that the cytotoxicity of a metal ion changes with the quantity of the metal ion incorporated into cells. It has been clarified by high-performance liquid chromatography (HPLC) that V ions are incorporated into cells through xanthine derived from fetal bovine serum. The strong interaction of Co, Ni, and Mo with amino acids has also been analyzed by HPLC.

In the orthopedic implant field, an increase in the concentration of cytokines such as interleukin-6 (IL-6) and tumor necrosis factor-α (TNF-α) causes osteoclast differentiation and promotes bone resorption. Bone resorption is promoted by osteoclasts around artificial hip joints. It has been reported that marked increases in TNF-α and IL-6 concentrations in patients with rheumatic disease cause accelerated bone resorption (Okazaki and Gotoh, 2013). The release of TNF-α from J774.1 cells starts at approximately 0.5 ppm V; the concentrations of IL-6 and transforming growth factor-β (TGF-β) show a marked increase in the rate of increase above 1 ppm V. The Ni concentration required to produce cytokines is higher than the V concentration (Okazaki and Gotoh, 2013).

2.5 Metal ion release

Concerns such as metal sensitivity remain regarding the long-term exposure to metal ions released from metal implants into the body. A 7-day static immersion test on alloys is performed to examine the quantities of metal released from each alloy in different solutions and their pH dependence is examined. The immersion test is performed in accordance with the JIS T 0304 standard (JIS T 0304, 2002). The immersion test is conducted using the solutions shown in Table 2.3 (Okazaki and Gotoh, 2008a). Ringer's solution and 0.9% NaCl are the recommended solutions for corrosion testing in the ISO 16428 standard. ISO 16428 also states that 0.9% NaCl solution adjusted to pH 2 by adding HCl meets the rigorous testing conditions (ISO 16428, 2005). The 0.9% NaCl+HCl solutions at lower pHs are prepared by adding HCl (pH = 2, 3, 4, and 5). Bottles of each solution without a specimen are prepared as blanks. The weekly quantity of each metal released (μg/cm^2) is estimated using formula (2.1).

$$(\text{Amount of solution}: 50\,\text{mL}) \times [(\text{Metal concentration in each solution}) - (\text{Mean metal concentration of three blank bottles})]/(\text{Surface area of specimen}) \quad (2.1)$$

Table 2.3 Solutions used in the immersion test

Solution	pH	Composition (g/L)	Cl (g/L)
α-Medium	7.5	NaCl: 6.8, KCl: 0.4, Na_2HPO_4: 1.15, $NaH_2PO_4 \cdot H_2O$: 0.2, Amino acids and vitamins: 0.27, Fetal bovine serum (10 vol%), 7.5% $NaHCO_3$ solution (1 vol%)	4.5
PBS (−)	7.5	NaCl: 8, KCl: 0.2, NaH_2PO_4: 0.14, KH_2PO_4: 0.2	5
Calf serum (Membrane-filtered)	7.4		
Artificial saliva*	6.4	NaCl: 0.844, KCl: 1.2, $CaCl_2$: 0.146, $MgCl_2$: 0.052, K_2PO_4: 0.342	1.2
Ringer's solution	6.1	NaCl: 8.36, KCl: 0.3, $CaCl_2$: 0.15	5.4
0.9/4.5% NaCl	5.6/5.4	NaCl: 9/45	5.5/27
0.9% NaCl + HCl	2/2.9/3.9/4.9	NaCl: 9, HCl added to adjust pH	5.5
4.5% NaCl + HCl	1.9	NaCl: 45, HCl added to adjust pH	28
0.01/0.05/1% Lactic acid	3.5/3/2.2		
1.2% L-cysteine	2.1	$HSCH_2CH(NH_2)COOH \cdot HCl \cdot H_2O$: 17.6	3.5
0.01% HCl (0.05 vol% Concentrated HCl)	2		0.2

Purchased from Teijin Ltd., Japan. It contains trace amounts of thickener and benzoic acid to adjust the viscosity to 6 mPa s.
The used HCl is an ultrahigh-purity concentrate.

2.5.1 Metal ions released from stainless steels and Co-Cr-Mo alloys

The effect of pH on the metal release rate in various solutions is examined with the aim of reducing the toxicity risk due to metal ion release. Fig. 2.9 shows the effect of pH on the quantities of metals released from three types of solution-treated stainless steel. The quantities of Fe and Ni and the total quantity of metal (Fe + Cr + Ni + Mo + Mn) released from the stainless steels linearly decrease with increasing pH (pH 2–7.5), while the quantity of Cr released gradually increases with decreasing pH ($pH \leq 6$) and plateaus at pH 6. The quantity of Mo released is slightly higher in Ringer's (pH 6.1) and 4.5% NaCl (pH 5.5) solutions than in the other solutions.

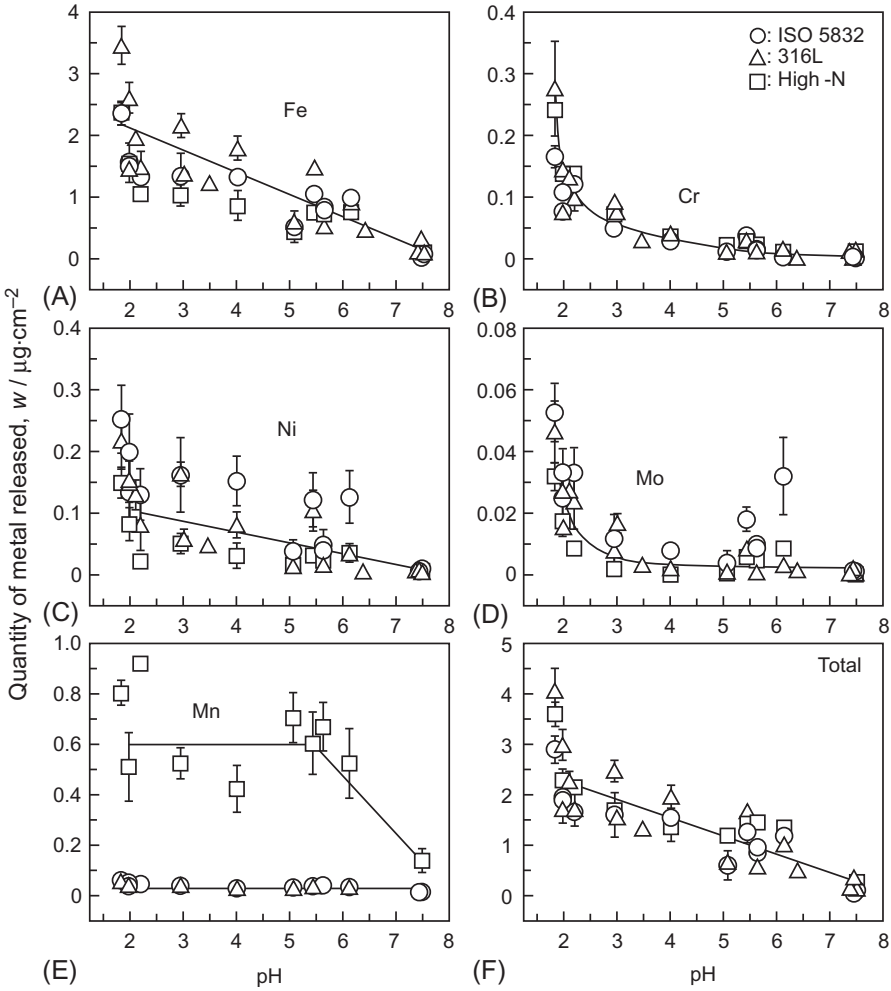


Fig. 2.9 Effect of pH on quantity of each metal element released from three solution-treated stainless steels (ISO 5832, 316L, and high-N) at 37°C for one week: (A) Fe, (B) Cr, (C) Ni, (D) Mo, (E) Mn, and (F) total.

The total quantity of metal released depends on the pitting resistance equivalent (PRE) (Okazaki and Gotoh, 2013), which can be evaluated by formula (2.2).

$$\mathrm{PRE} = \%\mathrm{Cr} + 3.3\%\mathrm{Mo} + 16\%\mathrm{N} \tag{2.2}$$

The PRE values of the ISO 5832, 316L, and high-N stainless steels are approximately 24, 32, and 35, respectively. Therefore, the total quantity of metal released weekly from the high-N stainless steel is the lowest among the three stainless steels.

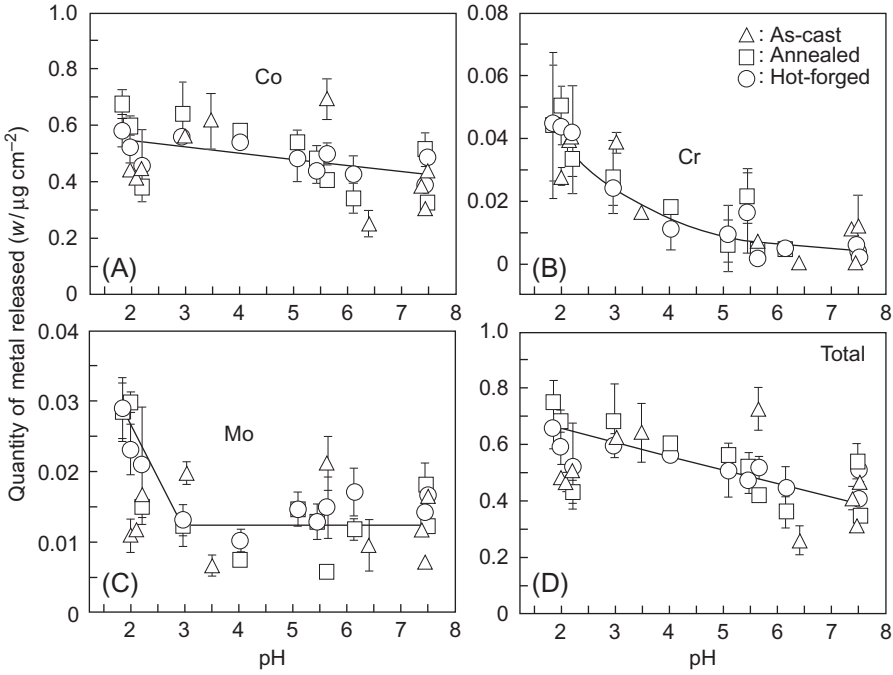


Fig. 2.10 Effect of pH on quantity of each metal element released from three types of Co-Cr-Mo alloy (as-cast, annealed, and hot forged) at 37°C in one week: (A) Co, (B) Cr, (E) Mo, and (D) total.

Fig. 2.10 shows effect of pH on the metal release from three types of Co-Cr-Mo alloy: as-cast, annealed, and hot-forged. The trends of the effect of pH on Co, Cr, and Mo release are nearly the same in the three alloys. In particular, the effect of pH on Co release is very small. The quantity of Cr released gradually increases as pH decreases (pH $\leq$ 6) and is low throughout the pH range. The quantity of Mo released is also very low at a pH of approximately 3 and higher.

2.5.2 *Stability of passive film formed on stainless steel and Co-Cr-Mo alloy*

A surface oxide film, referred to as a passive film, formed on metallic materials plays an important role as an inhibitor of ion release. Implants made of metallic materials with strong passive films exhibit lower quantities of metal ion release. Thus, the quantity of metal ions released depends on the nature and strength of the metal-oxide bond, the structure, the role of alloying elements, the composition, and the thickness of oxide films. The role of alloying elements in passive films formed on SUS 316L stainless

steel and Co-Cr-Mo alloys in a calf serum solution has been examined by X-ray photoelectron spectroscopy (XPS). The XPS spectra of the passive films exhibit peaks corresponding to Cr_2O_3, CoO, Fe oxide, and Mo oxide (Okazaki et al., 1997). The electrochemical strength and stability of oxide films formed on the surface of various alloys implanted into a living body can be examined via an anodic polarization test performed in accordance with the JIS T 0302 standard (JIS T 0302, 2000). In the anodic polarization test, a specimen is initially held at −1 V for 300 s and then at an open-circuit potential for 300 s. The test is conducted from −1 to 2 V at a sweep rate of 20 mV/min. The counter and reference electrodes are platinum and a saturated calomel electrode (SCE), respectively.

2.6 Highly biocompatible α-β-type Ti alloy

Among the metallic materials currently used for implants, C.P. Ti, and Ti alloys have attracted particular attention owing to their higher biomechanical and biochemical compatibility than conventional materials such as stainless steel and Co-based alloys. Recently, studies on Ti alloys have been carried out in consideration of their long-term use in the human body and possible long-term health problems associated with the release of toxic ions and fatigue fracture.

2.6.1 Role of alloying elements in Ti alloy

As summarized in Fig. 2.11, the Ti alloys specified in JIS, ISO, and ASTM are categorized into three types according to microstructural differences: α (alpha)-type alloys having a hexagonal-close-packed (hcp) structure (hcp), β (beta)-type having a body-centered-cubic (bcc) structure, and α-β-type having a mixed structure comprising α- and β-phases. ASTM-standardized alloys, such as the near-β alloy Ti-13Zr-

Alpha structure (Hcp)	Mixed alpha-beta structure	Beta structure (Bcc)
← Alpha-stabilizing elements [Al, O, Zr, etc.]		Beta-stabilizing elements → [Mo, Fe, Nb, Ta, etc.]
	← Higher fatigue strength	
	Improved fabricability →	
Unalloyed titanium (ISO 5832-2)	Ti-6Al-4V (ISO 5832-3) Ti-6Al-7Nb (ISO 5832-11) Ti-6Al-2Nb-1 Ta (JIS T7401-3) Ti-15Zr-4Nb-4Ta (JIS T 7401-4) Ti-13Zr-13Nb (ASTM F 1713) Ti-15Mo-5Zr-3Al (ISO 5832-14)	Ti-15Mo (ASTM F 2066) Ti-12Mo-6Zr-3Fe (ASTM F 1813)

Fig. 2.11 Effects of alloying elements on Ti alloy structure, and microstructures of Ti alloys specified in ISO, ASTM, and JIS.

13Nb (ASTM F 1713-08, 2013) and β-type alloys such as Ti-12Mo-6Zr-2Fe (ASTM F 1813-13, 2013), have a slightly lower Young's modulus than α-β-type alloys. Among the α-β-type Ti alloys, Ti-6Al-4V alloy has been extensively used for various orthopedic applications, as shown in Table 2.2 (ASTM F 1713-08, 2013; ASTM F 1813-13, 2013; JIS T 7401-3, 2002). The α-β-type Ti alloys exhibit better fatigue characteristics than the β-type alloys. Another α-β-type Ti alloy, Ti-15Zr-4Nb-(1–4)Ta alloy, has been developed in Japan as a highly biocompatible alloy for long-term biomedical applications and is standardized in JIS T 7401–4 (JIS T 7401-4, 2009).

Microstructural changes in the α-β-type Ti-15Zr-4Nb-4Ta alloy with the Al equivalence ([Al]eq) and Mo equivalence ([Mo]eq) can be expected. [Al]eq and [Mo]eq are calculated using formulas (2.3) and (2.4), respectively, with the mass% of each element (Welsch et al., 1994). With increasing [Al]eq, the volume fraction of the α-phase increases. Likewise, with increasing [Mo]eq, the volume fraction of the β-phase increases. Because the Ti-15Zr-4Nb-4Ta alloy does not contain Al, O has an effective role in determining the mechanical properties.

$$[\mathrm{Al}]\mathrm{eq} = [\mathrm{mass\%Al}] + 1/6[\%\mathrm{Zr}] + 10[\%\mathrm{O}] \tag{2.3}$$

$$[\mathrm{Mo}]\mathrm{eq} = [\%\mathrm{Mo}] + 1/3.6[\%\mathrm{Nb}] + 1/5[\%\mathrm{Ta}] + 2.5\,[\%\mathrm{Fe}] + 1/1.5[\%\mathrm{V}] + 1/2.5[\%\mathrm{W}] \tag{2.4}$$

2.6.2 Low-cost manufacturing process for highly biocompatible Ti alloy

Zr, Nb, and Ta are important alloying elements of Ti alloys for attaining superior long-term corrosion resistance and biocompatibility. However, note that the addition of excess Nb and Ta to Ti alloys leads to a higher manufacturing cost. To develop low-cost manufacturing processes, the effects of hot-forging and continuous-hot-rolling conditions on the microstructure, mechanical properties, hot forgeability, and fatigue strength of Ti-15Zr-4Nb-4Ta alloy are investigated (Okazaki, 2012a). Fig. 2.12 shows a Ti-15Zr-4Nb-4Ta alloy ingot and α-β-forged billets (100 mm square). Vacuum-arc melting is performed on the Ti-15Zr-4Nb-4Ta alloy, which is used for medical implants. A Ti-15Zr-4Nb-4Ta alloy ingot is homogenized at

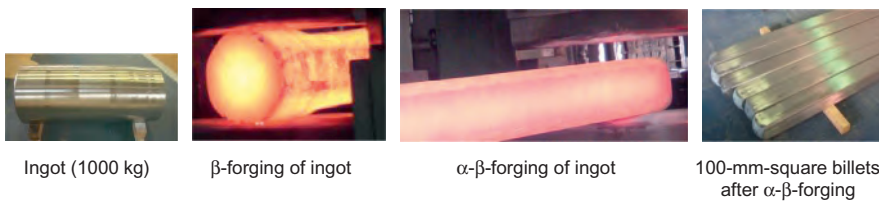


Fig. 2.12 Ti-15Zr-4Nb-4Ta alloy ingot and 100-mm-square billets after β- and α-β-forging.

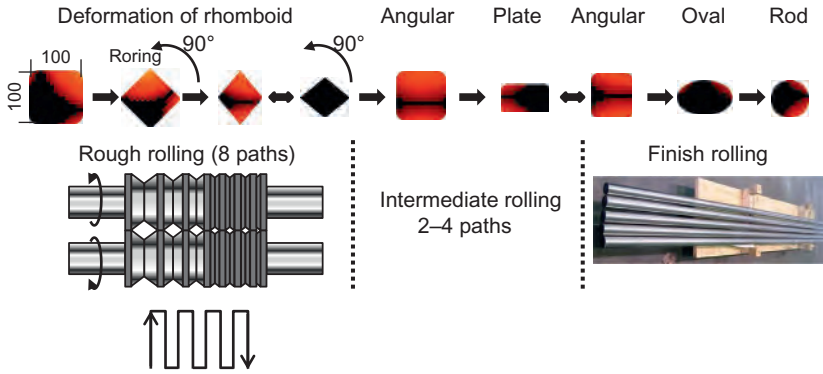


Fig. 2.13 Schematic illustration of continuous hot rotting of Ti alloy to obtain rod specimens.

approximately 1200°C for >3 h and β-forged at the same temperature to a forging ratio (cross section before forging/cross section after forging) of >3. Secondly, β-forging, while controlling the grain growth of the β-phase, is conducted to minimize the β-phase at 1000 to 1150°C relative to the size of the billet and the forging ratio. Afterwards, α-β-forging at T_β–60 to T_β–30°C is conducted to obtain the α- and β-structures by decoupling the fine β phase. T_β indicates the β-transus temperature (100 vol% β phase). 100-mm-square × 1-m-long billets of Ti alloy billets are manufactured by α-β-forging, which is performed under atmospheric conditions using a 1200 ton forging machine. To prevent the edge of the billet from cracking caused by heat loss, the forging time is minimized by adjusting the forging reduction and forging width/speed. Reheating of the ingot and forging are repeated once or twice to optimize the ingot size and microstructure. Between the β- and α-β-forging, the billet surface is ground with a grinder to prevent cracking due to the oxide scale formed on the ingot surface.

Fig. 2.13 shows a schematic illustration of a continuous hot-rolling process for Ti alloys. A continuous hot-rolling test is conducted with 100-mm-square × 1-m-long billets of Ti alloy. After maintaining them at T_β–60°C for 2 h, the Ti alloy billets are hot-rolled continuously in the α-β temperature region (below T_β) at a low rolling speed to prevent an increase in the internal temperature of the rolling rod. After α-β rolling, the annealing of the Ti alloy is generally followed by the removal of internal stress, heat treatment at 550–750°C for 2 h to optimize the microstructure, and then air-cooling.

Fig. 2.14 shows the changes in the volume fraction of the α-phase with the heat treatment temperature (Fig. 2.14A) and with the temperature difference (ΔT) between T_β and the heat-treatment temperature (Fig. 2.14B) (Okazaki, 2012a). T_β for the Ti-15Zr-4Nb-4Ta alloy is much lower than that for the Ti-6Al-4V alloy. The recorded changes in the volume fraction of the α-phase for both Ti-15Zr-4Nb-4Ta and Ti-6Al-4V alloys are almost the same, as shown in Fig. 2.14B. Thus, T_β is an important parameter for understanding the microstructural changes of α-β-type Ti alloy, and the microstructure at each temperature can be predicted using the temperature difference (ΔT) from T_β. In the Ti-15Zr-4Nb-4Ta alloy, the correlation between the β-phase

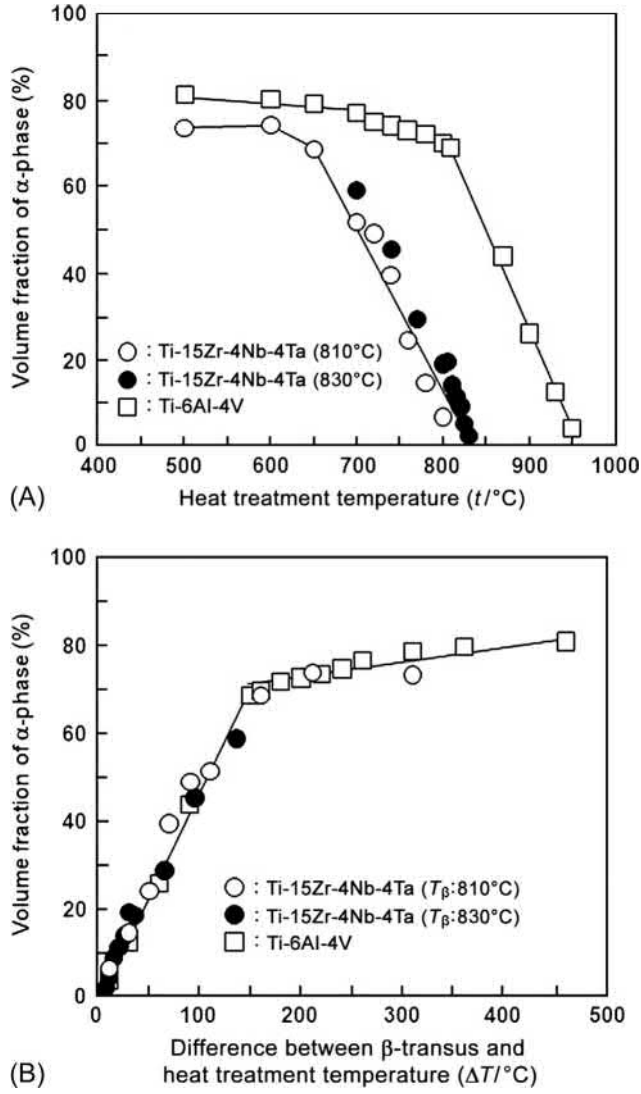


Fig. 2.14 Change in volume fraction of α-phase as a function of heat treatment temperature (A) and difference (ΔT) between β-transus (T_β) and heat treatment temperature (B).

transformation temperature (β-transus; T_β) and each element (mass%) is expressed using formula (2.5) (Okazaki et al., 1993), which predicts the effect of elements that increase or decrease β-transus.

$$T_\beta/^\circ\mathrm{C} = 848 - 4.2[\%\mathrm{Zr}] - 5.5[\%\mathrm{Ta}] - 6.3[\%\mathrm{Nb}] - 76[\%\mathrm{Pd}] + 343[\%\mathrm{O}] + 600[\%\mathrm{N}] \quad (2.5)$$

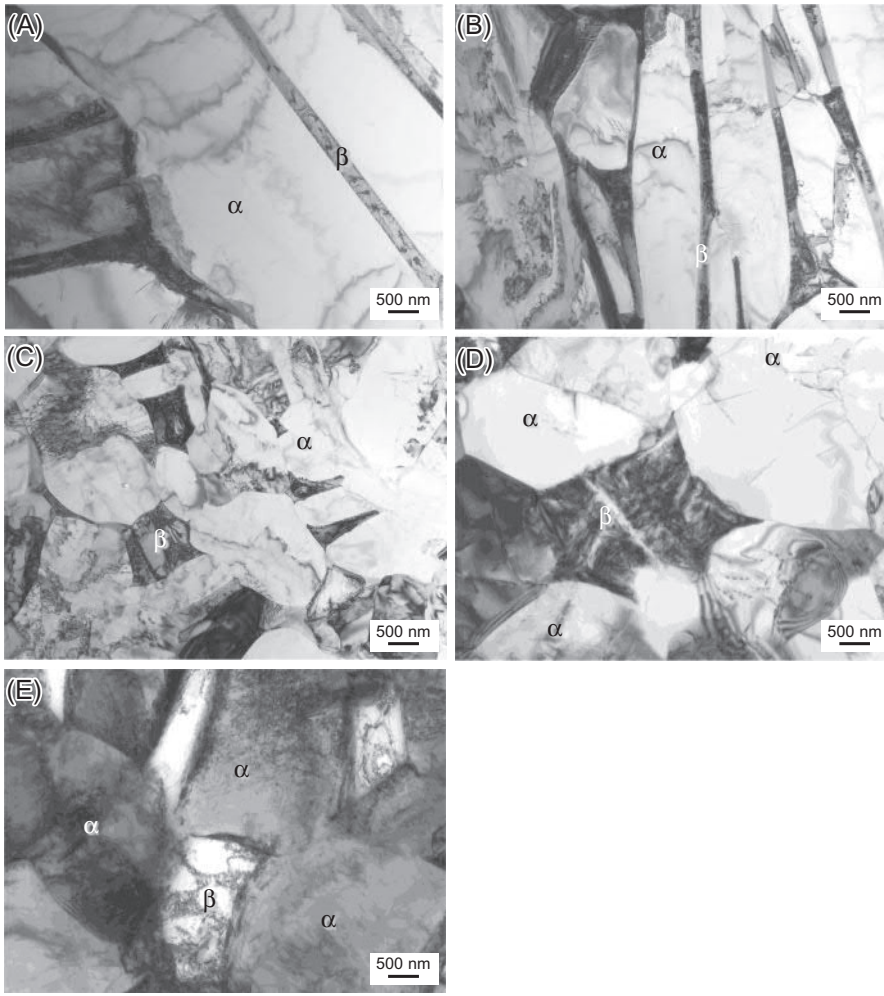


Fig. 2.15 TEM images of forged Ti-15Zr-4Nb-4Ta alloy (A)–(C), Ti-15Zr-4Nb-4Ta annealed at 700°C for 2 h (D), and Ti-6Al-4V alloy annealed at 700°C for 2 h (E). (A) β-annealed, (B) forging ratio of 2, and (C) forging ratio of 10.

Fig. 2.15 shows TEM images of the α-β-forged Ti-15Zr-4Nb-4Ta alloy. Electron beam diffraction analysis confirmed the existence of the β-phase at grain boundaries of the α-phase. In the Ti-15Zr-4Nb-4Ta alloy after β-annealing, an acicular α-phase structure is observed that contains a small amount of the elongated β-phase at grain boundaries of the acicular α-structure. Otherwise, at a forging ratio of 10 and above, a fine granular equiaxed α-phase structure containing a fine granular β-phase at grain boundaries is observed. TEM images of the annealed Ti-15Zr-4Nb-4Ta and Ti-6Al-4V alloys after α-β-forging are also shown in Fig. 2.15D and E, respectively. A similar α-β-structure can be seen in both annealed alloys. Fig. 2.16 shows the effects

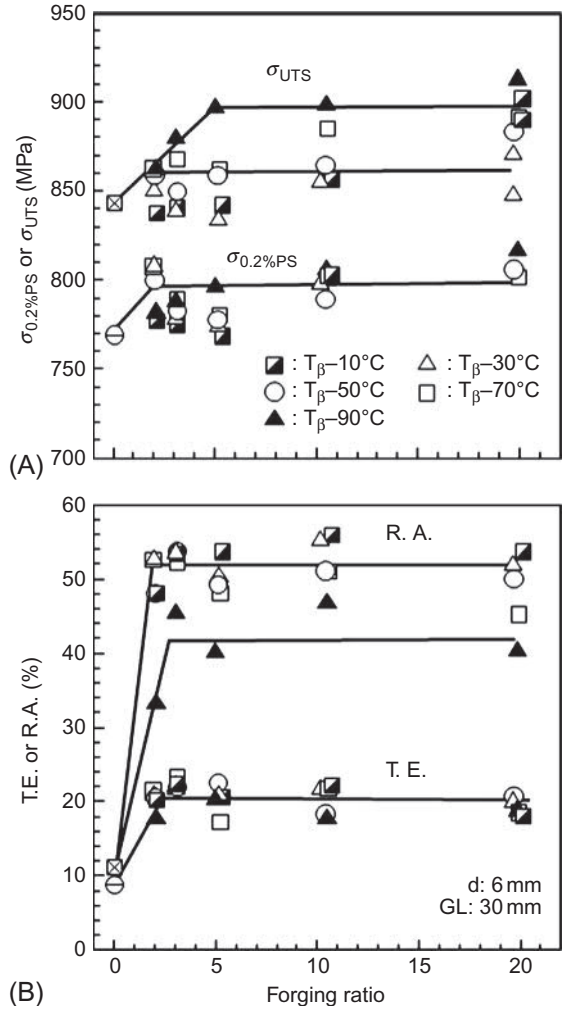


Fig. 2.16 Effects of forging temperature and forging ratio on (A) 0.2% proof strength ($\sigma_{0.2\ PS}$) and ultimate tensile strength (σ_{UTS}), and (B) total elongation (T.E.), and reduction of area (R.A.) obtained by room-temperature mechanical testing.

of the forging temperature and forging ratio on mechanical properties (0.2% proof strength: $\sigma_{0.2\%PS}$, ultimate tensile strength: σ_{UTS}, total elongation: T.E., and reduction in area: R.A.) at room temperature. Ti alloy with equiaxed fine grains has excellent mechanical properties compared with those of the alloy with an acicular microstructure. Fig. 2.17 shows the room-temperature mechanical properties of continuously hot-rolled Ti-15Zr-4Nb-4Ta alloy rods. High strength, high hardness, and excellent ductility are obtained in this continuous hot-rolling process for each rod diameter (12–50 mm) (Okazaki, 2012a). Formulas (2.6), (2.7), and (2.8) are used to express the relationships of the 0.2% proof stress ($\sigma_{0.2\%PS}$) or the tensile strength (σ_{UTS}) of the annealed Ti-15Zr-4Nb-4Ta alloy rods with the Vickers hardness (Hv) and the amount of each alloying element (mass%) (Okazaki, 2012a).

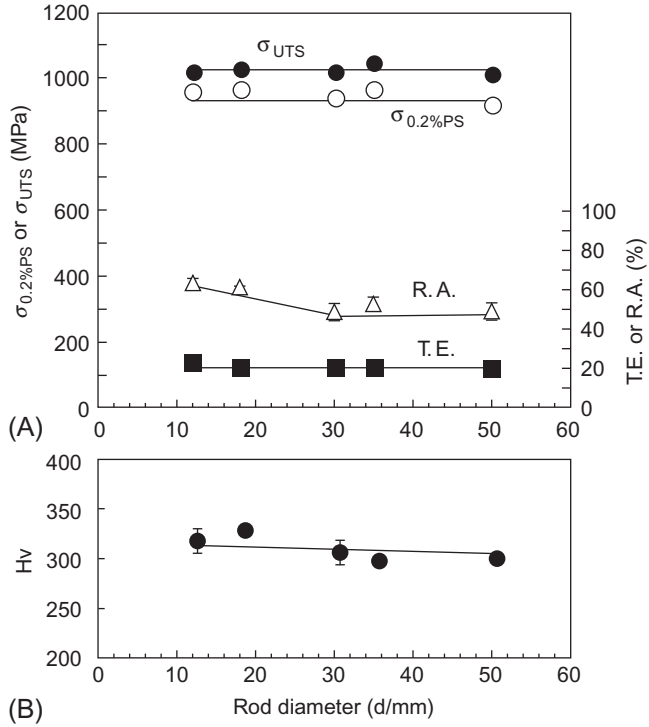


Fig. 2.17 Effects of rolling diameter on (A) mechanical properties ($\sigma_{0.2\ PS}$, σ_{UTS}, T.E., and R.A.) and (B) Vickers hardness (Hv) of hot-rolled Ti-15Zr-4Nb-4Ta alloy.

$$\sigma_{0.2\%PS}\,(\mathrm{MPa}) = -160 + 3.4[\mathrm{Hv}], \sigma_{UTS}\,(\mathrm{MPa}) = -91 + 3.5[\mathrm{Hv}] \tag{2.6}$$

$$\sigma_{0.2\%PS}\,(\mathrm{MPa}) = 472 + 9.8[\%\mathrm{Zr}] - 3.2[\%\mathrm{Nb}] + 10.7[\%\mathrm{Ta}] + 335[\%\mathrm{O}] + 1611[\%\mathrm{N}] \tag{2.7}$$

$$\sigma_{UTS}\,(\mathrm{MPa}) = 487 + 10.9[\%\mathrm{Zr}] + 4.9[\%\mathrm{Nb}] + 2.9[\%\mathrm{Ta}] + 514[\%\mathrm{O}] + 1491[\%\mathrm{N}] \tag{2.8}$$

Ti alloys can be strengthened by adding trace amounts of Fe and O.

2.6.3 Manufacturing equivalency of Ti alloys

The hot forgeability of Ti-15Zr-4Nb-4Ta alloy is excellent, as shown in Fig. 2.12. Since deformability is subject to the capacity of the forging machine, hot forgeability is analyzed by performing a high-temperature tensile test from room temperature up to a high temperature, focusing on changes in the maximum tensile strength (σ_{max}) and R.A. To compare the hot forgeability of the Ti-15Zr-4Nb-4Ta and Ti-6Al-4V alloys, a high-temperature tensile test and three types of Gleeble test are conducted. Fig. 2.18

shows the effects of the test temperature on the high-temperature mechanical properties (σ_{max}). Fig. 2.18A shows a comparison of σ_{max} for the Ti-15Zr-4Nb-4Ta and Ti-6Al-4V alloys, SUS 304 stainless steel, and commercially pure grade 3 Ti. σ_{max} markedly increases with decreasing testing temperature below T_β. Fig. 2.18B shows a comparison of σ_{max} for the Ti-15Zr-4Nb-4Ta and Ti-6Al-4V alloys as a function of the difference (ΔT) between T_β and the test temperature. The temperature dependences of σ_{max} for the Ti-15Zr-4Nb-4Ta and Ti-6Al-4V alloys are the same and might

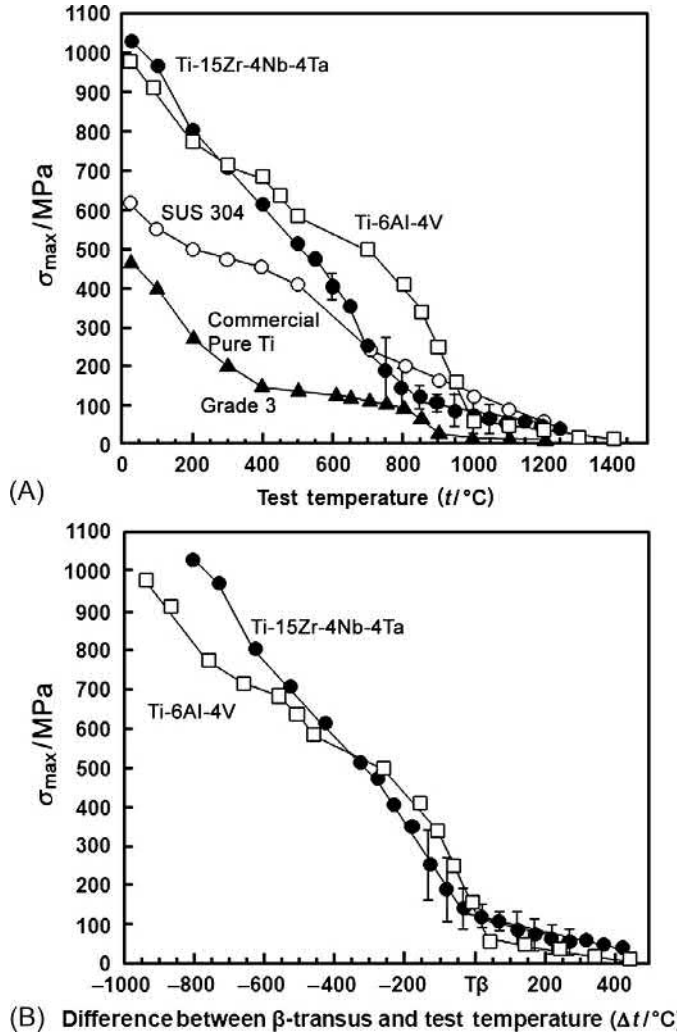


Fig. 2.18 Effects of test temperature on maximum strength (σ_{max}) obtained by high-temperature tensile tests. (A) Effect of test temperature on maximum strength (σ_{max}); (B) effect of temperature difference (ΔT) between β-transus and test temperature of tensile test.

be a result of the temperature difference (ΔT) from T_β. The temperature dependences of R.A. for the Ti-15Zr-4Nb-4Ta and Ti-6Al-4V alloys at high temperatures are shown in Fig. 2.19. R.A. slowly decreases with decreasing testing temperature below T_β. The temperature dependences of R.A. for both alloys are similar and might be a result of the temperature difference (ΔT) from T_β. In the Ti-6Al-4V alloy, R.A. of >60% is used to indicate the hot forgeability of the Ti-6Al-4V alloy (Okazaki, 2012a). From these results, it is clear that Ti-15Zr-4Nb-4Ta alloy can be manufactured by the same process as Ti-6Al-4V alloy provided the temperature difference (ΔT) between T_β and the test temperature is taken into account. Also, the manufacturing equivalency of Ti-15Zr-4Nb-4Ta alloy to obtain the marketing approval of implants has been established.

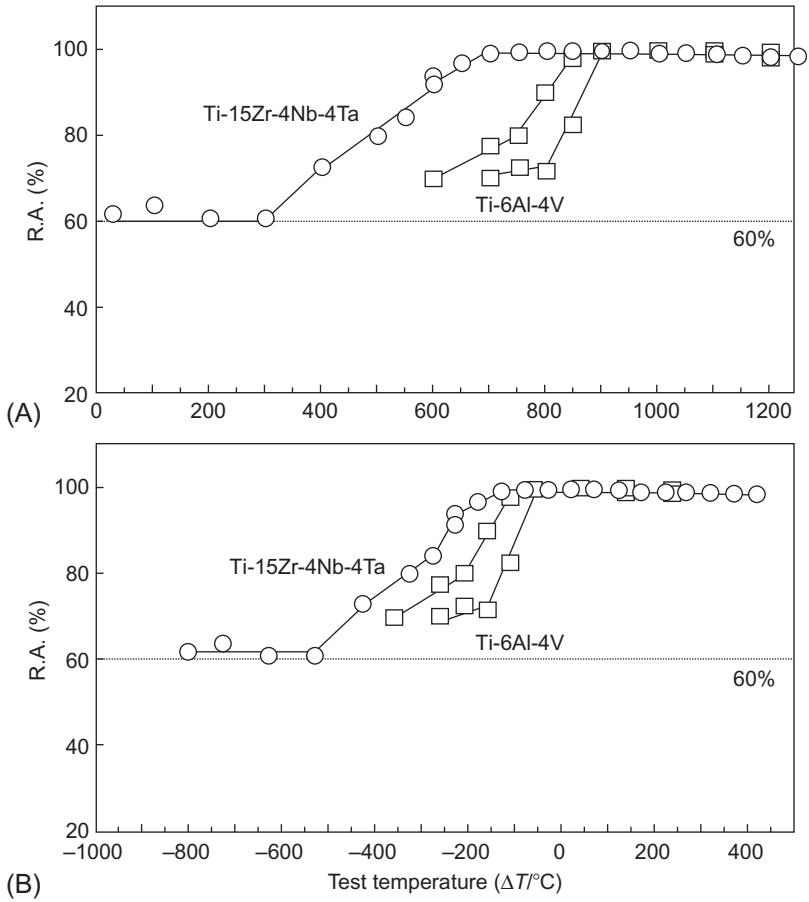


Fig. 2.19 Comparison of reduction in area (R.A.) of Ti-15Zr-4Nb-4Ta and H-6Al-4V alloys obtained by high-temperature tensile test. (A) Effect of test temperature on R.A.; (B) effect of temperature difference (ΔT) between β-transus and test temperature of tensile test.

2.6.4 Metal ions released from Ti alloys

Fig. 2.20 shows the amounts of Ni and Ti ions released from Ni-Ti alloy as a function of pH (Okazaki and Gotoh, 2008a). The quantities of both Ni and Ti released markedly increase with decreasing pH, particularly up to about pH 2, and level off above pH 4. For the Ni-Ti alloy, the critical current density for passivation (Ic) increases with decreasing pH and levels off after reaching 1.4 μA/cm^2 at pH 4. The potential (E_{10} vs SCE) at 10 μA/cm^2 rapidly increases up to pH 2 (Okazaki and Gotoh, 2008a). In terms of clinical application, the amount of Ni ions released is within the permissible range for in vivo application, thus satisfying the requirements for biliary stents, coronary stents, and stent grafts. Therefore, Ni-Ti alloy is specified in ASTM F 2063 (ASTM F 2063-12, 2012).

Figs. 2.21 and 2.22 show the effects of pH on the quantity of each metal released from Ti-6Al-4V and Ti-15Zr-4Nb-1Ta alloys, respectively. In Ti-6Al-4V the released quantities rapidly increase with decreasing pH from 4 to 2, although the changes are

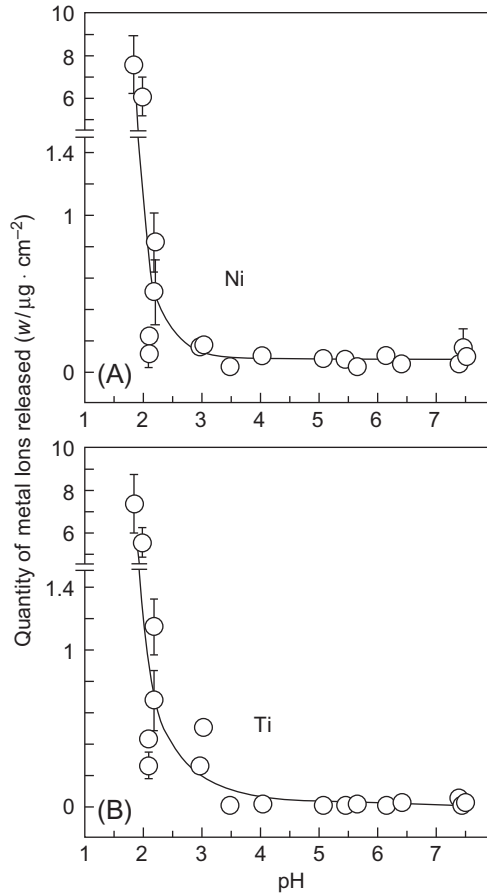


Fig. 2.20 Effects of pH on quantities of Ni and Ti ions released from Ni—Ti alloy at 37°C in one week: (A) Ni and (B) Ti.

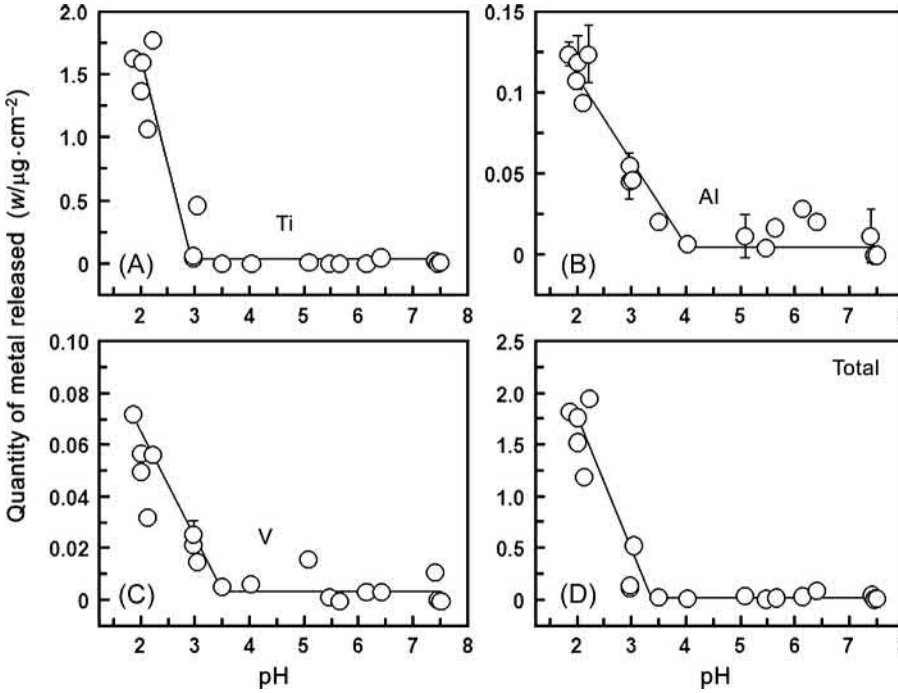


Fig. 2.21 Effects of pH on quantity of each metal element released from Ti-6Al-4V alloy at 37° C in one week: (A) Ti, (B) Al, (C) V, and (D) total.

relatively small above pH 4. In contrast, even a low pH has virtually no effect on the quantity of each metal released from Ti-15Zr-4Nb-4Ta, with the exception of Ti: the quantity of released Ti starts to increase below pH 3.5, although more gradually than in Ti-6Al-4V. Clearly, 0.9% NaCl+HCl solution adjusted to pH 2 is appropriate for accelerated immersion tests.

2.6.5 Passive film formed on Ti alloys

An oxide film formed on a Ti alloy mainly consists of TiO_2, which is thinner and stronger than a Cr_2O_3 film. Fig. 2.23 shows anodic polarization curves of Ti-6Al-4V and Ti-15Zr-4Nb-4Ta alloys tested in Ringer's solution, Eagle's medium, and 0.9% NaCl (Okazaki and Nagata, 2012). In the case of Ti-6Al-4V, the change in the current density is small at a potential of 1.2 V or lower but starts to increase at higher potentials. Meanwhile, the current density of the Ti-15Zr-4Nb-4Ta film does not increase until the potential reaches 4 V, revealing the higher strength and stability of the passive film on Ti-15Zr-4Nb-4Ta alloy than that on Ti-6Al-4V alloy.

Fig. 2.24 shows the critical current density for passivation (Ic) and the potential (E_{10} vs SCE) at a current density of 10 μA/cm^2 (see Fig. 2.23) estimated from the anodic polarization curves for Ti-6Al-4V, Ti-15Zr-4Nb-4Ta, Zr-2.5Nb, and

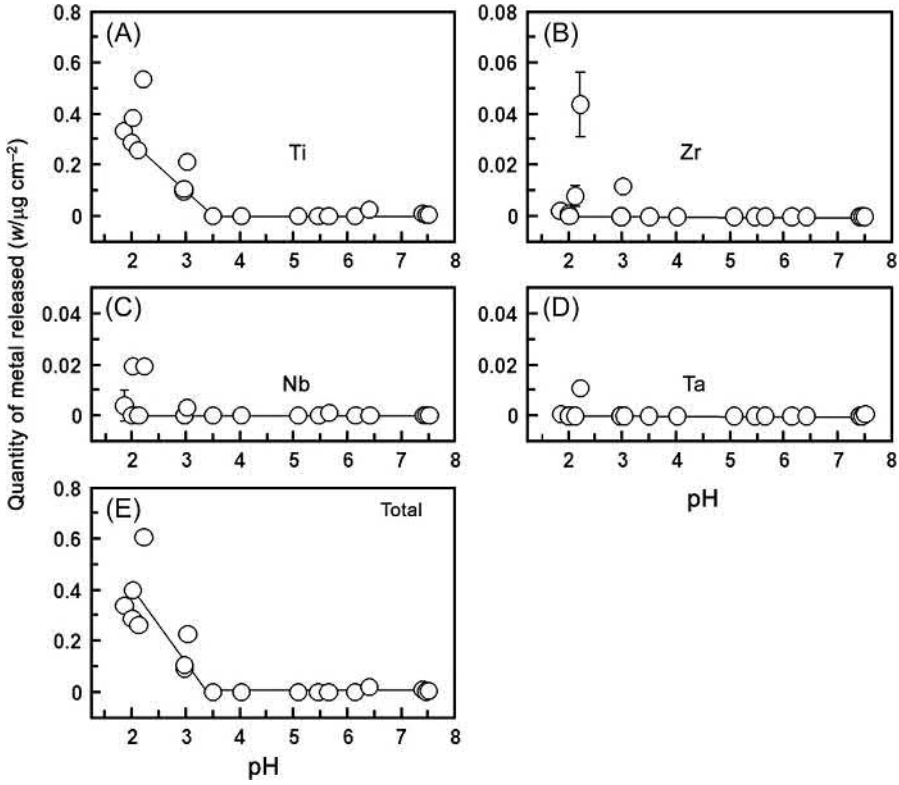


Fig. 2.22 Effects of pH on quantity of each metal element released from Ti-15Zr-4Nb-4Ta alloy at 37°C in one week: (A) Ti, (B) Zr, (C) Nb, (D) Ta, and (E) total.

Co-Cr-Mo alloys and stainless steel. The critical current density of the Ti-6Al-4V alloy gradually decreases with increasing pH and stabilizes at 2 μA/cm^2 above pH 3. On the other hand, Ic for the Ti-15Zr-4Nb-4Ta alloy remains stable in the pH range from 1 to 8. E_{10} for the Ti-15Zr-4Nb-4Ta alloy is within 4–5 V, twice that for the Ti-6Al-4V alloy, revealing that the Ti-15Zr-4Nb-4Ta alloy has a more stable passive film. The E_{10} values of the Ti alloys are higher than those of the Co-Cr-Mo and Zr-2.5Nb alloys and stainless steel, showing that the passive films on the Ti alloys are stronger (Fig. 2.24B). Fig. 2.25 shows a field-emission transmission electron microscopy (FE-TEM) image (Fig. 2.25A) and energy-dispersive X-ray (EDX) analysis (Fig. 2.25B) results of the oxide film formed on a Ti-15Zr-4Nb-4Ta alloy surface by anodic polarization up to 0.5 V vs SCE in Eagle's medium. An oxide film of approximately 7 nm thickness is observed on the alloy surface; it consists of TiO_2 and contains Zr and small amounts of Nb and Ta elements, as shown in Fig. 2.25B. The thickness of the oxide film increases from 4 to 7 nm with increasing anodic polarization potential from an open-circuit potential to 0.5 V vs SCE in Eagle's medium. The chemical bonding in the oxide films is examined by angle-resolved

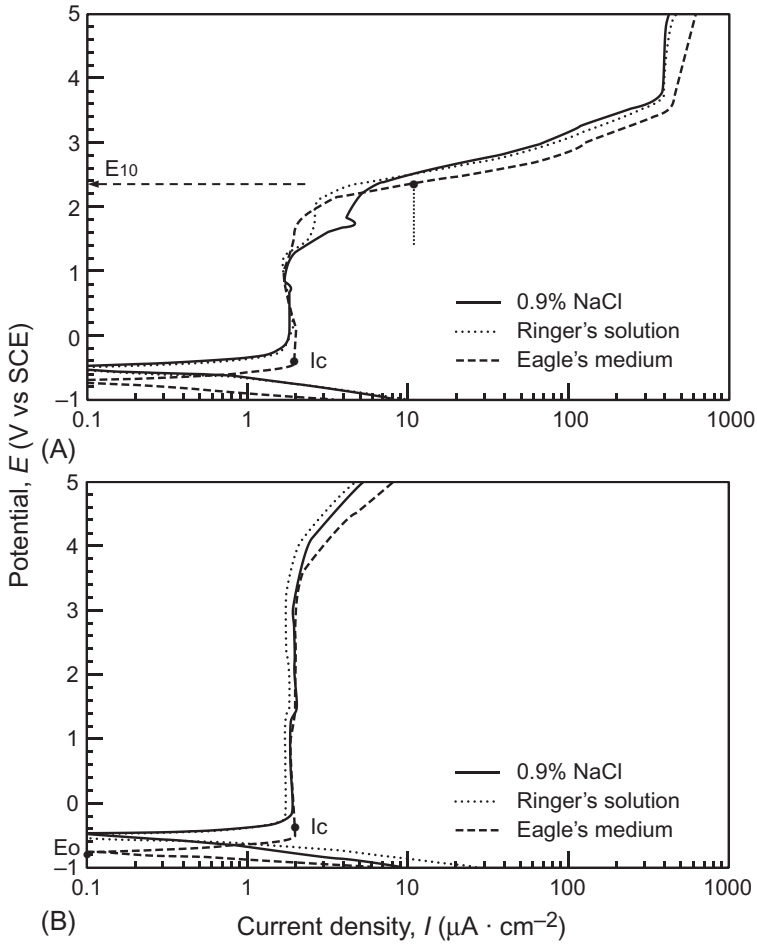
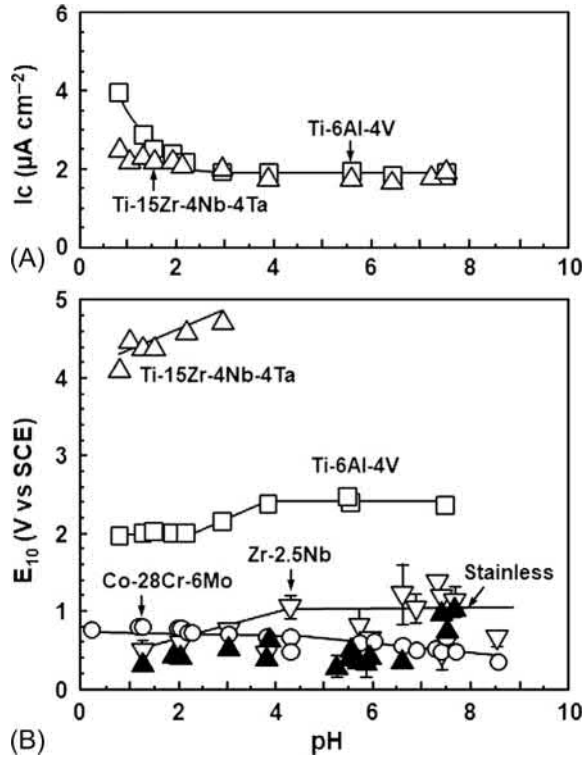


Fig. 2.23 Comparison of anodic polarization curves of (A) Ti-6Al-4V and (B) Ti-15Zr-4Nb-4Ta alloys in 0.9% NaCl. Ringer's solution, and Eagle's medium at 37°C.

X-ray photoelectron spectroscopy (ARXPS). Qualitative analysis of the mirror-like-finished Ti-15Zr-4Nb-4Ta alloy surface is conducted using wide-range photoelectron spectra (takeoff angle $\theta = 90°$). Fig. 2.26 shows the narrow-range spectra of the oxide film at takeoff angles of 20, 45, and 90°. The Ti in the oxide film is in the form of TiO_2, and a small peak originating from the base metal is detected at $\theta = 45$ and 90°. No Ti 2p peak is detected at $\theta = 20°$. Zr in the oxide film is in the form of ZrO_2, and a small peak originating from low-valence Zr is also detected at $\theta = 90°$. Nb and Ta in the oxide film are in the form of Nb_2O_5 and Ta_2O_5, respectively. No Nb or Ta peaks are detected at $\theta = 20$, 45, or 90°. Thus, when Zr, Nb, and Ta are added, the resultant ZrO_2, Nb_2O_5, and Ta_2O_5 formed in the TiO_2 passive film strengthen the film on the Ti alloy.

Fig. 2.24 Changes in (A) critical current density for passivation (Ic) and (B) in potential (E_{10}) at a current density of 10 μA/cm^2 obtained from anodic polarization curves for various solutions with different pHs.



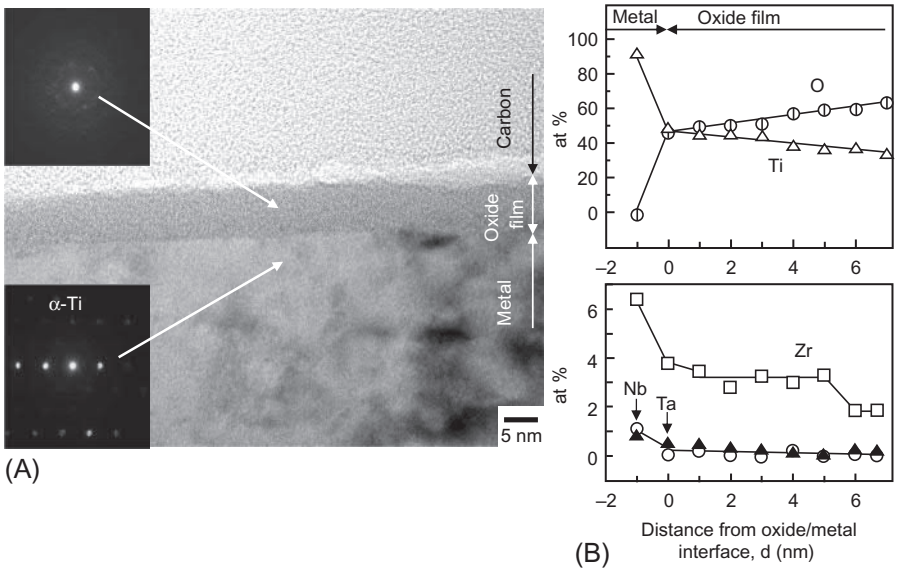


Fig. 2.25 (A) FE-TEM image and (B) results of EDX analysis of oxide film formed on Ti-15Zr-4Nb-4Ta alloy surface by anodic polarization up to 0.5 V vs SCE in Eagle's medium at 37°C.

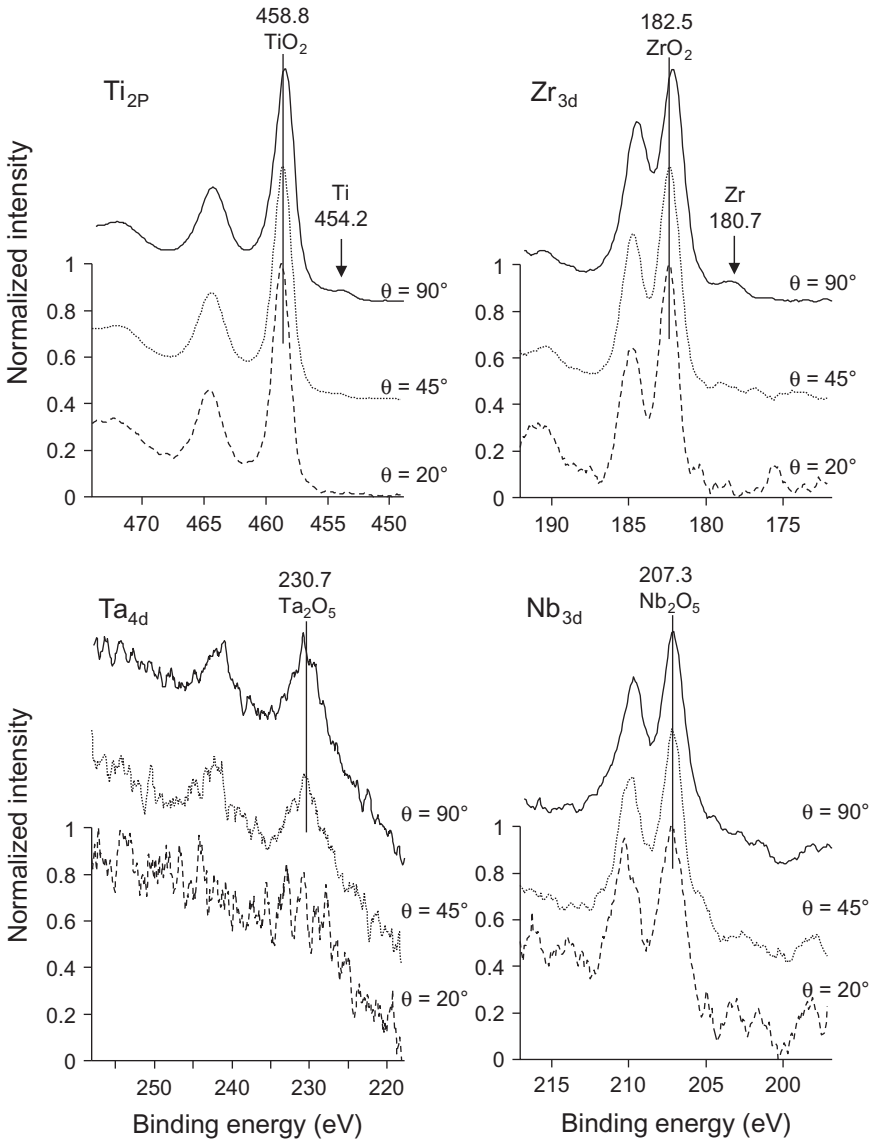


Fig. 2.26 ARXPS narrow-range spectra for oxide film formed on Ti-15Zr-4Nb-4Ta alloy by anodic polarization up to 0.5 V vs SCE in Eagle's medium at 37°C.

The metal surface of an oxide film (electric double layer) is equivalent to a capacitor (Okazaki and Nagata, 2012). Therefore, the equivalent circuit of an oxide film can be estimated as shown in Fig. 2.27. The following equation holds for this equivalent circuit:

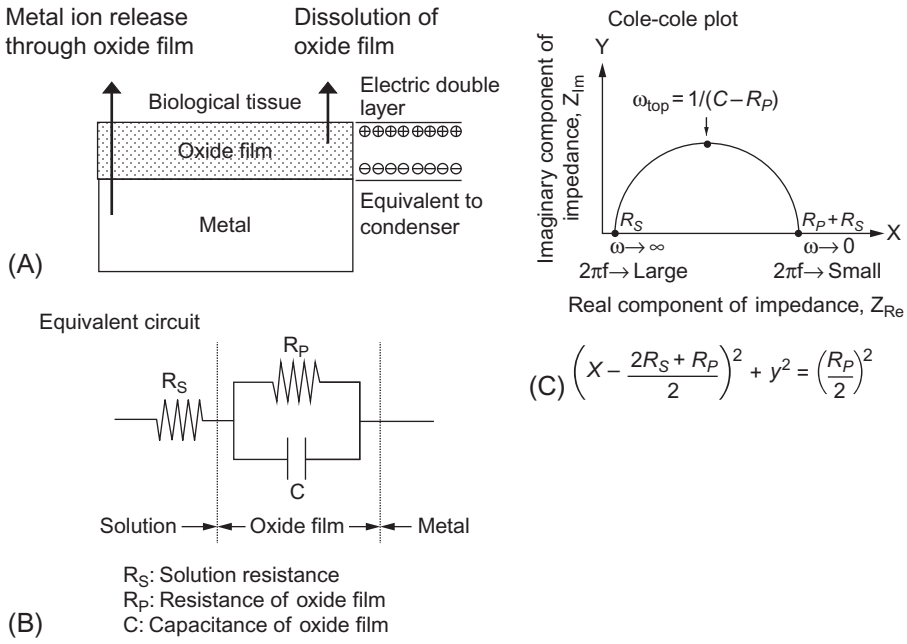


Fig. 2.27 (A) Role of oxide film, (B) equivalent circuit of oxide film, (C) Cole–Cole plot.

$$\left(x-\frac{2R_S+R_P}{2}\right)^2+y^2=\left(\frac{R_P}{2}\right)^2 \tag{2.9}$$

Here, x and y, respectively, represent the real and imaginary components of the alternating impedance $Z = E(t)/A(t) = [\mathrm{V/(A/cm^2)} = \Omega\cdot\mathrm{cm^2}]$, where E is the alternating voltage and A is the alternating current density ($\mathrm{A/cm^2}$). A semicircle with a center at $[(R_S + R_P/2), 0]$ and a radius of $R_P/2$ is also drawn. Thus, the resistances of the solution (R_S, $\Omega\cdot\mathrm{cm^2}$) and the oxide film (R_P, $\Omega\cdot\mathrm{cm^2}$) are determined by fitting the measurement data using analytical software, and the capacitance C is calculated from the maximum $\omega_{\mathrm{top}} = 1/(CR_P)$. The impedance is modified using a constant-phase element (CPE) since the actual measurement produces a semicircle on a Nyquist diagram (Cole–Cole plot) (Okazaki and Nagata, 2012). The CPE impedance is given by $\mathrm{CPE} = 1/((j\omega)^n Z_{\mathrm{CPE}})$, where Z_{CPE} corresponds to a capacitance-like element, ω ($=2\pi f$, f: frequency) is the angular frequency in rad/s, j is the unit imaginary number, and n is an exponent between 0 and 1. When $n = 1$, the system behaves as an ideal capacitor and when $n = 0$, it behaves as an ideal resistor; when n is close to 1, Z_{CPE} is close to C; the n values are 0.87–0.96 (Okazaki and Nagata, 2012). Fig. 2.28 shows values of R_P (a) and CPE (b) measured after anodic polarization up to 0 V vs SCE (x axis), and after 7-day immersion in 0.9% NaCl and Eagle's medium (y axis). R_P for the oxide film is determined after the anodic polarization from an open-circuit potential to

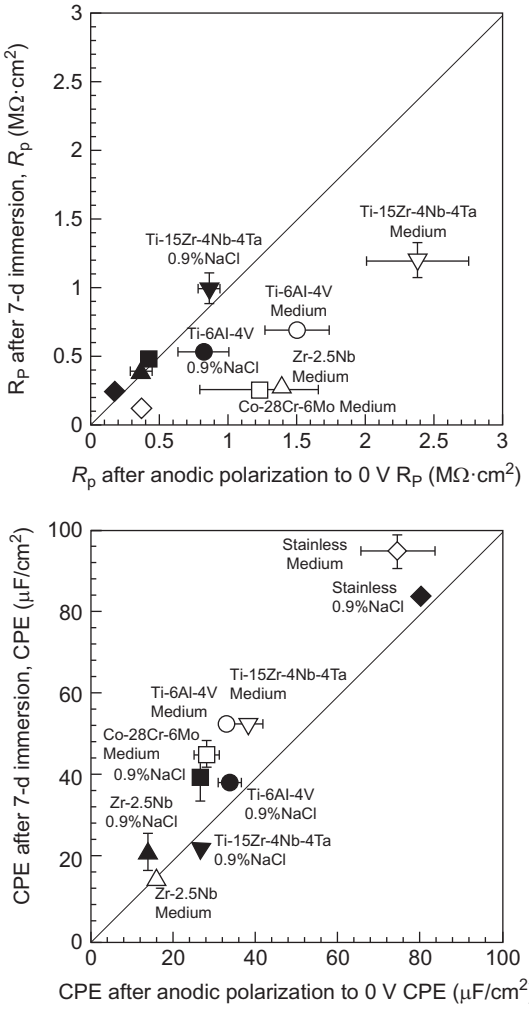


Fig. 2.28 Comparison of (A) R_P and (B) CPE measured after anodic polarization up to 0 V vs SCE and after 7-day immersion test in 0.9% NaCl and Eagle's medium at 37°C.

0 V vs SCE, similarly to that of the oxide film formed in the 7-day immersion test in 0.9% NaCl. For the comparison of the electrochemical properties of different materials, evaluation at 0 V vs SCE during anodic polarization in 0.9% NaCl is recommended on the basis of these results. Stainless steel, which has over 40 years of clinical use in the human body, has R_P of 0.2 MΩ in 0.9% NaCl. This means that materials with R_P of 0.2 MΩ or more in 0.9% NaCl can be used in the human body.

2.6.6 Osteocompatibility of Ti alloys

The behavior of newly formed bone tissue around implants can be calculated using the following four parameters (Okazaki et al., 2005).

$$\text{New bone formation rate}\,(\%) = (\text{total length of new bone formed around implant})/(\text{length of surrounding implant}) \tag{2.10}$$

$$\text{Bone contact rate}\,(\%) = (\text{total length in direct contact with implant as determined from} \times 100 \text{ optical micrograph})/(\text{length of surrounding implant}) \times 100 \tag{2.11}$$

$$\text{Thickness of new bone} = (\text{total area of new bone})/(\text{total length of new bone formed around implant}) \tag{2.12}$$

$$\text{Osteoid formation rate}\,(\%)\ \text{obtained using Villanueva stain} = [(\text{total area of osteoid bone})/\text{total area of new bone (osteoid plus calcified bone)}] \tag{2.13}$$

Fig. 2.29 shows optical micrographs of the new bone formed around a Ti-15Zr-4Nb-4Ta alloy implant. The newly formed bone is stained with toluidine blue 48 weeks after implantation (Fig. 2.29A) and the decalcified bone is stained with hematoxylin eosin (HE) 12 weeks after implantation (Fig. 2.29B). The Ti-15Zr-4Nb-4Ta alloy implant is completely surrounded by the new bone. Fig. 2.30 shows the changes in the above four morphometrical parameters over time for Ti-6Al-4V and Ti-15Zr-4Nb-4Ta alloy implants. The new bone formation rates are >90% in the early implantation period for both alloy implants. The bone contact rates gradually increase to >75% at 24 weeks after implantation then remain almost unchanged. No difference in the new bone thickness between the Ti-6Al-4V and Ti-15Zr-4Nb-4Ta alloy implants is observed. As shown in Fig. 2.30D, for the Ti-15Zr-4Nb-4Ta alloy implant, the osteoid formation rates are 10 ± 4, 6 ± 3, 6 ± 2, and $3 \pm 1\%$ at 4, 12, 24, and 48 weeks after implantation, respectively. In contrast, for the Ti-6Al-4V alloy implant, the osteoid formation rate slightly increases from 24 to 48 weeks after implantation, and the values are 9 ± 6 and $12 \pm 8\%$ at 24 and 48 weeks, respectively

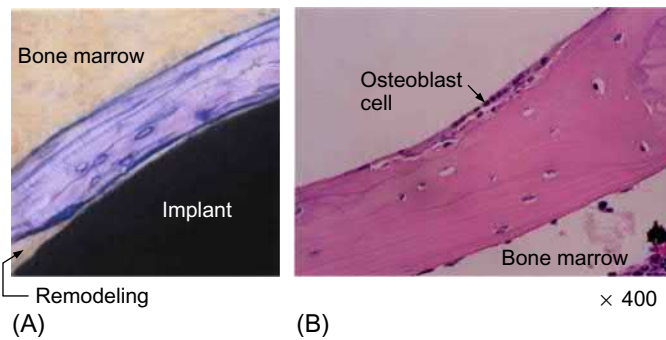


Fig. 2.29 Optical micrographs of (A) non-decalcified bone stained with toluidine blue around Ti-15Zr-4Nb-4Ta implant 48 weeks after implantation and (B) decalcified bone stained with H.E. 12 weeks after implantation. (For interpretation of the references to colour in this figure legend, the reader is referred to the web version of this article.)

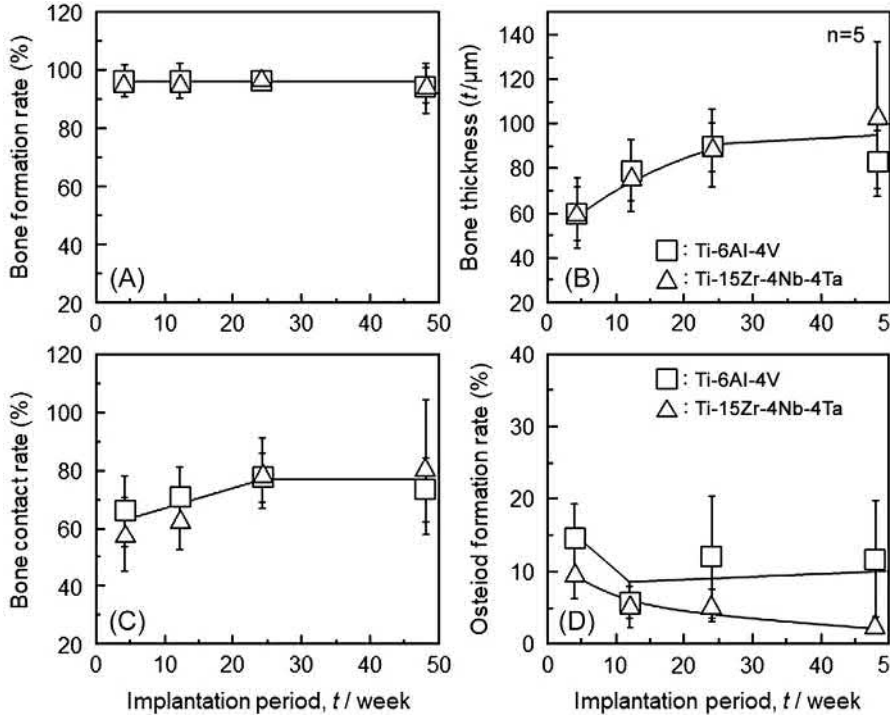


Fig. 2.30 Changes in newly formed bone around implants during implantation period (A) bone formation rate, (B) bone thickness, (C) bone contact rate, and (D) osteoid formation rate.

(Okazaki et al., 2005). The effect of a different surface treatment on Ti-6Al-4V and Ti-15Zr-4Nb-4Ta alloy implants is investigated by implantation into a rabbit femur. The pullout strength shows no statistical differences between blasted and machined implants at any stage after implantation, showing a linear increase between 4 and 24 weeks followed by a slight decrease at 48 weeks.

2.6.7 In vivo metal release

The metal concentration in a solution containing dissolved bone tissue is determined by ICP-MS. The concentrations (μg/g) of various metals in the bone tissue can be calculated by dividing the quantity of each metal (μg) in the dissolved bone tissue solution by the weight of lyophilized bone tissue (g) (Okazaki et al., 2004). As shown in Fig. 2.31, the Ti concentration in the rat tibia tissue with a Ti-15Zr-4Nb-4Ta implant is considerably lower than that in the tibia tissue with a Ti-6Al-4V implant. The Zr, Nb, and Ta concentrations are not significantly larger than those of the control sample (without an implant). The Ti concentration in the tibia tissue with the Ti-15Zr-4Nb-4Ta implant is approximately 40% lower than that in the tibia tissue with the

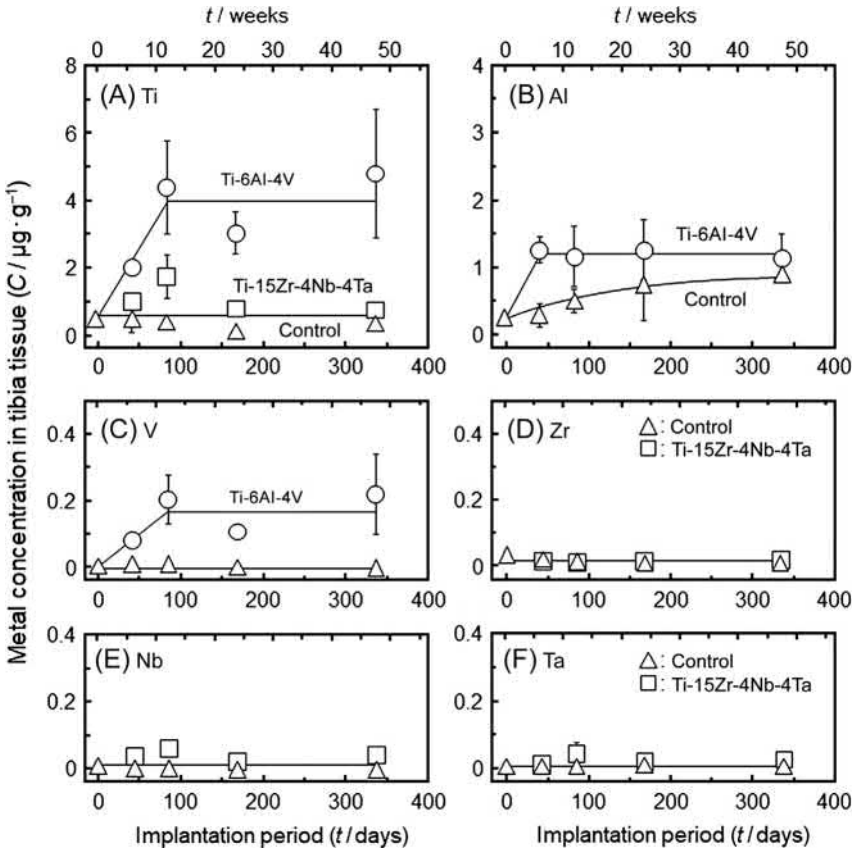


Fig. 2.31 Changes in metal concentration in lyophilized tibia tissue with Ti-6Al-4V or Ti-15Zr-4Nb-4Ta implant during implantation period. (A) Ti released from Ti6Al-4V or Ti-15Zr-4Nb-4Ta, (B) Al released from Ti6Al-4V, (C) V released from Ti6Al-4V, (D) Zr released from Ti-15Zr-4Nb-4Ta, (E) Nb released from Ti-15Zr-4Nb-4Ta, and (F) Ta released from Ti-15Zr-4Nb-4Ta.

Ti-6Al-4V implant. The (Zr + Nb + Ta) concentration is 20% less than the (Al + V) concentration.

2.6.8 Evaluation of biological properties under good laboratory practice (GLP) regulation

The quantity of released metal ions affects biocompatibility, including cytotoxicity, sensitization, and genotoxicity. In cytotoxicity tests performed under the GLP regulation, cell line V79 is cultured directly on Ti-15Zr-4Nb-4Ta alloy discs for a colony formation test. The aim is to evaluate the cytotoxicity of released substances and the interaction with the material surface such as cell adhesion. The result does not yield a

decrease in the cell adhesiveness level, colony forming ratio, or cytotoxicity. The same result was obtained previously with Ti-6Al-4V alloy used as a control sample. No sensitization is detected in a maximization test using guinea pigs. In a reverse mutation test with bacteria and a chromosomal aberration test with CHL/IU cells to evaluate genotoxicity, the clastogenic property is negative and both tests show no induction of genetic mutation. In implantation tests on a rabbit tibia and femur for 4, 12, 26, and 52 weeks, no degeneration in the bone marrow tissue around the implantation sites is observed under all implant conditions. Aggregation, degeneration, and necrosis are not induced by inflammatory cells such as macrophages, heterophils, and leukocytes. New bone is formed from 4 weeks, similarly to in the case using the reference material of Ti-6Al-4V alloy.

2.7 Fatigue assessment

Fatigue resistance is one of the most important mechanical characteristics of structural biomaterials because biomaterials are generally used under cyclic loading conditions. Fatigue tests are conducted in accordance with JIS T 0309 (JIS T 0309, 2009). The tests are mainly carried out in the tension-to-tension mode with a sine wave. The testing conditions are a stress ratio (R = (minimum stress)/(maximum stress)) of 0.1 and a frequency of 10 Hz. To obtain the profiles of maximum stress vs number of cycles (S-N curves), the specimens are cycled with a constant load amplitude for a maximum of 10^7 cycles or until they fail. For a uniform specimen, fatigue fracture occurs at different positions owing to the effect of machining; however, hourglass-shaped specimens fracture at the same position (at the position of minimum diameter). Plate-shaped specimens also exhibit lower fatigue strength than rod-shaped specimens.

Fig. 2.32 shows the S-N curves obtained from a tension-to-tension test on C.P. Ti and Ti alloy hourglass-shaped rod specimens (minimum diameter: 4.5 mm) using a sine wave. Higher-grade C.P. Ti shows a higher fatigue strength at 1×10^7 cycles: grade 2, 280 MPa; grade 3, 355 MPa; and grade 4, 485 MPa. Fig. 2.33 shows the S-N curves for hourglass-shaped rods of (A) annealed Ti-6Al-4V, Ti-6Al-7Nb, and Ti-6Al-2Nb-1Ta, and (B) solution-annealed Ti-15Mo-5Zr-3Al tested in the tension-to-tension mode with a sine wave in Ringer's solution at 37°C. The fatigue strengths of the annealed Ti-15Zr-4Nb-4Ta, Ti-6Al-4V, V-free Ti-6Al-7Nb, and Ti-6Al-2Nb-1Ta rods are approximately 730, 685, 600, and 700 MPa, respectively. Fig. 2.34 shows optical microscopy and TEM images of the Ti-6Al-4V and Ti-15Zr-4Nb-4Ta alloys. The annealed Ti-6Al-4V alloy consists of an α-phase matrix with approximately 20 vol% β-phase. As shown in Fig. 2.34C and D, the annealed Ti-15Zr-4Nb-4Ta mostly consists of an α-phase matrix with approximately 25 vol % β-phase. Table 2.4 shows the tensile properties of various implantable metals. The means of the $\sigma_{0.2\%PS}$, σ_{UTS}, T.E., and R.A., together with the standard deviations are calculated for three test specimens of each alloy. The ratios of the fatigue strength at 1×10^7 cycles to the ultimate tensile strength are also shown in Table 2.4 and are over 65% for the α- and α-β-type Ti materials.

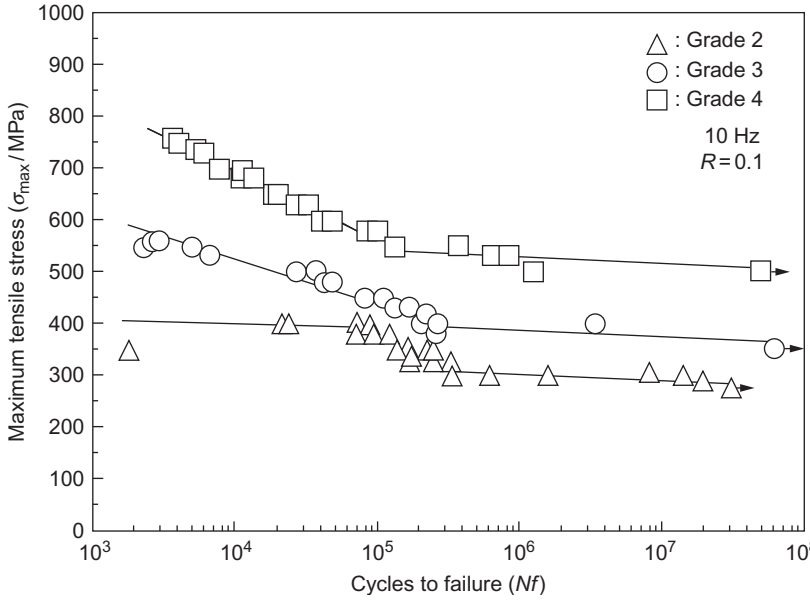


Fig. 2.32 S-N curves obtained from tension-to-tension fatigue test with sine wave in Ringer's solution at 37°C for three types of commercially pure titanium.

2.8 Performance evaluation of orthopedic devices

Mechanical testing methods for bone plates, CHSs, short femoral nails, intramedullary nails, screws, artificial hip joints, artificial knee joints, and spine fixtures have been developed over time. For bone plates and intramedullary nails, the bending strength, bending stiffness, and durability are evaluated by conducting a four-point bending test in accordance with JIS T 0312 (JIS T 0312, 2009), as shown in Fig. 2.35A and B. Durability tests on CHSs, and short femoral nails are conducted in accordance with JIS T 0313 (JIS T 0313, 2009). For CHSs and short femoral nails, the compression strength, compression stiffness, and durability are evaluated by performing a compression bending test in accordance with JIS T 0313 (Fig. 2.35D). For screws, a torsional breaking test, an evaluation of durability by a four-point bending test, a driving force test into artificial (model) bones, and a pullout test from model bones are performed (Figs. 2.35C and 2.36). The durability test on artificial hip stems is conducted in accordance with ISO 7206-4 (ISO 7206-4, 2010).

2.8.1 Mechanical properties of osteosynthesis devices

To evaluate the bending strength, bending structural stiffness, and fatigue properties of osteosynthesis devices, four-point and three-point bending tests are conducted on bone plates, intramedullary nail rods, and bone screws. Load vs displacement (L–D) curves are obtained at a crosshead speed of 10 mm/min in all tests. The bending

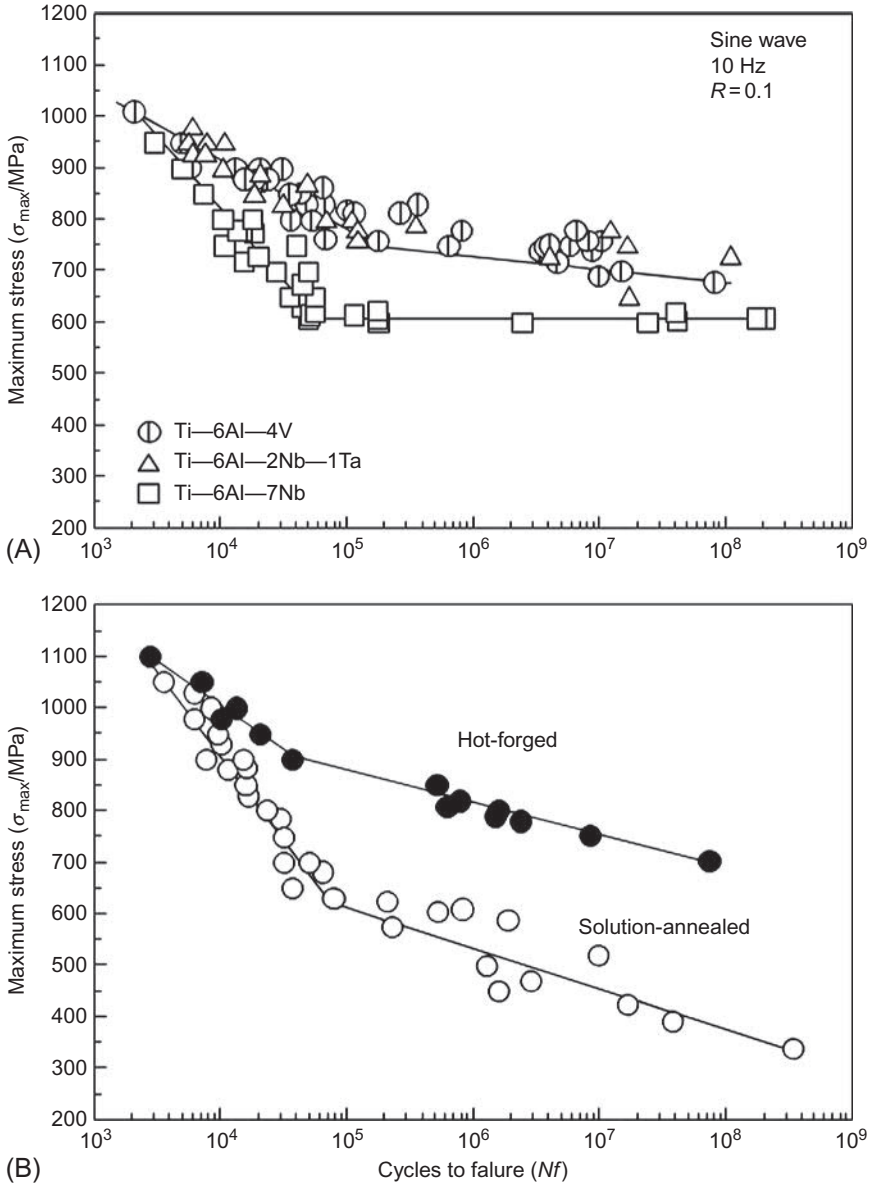


Fig. 2.33 S-N curves obtained from tension-to-tension fatigue test with sine wave in Ringer's solution at 37°C. (A) Annealed Ti-6Al-7Nb, Ti-6Al-4V, and Ti-6Al-2Nb-1Ta alloys; (B) solution-annealed and hot-forged Ti-15Mo-5Zr-3Al alloy.

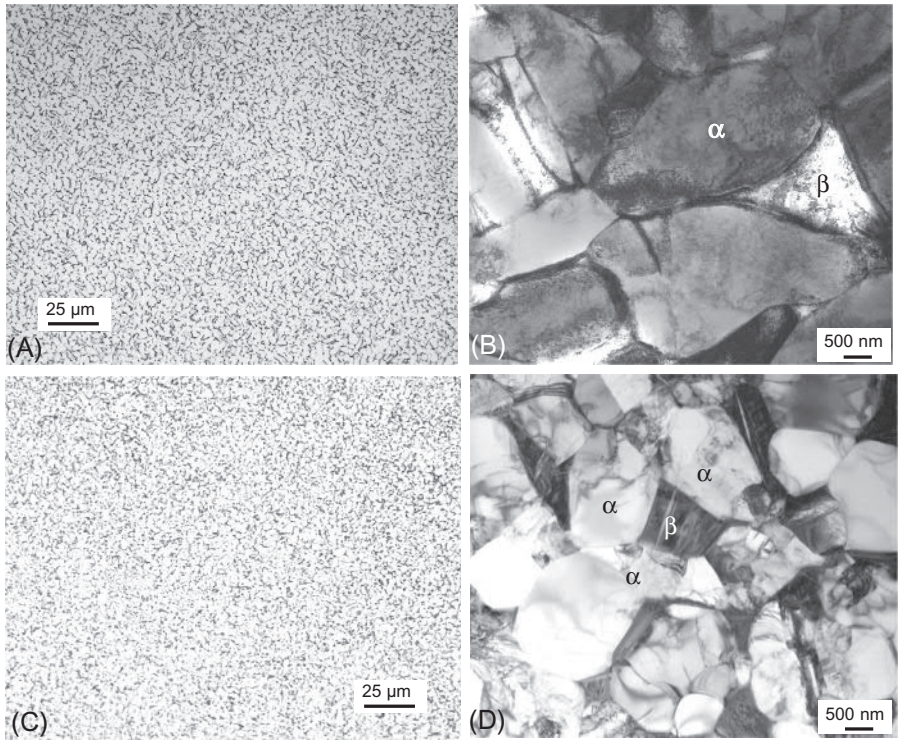


Fig. 2.34 Optical micrograph (A) and TEM image (B) of annealed Ti-6Al-4V, optical micrograph (C) and TEM image (D) of annealed Ti-15Zr-4Nb-4Ta.

strength and bending structural stiffness are determined using the following expressions:

$$\text{Bending strength } (\mathrm{N \cdot m}) \text{ in four-point and three-point bending tests} = \mathrm{Ph}/2 \tag{2.14}$$

$$\text{Bending structural stiffness } \left(\mathrm{N \cdot m^2}\right) \text{ in four-point bending test} = (2\mathrm{h} + 3\mathrm{k})\mathrm{Mh}^2/12 \tag{2.15}$$

(in the three-point bending test, h is 0), where P, h, k, and M are the offset load for 0.2% or 2% offset displacement, the distance between the loading roller and support roller, the loading span distance, and the bending stiffness estimated from the maximum slope of the linear part of the L–D curve, respectively.

In the four-point bending test on the bone plate, it is recommended that two support rollers be placed at two screw holes from the outside of the loading rollers. The offset displacement is 0.2% of the distance between the support rollers and loading rollers. On the basis of the four-point bending fatigue test on the bone plate, L–N curves are

Table 2.4 Tensile properties of implantable metals and ratios of fatigue strength at 10^7 cycles (σ_{FS}) to ultimate tensile strength (σ_{UTS}) shown for comparison among the alloys tested

Alloy	$\sigma_{0.2\%PS}$/ MPa	σ_{UTS}/ MPa	T.E. (%)	R.A. (%)	*E*/GPa	σ_{FS}/σ_{UTS}
Ti-15Zr-4Nb-4Ta						
Annealed (Plate)	800 ± 14	910 ± 10	19 ± 2			0.54
Annealed (Rod)	848 ± 2	915 ± 3	21 ± 2	55 ± 3	94 ± 2	0.80
S.T. + Aged (Rod)	894 ± 5	1020 ± 8	15 ± 2	48 ± 3	98 ± 2	0.89
C.P. Ti Grade 2	276 ± 6	410 ± 4	40 ± 2	60 ± 6	106 ± 2	0.68
C.P. Ti Grade 3	380 ± 2	540 ± 2	32 ± 2	54 ± 2	108 ± 3	0.66
C.P. Ti Grade 4	600 ± 6	701 ± 8	26 ± 2	46 ± 3	118 ± 2	0.69
Ti-6Al-4V	849 ± 1	934 ± 1	16 ± 1	42 ± 3	102 ± 4	0.73
Ti-6Al-7Nb	845 ± 8	960 ± 10	18 ± 2	47 ± 3	108 ± 2	0.63
Ti-6Al-2Nb-1Ta	842 ± 2	900 ± 3	18 ± 3	43 ± 4	110 ± 1	0.81
Ti-15Mo-5Zr-3Al						
Solution-annealed	910 ± 10	930 ± 8	19 ± 2	50 ± 2	92 ± 2	0.38
Hot-forged	963 ± 12	988 ± 10	18 ± 2	50 ± 6	102 ± 2	0.71
Stainless steel ISO 5832						
Solution-treated	338 ± 30	680 ± 8	68 ± 4	70 ± 2		0.55
20% Cold-worked	760 ± 5	878 ± 3	30 ± 11	70 ± 4		0.79
SUS 316L						
Solution-treated	262 ± 6	567 ± 2	56 ± 6	74 ± 7		0.67
High-N Solution-treated	436 ± 4	830 ± 4	37 ± 2	48 ± 7		0.57
Co-Cr-Mo						
As-cast	380 ± 30	550 ± 50	6 ± 3	14 ± 2		0.72
Annealed	552 ± 4	915 ± 15	20 ± 2	14 ± 1		0.75
Hot-forged	669 ± 40	1075 ± 20	7 ± 2	10 ± 2		0.74
Warm-worked	760 ± 5	1153 ± 16	12 ± 2	8 ± 2		0.84

E: Young's modulus.

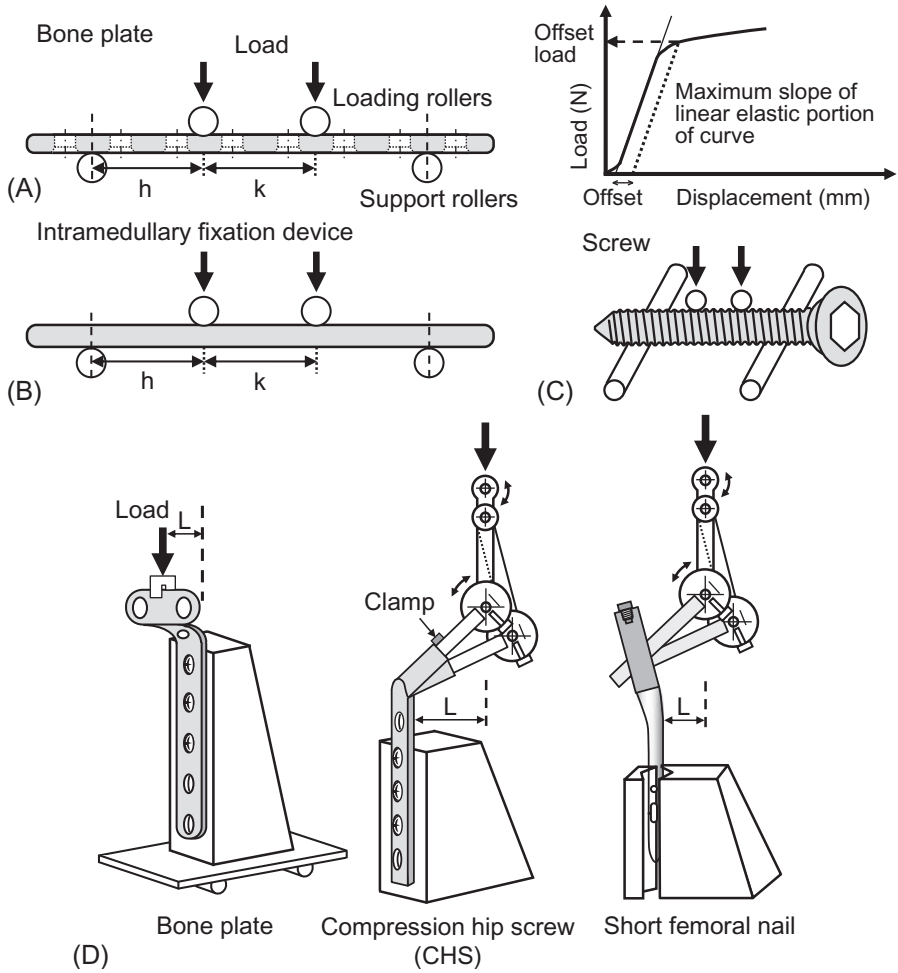


Fig. 2.35 (A–C) Static four-point bending and four-point bending fatigue tests. Loading rollers are placed at one-third of the way between the two support rollers. (D) Schematic illustration of compression bending tests.

measured with a sine wave, a load ratio of 0.1, and a frequency of 1–5 Hz for up to 10^6 cycles. Fig. 2.37 shows L–N curves obtained by the four-point bending durability test for various sizes and types of bone plate measured in air (Okazaki et al., 2017). Note that Fig. 2.37 is a useful reference for the development of new bone plates, providing basic data for the commercial approval of medical devices. Compression bending tests on CHSs, short femoral nails, and T-shaped metal plates (T-plates) are conducted to evaluate their compression bending strength, compression bending stiffness, and fatigue properties. Load vs displacement (L–D) curves are measured at a crosshead speed of 10 mm/min. The bending stiffness (N/m) is estimated from the

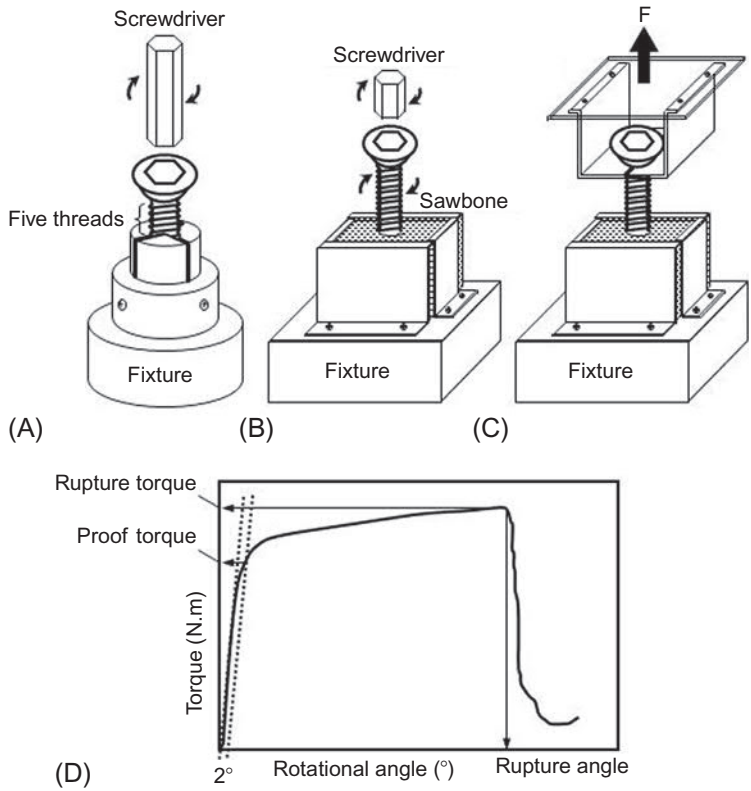


Fig. 2.36 Schematic illustration of (A) torsional breaking, (B) driving force, and (C) pullout tests. (D) Torque versus rotational angle curve.

maximum slope of the linear elastic part of the L–D curve. The bending strength (N·m) is defined by formula (2.16):

$$(\mathrm{N}\cdot\mathrm{m}) = \text{lever arm} \times \text{offset load}. \tag{2.16}$$

To estimate the offset load, 0.2% or 2% of the length of the lever arm is used as the offset displacement. The compression bending strength of a CHS with all the screw holes of the side plate anchored is approximately 1.3 times higher than that of the same CHS with the top screw hole unanchored. The bending stiffness decreases as the lag screw becomes longer, although the bending strength is not affected by the lag screw length. Short femoral nails show higher bending stiffness and strength than CHSs. The T-plate shows higher bending strength and a superior fatigue property to the T-buttress plate in all tests. As the maximum load in the fatigue test ($R = 0.1$) of a CHS decreases, the starting point of the fracture shifts from the lag screw to the side plate. The fatigue properties of the sliding-type CHS are markedly inferior to those of the tube-type. The effect of jig fixation on the fatigue properties of the CHSs is small. The

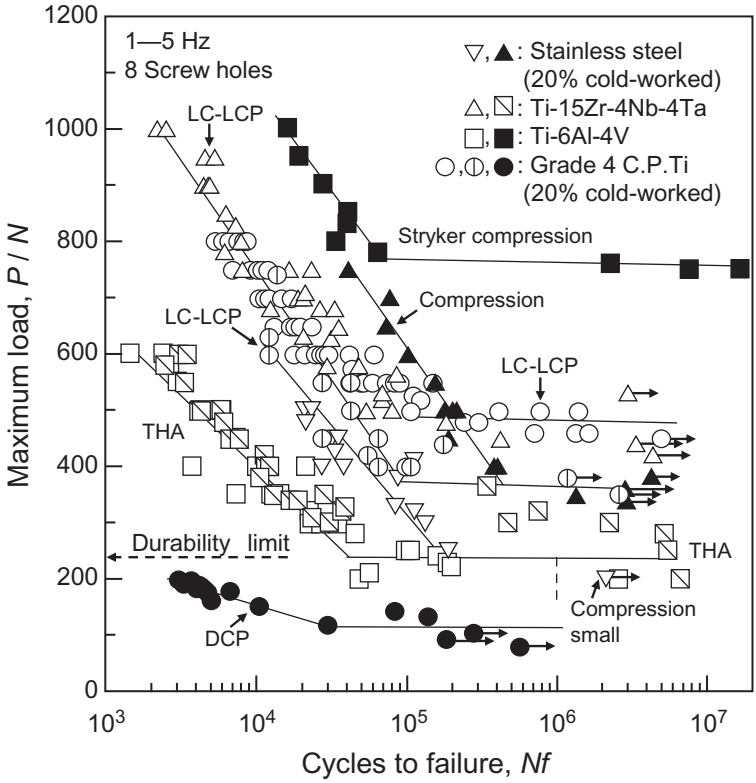


Fig. 2.37 L–N curves obtained by four-point bending durability tests for various metallic bone plates.

fatigue properties of short femoral nails are superior to those of the CHSs. The effect of the diameter of a proximal nail on its bending stiffness and strength is large, whereas the effect of the proximal shaft angle is small. Its fatigue properties deteriorate with decreasing proximal shaft angle and diameter of the nail. The fatigue properties of all implant devices are affected more by their design than by their material composition. Likewise, the intramedullary nail rod shows excellent fatigue properties. The fatigue properties of a screw made of Ti materials markedly changes from a core diameter of 3–3.5 mm.

2.8.2 Performance of metallic bone screws

To evaluate the torsional breaking and performance of cortical, cancellous, and locking screws widely used in thigh bones, a torsional breaking test (rotational speed: 1 rpm), a screw driving force test into a cortical sawbones (Solid Rigid Polyurethane Foam, 15 pcf) or cancellous sawbones (Cellular Rigid Polyurethane Foam, 20 pcf) with loading of 100 N, and a pullout test (crosshead speed: 10 mm/min) on screws driven and remaining in the sawbones after the driving force test are conducted

(Fig. 2.36) (Okazaki and Gotoh, 2008b). It is shown that the 2° proof and rupture torques of a screw estimated from torque versus rotational angle curves increase with increasing core diameter of the screw. The 2° proof torque of a stainless-steel screw is higher than that of screws made from Ti materials. The rupture torque is not affected by the material. Cortical double-threaded screws show the highest rupture torque among the cortical screws. The maximum pullout load tends to increase with the driving torque applied in a driving force test. The effects of the screw shape, namely, the height of the screw [(thread diameter–core diameter)/2], the pitch, and the aspect ratio (height of screw/pitch), on the driving torque are small while the maximum pullout load increases with these values. In general, the maximum pullout load of a pre-tap screw is larger than that of a self-tap screw.

2.8.3 Analysis of spatial stress distribution of implant devices by thermoelastic stress measurement

Four-point bending durability tests are carried out on bone plates and compression bending durability tests are carried out on CHSs, short femoral nails, and artificial hip stems to measure the surface stress distribution of implant devices. The surface stress produced by a bending moment is compared with that obtained by thermoelastic measurement (Okazaki et al., 2017). Moreover, to compare the durability limit of metallic bone plates and CHSs and the notch fatigue strength of the raw materials, fatigue tests with V-notched specimens are carried out (Okazaki et al., 2017). Fig. 2.38 shows the stress distribution of a bone plate surface generated by the bending

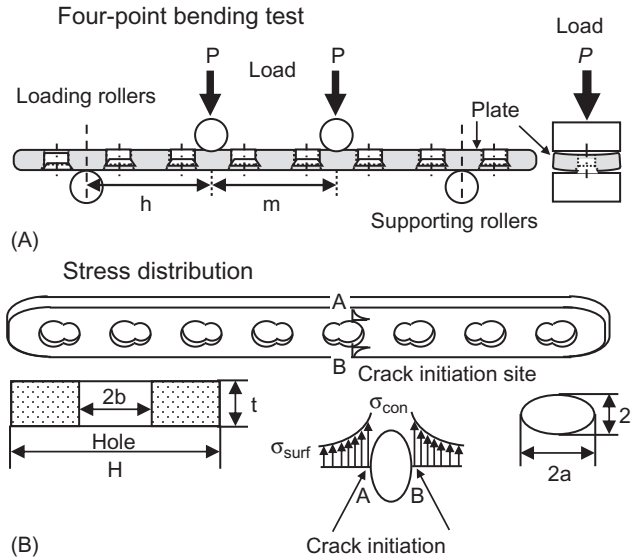


Fig. 2.38 (A) Four-point bending test. (B) Stress distribution of bone plate surface (AB) generated by bending moment in the durability test on a bone plate, and shape of cross section of bone plate.

moment in the durability test on a bone plate and the cross section of the bone plate. P shown in Fig. 2.38A is the applied load, m is the distance between the loading rollers, and h is the distance between a loading roller and the nearest supporting roller (h: $m = 1{:}1$). Fig. 2.38B shows the stress distribution at a bone plate surface when a bending moment is applied to the bone plate. Increases in tensile stress and compressive stress can be observed toward the exterior and interior surfaces from the center of the cross section of the bone plate, respectively. The maximum tensile strength (σ_{surf}) is at the exterior surface AB shown in Fig. 2.38B (support roller side). Stress concentration (σ_{con}) occurs at the middle of the hole of the exterior surface AB. A fatigue crack is initiated from the location where stress concentration (σ_{con}) occurs at the middle of the plate hole surface (side AB) shown in Fig. 2.38B when σ_{con} on the plate hole surface is higher than the fatigue strength (generally elastic deformation) of the raw material, and it propagates toward the opposite side (loading roller side) of the bone plate. σ_{surf} and σ_{con} at the bone plate surface relative to the bending moment can be estimated using formulas (2.17) and (2.18), respectively,

$$\sigma_{surf} = M/Z = P \times h/2/Z \tag{2.17}$$

$$\sigma_{con} = k \times \sigma_{surf} \tag{2.18}$$

where M is the bending moment ($P \times h/2$), P is the maximum applied load (N), h is the distance between the loading roller and the support roller, and k is the stress concentration factor, which depends on the hole shape. Z is the section modulus, which depends on the cross-sectional shape of the plate and is expressed as $Z = (H–2b) \times t^2/6$ (H–2b: length of the plate excluding the hole; t: thickness of the cross section) for a rectangular shape. The Z value is calculated at the rupture position. k can be geometrically determined from the rectangular shape of the hole and by using a relationship diagram, as shown later in Fig. 2.41D (ISO 7206-4, 2010). k is also approximately expressed as $(1 + 2b/a)$. σ_{surf} and σ_{con} are estimated by thermoelastic stress measurement while varying the applied load. These values are compared with the σ_{surf} ($=P \times h/2/Z$) and σ_{con} ($=k \times \sigma_{surf}$) values calculated from the durability test results, which change with the applied load, and k is determined from the shape of the hole using Fig. 2.41D. The k values of the bone plates and side plates of the CHSs are approximately 2. The fatigue strength at 10^7 cycles is determined using a V-notched fatigue specimen. It is then compared with the maximum stress σ_{surf} calculated with the durability data of the bone plate using formula (2.17). Fig. 2.39A shows the stress distribution of a bone plate surface obtained by thermoelastic stress measurement. Tensile stress σ_{surf} is observed at the exterior surface (support roller side). Stress concentration (σ_{con}) is observed near the hole of the exterior surface. Fig. 2.39B shows a comparison of σ_{surf} and σ_{con} calculated from the bending moment with two types of bone plate (types A and B), and σ_{surf} and σ_{con} obtained by thermoelastic stress measurement for each bone plate. σ_{surf} and σ_{con} calculated with formulas (2.17) and (2.18) are approximately equal to the values obtained by thermoelastic stress measurement. Fig. 2.40 shows changes in the value of $\sigma_{surf} = P \times h/Z/2$ calculated with the L–N data shown in Fig. 2.37. The L–N data

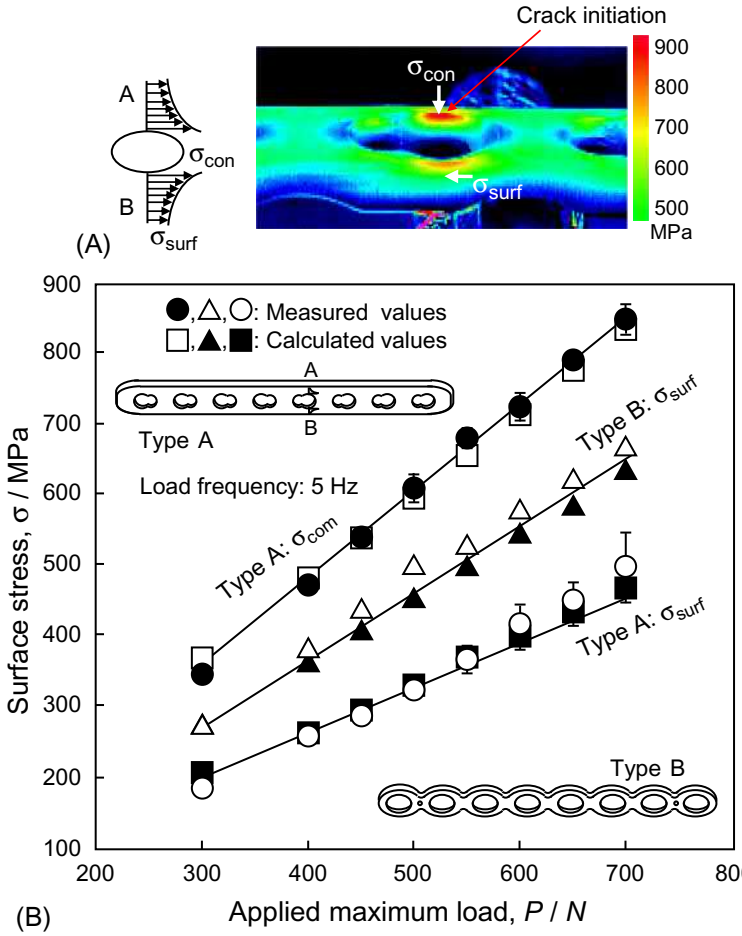


Fig. 2.39 (A) Stress distribution of bone plate surface. (B) Comparison between surface stress calculated from bending moment and that obtained by thermoelastic stress measurement based on four-point bending durability test.

of plates with different sizes converged to a fatigue limit of around 400 MPa. The durability limits of various types of bone plate calculated from maximum load vs number of cycles (L–N) data are close to the notch fatigue strength of the raw material. Formulas (2.17) and (2.18) concerning the bending moment can be used to estimate the stress concentration in the durability evaluation of bone plates.

Fig. 2.41 shows the stress distributions on (Fig. 2.41A) a CHS, (Fig. 2.41B) a short femoral nail, and (Fig. 2.41C) an artificial hip stem when a bending moment is applied to an implant device. An artificial hip stem is set with a fixed vertical distance from the tip of the stem to the upper level of the fixation jig of 80 mm. δ (in adduction), which is the angle between the load axis and the stem axis, is 10°, and ε (in flexion), which is

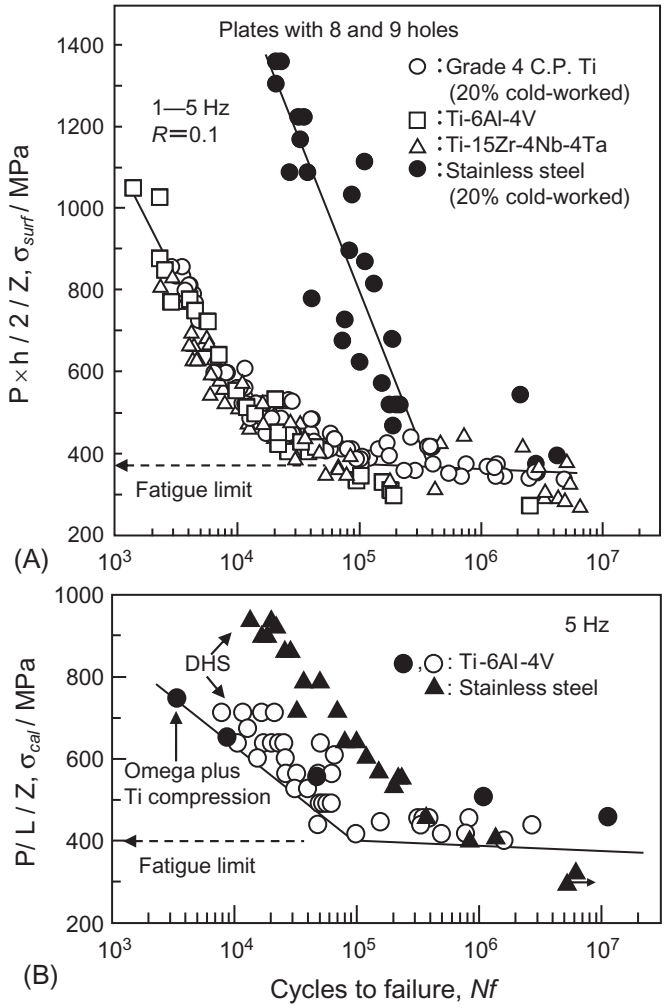


Fig. 2.40 Effects of stress concentration on (A) bone plates and (B) CHSs. (A) Changes in σ_{surf} calculated using L–N data measured in the four-point bending durability test. (B) Changes in surface stress ($\sigma_{cal} = P \times L/Z$, $\alpha = 1$) of side plates calculated from durability results for CHSs.

the angle between the line from the center of the head to the tip of the stem and the longitudinal-sectional stem axis when viewed from the back, is 9° (Okazaki et al., 2017). The maximum tensile strength (σ_A) and minimum compression strength (σ_B) occur at the exterior (A) and interior (B) surfaces, respectively. A fatigue crack is initiated from the location where stress concentration occurs on the tensile side A of the CHS, the short femoral nail, and the artificial hip stem, and it propagates toward the opposite side B. The thermoelastic stress generated on the compression and tensile sides is independently measured by applying a sinusoidal load with various

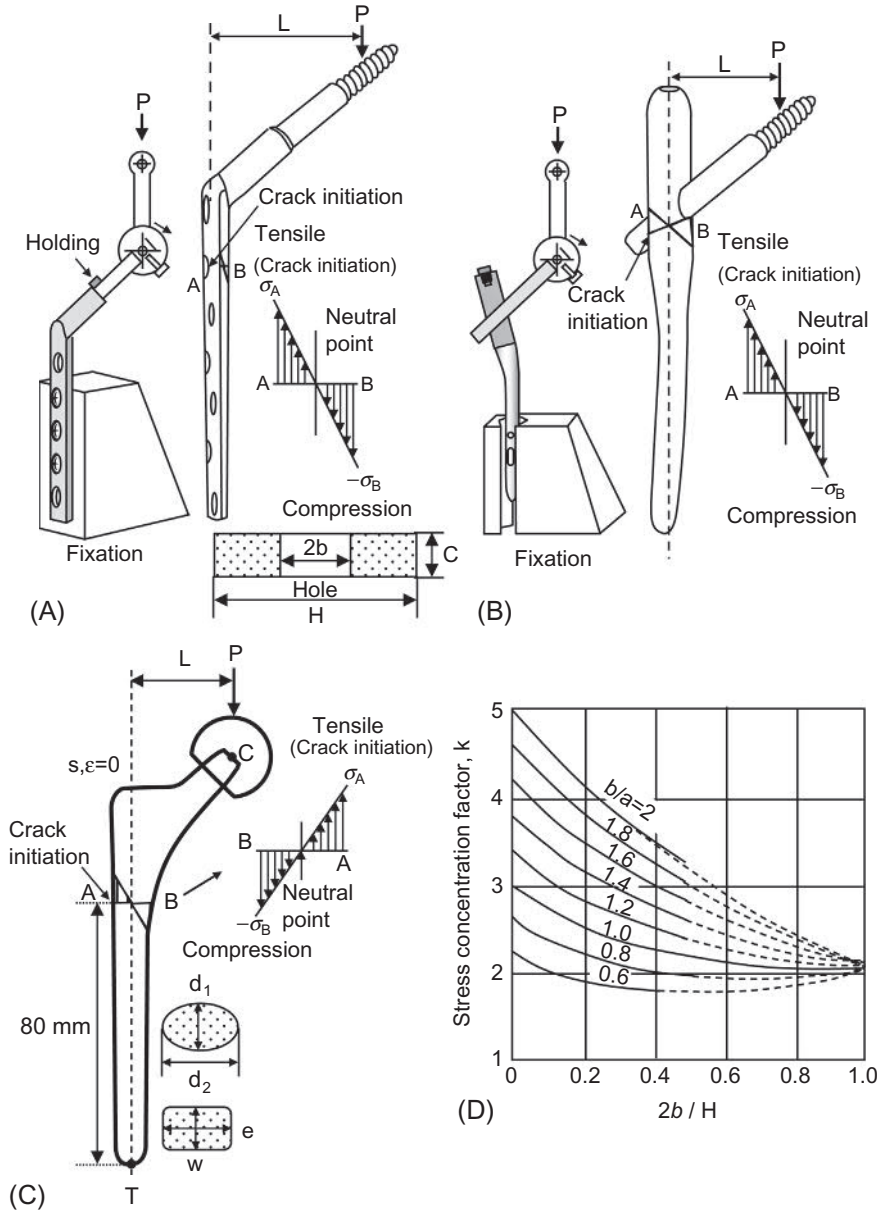


Fig. 2.41 (A, B) Fixation methods and stress distributions of CHS and short femoral nail in the cross section AB. (C) Stress distributions of stem generated by bending moment in the durability test using an artificial hip stem. (D) Relationship between the elliptical and cross-sectional shapes of the plate hole and the stress concentration factor (k).

amplitudes to each side. The durability tests are conducted with a sine wave, a load ratio of 0.1, and a frequency of 2–5 Hz.

The surface stress (σ_{surf}) generated by the bending moment is estimated using formula (2.19).

$$\sigma_{surf} = M/\alpha/Z \tag{2.19}$$

M (the bending moment) is expressed as $P \times L$, where P is the maximum applied load (N) and L is the length of the lever arm. Several equations for Z (the modulus of the section) are adopted depending on the cross-sectional shape. Three equations, for circular, elliptical, and rectangular shapes, are used in our examination: $\pi d^3/32$ for a circular cross section, where d is the diameter; $\pi d_1 \times d_2^2/32$ for an elliptical cross section, where d_1 is the short-axis length and d_2 is the long-axis length; $Z = w \times e^2/6$ for a rectangular cross section, where e is the length of the cross section and w is the width of the stem. α denotes the stress concentration factor at the implant surface, which is 1 for a smooth surface, although it depends on the surface finish as well as on the coating technique used, such as bead coating or plasma-spray coating for an artificial hip stem. The durability tests are carried out in accordance with ISO 7206-4 (JIS T 0313, 2009) in the tension-to-tension mode with a sine wave. The load ratio (minimum load/maximum load) is 0.1 and the wave frequency is 2 or 3 Hz. The absolute values of the tensile and compression stresses measured at the same amplitude are averaged. L-N curves are determined to estimate the effect of the surface treatment (stress concentration) on the durability of the stem. Tensile (at the crack initiation site) and compressive (negative) stresses are observed at the exterior and interior surfaces of the stem, respectively. The absolute values of the tensile and compressive stresses are approximately the same at the same load amplitude. The mean thermoelastic stress $[(\sigma_A + \sigma_B)/2]$ is the mean of the absolute values of the tensile and compressive stresses measured on both sides (A and B shown in Fig. 2.41C) of the stem surface, and $\sigma_{cal} = P \times L/Z \times 0.9$ ($\alpha = 1$). The σ_{cal} values calculated from the bending moment, which is in formula (2.19), are nearly equal to the actual surface stresses $[(\sigma_A + \sigma_B)/2]$ obtained by thermoelastic stress measurement. The stress concentration factor α is roughly 0.8 for the bead-coated stem and roughly 0.6 for the plasma-coated stem. Tensile stress σ_A or compressive stress σ_B is observed on the exterior or interior side of the CHS side plate, respectively. Stress concentration (σ_{con}: crack initiation position) is observed near the hole of the CHS side plate surface. Tensile stress (σ_A: crack initiation position) and compressive stress σ_B are similarly observed near the hole of the short femoral nail rod. Breakages of CHSs and short femoral nails in clinical use due to fatigue fracture have been reported to occur at the center of the side plate holes of the CHSs and at the lag screw holes of the short femoral rods (Okazaki et al., 2017).

2.8.4 Wear properties of artificial hip prostheses using hip simulator

For the hard-on-soft and hard-on-hard bearings of artificial hip joints, metal-on-polyethylene and ceramic-on-polyethylene bearings, and ceramic-on-ceramic and metal-on-metal bearings are in worldwide use, respectively. There are currently three

Table 2.5 Typical physical properties of ultrahigh-molecular-weight polyethylene (UHMWPE) inserts

Property	CPE	XLPE
Melting temperature (°C)	135–145	130–140
Crystallinity (%)	48–60	40–52
Density (mg/mm^3)	0.93–0.94	0.93
Poisson's ratio	0.46	0.46
Yield strength (MPa)	20–24	20–24
Ultimate tensile strength (MPa)	50–60	42–60
Elongation at breakage (%)	360–520	200–300
Modulus of elasticity (MPa)	800–900	800–900

types of ultrahigh-molecular-weight polyethylene (UHMWPE) material: conventional UHMWPE (CPE), highly cross-linked UHMWPE (XLPE), and vitamin *E*-containing highly cross-linked UHMWPE (VEPE) (FDA Draft Guidance, 2016). Table 2.5 shows physical properties of CPE and XLPE (Morrison et al., 2015). Recently, many adverse clinical experiences regarding metal-on-metal bearing devices have been reported (Okazaki, 2014). Consideration of the reactive chemical nature of these metallic particles has led to concerns about their potential to cause hypersensitivity and osteolysis. Moreover, the wear debris can damage bone and/or tissue surrounding the implant and joint. This is referred to as adverse local tissue reaction (ALTR) or adverse reaction to metal debris (ARMD). Recently, the presence of pseudotumors has attracted attention and caused concern. ALVALs are a typical example of pseudotumors and the number of reports on them has been increasing rapidly. A hip simulator is an efficient tool for preclinical tests to minimize patient risk. The history of simulator development, mainly driven by research, has led to the development of many diverse designs. The loading waves and angle of flexion or extension, angle of adduction or abduction, and angle of inward or outward rotation for hip simulator wear testing are specified in ISO 14242-1 (ISO 14242-1, 2014). ISO 14242-1 defines the load waveform (Fig. 2.42A) and angular changes (Fig. 2.42B) caused by abduction/adduction, flexion/extension, and outward/inward rotation of the hip joint. Many types of artificial hip joint simulator have been developed (Affatato et al., 2008a). GUR1050, GUR1020, and GUR 4150 UHMWPE materials are mainly used for the bearing inserts of artificial hip joints. Co-Cr-Mo femoral head surfaces affected by wear are finished to a smooth surface (Ra: approximately 0.01–0.03 μm) (Wang et al., 1988). Fig. 2.43 shows the weight changes during wear tests of an artificial hip joint consisting of a cross-linked UHMWPE insert and a 26 mm Co-Cr-Mo femoral head (Okazaki, 2014). A negative value on the vertical axis indicates a decrease in the weight (wear loss) of the UHMWPE insert. For control samples subjected to loading but without rotation, an increase in weight caused by water absorption is found for four polyethylene inserts. For a cross-linked UHMWPE bearing, the increase in wear is small even with increasing number of wear cycles. On the other hand, for a non-cross-linked bearing, the wear loss increases markedly with increasing number of

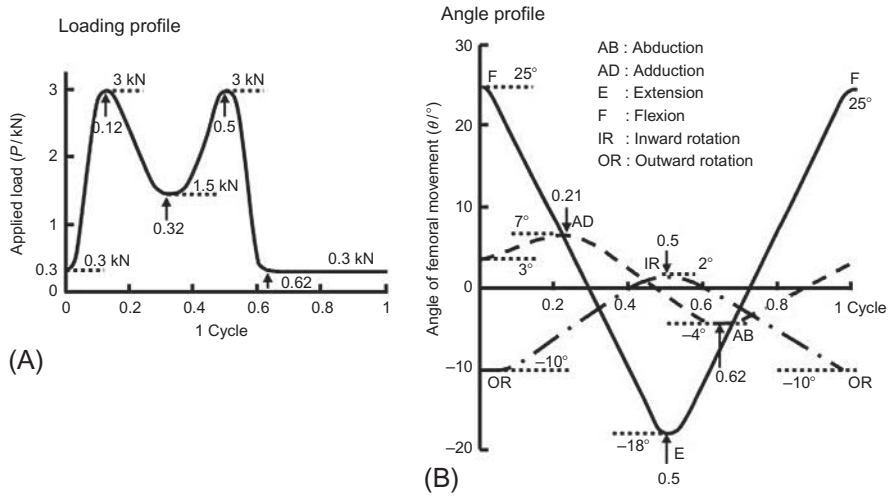


Fig. 2.42 (A) Loading and (B) angle profiles in the human hip joint simulation.

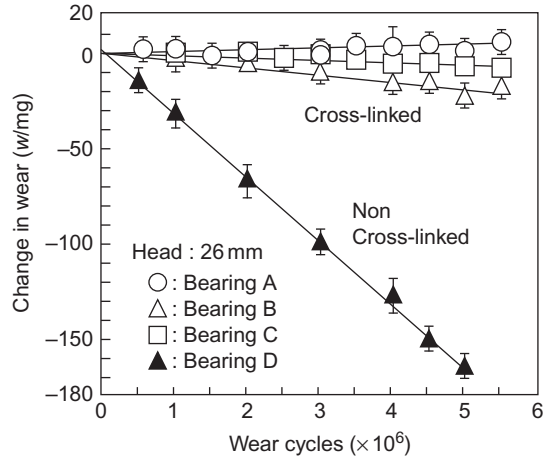


Fig. 2.43 Wear properties of 26-mm articular head metal-on-polyethylene bearings measured with hip simulator.

wear cycles (Okazaki, 2014). Fig. 2.44 shows the effects of the γ-radiation dose on the change in density (Fig. 2.44A) and the hip simulator volumetric wear rate per million cycles (mm^3/Mc) (Fig. 2.44B) (Morrison et al., 2015; Edidin et al., 1999; McKellop et al., 1999; Wang et al., 1998). The wear rate of various hip joints made of highly cross-linked UHMWPE (XLPE) markedly decreases when they are subjected to a radiation dose of 40 kGy or more. Simulator test results reported in the literature are summarized below. Fig. 2.45 shows the effect of the femoral head diameter on the hip simulator volumetric wear rates of CPE and XLPE reported in the literature

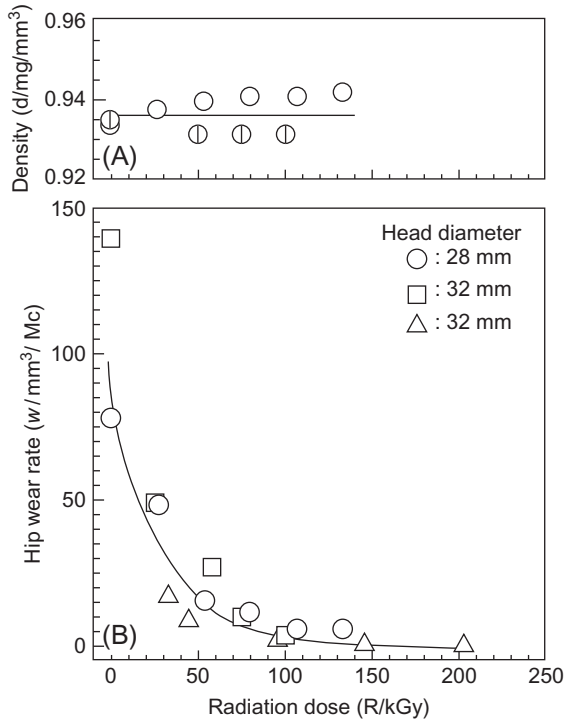


Fig. 2.44 Effect of γ-radiation dose on change in (A) density of UHMWPE and (B) hip simulator volumetric wear rate.

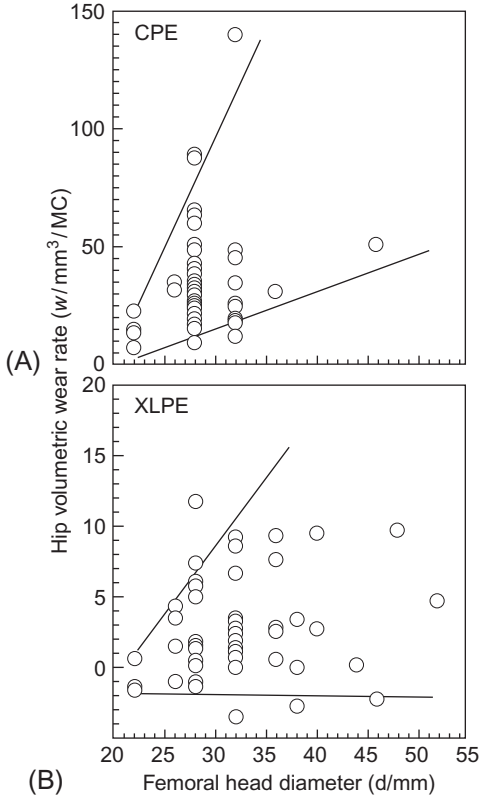


Fig. 2.45 Effect of femoral head diameter on (A) hip simulator volumetric wear rates of conventional UHMWPE and (B) highly cross-nked UHMWPE.

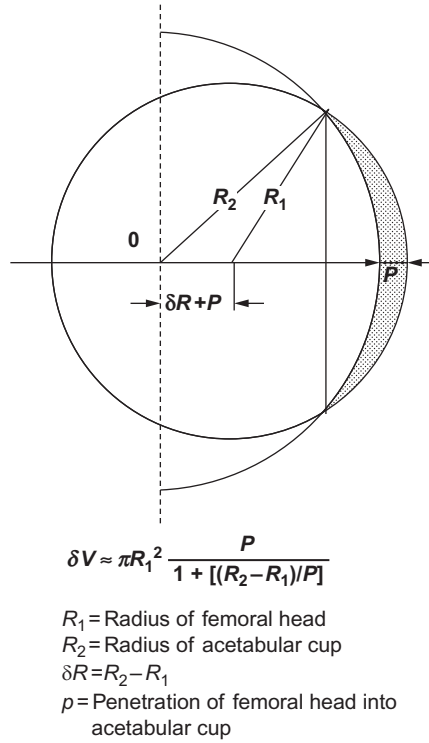


Fig. 2.46 Penetration of spherical femoral head into acetabular cup.

(Affatato et al., 2008a; Clarke et al., 1996; Moro et al., 2014; Hashimoto et al., 2013; Geerdink et al., 2006; Edidin and Kurtz, 2000; John, 2015; Moro et al., 2015; Biomet Biomaterials Laboratory, 2007; Trommer et al., 2015; Trommer and Maru, 2017; Taddei et al., 2008; Laurent et al., 2008; Saikko et al., 2001; Affatato et al., 2008b; González-Mora et al., 2009; Affatato et al., 2016; Loving et al., 2013; Bragdon et al., 2003; Herrera et al., 2007; Johnson et al., 2014; Muratoglu et al., 2001a; Saikko, 1995; McKellop et al., 2006; Shen et al., 2011; Oral et al., 2006; Essner et al., 2005; Liao et al., 2003; Estok II et al., 2007; Holley et al., 2005; Muratoglu et al., 2001b; Kang et al., 2009; Unsworth et al., 2000; Wang et al., 1997; Clarke and Gustafson, 2000; Mimnaugh et al., 2009; Hermida et al., 2003; McKellop et al., 2000; Galvin et al., 2008; Smith and Unsworth, 1999; Smith and Unsworth, 2000; Greer et al., 1955). The hip wear rates of both CPE and XLPE slightly increase with increasing femoral head diameter. Penetration of the femoral head into an UHMWPE acetabular cup is evaluated using formula (2.20), as shown in Fig. 2.46 (Dowson et al., 1993; Dowson, 1995).

$$\delta V = \pi R_1{}^2 \times p/[1 + (R_2 - R_1)/p] \tag{2.20}$$

Here, δV (volumetric wear) represents the volume of the UHMWPE removed by wear (mm^3), p is the penetration (linear wear) of the femoral head into the UHMWPE acetabular cup (mm/year), and R_1 and R_2 are the radii of the femoral head and acetabular cup (mm), respectively. When $p \gg (R_2 - R_1)$, the standard tunneling equation ($\delta V = \pi R_1^2 \times p$) emerges, but when p is equal to the radial clearance (R_2–R_1), the volumetric wear (δV) is only half that given by the tunneling equation (Dowson et al., 1993; Dowson, 1995). Fig. 2.47 shows the effect of the femoral head diameter on the linear head penetration (linear wear) rates of CPE and XLPE in clinical use reported in the literature (Tarasevicius et al., 2008; Eggli et al., 2002; Lachiewicz et al., 2009; Campbell et al., 2010; Capello et al., 2011; Lee et al., 2011; Mutimer et al., 2010; Ranawat et al., 2012; Reynolds et al., 2012; Devane et al., 1997;

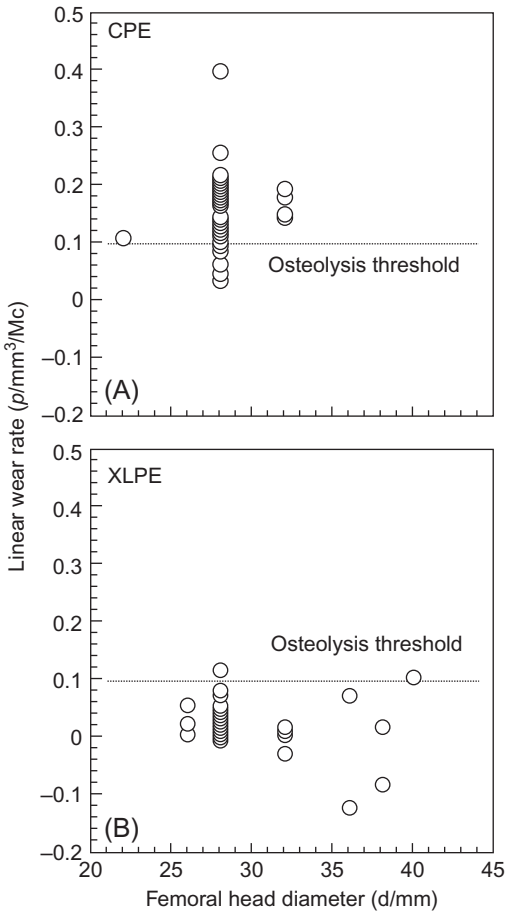


Fig. 2.47 Effect of femoral head diameter on linear wear (penetration) rates of femoral head in clinical use: (A) CPE and (B) XLPE.

Leung et al., 2007; Engh Jr et al., 2012; Rajadhyaksha et al., 2009; Martell et al., 2003; Bitsch et al., 2008; Engh Jr et al., 2006; Glyn-Jones et al., 2008a; Beksaç et al., 2009; Bragdon et al., 2006; Thomas et al., 2011; McCalden et al., 2009; Dorr et al., 2005; Kim, 2005; Hammerberg et al., 2010; Hopper Jr et al., 2003; Kawate et al., 2009; Krushell et al., 2005; Manning et al., 2005; Nakahara et al., 2010; Olyslaegers et al., 2008; Triclot et al., 2007; Geerdink et al., 2009; Calvert et al., 2009; D'Antonio et al., 2005; Geller et al., 2006; Callaghan et al., 1995; Bragdon et al., 2007; Kusaba et al., 2002; Heisel et al., 2004; Glyn-Jones et al., 2008b; Kurtz et al., 2011; Mu et al., 2009). It is found that the effect of the femoral head diameter on the linear head penetration rate is small. Linear wear of 0.1 mm/year or less is recommended so that osteolysis does not occur. This value is known as the osteolysis threshold. The UHMWPE wear rate in clinical use can be estimated using formula (2.20). For a bearing with an UHMWPE insert subjected to the wear rate of cross-linked UHMWPE, the wear rate is small, suggesting its excellent long-term clinical performance.

2.8.5 Wear properties of artificial knee prostheses using knee simulator

With the advent of a super-aging society, total knee replacement (TKR) is an increasingly common surgical intervention for the treatment of arthritis and joint degeneration. Also, TKR is projected to become increasingly common for younger, heavier, and more active patients. This generates a need for longer implantation periods to reduce the number of revision surgeries required in the lifetime of TKR patients. Longer implantation periods and younger, heavier, and more active patients both contribute to increased tribological wear on artificial knee joints. UHMWPE is widely used as a bearing material of artificial knee joints and is the key material for achieving excellent long-term results in total knee joint arthroplasties. UHMWPE wear or, more precisely, debris caused by wear can lead to cellular reactions resulting in osteolysis and consequently loosening of the implant. Experimental knee wear simulators have been developed in an effort to provide insight into UHMWPE wear mechanisms and preclinically evaluate implant designs and bearing materials.

There is variation in the constraint of the tibial insert depending on whether the posterior cruciate ligament is preserved (cruciate retaining; CR) or sacrificed (posterior stabilized; PS) at the time of knee joint surgery. The clinical use of fixed-bearing TKR is also increasing relative to the use of mobile-bearing (MBT) TKR. The wear rates of CR artificial knee joint UHMWPE inserts are examined using a knee joint simulator satisfying ISO 14243-1 (load control) and ISO 14243-3 (displacement control) (Fig. 2.48) (ISO 14243-1, 2009; ISO 14243-2, 2016; ISO 14243-3, 2014). Many types of knee joint simulator have been developed by Advanced Mechanical Technology Inc. (AMTI six-station), Simulation Solutions Ltd. (Prosim six-station), Instron Ltd. (Instron-Stanmore four-station), MTS Systems Corp. (Bionix six-station), and other companies. The wear rate of knee

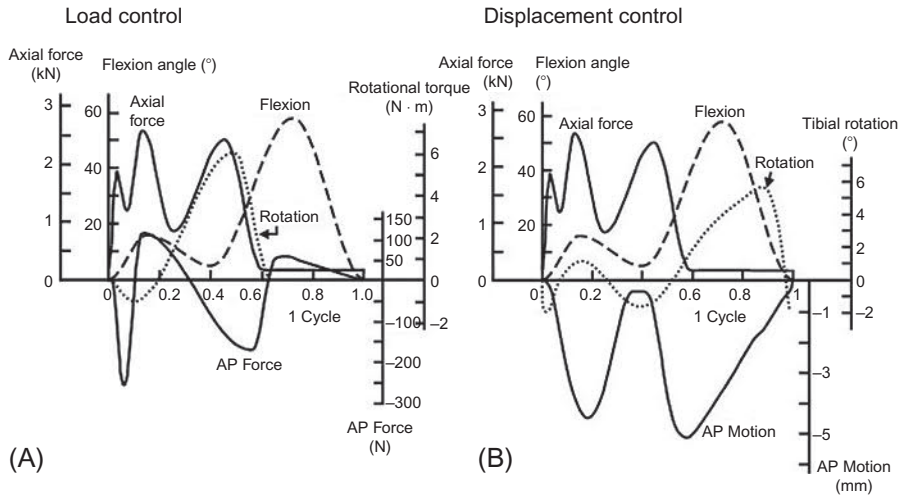


Fig. 2.48 Knee simulator input profiles for axial force, flexion angle, rotational torque (tibial rotation), and AP force (motion) for (A) load control and (B) displacement control.

joints composed of a UHMWPE insert and a Co-Cr-Mo alloy or oxidized Zr femoral component linearly increases with increasing number of wear cycles, and the volumetric wear rate per million cycles is approximately 6–18 mm^3/Mc (Okazaki, 2019). The wear rate of various knee joints made of XLPE markedly decreases when they are subjected to a radiation dose of 40 kGy or more. The 10-year cumulative percentage revision rate since the primary operation slightly decreases with decreasing volumetric knee simulator wear rate for CPE and XLPE knee joint inserts. The XLPE knee joint is shown to exhibit reduced in vivo wear and lower rates of revision for TKR. National joint replacement registries have been established in the National Joint Registry 14th Annual Report 2017 (NJR) and the Australian Orthopedic Association National Joint Replacement Registry 2017 Annual Report (AOA), and so forth, to monitor revision replacement surgery. On the other hand, Nexgen and PFC Sigma (both CPE) knee joints show the lowest revision rate in the AOA and NJR registries. Volumetric wear rates of 3 mm^3/Mc for XLPE knee joint inserts and 15 mm^3/Mc for CPE knee joint inserts are recommended as goals for the development of new knee joints as shown in Fig. 2.49.

2.9 Future trends

Zr, Nb, and Ta are important alloying elements for Ti alloys to attain long-term superior corrosion resistance and biocompatibility. Furthermore, the oxides ZrO_2, Nb_2O_5, and Ta_2O_5 strengthen the passive film and prevent the release of metal ions.

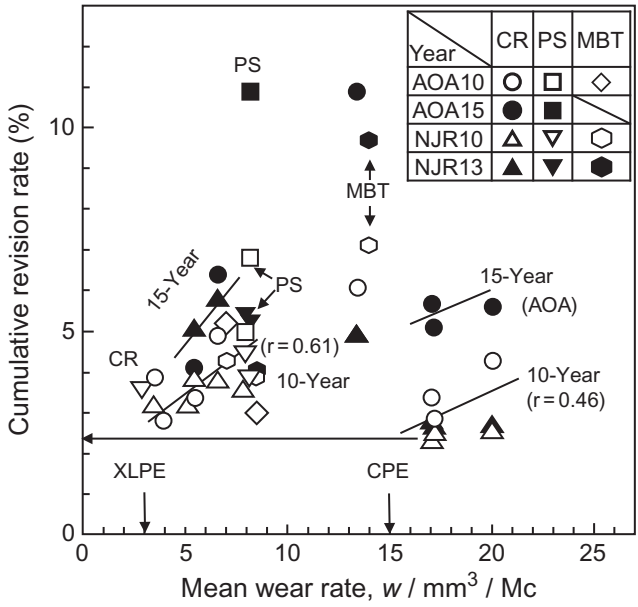


Fig. 2.49 Relationship between 10-, 13-, or 15-year cumulative percentage revision in AOA and NJR registries and mean knee simulator wear rate.

Ti-15Zr-4Nb-4Ta alloy has excellent room-temperature strength and fatigue properties with high biocompatibility. In fact, the biological safety of this alloy has already been proven in cytotoxicity tests, sensitivity tests, genetic damage tests, and rabbit implantation tests. This has created high expectations for the long-term future use of this alloy as a viable implant material.

With the advent of a super-aging society, there has been an increase in the number of operations to insert orthopedic implants (such as osteosynthetic materials and prosthetic joints) that compensate for impaired body functions. The development of orthopedic implants optimized for each patient's needs or skeletal structure (custom-made orthopedic implants) has been made possible owing to advances in fabrication techniques (Okazaki, 2012b). Custom-made orthopedic implants are medical devices that exhibit optimal mechanical compatibility and fixation while maintaining the function of basic orthopedic implants with only the minimal improvements applied to the incompatible part caused by the patient's condition (Fig. 2.50). "Average direction" in Fig. 2.50 indicates the conformational changes of a basic orthopedic implant and the standard for the maximum extent of change is approximately 20%. Owing to the rapid progress of three-dimensional (3D) layer manufacturing technologies, the development of orthopedic implants customized to the skeletal structure and the symptoms of each patient is now possible. Table 2.6 shows examples of the customizable contents of custom-made orthopedic implants.

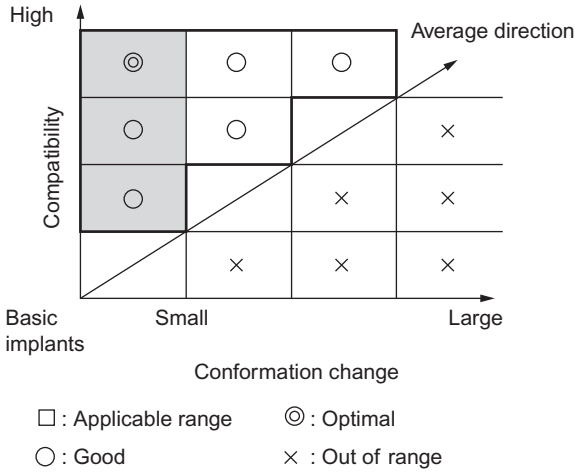


Fig. 2.50 Definition of custom-made orthopedic implants.

Table 2.6 Examples of custom-made orthopedic implants

Implant	Customizable content
Bone plate	• The width, thickness, and length are adjustable to enable optimal fixation. The location and number of holes are adjustable to enable sufficient fixation while avoiding the point of fracture • Adjustment of bone-contacting surface to the shape of the bone
Metaphyseal plate	• The width, thickness, and length are adjustable to enable optimal fixation • Adjustment of bone-contacting surface to the shape of the bone
Intramedullary nail	• The length and diameter are adjustable • Adjustment of curvature to shape of bone • The location, insertion direction, and number of rotation-preventing horizontal screws are adjustable
Short femoral nail	• The location, thickness, and length of the nail are adjustable • The curvature of the nail can be adjusted to the shape of the bone surface • The location, insertion direction, and number of rotation-preventing horizontal screws are adjustable
Artificial hip joint	• The cup shape can be optimized
Acetabular component	• The body-neck angle is adjustable
Femoral component	• Proximal: adjustable in lateral, medial, and anteroposterior directions • Distal: thickness and length can be optimized
Artificial knee joint	• The shape of the tibial tray can be optimized
Femoral component	• The length and thickness of the stem are adjustable to the bone shape
Tibial component	

References

Affatato, S., Spinelli, M., Zavalloni, M., Mazzega-Fabbro, C., Viceconti, M., 2008a. Tribology and total hip joint replacement: Current concepts in mechanical simulation. Med. Eng. Phys. 30, 1305–1317.

Affatato, S., Zavalloni, M., Taddei, P., Di Foggia, M., Fagnano, C., Viceconti, M., 2008b. Comparative study on the wear behaviour of different conventional and cross-linked polyethylenes for total hip replacement. Tribol. Int. 41 (8), 813–822.

Affatato, S., Freccero, N., Taddei, P., 2016. The biomaterials challenge: a comparison of polyethylene wear using a hip joint simulator. J. Mech. Behav. Biomed. Mater. 53, 40–48.

ASTM F 1713-08, 2013. Standard specification for wrought titanium-13niobium-13zirconium alloy for surgical implant applications. American Society for Testing and Materials, West Conshohocken, PA.

ASTM F 1813-13, 2013. Standard specification for wrought titanium-12molybdenum-6zirconium-2 iron alloy for surgical implant. American Society for Testing and Materials, West Conshohocken, PA.

ASTM F 2063-12, 2012. Standard specification for wrought nickel-titanium shape memory alloys for medical devices and surgical implants. American Society for Testing and Materials, West Conshohocken, PA.

Beksaç, B., Salas, A., Valle, A.G.D., Salvati, E.A., 2009. Wear is reduced in THA performed with highly cross-linked polyethylene. Clin. Orthop. Relat. Res. 467 (7), 1765–1772.

Biomet Biomaterials Laboratory, 2007. E-Poly HXLPE: The Revolutionary Second Generation, Vitamin E Stabilised Highly Crosslinked UHMWPE. .

R.G. Bitsch, T. Loidolt, C. Heisel, S. Ball, T.P. Schmalzried, Reduction of osteolysis with use of Marathon cross-linked polyethylene: a concise follow-up, at a minimum of five years, of a previous report, J. Bone Joint Surg. Am. 90-A (7) (2008) 1487–1491.

Bragdon, C.R., Jasty, M., Muratoglu, O.K., O'Connor, D.O., Harris, W.H., 2003. Third-body wear of highly cross-linked polyethylene in a hip simulator. J. Arthroplast. 18 (5), 553–561.

Bragdon, C.R., Barrett, S., Martell, J.M., Greene, M.E., Malchau, H., Harris, W.H., 2006. Steady-state penetration rates of electron beam-irradiated, highly cross-linked polyethylene at an average 45-month follow-up. J. Arthroplast. 21 (7), 935–943.

Bragdon, C.R., Kwon, Y.M., Geller, J.A., Greene, M.E., Freiberg, A.A., Harris, W.H., Malchau, H., 2007. Minimum 6-year followup of highly cross-linked polyethylene in THA. Clin. Orthop. Relat. Res. 465, 122–127.

Callaghan, J.J., Pedersen, D.R., Olejniczak, J.P., Goetz, D.D., Johnston, R.C., 1995. Radiographic measurement of wear in 5 cohorts of patients observed for 5 to 22 years. Clin. Orthop. Relat. Res. 317, 14–18.

Calvert, G.T., Devane, P.A., Fielden, J., Adams, K., Horne, J.G., 2009. A double-blind, prospective, randomized controlled trial comparing highly cross-linked and conventional polyethylene in primary total hip arthroplasty. J. Arthroplast. 24 (4), 505–510.

Campbell, D.G., Field, J.R., Callary, S.A., 2010. Second-generation highly cross-linked X3™ polyethylene wear: a preliminary radiostereometric analysis study. Clin. Orthop. Relat. Res. 468 (10), 2704–2709.

Capello, W.N., D'Antonio, J.A., Ramakrishnan, R., Naughton, M., 2011. Continued improved wear with an annealed highly cross-linked polyethylene. Clin. Orthop. Relat. Res. 469 (3), 825–830.

Clarke, I.C., Gustafson, A., 2000. Clinical and hip simulator comparisons of ceramic-on-polyethylene and metal-on-polyethylene wear. Clin. Orthop. Relat. Res. 379, 34–40.
Clarke, I.C., Gustafson, A., Jung, H., Fujisawa, A., 1996. Hip-simulator ranking of polyethylene wear: comparisons between ceramic heads of different sizes. Acta Orthop. Scand. 67 (2), 128–132.
D'Antonio, J.A., Manley, M.T., Capello, W.N., Bierbaum, B.E., Ramakrishnan, R., Naughton, M., Sutton, K., 2005. Five-year experience with crossfire® highly cross-linked polyethylene. Clin. Orthop. Relat. Res. 441, 143–150.
Devane, P.A., Horne, J.G., Martin, K., Coldham, G., Krause, B., 1997. Three-dimensional polyethylene wear of a press-fit titanium prosthesis: factors influencing generation of polyethylene debris. J. Arthroplasty 12 (3), 256–266.
Dorr, L.D., Wan, Z., Shahrdar, C., Sirianni, L., Boutary, M., Yun, A., 2005. Clinical performance of a Durasul highly cross-linked polyethylene acetabular liner for total hip arthroplasty at five years. J. Bone Joint Surg. Am. 87-A (8), 1816–1821.
Dowson, D., 1995. A comparative study of the performance of metallic and ceramic femoral head components in total replacement hip joint. Wear 190, 171–183.
Dowson, D., Jobbins, B., Seyed-Harraf, A., 1993. An evaluation of the penetration of ceramic femoral heads into polyethylene acetabular cups. Wear 162–164, 880–889.
Edidin, A.A., Kurtz, S.M., 2000. Influence of mechanical behavior on the wear of 4 clinically relevant polymeric biomaterials in a hip simulator. J. Arthroplast. 15 (3), 321–331.
Edidin, A.A., Pruitt, L., Jewett, C.W., Crane, D.J., Roberts, D., Kurtz, S.M., 1999. Plasticity-induced damage layer is a precursor to wear in radiation-cross-linked UHMWPE acetabular components for total hip replacement. J. Arthroplast. 14 (5), 616–627.
Eggli, S., z'Brun, S., Gerber, C., Ganz, R., 2002. Comparison of polyethylene wear with femoral heads of 22 mm and 32 mm. J. Bone Joint Surg. Br. 84-B (3), 447–451.
Engh Jr., C.A., Stepniewski, A.S., Ginn, S.D., Beykirch, S.E., Sychterz-Terefenko, C.J., Hopper Jr., R.H., Engh, C.A., 2006. A randomized prospective evaluation of outcomes after total hip arthroplasty using cross-linked Marathon and non–cross-linked Enduron polyethylene liners. J. Arthroplast. 21 (6 Suppl. 2), 17–25.
Engh Jr., C.A., Hopper Jr., R.H., Huynh, C., Ho, H., Sritulanondha, S., Engh Sr., C.A., 2012. A prospective, randomized study of cross-linked and non-cross-linked polyethylene for total hip arthroplasty at 10-year follow-up. J. Arthroplast. 27 (8 Suppl. 1), 2–7.
Essner, A., Schmidig, G., Wang, A., 2005. The clinical relevance of hip joint simulator testing: in vitro and in vivo comparisons. Wear 259 (7–12), 882–886.
Estok II, D.M., Burroughs, B.R., Muratoglu, O.K., Harris, W.H., 2007. Comparison of hip simulator wear of 2 different highly cross-linked ultra high molecular weight polyethylene acetabular components using both 32- and 38-mm femoral head. J. Arthroplast. 22 (4), 581–589.
FDA Draft Guidance, 2016. Characterization of Ultrahigh Molecular Weight Polyethylene (UHMWPE) Used in Orthopedic Devices. Center for Devices and Radiological Health.
Galvin, A., Brockett, C., Williams, S., Hatto, P., Burton, A., Isaac, G., Stone, M., Ingham, E., Fisher, J., 2008. Comparison of wear of ultra-high molecular weight polyethylene acetabular cups against surface-engineered femoral heads. Proc. Inst. Mech. Eng. Part H, J. Eng. Med. 222 (7), 1073–1080.
Geerdink, C.H., Grimm, B., Ramakrishnan, R., Rondhuis, J., Verburg, A.J., Tonino, A.J., 2006. Crosslinked polyethylene compared to conventional polyethylene in total hip replacement: pre-clinical evaluation, in-vitro testing and prospective clinical follow-up study. Acta Orthop. 77 (5), 719–725.

Geerdink, C.H., Grimm, B., Vencken, W., Heyligers, I.C., Tonino, A.J., 2009. Cross-linked compared with historical polyethylene in THA: An 8-year clinical study. Clin. Orthop. Relat. Res. 467 (4), 979–984.

Geller, J.A., Malchau, H., Bragdon, C., Greene, M., Harris, W.H., Freiberg, A.A., 2006. Large diameter femoral heads on highly cross-linked polyethylene: minimum 3-year results. Clin. Orthop. Relat. Res. 447, 53–59.

Glyn-Jones, S., Isaac, S., Hauptfleisch, J., McLardy-Smith, P., Murray, D.W., Gill, H.S., 2008a. Does highly cross-linked polyethylene wear less than conventional polyethylene in total hip arthroplasty? A double-blind, randomized, and controlled trial using roentgen stereophotogrammetric analysis. J. Arthroplasty 23 (3), 337–343.

Glyn-Jones, S., McLardy-Smith, P., Gill, H.S., Murray, D.W., 2008b. The creep and wear of highly cross-linked polyethylene. J. Bone Joint Surg. Br. 90-B (5), 556–561.

González-Mora, V.A., Hoffmann, M., Stroosnijder, R., Gil, F.J., 2009. Wear tests in a hip joint simulator of different CoCrMo counterfaces on UHMWPE. Mater. Sci. Eng. C 29, 153–158.

Greer, K.W., Schmodt, M.B., Tariah, I.B., 1955. A comparison of the wear properties of UHMWPE produced from two powder grades. In: 21st Annual Meeting of the Society for Biomaterials, March 18–22, San Francisco, California, p. 227.

Hammerberg, E.M., Wan, Z., Dastane, M., Dorr, L.D., 2010. Wear and range of motion of different femoral head sizes. J. Arthroplast. 25 (6), 839–843.

Hashimoto, M., Hayashi, K., Kitaoka, S., 2013. A comparative hip joint simulator study of the wear, debris and metal ion release of CoCrMo/CoCrMo and CoCrMo/CL-UHMWPE couplings. Nano Biomed. 5 (1), 25–30.

Heisel, C., Silva, M., Rosa, M.A.D., Schmalzried, T.P., 2004. Short-term in vivo wear of cross-linked polyethylene. J. Bone Joint Surg. Am. 86-A (4), 748–751.

Hermida, J.C., Bergula, A., Chen, P., Colwell Jr., C.W., D'Lima, D.D., 2003. Comparison of the wear rates of 28 mm and 32 mm femoral heads on cross-linked polyethylene acetabular cups in a wear simulator. J. Bone Joint Surg. Am. 85-A (12), 2325–2331.

Herrera, L., Lee, R., Longaray, J., Essner, A., Wang, A., 2007. Hip simulator evaluation of the effect of femoral head size on sequentially cross-linked acetabular liners. Wear 263 (7–12), 1034–1037.

Holley, K.G., Furman, B.D., Babalola, O.M., Lipman, J.D., Padgett, D.E., Wright, T.M., 2005. Impingement of acetabular cups in a hip simulator: comparison of highly cross-linked and conventional polyethylene. J. Arthroplast. 20 (7 Suppl. 3), 77–86.

Hopper Jr., R.H., Young, A.M., Orishimo, K.F., McAuley, J.P., 2003. Correlation between early and late wear rates in total hip arthroplasty with application to the performance of Marathon cross-linked polyethylene liners. J. Arthroplast. 18 (7 Suppl. 1), 60–67.

ISO 14242-1, 2014. Implants for Surgery—Wear of Total Hip-Joint Prostheses—Part 1: Loading and Displacement Parameters for Wear-Testing Machines and Corresponding Environmental Conditions for Test, second ed. International Organization for Standardization, Geneva, Switzerland.

ISO 14243-1, 2009. Implants for Surgery–Wear of Total Knee-Joint Prostheses–Part 1: Loading and Displacement Parameters for Wear-Testing Machines with Load Control and Corresponding Environmental Conditions for Test, second ed. International Organization for Standardization, Geneva, Switzerland.

ISO 14243-2, 2016. Implants for Surgery–Wear of Total Knee-Joint Prostheses–Part 2: Methods of Measurement, third ed. International Organization for Standardization, Geneva, Switzerland.

ISO 14243-3, 2014. Implants for Surgery–Wear of Total Knee-Joint Prostheses–Part 3: Loading and Displacement Parameters for Wear-Testing Machines with Displacement Control and Corresponding Environmental Conditions for Test, second ed. International Organization for Standardization, Geneva, Switzerland.
ISO 16428, 2005. Implants for Surgery—Test Solutions and Environmental Conditions for Static and Dynamic Corrosion Tests on Implantable Materials and Medical Devices. International Organization for Standardization, Geneva, Switzerland.
ISO 5832-1, 2016. Implants for Surgery – Metallic Materials—Part 1: Wrought Stainless Steel. International Organization for Standardization, Geneva, Switzerland.
ISO 5832-11, 2014. Implants for Surgery—Metallic Material—Part 11: Wrought Titanium 6-Aluminium 7-Niobium Alloy. International Organization for Standardization, Geneva, Switzerland.
ISO 5832-12, 2007. Implants for Surgery—Metallic Materials—Part 12: Wrought Cobalt-Chromium-Molybdenum Alloy. International Organization for Standardization, Geneva, Switzerland.
ISO 5832-14, 2007. Implants for Surgery—Metallic Materials—Part 14: Wrought Titanium 15-Molybdenum 5-Zirconium 3-Aluminium Alloy. International Organization for Standardization, Geneva, Switzerland.
ISO 5832-2, 2018. Implants for Surgery – Metallic Materials—Part 2: Unalloyed Titanium. International Organization for Standardization, Geneva, Switzerland.
ISO 5832-3, 2016. Implants for Surgery – Metallic Materials—Part 3: Wrought Titanium 6-Aluminium 4-Vanadium Alloy. International Organization for Standardization, Geneva, Switzerland.
ISO 5832-4, 2014. Implants for Surgery—Metallic Materials—Part 4: Cobalt-Chromium - Molybdenum Casting Alloy. International Organization for Standardization, Geneva, Switzerland.
ISO 5832-9, 2007. Implants for Surgery – Metallic Materials—Part 9: Wrought High Nitrogen Stainless Steel. International Organization for Standardization, Geneva, Switzerland.
ISO 7206-4, 2010. Implants for Surgery—Partial and Total Hip Joint Prostheses—Part 4: Determination of Endurance Properties of Stemmed Femoral Components. International Organization for Standardization, Geneva, Switzerland.
JIS T 0302, 2000. Testing Method for Corrosion Resistance of Metallic Biomaterials by Anodic Polarization Measurement. Japanese Standards Association, Tokyo, Japan.
JIS T 0304, 2002. Testing Method for Metal Release from Metallic Biomaterials. Japanese Standards Association, Tokyo, Japan.
JIS T 0309, 2009. Testing Method for Fatigue Properties of Metallic Biomaterials. Japanese Standards Association, Tokyo, Japan.
JIS T 0312, 2009. Testing Methods for Bending Properties of Metallic Osteosynthesis Devices. Japanese Standards Association, Tokyo, Japan.
JIS T 0313, 2009. Testing Methods for Compression Bending Properties of Metallic Osteosynthesis Devices. Japanese Standards Association, Tokyo, Japan.
JIS T 7401-3, 2002. Titanium Materials for Surgical Implant Applications Part 3: Wrought Titanium 6-Aluminium 2-Niobium 1-Tantalum Alloy. Japanese Standards Association, Tokyo, Japan.
JIS T 7401-4, 2009. Titanium Materials for Surgical Implant Applications Part 4: Wrought Titanium 15-Zirconium 4-Niobium 4-Tantalum Alloy. Japanese Standards Association, Tokyo, Japan.
John, K.R.S., 2015. Evaluation of two total hip bearing materials for resistance to wear using a hip simulator. Lubricants 3 (2), 459–474.

Johnson, A.J., Loving, L., Herrera, L., Delanois, R.E., Wang, A., Mont, M.A., 2014. Short-term wear evaluation of thin acetabular liners on 36-mm femoral heads. Clin. Orthop. Relat. Res. 472 (2), 624–629.

Kang, L., Galvin, A.L., Fisher, J., Jin, Z., 2009. Enhanced computational prediction of polyethylene wear in hip joints by incorporating cross-shear and contact pressure in additional to load and sliding distance: effect of head diameter. J. Biomech. 42 (7), 912–918.

Kawate, K., Ohmura, T., Kawahara, I., Tamai, K., Ueha, T., Takemura, K., 2009. Differences in highly cross-linked polyethylene wear between zirconia and cobalt-chromium femoral heads in Japanese patients: a prospective, randomized study. J. Arthroplasty 24 (8), 1221–1224.

Kim, Y.-H., 2005. Comparison of polyethylene wear associated with cobalt-chromium and zirconia heads after total hip replacement: a prospective, randomized study. J. Bone Joint Surg. Am. 87-A (8), 1769–1776.

Krushell, R.J., Fingeroth, R.J., Cushing, M.C., 2005. Early femoral head penetration of a highly cross-linked polyethylene liner vs a conventional polyethylene liner: a case-controlled study. J. Arthroplast. 20 (7 Suppl. 3), 73–76.

Kurtz, S.M., Gawel, H.A., Patel, J.D., 2011. History and systematic review of wear and osteolysis outcomes for first-generation highly crosslinked polyethylene. Clin. Orthop. Relat. Res. 469, 2262–2277.

Kusaba, A., Kuroki, Y., Kondo, S., Hirose, I., Ito, Y., Shirasaki, Y., Tateishi, T., Scholz, J., 2002. Frictional torque and wear of retrieved hip prostheses: a comparison between alumina/PE and Co-Cr/PE prostheses. J. Long-Term Eff. Med. Implants 12 (1), 53–62.

Lachiewicz, P.F., Heckman, D.S., Soileau, E.S., Mangla, J., Martell, J.M., 2009. Femoral head size and wear of highly cross-linked polyethylene at 5 to 8 years. Clin. Orthop. Relat. Res. 467 (12), 3290–3296.

Laurent, M.P., Johnson, T.S., Crowninshield, R.D., Blanchard, C.R., Bhambri, S.K., Yao, J.Q., 2008. Characterization of a highly cross-linked ultrahigh molecular-weight polyethylene in clinical use in total hip arthroplasty. J. Arthroplast. 23 (5), 751–761.

Lee, J.-H., Lee, B.W., Lee, B.-J., Kim, S.-Y., 2011. Midterm results of primary total hip arthroplasty using highly cross-linked polyethylene: minimum 7-year follow-up study. J. Arthroplast. 26 (7), 1014–1019.

Leung, S.B., Egawa, H., Stepniewski, A., Beykirch, S., Engh Jr., C.A., Engh Sr., C.A., 2007. Incidence and volume of pelvic osteolysis at early follow-up with highly cross-linked and noncross-linked polyethylene. J. Arthroplast. 22 (6 Suppl. 2), 134–139.

Liao, Y.-S., McNulty, D., Hanes, M., 2003. Wear rate and surface morphology of UHMWPE cups are affected by the serum lubricant concentration in a hip simulation test. Wear 255 (7–12), 1051–1056.

Loving, L., Lee, R.K., Herrera, L., Essner, A.P., Nevelos, J.E., 2013. Wear performance evaluation of a contemporary dual mobility hip bearing using multiple hip simulator testing conditions. J. Arthroplast. 28 (6), 1041–1046.

Manning, D.W., Chiang, P.P., Martell, J.M., Galante, J.O., Harris, W.H., 2005. In vivo comparative wear study of traditional and highly cross-linked polyethylene in total hip arthroplasty. J. Arthroplast. 20 (7), 880–886.

Martell, J.M., Verner, J.J., Incavo, S.J., 2003. Clinical performance of a highly cross-linked polyethylene at two years in total hip arthroplasty: a randomized prospective trial. J. Arthroplast. 18 (7 Suppl. 1), 55–59.

McCalden, R.W., MacDonald, S.J., Rorabeck, C.H., Bourne, R.B., Chess, D.G., Charron, K.D., 2009. Wear rate of highly cross-linked polyethylene in total hip arthroplasty: a randomized controlled trial. J. Bone Joint Surg. Am. 91-A (4), 773–782.

McKellop, H., Shen, F.-W., Lu, B., Campbell, P., Salovey, R., 1999. Development of an extremely wear-resistant ultra high molecular weight polyethylene for total hip replacements. J. Orthop. Res. 17, 157–167.

McKellop, H., Shen, F.-W., Lu, B., Campbell, P., Salovey, R., 2000. Effect of sterilization method and other modifications on the wear resistance of acetabular cups made of ultra-high molecular weight polyethylene: a hip-simulator study. J. Bone Joint Surg. Am. 82-A (12), 1708–1725.

McKellop, H., Liao, Y.-S., Shen, F.-W., McGarry, W., 2006. Effect of femoral head size, material, surface roughness and serum concentration on the wear of 5 Mrad crosslinked- remelted UHMWPE acetabular cups. In: 52nd Annual Meeting of the Orthopaedic Research Society, March 19–22, Chicago, Illinois, USA, Vol. 31, Paper no: 0638.

Mimnaugh, K.D., Yao, J.Q., Laurent, M.P., Crowninshield, R., Mason, J.J., Blanchard, C., 2009. The effect of entrapped bone particles on the surface morphology and wear of polyethylene. J. Arthroplast. 24 (2), 303–309.

Moro, T., Takatori, Y., Kyomoto, M., Ishihara, K., Hashimoto, M., Ito, H., Tanaka, T., Oshima, H., Tanaka, S., Kawaguchi, H., 2014. Long-term hip simulator testing of the artificial hip joint bearing surface grafted with biocompatible phospholipid polymer. J. Orthop. Res. 32 (3), 369–376.

Moro, T., Takatori, Y., Kyomoto, M., Ishihara, K., Kawaguchi, H., Hashimoto, M., Tanaka, T., Oshima, H., Tanaka, S., 2015. Wear resistance of the biocompatible phospholipid polymer-grafted highly cross-linked polyethylene liner against larger femoral head. J. Orthop. Res. 33 (7), 1103–1110.

Morrison, M.L., Jani, S., Parikh, A., 2015. Design of an advanced bearing system for total knee arthroplasty. Lubricants 3 (2), 475–492. https://doi.org/10.3390/lubricants3020475.

Mu, Z., Tian, J., Wu, T., Yang, J., Pei, F., 2009. A systematic review of radiological outcomes of highly cross-linked polyethylene versus conventional polyethylene in total hip arthroplasty. Int. Orthop. 33, 599–604.

Muratoglu, O.K., Bragdon, C.R., O'Connor, D.O., Jasty, M., Harris, W.H., 2001a. A novel method of cross-linking ultra–high-molecular-weight polyethylene to improve wear, reduce oxidation, and retain mechanical properties. J. Arthroplast. 16 (2), 149–160.

O.K. Muratoglu, C.R. Bragdon, D. O'Connor, R.S. Perinchief, D.M. Estok II, M. Jasty, W.H. Harris, Larger diameter femoral heads used in conjunction with a highly cross-linked ultra-high molecular weight polyethylene: a new concept, J. Arthroplast. 16 (8 Suppl. 1) (2001b) 24–30.

Mutimer, J., Devane, P.A., Adams, K., Horne, J.G., 2010. Highly crosslinked polyethylene reduces wear in total hip arthroplasty at 5 years. Clin. Orthop. Relat. Res. 468 (12), 3228–3233.

Nakahara, I., Nakamura, N., Nishii, T., Miki, H., Sakai, T., Sugano, N., 2010. Minimum five-year follow-up wear measurement of longevity highly cross-linked polyethylene cup against cobalt-chromium or zirconia heads. J. Arthroplast. 25 (8), 1182–1187.

Okazaki, Y., 2008a. Effects of heat treatment and hot forging on microstructure and mechanical properties of co-Cr-Mo alloy for surgical implants. Mater. Trans. 49, 817–823.

Okazaki, Y., 2008b. Effects of solution treatment and cold rolling on microstructure and mechanical properties of stainless steel for surgical implants. Mater. Trans. 49, 1423–1427.

Okazaki, Y., 2012a. On the effects of hot forging and hot rolling on the microstructural development and mechanical response of a biocompatible Ti alloy. Materials 5, 1439–1461.

Okazaki, Y., 2012b. Development trends of custom-made orthopedic implants. J. Artif. Organs 15, 20–25.

Okazaki, Y., 2014. Effect of head size on wear properties of metal-on-metal bearings of hip prostheses, and comparison with wear properties of metal-on-polyethylene bearings using hip simulator. J. Mech. Behav. Biomed. Mater. 31, 152–163.
Okazaki, Y., 2019. Effects of knee simulator control method, and radiation dose on UHMWPE wear rate, and relationship between wear rate and clinical revision rate in national joint registry. J. Mech. Behav. Biomed. Mater. 90, 182–190.
Okazaki, Y., Gotoh, E., 2008a. Metal release from stainless steel, Co-Cr-Mo-Ni-Fe and Ni-Ti alloys in vascular implants. Corros. Sci. 50, 3429–3438.
Okazaki, Y., Gotoh, E., 2008b. Evaluation of torsional breaking and performance properties of bone screws using sawbone. Jpn. J. Clin. Biomech. 29, 443–448.
Okazaki, Y., Gotoh, E., 2013. Metal ion effects on different types of cell line, metal ion incorporation into L929 and MC3T3-E1 cells, and activation of macrophage-like J774.1 cells. Mater. Sci. Eng. C 33, 1993–2001.
Okazaki, Y., Nagata, H., 2012. Comparisons of immersion and electrochemical properties of highly biocompatible Ti-15Zr-4Nb-4Ta alloy and other implantable metals for orthopedic implants. Sci. Technol. Adv. Mater. 13, 0642161-13.
Okazaki, Y., Ito, Y., Ito, A., Tateishi, T., 1993. Effect of alloying elements on mechanical properties of titanium alloys for medical implants. Mater. Trans. JIM 34, 1217–1222.
Okazaki, Y., Tateishi, T., Ito, Y., 1997. Corrosion resistance of implant alloys in pseudo physiological solution and role of alloying elements in passive films. Mater. Trans. JIM 38, 78–84.
Okazaki, Y., Rao, S., Asao, S., Tateishi, T., Katsuda, S., Furuki, Y., 1998. Effects of Ti, Al and V concentrations on cell viability. Mater. Trans. JIM 39, 1053–1062.
Okazaki, Y., Gotoh, E., Manabe, T., Kobayashi, K., 2004. Comparison of metal concentrations in rat tibia tissues with various metallic implants. Biomaterials 25, 5913–5920.
Okazaki, Y., Gotoh, E., Nishimori, M., Katsuda, S., Manabe, T., Kobayashi, K., 2005. Osteocompatibility of stainless steel, Co-Cr-Mo, Ti-6Al-4V and Ti-15Zr-4Nb-4Ta alloy implants in rat bone tissue. Mater. Trans. JIM 46, 1610–1617.
Okazaki, Y., Ishii, D., Ogawa, A., 2017. Spatial stress distribution analysis by thermoelastic stress measurement and evaluation of effect of stress concentration on durability of various orthopedic implant devices. Mater. Sci. Eng. C 75, 34–42.
Olyslaegers, C., Defoort, K., Simon, J.-P., Vandenberghe, L., 2008. Wear in conventional and highly cross-linked polyethylene cups: a 5-year follow-up study. J. Arthroplast. 23 (4), 489–494.
Oral, E., Christensen, S.D., Malhi, A.S., Wannomae, K.K., Muratoglu, O.K., 2006. Wear resistance and mechanical properties of highly cross-linked, ultrahigh-molecular weight polyethylene doped with vitamin E. J. Arthroplast. 21 (4), 580–591.
Rajadhyaksha, A.D., Brotea, C., Cheung, Y., Kuhn, C., Ramakrishnan, R., Zelicof, S.B., 2009. Five-year comparative study of highly cross-linked (crossfire) and traditional polyethylene. J. Arthroplast. 24 (2), 161–167.
Ranawat, A.S., Tsailis, P., Meftah, M., Koob, T.W., Rodriguez, J.A., Ranawat, C.S., 2012. Minimum 5-year wear analysis of first-generation highly cross-linked polyethylene in patients 65 years and younger. J. Arthroplast. 27 (3), 354–357.
Reynolds, S.E., Malkani, A.L., Ramakrishnan, R., Yakkanti, M.R., 2012. Wear analysis of first-generation highly cross-linked polyethylene in primary total hip arthroplasty: an average 9-year follow-up. J. Arthroplast. 27 (6), 1064–1068.
Saikko, V.O., 1995. Wear of the polyethylene acetabular cup: The effect of head material, head diameter, and cup thickness studied with a hip simulator. Acta Orthop. Scand. 66 (6), 501–506.

Saikko, V., Ahlroos, T., Calonius, O., Keränen, J., 2001. Wear simulation of total hip prostheses with polyethylene against CoCr, alumina and diamond-like carbon. Biomaterials 22 (12), 1507–1514.

Shen, F.-W., Lu, Z., McKellop, H.A., 2011. Wear versus thickness and other features of 5-Mrad crosslinked UHMWPE acetabular liners. Clin. Orthop. Relat. Res. 469 (2), 395–404.

Smith, S.L., Unsworth, A., 1999. A comparison between gravimetric and volumetric techniques of wear measurement of UHMWPE acetabular cups against zirconia and cobalt-chromium-molybdenum femoral heads in a hip simulator. Proc. Inst. Mech. Eng. Part H, J. Eng. Med. H 213 (6), 475–483.

Smith, S.L., Unsworth, A., 2000. Simplified motion and loading compared to physiological motion and loading in a hip joint simulator. Proc. Inst. Mech. Eng. Part H, J. Eng. Med. 214 (3), 233–238.

Steinemann, S.G., 1980. Corrosion of surgical implants-in vivo and in vitro tests. In: Winter, G.-D., Leray, J.L., de Groot, K. (Eds.), Evaluation of Biomaterials. Wiley, Chichester, pp. 1–34.

Steinemann, S.G., 1999. Compatibility of titanium in soft and hard tissue-the ultimate is osseointegration. In: Stallforth, H., Revell, P. (Eds.), Materials for Medical Engineering. Wiley–VCH, Weinheim, pp. 199–203.

Taddei, P., Affatato, S., Rocchi, M., Fagnano, C., Viceconti, M., 2008. The effects of irradiation and EtO-treatment on ultrahigh molecular weight polyethylene acetabular cups following accelerated aging: Degradation of mechanical properties and morphology changes during hip simulator tests. J. Mol. Struct. 875, 254–263.

Tarasevicius, S., Robertsson, O., Kesteris, U., Kalesinskas, R.J., Wingstrand, H., 2008. Effect of femoral head size on polyethylene wear and synovitis after total hip arthroplasty: a sonographic and radiographic study of 39 patients. Acta Orthop. 79 (4), 489–493.

Thomas, S.R., Shukla, D., Latham, P.D., 2004. Corrosion of cemented titanium femoral stems. J. Bone Joint Surg. Br. 86-B, 974–978.

Thomas, G.E.R., Simpson, D.J., Mehmood, S., Taylor, A., McLardy-Smith, P., Gill, H.S., Murray, D.W., Glyn-Jones, S., 2011. The seven-year wear of highly cross-linked polyethylene in total hip arthroplasty: a double-blind, randomized controlled trial using radiostereometric analysis. J. Bone Joint Surg. Am. 93-A (8), 716–722.

Triclot, P., Grosjean, G., El Masri, F., Courpied, J.P., Hamadouche, M., 2007. A comparison of the penetration rate of two polyethylene acetabular liners of different levels of cross-linking: a prospective randomised trial. J. Bone Joint Surg. Br. 89-B (11), 1439–1445.

Trommer, R.M., Maru, M.M., 2017. Importance of preclinical evaluation of wear in hip implant designs using simulator machines. Rev. Bras. Ortop. 52 (3), 251–259.

Trommer, R.M., Maru, M.M., Filho, W.L.O., Nykanen, V.P.S., Gouvea, C.P., Archanjo, B.S., Martins Ferreira, E.H., Silva, R.F., Achete, C.A., 2015. Multi-scale evaluation of wear in UHMWPE-metal hip implants tested in a hip joint simulator. Biotribology 4, 1–11.

Unsworth, A., Scholes, S.C., Smith, S.L., Elfick, A.P.D., Ash, H.A., 2000. Tribology of replacement hip joints, thinning films and tribological interface. In: Dowson, D. et al., (Ed.), Tribology Series. In: vol. 38. Elsevier Science BV, pp. 195–202.

Wang, A., Polineni, V.K., Stark, C., Dumbleton, J.H., 1988. Effect of femoral head surface roughness on the wear of ultrahigh molecular weight polyethylene acetabular cups. J. Arthroplast. 13 (6), 615–620.

Wang, A., Sun, D.C., Yau, S.-S., Edwards, B., Sokol, M., Essner, A., Polineni, V.K., Stark, C., Dumbleton, J.H., 1997. Orientation softening in the deformation and wear of ultra-high molecular weight polyethylene. Wear 203-204, 230–241.

Wang, A., Essner, A., Polineni, V.K., Stark, C., Dumbleton, J.H., 1998. Lubrication and wear of ultra-high molecular weight polyethylene in total hip replacements. Tribol. Int. 31 (1–3), 17–33.
Welsch, G., Boyer, R., Collings, E.W., 1994. Materials Properties Handbook: Titanium Alloys. ASM International, p. 10.

Further reading

Okazaki, Y., Gotoh, E., 2011. Comparison of fatigue strengths of biocompatible Ti-15Zr-4Nb-4Ta alloy and other titanium materials. Mater. Sci. Eng. C 33, 325–333.

Part Two

Mechanical behavior, degradation, and testing of metals for biomedical devices

Physical and mechanical properties of metallic biomaterials

3

Takayoshi Nakano
Graduate School of Engineering, Osaka University, Osaka, Japan

3.1 Introduction

Metallic materials have outstanding mechanical reliability in in vivo environments; thus, they are the most widely used materials from which to manufacture implantations. They are particularly useful in load-bearing parts in orthopedic surgery and dentistry, to support the body weight on the bones and joints and enable the reconstruction of motor functions (Williams et al., 1990). Although there was a time when the future use of metallic biomaterials was doubted because they remain in the body, progress in regenerative medicine in recent years has indicated that it would not be possible to develop biomedical devices without taking advantage of the mechanical properties and other outstanding functions of metallic materials, except in the case of special preliminary treatment with some embryonic stem cells or induced pluripotent stem (iPS) cells (Kikuchi et al., 2017).

In this chapter, I build a foundation for understanding and controlling the basic properties of metallic biomaterials, and provide a general explanation of the crystal structure, slip deformation and dislocation, phase diagram and phase selection, and deformation and recrystallization process, with a focus on the relationship between the microstructure and mechanical properties of metallic biomaterials. Finally, I consider the requirements that would have to be imposed on metallic biomaterials for implantation when these materials are considered with respect to the microstructure of bones. Strategies, including those pertaining to metal additive manufacturing, for improving the in vivo mechanical properties by combining metallic biomaterials and bones are suggested.

3.2 Metallic biomaterials which can realize sufficient mechanical properties for use in vivo

The purpose of biomaterials is to save lives, to provide medical treatment, and to improve the quality of life (QOL), and metallic biomaterials are no exception. The advantages of metallic materials include high strength, superior ductility, superior fracture toughness, abrasion resistance, fatigue-resistant properties, high elastic modulus, and high electric conductivity. In this regard, some metallic materials show outstanding magnetic qualities (Williams, 1981). As a result, as shown in Fig. 3.1, considering only bone-related implants, metallic biomaterials are used in the majority

Metals for Biomedical Devices. https://doi.org/10.1016/B978-0-08-102666-3.00003-1
© 2019 Elsevier Ltd. All rights reserved.

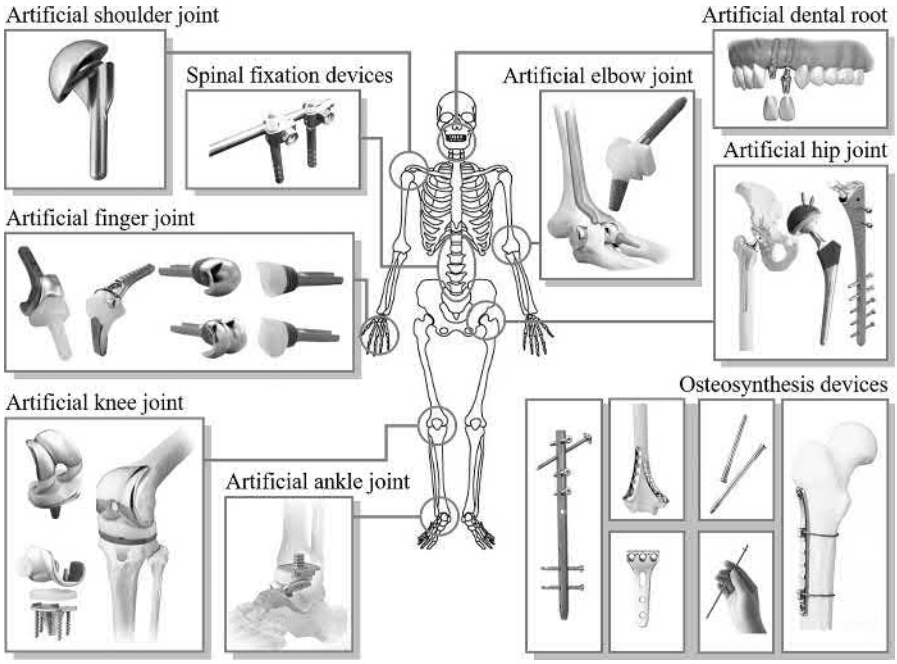


Fig. 3.1 Various bone-related implants (for use in orthopedic surgery and dentistry) that are used in vivo. The majority of them are made uniquely of metal.
Photos provided by Teijin Nakashima Medical Co., Ltd., Japan and Kyocera Co., Ltd., Japan.

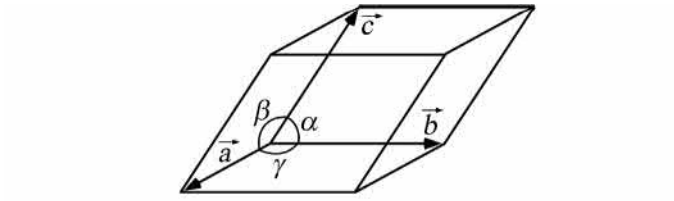
of bone devices as load-bearing parts, including artificial joints, osteosynthesis devices, and spinal fixation devices. These biomaterials have a wide range of applications as dental restorations, artificial tooth roots, denture bases, wires for use in orthodontics, prosthetic valves, electrodes, clips, etc. Moreover, metallic stents are used to expand constricted areas in blood vessels, the intestines, etc., and their use is increasing every year.

Many of these metallic biomaterials are crystalline materials with a periodic arrangement of metallic atoms, and the mechanical properties on which most importance is placed when they are applied in load-bearing parts are governed by dislocation and twinning based on their crystal structure. Moreover, the so-called phase transformation the crystal structure undergoes, in particular the expression of superelasticity based on the martensitic transformation, has led to the application of these metallic biomaterials in vivo because the metal appears to behave in a way that produces flexibility. In other words, metallic biomaterials aim to improve their mechanical properties by controlling their lattice defects and phase transformation at the atomic level because of the electronic state. Currently, the typical metallic biomaterials used in clinical settings include stainless steel, cobalt-chromium (Co-Cr) alloys, pure titanium (Ti) and titanium alloys, pure tantalum (Ta), and noble metallic alloys. All of

these are crystalline materials, with their mechanical and physical properties governed by their atomic arrangements and crystal structures, and the symmetry/asymmetry and/or isotropy/anisotropy of these structures.

3.2.1 Crystals and crystal structure

Crystals are solids with long-range periodicity of which the constituent atoms, ions, or molecules are arranged in an orderly repeating pattern that extends in all three spatial dimensions (Wert and Thomson, 1970; Cullity and Stock, 2001). Crystals are distinguished from amorphous materials and their crystal structure consisting of a three-dimensional periodic arrangement is deeply related to the mechanical properties of the materials. The crystal structure does not necessarily depend on the arrangement of individual atoms, for example; instead, it is expressed by the distribution of imaginary points reflecting the periodicity in crystals, which are known as the lattice points. As shown in Fig. 3.2, the arrangement of all of the lattice points is divided into seven



Crystal system	Axial lengths and angles	Bravais lattice
Cubic	$a=b=c, \alpha=\beta=\gamma=90^\circ$	Simple (P) Body-centered (I) Face-centered (F)
Tetragonal	$a=b\neq c, \alpha=\beta=\gamma=90^\circ$	Simple (P) Body-centered (I)
Orthorhombic	$a\neq b\neq c, \alpha=\beta=\gamma=90^\circ$	Simple (P) Body-centered (I) Base-centered (C) Face-centered (F)
Rhombohedral	$a=b=c, \alpha=\beta=\gamma\neq 90^\circ\ (<120^\circ)$	Simple (P)
Hexagonal	$a=b\neq c, \alpha=\beta=90^\circ, \gamma=120^\circ$	Simple (P)
Monoclinic	$a\neq b\neq c, \alpha=\gamma=90^\circ\neq\beta$	Simple (P) Base-centered (C)
Triclinic	$a\neq b\neq c, \alpha\neq\beta\neq\gamma\neq 90^\circ$	Simple (P)

Fig. 3.2 Unit cells and crystal systems that determine the crystal structure and the categories of Bravais lattice. All crystals can be classified into the 7 crystal systems and the 14 Bravais lattices.

crystal systems determined by three vectors, $\vec{a}$, $\vec{b}$, and $\vec{c}$ and the angles between them, α, β, and γ; furthermore, these systems are finally classified into 14 types of Bravais lattice on the basis of the distribution of the lattice points. Here the lattice points have exactly the same ambient environment. It is surprising that the crystal structures are classified into only 14 types even though the distribution of atoms relative to each lattice point has infinite variations that give rise to a great variety of crystal structures.

In metallic materials, most often a single metallic atom occupies the lattice points of a simple lattice, and those with a highly symmetric crystal structure are widely used in industrial applications. This is because in combinations of crystal grains with differing crystal orientations, in other words, in polycrystals, the highly symmetric crystals easily satisfy the von Mises criterion, which is the condition necessary for maintaining the continuity of the strain through the crystal grain boundaries. Fig. 3.3 shows the typical crystal structures: the body-centered cubic (bcc) structure, the face-centered cubic (fcc) structure, and the hexagonal close-packed (hcp) structure. The symmetry of the crystal structure is lower for hcp than bcc and fcc, and the packing density of the atoms is lower in bcc than fcc and hcp. These atomic arrangements of metallic biomaterials are deeply related to the mechanical properties resulting from the displacement of atoms.

In current metallic biomaterials of major importance, the crystal structure of the constituent phases is characterized by highly symmetric atomic arrangement. For example, stainless steel depends on the composition of the alloy and heat treatment to which it is subjected, and generally has a bcc or fcc structure, and 316L stainless steel, which is highly corrosion resistant and which is used as a metallic biomaterial, has fcc as its parent phase. Moreover, Co-Cr alloys for biomedical applications are basically fcc, and pure titanium (Ti) has an hcp (α-phase) as its stable crystal structure at ambient temperature and bcc (β-phase) as its stable crystal structure at high temperatures of approximately 882.5°C. Ti-6Al-4V alloys and Ti-6Al-7Nb alloys, which exclude the bio-toxic element, vanadium (V), have (α + β) duplex phases, including a bcc (β-phase) in addition to the hcp (α-phase).

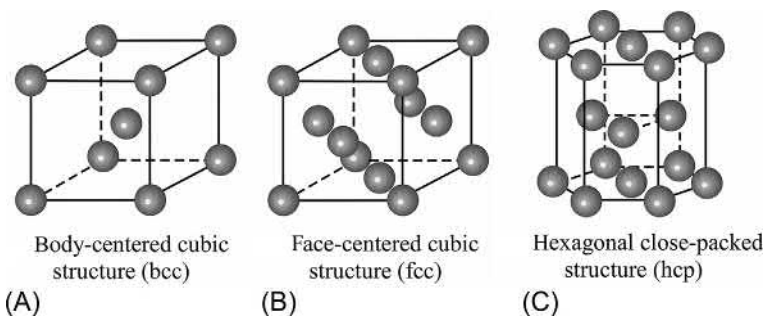


Fig. 3.3 Atomic arrangement in (A) body-centered cubic (bcc), (B) face-centered cubic (fcc), and (C) hexagonal close-packed (hcp) crystal. These are the basic crystal structures of metallic materials that are widely used in practical applications due to their high crystal symmetry. This also applies to metallic biomaterials, in which most of the crystal structures of the parent phase are one of these three structures.

In recent years, alloys with a low Young's modulus have been the topic of research and development, and are aimed at alleviating the stress shielding caused by the difference in the elastic modulus between bone tissue and metallic implants (Tonino et al., 1976). Stress shielding is defined as the phenomenon in which bone mass, bone density, and bone quality declines compared to normal levels when stress in bone is shielded (Noyama et al., 2012). A typical example of a material that avoids stress shielding is β-type Ti alloys. These alloys have a low Young's modulus and a bcc crystal structure as their stable crystal structure. However, from the perspective of the improvement of mechanical properties, alloy compositions with low bcc stability are the focus of attention, and the expression of several types of martensitic phases using martensitic phase transformation and the control of precipitation using heat treatment are possible. Most of the several structures that are formed in this way belong to hexagonal crystal systems with an α-phase. Here, the martensitic transformation is a "non-diffusive transformation" in which the crystal structure changes without requiring thermal activation energy and is the cause of the superelasticity and shape memory phenomenon. In particular, the superelasticity derives from the fact that the crystal structure changes reversibly due to the martensitic transformation when loading and unloading stress, and this creates flexibility as a rubber-like metal. Apart from this, as mentioned in Section 3.7.3, Young's modulus also exhibits an even orientation dependence in the single-crystalline form (Tane et al., 2008; Lee et al., 2012). In addition, the crystal structure of noble alloys for dental use depends on the alloy composition; however, many gold and platinum series (Au-Pt) alloys have fcc as their matrix crystal structure.

3.2.2 Deformation of crystalline metallic biomaterials

The deformation of crystal metallic materials can be classified into two types: "elastic deformation" and "plastic deformation" (Wert and Thomson, 1970; Dieter, 1986). "Elastic deformation" is a region governed by Hooke's law and is equivalent to the deformation of a spring, with unloading returning the materials to their original shape. On the other hand, if a load greater than a certain level is applied, the shape of the deformed materials is not restored to its original state even after the weight is removed. This kind of permanent deformation is known as "plastic deformation." Fig. 3.4 shows the typical stress-strain curve of a single crystal of a β-type Ti alloy for biomedical application. In the low-strain region, stress rises linearly due to elastic deformation; after reaching a certain level of stress, the gradient declines, and plastic deformation commences. This stress at which the transition from elastic deformation to plastic deformation takes place is termed the "yield stress" or the "elastic limit" and is an important indicator reflecting the strength of materials. However, it is important to note that even above the yield stress the elastic strain increases as the stress increases.

The slope of the stress-strain curves in elastic deformation is known as Young's modulus, and it reflects the elastic property of materials. Generally, when metallic biomaterials are applied in implantations, etc., they are used within their elastic limit. Therefore, when these materials are implanted in bones, the difference in the elastic modulus compared to that of bones is important.

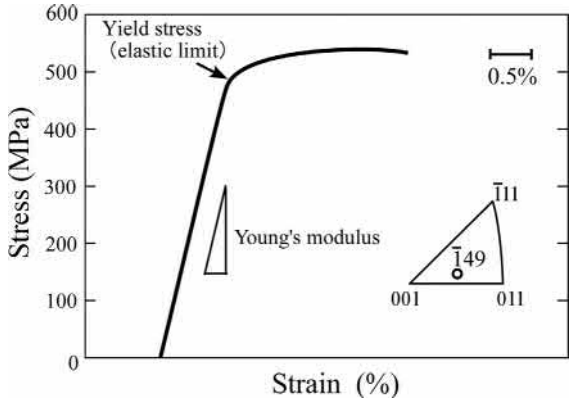


Fig. 3.4 Typical stress-strain curve of a single crystal of a β-type Ti alloy for medical application at room temperature. After elastic deformation, macroscopic plastic deformation starts at the yield stress, and the material undergoes permanent deformation. In this case, the slip deformation due to the dislocation is responsible for the plastic deformation.

In the plastic deformation region after yielding, along with an increase in the strain, the crystalline materials harden and their deformation proceeds. Metallic biomaterials are never used at the yield stress or above; however, plastic deformation behavior is extremely important with respect to fabrication to give the materials their shape, to introduce strain for microstructure control, and for deformation to progress as a result of metal fatigue. Elongation up to the point of fracture in tension shows the ductility of the materials, and the larger this value, the easier the plastic deformation becomes. However, the ductility of materials tends to be inversely related to the yield stress or maximum strength; therefore, it is important to adjust both of these according to the application, and to design the materials to increase both the strength and ductility.

Fig.3.5 shows typical stress-strain curves obtained when tension is applied to metallic biomaterials, ceramics-base biomaterials, ultrahigh molecular weight polyethylene (UHMWPE), and cortical bone. In the case of metallic materials, the stress increases linearly due to elastic deformation in the low-strain region, the inclination decreases after reaching a certain stress, and plastic deformation proceeds along with work hardening. In the plastic deformation region after yielding, the crystalline material hardens as the amount of strain increases and the deformation progresses. Metallic biomaterials are never used at yield stress or higher, but the plastic strain is used to impart shape. Although the plastic deformation behavior is characteristic depending on the type of material such as metallic, ceramic, or polymeric, metals with the best balance between strength and ductility are excellent biomaterials.

Generally, the rise in yield stress due to the decline in temperature (temperature dependence) is larger for bcc than fcc and hcp; therefore, bcc is more strongly affected by interstitial elements with small comparative atomic radii such as carbon (C) and nitrogen (N). In view of the dislocation, which is discussed later, this is deeply related to the structures of the formation of the surrounding strain field and the dislocation core.

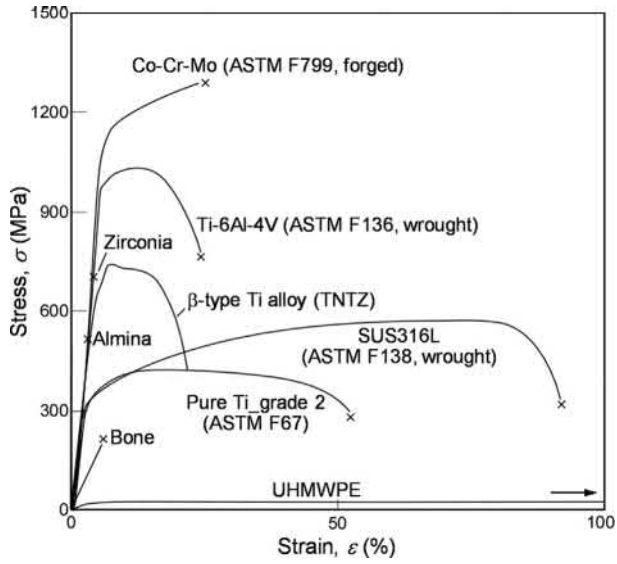


Fig. 3.5 Typical stress-strain curves obtained by conducting tensile tests of various metallic biomaterials, ceramics-based biomaterials, ultrahigh molecular weight polyethylene (UHMWPE), and cortical bone.

This core is the part at which the rearrangement of the atomic arrangement in the center of the dislocation occurs, a portion that cannot be calculated by the theory of linear elasticity.

3.2.3 Slip deformation based on crystal structure

From the macroscopic perspective presented in the previous paragraph, both the elastic and plastic deformation behavior is deeply related to the crystal structure, which is a spatial atomic arrangement. Fig. 3.6 shows the stylized movement of atoms in two dimensions inside crystals upon the first elastic deformation and subsequent plastic deformation. For example, if a tensile load is added under elastic deformation (Fig. 3.6B) the atomic distance changes relative to that before deformation (Fig. 3.6A); however, the bonding relationships among adjacent atoms remain unchanged. Therefore, elastic deformation is deeply related to the shape of the potential between atoms with respect to atomic distance.

On the other hand, plastic deformation progresses as a result of slip deformation of the crystals as in Fig. 3.6C. Slip deformation occurs because of the relative displacement of atoms in a specific direction, which is termed the slip direction on a specific crystal plane known as the slip plane (Wert and Thomson, 1970; Dieter, 1986; Hirth and Lothe, 1968; Nabarro, 1979). Generally, the plane in which the separation between slip planes (lattice spacing) is large and the atoms are closely packed is selected as the slip plane, and the direction in which the atoms are most closely arranged is selected as the slip direction. This kind of deformation can be said to

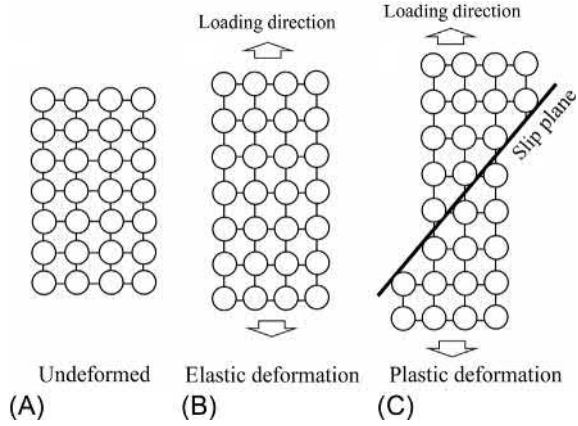


Fig. 3.6 Stylized diagram showing the movements of atoms from undeformed structure (A) within crystals in two dimensions when elastic deformation and plastic deformation progress. (B) With elastic deformation, after unloading, the atomic distance and external shape return to their original formats. (C) In plastic deformation, slip occurs due to the atomic arrangement in the crystalline metallic materials; however, the slip plane and slip direction in this case are strongly constrained.

be a constraint condition for enabling plastic deformation to progress in metallic biomaterials and other crystalline metals while breaking down the stable crystal structure as little as possible. Therefore, there is a tendency to believe that deformation is generally easy for metallic materials; however, it is necessary to be strongly aware of the fact that actually plastic deformation progresses under constraints, which result in the selection of the slip plane and slip direction based on the crystal structure. As a result, appropriate material design involves producing metallic biomaterials that combine mechanical safety and outstandingly high strength.

Fig. 3.7 illustrates the typical slip systems as combinations of the slip planes and slip directions, found in bcc, fcc, and hcp, the most common structures in metallic biomaterials. The slip plane and slip direction are written in their respective separate spaces, which are termed the reciprocal lattice space and the real lattice space, respectively. The Miller indices as representing the reciprocal lattice space are well known, whereas the Miller-Bravais indices are utilized only in the hexagonal crystal system due to the special symmetry. The fcc and bcc structures are cubic crystal systems; therefore, the spaces that express the slip plane and the slip direction coincidentally correspond, and it is possible to include them in an orthonormal coordinate system. The slip plane in Fig. 3.7 is displayed as a vector of the normal direction of the slip plane and the slip direction is displayed as a vector parallel to that direction. As a result, for the fcc structure, which has the greatest packing density of atoms, the slip plane is uniquely determined to be $\{111\}$ (the plane for which $\langle 111 \rangle$ is the normal) and the slip direction to be $\langle \bar{1}\,10 \rangle$ therefore, from the symmetry of the crystals, a total of 12 combinations of slip systems exist. On the other hand, for the bcc crystal structure, the $\langle 111 \rangle$ direction is selected as the closest packed arrangement of atoms as the slip direction; however,

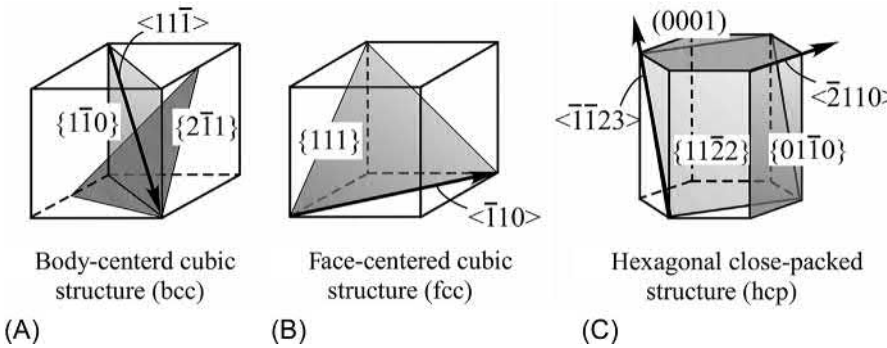


Fig. 3.7 Typical slip system (slip plane and slip direction) in (A) body-centered cubic (bcc), (B) face-centered cubic (fcc), and (C) hexagonal close-packed (hcp) crystal structures. Generally the plane in which the atoms are closely packed is selected as the slip plane, and the direction in which the atoms are most closely arranged is selected as the slip direction.

for planes other than the {110} plane, for example, the {211} plane, the closest packed plane becomes the slip plane. The selection of the slip system based on the crystal structure is extremely important when considering the strength of metallic biomaterials. This is because the degree of difficulty of slip deformation corresponds directly to the difference in the strength of the materials. In other words, resistance and impedance of the slip deformation lead to high strength metallic materials.

3.2.4 Dislocation motion in crystals

In the case in which shear deformation of the slip plane progresses in line with the slip direction, the relative displacement of atoms, as shown in Fig. 3.8, is expected. The shear stress necessary to carry out the (A)→(B)→(C) series of atomic displacements at a time in Fig. 3.8 is known as the theoretical strength (Hirth and Lothe, 1968). This value is estimated to be approximately one-sixth of the shear modulus of rigidity in metals; however, the actual stress for the slip is more than two or three digits smaller than this. The lattice defect that was introduced to explain the reason for this large difference is dislocation (Hirth and Lothe, 1968). In other words, at the time of a plastic deformation, a slip does not progress all at once; rather, in the process shown in Fig. 3.8(A)→(C), overall, slip occurs via a progression of partial slip deformation steps equivalent to the situation in (D), in other words a "disarray of atomic arrangement" as shown by "⊥ (Caution: this mark is an inverse "T")." The strain component resulting from this slip motion of the dislocation is defined as the Burgers vector ($\vec{b}$). The self-energy of the dislocation is proportionate to the square of the Burgers vector; therefore, the length of the Burgers vector has a strong effect on the formation, dissolution, and motion of the dislocation. A transmission electron microscope can be used to directly observe dislocation depending on the strain field of the surrounding lattice. For example, as shown in Fig. 3.9, the dislocation can be directly observed as white lines of contrast, and we can determine the direction of the Burgers vector by using the conditions under which the dislocation is extinguished.

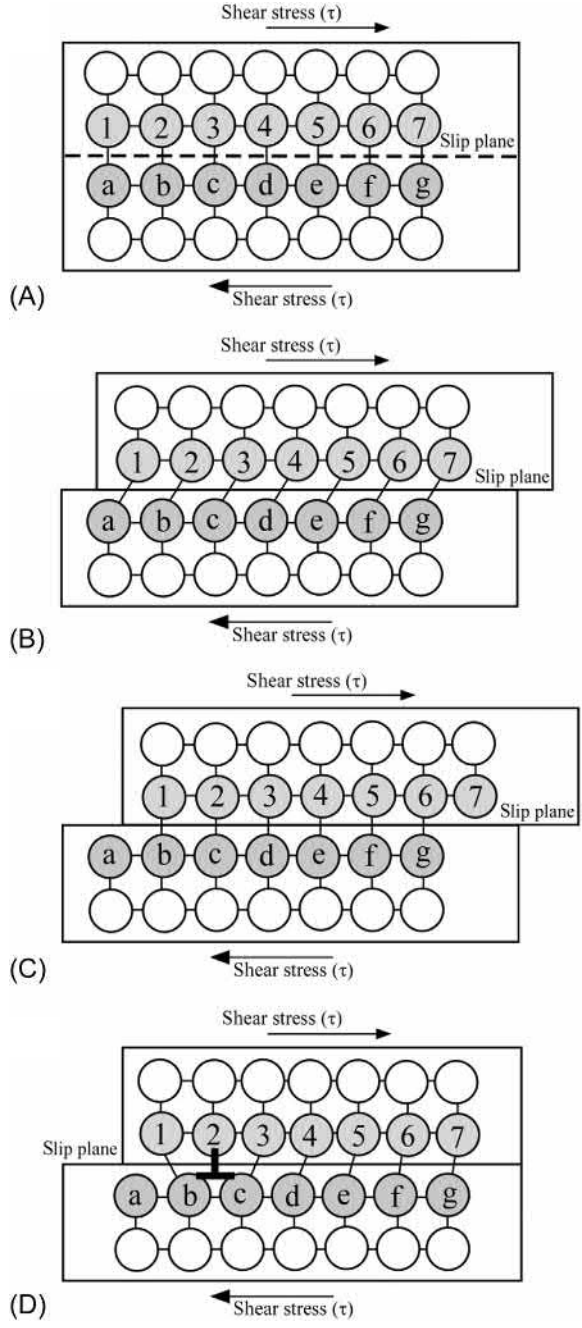


Fig. 3.8 Relative displacement of atoms and change in the external shape when shear deformation on the slip plane progresses in line with the slip direction. Extremely high shear stress is thought to be necessary to carry out the series of atom movements in figure (A)→(B)→(C) all at once, and actually the movement of the atoms is carried out in the order figure (A)→(D)→(C). Owing to the progress of partial slip equivalent to a "disarray of atomic arrangement" such as that shown by "⊥ (Caution: this mark is an inverse "T")" in figure (D), overall slip deformation occurs, which is known as "dislocation."

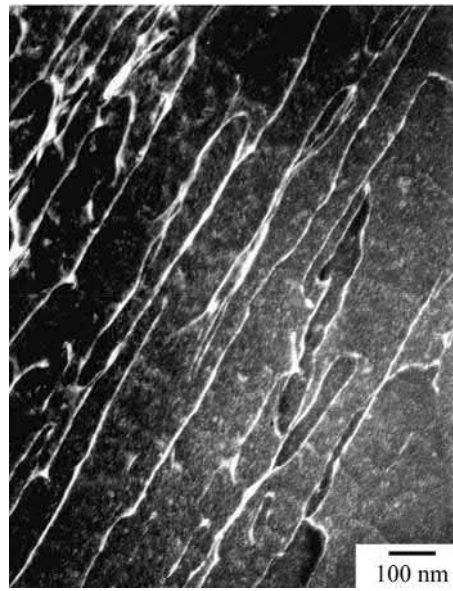


Fig. 3.9 Dislocation discernible after deformation in a single crystal of a β-type Ti-based alloy (white curve). This dislocation can be directly observed using transmission electron microscopy (TEM: dark field image) on the basis of the strain field of the surrounding dislocation core.

A dislocation is a partial rearrangement of atoms in the crystal structure such that a large strain field occurs in the area surrounding the dislocation. These dislocations can be classified into three types on the basis of the relationship of the angles of the slip direction (the direction of the Burgers vector) and the direction in which the dislocation is arranged (the direction of the dislocation lines): edge dislocations, screw dislocations, and mixed dislocations. As shown in Fig. 3.10, the case in which the relationship between the slip direction (the direction of the Burgers vector) and the dislocation line is perpendicular is referred to as the edge dislocation (Fig. 3.10A) and the case in which that relationship is parallel is termed screw dislocation (Fig. 3.10B). Other cases in which the dislocation is composed of both edge and screw dislocation components are referred to as mixed dislocations. For an edge dislocation, the slip plane is uniquely determined from the relationship between the dislocation lines and the Burgers vector, whereas with screw dislocation, motion of the identical slip plane is not inevitable. As a result, especially for the bcc structure in which the slip plane is not uniquely selected, dislocation motion known as "cross slip," which moves while changing the slip plane due to screw dislocation can be observed. As a result, the curved slip traces can be discerned on the sample surface after deformation in the bcc structure. As an example thereof, Fig. 3.11A and B show the condition of the sample surface after deformation of a β-type Ti alloy single crystal newly developed for biomedical application. Wavy slip traces can be observed and the transition of the operative slip plane arising from the change in the loading axis (corresponding to Fig. 3.11A and B) can be discerned, and in these two subfigures, the {101} and {211} planes, respectively, are mainly selected as the slip plane. This means that

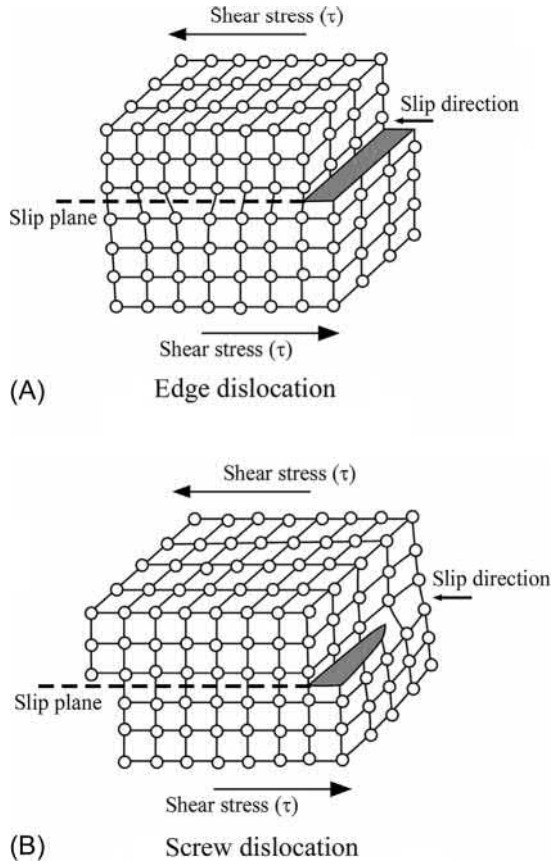


Fig. 3.10 Stylized diagram of the atomic arrangement showing (A) edge dislocation and (B) screw dislocation. The relationship between the slip direction (the Burgers vector) and the dislocation lines is perpendicular (A) and parallel (B), respectively. If both components occur in combination, the dislocation is termed mixed dislocation, and the slip deformation differs depending on the respective types of dislocation.

the operative slip plane of the dislocation undergoes a transition while adhering to the maximum resolved shear stress plane (MRSSP: the crystal plane in which the resolved shear stress is loaded most efficiently with respect to the external stress loading) to some extent (Taoka et al., 1964; Takeuchi et al., 1967). This transition phenomenon of the slip plane differs greatly in the case of fcc and hcp owing to the characteristics of the crystal structure and the dislocation core structure on the basis of the atomic arrangement. For reference purposes, the slip line at room temperature in the pure Ti single crystal with the hcp structure is shown in Fig. 3.11C. Unlike the cases shown in Fig. 3.11B and C, a large number of slip lines that appear to be linear on the trace of the $\{10\bar{1}0\}$ prism plane can be found (Fig. 3.11C).

The differences in the operative slip planes depending on these crystal structures are also strongly expressed in the critical resolved shear stress (CRSS), which

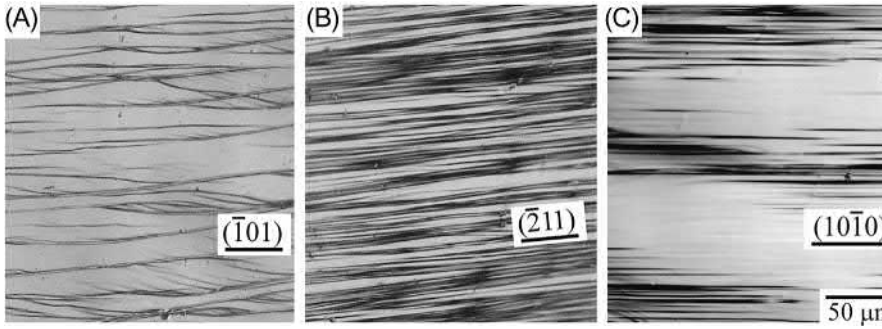


Fig. 3.11 Slip trances on the sample surface after deformation of a single crystal of a β-type Ti-based alloy newly developed for biomedical application (A, B) and a pure Ti single crystal (C). With the β-type Ti alloys that have a bcc structure, a curved slip trace showing the cross slip events can be discerned; with the slip plane for which the maximum resolved shear stress plane (MRSSP) depending on the loading axis is selected, the curved slip trace of the crystal structure (A, B) can be observed, and the dominant slip plane depending on the loading axis transitions from the $(\bar{1}01)$ plane (A) to the $(\bar{2}11)$ plane (B). On the other hand, in a pure Ti single crystal with an hcp structure, a linear slip trace in line with the $(10\bar{1}0)$ prism plane (C) can be discerned, and this is deeply related to the dislocation core structure based on the crystal structure.

determines the strength of the materials. CRSS is the effective stress with respect to the slip direction on the slip plane for starting macroscopic plastic shear deformation, and in fcc structures; excluding some exceptions, it does not depend on the loading axis orientation and is largely constant. On the other hand, in bcc alloys, changes in the slip plane arising from the complexity of the dislocation core structure and even crystal orientation dependence of the CRSS frequently appear. Thus, the motion of the dislocation that determines the strength of the materials has a close relationship to the atomic arrangement within the crystals introduced by the dislocation; in other words, the dislocation mode is strongly influenced by the crystal structure of the contained constituent phase and its combinations.

Taking the β-type Ti alloys as an example, their deformation is closely related to the stability of β (bcc) structures. Fig. 3.12 shows the trace on the specimen plane after deformation, and the deformation mode changes substantially along with stabilization of the β-phase (Sakaguchi et al., 2005; Nakano et al., 2007; Hagihara and Nakano, 2017). The motion of the dislocation is important as the deformation mode of crystalline metallic materials; however, the deformation is frequently borne by this deformation twin and martensitic transformation. Here, the deformation twin creates a mirror relationship (180° symmetry) with respect to the specific plane (twinning plane) with respect to the original crystals. Generally, with bcc structures the {112} plane is the twinning plane, which is displaced in the ⟨111⟩ direction. With β-type Ti alloys, as the stability of the β-phase of the parent phase increases, the deformation mode changes according to stress-induced martensitic transformation, {332} ⟨113⟩ deformation twin, and ⟨111⟩ dislocation in this order. At the same time, the mechanical properties change substantially corresponding to the variations in the deformation mode.

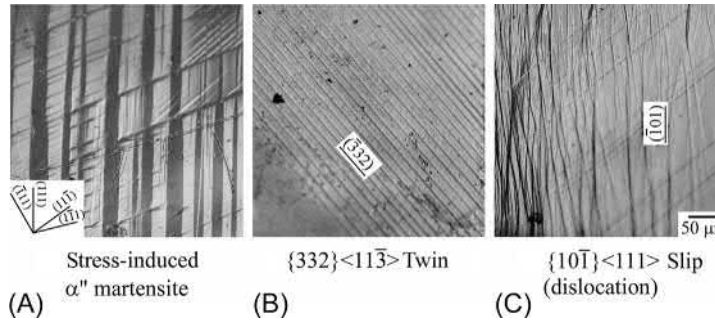


Fig. 3.12 Dependence of the stability of the bcc atomic structure on the deformation mode of β-type Ti alloys for biomedical application. This mode closely correlates with the stability of the β phase. The major deformation mode changes along with the stabilization of the β phase from stress-induced martensitic transformation (A) to deformation twin (B) and finally to motion of dislocation (C).

3.3 Methods for strengthening metallic biomaterials

The strengthening of metallic materials is basically achieved by impeding the dislocation motion (Dieter, 1986; Cahn and Haasen, 1996).

(A) *Work hardening*:
This is the phenomenon in which mobile dislocation undergoes interactions due to the pile-up dislocations introduced by plastic deformation, and therefore dislocation motion becomes difficult. Generally, it rises in proportion to the square root of the dislocation density. In the case of as-wrought Co-Cr alloys, improvement of their strength through work hardening is possible.

(B) *Solution hardening*:
This is the phenomenon by which introduction of a heterogeneous solute atom to a pure metal impedes the dislocation motion, thereby resulting in hardening. In particular, hardening is promoted by differences in the atomic size and atomic modulus of rigidity. The addition of aluminum to Ti alloys makes the same contribution to strengthening as a substitutional element.

(C) *Precipitation hardening*:
This is the phenomenon in which the dislocation motion is impeded and the material is hardened by precipitating and dispersing an extremely fine precipitation in the parent phase using the differences in solubility of the solute atoms at different temperatures. Hardening due to the uniform dispersion of carbide in Co-Cr alloys and the precipitation of the ordered phase of gold alloys fall into this category.

(D) *Particle dispersion hardening*:
Powder metallurgy (the method of hardening raw powder by subjecting it to pressure and heat, to mold or synthesize it as a bulk material) and other methods are used to harden the material by finely dispersing particles that harden and stabilize at high temperatures, such as alumina (Al_2O_3). Along with precipitation hardening, mobile dislocation leads to hardening by cutting particles or proceeding by an indirect route. In case the loop of the dislocation surrounding the particle (the Orowan loop) is left behind, owing to the resulting

internal stress, the motion of the dislocation, which continues to move, is impeded, and significant hardening will occur. A particle distribution that exhibits an interdistance between particles of approximately the order of length for a Burgers vector is considered to be necessary for hardening.

(E) *Composite strengthening*:

Compared to precipitation hardening and particle dispersion hardening, the volume fraction of the second phase for strengthening is larger, and this approach aims to strengthen by receiving the load in accordance with the volume fraction in both the parent phase and the second phase.

(F) *Grain refining hardening*:

Deformation progresses through grain boundaries due to the multiplication of dislocation within the adjacent crystal grains after stress concentration by the pile-up dislocations in the original grain. Thus, the material becomes harder if the crystal grains are smaller, and both the yield stress and maximum stress change in inverse proportion to the square root of the size of the crystal grains. Grain refining is achieved by using processes such as deformation & recrystallization and severe plastic deformation, which are mentioned later.

3.4 Phase rule and phase diagram

Controlling the strength of crystalline metallic materials requires the properties of the slip system to be taken into consideration on the basis of the crystal structure and to have an alloying design to control the motion of the dislocation. Therefore, not only alloys comprised of a single phase but also an alloy design comprised of a multiphase consisting of two or more phases is important. In reality, most of the metallic biomaterials that are being used in applications use the multiphase design, which allows the exclusion of pure metals such as Ti. Moreover, it is also possible to not only use the stable phase but also the meta-stable phase. However, taking into consideration the phase rule as an indicator as to whether multiple stable phases can coexist is extremely important when following the alloy design. Currently, at constant pressure, the degrees of freedom f′ are expressed in terms of C − P + 1 (C: number of alloy components, P: number of stable phases) (Cahn and Haasen, 1996). Using this relationship, for example, equilibrium can be achieved up to a maximum of four phases in ternary alloys (i.e., alloys with three components).

A diagram that describes this stable phase equilibrium (the situation in which free energy is at a minimum) with respect to temperature, composition, and pressure is known as a phase diagram, and these diagrams are indispensable when determining the strategies for alloy design (Wert and Thomson, 1970; Cahn and Haasen, 1996).

As an example, Fig. 3.13 shows a stylized binary phase diagram that can be used as the guideline when designing Ti alloy, which is highly biocompatible. When Ti is replaced with the secondary element (X), the transformation temperature for α (hcp)/β (bcc) fluctuates depending on the type of element, and cases are seen where the (α + β) duplex phase region exists in a stable state even at room temperature.

First, Fig. 3.13A is utilized to explain how to read and use a general binary phase diagram. The vertical axis shows the temperature (T) and the horizontal axis corresponds to the alloy composition (concentration of X). In this case, the vertical lines

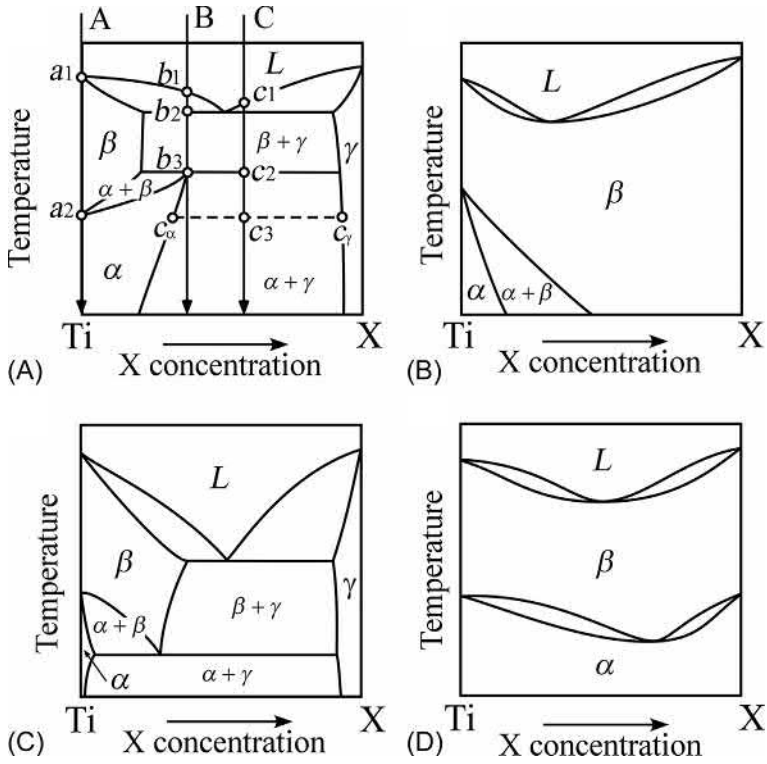


Fig. 3.13 Binary phase diagrams when a second element is added to Ti alloy. The transformation temperature for α (hcp)/β (bcc) fluctuates depending on the nature of X. Phase diagram for the (A) α region expansion type (X = Al, Ga, C, N, O, etc.), (B) β region expansion type (X = Mo, Nb, Re, Ta, V, etc.), (C) β eutectoid type (X = Ag, Au, Co, Cr, H, Si, Pt, W, etc.), and (D) continuous solid solution type (X = Hf, Zr).

on the extreme left and right represent pure Ti and pure X element, respectively. Thus, moving along the horizontal axis to the right means a greater amount of pure Ti has been replaced with X element, and the phase state of the equilibrium condition combining the respective compositions and temperatures is shown. In other words, the phase state with the least amount of free energy for each temperature and composition is reflected. This kind of phase diagram is drawn according to the free energy-composition curve at each temperature; therefore, it is necessary to understand the phase diagram while taking this curve into consideration at all times. Fig. 3.13A shows the three straight lines, A, B, and C, of different alloy compositions, and it shows the change in the equilibrium phase resulting from the decline in temperature for each of them.

A (Pure Ti): L $(T > a_1) \rightarrow L + \beta$ $(T = a_1) \rightarrow \beta$ $(a_2 < T < a_1) \rightarrow \alpha + \beta$ $(T = a_2) \rightarrow \alpha$ $(T < a_2)$.
B (Ti-X (low concentration of X) alloy): L $(T > b_1) \rightarrow L + \beta$ $(b_2 < T \leqq b_1) \rightarrow L + \beta + \gamma$ $(T = b_2) \rightarrow \beta + \gamma$ $(b_3 < T < b_2) \rightarrow \alpha + \beta + \gamma$ $(T = b_3) \rightarrow \alpha + \gamma$ $(T < b_3)$.

C (Ti-X (high concentration of X) alloy): L $(T > c_1) \rightarrow L + \beta + \gamma$ $(T = c_1) \rightarrow \beta + \gamma$ $(c_2 < T < c_1) \rightarrow \alpha + \beta + \gamma$ $(T = c_2) \rightarrow \alpha + \gamma$ $(T < c_2)$.

As can be understood from the phase rule, the maximum number of phase equilibriums in pure Ti is two-phase equilibriums ($T = a_1$: $L + \beta$, $T = a_2$: $\alpha + \beta$), and in the binary alloys of the B and C compositions, the maximum is three-phase equilibriums [B composition ($T = b_2$): $L + \beta + \gamma$, $T = b_3$: $\alpha + \beta + \gamma$; C composition ($T = c_1$): $L + \beta + \gamma$, $T = C_2$: $\alpha + \beta + \gamma$], making multiphase compositions possible because phases have different crystal structures and different mechanical properties. In case the maximum number of equilibrium phases is reached, the degrees of freedom at constant pressure becomes zero and it is termed an invariant reaction in which the composition and temperature required for phase equilibrium are uniquely determined. Therefore, when designing an alloy, an increase in the number of elements is an important method for increasing the number of degrees of freedom in the case of a multiphase equilibrium.

The equilibrium composition and even the quantitative ratio of the equilibrium phase can be understood from the alloy phase diagram. For example, looking at C alloy (Fig. 3.13A), in $T = c_3$ the $(\alpha + \gamma)$ two-phase equilibrium is maintained; however, the equilibrium compositions in that case are C_α and C_γ for the α-phase and γ-phase, respectively, and the quantitative ratio of the phases is expressed through the relationship of the values of $(C_\gamma\text{-}C)/(C_\gamma\text{-}C_\alpha)$ and $(C\text{-}C_\alpha)/(C_\gamma\text{-}C_\alpha)$, respectively. The important point here is that even in cases where $T = c_3$, the alloy composition changed from C_α to C_γ, the compositions of the α-phase and the γ-phase are constant at C_α and C_γ, respectively, and only the quantitative ratio of the α-phase and the γ-phase changes. This reflects the fact that the free energy of the α-phase and the γ-phase in equilibrium is minimized in the C_α composition and the C_γ composition, respectively.

Using our basic knowledge about the above phase diagram, let us look at the Ti-based two-dimensional phase diagram. It is classified into "α-phase stabilized elements," for which the addition of a second element raises the transformation temperature of α/β and expands the α-phase region; "β-phase stabilized elements," for which conversely the transformation temperature is lowered; and the β-phase region expands, and "neutral elements," which do not belong to either of the previous categories. The respective phase diagrams have special characteristics. In Fig. 3.13A, it is seen that X = Al, Ga, C, N, O, etc., and the α-phase region expands as an α-phase stabilized element. In Fig. 3.13B, X = Mo, Nb, Re, Ta, V, etc., and the β-phase region expands and also in Fig. 3.13C, the β-phase region is expanded, and the β-phase undergoes a solid phase transformation to the α-phase and the γ-phase due to the eutectoid reaction (X = Ag, Au, Co, Cr, H, Si, Pt, W, etc.). Here, the eutectoid reaction is one type of invalid reaction in the binary system, and it means the resolution from one solid phase to two different solid phases due to a decline in temperature, resulting in a three-phase equilibrium. Moreover, in Fig. 3.13D it is seen that for X = Hf, Zr, the temperature of the α/β transformation does not change substantially, and X behaves as a neutral element because it becomes a continuous solid solution.

If we view the history of the development of Ti and Ti alloys as metallic biomaterials in terms of phase equilibrium, pure Ti with an hcp structure (α-phase) has been used often; however, owing to their lack of strength, metals such as Al, V, and Nb were

added to transform them into (α + β) duplex alloys and thus achieve precipitation hardening and solution hardening. Moreover, recently β-type Ti alloys with a low Young's modulus have been gaining attention as a way to reduce the stress shielding effect on bone tissue, and alloys are being designed using β-stabilized elements such as Ta, Nb, and Mo with low toxicity is being carried out (Niinomi, 2003).

In Fe-based alloys as well, the binary phase diagram is broadly classified into four (order of the change of stability from the α-phase to the γ-phase: γ-loop formation type, γ-region contraction type, γ-region expansion type, γ-region open type) according to the expansion and contraction of the stable region of the α-phase (ferrite: bcc) and the γ-phase (austenite: fcc). Cr is a γ-loop formation type element, thus the γ-region contracts; however, with the addition of 12% or more it forms a passivated membrane as a hydrated chrome oxyhydroxide, and this increases its corrosion resistance. Another example is 316L stainless steel, which is used as a metallic biomaterial. The γ-phase of this biomaterial is stabilized by adding nickel (Ni), a γ-region expansion type element, to improve the toughness. In other words, Cr and Ni, elements with different γ-phase stabilization tendencies, are added to improve both the corrosion resistance and the mechanical properties at the same time. In recent years, Ni-free stainless steel was developed in consideration of the allergenic properties of Ni by adding the γ-region expansion type element N instead of Ni (Sumita et al., 2004).

3.5 Deformation and recovery, recrystallization, and grain ripening

If plastic deformation of crystalline materials is carried out at a temperature below the melting point, the microstructure and the mechanical properties change. The dislocations introduced as a result of plastic deformation at low temperatures and other lattice defects rearrange and decrease through the processes of recovery and recrystallization at a relatively high temperature; at the same time, the microstructure is once refined by recrystallization, and subsequently the crystal grains become coarser through grain ripening achieved with further heat treatment (Cahn and Haasen, 1996). In the recovery process, the extinguishment of excess point defects, such as vacancies and interstitial atoms, that occurred in the crystal and rearrangement of the dislocation do not result in a change in the structure at the micrometer level; however, there is a slight decline in strength and rise in ductility. Moreover, raising the temperature or exposing the material to lengthy heat treatment results in recrystallization as the driving force for reducing the energy based on the extinguishment of lattice defects, especially dislocations. At this time, the new crystal grains with a low lattice defect density undergo nucleation, and the overall material is covered with new crystal grains with a low density of lattice defects, and at the same time refinement progresses. During this recrystallization process, because the crystal grains with work hardening are extinguished, a marked decline in strength can be discerned; however, as a result of the refinement of the crystal grains the increase in strength is greater than that of the structure containing the coarse crystal grains before the work hardening. Moreover, continuation of the heat treatment becomes a driving force that decreases the total energy of the crystal

grain boundaries, ripens the crystal grains, and causes a decline in strength that corresponds to the increase in the crystal grain size. In metallic biomaterials, carrying out structure control by using a combination of plastic deformation and heat treatment enables the mechanical properties to be controlled so as to suit the application.

3.6 Microstructure and related mechanical properties in typical metallic biomaterials

The 316L stainless steel, which is used for biomedical application, was developed from the basic composition of 304 stainless steel (Fe-18 wt% Cr-8 wt% Ni), which is widely used as austenitic stainless steel. The addition of molybdenum (Mo) to this stainless steel improves its corrosion resistance, and reduction of the C content, which has a low solid solubility range, enables maintaining precipitation at the grain boundary of chromium carbide ($Cr_{23}C_6$) at an acceptably low level to further improve the corrosion resistance (Sumita et al., 2004; Uhlig, 1963). Solution treatment at approximately 1000°C ensures that the carbon reaches a state of solid supersaturation and precipitation of the carbide is reduced. Moreover, because the amount of carbon itself in the solid solution is maintained at a low level, it has relatively low strength properties, such as yield stress, compared with 316L stainless steel, which contains a large amount of carbon.

Co-Cr alloys for biomedical applications are known as "Vitarium" and are classified into those used for casting and those used for wrought alloys (ASTM standards, 2004a,b). In casted Co-Cr alloys, various defects are introduced during solidification; thus, their toughness is lower than that of wrought alloys, and it is difficult to improve their strength. Therefore, cast defects are removed using hot isostatic pressing (HIP). When doing this, we adjust the solidification structure and crystal grain size distribution using the molten metal temperature and the casting mold temperature to impose certain mechanical properties. In contrast, wrought Co-Cr alloys have outstanding ductility compared to casting alloys because the cast defect and structure are destroyed, and the internal defects are extinguished; however, it is difficult to form them into complex shapes. For both casting and wrought materials, the carbide disperses during the Co-based parent phase hence strengthening can be expected; however, in wrought alloys, the solution treatment temporarily extinguishes the carbide, which plastically deforms under the recrystallization temperature and introduces dislocation inside the crystal grain. The following ageing treatment for a process intended to change the microstructure of the materials by extended heat treatment, creates a homogeneous dispersion of the carbide inside the parent grains; therefore, high strength is achieved through precipitation hardening without reducing toughness. As a result, Co-Cr alloys demonstrate high strength and abrasion resistance even though they have a higher Young's modulus than bone. As a result, Co-Cr alloys are used in many artificial hips, especially, femoral head prosthesis.

Pure Ti and Ti alloys have a strong affinity for oxygen (O), and their mechanical properties tend to degrade with an increase in oxygen concentration. Furthermore, the same is true for N; therefore, the concentrations of these two elements are maintained

at low levels (Finlay and Snyder, 1950). Furthermore, the mechanical properties of (α + β) duplex alloys strongly depend on the amount of precipitation and the shape of precipitation of the α-phase. In particular, using hot forging in the duplex phase region to control the α-phase, such that the needle-shaped structure is changed to the equiaxed grain-shaped structure, results in a decline in strength but an improvement in ductility, enabling a balance between the two structures to be achieved. Moreover, the microstructure and even mechanical properties of β-type Ti alloys can be controlled with heat treatment. Precipitation of the α-phase and ω-phase, both of which belong to the hexagonal crystal system, causes the strength to increase owing to heat treatment in the unstable regions of the β-phase; at the same time, it causes the ductility to decline. Therefore, microstructural control is generally implemented to optimize the mechanical properties by reducing the precipitation of the ω-phase and controlling the precipitation of the α-phase.

3.7 Development of metallic biomaterials based on biological bone tissues

3.7.1 Anisotropic nature of bone microstructure for optimal mechanical design of metallic biomaterials

Up until the previous paragraph, the properties of metallic biomaterials and the factors that control these properties from the perspective of metallic implants are discussed. On the other hand, because most metallic implants are used by embedding them in biological structures, particularly in biological bone tissues, it is necessary to develop metallic biomaterials such that the mechanical characteristics and microstructure of bone tissue, and also the environment for bone cells, are maintained. Meanwhile, since the consensus statement by the US National Institutes of Health (NIH) in 2000, bone quality has received attention as one of the factors governing bone strength other than the traditional indicator of bone mineral density (NIH Consensus, 2001). In 2000, leading candidates for bone quality that were proposed included the formation and restoration of bone microstructure—typically the network structure of trabecular bone—and microcracks, the state of the collagen, bone turnover, and cell viability; however, our current understanding of the essential factors responsible for controlling bone quality remains insufficient.

Bones possess a hierarchical structure that is precisely controlled at various levels. Its major components, excluding water, minor proteins, and bone cells, are basically type I collagen and biological apatite (BAp), with a combination of these two components giving the bones their flexibility and strength, respectively.

Of these components, BAp, as shown in Fig. 3.14, is a highly anisotropic ionic crystal with a crystal structure similar to a hexagonal column as its basic unit cell; therefore, the mechanical, chemical, and biological characteristics of bones strongly depend on the crystallographic orientation, that is, along the *a*-axis and *c*-axis (Elliot, 1994). Moreover, in the bone structure, the nucleation site of the BAp crystals

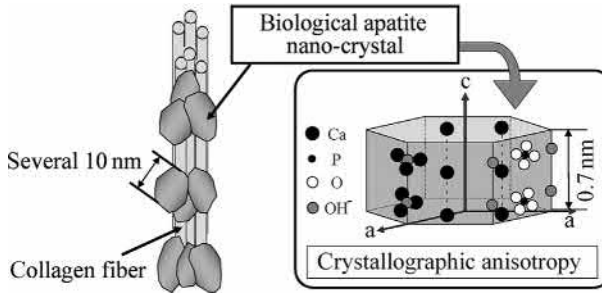


Fig. 3.14 Bone structure mainly comprises collagen (type I) and biological apatite (BAp) crystal, with the *c*-axis of the BAp crystallite arranged in the running direction of the collagen. Bone structure exhibits strongly anisotropic mechanical properties owing to the orientation of both of these components.

seems to be inside the collagen hole zone, and it is thought that calcification, also known as mineralization, progresses as a result of epitaxial nucleation and growth on the basis of the existence of the matrix vesicle. Therefore, analyses of the orientation degree of BAp crystals also reflect collagen organization, and the orientated structure formation of the BAp/collagen composite as bone tissue is thought to be an extremely important factor for determining bone function (Sasaki et al., 1989; Landis et al., 1993; Nakano et al., 2005).

The preferential alignment of BAp crystals in the bone structure changes substantially depending on bone pathology and bone regeneration; even in the case of normal bones, it changes substantially depending on various parameters such as the animal species, bone position, and maturation (Nakano et al., 2005). Fig. 3.15 shows the orientation degree of the BAp *c*-axis as the relative diffraction intensity ratio of (002)/(310) in various mature animal bones analyzed using microbeam X-ray diffraction (μXRD) (Nakano et al., 2002). In the case of non-orientation, intensity ratio of(002)/(310) indicate approximately 2, meaning that, in cases with higher diffraction intensity than this, it exhibits the preferential orientation degree of the BAp crystal *c*-axis. The bone mineral density of mature bone tissue does not change substantially; however, the structure of BAp has a uniaxial orientation with the *c*-axis preferentially aligned in the longitudinal, mesiodistal, and craniocaudal axis directions in the rabbit ulna, monkey mandible, and monkey lumber vertebra, respectively, in cortical bone sites. On the other hand, the bone of the rabbit skull, which is a flat bone, has a two-dimensional orientation within the bone surface. This characteristic orientation distribution is deeply related to the in vivo stress distribution and bone growth direction of normal metabolic turnover. In particular, the orientation for which a strong *c*-axis orientation is recognized corresponds with the maximum load orientation (Nakano et al., 2002).

The monkey mandible basically has a BAp orientation, which is in line with the mesiodistal direction parallel to the C-orientation in Fig. 3.15; however, directly below the coronal portion it starts to show the maximum orientation with respect

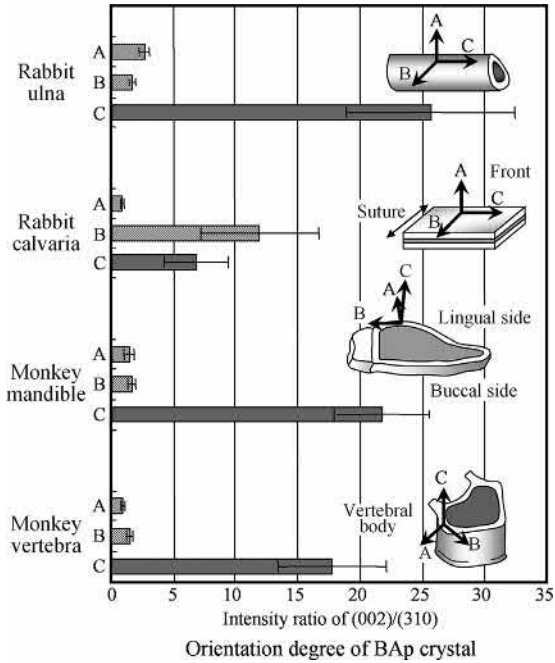


Fig. 3.15 Orientation degree of the *c*-axis of BAp crystallite in mature cortical bone analyzed with microbeam X-ray diffraction (μXRD). The bones show the characteristic anisotropic microstructure for each portion, and the preferential degree of orientation can be found. In this case, when there is non-orientation the value of 2 is shown.
Reproduced from Nakano et al. (Nakano et al., 2002) with modifications.

to the mastication load orientation along the B-orientation. This tendency is strong on the buccal side, which is easily exposed to the mastication load, and it controls the BAp orientation by handling the complex local changes in the in vivo local stress distribution due to mastication (Nakano et al., 2002).

As shown in Fig. 3.16, various factors including bone pathology, bone regeneration, and gene mutation have been found to affect the collagen/BAp orientation (Nakano et al., 2002, 2012; Nakano, 2015; Matsugaki et al., 2012, 2015; Noyama et al., 2013; Ishimoto et al., 2013, 2017a, 2018; Shinno et al., 2016; Sekita et al., 2017a,b; Kimura et al., 2017; Kuroshima et al., 2017a,b; Wang et al., 2017; Sasaki et al., 2018). Formation of the preferential orientation is closely related to the external environment such as the stress distribution and the in vivo environment, and is strongly controlled by the cellular level actions of osteoblast, osteoclast, and osteocyte. Research is currently progressing to elucidate the formation mechanism of the preferential orientation of the bone extracellular matrix from the molecular level and gene level responsible for biological signal transduction to specify the factors controlling its orientation.

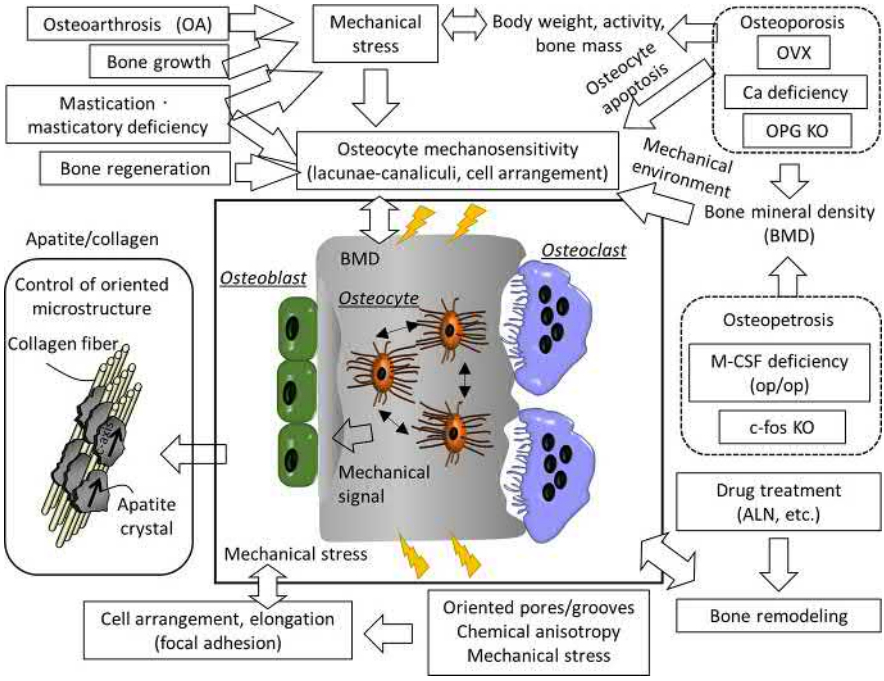


Fig. 3.16 Numerous controlling factors that determine the degree of *c*-axis orientation of BAp crystallite.
Reproduced from Nakano, T., 2015. Bone tissue and biomaterial design based on the anisotropic microstructure. In: Niinomi, M., Narushima, T., Nakai, M. (Eds.) Advances in Metallic Biomaterials: Tissues, Materials and Biological Reactions, Springer Berlin Heidelberg, Berlin, Heidelberg, 2015, pp. 3–30; Nakano, T., Ishimoto, T., 2015. Powder-based additive manufacturing for development of tailor-made implants for orthopedic applications. KONA Powder Part. J. 32, 75–84.; Ikeo, N., Ishimoto, T., Nakano, T., 2015. Novel powder/solid composites possessing low Young's modulus and tunable energy absorption capacity, fabricated by electron beam melting, for biomedical applications. J. Alloys Compd. 639, 336–340, with modifications.

3.7.2 Improvement of the mechanical functions based on the combination of both metallic biomaterials and biological bones

The orientation of collagen/BAp inside biological bones strongly depends on the in vivo stress distribution. In particular, the principal stress direction and the *c*-axis preferential orientation of the BAp correspond well; therefore, metallic implants should be optimally designed to maintain the healthiness of this bone microstructure. Generally, the homeostasis of bone microstructure is maintained and bone remodeling progresses due to osteoblasts that form the bone, osteoclasts that resorb the bone, and osteocytes that sense the stress distribution within the bones. Ensuring that the

direction of the grooves and pores correspond with the principal stress direction provides an optimal environment for the bone cells (Noyama et al., 2013; Kuroshima et al., 2017b; Nakano et al., 2006); this, in particular, enables the sensing of the stress by the osteocytes to approach a more normal state. Broadly classified, three necessary points are required for future types of artificial joints: (1) surface design, (2) improvement of the properties of the materials themselves, and (3) switching to tailor-made macroshapes. Regarding (1) surface design, a surface shape to maintain the bone quality surrounding the metallic implants is extremely important to encourage autonomic bone conductivity, finally making fixation over a long time feasible. As a result, this leads to an improvement in the mechanical functions of metallic biomaterials and biological bones in combination. Moreover, as mentioned before in this chapter, controlling the properties of the materials is extremely effective. In particular, designing the composition and shock absorption properties of future types of metallic biomaterials such that the difference in the elastic modulus is largely eliminated compared to bone is an important challenge. Moreover, the switch to tailor-made shapes that accurately fit the shape of the medullary cavity in the bones of individual patients, made possible by the combination of CT image construction and the development of additive manufacturing technology as mentioned in Section 3.8, is expected to accelerate even more in the future along with changes in medical standards.

3.7.3 Development of metallic implants with low Young's modulus based on single crystals of β-type Ti alloys

In addition to controlling the balance between strength and ductility as an approach to achieving microstructural control and alloying design, reduction of the elastic modulus of the implant is a major challenge a metallic implant would have to overcome. This is because the cortical long bone shows a low Young's modulus of about 30 GPa along the longitudinal axis, whereas most metallic biomaterials exhibit a high Young's modulus derived from a strong interatomic bonding force. In 316L stainless steel, the Young's modulus is approximately 160 GPa, in Co-Cr alloys it is approximately 200 GPa, and in pure titanium it is approximately 110 GPa. As a result, when metallic biomaterials are introduced into bone in parallel, the difference in Young's modulus with bone causes stress shielding, thereby inhibiting the signal transduction of stress through the osteocyte, which can sense in vivo stress distribution to ultimately result in the promotion of bone loss and the degradation of bone quality (Noyama et al., 2012).

Single crystallization of some metal biomaterials can create bone implants that can suppress stress shielding. In this regard, β-type Ti alloy with a bcc structure shows a relatively low Young's modulus even in polycrystalline form. However, it is possible to further lower the Young's modulus by manifesting the anisotropy of the modulus depending on the crystal orientation by single crystallization of some β-type Ti alloys.

Fig. 3.17 shows the dependency of Young's modulus on the crystal orientation in a single crystal of a β-type Ti-15Mo-5Zr-3Al alloy, which is regulated by ISO (ISO 5832-14) (ISO 5832-14, 2007). This figure also exhibits the dependence of Young's modulus on the orientation of a single crystal of β-type Ti alloy with a different mean

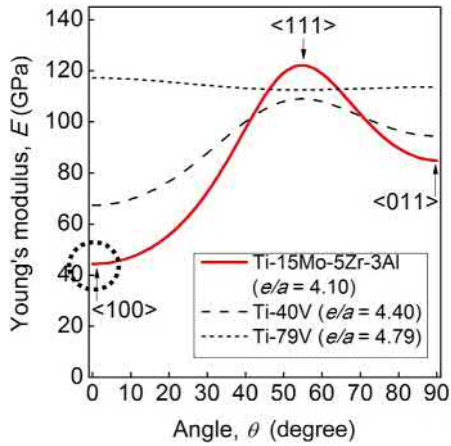


Fig. 3.17 Orientation dependence of Young's modulus in Ti-15Mo-5Zr-3Al single crystals and other β-type Ti single crystals. The *e*/*a* ratio strongly affects the anisotropy of Young's modulus in β-type Ti single crystals. The areas enclosed by broken lines show minimum Young's modulus of Ti-15Mo-5Zr-3Al alloy in single crystalline form.
Reproduced from Lee, S.H., Todai, M., Tane, M., Hagihara, K., Nakajima, H., Nakano, T., 2012. Biocompatible low Young's modulus achieved by strong crystallographic elastic anisotropy in Ti–15Mo–5Zr–3Al alloy single crystal. J. Mech. Behav. Biomed. Mater. 14, 48–54 with modifications.

valence electron number, *e*/*a*, which is the number of valence electrons per atom. Furthermore, the Young's modulus value of E_{100} and its anisotropy, E_{100}/E_{111}, depend on the *e*/*a* (Tane et al., 2008; Lee et al., 2012; Hagihara et al., 2016). As the ratio of *e*/*a* decreases and approaches 4, the anisotropy of E_{100}/E_{111} and E_{100} decrease remarkably.

The β-type Ti-15Mo-5Zr-3Al alloy has a low *e*/*a* ratio of 4.1 as well as a low Young's modulus of approximately 85 GPa even in the polycrystalline form. As a result, owing to the large anisotropy caused by single crystallization and the reduction in E_{100}, the Young's modulus in ⟨100⟩, E_{100}, decreases to 44.4 GPa (Lee et al., 2012).

This low value is comparable to ∼ 30 GPa, which is the Young's modulus of the long bone along the longitudinal bone axis as shown in Fig. 3.17. Thus, implantation of a β-type Ti-15Mo-5Zr-3Al alloy single crystal parallel to the ⟨100⟩ would be expected to suppress the stress shielding by implanting in a direction parallel to the longitudinal axis of the long bone (Lee et al., 2012; Nakano and Ishimoto, 2015).

3.8 Additive manufacturing technology for developing metallic biomaterials

Metal additive manufacturing allows the creation of metallic biomaterials with superior mechanical properties by simultaneously controlling the shape parameters and microstructural parameters. In other words, besides bone-like anisotropic design that

entails shaping the external and internal structures of complicated shapes by tailoring designs, it is possible to control the atomic arrangement to resemble that of a single crystal to achieve the desired mechanical properties in a specific direction. The powder bed fusion method of metal additive manufacturing provides a certain directionality; moreover, because the irradiation direction of the heat source beam and the stacking-layered plane are close to perpendicular to each other, high functionality products can be demonstrated in a specific direction by fabrication under optimal conditions. It is also possible to demonstrate anisotropy and conversely isotropic properties (Nakano and Ishimoto, 2015).

3.8.1 Control of mechanical anisotropy by controlling the shape of biomaterials with additive manufacturing

The shape parameters hierarchically include both external and internal shapes such as the microstructural and/or cellular shape and the arrangement of the solid parts. The important microstructural parameters are obtained by the selection of materials with different physical properties and different atomic arrangements such as polycrystalline, columnar-like crystalline, and single crystalline. Ultimately, it is possible to simultaneously control the hierarchical shape and a microstructure such as a single crystal for metallic biomaterials (Tane et al., 2008; Lee et al., 2012; Nakano and Ishimoto, 2015). The most important feature of shape parameter control and hierarchical additive manufacturing technology is to enable the production of highly functional complex, arbitrarily shaped products. In addition, from the viewpoint of mimicking natural creatures, products obtained by additive manufacturing can be expressed by the features and anisotropies of the hierarchy of each size scale as shape parameters, and also expressed by the functionality by organically combining them. Even the most advanced forming and cutting method allows shape parameters to be imparted to a certain extent, but it is difficult to impart characteristics such as a hierarchical structure, a complicated shape, and an inner hole structure in one step.

Fig. 3.18 (Nakano et al., 2017) shows the typical nominal stress-nominal strain curves in a product fabricated with anisotropic inner bodies along the X-, Y-, and *Z*-axes with $3 \times 3 \times 3 = 27$ cubic compartments as a model case for anisotropy. In this case, 14 of the 27 cubic compartments were melted and then solidified, and the other part was filled with Ti-6Al-4V ELI alloy powder with a bulk density approximating 50%. Even in the internal structure of only 27 cubic compartments, when the X-, Y-, and Z-axes are fixed, the number of combinations of solid cubic arrangements exceeds 100 million. Thus, it is necessary to estimate the mechanical properties of the products by using computer simulation based on the mixing rule to design products before they are fabricated.

As shown in Fig. 3.18, Young's modulus and the yield stress decrease in the order of compression along the Z-, Y-, and X-axes (Nakano and Ishimoto, 2015; Nakano et al., 2017). In this case, the number of through-column structures is 4, 2, and 0, respectively. This suggests that the arrangement of the columnar structure as the internal shape structure strongly influences the mechanical properties. The unmelted cubic compartments contain metallic powder, which is the raw material that should

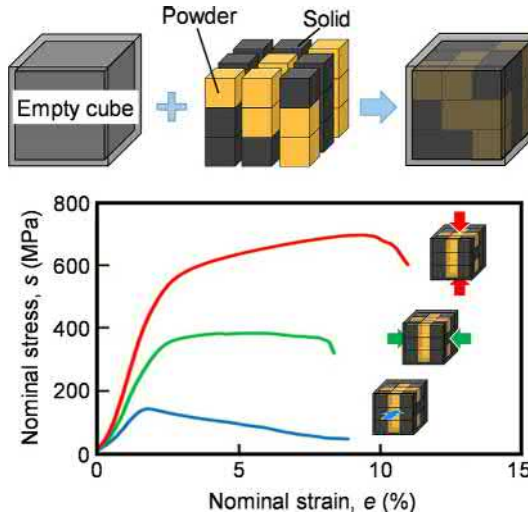


Fig. 3.18 Typical anisotropic nominal stress-nominal strain curves depending on the loading axis in the powder/solid product fabricated with anisotropic inner bodies along the X-, Y-, and *Z*-axes with $3 \times 3 \times 3 = 27$ cubic compartments as a model case for anisotropy. Reproduced from Nakano, T., Ishimoto, T., 2015. Powder-based additive manufacturing for development of tailor-made implants for orthopedic applications. KONA Powder Part. J. 32, 75–84; Nakano, T., Fukuda, H., Takahashi, H., 2017. Development of a new powder/solid composite for biomimic implant materials by electron-beam additive manufacturing. Mater. Sci. Forum 879, 1361–1364 with modifications.

originally have been removed. This powder has been enclosed for hierarchical design, and this structure was named the powder (P)/solid (S) composite (Ikeo et al., 2015). The powder (P) hardly affects the mechanical properties in the AMed condition. However, as shown in Fig. 3.19, optimal heat treatment produces strong necking within the powder and/or between the powder and the inner walls of the structure, thus giving rise to impact absorption energy approximately 10 times higher than before the heat treatment. That is, from the powder particles (of the order of tens of micrometers) to the internal structure of the inner wall (of the order of several millimeters) and the entire body surrounded by the external wall (of the order of several centimeters), a product with a hierarchical structure exerts macroscopic mechanical properties (Ikeo et al., 2015).

3.8.2 Control of crystallographic anisotropy to suppress stress shielding by additive manufacturing

The conditions under which metal additive manufacturing are carried out according to the process parameters of additive manufactured fabrication (e.g., the solubility/solidification, heat transfer/transmission direction, and thermal history) enable not only the shape but also the microstructural parameters to be controlled (Nakano and Ishimoto, 2015; Nakano et al., 2017; Ikeo et al., 2015; Nie et al., 2014; Hagihara et al., 2017;

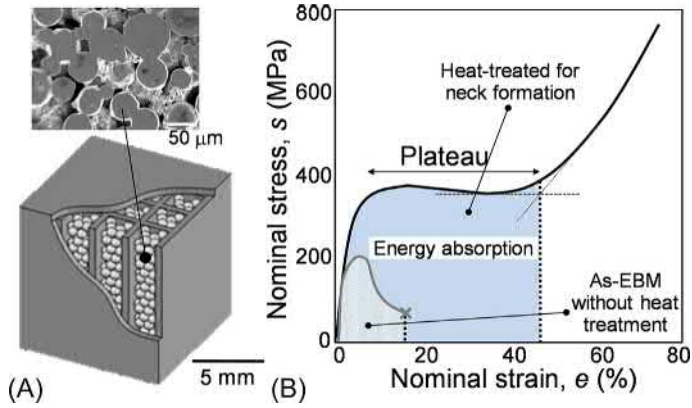


Fig. 3.19 (A) Schematic illustration of an AM fabricated product in which unmelted powder remains and SEM image of the powder part after heat treated. (B) Nominal stress-nominal strain curves of the products with and without heat treatment that makes powders necked. The product with the necked powder inside becomes highly energy absorptive due to the stress transmission between powders through the necks.
Reproduced from Ikeo, N., Ishimoto, T., Nakano, T., 2015. Novel powder/solid composites possessing low Young's modulus and tunable energy absorption capacity, fabricated by electron beam melting, for biomedical applications. J. Alloys Compd. 639, 336–340 with modifications.

Sun et al., 2018). In metals, various microstructural parameters such as the crystal grain size, shape and distribution, crystal grain boundary character, crystallographic texture, and porosity, all of which are directly related to the functionality of the fabricated products, can be controlled. In particular, additive manufacturing is an excellent way to control the crystallographic orientation relationship based on the formation of the melt pool owing to the directionality of the heat source.

Fig. 3.20 shows the dependence of the crystallographic orientation of products manufactured using the laser powder bed fusion method by employing β-type Ti-15Mo-5Zr-3Al alloy powder for the scan strategy (Scan Strategy X, and Scan Strategy XY) on the two-dimensional XY plane. In this case, the two types of scanning strategies were as follows: the first entailed bidirectional (zigzag) scanning along the X-axis (Scan Strategy X), as illustrated in Fig. 3.20A, whereas the other involved bidirectional scanning with a rotation of 90° between layers (Scan Strategy XY) in which the X-scan and Y-scan are repeated [Fig. 3.20C]. The figure shows the IPF maps obtained by the electron back scatter diffraction patterns (EBSD) method using each scanning strategy (Ishimoto et al., 2017b). Although low-angle grain boundaries with slight orientation differences are observed, single-crystal-like crystalline structures are formed independent of the scan strategies. In Scan Strategy X, ⟨100⟩ orients in the scan (X) direction and ⟨011⟩ orients in the scan (Y) and (Z) directions, but in Scan Strategy XY, ⟨100⟩ oriented preferentially in the scan (X), (Y), and

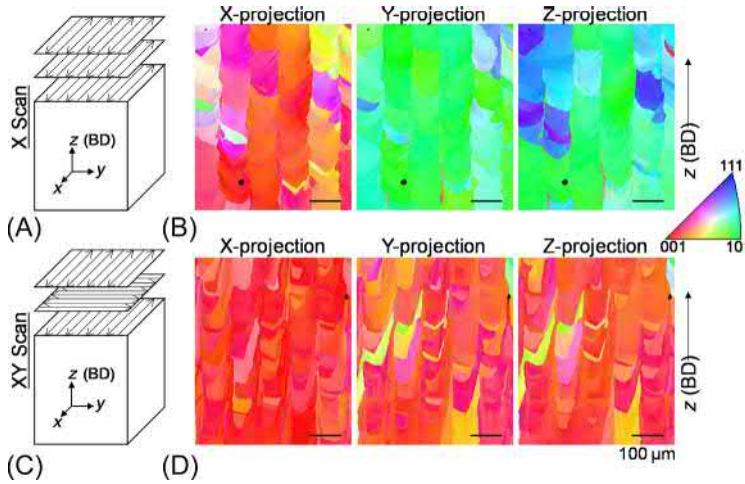


Fig. 3.20 Variations in crystallographic orientation depending on the scan strategy, (A, B) Scan Strategy X and (C, D) Scan Strategy XY.
Reproduced from Ishimoto, T., Hagihara, K., Hisamoto, K., Sun, S.-H., Nakano, T., 2017b. Crystallographic texture control of beta-type Ti–15Mo–5Zr–3Al alloy by selective laser melting for the development of novel implants with a biocompatible low Young's modulus. Scr. Mater. 132, 34–38 with modifications.

(Z) directions (Ishimoto et al., 2017b). That is, bidirectional scanning with and without a rotation of 90° between the layers gave rise to different crystallographic textures with preferential orientations of ⟨001⟩ and ⟨011⟩ along the building direction, respectively. Control of the growth behavior of the columnar cells in the melt pools via scan strategies enabled the generation of these different textures. The selection of such a crystal orientation is formed by a competitive relationship between the stability of the crystal orientation and epitaxial growth in the melt pool. ⟨100⟩ orients parallel to the migration direction of the solid-liquid interface in the melt pool according to the thermal gradient. As stacking progresses, however, a single crystalline-like crystal orientation is formed and epitaxial growth is prioritized rather than the stability of the crystal orientation. This leads to the formation of columnar-like crystalline or single crystalline-like bodies with different crystal orientations depending on the scan strategy.

In addition, it is possible to seed specific crystal directions by subsequent epitaxial growth by using a seed consisting of a single crystal (Nakano et al., 2014). Because low elasticity in bone substitute implant material is effective for reducing stress shielding, crystal growth to ⟨100⟩ in β-type Ti alloy is very important.

Controlling the scan strategy in additive manufacturing is expected to stabilize the crystal orientation and promote epitaxial growth; furthermore, the method of additive manufacturing finally enables a single crystal to be obtained at an early stage by seeding. As a result, it is possible to develop a metal biomaterial with low elasticity of which the behavior mimics that of bone.

3.9 Summary

Metallic materials have a long history as structural materials, and currently metallic biomaterials are expansively being understood and developed. On the other hand, the properties of metallic biomaterials need to be such that they can endure use in special environments, for example it is necessary to reduce the toxic elements in these materials so they can be used in vivo. Moreover, structural inducibility and other interactions of metallic biomaterials with cells and biological structures are also important. Space constraints prevented me from fully explaining these issues in this chapter. However, I described the way in which the mechanical properties of metallic biomaterials can be controlled at the atomic level, and how these materials inherently have the potential to play an extremely important future role as structural materials centered on the load support function. Many current metallic biomaterials were initially developed for other applications, for example heat-resistant structural materials, and were subsequently diverted to biomedical applications. From this perspective, the developmental research of metallic materials specifically for biomedical applications has only just begun. Research into materials from which to manufacture implantations intended to serve as load-bearing parts is a field foreseen to undergo major development and contribute to building new theories in the future. These materials are centered on the assignment of mechanical properties and the maintenance of an intact bone microstructure, especially the degree of orientation of the BAp crystal as an index of bone quality surrounding the metallic implants. Metal additive manufacturing is also expected to contribute to customized medical treatment as a technique for modeling new future anisotropic/isotropic biomaterials.

Acknowledgments

This work was supported in part by Grants-in-Aid for Scientific Research (S) (grant numbers JP25220912 and JP18H05254) and (A) (grant number JP18H03844) from the Japan Society for the Promotion of Science.

References

ASTM standards, 2004a. Standard specification for cast cobalt-28 chromium-6 molybdenum alloy castings and casting alloy for surgical implants. In: Annual Book of ASTM standards, F75–01.pp. 44–47.

ASTM standards, 2004b. Standard specification for wrought cobalt-28 chromium-6 molybdenum alloys for surgical implants. In: Annual Book of ASTM standards, F1537-00. pp. 675–677.

Cahn, R.W., Haasen, P., 1996. Physical Metallurgy, fourth ed. vol. 1–3. Elsevier Science B.V, Amsterdam.

Cullity, B.D., Stock, S.R., 2001. Elements of X-Ray Diffraction, third ed. Prentice Hall, New Jersey.

Dieter, G.E., 1986. Mechanical Metallurgy, third ed. McGraw-Hill, New York.

Elliot, J.C., 1994. Structure and Chemistry of the Apatites and Other Calcium Phosphates. Elsevier, Amsterdam.

Finlay, W.L., Snyder, J.A., 1950. Effect of three interstitial solutes (nitrogen, oxygen, and carbon) on the mechanical properties of high-purity alpha titanium. Transactions of the AIME 188, 277–286.

Hagihara, K., Nakano, T., 2017. Experimental clarification of the cyclic deformation mechanisms of β-type Ti-Nb-Ta-Zr-alloy single crystals developed for the single-crystalline implant. Int. J. Plast. 98, 27–44.

Hagihara, K., Nakano, T., Maki, H., Umakoshi, Y., Niinomi, M., 2016. Isotropic plasticity of beta-type Ti-29Nb-13Ta-4.6Zr alloy single crystals for the development of single crystalline beta-Ti implants. Sci. Rep. 6, 29779.

Hagihara, K., Nakano, T., Suzuki, M., Ishimoto, T., Suyalatu, S.-H.S., 2017. Successful additive manufacturing of $MoSi_2$ including crystallographic texture and shape control. J. Alloys Compd. 696, 67–72.

Hirth, J.P., Lothe, J., 1968. Theory of Dislocations. McGraw-Hill, New York.

Ikeo, N., Ishimoto, T., Nakano, T., 2015. Novel powder/solid composites possessing low Young's modulus and tunable energy absorption capacity, fabricated by electron beam melting, for biomedical applications. J. Alloys Compd. 639, 336–340.

Ishimoto, T., Nakano, T., Umakoshi, Y., Yamamoto, M., Tabata, Y., 2013. Degree of biological apatite c-axis orientation rather than bone mineral density controls mechanical function in bone regenerated using recombinant bone morphogenetic protein-2. J. Bone Miner. Res. 28, 1170–1179.

Ishimoto, T., Sato, B., Lee, J.W., Nakano, T., 2017a. Co-deteriorations of anisotropic extracellular matrix arrangement and intrinsic mechanical property in c-src deficient osteopetrotic mouse femur. Bone 103, 216–223.

Ishimoto, T., Hagihara, K., Hisamoto, K., Sun, S.-H., Nakano, T., 2017b. Crystallographic texture control of beta-type Ti–15Mo–5Zr–3Al alloy by selective laser melting for the development of novel implants with a biocompatible low Young's modulus. Scr. Mater. 132, 34–38.

Ishimoto, T., Yamada, K., Takahashi, H., Takahata, M., Ito, M., Hanawa, T., Nakano, T., 2018. Trabecular health of vertebrae based on anisotropy in trabecular architecture and collagen/apatite micro-arrangement after implantation of intervertebral fusion cages in the sheep spine. Bone 108, 25–33.

ISO 5832-14:2007, Implants for surgery -Metallic materials- Part 14: Wrought titanium 15-molybdenum 5-zirconium 3-aluminium alloy, 2007.

Kikuchi, T., Morizane, A., Doi, D., Magotani, H., Onoe, H., Hayashi, T., Mizuma, H., Takara, S., Takahashi, R., Inoue, H., Morita, S., Yamamoto, M., Okita, K., Nakagawa, M., Parmar, M., Takahashi, J., 2017. Human iPS cell-derived dopaminergic neurons function in a primate Parkinson's disease model. Nature 548, 592.

Kimura, Y., Matsugaki, A., Sekita, A., Nakano, T., 2017. Alteration of osteoblast arrangement via direct attack by cancer cells: new insights into bone metastasis. Sci. Rep. 7. 44824.

Kuroshima, S., Kaku, M., Ishimoto, T., Sasaki, M., Nakano, T., Sawase, T., 2017a. A paradigm shift for bone quality in dentistry: a literature review. Journal of Prosthodontic Research 61, 353–362.

Kuroshima, S., Nakano, T., Ishimoto, T., Sasaki, M., Inoue, M., Yasutake, M., Sawase, T., 2017b. Optimally oriented grooves on dental implants improve bone quality around implants under repetitive mechanical loading. Acta Biomater. 48, 433–444.

Landis, W.J., Song, M.J., Leith, A., McEwen, L., McEwen, B.F., 1993. Mineral and organic matrix interaction in normally calcifying tendon visualized in three dimensions by high-voltage electron microscopic tomography and graphic image reconstruction. J. Struct. Biol. 110, 39–54.

Lee, S.H., Todai, M., Tane, M., Hagihara, K., Nakajima, H., Nakano, T., 2012. Biocompatible low Young's modulus achieved by strong crystallographic elastic anisotropy in Ti–15Mo–5Zr–3Al alloy single crystal. J. Mech. Behav. Biomed. Mater. 14, 48–54.

Matsugaki, A., Aramoto, G., Nakano, T., 2012. The alignment of MC3T3-E1 osteoblasts on steps of slip traces introduced by dislocation motion. Biomaterials 33, 7327–7335.

Matsugaki, A., Aramoto, G., Ninomiya, T., Sawada, H., Hata, S., Nakano, T., 2015. Abnormal arrangement of a collagen/apatite extracellular matrix orthogonal to osteoblast alignment is constructed by a nanoscale periodic surface structure. Biomaterials 37, 134–143.

Nabarro, F.R.N., 1979. Dislocations in Solid. North-Holland Publishing Company, Amsterdam.

Nakano, T., 2015. Bone tissue and biomaterial design based on the anisotropic microstructure. In: Niinomi, M., Narushima, T., Nakai, M. (Eds.), Advances in Metallic Biomaterials: Tissues, Materials and Biological Reactions, Springer Berlin Heidelberg, Berlin, Heidelberg. pp. 3–30.

Nakano, T., Ishimoto, T., 2015. Powder-based additive manufacturing for development of tailor-made implants for orthopedic applications. KONA Powder and Particle Journal 32, 75–84.

Nakano, T., Kaibara, K., Tabata, Y., Nagata, N., Enomoto, S., Marukawa, E., Umakoshi, Y., 2002. Unique alignment and texture of biological apatite crystallites in typical calcified tissues analyzed by microbeam x-ray diffractometer system. Bone 31, 479–487.

Nakano, T., Tabata, Y., Umakoshi, Y., 2005. Texture and bone reinforcement. In: Buschow, K.-H.J., Cahn, R.W., Flemings, M.C., Ilschner, B., Kramer, E.J., Mahajan, S., Veyssière, P. (Eds.), Encyclopedia of Materials: Science and Technology. Elsevier, Oxford, pp. 1–8.

Nakano, T., Kan, T., Ishimoto, T., Ohashi, Y., Fujitani, W., Umakoshi, Y., Hattori, T., Higuchi, Y., Tane, M., Nakajima, H., 2006. Evaluation of bone quality near metallic implants with and without lotus-type pores for optimal biomaterial design. Mater. Trans. 47, 2233–2239.

Nakano, T., Hagihara, K., Maki, H., Umakoshi, Y., Niinomi, M., 2007. Crystal growth and plastic deformation behavior of Ti-29Nb-13Ta-4.6Zr Bcc-based single crystal, Ti-2007. In: Proceedings of the Eleventh World Conference on Titanium, JIMIC-5, 4–8 September 2007, City, Country, pp. 1437–1439.

Nakano, T., Kaibara, K., Ishimoto, T., Tabata, Y., Umakoshi, Y., 2012. Biological apatite (BAp) crystallographic orientation and texture as a new index for assessing the microstructure and function of bone regenerated by tissue engineering. Bone 51, 741–747.

Nakano, T., Nakamoto, T., Serizawa, A., Inoue, T., Sugawara, T., Shirakawa, N., Yamaguchi, K., 2014. Method for Producing Single Crystal, Japanese Unexamined Patent Application Publication No. 2014–06729.

Nakano, T., Fukuda, H., Takahashi, H., 2017. Development of a new powder/solid composite for. Biomimic Implant Materials by Electron-Beam Additive Manufacturing, Materials Science Forum 879, 1361–1364.

Nie, P., Ojo, O.A., Li, Z., 2014. Numerical modeling of microstructure evolution during laser additive manufacturing of a nickel-based superalloy. Acta Mater. 77, 85–95.

NIH Consensus, 2001. Osteoporosis prevention, diagnosis, and therapy. J. Am. Med. Assoc. 285, 785–795.

Niinomi, M., 2003. Fatigue performance and cyto-toxicity of low rigidity titanium alloy, Ti–29Nb–13Ta–4.6Zr. Biomaterials 24, 2673–2683.

Noyama, Y., Miura, T., Ishimoto, T., Itaya, T., Niinomi, M., Nakano, T., 2012. Bone loss and reduced bone quality of the human femur after Total hip arthroplasty under stress-shielding effects by titanium-based implant. Mater. Trans. 53, 565–570.

Noyama, Y., Nakano, T., Ishimoto, T., Sakai, T., Yoshikawa, H., 2013. Design and optimization of the oriented groove on the hip implant surface to promote bone microstructure integrity. Bone 52, 659–667.

Sakaguchi, N., Niinomi, M., Akahori, T., Takeda, J., Toda, H., 2005. Relationships between tensile deformation behavior and microstructure in Ti-Nb-Ta-Zr system alloys. Mater. Sci. Eng. C 25, 363–369.

Sasaki, N., Matsushima, N., Ikawa, T., Yamamura, H., Fukuda, A., 1989. Orientation of bone mineral and its role in the anisotropic mechanical properties of bone–transverse anisotropy. J. Biomech. 22, 157–164.

Sasaki, M., Chubachi, S., Kameyama, N., Sato, M., Haraguchi, M., Miyazaki, M., Takahashi, S., Nakano, T., Kuroda, Y., Betsuyaku, T., Matsuo, K., 2018. Effects of long-term cigarette smoke exposure on bone metabolism, structure, and quality in a mouse model of emphysema. PLoS One. 13. e0191611.

Sekita, A., Matsugaki, A., Ishimoto, T., Nakano, T., 2017a. Synchronous disruption of anisotropic arrangement of the osteocyte network and collagen/apatite in melanoma bone metastasis. J. Struct. Biol. 197, 260–270.

Sekita, A., Matsugaki, A., Nakano, T., 2017b. Disruption of collagen/apatite alignment impairs bone mechanical function in osteoblastic metastasis induced by prostate cancer. Bone 97, 83–93.

Shinno, Y., Ishimoto, T., Saito, M., Uemura, R., Arino, M., Marumo, K., Nakano, T., Hayashi, M., 2016. Comprehensive analyses of how tubule occlusion and advanced glycation end-products diminish strength of aged dentin. Sci. Rep. 6. 19849.

Sumita, M., Hanawa, T., Teoh, S.H., 2004. Development of nitrogen-containing nickel-free austenitic stainless steels for metallic biomaterials—review. Mater. Sci. Eng. C 24, 753–760.

Sun, S.-H., Ishimoto, T., Hagihara, K., Tsutsumi, Y., Hanawa, T., Nakano, T., 2018. Excellent mechanical and corrosion properties of austenitic stainless steel with a unique crystallographic lamellar microstructure via selective laser melting. Scr. Mater. https://doi.org/10.1016/j.scriptamat.2018.09.017.

Takeuchi, S., Furubayashi, E., Taoka, T., 1967. Orientation dependence of yield stress in 4.4% silicon iron single crystals. Acta Metall. 15, 1179–1191.

Tane, M., Akita, S., Nakano, T., Hagihara, K., Umakoshi, Y., Niinomi, M., Nakajima, H., 2008. Peculiar elastic behavior of Ti–Nb–Ta–Zr single crystals. Acta Mater. 56, 2856–2863.

Taoka, T., Takeuchi, S., Furubayashi, E., 1964. Slip systems and their critical shear stress in 3% silicon Iron. J. Phys. Soc. Jpn. 19, 701–711.

Tonino, A.J., Davidson, C.L., Klopper, P.J., Linclau, L.A., 1976. Protection from stress in bone and its effects. Experiments with stainless steel and plastic plates in dogs. Journal of Bone and Joint Surgery Br. 58, 107–113.

Uhlig, H.H., 1963. Corrosion and Corrosion Control. Wiley, New York.

Wang, J., Ishimoto, T., Nakano, T., 2017. Unloading-induced degradation of the anisotropic arrangement of collagen/apatite in rat femurs. Calcif. Tissue Int. 100, 87–94.

Wert, C.A., Thomson, R.M., 1970. Physics of Solids, second ed. McGraw-Hill, New York.

Williams, D.F., 1981. Biocompatibility of Clinical Implant Materials. CRC Press, Boca Raton.

Williams, D.F., Cahn, R.W., Bever, M.B., 1990. Concise Encyclopedia of Medical & Dental Materials. Pergamon Press, Oxford.

Corrosion of metallic biomaterials

4

Sachiko Hiromoto
National Institute for Materials Science, Tsukuba, Ibaraki, Japan

4.1 Importance of corrosion

Corrosion is defined as the destructive attack of a metal by chemical or electrochemical reaction with water, oxygen (O_2), sulfur (S), and so on in its environment (Revie and Uhlig, 2008). The corrosion of metals in aqueous solutions is inevitable because metal elements, except noble metal elements, are thermodynamically more stable in the oxide state than in the metal state, according to their ionization tendency. The corrosion of metallic biomaterials causes the loss of their structural integrity and surface function. It accelerates their fatigue, fretting fatigue, and wear and, conversely, such damage accelerates the corrosion. The corrosion processes of metallic biomaterials can cause alterations to bioenvironments, such as change in pH, decrease in dissolved O_2, change in chemical components, and so on. Moreover, the very small amount of released metal ions may cause allergic response and carcinogenesis in the human body. Because of these problems, the allowable amount of corrosion of metallic biomaterials is much smaller than that for the structural materials of bridges, buildings, and so on. So, the corrosion process is one of the most important mediators of the tissue response to metallic biomaterials and an understanding and accurate evaluation of the corrosion behavior of metallic biomaterials are necessary.

Titanium (Ti) alloys, cobalt (Co)-chromium (Cr) alloys, and stainless steels are mainly used for orthopedic and cardiovascular implants not only because of their high strength but also due to the high corrosion resistance of their passive surface films (oxide film). Passive films of Ti, Cr, and so on show very high protectiveness against general corrosion. Noble metal alloys consisting of gold (Au), silver (Ag), platinum (Pt), and palladium (Pd) are used for dental materials and Pt is used for the electrodes of pace makers. Because of their low ionization tendency, the noble metals show relatively high thermodynamic stability, that is, high corrosion resistance. Here, "high corrosion resistance" means that the corrosion rate is sufficiently low from the viewpoint of the lifetime of the materials.

Release of metal ions from the passive and noble metals and alloys continues at a low level inside the human body. However, such materials as magnesium (Mg), iron (Fe), and zinc (Zn) alloys might be utilized for biodegradable/bioabsorbable metallic biomaterials in stents, mini/microplate systems, and so on. Since Mg exhibits very high ionization tendency and does not form protective film at around neutral pH, Mg alloys are expected to be easily corroded and to generate H_2 gas and hydroxide ions inside the human body. The corrosion rate of biodegradable metallic materials needs to be precisely controlled, depending on the sort of devices and the condition

Metals for Biomedical Devices. https://doi.org/10.1016/B978-0-08-102666-3.00004-3
© 2019 Elsevier Ltd. All rights reserved.

of the affected parts. As mentioned, the corrosion behavior and the expected corrosion rate of metallic biomaterials depend on various factors in a complicated manner. The parameters of the corrosion test should be carefully considered depending on the purpose.

4.2 Principle of corrosion

4.2.1 Corrosion process

Since corrosion processes are mostly electrochemical, an understanding of electrochemistry is very important. Furthermore, a fundamental understanding of physical metallurgy is also important because the structure and the composition of metallic materials often determine corrosion behavior (Revie and Uhlig, 2008).

On the surface of metallic materials immersed in an electrolyte, infinite number of atomic-size anodes and cathodes are formed as shown in Fig. 4.1. Short-circuit current (i) flows between local anodes and cathodes. A pair of local anode and cathode is called a local cell and the current flowing between them is called local current. The place of local anodes and cathodes changes every moment in the case of general corrosion. Moreover, the total anodic current is equivalent to the total cathodic current. As a result, the whole surface is uniformly attacked.

On local anodes, the dissolution (ionization) reaction of the metal M with releasing electrons (anodic reaction) (Eq. 4.1) takes place. On local cathodes, the reduction reaction of hydrogen (H^+) ions, dissolved O_2, or water molecules with receiving electrons (cathodic reaction) takes place. The kind of cathodic reaction depends on the pH of the electrolyte and the standard electrode potential of the metal. Cathodic reaction in acid and neutral electrolyte is generally the reduction of H^+ ions and dissolved O_2, respectively (Eqs. 4.2, 4.3). When the standard electrode potential of the metal, such

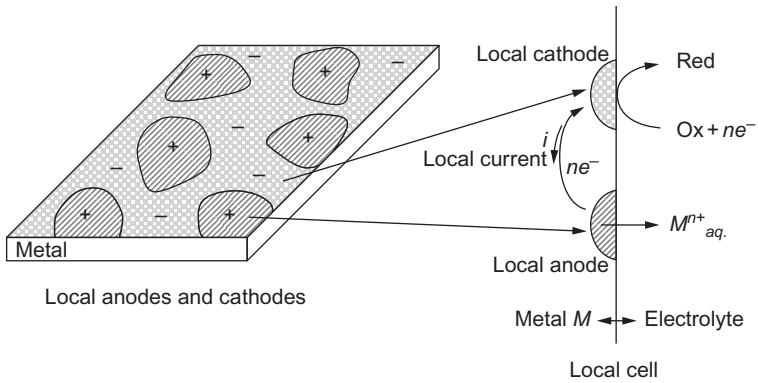


Fig. 4.1 Schematic illustration of the local anodes and cathodes, and a local-cell formed between them.

as Mg, is lower than that of water, the cathodic reaction in neutral electrolyte is the reduction of water (Eq. 4.4).

$$\mathrm{M} \rightarrow \mathrm{M}^{n+} + n\mathrm{e}^- \tag{4.1}$$

$$2\mathrm{H}^+ + 2\mathrm{e}^- \rightarrow \mathrm{H}_2 \tag{4.2}$$

$$\mathrm{O}_2 + 2\mathrm{H}_2\mathrm{O} + 4\mathrm{e}^- \rightarrow 4\mathrm{OH}^- \tag{4.3}$$

$$2\mathrm{H}_2\mathrm{O} + 2\mathrm{e}^- \rightarrow 2\mathrm{OH}^- + \mathrm{H}_2 \tag{4.4}$$

When a metal M is immersed in the solution of its own salt, such as Fe in iron sulfate ($FeSO_4$) solution, the redox reaction of Eq. (4.5) takes place as a single electrode reaction.

$$M \Leftrightarrow M^{n+} + n\mathrm{e}^- \tag{4.5}$$

The free energy change (ΔG) of the redox reaction is expressed by Eq. (4.6) with the standard free energy change (ΔG^0) and the activity of M^{n+} ions and metal M ($[M^{n+}]$ and $[M]$).

$$\Delta G = \Delta G^0 + RT \ln \frac{[M^{n+}]}{[M]} \tag{4.6}$$

where R and T are the gas constant and the absolute temperature, respectively. When the redox reaction is in an equilibrium state, $\Delta G = 0$. Then, the standard free energy change is given by Eq. (4.7).

$$-\Delta G^0 = RT \ln \frac{[M^{n+}]}{[M]} \tag{4.7}$$

At constant temperature, $-\Delta G^0/RT$ becomes constant, so that $[M^{n+}]/[M]$ becomes constant. In this case $[M^{n+}]/[M]$ is called equilibrium constant (K) of the redox reaction. The standard free energy change is then expressed as a function of the equilibrium constant [Eq. (4.8)].

$$-\Delta G^0 = RT \ln K \tag{4.8}$$

Here, the free energy change gives the electrode potential (E) of the redox reaction according to Eq. (4.9).

$$\Delta G = -nFE \tag{4.9}$$

where F is the Faraday number. According to Eqs. (4.6)–(4.9), the electrode potential of the redox reaction is given by Eq. (4.10).

$$E = -\frac{\Delta G^0}{nF} - \frac{RT}{nF}\ln\frac{\lfloor M^{n+}\rfloor}{[M]} = E_0 - \frac{RT}{nF}\ln\frac{[M^{n+}]}{[M]} \tag{4.10}$$

where $\Delta G^0 = -nFE^0$ and E^0 is the standard electrode potential. Eq. (4.10) is called Nernst equation and it gives the equilibrium potential of redox reactions. The tendency of the dissolution reaction of the metals can be estimated according to the Nernst equation.

The equilibrium potential of elements in the standard state is called the standard electrode potential which is expressed relative to the standard H_2 electrode (SHE) or normal H_2 electrode (NHE). The standard electrode potential of the elements relevant to metallic biomaterials is summarized in Table 4.1 (Revie and Uhlig, 2008; Kita and Uosaki, 1983). The standard electrode potential is equivalent to the electromotive force of elements, in the other words, the tendency of its dissolution reaction to proceed. However, the order of the standard electrode potential of the metallic elements does not directly correspond to that of the corrosion rate because the solubility of the metal salts is limited by a protective film which is often formed on the metal surface.

Because the redox reaction (electrochemical reaction) of a metal in its solution involves electrons and/or H^+ ions, the equilibrium potential of the electrochemical reaction can be thermodynamically calculated as a function of pH based on the Nernst equation. The potential is plotted as a function of pH and the potential-pH diagram is often called Pourbaix diagram (Pourbaix, 1966). The Pourbaix diagram is used to

Table 4.1 Standard electrode potential of elements relevant to metallic biomaterials (298 K) (Revie and Uhlig, 2008; Kita and Uosaki, 1983)

Electrode reaction	Standard electrode potential, E^0/V vs NHE
$Mg \leftrightarrow Mg^{2+} + 2e^-$	−2.36
$Al \leftrightarrow Al^{3+} + 3e^-$	−1.66
$Ti \leftrightarrow Ti^{2+} + 2e^-$	−1.63
$H_2 + 2OH^- \leftrightarrow 2H_2O + 2e^-$	−0.8281
$Zn \leftrightarrow Zn^{2+} + 2e^-$	−0.763
$Cr \leftrightarrow Cr^{3+} + 3e^-$	−0.744
$Fe \leftrightarrow Fe^{2+} + 2e^-$	−0.440
$Co \leftrightarrow Co^{2+} + 2e^-$	−0.277
$Ni \leftrightarrow Ni^{2+} + 2e^-$	−0.250
$H_2 \leftrightarrow 2H^+ + 2e^-$	±0.000
$Ag \leftrightarrow Ag^+ + e^-$	0.799
$Pd \leftrightarrow Pd^{2+} + 2e^-$	0.987
$Pt \leftrightarrow Pt^{2+} + 2e^-$	1.188
$2H_2O \leftrightarrow O_2 + 4H^+ + 4e^-$	1.229
$Au \leftrightarrow Au^{3+} + 3e^-$	1.498

estimate the corrosion behavior of metals in aqueous solutions. For more details, please refer text books on corrosion.

When the metal M is at the equilibrium potential discussed above, the rate of the anodic (oxidation) and the cathodic (reduction) reaction is equal. When the potential of the metal M is shifted by η (overpotential) from the equilibrium potential, the anodic reaction is promoted and the anodic current flows externally. The apparent anodic current at the potential shifted by η is given by the Butler-Volmer equation (Eq. 4.11) as a difference between true anodic and cathodic current.

$$i = i_0 \left\{ \exp\left(\frac{\alpha n F \eta}{RT}\right) - \exp\left[-\frac{(1-\alpha) n F \eta}{RT}\right] \right\} \tag{4.11}$$

where i_0 and α are the exchange current and the transfer coefficient (symmetry factor), respectively. The exchange current is the anodic and cathodic current at the equilibrium potential as shown in Fig. 4.2. The magnitude of α is generally 0.3–0.7 (Sugimoto, 2009). Based on the Butler-Volmer equation, the corrosion rate of metals is estimated by electrochemical measurements since the magnitude of current corresponds to the rate of the electrochemical reactions.

In practice, the potential of the metal M immersed in electrolytes is settled at the potential at which anodic and cathodic reactions are of equal rate, but are different

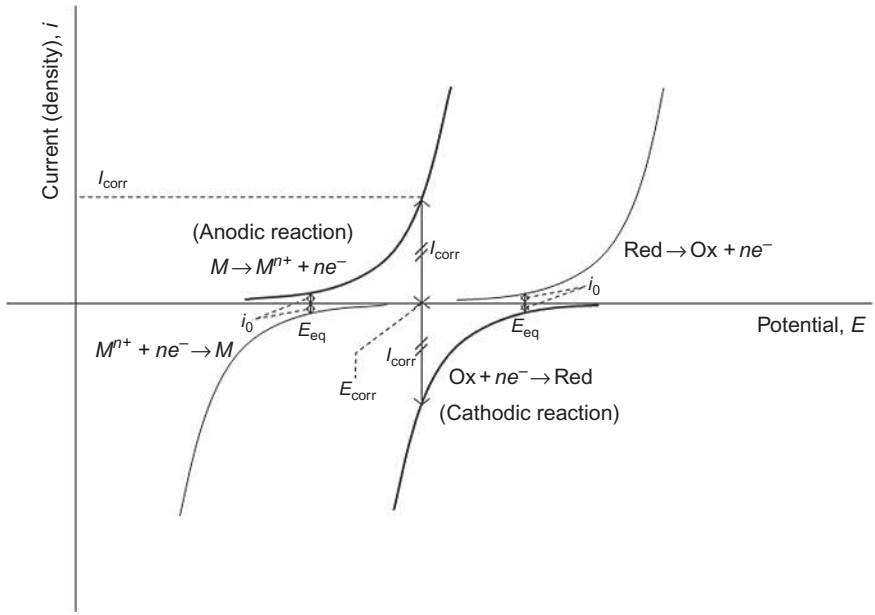


Fig. 4.2 Schematic illustration of potential-current (density) curves in the corrosion system of a metal [E_{corr}: corrosion potential, E_{eq}: equilibrium potential, I_{corr}: corrosion current (density), and i_0: exchange current (density)].

processes as shown in Fig. 4.2. This "mixed potential" is called corrosion potential (E_{corr}), open-circuit potential (OCP) or rest potential. Note that the corrosion potential is not the equilibrium potential because it is determined by the balance between several anodic and cathodic reactions. The rate of the anodic partial reaction at the corrosion potential in Fig. 4.2 is called corrosion current (density) (I_{corr}) which corresponds to the corrosion rate.

4.2.2 Passivity

Some metals and alloys, such as Ti alloys, Co-Cr alloys and stainless steels, show very low corrosion rate in an environment in which a very high corrosion rate would be predicted according to the low-standard electrode potential of the alloying elements. These metals and alloys are classified in passive metals and alloys. Their very low corrosion rate is due to the very thin but very protective oxide film (passive film) formed on the surface. The passive alloys generally include Cr, Ti, zirconium (Zr), and so on.

When the passive metals and alloys are anodically polarized (Fig. 4.3), the anodic current density increases with an increase in overpotential (η) according to the Butler-Volmer equation (Eq. 4.11). Anodic current density achieves a critical passive current

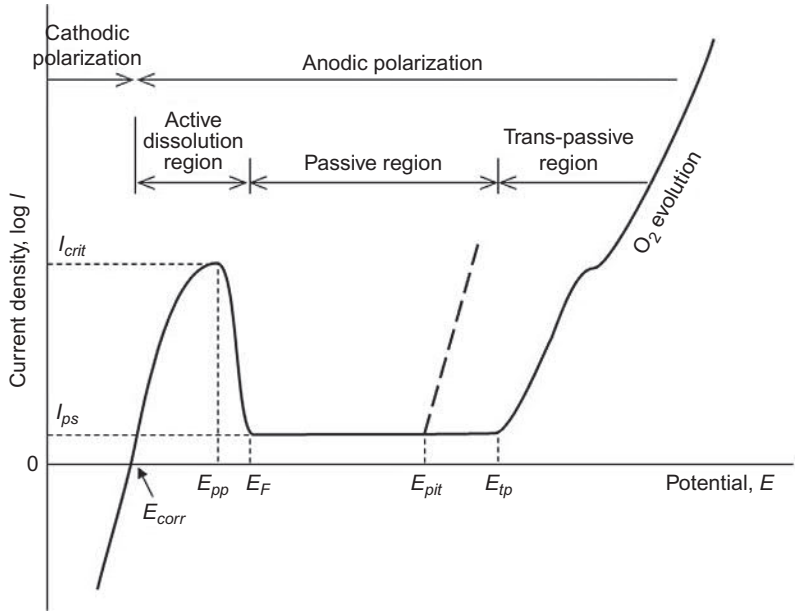


Fig. 4.3 Schematic illustration of anodic polarization curve of passive metal (E_{corr}: corrosion potential, E_{pp}: passivation potential, E_F: Flade potential, E_{pit}: pitting potential, E_{tp}: transpassive potential, I_{crit}: critical passive current density, and I_{ps}: passive current density).

density (I_{crit}), and subsequently it suddenly drops by orders of magnitude lower to a passive current density (I_{ps}). The magnitude of passive current density represents the protectiveness of the passive film against the general corrosion. An important point for metallic biomaterials is that the release of metal ions equivalent to the magnitude of passive current density takes place continuously, although the passive alloys are in a passive state. On further increase in overpotential, the current density increases rapidly with the initiation of pitting corrosion, transpassive dissolution, and/or O_2 evolution. In pitting corrosion, the passive film is locally broken by halogen species such as chloride (Cl^-) ion, fluoride (F^-) ion, and hydrogen fluoride (HF). In transpassive dissolution, metal ions in the passive film are further oxidized to polyvalence metal ions and are released in the electrolyte. The O_2 evolution takes place with the electrolysis of water.

Ti alloys, Co-Cr alloys and stainless steels in physiological environments generally are not in an active state and are spontaneously passivated. The passive film of stainless steels is more sensitive to Cl^- ion than those of Ti alloys and Co-Cr alloys.

4.3 Corrosion morphology

Metals show various corrosion morphologies since their corrosion behavior is influenced by various factors such as microstructure and composition of the metal and pH, temperature, and concentration of dissolved O_2 of the electrolyte. Corrosion morphology is roughly classified into general corrosion (uniform corrosion) and local corrosion (nonuniform corrosion).

4.3.1 General corrosion

The whole surface of the metal is uniformly corroded in general corrosion, as shown in Fig. 4.4A. General corrosion of the passive alloys such as Ti alloys, Co-Cr alloys, and stainless steels is rarely observed in the human body. On the other hand, for the electrolytic polishing of passive alloys, the general corrosion is promoted using aggressive electrolytes in which the alloys are in active state.

4.3.2 Local corrosion

Local corrosion is classified into pitting corrosion, crevice corrosion, intergranular corrosion, galvanic corrosion, selective corrosion, erosion-corrosion, and stress corrosion cracking (Fontana, 1987; Revie and Uhlig, 2008). Local corrosion forms holes on the surface of the metals. The corrosion holes may initiate cracks and accelerate the fracture of metals.

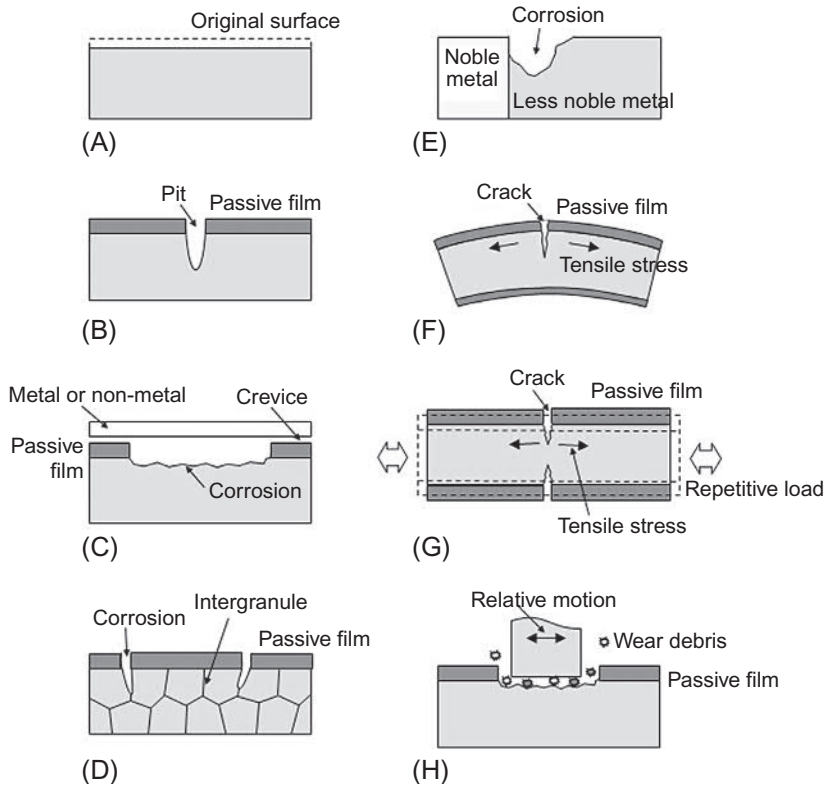


Fig. 4.4 Schematic illustration of corrosion morphologies. (A) General corrosion, (B) pitting corrosion, (C) crevice corrosion, (D) intergranular corrosion, (E) galvanic corrosion, (F) stress corrosion cracking, (G) fatigue corrosion, and (H) wear/fretting corrosion.

4.3.2.1 Pitting corrosion

Pitting corrosion is a type of local corrosion which proceeds at a very limited area while the greater part of the passivated surface is intact. Pitting corrosion is identified by the shape of pits, of which the depth is larger than the diameter in many cases (Fig. 4.4B). Pitting corrosion tends to take place on passive alloys in the presence of halogen species such as Cl^-, bromide (Br^-), and iodide (I^-) ions, and HF. These halogen species attack the defects of passive films and locally break the film. Because the magnitude of anodic reaction inside the pits is balanced with that of cathodic reaction outside the pits, a large amount of metal ions is dissolved inside the pits. The sensitivity to pitting corrosion of the metal can be estimated based on the pitting potential obtained by electrochemical measurements. It has been reported that the austenitic stainless steels and Co-Cr alloys have the possibility of pitting in unfavorable conditions in physiological environments (Scharnweber, 1998). The possibility of pitting corrosion of Ti alloys is low; however, pitting corrosion can occur on Ti alloys when

active O_2 species and the other factors, which break the passive film and prevent the re-passivation, coexist (Wang et al., 2017). In the case of metallic biomaterials, pitting corrosion is observed at a screw hole of bone plates made of a stainless steel (Williams and Williams, 2004; Virtanen et al., 2008).

4.3.2.2 Crevice corrosion

Crevice corrosion is a type of the local corrosion that takes place inside a metal-metal crevice and a metal-nonmetal crevice (Fig. 4.4C). Inside the crevice, where the mass diffusion is restricted, dissolved O_2 and pH decrease and Cl^- ions are enriched finally. Such change in the chemical environment inside the crevice causes the de-passivation of the metal surface inside the crevice. Because the rate of anodic reaction inside the crevice is balanced with that of cathodic reaction outside the crevice, corrosion inside the crevice proceeds intensively. In the case of metallic biomaterials, the crevice corrosion can take place on mating interfaces such as the head-stem interface in artificial hip joints and the screw-hole interface in bone plates (Williams and Williams, 2004; Virtanen et al., 2008).

4.3.2.3 Intergranular corrosion

Intergranular corrosion is a type of corrosion that selectively and deeply progresses at grain boundaries while the inside of grains is intact (Fig. 4.4D). Intergranular corrosion of stainless steels is the selective dissolution of the Cr-depleted zone formed along the grain boundaries. The chromium-depleted zone is formed with the precipitation of chromium carbides at the grain boundaries by the heat treatment.

4.3.2.4 Galvanic corrosion

When two types of metals show different corrosion potential individually and are placed in electrical contact with each other in an electrolyte, galvanic corrosion takes place on the metal at less noble potential, while cathodic protection takes place on the other metal at noble potential, as shown in Fig. 4.4E. Some stainless steel stents are partially coated with Au as a contrast marker for an angiographic X-ray apparatus; the standard electrode potential of Au is higher than that of stainless steel as indicated in Table 4.1. In the field of dentistry, the crown is made of various noble metal alloys, it often happens that the crowns made of different sorts of alloys are used in the neighborhood. In the case of the coupling of Ag-Pd-copper (Cu)-Au alloy and Ag alloy, the former alloy becomes the anode and the latter becomes the cathode (Table 4.1). In the case of artificial joints, the coupling of a Ti alloy stem and a Co-Cr alloy head is often used. However, galvanic corrosion does not always take place. When the difference in corrosion potential between the coupled alloys is relatively small, galvanic corrosion may not occur.

4.3.2.5 Corrosion under mechanical loading

Under mechanical loading, such as static tensile or compressive stress, fatigue stress, and wear/fretting, the surface of metallic materials is deformed, and the passive film is locally and repetitively broken, as shown in Fig. 4.4F–H. Thus, the bare metal surface, which can be rapidly corroded, is exposed to the environment repetitively. Because the re-passivation of the bare metal surface is prevented by the repetitive removal of the passive film, local corrosion is accelerated under the mechanical loading. Corrosion under the mechanical loading thus often takes place at a stress concentration area of metals. Because the progress of corrosion under mechanical loadings can promote crack initiation, fatigue, fretting fatigue, and fretting/wear are accelerated, and vice versa. Metallic biomaterials are often subjected to mechanical loadings, so corrosion under such loadings is important. Fretting corrosion takes place on mating interfaces such as the head-stem interface in artificial joints and the screw-hole interface in bone plates (Hallab et al., 2004; Rodrigues et al., 2008).

4.4 Evaluation methods of corrosion behavior

4.4.1 Electrochemical methods

4.4.1.1 Anodic polarization tests

Since the corrosion reaction is mostly electrochemical, corrosion behavior of metals can be evaluated with electrochemical techniques. A polarization test is one of the common techniques (ASTM Standard F1089-02, 2002; ASTM Standard F746-04, 2004; JIS T 0302, 2000). In anodic polarization tests, the anodic reaction of the specimen is accelerated by applying anodic overpotential and the current response is measured. According to various parameters obtained, such as the magnitude of current density and pitting potential, the corrosion behavior of the metals can be evaluated. In practice, the anodic reaction is accelerated by applying anodic current using a potentiostat. A potentiodynamic polarization test (linear sweep voltammetry), in which the potential of the specimen is swept at a constant speed, is generally carried out. To obtain the response near the steady state, the sweep rate of potential should be as slow as possible. On the other hand, a potentiostatic polarization test is recommended to obtain the response at a steady state because the response can reach the steady state during the period when the potential is kept for several minutes.

Fig. 4.5 shows a schematic illustration of electrochemical cell equipped with three electrodes: a working electrode (WE, specimen), a reference electrode (RE), and a counter electrode (CE). The potential of the WE is measured against the RE and the current flowing between the WE and CE is measured using a potentiostat. A saturated calomel electrode (SCE) or standard silver-silver chloride (Ag-AgCl) electrode (SSE) is used for an RE and Pt or carbon (C) is used for a CE. The tip of RE is set close to the surface of the WE to minimize the *IR* drop due to solution resistance. The *IR* drop rarely becomes a problem in practical corrosion tests because the test solution for metallic biomaterials generally shows low solution resistance.

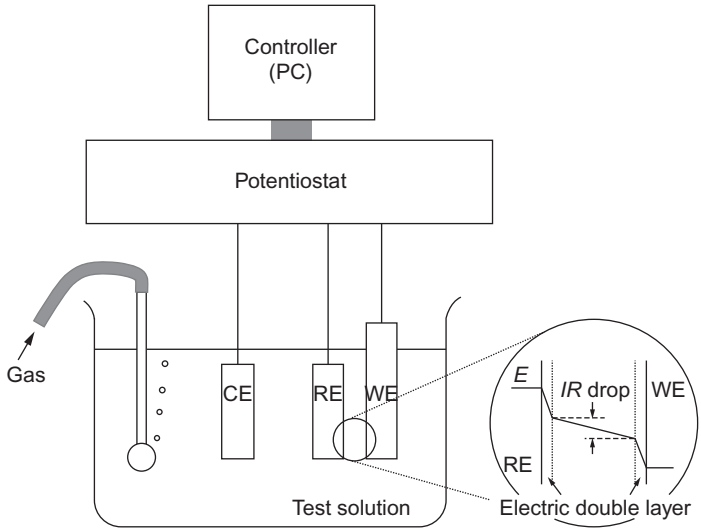


Fig. 4.5 Schematic illustration of three-electrode electrochemical cell (WE: working electrode, RE: reference electrode, and CE: counter electrode).

The electrochemical cell is filled with a test solution. The test solution should be selected depending on the environment in the body and the purpose of the test. Saline (0.9 mass% NaCl solution) is used as a simple test solution. To simulate the pH and/or the inorganic composition of body fluids, phosphate buffer saline (PBS), Hanks' solution, Ringer solution, or minimum essential medium (MEM) is used. The test temperature is 310 K of body temperature and the concentration of dissolved O_2 is controlled by bubbling Ar, N_2, or O_2-N_2 gas depending on the relevant environment and the purpose of the test.

Fig. 4.6 shows anodic polarization curves of pure Ti, 316 L stainless steel, and Co-Cr alloy measured after 1 week immersion in Hanks' solution (Hiromoto and Hanawa, 2006b), as examples. On the curve of 316 L stainless steel an abrupt increase in current density due to pitting corrosion finishes the passive region. The Co-Cr alloy shows an increase in current density due to transpassive dissolution following the passive region. Pure Ti shows a constant passive current density in the potential region of this study. This result indicates that each metal shows characteristic polarization behavior.

4.4.1.2 Tafel extrapolation method

Corrosion current density, which corresponds to the corrosion rate at the corrosion potential, can be obtained by the Tafel extrapolation method. Sufficiently apart from the corrosion potential by ±50 mV, the current density (I) increases with the increase in overpotential following to the Tafel equation (Eq. 4.12) which is derived from the Butler-Volmer equation

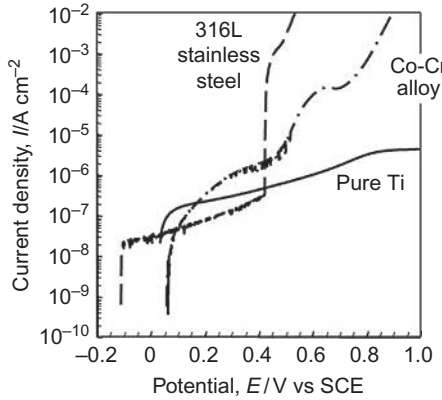


Fig. 4.6 Anodic polarization curves of pure Ti, 316 L stainless steel, and Co-Cr alloy in Hanks' solution.

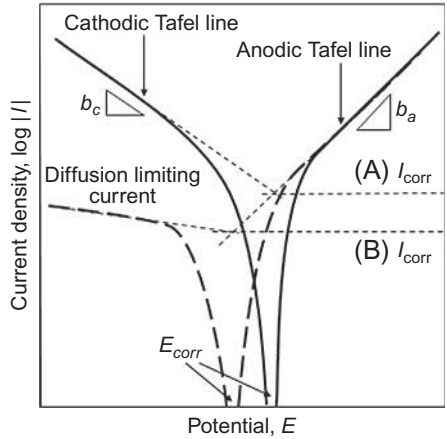


Fig. 4.7 Schematic illustration of the Tafel extrapolation method (E_{corr}: corrosion potential, I_{corr}: corrosion current density, b_c: cathodic Tafel slope, and b_a: anodic Tafel slope. (A) I_{corr} in the case that both cathodic and anodic polarization curves show a Tafel line and (B) I_{corr} in the case that cathodic polarization curve shows diffusion limiting current.

$$\eta = a + b\log I \tag{4.12}$$

where a and b are the constant and the Tafel slope, respectively. As shown in Fig. 4.7, the intersection of the straight lines on anodic and cathodic polarization curves corresponds to the corrosion current density. Typical values of Tafel slope are 0.05–0.23 V/decade (Sugimoto, 2009). When the cathodic current is limited by

diffusion of the cathodic reactant, as shown by the dashed line in Fig. 4.7, the intersection of anodic Tafel line and the limiting current line corresponds to the corrosion current density. It should be noted that the typical anodic Tafel line does not often appear on alloys in physiological solutions because several redox reactions take place in parallel.

In the case of Mg alloys, the corrosion current density obtained from potentiodynamic polarization curves may not reflect the actual corrosion rate (Esmaily et al., 2017) because the formation of corrosion product layers affects the exposed area and the H_2 evolution during polarization causes *IR* drops. The potentiodynamic polarization results are advisably used to examine the relative changes in corrosion resistance.

4.4.1.3 Linear polarization resistance method

The polarization resistance (R_p), which corresponds to corrosion resistance, is obtained by the linear polarization resistance method. Current linearly depends on the potential in a narrow potential region of $E_{corr} \pm 10$ mV, as expressed by Eq. (4.13), called the Stern-Geary equation

$$I_{corr} = \left(\frac{b_a b_c}{2.30(b_a + b_c)}\right)\left(\frac{\eta}{I}\right)^{-1} = KR_p^{-1} = \frac{K}{R_p} \tag{4.13}$$

where b_a and b_c correspond to the anodic and the cathodic Tafel slope, respectively. K is called the conversion factor, and η/I, which is the slope of the polarization curve around the corrosion potential (E_{corr}), as shown in Fig. 4.8, corresponds to the polarization resistance. When the conversion factor is already known, the corrosion current density can be calculated based on the polarization resistance obtained by the linear polarization. Generally, the conversion factor is 0.02–0.05 V (Sugimoto, 2009).

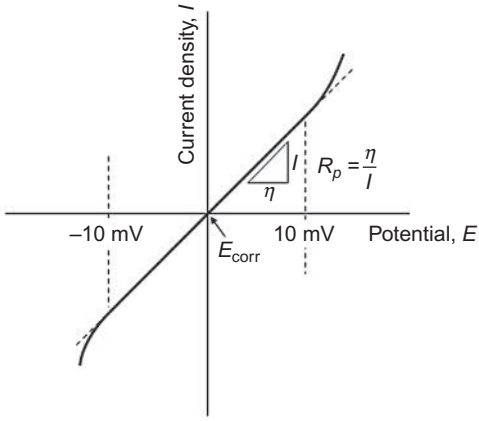


Fig. 4.8 Schematic illustration of linear polarization test (R_p: polarization resistance, E_{corr}: corrosion potential, η: overpotential, and I = current density).

4.4.1.4 Impedance test

The impedance test is performed by imposing an alternating potential with a small amplitude of less than 10 mV around the corrosion potential. The polarization resistance can be determined, based on the impedance at low frequency around 1–10 mHz. An amplitude less than 10 mV does not disturb the corrosion system, which enables the continuous in situ measurement of the impedance behavior. The frequency is varied in a wide range, typically from 1 mHz to 1 MHz, to obtain the frequency dependence of impedance.

The corrosion interface of the metal under dissolution is simulated with the simple electrical equivalent circuit shown in Fig. 4.9. When alternating potential is imposed in this equivalent circuit, the value of impedance follows (Eq. 4.14).

$$\begin{aligned} Z_{ct} &= R_s + \frac{1}{j\omega C_{dl} + \frac{1}{R_{ct}}} \\ &= R_s + \frac{R_{ct}}{1+\omega^2 C_{dl}^2 R_{ct}^2} - j\frac{\omega C_{dl} R_{ct}^2}{1+\omega^2 C_{dl}^2 R_{ct}^2} \end{aligned} \tag{4.14}$$

where j, ω, and f are the imaginary number ($j = \sqrt{-1}$), the angular velocity ($\omega = 2\pi f$), and the frequency of the alternating potential, respectively. Additionally, R_s, R_{ct}, and C_{dl} are solution resistance, polarization resistance (charge transfer resistance), and capacitance of the electric double layer, respectively. When ω is eliminated and Z_{ct} is rearranged by dividing into a real part (Z_{Re}) and an imaginary part (Z_{Im}), then Eq. (4.15) is derived from Eq. (4.13).

$$\left[Z_{Re} - \left(R_s + \frac{R_{ct}}{2}\right)\right]^2 + {Z_{Im}}^2 = \left(\frac{R_{ct}}{2}\right)^2 \tag{4.15}$$

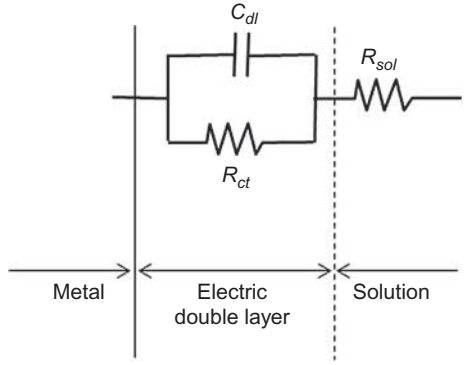


Fig. 4.9 Equivalent electric circuit of the interface of the metal under dissolution (R_{sol}: solution resistance, R_{ct}: polarization resistance (charge transfer resistance), and C_{dl}: capacitance of the electric double layer).

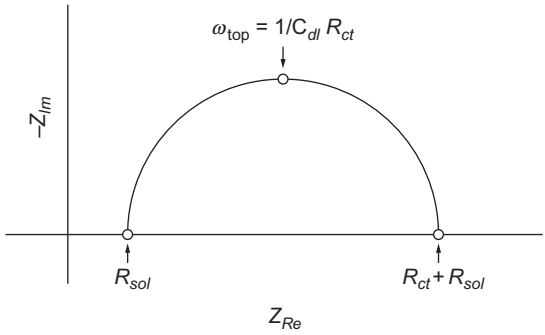


Fig. 4.10 Nyquist plot obtained from Eq. (4.14) (Z_{Im}: impedance in imaginary part, and Z_{Re}: impedance in real part).

The Z_{Im}–Z_{Re} plot is called the Nyquist plot. The Z_{Re}–Z_{Im} plot will show a semicircle as shown in Fig. 4.10 when the impedance measurement is carried out in a wide frequency range. The center of this semicircle is at $[(R_s + R_{ct}/2), 0]$ and the radius is $R_{ct}/2$. Thus, the charge transfer resistance at the interface, which corresponds to polarization resistance, can be obtained from the impedance at the low frequency.

4.4.1.5 Monitoring of corrosion potential

Long-term change of corrosion potential (ocp) reflects a change in a corrosion system because the change in corrosion potential depends on the change in one or both the anodic and cathodic reactions. For example, an increase in corrosion potential can be attributed to a decrease in the anodic reaction with the growth of a passive film or to an increase in the cathodic reaction with an increase in dissolved O_2. A decrease in corrosion potential can be attributed to an increase in the anodic reaction or to a decrease in the cathodic reaction. The monitoring of corrosion potential is therefore often carried out (ISO 16429, 2004; JIS T 6002, 2005). For the test solution, saline, PBS, Ringer solution, culture medium, serum, and artificial saliva are typically used. The corrosion potential of the specimen can be monitored against an RE using an electrometer with high input impedance (10^{11}–10^{14} Ω) or a potentiostat.

4.4.2 Immersion tests

The total amount of metal ions released in test solutions is quantified by gravimetric analysis or by solution analysis in immersion tests (dissolution tests) (ISO 10271, 2001; BS EN 1811:1998+A1:2008, 2008; JIS T 0304, 2002). When the test solution is carefully selected, results similar to that in the human body can be obtained. For example, the selective dissolution of alloying elements can be reproduced in vitro. The test solution is selected from saline, PBS, Ringer solution, culture medium, serum, and artificial saliva. Additionally, 0.1 mol L^{-1} lactic acid solution and 0.1 mol L^{-1} HCl solution are used for accelerated tests. The test temperature is kept at 310 K and the test period (immersion period) is advisably longer than 7 d. The pH of

the test solution should be checked before and after the immersion. The concentration of dissolved metal ions is quantified using inductively coupled plasma (ICP), atomic absorption spectrometry, and so on. In the case of Mg alloys, the volume of H_2 gas generated in the cathodic reaction is quantified because the number of moles of dissolved Mg ions is equal to that of the generated H_2 gas. The monitoring of the pH of the test solution is helpful to estimate the magnitude of the corrosion of Mg alloys.

4.4.3 Other methods

The environment around the metallic biomaterial implanted in patients or immersed in test solutions is estimated from the corrosion morphology and the composition of corrosion products. Corrosion morphology is determined by observing the surface morphology using an optical microscope or a scanning electron microscope (SEM). The area and depth of corrosion region are measured by a profilometer such as a laser profilometer and a laser scanning confocal microscope. X-ray computed tomography (CT) is used to measure the three-dimensional (3D) morphology of corrosion pits and cracks and the volume of remaining metal part of biodegradable metals. Corrosion products are qualified and quantified by electron dispersion spectroscopy (EDS), X-ray photoelectron spectroscopy (XPS) (JIS T 0306, 2002), auger electron spectroscopy (AES), and so on.

A tarnish test is performed for metallic dental materials because change in color (tarnish) of the surface should be avoided for cosmetic reasons. Dental Au alloys and Ag alloys are, however, easily tarnished with a slight amount of soluble sulfide in foods and drinks. The tarnish test is performed by immersion in 0.1 mol L^{-1} sodium sulfide (Na_2S) for 3 d (ISO/TR 10271, 2001; JIS T 6002, 2005). The degree of tarnish is determined by the naked eye, by comparing with the as-prepared surface.

As discussed in Section 4.5.4, the presence of cells on the surface of metallic biomaterials can change the chemical and/or physical environment on the surface. Electrochemical measurements under cell-culturing environments have been suggested to understand the in vivo corrosion reactions (Hiromoto et al., 2002; Lin and Bumgardner, 2004).

When biodegradable metals such as Mg are implanted under blood flow, their corrosion is expected to be accelerated with the promotion of mass diffusion. Flow cells or rotating disk electrodes have been suggested for the electrochemical measurements and immersion tests for the biodegradable metals to simulate the influence of blood flow (Lévesque et al., 2008; Hiromoto et al., 2008a). Periodical replacement of test solution is another way to simulate the circulation of body fluids (Yamamoto and Hiromoto, 2009).

4.5 Biological environments

The internal environment of a living body is maintained at a stable and constant condition (homeostasis). However, local environments have large variations in pH, concentration of dissolved O_2, temperature, and so on (Hayashi, 1987). Additionally, body fluids circulate inside the body by blood flow and natural convection.

Inside the living body, the implanted metals are firstly exposed to body fluids containing inorganic ions [Cl^-, carbonate, phosphate, calcium (Ca^{2+}) ions and so on], proteins, lipids, and amino acids. The kind of cells assemble around the implanted metal varies with time. Devices made of metallic biomaterials have various designs and static and dynamic mechanical loadings are applied. These various factors affect the corrosion of metallic biomaterials in a complicated way.

4.5.1 Temperature and pH

Body temperature is kept at around 310 K (homeostasis). ISO 16428 recommends that the temperature of the test solution be kept at 310 ± 1 K. The temperature of the oral cavity varies over a wide range with eating and drinking. Because the adsorption and chelating behavior of proteins and amino acids depends on the temperature (Ivarsson and Lundström, 1986), the temperature of test environments containing proteins and amino acids should be kept at 310 K.

The pH of body fluids is normally kept close to neutral by buffering with phosphate, carbonate, proteins, and so on (homeostasis). Since the test solutions, such as 0.9% NaCl and Ringer solutions, that ISO 16428 recommends, have a near-neutral pH value, it is recommended that the pH value during long-term tests is recorded. Phosphate, carbonate, and Good's buffer are used to buffer test solutions; however, some buffering reagents have an influence on the corrosion behavior of metallic biomaterials (Hiromoto and Mischler, 2006). Phosphate ions react with Ca^{2+}, Ti^{4+}, Zr^{4+}, and Mg^{2+} ions and deposit as phosphate salts; therefore, high concentration of phosphate ions sometimes alter the corrosion environment. Carbonate buffer is recommended for Mg alloys.

The pH of body fluids decreases to ca. 5.2 with inflammation (Hench and Ethridge, 1975). Inside the oral cavity, pH varies in wide range when eating and drinking, and the recovery of pH from a low value after eating and drinking sometimes takes more than 40 min (Stephan and Miller, 1943a, p45; Stephan and Miller, 1943b, p53). The decrease in pH accelerates the corrosion of metals by enhancing the dissolution of the passive film and cathodic reaction. Probability of local corrosion due to Cl^- ions also increases because the corrosion potential increases with a decrease in pH. Metallic biomaterials rarely show unexpected corrosion and fracture in the human body, which may be attributed to the decrease in pH. Citric acid-phosphate buffer was used to simulate low pH within inflammation (Maruyama et al., 2011).

4.5.2 Concentration of dissolved O_2

Since body fluids are neutral, cathodic reaction inside the body is the reduction of dissolved O_2 (Hayashi, 1987) except for Mg alloys. The corrosion potential of metals then depends on the concentration of dissolved O_2. The concentration of dissolved O_2 of transcellular fluids is 1/80–1/4 of that under ambient condition (Hayashi, 1987). Those of arterial blood and venous blood are 5/8 and 1/40 of that under ambient condition, respectively (Hayashi, 1987). When the concentration of dissolved O_2 is low, the corrosion potential shifts in a negative direction, so that the re-passivation of fractured passive film is delayed. The concentration of dissolved O_2 of the test

solutions is advisably controlled, depending on that inside the body. The test solution shall be purged with pure O_2 or pure nitrogen (N_2) to allow or prevent the passivation of the metal surface (ISO 16428). Since the cathodic reaction on Mg alloys is the reduction of water, the gas purge is not always necessary.

4.5.3 Calcium (Ca) and phosphate ions, proteins, and amino acids

Calcium phosphate deposits on Ti and its alloys spontaneously inside the body, while the deposition of calcium phosphate on stainless steel is relatively small (Sundgren et al. 1986; Espostito et al., 1999; Hiromoto and Hanawa, 2006b). The deposited calcium phosphate layer isolates the metal surface from the environment and may decelerate the corrosion. The deposition of calcium phosphate possibly affects adsorption behavior of proteins because calcium phosphate is a good adsorbent of proteins (MacConnell, 1973). In the case of Mg and its alloys, the presence of Ca^{2+} and phosphate ions in the test solution noticeably decelerates the dissolution of metal (Yamamoto and Hiromoto, 2009) by forming a calcium phosphate layer.

Proteins and amino acids are adsorbed by metal surfaces subsequent to inorganic ions in the very initial stages of implantation. The variety of proteins adsorbed by metal surfaces changes from low-molecular-weight proteins to relatively high-molecular-weight proteins in the course of time (Vroman effect) (Wahlgren and Arnebrant, 1991). Because these biological molecules have carboxyl groups, amino groups, and/or thiol groups, they are adsorbed by metal surfaces or form complex compounds with metal ions. Whether the corrosion of metallic biomaterials is accelerated or decelerated by proteins and amino acids depends on their adsorption and complexation abilities. However, the influence of the biological molecules on the corrosion is not systematically understood. Because the adsorption and complexation behavior of proteins depends on the conformation of molecules, which changes with temperature and pH (Ivarsson and Lundström, 1986), it is important to control the temperature and pH of test solutions at 310 ± 1 K and neutral, respectively.

4.5.4 Cells and extracellular matrix

Macrophages assemble around implanted materials in the initial inflammation reaction (Yoshikawa, 1993). Macrophages generate active O_2 species which dissolve and/or weaken the passive film of Ti alloys and stainless steels, forming oxyhydroxide of Ti, Fe, and Cr in passive films (Pan et al., 1994; Hanawa, 2002). Hydrogen peroxide (H_2O_2) weaken a passive film of Ti alloys by forming a complex of Ti(IV)-H_2O_2, as mentioned in Section 4.3.2 (Wang et al., 2017). It has been reported that the dissolution of pure Ti is enhanced in the presence of macrophages (Mu et al., 2000). Corrosion of metallic biomaterials is expected to be enhanced under the inflammatory condition due to active O_2 species from macrophages in addition to the low pH.

After the initial inflammation for a few weeks, the cells of the surrounding tissues adhere to the metal surface, generate extracellular matrix, and initiate the formation of bone or soft tissue, depending on the part of body (Yoshikawa, 1993). When the metal is recognized as a foreign body, a fibrous tissue layer is formed around the metal to

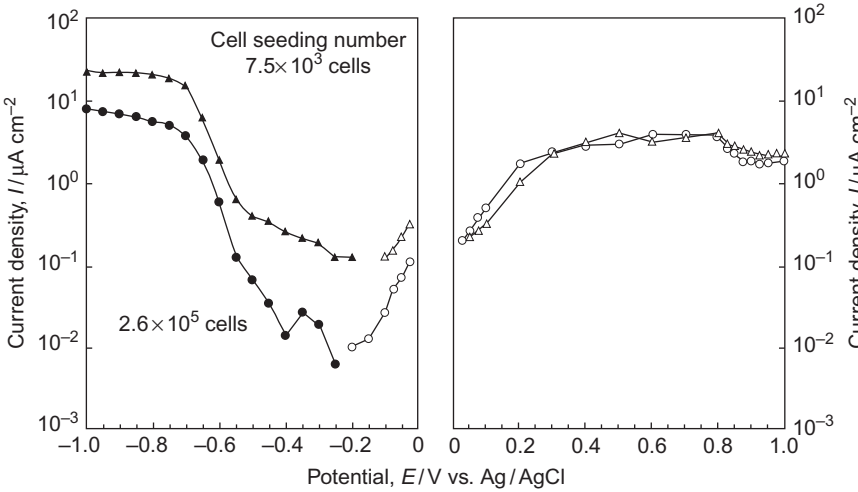


Fig. 4.11 Potentiostatic polarization curves of pure titanium immersed in a medium with culturing different numbers of fibroblast L929.

isolate the metal from the local tissue environment (encapsulation). The main components of the extracellular matrix are fibrous proteins and polysaccharides such as collagen and chondroitin sulfate. When the inflammation reaction is subsided, the pH of body fluid around the implanted materials reverts to neutral. The fibrous molecules form a gel which can retard the diffusion of ions and molecules around the metal surface. Culturing fibroblasts, which mainly generates collagen as extracellular matrix, causes a decrease in cathodic reaction of the reduction of dissolved O_2 on stainless steel and pure Ti, as shown in Fig. 4.11 (Hiromoto et al., 2008b). Also, the culturing of fibroblasts causes a decrease in the pitting corrosion potential of stainless steels (Hiromoto and Hanawa, 2006a; Tang et al., 2006).

During long-term implantation, metallic biomaterials may be gradually degraded and release wear debris and metal ions. These wear debris and metal ions may induce macrophages around the materials, which lead to the postinflammation. The corrosion of metallic biomaterials is then expected to accelerate postinflammation.

4.5.5 Circulation of body fluids

Body fluids are circulating inside the body to transport nourishment to the cells. Blood circulates inside the blood vessel by the pumping of the heart. The rate of blood flow varies from 0.1 to 1.0 m s^{-1}, depending on the diameter of blood vessel (Kaibara and Sakanishi, 1999; Sugawara and Maeda, 2003). The circulation of body fluids enhances the diffusion of released metal ions and corrosion products away from the metal surface, so that it possibly accelerates the corrosion of metallic biomaterials. Especially in the case of biodegradable metallic biomaterials such as Mg, Fe, and Zn alloys, flow rate on the surface can affect the corrosion behavior.

In the case of passive metals, the flow rate may enhance the reduction of dissolved O_2. On the other hand, the flow rate on the surface does not accelerate the corrosion, because the dissolution of metal ions (anodic reaction) is limited by the passive film. Therefore, agitation of the test solution in addition to the gas purge is not always recommended unless portions of the test solution are seen to stagnate at certain specimen areas (ISO 16428).

4.5.6 Design of devices and mechanical loadings

The design of biomedical devices often determines the corrosion morphology of metallic biomaterials. Corrosion of metallic biomaterials is accelerated inside the crevices (crevice corrosion) and at sliding parts with the repetitive removal of the passive film (wear/fretting corrosion). It is reported that fretting corrosion takes place on the surface at the screw-hole contact of bone plates and at the neck-head contact of artificial hip joints (Hallab et al., 2004; Virtanen et al., 2008). Repetitive load with walking or beating of heart, which is applied on the artificial hip joints and the bone plates or the struts of stents and the leads of pace makers, also causes the fracture of the surface film and accelerates the corrosion and crack initiation. Wear, fretting, fatigue, and fretting fatigue are accelerated by the promotion of corrosion, and vice versa.

Stents made of stainless steels, Co-Cr alloys, and Mg alloys are expanded by plastically deforming the metal struts in blood vessel. The effect of the plastic deformation on the corrosion behavior is advisably examined for metals with a coating.

References

ASTM Standard F1089-02, 2002. Standard Test Method for Corrosion of Surgical Instruments. ASTM.

ASTM Standard F746-04, 2004. Standard Test Method for Pitting or Crevice Corrosion of Metallic Surgical Implant Materials. ASTM.

BS EN 1811:1998+A1:2008, 2008. Reference Test Method for Release of Nickel from Products Intended to Come into Direct and Prolonged Contact with the Skin.

Esmaily, M., Svensson, J.E., Fajardo, S., Birbilis, N., Frankel, G.S., Virtanen, S., Arrabal, R., Thomas, S., Johansson, L.G., 2017. Fundamentals and advances in magnesium alloy corrosion. Prog. Mater. Sci. 89, 92–193.

Espostito, M., Lausmaa, J., Hirsch, J.M., Thomsen, P., 1999. Surface analysis of failed oral titanium implants. J. Biomed. Mater. Res. Appl. Biomater. 48, 559–568.

Fontana, M.G., 1987. Corrosion Engineering, third ed. McGraw-Hill, New York.

Hallab, N.J., Messina, C., Skipor, A., Jacobs, J.J., 2004. Differences in the fretting corrosion of metal-metal and ceramic-metal modular junctions of total hip replacements. J. Orthop. Res. 22, 250–259.

Hanawa, T., 2002. Evaluation techniques of metallic biomaterials in vitro. Sci. Tech. Adv. Mater. 3, 289–295.

Hayashi, K., 1987. Biodegradation of implant materials. JSME Int. J. 30 (268), 1517–1525.

Hench, L.L., Ethridge, E.C., 1975. Biomaterials—the interfacial problem. Adv. Biomed. Eng. 5, 35–150.

Hiromoto, S., Noda, K., Hanawa, T., 2002. Development of electrolytic cell with cell-culture for metallic biomaterials. Corros. Sci. 44, 955–965.

Hiromoto, S., Hanawa, T., 2006a. Electrochemical properties of 316L stainless steel with culturing L929 fibroblasts. J. Roy. Soc. Interface 3, 495–505.
Hiromoto, S., Mischler, S., 2006. The influence of proteins on the fretting–corrosion behaviour of a Ti–6Al–4V alloy. Wear 261, 1002–1011.
Hiromoto, S., Hanawa, T., 2006b. Corrosion of implant metals in the presence of cells. Corrosion Rev. 24 (5–6), 323–351.
Hiromoto, S., Yamamoto, A., Maruyama, N., Somekawa, H., Mukai, T., 2008a. Polarization behavior of pure magnesium under a controlled flow in a NaCl solution. Mater. Trans. 49 (6), 1456–1461.
Hiromoto, S., Ziegler, J., Yamamoto, A., 2008b. Morphological change of fibroblast cells on titanium and platinum cultured at anodic and cathodic potentials. Zairyo-to-Kankyo 57 (9), 400–408.
ISO 16429, 2004. Implants for Surgery—Measurements of Open-Circuit Potential to Assess Corrosion Behaviour of Metallic Implantable Materials and Medical Devices Over Extended Time Periods.
ISO 10271, 2001. Dental Metallic Materials—Corrosion Test Methods.
Ivarsson, B., Lundström, I., 1986. Physical characterization of protein adsorption on metal and metaloxide surfaces. Crit. Rev. Biocompat. 2 (1), 1–96.
JIS T 0302, 2000. Testing Method for Corrosion Resistance of Metallic Biomaterials by Anodic Polarization Measurement.
JIS T 0304, 2002. Testing Method for Metal Release From Metallic Biomaterials.
JIS T 0306, 2002. Analysis of State for Passive Film Formed on Metallic Biomaterials by X-Ray Photoelectron Spectroscopy.
JIS T 6002, 2005. Dental Metallic Materials—Corrosion Test Methods.
Kaibara, M., Sakanishi, A., 1999. Biorheology. Sangyo-tosho, Tokyo, p. 78 (in Japanese).
Kita, H., Uosaki, K., 1983. Basic of Electrochemistry. Gihodoshuppan, Tokyo.
Lin, H.-Y., Bumgardner, J.D., 2004. In vitro biocorrosion of Co–Cr–Mo implant alloy by macrophage cells. J. Orthop. Res. 22, 1231–1236.
Lévesque, J., Hermawan, H., Dube, D., Mantovani, D., 2008. Design of a pseudo-physiological test bench specific to the development of biodegradable metallic biomaterials. Acta Biomater. 4, 284–295.
MacConnell, D., 1973. Apatite: Its Crystal Chemistry, Mineralogy, Utilization, and Geologic and Biologic Occurrences. Springer-Verlag, New York (chapter 5).
Maruyama, N., Mori, D., Hiromoto, S., Kanazawa, K., Nakamura, M., 2011. Fatigue strength of 316L-type stainless steel in simulated body fluids. Corros. Sci. 53, 2222–2227.
Mu, Y., Kobayashi, T., Sumita, M., Yamamoto, A., Hanawa, T., 2000. Metal ion release from titanium with active oxygen species generated by rat macrophages in vitro. J. Biomed. Mater. Res. 49, 238–243.
Pan, J., Thierry, D., Leygraf, C., 1994. Electrochemical and XPS studies of titanium for biomaterial applications with respect to the effect of hydrogen-peroxide. J. Biomed. Mater. Res. 28, 113–122.
Pourbaix, M., 1966. Atlas of Electrochemical Equilibria in Aqueous Solutions. Pergamon Press, London.
Revie, R.W., Uhlig, H.H., 2008. Corrosion and Corrosion Control, An Introduction to Corrosion Science and Engineering, fourth ed. Wiley-Interscience, NJ.
Rodrigues, D.C., Urban, R.M., Jacobs, J.J., Bilbert, J.L., 2008. In vivo severe corrosion and hydrogen embrittlement of retrieved modular body titanium alloy hip-implants. J. Biomed. Mater. Res. 88B, 206–219.
Scharnweber, D., 1998. Degradation (in vitro-in vivo corrosion). In: Helsen, J.A., Breme, H.J. (Eds.), Metals as Biomaterials. John Wiley & Sons, Chichester, pp. 101–152.

Stephan, R.M., Miller, B.F., 1943a. A Quantitative method for evaluating physical and chemical agents which modify production of acids in bacterial plaques on human teeth. J. Dent. Res. 22, 45–51.

Stephan, R.M., Miller, B.F., 1943b. The effect of synthetic detergents on pH changes in dental plaques. J. Dent. Res. 22, 53–61.

Sugawara, M., Maeda, N., 2003. Hemorheology and Blood Flow. Corona Publishing, Tokyo, p. 75 (in Japanese).

Sugimoto, K., 2009. Kinzoku-Fushoku-Kogaku (Corrosion Engineering of Metals). Uchida Rokakuho Publishing, Tokyo (in Japanese).

Sundgren, J.L., Bodo, P., Lundstrom, I., 1986. Auger electron spectroscopic studies of the interface between human tissue and implants of Ti and stainless steel. J. Colloid Interface Sci. 110, 9–20.

Tang, Y.-C., Katsuma, S., Fujimoto, S., Hiromoto, S., 2006. Electrochemical study on type 304 and 316L stainless steels in simulated body fluids and cell cultures. Acta Biomater. 2 (6), 709–715.

Virtanen, S., Milosev, I., Gomez-Barrena, E., Trebse, R., Salo, J., Konttinen, Y.T., 2008. Special modes of corrosion under physiological and simulated physiological conditions. Acta Biomater. 4, 468–476.

Wahlgren, M., Arnebrant, T., 1991. Protein Adsorption to Solid Surfaces. 9, Tibtech, pp. 201–208.

Wang, J.-L., Liu, R.L., Majumdar, T., Mantri, S.A., Ravi, V.A., Banerjee, R., Birbilis, N., 2017. A closer look at the in vitro electrochemical characterisation of titanium alloys for biomedical applications using in-situ methods. Acta Biomater. 54, 469–478.

Williams, D.F., Williams, R.L., Ratner, B.D., Hoffman, A.S., Schoen, F.J., Lemons, J.E., 2004. Degradative effects of the biological environment on metals and ceramics. In: Biomaterials Science, An Introduction to Materials in Medicine. second ed. Elsevier, San Diego, pp. 430–439.

Yamamoto, A., Hiromoto, S., 2009. Effect of inorganic salts, amino acids and proteins on the degradation of pure magnesium in vitro. Mater. Sci. Eng. C 29, 1559–1568.

Yoshikawa, S., 1993. Foreign-body reaction. In: Ikada, Y. (Ed.), Introduction to Biomaterials. Japan Scientific Societies Press, Tokyo, pp. 95–123 (in Japanese).

Fatigue failure of metallic biomaterials

5

Mitsuo Niinomi
Tohoku University, Sendai, Japan; Osaka University, Osaka, Japan; Nagoya University, Nagoya, Japan; Meijo University, Nagoya, Japan

5.1 Introduction

Implants that function as bones—for example, implants that are used to replace failed hard tissue, such as artificial hip joints, artificial joints, bone plates, and dental implants—are usually used under severe cyclic loading conditions. Therefore, metallic materials that typically exhibit high strength, ductility, and toughness are the main candidates for the structural biomaterials of these implants. Further, the abovementioned implants must exhibit high biocompatibility, high performance, and reliability for long-term use.

The reliability of implants after implantation is determined by their fracture and wear after the critical period of infection. Nowadays, implants are required to exhibit much greater mechanical and biological performance. Therefore, the mechanical properties of structural biomaterials in a living body environment such as fatigue, toughness, and wear resistance need to be evaluated and improved considerably in order for these materials to be applied to implants for a long-term use.

With regard to the fracture of structural biomaterials, fatigue fracture occurs occasionally; it is considered a crucial problem among the various types of fractures.

Fatigue with fretting, that is, fretting fatigue, is a type of fatigue that can occur between two bodies, such as between a bone plate and screw. Fatigue characteristics are closely related to microstructures. The microstructures in metallic structural biomaterials change according to the processing and heat treatment employed.

Currently, the main metallic biomaterials used in practical applications are austenitic stainless steel, cobalt (Co)-chromium (Cr) alloys, and titanium (Ti) and its alloys. Among them, Ti and its alloys are receiving considerable attention for biomedical applications because of their high biocompatibility, specific strength, and corrosion resistance (Niinomi, 2001). In particular, low-modulus β-type Ti alloys composed of nontoxic and allergy-free elements have been recently developed and examined (Niinomi, 2003). With regard to stainless steels and Co-Cr alloys, Ni-free high nitrogen austenitic stainless steel (Kuroda et al., 2002), and nickel (Ni)- and carbon (C)-free Co-Cr alloy (Lee et al., 2006) have also been developed recently and examined.

Metals for Biomedical Devices. https://doi.org/10.1016/B978-0-08-102666-3.00005-5
© 2019 Elsevier Ltd. All rights reserved.

Therefore, in this chapter, the fatigue characteristics of the main metallic structural biomaterials such as stainless steels, Co-Cr alloys, and Ti and its alloys including those that are currently in use as well as those in development stage are described.

5.2 Fatigue strength

5.2.1 Fatigue strength level of various metallic biomaterials

The fatigue life of metallic biomaterials such as Ti alloys, Co alloys, and stainless steels for biomedical applications are shown in Fig. 5.1 (Niinomi, 1998): this figure shows the fatigue limits of stainless steels, Co alloy, and Ti and its alloys as representative metallic biomaterials in air. The fatigue limits are scattered depending on factors such the fabrication process, surface condition, microstructure, and fatigue condition. The fatigue limit of bovine bone (Kim et al., 2005) is also shown in Fig. 5.1 The limit decreases in the following order: Co alloy ≧ Ti-6 aluminum (Al)-4 vanadium (V) ≧ 316L stainless steel. Among the Ti alloys, the fatigue limits of (α + β)-type Ti alloys such as Ti-6Al-4V ELI and Ti-6Al-7 niobium (Nb) are greater than those of β-type Ti alloys such as Ti-13Nb-13 zirconium (Zr), Ti-15 molybdenum (Mo)-5Zr-3Al, and Ti-35.3Nb-5.1 tantalum (Ta)-7.1Zr. The fatigue limits of β-type Ti alloys increase by aging treatment after solution treatment (ST); the fatigue limit of β-type Ti alloy such as Ti-29Nb-13Ta-4.6Zr, which is referred to as TNTZ (Kuroda et al., 1998), has been reported to increase and become comparable to that of Ti-6Al-4V ELI. However, the fatigue limit of each metallic biomaterial shows a fairly large scatter due to the abovementioned factors. The fatigue limit of each metallic biomaterial is higher than that of bovine bone.

Figs. 5.2 and 5.3 (Breme and Helsen, 1998; Akahori et al., 2003) show the relationship between the rotating bending fatigue limit and the elongation up to fracture and that between the fatigue strength and Young's modulus for various metallic biomaterials, respectively. The rotating bending fatigue strength decreases with the elongation up to fracture. The rotating bending fatigue strength is relatively higher and the Young's modulus is relatively low in (α + β)-type Ti alloys. Therefore, the BF value of Ti alloys, which is obtained by dividing the fatigue strength with Young's modulus, is high (≃5.2). The biofunctionality index (BF) values of materials such as 316L stainless steel, Co-Cr alloy, Co-Ni-Cr alloy, pure Ti, and pure Nb, lie between 1.2 and 2.3 (Breme and Helsen, 1998). This indicates that the mechanical biocompatibility of Ti alloys is excellent in comparison with that of other metallic biomaterials. The BF value of aged TNTZ is very high (≃9.6) (Akahori et al., 2003).

Among the Ti alloys that have received considerable attention as metallic biomaterials, the fatigue limit of pure Ti, which is an α-type alloy, is the lowest. The fatigue limits of Ti-6Al-4V and Ti-6Al-7Nb, which are (α + β)-type alloys, are among the highest. The fatigue limit of β-type alloy subjected to ST is low; however, it increases drastically to approximate that of an (α + β)-type alloy by aging after ST due to the precipitation of the α-phase. The fatigue strength of (α + β)- and β-type Ti alloys varies considerably with the microstructure. In (α + β)-type Ti alloys, the fatigue

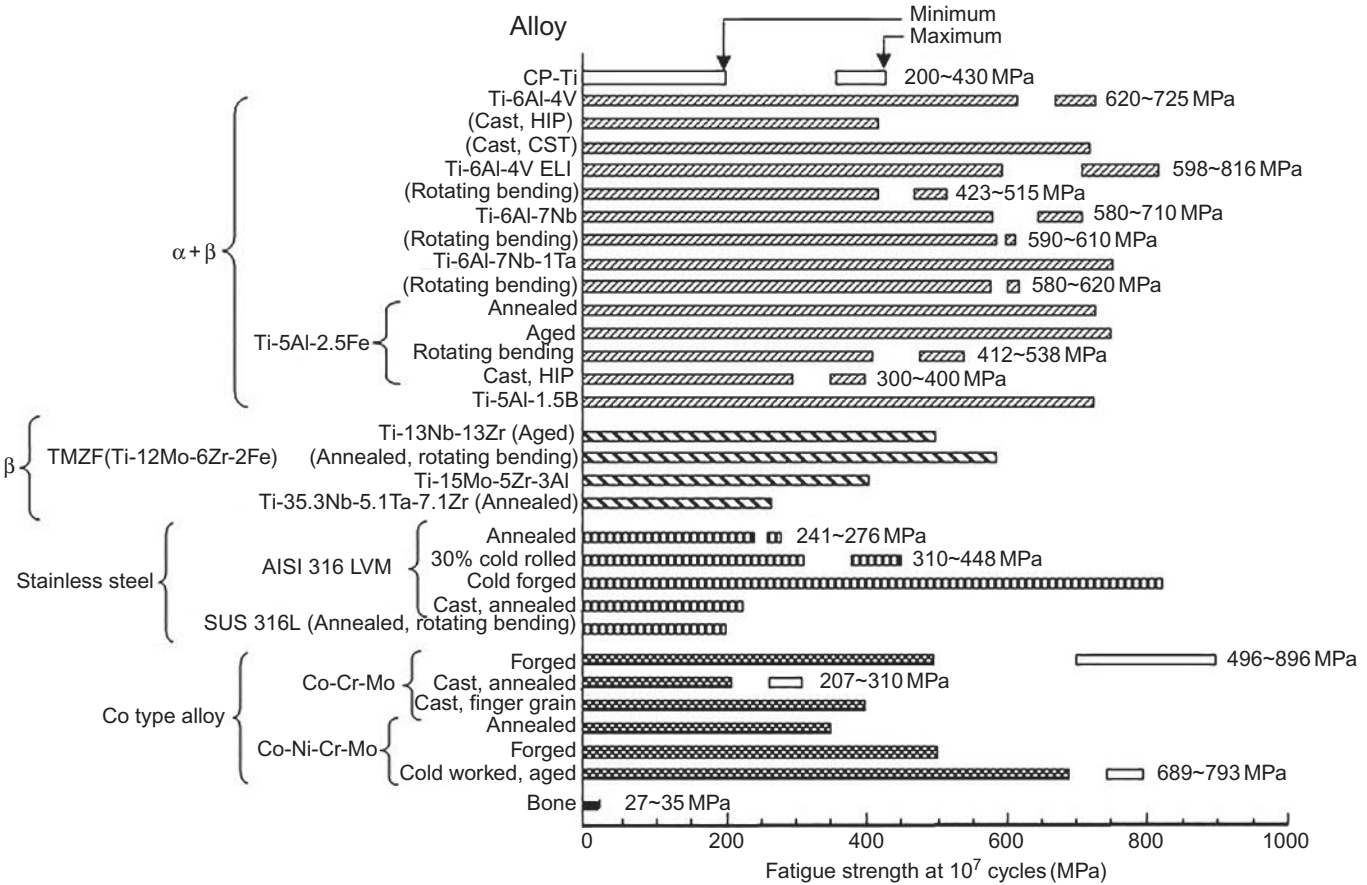


Fig. 5.1 Fatigue strength at 10^7 cycles of biomedical stainless steel, Co alloys, titanium and its alloys, and bone. Data without designation of rotating bending are those obtained from uniaxial fatigue tests.

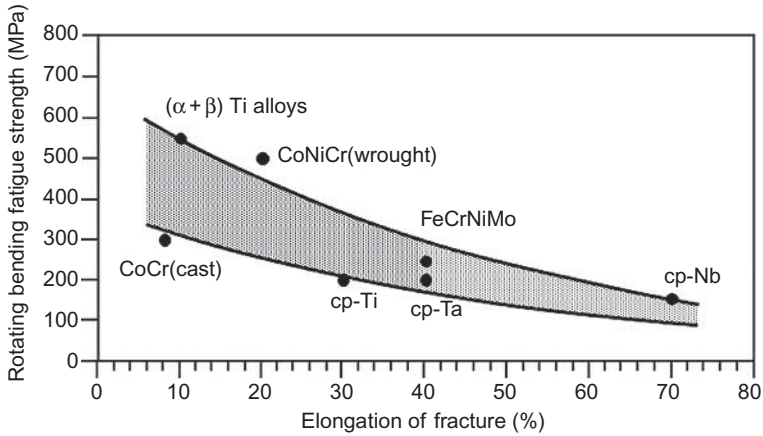


Fig. 5.2 Elongation at fracture as a function of the fatigue strength of metallic biomaterials.

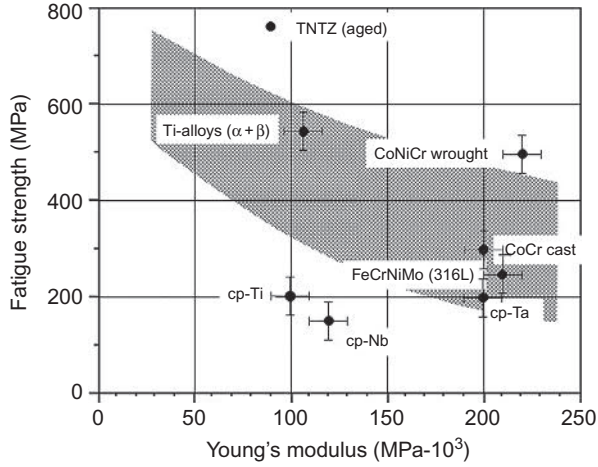


Fig. 5.3 Fatigue strength and Young's modulus of each metallic biomaterial.

strengths of an equiaxed α structure are, in general, higher than that of an acicular or Widmanstätten α structure (Niinomi et al., 1992).

5.2.2 *Fatigue strength in vitro and in vivo*

In order to estimate the fatigue strength of metallic biomaterials in a living body environment, it is essential to evaluate it in a simulated body environment. Fig. 5.4 (Niinomi et al., 1996) compares the rotating bending fatigue strength of Ti-6Al-4V ELI and SUS 316L stainless steel in Ringer's solution with those in air. The fatigue strength of Ti-6Al-4V ELI in Ringer's solution is similar to that in air, while that of

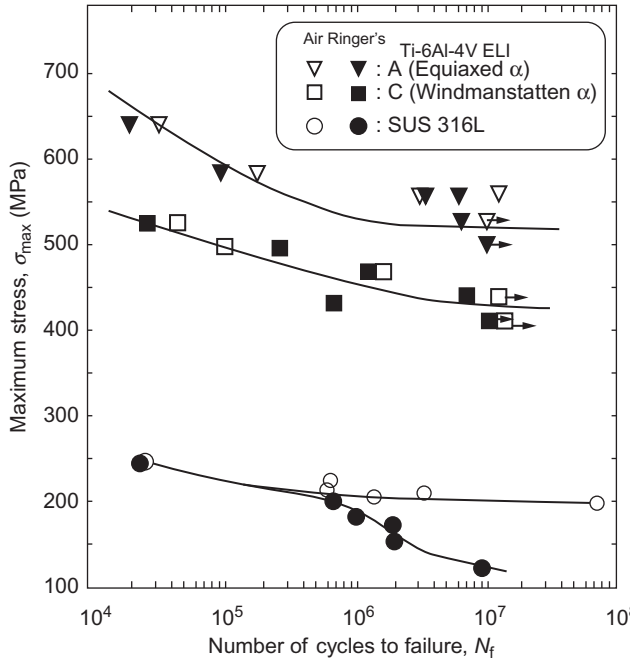


Fig. 5.4 S-N curves of Ti-6Al-4V ELI and SUS 316L in air and Ringer's solution.

SUS 316L stainless steel in Ringer's solution is lower than that in air. Therefore, corrosion fatigue occurs in Ringer's solution for SUS 316L stainless steel. The fatigue strength of Co-Cr-Mo is also reported to decrease in Ringer's solution as shown in Fig. 5.5 (Kumar et al., 1985).

As shown in Fig. 5.6 (Niinomi et al., 1996), the fatigue strength of Ti-5Al-2.5 iron (Fe) in Ringer's solution decreases when the oxygen (O) content is reduced by degassing with nitrogen (N) whereas it does not decrease without degassing. However, as shown in Fig. 5.7 (Niinomi, 2002a), the fatigue strength of Ti-6Al-4V ELI obtained by uniaxial fatigue tests does not degrade in a living body environment, for example, in the body of a living rabbit, which is in contrast to the fatigue strength of Ti-6Al-4V ELI in air. Therefore, there is a higher possibility of corrosion fatigue occurring under the bending fatigue condition in Ti alloys. In other words, the passive film formed on the surface of Ti alloys is considered to fracture more easily under the bending condition, and corrosion fatigue may occur because it takes a relatively longer time for a fractured passive film to recover due to the low O content.

Fig. 5.8 (Maruyama et al., 1999) compares the result of the fatigue test of Co-Cr alloy in PBS (−), which is phosphate-buffered saline (PBS) without calcium (Ca) and magnesium (Mg). The fatigue strength of Co-Cr alloy in PBS is lower than that in air in the low-cycle fatigue life region, while it is almost similar to that in air in the high-cycle fatigue life region.

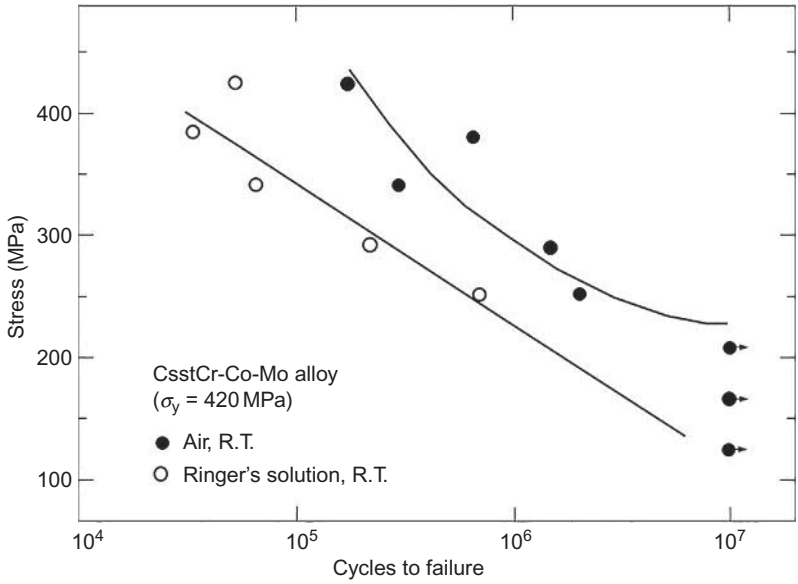


Fig. 5.5 Comparison of fatigue lives for cast Co-Cr-Mo alloy (type 1) in air and in simulated body solution.

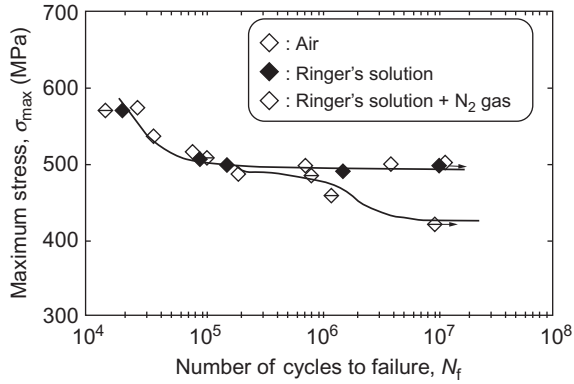


Fig. 5.6 S-N curves of Ti-5Al-2.5Fe in air, in Ringer's solution, and in Ringer's solution with N_2 gas.

5.2.3 Notch-fatigue strength

Since implants generally have complex shapes that have stress concentration sites such as sharp corners, it is imperative that the notch-fatigue strengths of medical Ti alloys be understood. Figs. 5.9 and 5.10 (Akahori et al., 2005a) show the S-N curves obtained from plain-fatigue and notch-fatigue tests on TNTZ. The stress concentration factors ($K_t = 1 + (t/\rho)$ 1/2, where t and ρ are the depth of the notch and the notch root radius) for plain-fatigue and notch-fatigue tests are 1 and 6, respectively. The notch-fatigue strength is much smaller in comparison with the plain-fatigue strength. Both

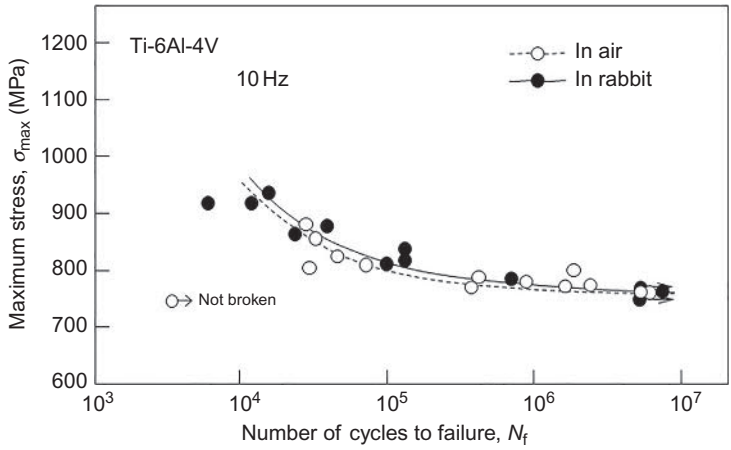


Fig. 5.7 S-N curves of Ti-6Al-4V obtained from uniaxial fatigue tests in air and rabbit.

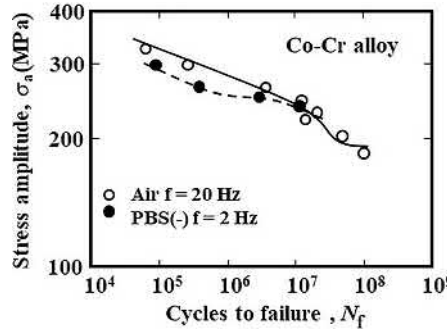


Fig. 5.8 S-N curves of Co-Cr alloy in air and in PBS(−).

the plain- and notch-fatigue limits of $STCR_{723}$ are the highest, where TNTZ was subjected to ST and then cold rolling (CR) followed by aging at 723 K. In this case, relatively coarse α-phases are homogeneously precipitated, and the elongation is relatively higher at 10% (Akahori et al., 2005a). Fig. 5.11 (Akahori et al., 2005a) shows the relationships between K_t and notch factor ($K_f = \sigma_{pf}/\sigma_{nf}$ where σ_{pf} and σ_{nf} are the fatigue limit and the notch-fatigue limit) for TNTZ, Ti-6Al-4V, and SUS 316L stainless steel subjected to various thermomechanical treatments. K_f of TNTZ subjected to each thermomechanical treatment is less than those of Ti-6Al-4V and SUS 316L stainless steel for the same K_t values. Fig. 5.12 (Akahori et al., 2005a) shows the relationship between the K_t and the notch sensitivity factor ($\eta = (K_f - 1)/(K_t - 1)$) of TNTZ, Ti-6Al-4V, pure Ti (CP-Ti), carbon steel (S45C), and SUS 316L stainless steel. The η of TNTZ subjected to each thermomechanical treatment is found to be less than those of the other materials.

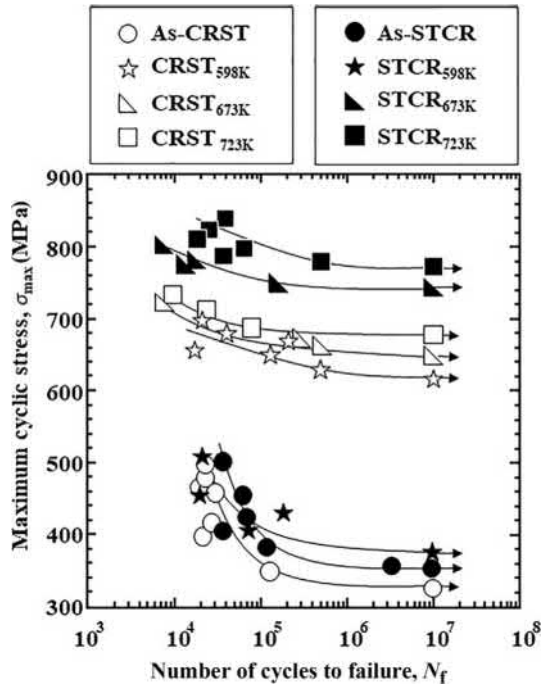


Fig. 5.9 S-N curves of TNTZ subjected to various thermomechanical treatments obtained from plain-fatigue tests ($K_t = 1$) in air.

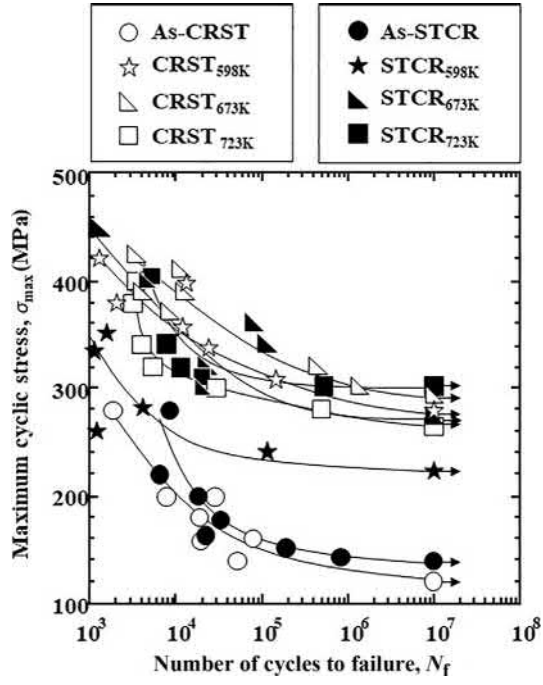


Fig. 5.10 S-N curves of TNTZ subjected to various thermomechanical treatments obtained from notch-fatigue tests ($K_t = 6$) in air.

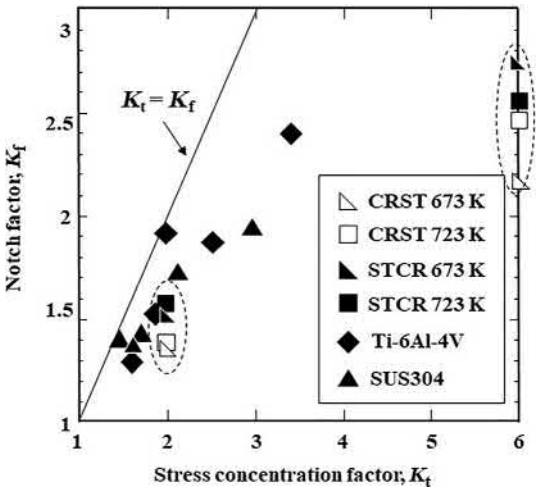


Fig. 5.11 Relationships between stress concentration factor, K_t, and notch factor, K_f, of TNTZ, Ti-6Al-4V, and SUS 304 subjected to various thermomechanical treatments.

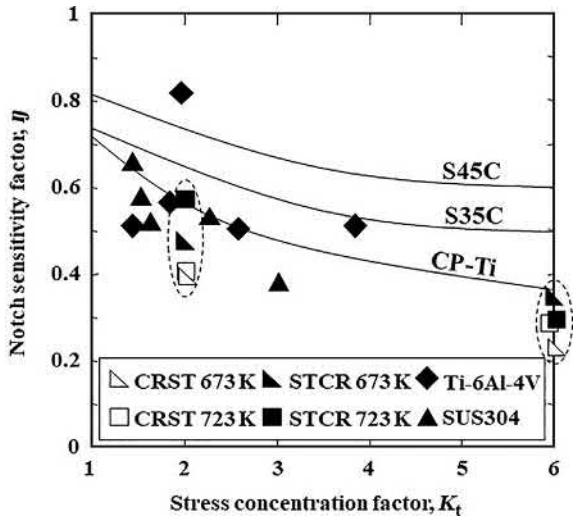


Fig. 5.12 Relationships between stress concentration factor, K_t, and notch sensitivity factor, η, of TNTZ, Ti-6Al-4V, CP-Ti, S35C, S45C, and SUS 304 stainless steel subjected to various thermomechanical treatments.

5.2.4 Fatigue strength and surface modification

In order to improve the wear resistance of Ti alloys, surface hardening treatments such as nitriding (Nakai et al., 2008) and oxidation (Niinomi et al., 2002b) are applied. On the other hand, bioactive ceramic surface modifications (Kasuga et al., 2003; Sato et al., 2007; Hanawa et al., 2001) are applied in order to improve the bone conductivity because metallic biomaterials, even Ti and its alloys, are not bioactive. In these cases, understanding the effects of surface modifications on the fatigue life of metallic biomaterials is important.

5.2.4.1 Fatigue strength and surface hardening treatment

The S-N curves of Ti alloys such as Ti-6Al-4V ELI and TNTZ subjected to nitriding are shown in Fig. 5.13 (Akahori et al., 2008). In this figure, $TNTZ_{ST}$, $TNTZ_{1123NP}$, $TNTZ_{1223NP}$, $Ti64_{ST}$, $Ti64_{1123NP}$, and $Ti64_{1223NP}$ indicate TNTZ subjected to ST and gas nitriding at 1123 and 1223 K, and Ti-6Al-4V ELI subjected to ST and gas nitriding at 1123 and 1223 K, respectively. The fatigue strengths of TNTZ and Ti-6Al-4V ELI are lowered by nitriding. The hard brittle layers, TiN or Ti_2N, formed on the surface of both alloys, are brittle leading to easy fatigue crack initiation. The intensity of the TiN peak has been found to increase with the nitriding temperature by XRD (X-ray diffraction) analysis. The Vickers hardness near the specimen surface of nitrided Ti-6Al-4V ELI has been reported to be greater than that of TNTZ.

The run out, which is the maximum cyclic stress that can be applied without causing fracture after 10^7 cycles, of $TNTZ_{1123NP}$ was around 300 MPa and is nearly equal to that of $Ti64_{1123NP}$, although the tensile strength of $TNTZ_{1123NP}$ was around 200 MPa lower than that of $Ti64_{1123NP}$. This value was slightly lower than that of $TNTZ_{ST}$. The fatigue crack seems to be easily initiated when the brittle nitride layer is slightly thicker in nitrided Ti-6Al-4V ELI, such as TiN or Ti_2N, as compared with the case for nitrided TNTZ. Particularly, the elastic modulus of TiN is two or more times higher of the matrix (Yan et al., 2001). Thus, the TiN layer of nitrided TNTZ and Ti-6Al-4V ELI is severely deformed under cyclic loading, wherein localized fatigue deformation could take place. This seems to result in brittle cracking and shortening of crack initiation life, in particular, in nitrided Ti-6Al-4V ELI with a relatively

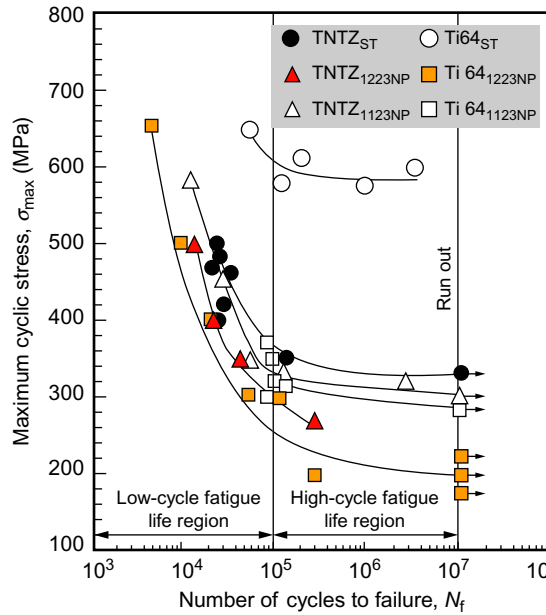


Fig. 5.13 S-N curves of TNTZ and Ti64 subjected to solution treatment and nitriding process.

high Vickers hardness, and the thickness of nitride- and nitrogen-rich layers. In addition, the notch factor (run out of smooth specimen/run out of notch specimen), which indicates that the notch sensitivity of aged TNTZ decreases with an increase in the volume fraction of the β-phase, and it is lower than that of annealed Ti-6Al4V ELI with an equiaxed β structure (Akahori et al., 2008). From these points of view, it follows that by the nitriding process, the plain-fatigue strength of TNTZ is not as degraded as that of Ti-6Al4V ELI.

5.2.4.2 *Fatigue strength and bioactive surface modification*

Among the metallic biomaterials, the biocompatibility of Ti alloys is the highest, but these alloys are not bioactive as stated above. Therefore, they are subjected to surface modification by bioactive ceramics in order to further improve their biocompatibility.

There exist many processes for bioactive ceramic surface modification. They are roughly grouped into dry process, for example, spray method (Niinomi, 2003), and wet processes, for example, alkali method (Kim et al., 1997) and dip-coating method (Niinomi et al., 2003). The fatigue characteristics of metallic biomaterials subjected to these different surface modification processes are also significant.

For example, Fig. 5.14 (Li et al., 2004) shows the results of fatigue tests for TNTZ coated with calcium phosphate invert glass-ceramic by the dip-coating method. In this method, a mixture of calcium phosphate invert glass-ceramic and distilled water is coated on the specimen by dipping the specimen into the mixture. The specimen is then fired in order to precipitate the calcium phosphate system ceramics. The firing temperature is above the β transus temperature of TNTZ; thus the fatigue strength of TNTZ cannot be maintained when the dip-coating method is employed. Therefore, it is necessary to finally age the specimen in order to improve the fatigue. As shown in Fig. 5.14, the fatigue strength of TNTZ coated with calcium phosphate invert-glass ceramic increases remarkably after aging. It is possible to inhibit cracking or exfoliation of the calcium phosphate invert glass-ceramic layer or cracking between the layer and the substrate by controlling the thickness of the layer (Li et al., 2004; Niinomi, 2003). Fig. 5.15 (Li et al., 2004) shows an SEM fractograph of calcium

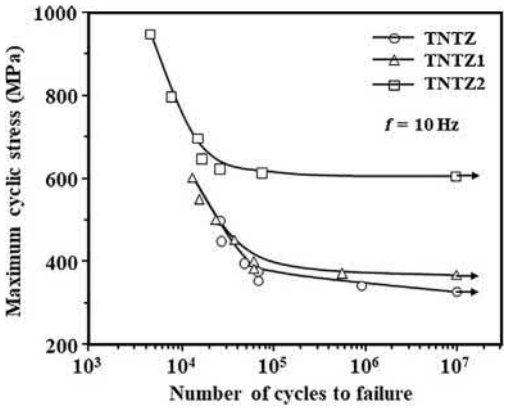


Fig. 5.14 S-N curves of as-solutionized TNTZ, glass-ceramic-coated TNTZ (TNTZ1), and glass-ceramic-coated TNTZ followed by aging (TNTZ2).

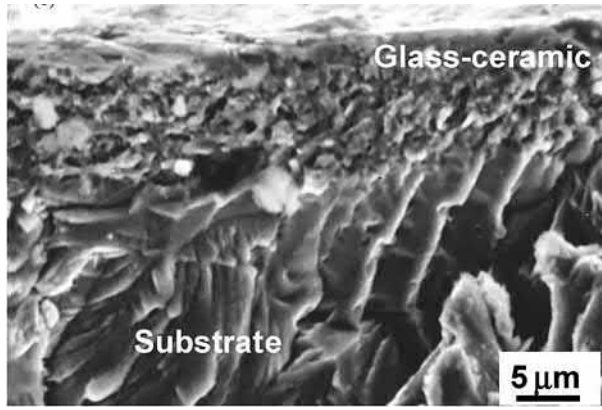


Fig. 5.15 General view of fatigue fracture surface of glass-ceramic-coated TNTZ (TNTZ1) ($N = 557{,}862$).

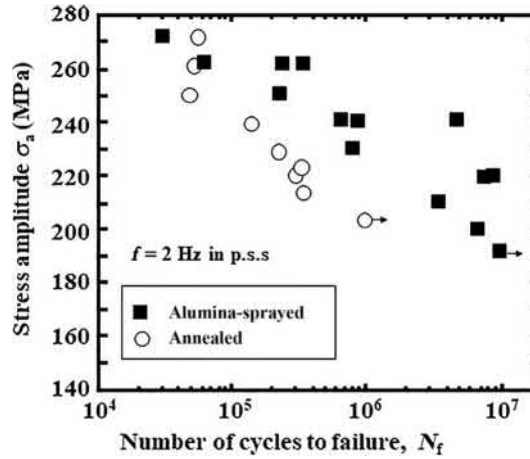


Fig. 5.16 S-N curves for annealed or alumina-sprayed SUS 316L stainless steels in physiological saline solution.

phosphate invert glass-ceramic-coated TNTZ after the fatigue test. The cracking or exfoliation of the layer cannot be observed on the SEM fractograph. It should be noted that the crack initiation sites in this case are the pits formed on the surface of the substrate by sand blasting, which is a pretreatment applied to the surface of the substrate.

Fig. 5.16 (Breme and Helsen, 1998) shows the fatigue strength of SUS 316L stainless steel coated with alumina (Al_2O_3), which is not a bioactive ceramic but is highly biocompatible, by the plasma spray method and evaluated in physiological saline. For comparison, the figure also shows the fatigue strength of SUS 316L stainless steel without alumina coating. The fatigue strength of SUS 316L stainless steel with alumina coating is higher than that without coating because the corrosion of steel (with coating) is inhibited by the dense alumina-coated layer.

5.2.5 Improvement in fatigue strength by various treatments

5.2.5.1 Heat treatment

The S-N curves of a fairly new (α + β)-type biomedical Ti alloy, Ti-6Al-7Nb, subjected to ST beyond and below the β transus temperature, respectively, followed by air cooling, AC, and aging, which yield equiaxed α and Widmanstätten α structures, respectively, are shown in Fig. 5.17 in comparison with those of conventional (α + β)-type biomedical Ti alloy, Ti-6Al-4V ELI, obtained by heat treatments similar to those of Ti-6Al-7Nb (Akahori et al., 2000). The fatigue strength of Ti-6Al-7Nb is nearly equal to that of Ti-6Al-4V ELI when the microstructure is Widmanstätten α. However, the fatigue strength of Ti-6Al-7Nb is inferior to that of Ti-6Al-4V ELI when the microstructure is equiaxed α. This inferiority of the fatigue strength is supposed to be one of the reasons why Ti-6Al-7Nb is not used widely. The fatigue strength of Ti-6Al-7Nb with the equiaxed α structure can be controlled by changing the volume fraction of primary α. The fatigue strength of Ti-6Al-7Nb increases with the volume fraction of primary α, which leads to an increased fatigue life of Ti-6Al-7Nb. The fatigue strength of Ti-6Al-7Nb is still lower than that of Ti-6Al-4V ELI when the volume fraction of primary α is relatively greater. When a fairly high cooling rate is adopted, for example, water quenching after ST in (α + β) region followed by aging, the fatigue strength of Ti-6Al-7Nb is nearly equal to that of Ti-6Al-4V ELI as shown in Fig. 5.18 (Akahori et al., 2000). Further advanced microstructural control processing is expected to develop the fatigue strength of Ti-6Al-7Nb such that it exceeds the fatigue strength of Ti-6Al-4V ELI.

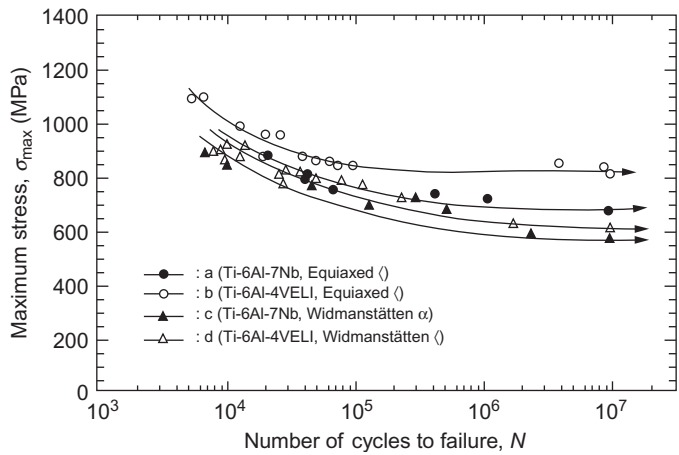


Fig. 5.17 S-N curves of Ti-6Al-7Nb and Ti-6Al-4V ELI with equiaxed α and Widmanstätten α structures.

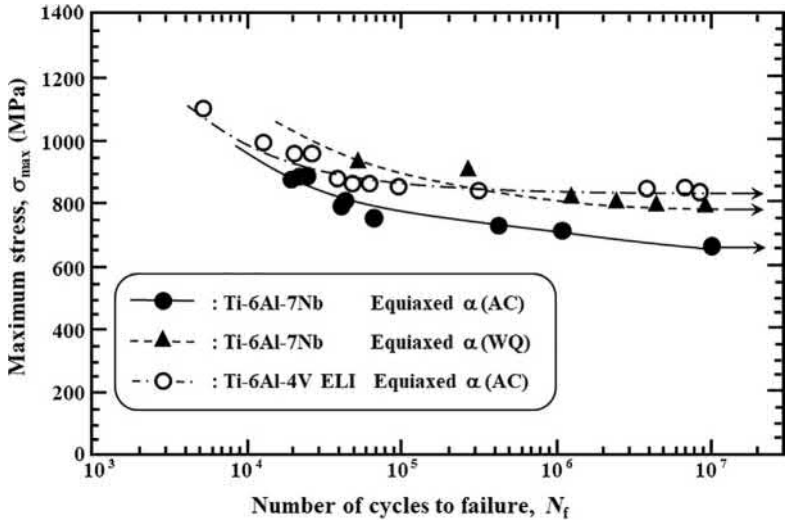


Fig. 5.18 S-N curves of Ti-6Al-7Nb and Ti-6Al-4V ELI with each heat treatment. AC and WQ correspond to air cooling and water cooling, respectively, after solution treatment.

5.2.5.2 *Aging treatment*

In general, the fatigue strength of Ti alloys is improved by aging after ST. The fatigue strength is drastically improved by aging treatment after ST for β-type Ti alloys. Fig. 5.19 (Akahori et al., 2006) shows the S-N curves obtained from fatigue tests in air on TNTZ samples subjected to ST at 1023 K (A_{ST}) and aging treatments at 723 K for various durations after ST—under-aging ($UA_{723\ K}$), peak-aging ($PA_{723\ K}$), and over-aging ($OA_{723\ K}$); these curves were obtained from fatigue tests in air. The fatigue limit of TNTZ increases drastically by aging treatments, and the fatigue limit of peak-aged TNTZ is the highest. The fatigue limits of each aged TNTZ sample is equivalent to that of Ti-6Al-4V ELI.

5.2.5.3 *Thermomechanical treatment*

It is possible to improve the fatigue strength of β-type Ti alloys by thermomechanical treatment involving cold working and heat treatment. Cold working can be performed very easily in β-type Ti alloys. Fig. 5.20 (Akahori et al., 2003) shows the fatigue strength of low-modulus TNTZ obtained by aging after ST ($TNTZ_{ST}$ aged at 598 K and $TNTZ_{ST}$ aged at 673 K) severe CR and aging ($TNTZ_{CR}$ aged at 598 K and $TNTZ_{CR}$ aged at 673 K) with the fatigue limits of Ti-6Al-4V ELI and Ti-6Al-7Nb. The fatigue limit of TNTZ is found to reach the upper limit of the fatigue limit range of Ti-6Al-4V ELI by aging after severe CR.

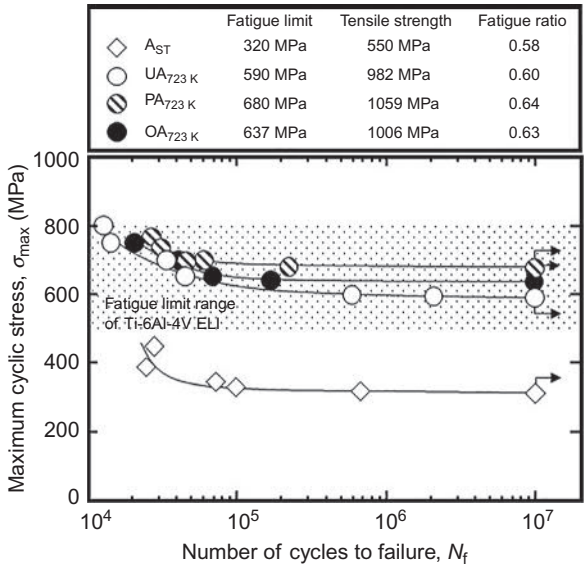


Fig. 5.19 S-N curves of A_{ST}, $UA_{723\,K}$, $PA_{723\,K}$, and $OA_{723\,K}$ obtained from fatigue tests in air.

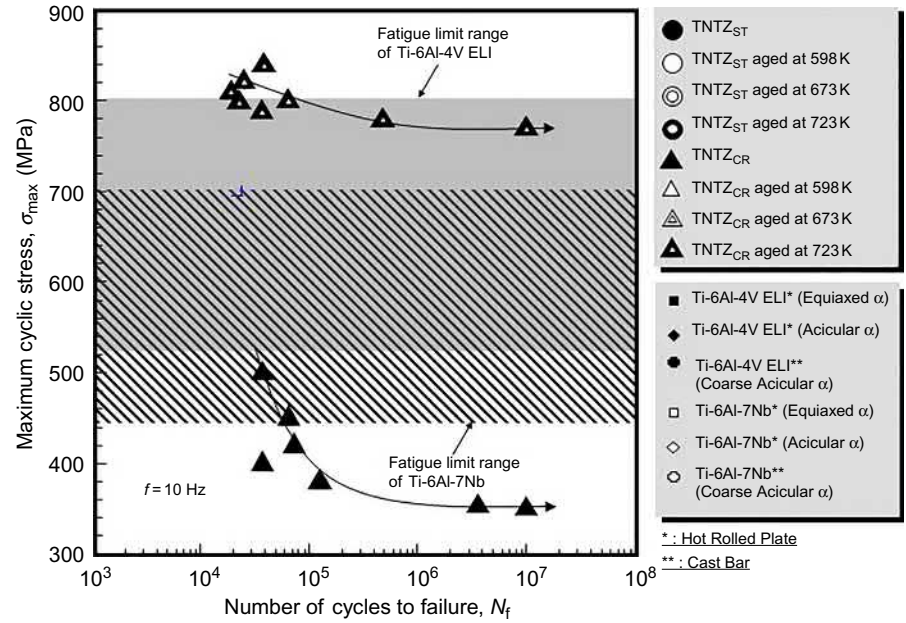


Fig. 5.20 S-N curves of $TNTZ_{CR}$ and $TNTZ_{CR}$ conducted with aging at 723 K for 259.2 ks with fatigue limit ranges of Ti-6Al-4V ELI and Ti-6Al-7Nb in air. $TNTZ_{CR}$ indicates severe cold-rolled TNTZ.

5.2.5.4 Thermochemical treatment

It is well known that the microstructures of (α + β)-type Ti alloys are significantly refined through the hydrogenation and dehydrogenation process, which is also referred to as thermochemical processing (TCP), as shown representatively in Fig. 5.21 (Akahori et al., 2002) for the case of cast Ti-6Al-7Nb. The size of the α-phase is significantly small in cast Ti-6Al-7Nb that has been subjected to TCP. In this case, the diameter of the α-phase is of the order of several micrometers. The tensile strength and fatigue strengths of (α + β)-type Ti alloys increase significantly after they are subjected to TCP, as shown in Fig. 5.22 (Akahori et al., 2002) and Fig. 5.23 (Niinomi et al., 1995), respectively, in the cases of cast Ti-6Al-7Nb and Ti-6A-4V for tensile strength and Ti-6Al-4V and Ti-6Al-2.5Fe for fatigue strength. In general, contrary to the increasing trends exhibited in the cases of tensile and fatigue strengths, ductility and fracture toughness tend to decrease. In order to inhibit this decrease in ductility or fracture toughness, it is effective to perform TCP below the β-transus temperature or to perform a postheat treatment where ST below the β-transus temperature is performed during the final stage of the TCP (Akahori et al., 2002; Niinomi et al., 1995). By means of these treatments, relatively significant amounts of unstable β-phase are retained in the microstructure at room temperature. The unstable β-phase enhances the ductility or fracture toughness of the alloy.

5.2.5.5 Cavitation peening

Peening treatments such as shot peening are effective to improve the fatigue strength of metallic biomaterials because of the residual stress, but their surfaces are roughened. The rough surface sometimes becomes stress concentration site, which lowers the fatigue strength. Cavitation peening schematically shown in Fig. 5.24 (Niinomi et al., 2016) can produce the residual stress on the surfaces of metallic biomaterials without roughening the surfaces.

To employ the alloy in practical applications for rods of spinal fixation devices, its endurance must be evaluated in a laboratory according to ASTM F1717

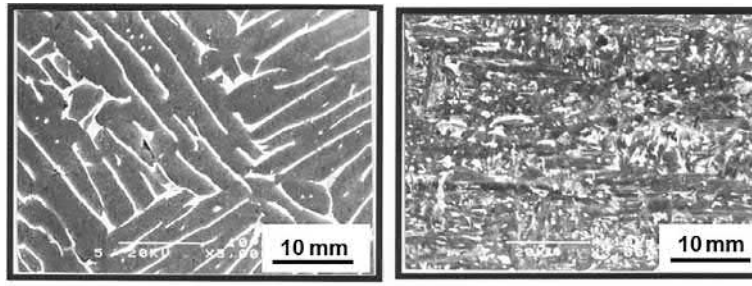


Fig. 5.21 Scanning electron micrographs of (A) as-HIP'ed cast Ti-6Al-7Nb and HIP'ed cast Ti-6Al-7Nb subjected to (B) TCP.

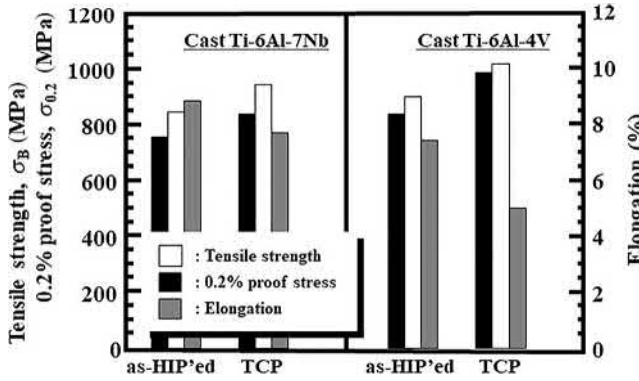


Fig. 5.22 Tensile strength, 0.2% proof stress and elongation of as-HIP'ed cast Ti-6Al-7Nb and Ti-6Al-4V, and HIP'ed cast Ti-6Al-7Nb and Ti-6Al-4V conducted with TCP.

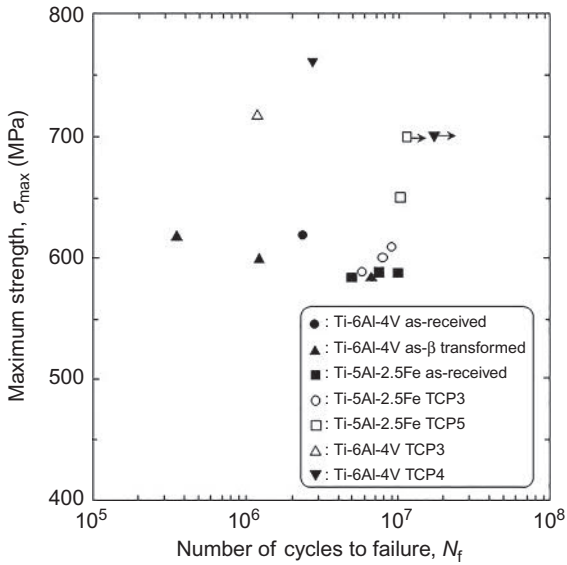


Fig. 5.23 Comparison of high-cycle fatigue strength of as-received, as-transformed, and TCP-treated Ti-6Al-4V, as-received and TCP-treated Ti-5Al-2.5Fe.

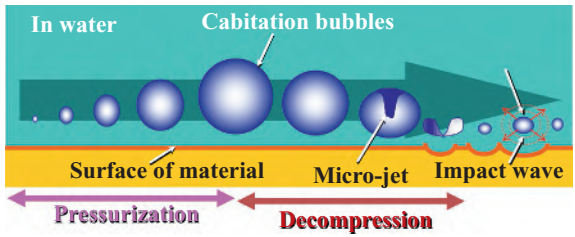


Fig. 5.24 Schematic drawings of development and crashing of cavitation.

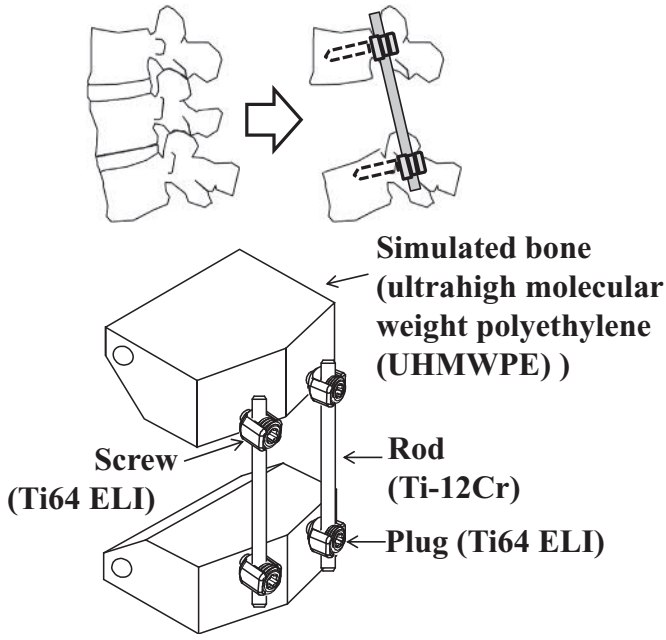


Fig. 5.25 Schematic drawing of compressive fatigue strength test method according to ASTM F1717.

(Niinomi et al., 2016). ASTM F1717 describes a testing method for evaluating the compressive fatigue strength of rods of spinal fixation devices. In that test, a simulated spinal fixation model as shown in Fig. 5.25 (Niinomi et al., 2016) is used. The spinal fixation device comprises screw and plug made of Ti-6Al-4V ELI, and a rod made of Ti-12Cr, which is expected to be used for rods. A Ti-6Al-4V ELI rod is also used for comparison. Bone is simulated using ultrahigh molecular weight polyethylene (UHMWPE). The compressive fatigue limit of Ti-12Cr subjected to ST is less than that of Ti-6Al-4V ELI, as shown in Fig. 5.26 (Niinomi et al., 2016). The rod typically failed at the contact area between the rod and the plug in the ASTM F1717 compressive fatigue test. Therefore, fretting that occurs between the rod and the plug is considered to lower the compressive fatigue strength of the rod. Improving the mechanical properties and tribological characteristics of the rod are expected to be an effective solution to this problem. The introduction of a hardened layer due to compressive residual stress on the surface of the rod is expected to prevent fretting fatigue. Peening techniques can introduce these hardened layers through plastic deformation, that is, work hardening, by delivering a large impact on the material's surface. Therefore, cavitation peening was performed on Ti-12Cr rods to improve their compression fatigue strength evaluated according to ASTM F1717. The cavitation peening significantly increases the compressive fatigue strength of the rods made of Ti-12Cr as shown in Fig. 5.26 (Niinomi et al., 2016). In this case, deformation-induced ω-phase, which increased the hardness and strength of the alloy, was formed simultaneously.

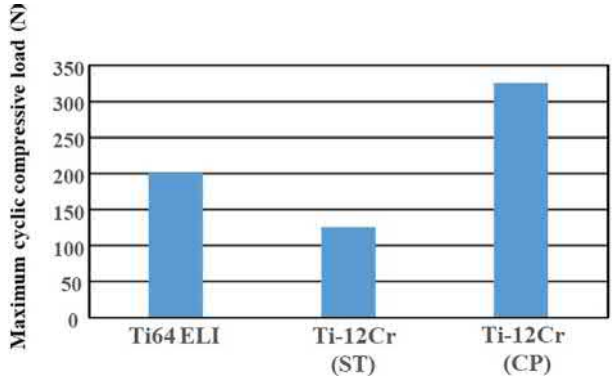


Fig. 5.26 Compressive fatigue limit of Ti-6Al-4V ELI (Ti64 ELI), and Ti-12Cr subjected to solution treatment (ST) and cavitation peening (CP) after solution treatment evaluated according to ASTM F 1717.

The deformation-induced ω-phase also contribute to increase the compressive fatigue strength of the rod made of Ti-12Cr.

5.2.5.6 Deformation-induced transformation

On the application of stress, martensitic transformation occurs in steels, which contain residual austenite in their microstructures. This phenomenon is called stress- or strain-induced martensitic transformation; it enhances the ductility or fracture toughness of the steels (Kobayashi and Yamamoto, 1998). Deformation-induced martensitic transformation also occurs in Ti alloys that contain unstable β-phase in their microstructures, and this transformation enhances the fatigue strength (Imam and Gilmore, 1983), fatigue crack propagation resistance (Niinomi et al., 1993), fracture toughness (Niinomi et al., 1990), and ductility (Gunawarman et al., 2002) of the Ti alloys. In general, the unstable β-phase is retained at room temperature by rapid cooling such as water quenching from a high temperature near the β transus temperature.

Fig. 5.27 (Imam and Gilmore, 1983) shows the S-N curves of Ti-6Al-4V subjected to annealing treatment and ST at 1173 K followed by water quenching. The fatigue strength of Ti-6Al-4V when subjected to ST followed by water quenching is higher than that when it is subjected to subsequent annealing treatment because of the deformation-induced martensitic transformation of the unstable β-phase, which is introduced by the water quenching after the ST.

5.2.5.7 Oxygen addition

Oxygen is generally regarded as an impurity in Ti and its alloys. However, O is currently being recognized as an effective alloying element to improve the mechanical biocompatibility of Ti alloys.

The S-N curves of TNTZ with an O content of 0.06 mass% (TNTZ-0.06O) and 0.14 mass% (TNTZ-0.14O) heat treated at 923 K for 3.6 ks and ST after severe cold

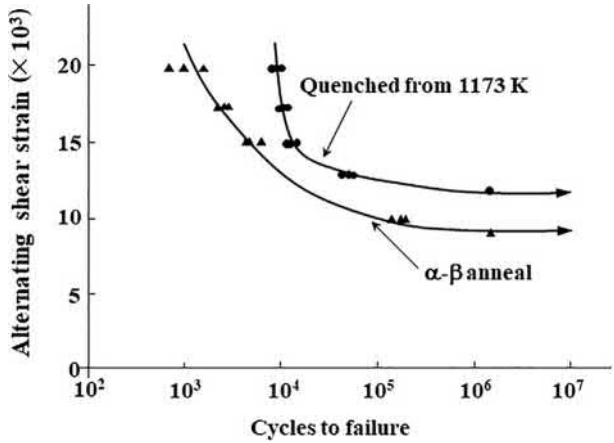


Fig. 5.27 Cycles to failure as a function of the applied alternating shear strain for Ti-6Al-4V α-β annealed and heat treated at 1173 K followed by a water quench.

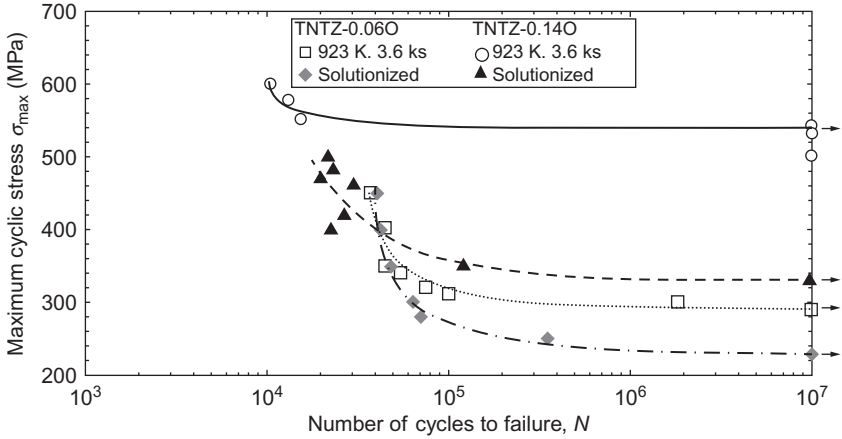


Fig. 5.28 S-N curves of TNTZ-0.06O subjected to a heat treatment at 923 K for 3.6 ks and solution treatment (ST) after severe cold waging, and TNTZ-0.14O subjected to a heat treatment at 923 K for 3.6 ks and ST after severe cold swaging. S-N curve for TNTZ subjected to ST is also shown.

swaging are shown in Fig. 5.28 (Cho et al., 2013). TNTZ-0.06O subjected to a heat treatment at 923 K for 3.6 ks after severe cold swaging had an average grain diameter of 1.7 μm. TNTZ-0.06O subjected to ST after severe cold swaging had an average grain diameter of 27 μm. TNTZ-0.14O subjected to a heat treatment at 923 K for 3.6 ks after severe cold swaging had an average grain diameter of 1.0 μm. TNTZ-0.14O subjected to ST after severe cold swaging had an average grain diameter of 33 μm. TNTZ-0.14O subjected to a heat treatment at 923 K for 3.6 ks after severe cold swaging exhibits significantly better fatigue strength than those of TNTZ-0.06O

subjected to a heat treatment at 923 K for 3.6 ks and ST after severe cold swaging, and TNTZ-0.14O subjected to solutionizing after severe cold swaging.

Therefore, the fatigue strength of TNTZ can be improved by solid-solution strengthening with O solutes and grain refinement.

The fatigue strength of TNTZ can be improved by adding a large amount of O, up to approximately 0.7 mass% as shown in Fig. 5.29 (Liu et al., 2017), with a fatigue limit range of Ti-6Al-4V ELI. In this case, TNTZ with various oxygen contents comprising a single β-phase obtained by ST and deformation-induced martensite is formed. The width of the deformation-induced martensite decreases with increasing O content as shown in Fig. 5.30. Thus, the increment in the fatigue strength of TNTZ with

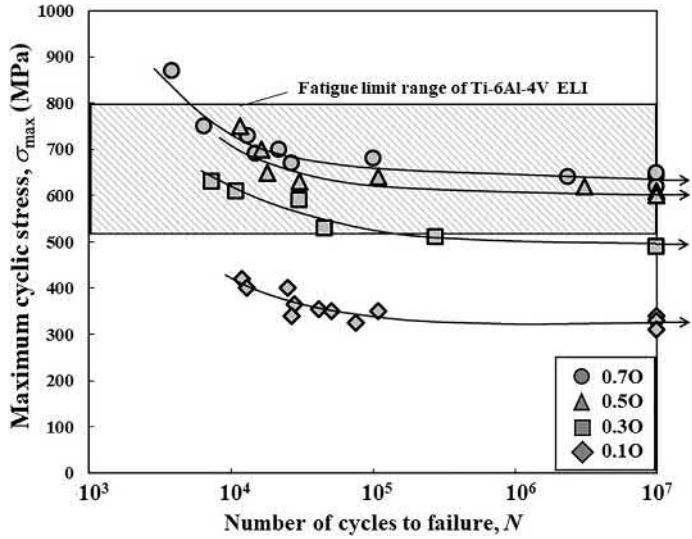


Fig. 5.29 S-N curves of TNTZ with oxygen contents of 0.1 (0.1O), 0.3 (0.3O), 0.5 (0.5O), and 0.7 (0.7O) mass% with fatigue limit range of Ti-6Al-4V ELI.

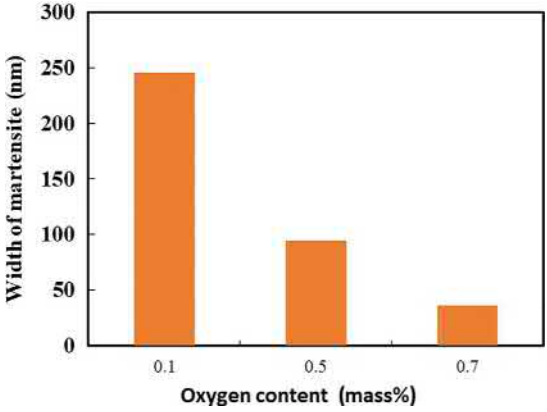


Fig. 5.30 Width of martensite in TNTZ with oxygen contents of 0.1, 0.5, and 0.7 mass%.

O content can be considered to be due to O solid-solution strengthening and microstructural refinement by deformation-induced martensite (Liu et al., 2017).

5.2.6 Improvement in fatigue strength by maintaining low Young's modulus

It is very important for metallic biomaterials such as β-type Ti alloys, which exhibit the lowest Young's modulus when the single β-phase is obtained by ST; low Young's modulus close to that of bone is effective to inhibit bone resorption and lead to good bone remodeling.

It was found that the static strength such as tensile strength of β-type Ti alloys such as TNTZ was significantly improved by the severe cold working such as severe cold-rolling, cold-swaging, and cold-drawing, and severe plastic deformation such as high-pressure torsion as compared to that of the TNTZ subjected to ST (Niinomi and Akahori, 2010), but the dynamic strength such as the fatigue strength was not improved. The fatigue strength can be improved considerably when aging treatment was provided after ST or after thermomechanical processing including severe cold working and aging treatment, which produces the α-phase or ω-phase precipitates in the β-matrix phase.

The strength and the Young's modulus increase significantly by the ω-phase precipitation as compared to α-phase precipitation, although the brittleness of the alloy is enhanced by the ω-phase precipitation. Therefore, the fatigue strength of TNTZ is expected to be improved by a small amount of the ω-phase precipitation while maintaining low Young's modulus. For this purpose, short-time aging at fairly low temperatures, which enhances a small amount of the ω-phase precipitation, was investigated. The Young's moduli of TNTZ subjected to ST, severe CR, and aging after CR at 573 K as a function of aging time (AT) are shown in Fig. 5.31 (Nakai et al., 2012). The Young's modulus is below 80 GPa, which is a tentative target value for a low Young's modulus, up to approximately 10.8 ks of AT. The S-N curves for TNTZ subjected to ST, severe CR, and aging for 3.6 and 10.8 ks at 573 K are shown in Fig. 5.32 (Nakai et al., 2012). The fatigue strength of TNTZ increases by aging treatment for 10.8 ks, while the Young's modulus remained lower than 80 GPa. Therefore, it is possible to improve the fatigue strength of TNTZ while maintaining a low Young's modulus by introducing a small amount of ω-phase precipitation using a short-time aging at relatively low temperatures.

Furthermore, the fatigue strength of β-type Ti alloys is expected to be improved by the addition of a small amount of ceramics particles in the β-phase matrix while maintaining a low Young's modulus. The Young's modulus of TNTZ with TiB_2 or Y_2O_3 additions subjected to severe CR is shown in Fig. 5.33 (Song et al., 2011, 2012) as a function of B or Y concentration. The Young's modulus is nearly constant with increasing B or Y concentration and is around 60 GPa, which is a value equal to that of TNTZ comprising single β-phase showing the lowest Young's modulus. The S-N curves of TNTZ with 0.1% and 0.2% B concentration or 0.2% and 0.5% Y concentrations subjected to CR after ST are shown in Fig. 5.34 (Song et al., 2011,

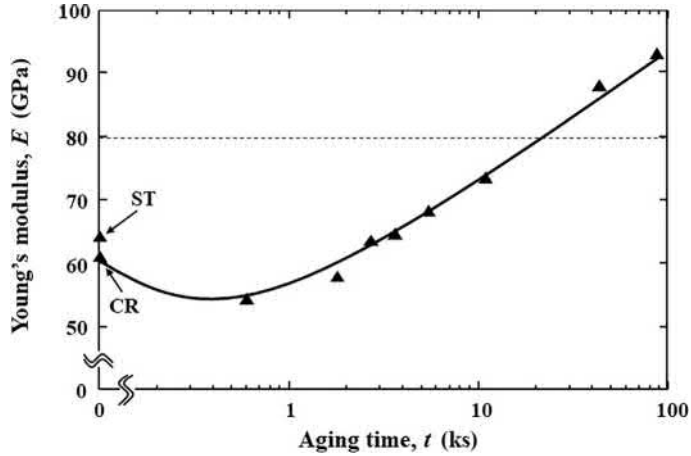


Fig. 5.31 Young's moduli of TNTZ subjected to solution treatment (ST), severe cold rolling (CR), and aging AT as a function of aging time.

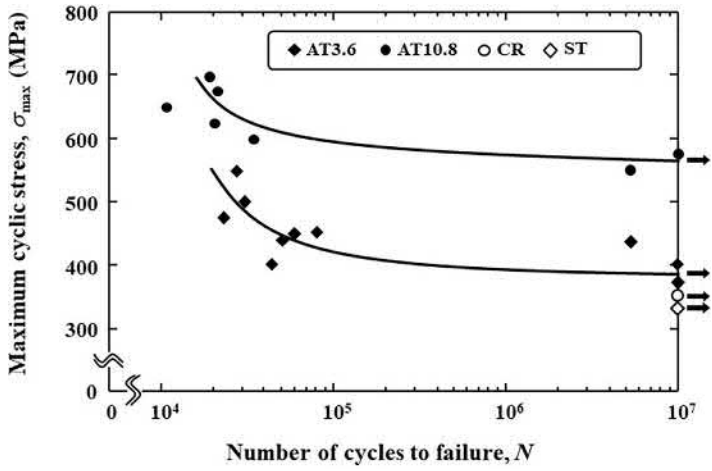


Fig. 5.32 S-N> curves of TNTZ subjected to aging at 573 K for 3.6 ks >(AT3.6) and 10.8 ks (AT10.8), and fatigue limits of TNTZ subjected to solution treatment (ST) and severe cold rolling (CR).

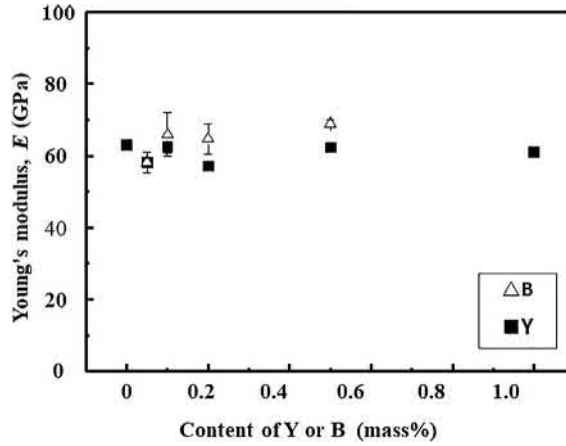


Fig. 5.33 Young's modulus as a function of Y or B concentration in TNTZ with TiB_2 or Y_2O_3 additions subjected to cold rolling after solution treatment.

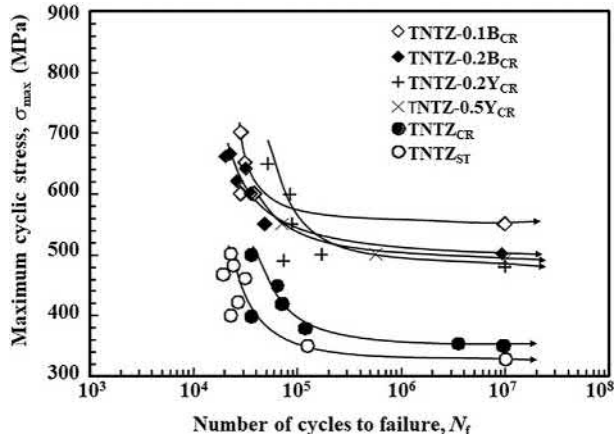


Fig. 5.34 S-N curves of TNTZ with TiB_2 or Y_2O_3 additions subjected to cold rolling after solution treatment along with those of TNTZ subjected to solution treatment or cold rolling after solution treatment.

2012) along with those of TNTZ subjected to ST or CR after ST. The fatigue strength of TNTZ is increased to the applicable level by adding a small amount of TiB_2 or Y_2O_3.

5.3 Fatigue crack propagation

In order to inhibit the catastrophic failure of biomaterials, it is necessary to understand the fatigue crack initiation and fatigue crack propagation characteristics. The crack propagation characteristics are important for arriving at a fail-safe design for structural materials. It is considered that the catastrophic failure of these materials can

be avoided by stopping the crack extension during the stable crack propagation stage, even if the crack has already been initiated.

It is important to evaluate both long and short crack (small crack) propagation characteristics. The trends in propagation rates of long and short cracks are not always similar.

5.3.1 Short fatigue crack propagation in air and in vitro

The relationships between the surface fatigue crack length, $2a$, and the ratio of the number of cycles to the number of cycles to failure, N/N_f, in Ti-6Al-7Nb and Ti-6Al-4V ELI with an equiaxed α structure are shown in Fig. 5.35 (Akahori et al., 2000) The number of cycles required for the first observation of an initial fatigue crack by light microscope is defined as the short fatigue crack initiation life; in this case, $2a < 50$ μm (approximately). The fraction of the fatigue crack initiation life in the total fatigue life that is equal to the number of cycles to failure is around 5% in Ti-6Al-7Nb and around 20% in Ti-6Al-4V ELI. Assuming that the short fatigue crack initiation and propagation life is the period for the surface crack to grow a length of five times or less than the size of the primary α grain, approximately $2a < 50$ μm, the short fatigue crack initiation and propagation life is around 50% of the total fatigue life in Ti-6Al-7Nb with an equiaxed α structure, while around 70% in Ti-6Al-4V ELI with an equiaxed α structure.

The observation of the fatigue crack propagation behavior revealed that the fatigue crack in the equiaxed α structure tends to initiate mainly at the primary α grain boundaries, while the crack tends to propagate preferentially along the β region near the interface between the primary α and β regions as shown in Fig. 5.36 (Akahori et al., 2000).

On the other hand, in the Widmanstätten α structure of both alloys, the observation of the fatigue crack behavior revealed that the fatigue crack initiates at the very early stage of the fatigue. After a few hundred cycles, the crack initiates and grows to a

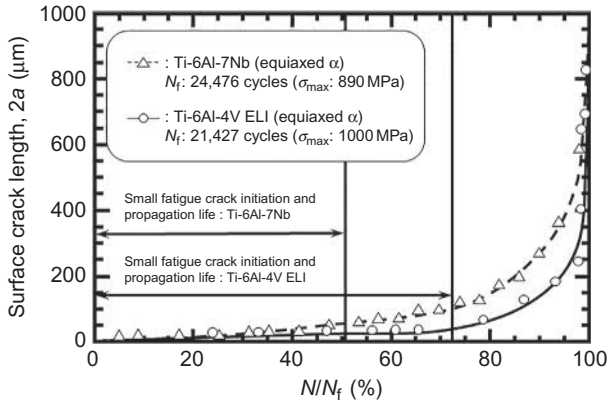


Fig. 5.35 Surface crack lengths in Ti-6Al-7Nb and Ti-6Al-4V ELI with equiaxed α structure. Maximum stresses, σ_{max}, are 890 and 1000 MPa for Ti-6Al-7Nb and Ti-6Al-4V ELI, respectively. N_f and N are the number of cycles to failure and the number of cycles, respectively.

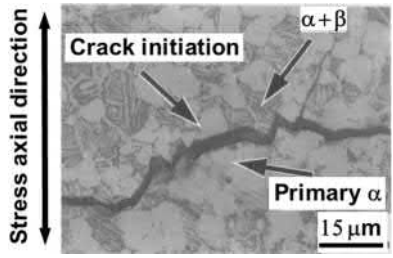


Fig. 5.36 Crack initiation site and propagation path in Ti-6Al-7Nb with equiaxed α structure.

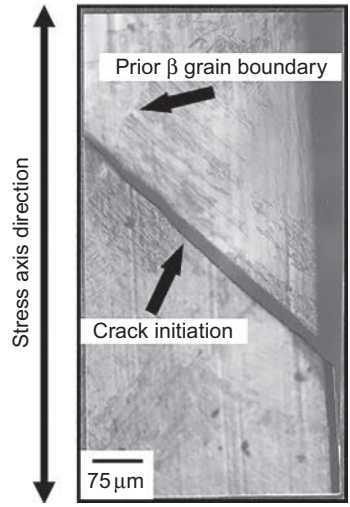


Fig. 5.37 Crack initiation site of Ti-6Al-7Nb with Widmanstätten α structure.

length that is nearly equal to the size of the colony or prior β grain. The colony of the prior β grain and crack propagation is retarded at the colony boundary or at the prior β grain boundary. However, the crack propagates in an unstable manner soon after passing through these boundaries, and this ultimately results in specimen fracture. These crack behaviors are shown in Fig. 5.37 (Akahori et al., 2000). The arresting period of the crack blocked in the α colony or the prior β grain boundaries occupies more than 90% of the total fatigue life in both alloys.

It is reported that the fatigue crack propagation rates of SUS 304 stainless steel, which is also austenitic stainless steel, evaluated in air and 3% NaCl solution are clearly different in the very short fatigue crack region, and the short crack propagation rate in 3% NaCl solution is higher than that in air, as shown in Fig. 5.38 (Nakajima et al., 1997).

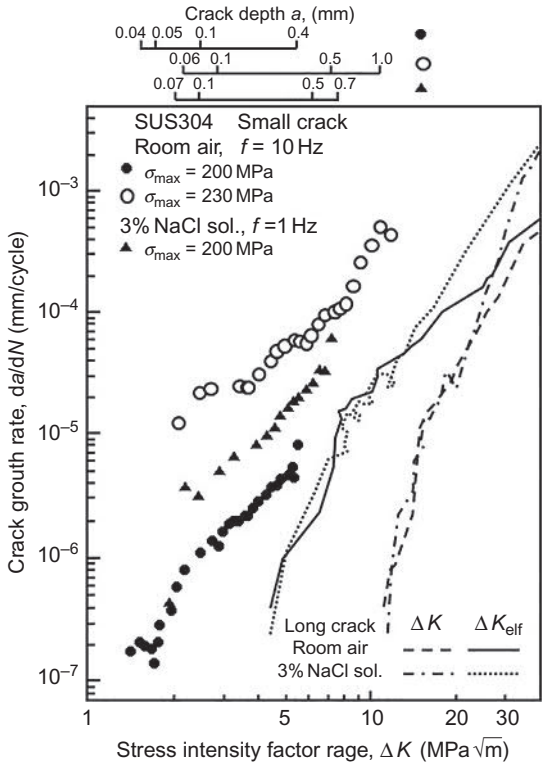


Fig. 5.38 da/dN-ΔK relationships for small cracks in SUS 304 stainless steel in air and in 3% NaCl solution.

5.3.2 Long fatigue crack propagation in air and in vitro

Fig. 5.39 (Niinomi et al., 2000) shows the relationship between the fatigue crack propagation rate, da/dN, and the nominal cyclic stress intensity factor, ΔK, and that between da/dN and the effective cyclic stress intensity factor, ΔK_{eff}, for Ti-6Al-4V ELI with Widmanstätten α and equiaxed α structures, and SUS 316L stainless steel obtained in air. When da/dN is plotted against ΔK, it is observed to decrease in the following order: Ti-6Al-4V ELI with the Widmanstätten α structure ≥ SUS 316L stainless steel ≥ Ti-6Al-4V ELI with the equiaxed α structure. On the other hand, when da/dN is plotted against ΔK_{eff}, the crack propagation rate of Ti-6Al-4V ELI with the Widmanstätten α structure is nearly the same as that of SUS 316L stainless steel. The crack propagation rate of Ti-6Al-4V ELI with the equiaxed α structure is the highest. However, the differences in the crack propagation rates among these materials become relatively small. In particular, the crack propagation rate of T-6Al-4V ELI with the Widmanstätten α structure approaches that of Ti-6Al-4V ELI with the equiaxed α structure. Therefore, the crack closure effect in Ti-6Al-4V ELI with the Widmanstätten α structure is greater than that in Ti-6Al-4V ELI with the equiaxed α structure.

The microstructure strongly affects the crack propagation rate in (α + β)-type Ti alloys. In a representative (α + β)-type Ti alloy, Ti-6Al-4V, the long crack propagation

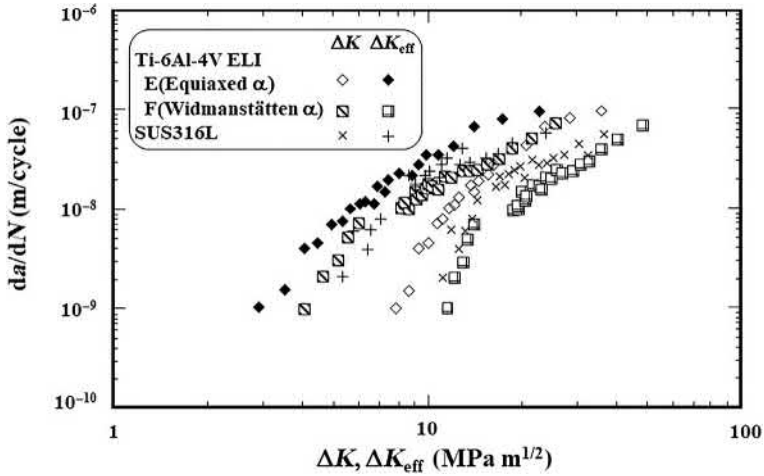


Fig. 5.39 The fatigue crack propagation rate, da/dN, as a function of the nominal cyclic stress intensity factor range, ΔK, and as a function of the effective cyclic stress intensity factor range, ΔK_{eff}, in the case of variously heat-treated Ti-6Al-4V ELI and SUS 316L stainless steel.

rate in the Widmanstätten α structure is, in general, lower than that in the equiaxed α structure. The main reason for this phenomenon is the large crack deflection in the Widmanstätten α structure (Niinomi et al., 1992). Therefore, the crack closure behavior in the Widmanstätten α structure is greater than that in the equiaxed α structure (Niinomi et al., 1992).

On the other hand, the short crack propagation rate in the equiaxed α structure is, in general, lower than that in the Widmanstätten α structure as mentioned above. The ratio of the short fatigue crack propagation life to the total fatigue life is fairly high. Therefore, improving resistance against short fatigue crack propagation is very effective in improving the total fatigue life (Akahori et al., 2000; Niinomi, 2000).

When da/dN is plotted against ΔK, the long fatigue crack propagation rates of Ti-6Al-4V ELI and Ti-5Al-2.5Fe in Ringer's solution are higher than those in air, but they are nearly the same in air and Ringer's solution when da/dN is plotted against ΔK_{eff}, as shown in Fig. 5.40. In this case, it is reported that the crack closure reduces in Ringer's solution because the number of secondary cracks and the fatigue fracture surface in Ringer's solution are smaller than those in air. This suggests that the fatigue fracture surface corrodes and dissolves in Ringer's solution.

The short fatigue crack propagation rates of SUS 304 stainless steel evaluated in air and 3% NaCl solution are higher than those in air, as already shown in Fig. 5.39 (Nakajima et al., 1997). However, the long fatigue crack propagation rate of SUS 304 stainless steel in air is almost the same as that in 3% NaCl solution, as shown in Fig. 5.41 (Nakajima et al., 1997); however, in the range of high stress intensity factor, the crack propagation rate in 3% NaCl solution is slightly higher than that in air.

It has been reported that for Co-Cr alloy, the long fatigue crack propagation rate in Ringer's solution is higher than that in air (Hanawa et al., 2000).

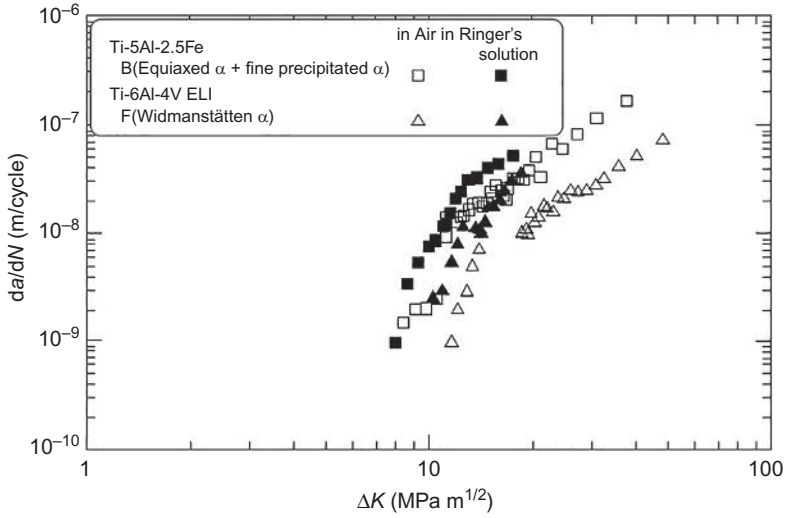


Fig. 5.40 Fatigue crack propagation rate, d*a*/d*N*, as a function of nominal cyclic stress intensity factor range, ΔK, in the case of Ti-5Al-2.5Fe with (equiaxed α + fine precipitated α) and Ti-6Al-4V ELI with Widmanstätten α in air and in Ringer's solution.

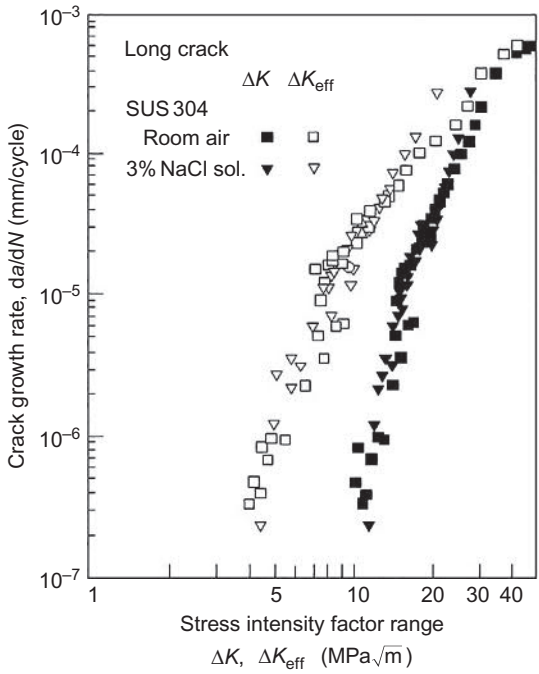


Fig. 5.41 d*a*/d*N*-ΔK and ΔK_{eff} relationships for long cracks of SUS 304 stainless steel in air and in 3% NaCl solution.

5.3.3 Improvement in long fatigue crack propagation resistance

The crack propagation resistance of Ti-6Al-4V also increases due to the deformation-induced transformation of the retained unstable β-phase, as shown in Fig. 5.42 (Niinomi et al., 1990, 1993), as well as the fatigue strength as mentioned above. This figure shows the relationship between the crack propagation rate (da/dN) and the effective cyclic stress intensity factor divided by the Young's modulus ($\Delta K_{\mathrm{eff}}/E$) for rolled plates of Ti-6Al-4V subjected to ST at 1173 and 1088 K, respectively, followed by water quenching (referred to as STQ1173R and STQ1088R) or aging treatment after water quenching (referred to as STA1173R). The da/dN of STQ1088R in the IIb and IIc regions is the least among all the specimens. In the case of STQ1088R, the deformation-induced martensitic transformation of the retained β-phase occurs, as shown in Fig. 5.43 (Niinomi et al., 1990, 1993).

In order to enhance the mechanical properties of Ti alloys by using the deformation-induced martensitic transformation of the retained unstable β-phase, the stability of the unstable β-phase is important. If the stability of the retained β-phase is considerably low, the mechanical properties may, on the contrary, be degraded because the unstable β-phase transforms into martensite before crack initiation or propagation (Akmoulin et al., 1993).

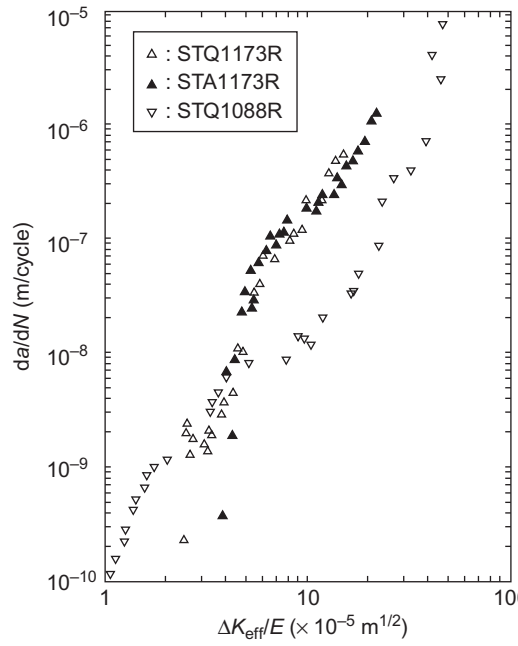


Fig. 5.42 Relationships between da/dN and $\Delta K_{\mathrm{eff}}/E$ in solution-treated specimen and aged specimens of rolled Ti-6Al-4V plates.

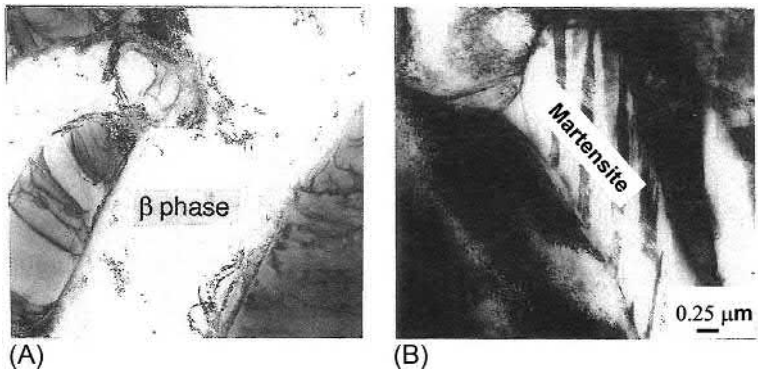


Fig. 5.43 Typical TEM micrographs of b regions in (A) under-formed and (B) deformed parts near the fracture surface formed in IIb region in the STQ1088R specimen.

5.4 Fatigue strength of wire

The wires composed of metallic biomaterials are useful in biomedical and dental applications, that is, stents, guide wire of a catheter, surgical wire, and orthodontic wire.

An interesting application of metallic wires is the use of the high-nitrogen stainless steel wire for the electrode of an FES (functional electrical stimulation). From the viewpoint of allergic reactions, low-Ni stainless steel wire, that is, high-nitrogen stainless steel wire (22.0% Cr, 10% Ni, 6.02% manganese (Mn), 2% Mo, 0.41% N and balance Fe) is preferred to SUS 316L stainless steel. In the case of a wire, the rotating bending fatigue strength is important. Fig. 5.44 (Iguchi, 1999) shows the relationship

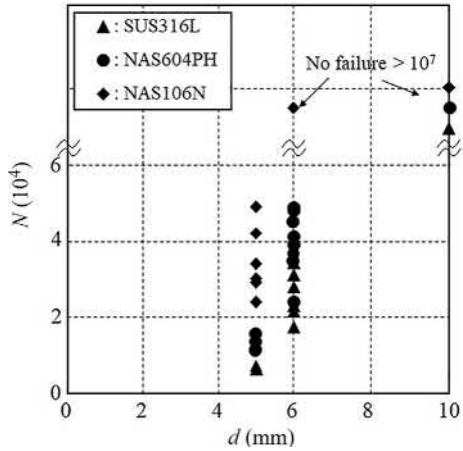


Fig. 5.44 Relationship between number of rotation of electrode materials to failure, *N*, and distance between chucks, *d*, by a dual-driven rotating-bending failure method in air.

between the number of rotations to failure, N_f, of electrode wires composed of SUS 316L stainless steel, NAS604PH (Co alloy), and NAS106N (high N stainless steel) and the distance between chucks, d, obtained from a dual-driven rotating-bending failure method in air. The rotating-bending fatigue strength of high-N stainless steel is the highest. Ti is expected to be a suitable material for this type of wire.

Low-modulus β-type Ti alloys are also used for wires for stents, catheters, and orthopedic, surgical, and orthodontic equipment. The shape memory alloy TiNi is widely used for catheters or orthodontic wires. However, TiNi contains a large amount of Ni, which has been reported to be an allergen and is also brittle. Therefore, Ni-free shape memory or super elastic Ti alloys with low moduli are being developed. As orthodontic wires, β-type Ti-Mo-Zr-tin (Sn) has been put to practical use. Very recently, low modulus β-type TNTZ subjected to severe cold working and heat treatment has exhibited super elastic behavior as shown in Fig. 5.45 (Niinomi, 2003). Fig. 5.46 (Akahori et al., 2005b) shows the notched fatigue strength of TNTZ wire with a diameter of 1.0 mm along with those of pure Ti, TiNi, and SUS 316L stainless steel wires with diameters of 1.0 mm. The notched fatigue strength of SUS 316L stainless steel wire is the highest in both the low- and high-cycle fatigue life regions. The notched fatigue strength of pure Ti wire is the lowest in the low-cycle fatigue life region, and that of TNTZ wire is slightly higher than that of TiNi wire. However, in the high-cycle fatigue life region, the notched fatigue strengths of pure Ti, TiNi, and TNTZ wires are nearly the same. In Japan, the official license for the application of TNTZ for orthodontic wire has been issued very recently. Thus, TNTZ wire will be put to practical use as orthodontic wire in the very near future.

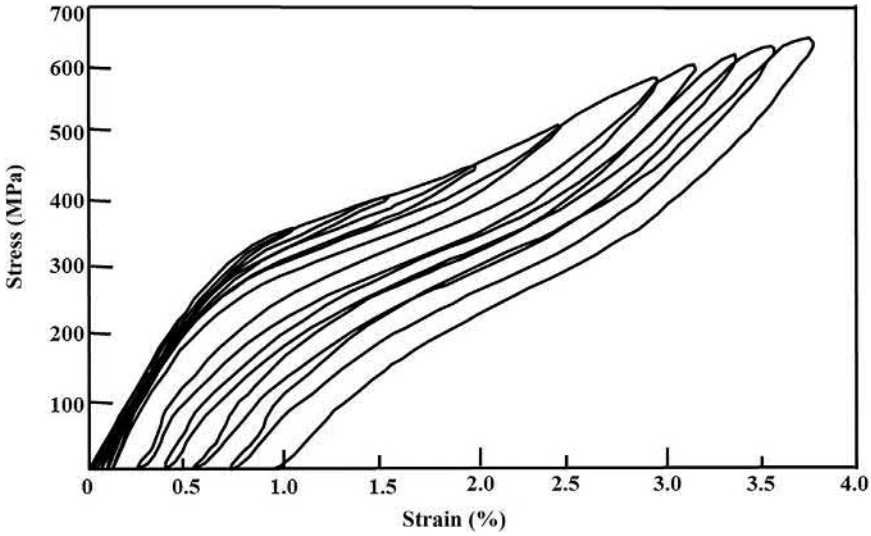


Fig. 5.45 Tensile loading-unloading stress-strain curves of drawn wire of Ti-29Nb-13Ta-4.6Zr with a diameter of 1.0 mm; total elastic strain: 2.7%.

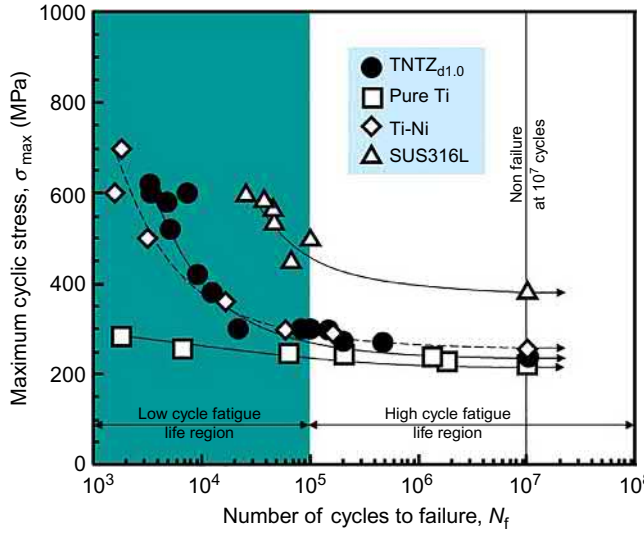


Fig. 5.46 S-N curves of TNTZr ($TNTZ_{d1.0}$) and pure Ti, Ti-Ni, and SUS316L stainless steel wires with a diameter of 1.0 mm obtained from notch-fatigue tests.

5.5 Summary

With regard to the long-term usage of implants, the understanding and improvement of fatigue properties of metallic biomaterials in complexed conditions such as fretting overlapped conditions, in air, and in vitro and in vivo are significantly important. In this chapter, these fatigue properties are described as possibilities. Because of the present trend toward the development of metallic biomaterials, the descriptions of Ti alloys occupy a large portion of this chapter. Fatigue data on metallic biomaterials in vivo are lacking, although they are very important from the viewpoint of practical applications. It is desirable to report much more data on the fatigue properties in vivo in future.

References

Akahori, T., Niinomi, M., Fukunaga, K., Inagaki, I., 2000. Effects of microstructure on the short fatigue crack initiation and propagation characteristics of biomedical α/β titanium alloys. Metall. Mater. Trans. A 31A, 1949–1958.

Akahori, T., Niinomi, M., Matsuda, K., Suzuki, A., 2002. Microstructure and fatigue crack initiation and propagation characteristics of dental cast (α + β)-type titanium alloy subjected to thermochemical treatment. J. Jpn. Inst. Metals 66, 1098–1106.

Akahori, T., Niinomi, M., Ishimizu, K., Fukui, H., Suzuki, A., 2003. Effect of thermomehcanical treatment on fatigue characteristics of Ti-29NB-13Ta-4.6Zr for biomedical applications. J. Jpn. Inst. Metals 67, 652–660.

Akahori, T., Niinomi, M., Otani, M., Toda, H., Fukui, H., Ogawa, M., 2005a. Notch fatigue properties of a Ti-29Nb-13Ta-4.6Zr alloy for biomedical applications. J. Jpn. Inst. Light Metals 55, 575–581.

Akahori, T., Niinomi, M., Toda, H., Yamauchi, K., Fukui, H., Ogawa, M., 2005b. Mechanical properties and deformation behavior of β-type titanium alloy (TNTZ) drawn wires. J. Jpn. Inst. Metals 69, 530–537.

Akahori, T., Niinomi, M., Noda, A., Toda, H., Fukui, H., Ogawa, M., 2006. Effect of aging on mechanical properties of Ti-29Nb-13Ta-4.6Zr alloy for biomedical applications. J. Jpn. Inst. Metals 70, 295–303.

Akahori, T., Niinomi, M., Nakai, M., Nishimura, Takei, H., Fukui, H., Ogawa, M., 2008. Wear and mechanical properties, and cell viability of gas-nitrided beta-type Ti-Nb-Ta-Zr system alloys for biomedical applications. Mater. Trans. 49, 166–174.

Akmoulin, I.A., Niinomi, M., Kobayashi, T., 1993. Dynamic fracture toughness of Ti-6Al-4V alloy with various stabilities of β phase. Metall. Trans. A. 25A, 1655–1666.

Breme, H.J., Helsen, J.A., Breme, H.J., 1998. In: Helsen, J.A. (Ed.), Selection of Materials. John Wiley & Sons, New York, pp. 1–36.

Cho, K., Niinomi, M., Nakai, M., Hieda, J., Kanekiyo, R., 2013. Improvement of tensile and fatigue properties of β-titanium alloy while maintaining low Young's modulus through grain refinement and oxygen addition. Mater. Trans. 54, 2000–2006.

Gunawarman, Niinomi, M., Eylon, D., Fujishiro, S., Ouchi, C., 2002. Effect of β phase stability at room temperature on mechanical properties in β-rich α+β type Ti-4.5Al-3V-2Mo-2Fe alloy. ISIJ 42, 191–199.

Hanawa, T., Nakazaw, K., Maruyama, N., Yamamoto, A., Hiromoto, S., Sumita, M., Ying, M., Kobayashi, T., 2000. Study on structural biomaterials with excellent biocompatibility. Research Report of National Inst. of Metals 22, pp. 223–239.

Hanawa, T., Hiromoto, A., Yamamoto, A., Maruyama, N., Nakazawa, K., Niinomi, M., Okabe, T., Taleff, E.M., Lesure, D.R., Lippard, H.E., 2001. Metallic biomaterials in body fluid and their surface modification. In: Structural Biomaterials for the 21st Century. TMS, pp. 145–156.

Iguchi, Y., 1999. Development of the implanted stainless steel electrode for functional electrical stimulation based on ultra clean refining processes. Bull. Iron Steel Inst. Jpn. 4, 737–740.

Imam, M.A., Gilmore, C.M., 1983. Fatigue and microstructural properties of quenched Ti-6Al-4V. Metall. Trans. A 14A, 233–240.

Kasuga, T., Nogami, M., Niinomi, M., Hattori, T., 2003. Bioactive calcium phosphate invert glass-ceramic coating on β-type Ti-29Nb-13Ta-4.6Zr. Biomaterials 24, 283–290.

Kim, H.M., Miyaji, F., Kokubo, T., 1997. Effect of heat treatment on apatite-forming ability of Ti metal induced by alkali treatment. J. Mater. Sci. Mater. Med. 8, 341–347.

Kim, J.H., Niinomi, M., Akahori, T., 2005. Influence of bone structure on mechanical properties of bovine and swine compact bones. Mater. Sci. Forum 475–479, 2407–2410.

Kobayashi, T., Yamamoto, H., 1998. Development of high toughness in austempered type ductile cast iron and evaluation of its properties. Metall. Trans. A. 19A, 319–327.

Kumar, P., Hickl, A.J., Asphahani, A.I., Lawley, A., 1985. Properties and Characteristics of Cast, Wrought, and Powder Metallurgy (P/M) Processed Cobalt-Chromium-Molybdenum Implant Materials. ASTM STP 859, pp. 30–56.

Kuroda, D., Niinomi, M., Morinaga, M., Kato, Y., Yashiro, T., 1998. Design and mechanical properties of new beta type titanium alloys for implant materials. Mater. Sci. Eng. A A243, 244–249.

Kuroda, D., Hiromoto, S., Hanawa, T., Katada, Y., 2002. Corrosion behavior of nickel-free nitrogen austenitic stainless steel in simulated biological environments. Mater. Trans. 43, 3100–3104.

Lee, S.H., Takahashi, E., Nomura, N., Chiba, A., 2006. Effect of heat treatment on microstructure and mechanical properties of Ni- and C-free Co-Cr-Mo alloys for medical applications. J. Jpn. Inst. Metals 70, 260–264.

Li, S.J., Niinomi, M., Akahori, T., Kasuga, T., Yang, R., Hao, Y.L., 2004. Fatigue characteristics of bioactive glass-ceramic-coated Ti-29Nb-13Ta-4.6Zr for biomedical applications. Biomaterials 25, 3341–3349.

Liu, H., Niinomi, M., Nakai, M., Obara, S., Fujii, H., 2017. Improved fatigue properties with maintaining low Young's modulus achieved in biomedical beta-type titanium alloy by oxygen addition. Mater. Sci. Eng. A 704, 10–17.

Maruyama, N., Kobayashi, T., Nakazawa, K., Sumita, M., Sato, M., 1999. Fatigue and fretting behavior of Ni free Co-Cr alloy in a pseudo-body fluid. J. Jpn. Biomater. Soc. 17, 172–179.

Nakai, M., Niinomi, M., Akahori, T., Ohtsu, N., Nishimura, H., Toda, H., Fukui, H., Ogawa, M., 2008. Surface hardening of biomedical Ti-29Nb-13Ta-4.6Zr and Ti-6Al-4V ELI by gas nitriding. Mater. Sci. Eng. A 486, 193–201.

Nakai, M., Niinomi, M., Oneda, T., 2012. Improvement in fatigue strength of biomedical β-type Ti–Nb–Ta–Zr alloy while maintaining low Young's modulus through optimizing ω-phase precipitation. Metal. Mater. Trans. A 43, 294–302.

Nakajima, M., Tokaji, K., Akatsuka, Y., 1997. Corrosion fatigue crack initiation and early growth behavior in stainless steel. J. Jpn. Soc. Eng. A 63, 487–492.

Niinomi, M., 1998. Mechanical properties of biomedical titanium alloys. Mater. Sci. Eng. A 243, 231–236.

Niinomi, M., 2000. Fatigue. Bull. Iron Steel Inst. Jpn. 5, 82–88.

Niinomi, M., 2001. Recent metallic materials for biomedical applications. Metall. Mater. Trans. A 32A, 477–486.

Niinomi, M., 2002a. Fatigue characteristics and microstructure of titanium alloys for biomedical applications. In: Blom, A.F. (Ed.), Proceedings Fatigue'2002. 3/5, EMAS, pp. 2073–2083.

Niinomi, M., Akahori, T., Nakamura, S., Fukui, H., Suzuki, A., 2002b. Friction wear characteristics of surface oxidized new β-type titanium alloy in simulated body environment. Tetsu-to-Hagane 88, 567–574.

Niinomi, M., 2003. Recent research and development in titanium alloys for biomedical applications and healthcare goods. Sci. Technol. Adv. Mater. 4, 445–454.

Niinomi, M., Akahori, T., 2010. Improvement of fatigue life of titanium alloys for biomedical devices through microstructural control. Expert Rev. Med. Devices 7 (4), 481–488.

Niinomi, M., Kobayashi, T., Inagaki, I., Thompson, A.W., 1990. The effect of deformation-induced transformation on the fracture toughness of commercial titanium alloys. Metall. Trans. A. 21A, 1733–1744.

Niinomi, M., Kobayashi, T., Akmoulin, I.A., 1992. Mechanical properties of titanium alloys. J. Jpn. Inst. Light Metals 42, 605–613.

Niinomi, M., Kobayashi, T., Shimokawa, S., 1993. In: Froes, F.H., Caplan, I. (Eds.), Fatigue Crack Propagation in Ti-6Al-4V Alloys, Titanium'92. TMS, pp. 1835–1842.

Niinomi, M., Gong, B., Kobayashi, T., Oyabu, Y., Toriyama, O., 1995. Mechanical properties and fracture characteristics of Ti-6Al-4V and Ti-5Al-2.5Fe with refined microstructure using hydrogen. Metall. Mater. Trans. A 26A, 1141–1151.

Niinomi, M., Kobayashi, T., Toriyama, O., Kawakami, N., Ishida, Y., Matsuyama, Y., 1996. Fracture characteristics, microstructure, and tissue reaction of Ti-5Al-25Fe for orthopedic surgery. Metall. Mater. Trans. A 27A, 3925–3935.
Niinomi, M., Saga, A., Fukunaga, K., 2000. Long crack growth behavior of implant materials Ti-5Al-2.5Fe in air and simulated body environment with relating microstructure. Int. J. Fatigue 22, 887–897.
Niinomi, M., Akahori, T., Nakamura, S., Fukui, H., Suzuki, A., 2002a. Friction wear characteristics of surface oxidized new β-type titanium alloy in simulated body environment. Tetsu-to-Hagane 88, 567–574.
Niinomi, M., Hattori, T., Morikawa, K., Kasuga, T., Suzuki, A., Fukui, H., Niwa, S., 2002b. Development of low rigidity β-type titanium alloy for biomedical applications. Mater. Trans. 43, 2970–2977.
Niinomi, M., Li, H., Nakai, M., Liu, H., Liu, Y., 2016. Biomedical titanium alloys with Young's moduli close to that of cortical bone. Regen. Biomater. 3, 1–13.
Sato, M., Tu, R., Goto, T., Ueda, K., Narushima, T., 2007. Hydroxyapatite formation on calcium phosphate coated titanium. Mater. Sci. Forum 561–565, 1513–1516.
Song, X., Niinomi, M., Tsutsumi, H., Nakai, M., Wang, L., 2011. Effects of TiB on mechanical properties of β-type titanium alloy for use in biomedical applications. Mater. Sci. Eng. A, 5285600–5285609.
Song, X., Niinomi, M., Tsutsumi, H., Nakai, M., Wang, L., 2012. Improvement in fatigue strength while keeping low Young's modulus of a β-type titanium alloy through yttrium oxide dispersion. Mater. Sci. Eng. C, 32542–32549.
Yan, X., Kato, M., Nakasa, K., Morit, K., 2001. Evaluation of fracture strength and interfacial strength of titanium-nitride layers formed by gas-nitriding of titanium. J. Soc. Mat. Sci. Jpn. 50, 764–771.

Further reading

Gunawarman Niinomi, M., Akahori, T., Souma, T., Ikeda, M., Toda, H., Terashima, K., 2005. Fatigue characteristics of low cost β titanium alloys for healthcare and medical applications. Mater. Trans. 46, 1570–1777.
Maruyama, N., Kobayashi, T., Sumita, M., 1995. Fretting fatigue strength of a Ti-6Al-4V alloy in a pseudo-body-fluid and quantitative analysis of the substances in the fluid. J. Jpn. Soc. Biomater. 13, 14–20.
Niinomi, M., Akahori, T., Yabunaka, T., Fukui, H., Suzuki, A., 2002c. Fretting fatigue characteristics of new biomedical β-type titanium alloy in air and simulated body environment. J. Iron Steel Inst. Jpn. 88, 553–560.
Niinomi, M., Akahori, T., Yamaguchi, T., Kasuga, T., Fukui, H., Suzuki, A., 2003. Aging characteristics and mechanical properties of calcium phosphate invert glass-ceramic coated Ti-29Nb-13Ta-4. 6Zr for biomedical applications. J. Jpn. Inst. Metals 67, 604–613.
Sumita, M., Kawabe, Y., Nishijima, T., Fujii, T., Sitou, K., 1993. Study on improvement of fretting fatigue characteristics of high strength structural materials. Research Reports of National Institute for Materials Science 14, pp. 207–218.
Takeda, J., Niinomi, M., Akahori, T., Suzuki, Y., Toda, H., 2005. Contact pressure and fretting fatigue characteristics of highly workable titanium alloy with equiaxed α and Widmanstätten α structure. J. Jpn. Inst. Light Metals 55, 661–667.

Mechanical testing of metallic biomaterials

6

Hideaki Nishikawa[*], *Norio Maruyama*[†]
[*]Research Center for Structural Materials, National Institute for Materials Science, Tsukuba-shi, Japan, [†]Collaboration Planning Office, National Institute for Materials Science, Tsukuba-shi, Japan

6.1 Fracture of metal implants and test methods

Metallic materials are often used for implants to load-bearing parts of the living body. Metal implants used under a static load will not fail before reaching the end of their estimated lifetime except in special circumstances. On the other hand, orthopedic implants such as artificial hip joints, bone plates, and intramedullary nails may fail before reaching the end of their estimated lifetime due to the cyclic load applied by periodic motion such as walking (Sasada et al., 1988). The Implant Committee of the Japanese Orthopedic Association distributed a questionnaire survey on implant fracture to 2032 authorized organizations in 1994. A total of 950 organizations responded to the survey, and the results were as follows:

- In terms of implant type, fracture occurred to bone-connecting materials used for intramedullary nails, plates and screws, spinal-fixation materials, and artificial joints, in descending order of prevalence.
- In terms of body area, fracture occurred mainly in the femoral region, followed by spine, knee, shinbone, and hip joint.

Fig. 6.1 shows a bone plate made of pure titanium (Ti) (JIS grade 2) that failed 1 year after it was implanted. Failure occurred in the screw hole of the plate. The implant procedure involved screwing the plate to the bone, and fretting (contact damage process arising from surface micro-slip associated with small-scale oscillatory motion of clamped structural members.) occurred between the screw head and the surface

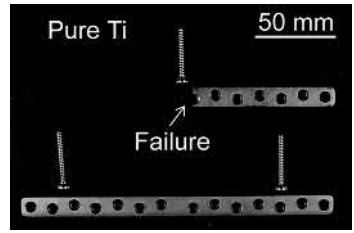


Fig. 6.1 Bone plate fractured after 1 year from implantation.

Metals for Biomedical Devices. https://doi.org/10.1016/B978-0-08-102666-3.00006-7
© 2019 Elsevier Ltd. All rights reserved.

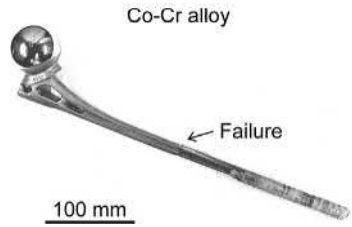


Fig. 6.2 Stem fractured 9 years after implantation. The *arrow* indicates the crack.

around the screw hole. Subsequently, a crack nucleated and grew, presumably leading to failure. In the human body environment, it is highly likely that the failure was also affected by corrosion. Fig. 6.2 shows a cobalt (Co)-chromium (Cr) alloy (vitallium) stem that failed 10 years after it was implanted. The stem failed in the center, where fretting occurred between the stem and the fitting mounted in the stem to prevent turning. Most of orthopedic implants which failed are affected by cyclic loading. However, such failure is rarely caused only by plain fatigue. In most cases, the fatigue is accompanied by fretting, corrosion, or both. It is known that the fatigue strength of metallic materials is significantly reduced by fretting or corrosion (Waterhouse, 1984).

Metallic materials have excellent tensile strength, fatigue strength, ductility, and toughness, and the scattering in the strength is very small compared to ceramic or polymer materials. Thus, metallic materials are often used for medical implants.

For example, metallic materials are used for:

- orthodontic wires and artificial tooth roots in dentistry,
- fracture prostheses such as artificial joints, bone plates, and spinal fixation in orthopedics,
- stents, catheters, and guide wires in medical management.

To ensure that the abovementioned metal implants function properly for the required period of time, sufficient durability must be provided to maintain the desired performance. Thus, different tests are employed to evaluate mechanical properties of metallic materials, because metal implants require various properties depending on the application.

These tests include, for example:

- tensile test and twist test (torque test) for orthodontic wires and guide wires,
- tensile test and abrasion test for artificial joint slip parts,
- tensile test, fatigue test, and fretting fatigue test for bone plates and spinal fixation,
- fatigue test and bend test for stents.

6.2 Living body environment

For the mechanical test of biomedical metallic materials, the living body environment should be considered. Generally, fatigue strength and fretting fatigue strength of metallic materials decrease in a corrosive environment.

In the living body, the salt concentration is about 1%, and the temperature is 310 K (37°C). Oxygen (O) partial pressure in the living body is 1/4–1/5 of that in air. Between two materials or between the material and cells, however, the dissolved O concentration is lowered, which is caused by crevice corrosion. Therefore, it takes longer to repair damaged oxide layers in the living body than in air. The pH level which affects corrosion of metallic materials is generally 7–7.35 in the living body. However, the level drops to 5.2 due to inflammation or foreign body reaction when an implant is inserted into the body (Hench and Ethridge, 1975). As mentioned above, the living body provides metallic materials with a severe environment.

Recently, it was clarified that the active O produced by immune cells (macrophage) and organic substances in the body, such as amino acids and proteins, accelerates corrosion of Ti materials (Mu et al., 2000). However, in corrosion fatigue and fretting corrosion fatigue tests for metallic biomaterials, PBS(−) (phosphate buffered saline), physiological saline, 0.9% NaCl water solution, Hank's balanced salt solution, Ringer's solution, and cell culture medium are frequently used as a simulated body fluid. This chapter describes the methods for fatigue and fretting fatigue tests in a simulated body fluid to evaluate mechanical properties of metallic materials to be used as fracture prostheses in the orthopedic field in particular. Next, the fatigue/fretting fatigue behavior in a simulated body fluid and in air is discussed for 316L stainless steel, nickel (Ni)-free high-nitrogen (N) stainless steel, Ti-6% aluminum (Al)-4% vanadium (V) (Ti-6Al-4V) alloy, pure Ti for industrial use (CP Ti), and Co-Cr-molybdenum alloy. Finally, a new method for fatigue tests using a living cell environment is also described.

6.3 Tensile strength of metallic materials

Tensile properties of materials can be obtained by the following method. When a tensile specimen is loaded in a given direction until it fractures, a curve called stress-strain (S-S) curve is obtained (Fig. 6.3). The S-S curve is divided into the elastic and plastic deformation regions, although the shape of the curve depends on the material. In Fig. 6.3, 0 − a is the elastic deformation region where Hooke's law holds true, that is, the stress is proportional to the strain. The slope of this region is called Young's modulus. For many metallic materials, the boundary between the elastic and plastic deformation is not clearly visible in the S-S curve. The stress (Point b) where plastic deformation is 0.2% is called 0.2% proof stress in the S-S curve and is often regarded as the yield strength. Beyond Point b, there is a region in which macroscopic plastic deformation is observed, and the stress has a maximum value at Point c. This stress is called the ultimate tensile strength (UTS). Then the specimen fails at Point d. The configuration change of the specimen before and after the tensile test can provide the elongation and the reduction of area, which are indexes of material ductility.

Tensile properties of metallic materials are affected by the chemical compositions and microstructures, and also depend on processing or heat treatment.

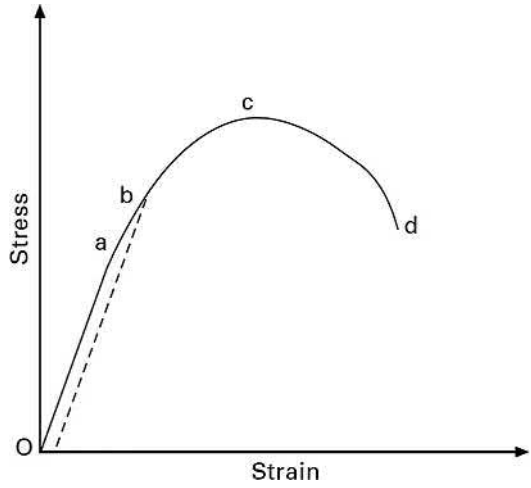


Fig. 6.3 Schematic diagram of a tensile stress-strain curve.

6.4 Fatigue and fretting fatigue of metallic materials

The corrosion fatigue test method for metal orthopedic implants is specified in ASTM F1801-97 (ASTM Standard F1801-97, 1997). In this standard, the recommended test environments are room temperature air and 37°C physiological saline, and the cyclic load frequency can be accelerated up to 30 Hz. However, a test at 1 Hz (similar to man's walking speed) should be conducted, when fatigue behavior in the living body is affected by corrosion. The number of specimens tested at each stress level should be three or more, and the stress amplitude vs number of cycles to failure (S-N) curve up to 10^6 cycles should be obtained.

The fretting corrosion test method for metallic biomaterials is specified in F897-84 (ASTM Standard F897-84, 2002). As there is no standard method for the fretting corrosion fatigue test, the method proposed by Nakazawa et al. is often used (Nakazawa et al., 1992).

6.4.1 Fatigue of metallic materials

Fatigue failure is a phenomenon caused by a cyclic load equal to or lower than the tensile strength, as shown in Fig. 6.4. As shown in Fig. 6.5, fatigue failure of metallic materials is caused by localized plastic deformation on the material surface, accumulation of damage, and nucleation and growth of a crack as the number of load cycles is increased.

Metallic materials are usually composed of many crystal grains, each of which has its own slip planes and slip directions. The slip planes and directions of each crystal grain are randomly distributed in the materials. Therefore, even though the maximum stress applied to a specimen is macroscopically within the elastic deformation region, plastically deformed grains locally exist on the specimen's surface. If the plastic

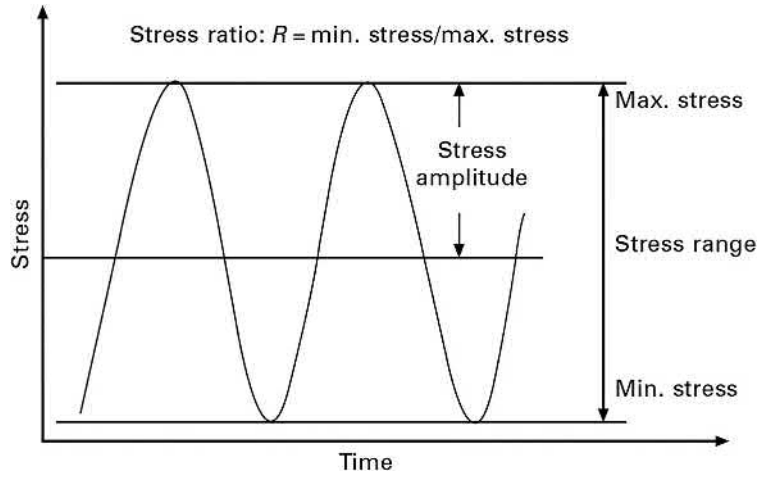


Fig. 6.4 Schematic diagram of stress change with time.

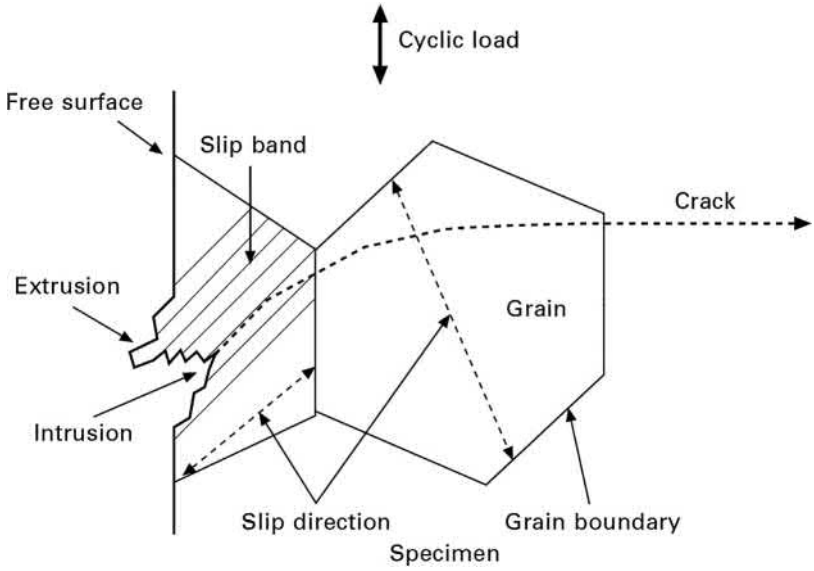


Fig. 6.5 Schematic drawing of fatigue crack initiation.

deformation induced by applied load disappears when the load is removed, fatigue will not occur. In practice, however, slight plastic deformation remains in one load cycle. Thus, cyclic load causes fatigue damage. Along with an increase in the number of load cycles, this damage accumulates locally in a crystal grain, causing a crack. The number of load cycles until the material fails is called fatigue life. The fatigue life is expressed by the sum of the number of cycles until a crack nucleates and the number until the crack grows to failure.

6.4.1.1 Fatigue life test

The fatigue test can be largely classified into fatigue life test and fatigue crack propagation test. Fatigue life test results are usually given by cyclic stress amplitude vs number of cycles to failure (S-N) curves as shown in Fig. 6.6. A stress amplitude, below which the specimen does not fail, is called the fatigue limit or durability limit. Generally, the fatigue strength at 10^7 cycles is regarded as the fatigue limit. To obtain 1 S-N curve, at least 10 specimens are required.

Fig. 6.6 shows a schematic diagram of S-N curves for fatigue, fretting fatigue, and fretting corrosion fatigue. Generally, corrosion and fretting decrease the fatigue strength of metallic materials (Waterhouse, 1984). In air, the fatigue limit is 1/2–1/3 of that the tensile strength (Klesnil and Lukas, 1984, pp. 4–37). This is partly because the fatigue strength is controlled by the weakest part of the material while the tensile strength is determined by the average properties of the whole material. Generally, as the tensile strength of materials increases the fatigue strength increases. In materials with very high tensile strength, however, the fatigue strength is lowered in sensitive response to defects in the specimen. If there is a stress concentration site such as bone plate hole or screw, the fatigue test is conducted using specimens with a notch with a similar stress concentration The number of cycles to crack nucleation for notched specimens is significantly lower than that for smooth specimens.

6.4.1.2 Fatigue crack propagation test

As shown in Fig. 6.5, a fatigue crack nucleates in a direction inclined at 45 degrees to the stress axis. Then, the crack propagates perpendicular to the stress axis. Generally, the fatigue crack propagation test is conducted with a constant stress amplitude. In this case, the fatigue crack growth rate increases exponentially with the number of stress cycles. The experimental results are typically summarized by a log (crack growth rate,

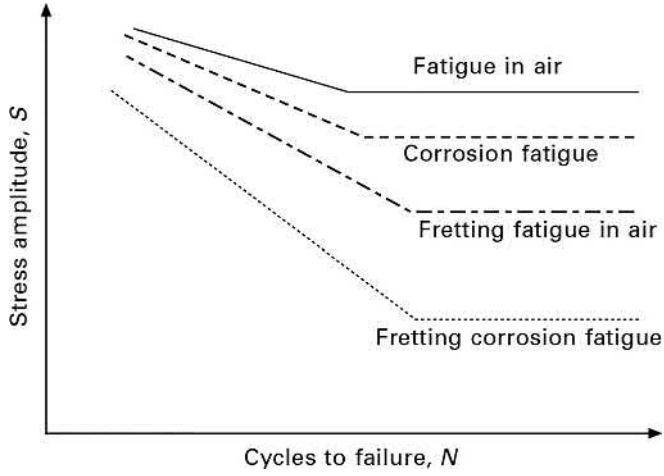


Fig. 6.6 Schematic diagrams of S-N curves for fatigue, fretting fatigue, and fretting corrosion fatigue.

da/dN, where a and N are the crack length and the number of cycles, respectively)-log (stress intensity factor range, ΔK) curve as shown in Fig. 6.7. Here, the stress intensity factor range ΔK is expressed by the cyclic stress range and the crack length. This figure shows the lower limit of ΔK, ΔK_{th} below which the crack does not propagate, the intermediate region, where log(da/dN) varies linearly with log(ΔK), and the unstable fracture region, where the crack propagates unstably and finally the specimen fractures. The stress intensity factor, K, at which the specimen unstably fractures, is called the fatigue fracture toughness, K_{fc}, which is similar to fracture toughness, K_{IC}. The fracture toughness is a material constant, depending on processing or heat treating, even though the chemical composition is the same. The linear relationship (Eq. 6.1) in the intermediate region was given by Paris (Klesnil and Lukas, 1984) and holds true for most metallic materials

$$da/dN = C\Delta K^m \tag{6.1}$$

where C and m are the material constants. The value of m, which is experimentally obtained, is between 2 and 4 for metallic materials.

A typical fracture surface of metallic materials caused by fatigue exhibits striations that show crack extension induced by cyclic stress. An example of striations of SUS 316L stainless steel is shown in Fig. 6.8. The distance between striations shows the distance that the crack grows during each stress cycle. Striations appear at a right angle to the crack propagation direction. Thus, for fatigue-failed materials, the cyclic stress applied to the material can be analyzed based on the orientation of the striations and the distance between them.

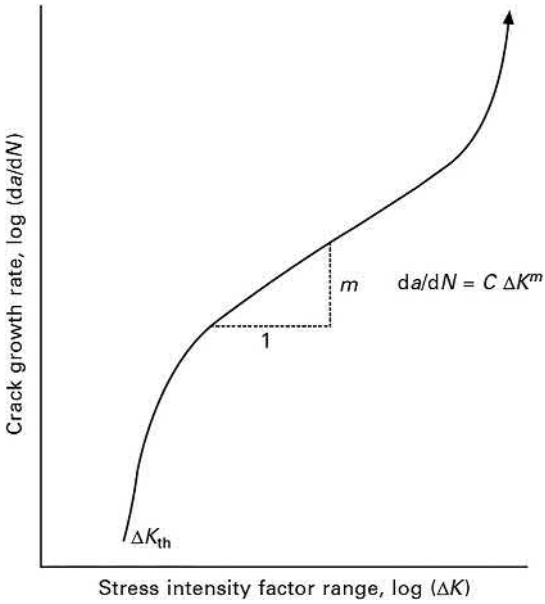


Fig. 6.7 Schematic diagram of crack growth rate as a function of stress intensity factor range.

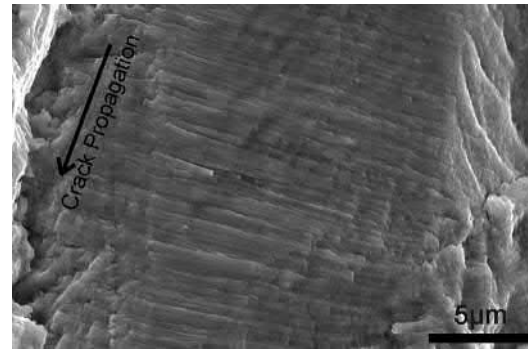


Fig. 6.8 Striation on fracture surface of SUS 316L stainless steel.

6.4.2 *Fretting fatigue of metallic materials*

Fretting means a contact damage process arising from surface micro-slip associated with small-scale oscillatory motion of clamped structural members. The contact surfaces are worn and, at the same time, they are affected by cyclic friction stress. Fatigue with fretting is called fretting fatigue. Mechanical factors affecting the fretting properties include coefficient of friction, pressing force, and amount of relative slip. In fretting fatigue, cyclic stress, which is the sum of cyclic applied stress and cyclic friction stress caused by fretting, is applied to the material. The friction stress is maximum on the contact surface of the material and decreases drastically toward the inside of the material. Therefore, fretting fatigue crack growth behavior differs significantly from fatigue crack growth behavior shown in Fig. 6.7. In fretting fatigue, the growth rate of a crack near the contact surface decreases drastically with increasing crack length, as shown in Fig. 6.9. Then, after showing a minimum value, it is well accorded with the plain fatigue crack growth rate. As show in Fig. 6.6, the fretting fatigue strength is often 1/2 or less of the plain fatigue strength and it will not become higher even though the tensile strength of the material is increased (Waterhouse, 1984).

Fretting fatigue life is shorter than plain fatigue life. In fretting fatigue, a crack easily nucleates due to friction stress even at a small stress amplitude at which plain fatigue failure may not occur, and the crack grows, leading to material failure. In orthopedic implants, fretting occurs where two materials come into contact with each other such as in bone plates or screws.

6.5 Effect of corrosion on fatigue and fretting fatigue

The fatigue strength of metallic materials in a corrosive environment varies depending on the effect of the corrosion on the nucleation and propagation of a fatigue crack. The effect of corrosion on crack nucleation is limited to the vicinity of the material surface. If crack nucleation is stimulated by the corrosion, in general, the crack growth rate is also increased by the corrosion.

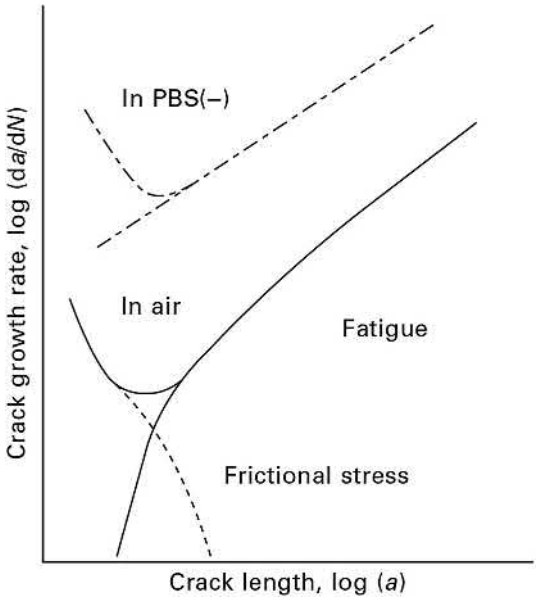


Fig. 6.9 Schematic diagram of relationship between crack growth rate and crack length in fretting fatigue test.

Corrosion of metallic materials is largely classified into uniform corrosion and local corrosion from surface appearance. Fatigue strength of metallic materials is degraded by local corrosion. However, the surface of metallic biomaterials is covered with dense oxide layers (passive films), which play a role as a corrosion prevention film. Therefore, the plain fatigue strength is not so different between that in air and that in a simulated body fluid.

In fretting fatigue, the surface oxide layers are damaged by fretting. As a result, the newly exposed surface is largely affected by corrosion and the fretting fatigue strength is significantly lowered. However, when wear caused by fretting is heavy, cracks induced by fretting corrosion are grounded. Therefore, the effect of fretting corrosion on crack nucleation may be relatively small in some cases.

6.6 Corrosion fatigue and fretting corrosion fatigue tests in a simulated body environment

A schematic diagram of the fretting fatigue test in a simulated body fluid is shown in Fig. 6.10 (Yamamoto et al., 1995). In fretting fatigue, the pads that cause fretting are attached to the parallel part of a specimen. Therefore, it is necessary to provide the fretting fatigue specimen with a parallel part for attaching the fretting pads, although various types of specimens are used in the fatigue test, such as a round bar smooth specimen, an hourglass specimen, a notched specimen, or a plate specimen. If a cyclic

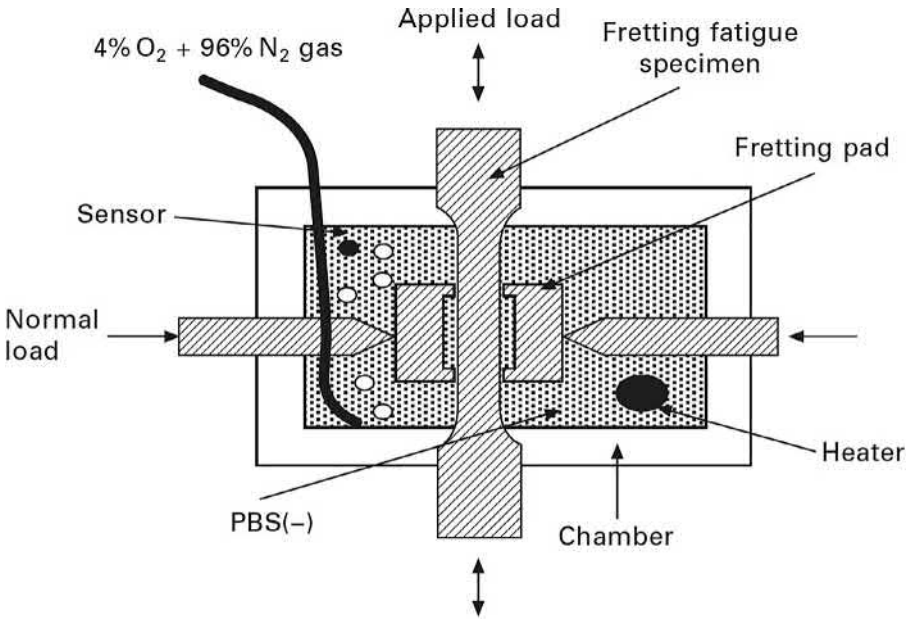


Fig. 6.10 Schematic diagram of fretting fatigue test in PBS(−).

load is applied to the specimen with the bridge-shaped pad pressed on either side of the parallel part of the specimen by a given force, relative slip is caused on the contact surface between the specimen and the pad by the expansion and contraction of the specimen, which causes fretting. The frictional force between the pad and the specimen can be measured based on the output from a strain gage affixed inside the center of the pad. Here, it is necessary to obtain a calibration curve of the load applied to the pad and the strain in advance. If the frictional force amplitude is f, the pressing force is p and the coefficient of friction is μ, μ can be defined by the following equation:

$$\mu = f/p \tag{6.2}$$

The relative slip distance between the specimen and the pad, S_a, is measured experimentally. In addition, as the pad can be considered a rigid body, it can be expressed as follows:

$$S_a = \sigma_a \cdot L/(2E) \tag{6.3}$$

where σ_a is the stress amplitude, E the Young's modulus, and L is the span of the pad.

The fretting fatigue life depends on the contact pressure of the pad.

From a mechanical viewpoint, cyclic shear stress on the specimen surface is a major factor that nucleates fretting fatigue cracks. Cyclic shear stress arises from the frictional force induced by the oscillatory motion of the pad. The maximum cyclic

stress amplitude, σ_1, at the edge of the fretted area on the specimen surface is calculated as follows:

$$\sigma_1 = \sigma_a + 2f_a \tag{6.4}$$

where σ_a is the plain fatigue stress amplitude and f_a is the friction stress amplitude. The region affected by fretting is limited to the shallow surface layers. Thus, fretting fatigue strength is almost equal to the fatigue strength of a specimen with short cracks (Nishioka and Hirakawa, 1969).

Generally, as the contact pressure of the pad increases, the frictional force increases and the fretting fatigue life decreases. In the low contact pressure region, however, the fretting fatigue life may show the minimum value in some cases (Maruyama et al., 1990). Fig. 6.11 shows the relationship between the contact pressure and the fretting fatigue life for a Ti-6Al-4V alloy when the applied stress amplitude is constant. This is because the contacting behavior of the area between the pad and the specimen differs depending on the contact pressure. Generally, if the contact pressure is high, the whole contact area will be the stick region. In this case, the highest stress concentration is obtained at the edge of the contact area, where a crack nucleates. If the contact pressure is low, however, the contact area is divided into a stick region to receive the contact pressure and two slip regions where wear is caused on both sides of the stick region, as shown in Fig. 6.12 (Nakazawa et al., 1992). In fretting fatigue, the highest stress concentration is obtained at the boundary between the stick region and the slip region, where a crack nucleates. The behavior of the contact area changes with an increase in the number of stress cycles. As the number of cycles increases, the area of the stick region becomes smaller than the initial contact area, and thus the net contact pressure rises, although the pressing force is constant. Then, the friction stress

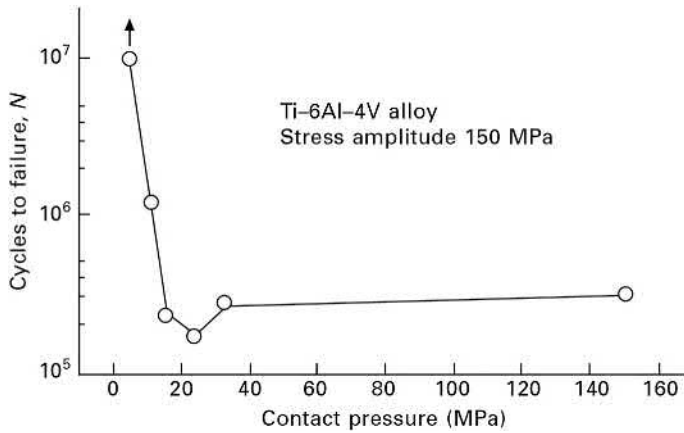


Fig. 6.11 Effect of contact pressure on fretting fatigue life of Ti-6Al-4V alloy in air. Maruyama, N., Sumita, M., Nakazawa, K., 1990. Fretting fatigue strength analysis of Ti-6Al-4V in air. Tetsu-to-Hagane 76, 262–269, in courtesy of The Iron and Steel Institute of Japan.

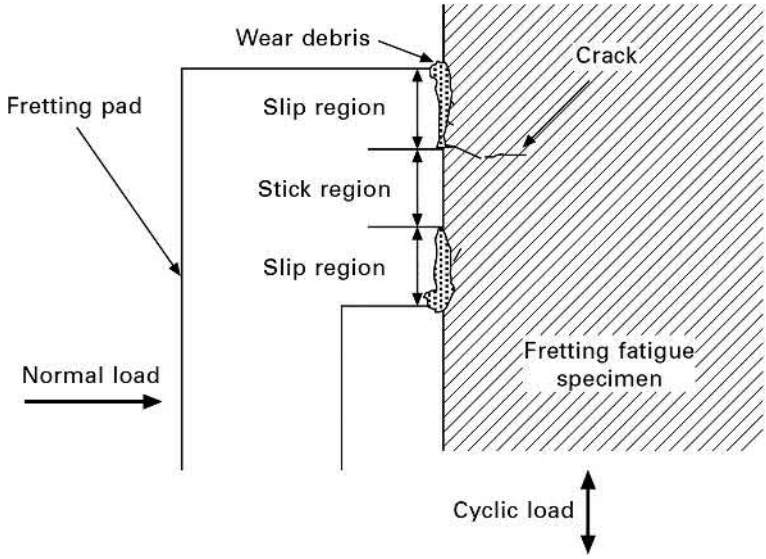


Fig. 6.12 Schematic drawing of fretting damage on contact area.
Maruyama, N., Kobayashi, T., Sumita, M., 1995. Fretting fatigue strength of a Ti-6AI-4V alloy in a pseudo-body-fluid and quantitative analysis of the substances in the fluids. J. Jpn. Soc. Biomater. 13, 14–20, in courtesy of Japanese Society for Biomaterials.

increases with the contact pressure and the fatigue life decreases. In the orthopedic field, this contact pressure is, empirically, 20–50 MPa.

The following are important points to keep in mind concerning fatigue and fretting fatigue tests in the living body environment:

- As fatigue is a phenomenon that depends on time, it is necessary to pay close attention to the frequency of cyclic stress. A frequency of approximately 1 Hz, which corresponds to man's walking speed, must be used for fatigue and fretting fatigue tests. Fig. 6.13 shows the relationship between the number of cycles to failure and the frequency of the cyclic stress for Ti-6Al-4V alloy and CP Ti, which are typical metallic biomaterials (Maruyama et al., 2000). Fatigue properties of Ti alloys depend on the frequency in air and the number of cycles to failure is lowered when the frequency is reduced.
- In many cases, PBS(−), 0.9% NaCl aqueous solution, Hank's balanced salt solution, Ringer's solution, and cell culture medium are used as a simulated body fluid. These solutions do not contain cell-producing active O such as macrophage. Moreover, O partial pressure in the living body is 1/4–1/5 of that in air. Therefore, repairing oxide layers damaged by fretting takes more time in a simulated body fluid than in air. The pH level, affecting corrosion of metallic materials, differs depending on the region of the human body and the presence of inflammation. Therefore, it is important to be aware of the fact that in the living body there are factors that are different from those in a simulated body fluid.
- In a fretting fatigue test in a simulated body fluid, it is necessary to use a pad and a pad-pressing bar made of the same material as that of the specimen, as in the case of an actual device, to prevent corrosion (galvanic corrosion) caused by the contact of different metallic materials.

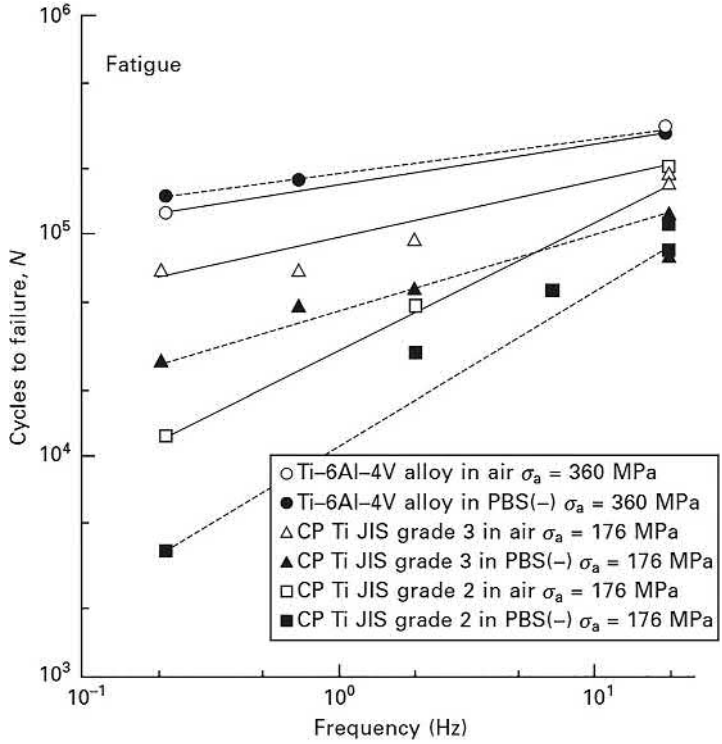


Fig. 6.13 Effect of frequency on cycles to failure in fatigue tests.
Maruyama, N., Nakazawa, K., Sumita, M., Sato, M., 2000. Effect of stress frequency on fatigue and fretting life for commercially pure Ti and Ti-6AI-4V alloy in pseudo-body fluid. J. Jpn. Soc. Biomater. 18, 17–23, in courtesy of Japanese Society for Biomaterials.

6.7 Results of fatigue and fretting fatigue tests of metallic biomaterials

The following describes the S-N curve characteristics of fatigue and fretting fatigue in air and in a simulated body fluid for typical metallic biomaterials such as 316L stainless steel, Ni-free high-N stainless steel, Ti-6Al-4V alloy, pure Ti (CP Ti), and Co-Cr alloy. Here, the test conditions are as follows: The stress ratio (ratio of the minimum stress to the maximum stress in cyclic loading) is 0.1, the cyclic stress waveform is sinusoidal, and the frequency of the cyclic stress is 20 Hz in air and 2 Hz in a simulated body fluid. The pad span is 20 mm, and the contact pressure between the specimen and the pad is 30 MPa. PBS(−) is used as a simulated body fluid. The amount of the fluid is 160 mL, dissolved O concentration is 4%, temperature is 310 K, and pH is 7.5. The components of the PBS(−) are 8000 mg/L NaCl, 200 mg/L $KH_{2P}O_4$, 1150 mg/L Na_2HPO_4, and 200 mg/L KH_2PO_4.

6.7.1 316L stainless steel

The S-N curve for a JIS 316L stainless steel (iron (Fe)-0.019% carbon (C)-0.48% silicon (Si)-1.18% manganese (Mn)-0.038% phosphorus (P)-0.013% sulfur (S)-12.10% Ni-16.72% Cr-2.05% Mo, 0.2% proof stress: 328 MPa, UTS: 602 MPa) is shown in Fig. 6.14 (Nakazawa et al., 1999). The fatigue strength at 10^7 cycles is approximately 205 MPa in air and 200 MPa in PBS(−). In the high-stress amplitude region, the fretting fatigue strength is almost the same in air and in PBS(−). In the low-stress amplitude region, however, it is lower in PBS(−) than in air. The fretting fatigue strength at 10^7 cycles is approximately 140 MPa in air, and 110 MPa in PBS(−). Thus, it is lowered to about 2/3–1/2 of the plain fatigue strength.

The S-N curve for a cold-rolled JIS 316L stainless steel (Fe-0.024% C-0.50% Si-1.40% Mn-0.033% P-0.024% S-12.23% Ni-17.14% Cr-2.04% Mo, 0.2% proof stress: 791 MPa, UTS: 883 MPa) is shown in Fig. 6.15 (Maruyama et al., 2013). The fatigue strength at 10^7 cycles is approximately 350 MPa in air and 320 MPa in PBS(−). The fretting fatigue strength at 10^7 cycles is approximately 180 MPa both in air and in PBS(−). Thus, it is lowered to about half of the plane fatigue strength.

6.7.2 Ni-free high-N stainless steel

The S-N curve for a Ni-free high-N stainless steel (Fe-0.022% C-0.15% Si-0.10% Mn-0.040% Ni-23.78% Cr-0.96% Mo, 0.005% O-1.05% N, 0.2% proof stress: 805 MPa, UTS: 1206 MPa) is shown in Fig. 6.16 (Maruyama et al., 2013). The fatigue strength at 10^7 cycles is approximately 320 MPa both in air and in PBS(−). The fretting fatigue strength is approximately 280 MPa in air and 240 MPa in PBS(−). Thus, it is lowered to about 3/4 of the plane fatigue strength.

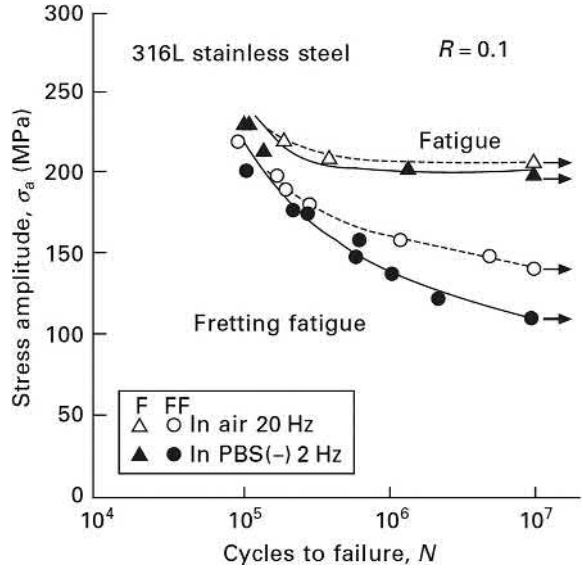


Fig. 6.14 S-N curves of 316L stainless steel in air and in PBS (−) (*F*, fatigue; *FF*, fretting fatigue).
Nakazawa, K., Sumita, M., Maruyama, N., 1999. Fatigue and fretting fatigue of austenitic and ferritic stainless steels in pseudo-body fluid. J. Jpn. Inst. Metals 63, 1600–1608, in courtesy of The Japan Institute of Metals.

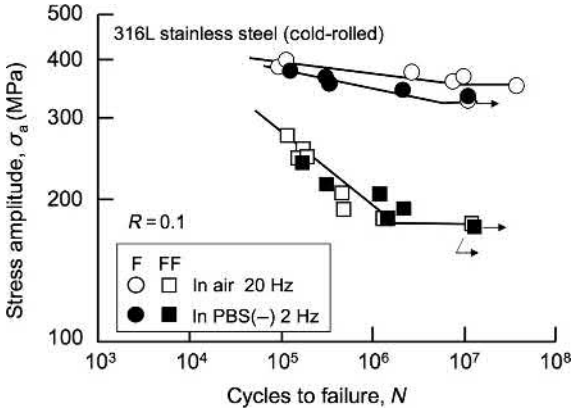


Fig. 6.15 S-N curves of cold-rolled 316L stainless steel in air and in PBS(−) (*F*, fatigue; *FF*, fretting fatigue).

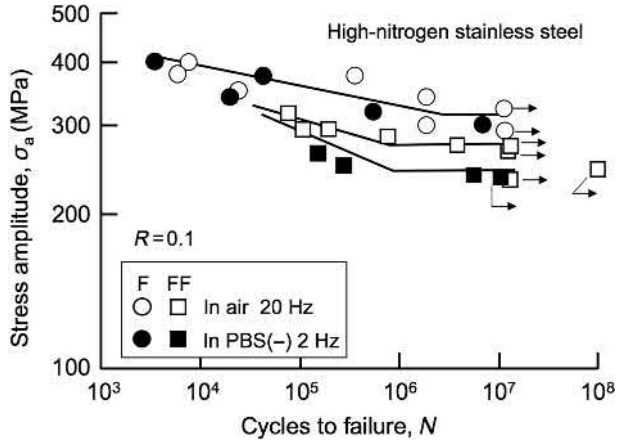


Fig. 6.16 S-N curves of Ni-free high-N stainless steel in air and in PBS(−) (*F*, fatigue; *FF*, fretting fatigue).

6.7.3 Ti-6Al-4V alloy

The S-N curve for a Ti-6Al-4V alloy solution treated and aged (Ti-6.15% Al-4.19% C-0.200% Fe-0.143% O-0.006% N-0.005% C, 0.2% proof stress: 974 MPa, UTS:1010 MPa) is shown in Fig. 6.17 (Maruyama et al., 1995). The fatigue strength at 10^7 cycles is approximately 300 MPa both in air and in PBS(−). The fretting fatigue strength is higher in PBS(−) than in air in the intermediate stress amplitude region. In the high- and low-stress amplitude regions, however, it tends to be lower in PBS(−) than in air. The fretting fatigue strength at 10^7 cycles is approximately 120 MPa in air, and 100 MPa in PBS(−). Thus, it is lowered to about 1/3 of the plain fatigue strength.

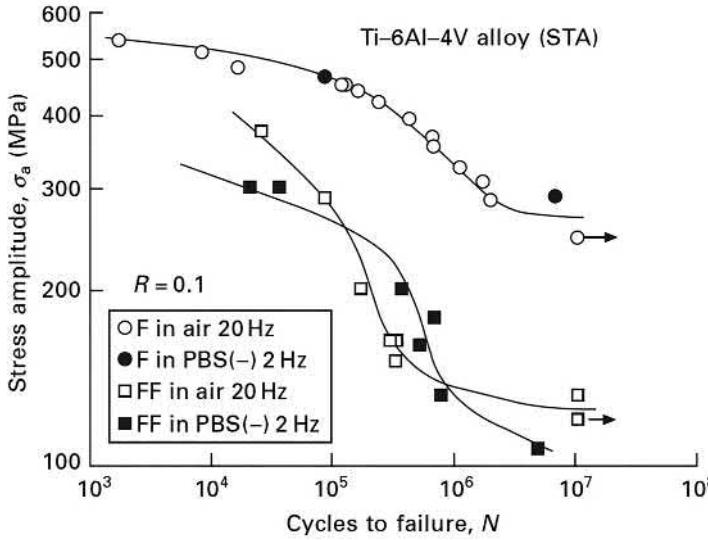


Fig. 6.17 S-N curves of Ti-6Al-4V alloy in air and in PBS(−) (*F*, fatigue; *FF*, fretting fatigue). Yamamoto, A., Kobayashi, T., Maruyama, N., Nakazawa, K., Sumita, M., 1995. Fretting fatigue properties of Ti-GAL-4V alloy in pseudo-body fluid and evaluation of biocompatibility by cell culture method. J. Jpn. Inst. Metals 59, 463–470, in courtesy of The Japan Institute of Metals.

6.7.4 CP Ti

The S-N curve for CP Ti (JIS grade 3; Ti-0.123% Fe-0.144% O-0.004% N, 0.2% proof stress: 416 MPa, UTS: 538 MPa) is shown in Fig. 6.18 (Maruyama et al., 1995). The fatigue strength for 10^7 cycles is approximately 150 MPa in air and 140 MPa in PBS (−). The fretting fatigue strength for 10^7 cycles is approximately 100 MPa in air and 85 MPa in PBS(−). Therefore, it is lowered to about 1/3–1/2 of the plain fatigue strength.

6.7.5 Co-Cr alloy

The S-N curve for a forged Ni-free Co-Cr alloy (64.81% Co-28.99% Cr-5.93% Mo-0.02% Ni-0.03% Fe, 0.2% proof stress: 432 MPa, UTS: 956 MPa) is shown in Fig. 6.19 (Maruyama et al., 1999). The asterisk "*" in the drawing means that in the fretting fatigue test, failure occurred in the parallel part of the specimen, and not in the fretting part. For the fatigue strength in air, no fatigue limit is obtained at 10^7 cycles, and at around 10^7 cycles it drops significantly. The fatigue strength at 10^7 cycles in air is approximately 240 MPa and is lower by 20–30 MPa in PBS (−) than in air in the low-cycle region. The fatigue strength at 10^7 cycles in PBS (−) is the same as that in air. The fretting fatigue strength in air and in PBS(−) is lower

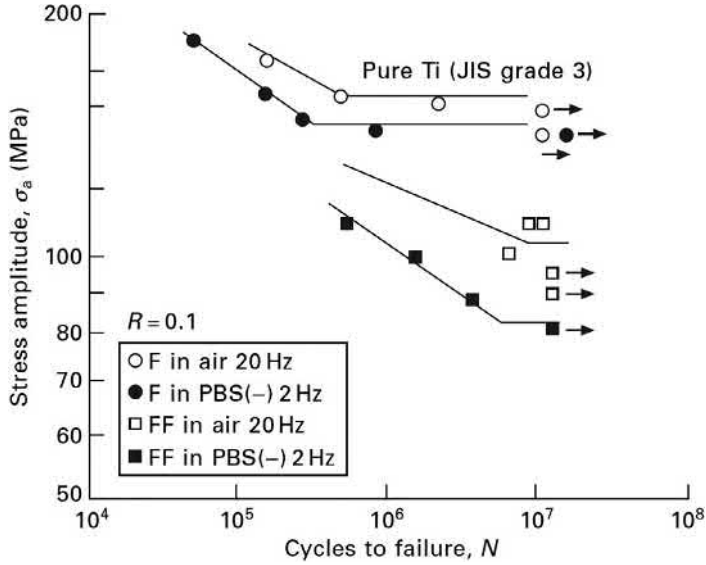


Fig. 6.18 S-N curves of CP Ti (JIS grade 3) in air and in PBS(−) (*F*, fatigue; *FF*, fretting fatigue).
Maruyama, N., Nakazawa, K., Sumita, M., Sato, M., 2000. Effect of stress frequency on fatigue and fretting life for commercially pure Ti and Ti-6AI-4V alloy in pseudo-body fluid. J. Jpn. Soc. Biomater. 18, 17–23, in courtesy of Japanese Society for Biomaterials.

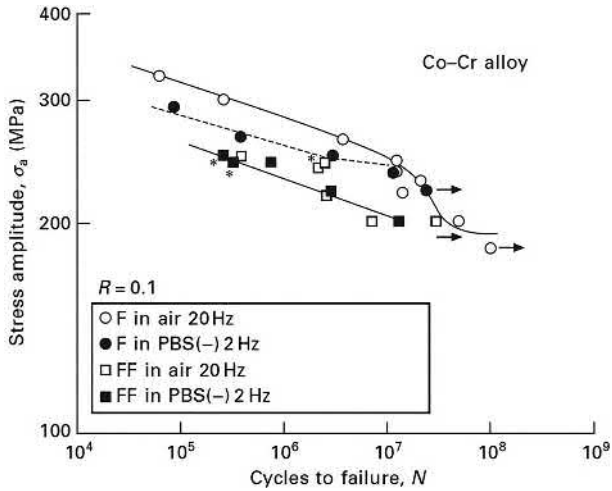


Fig. 6.19 S-N curves of Co-Cr alloy in air and in PBS(−) (*F*, fatigue; *FF*, fretting fatigue).
Maruyama, N., Kobayashi, T., Nakazawa, K., Sumita, M., Sato, M., 1999. Fatigue and fretting fatigue behaviour of Ni free Co-Cr alloy in a pseudo-body fluid. J. Jpn. Soc. Biomater. 17, 172–179, in courtesy of Japanese Society for Biomaterials.

by about 30 MPa, respectively, than the fatigue strength. The fretting fatigue strength in air and in PBS(−) exhibits no difference, remaining at approximately 210 MPa.

Fig. 6.20 shows the relationship between the tensile strength and the fatigue strength/fretting fatigue strength of metallic biomaterials at 10^7 cycles in air at room temperature and in a simulated body fluid (Maruyama et al., 1995, 1999, 2000; Nakazawa et al., 1999). For all of the biomaterials tested, the fatigue strength at 10^7 cycles is similar in air and in a simulated body fluid. The fatigue strength is closely correlated to the tensile strength: as the tensile strength increases, the fatigue strength also increases. However, a correlation is not observed between the fretting fatigue strength at 10^7 cycles and the fatigue strength or the tensile strength.

For example, if the plain fatigue strength and the fretting fatigue strength are compared for a Ti-6Al-4V alloy and a Co-Cr alloy with the same tensile strength, approximately 1000 MPa, the fretting fatigue strength of the Ti-6Al-4V alloy at 10^7 cycles is lower by 1/2 than the fatigue strength in both air and PBS(−). However, the fretting fatigue strength of the Co-Cr alloy at 10^7 cycles is the same as the fatigue strength in both air and PBS(−). This is because the contacting behavior of the area between the pad and the specimen differs from that of the Ti-6Al-4V alloy. Generally, fretting fatigue strength is affected by wear properties of materials since severe wear removes nucleated microscopic fatigue crack. On the contact area of the Ti-6Al-4V alloy in both air and in PBS(−), wear is relatively small and a crack caused by fretting fatigue grows to failure without being grounded. On the contact area of the Co-Cr alloy, particularly in PBS(−), however, significant wear is produced, as shown in Fig. 6.21 (Maruyama et al., 1999). Therefore, a crack caused by fretting fatigue is grounded and it is difficult for the crack to propagate. As a result, the fretting fatigue strength is similar to the plane fatigue strength.

Therefore, for orthopedic implants with fretting parts, failure can be prevented by a design that considers the fretting fatigue strength of metallic materials to be used in a

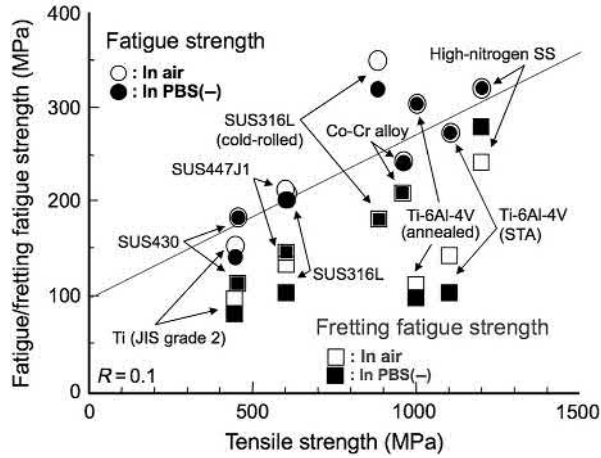


Fig. 6.20 Relationship between tensile strength and fatigue strength/fretting fatigue strength at 10^7 in air and in PBS(−) for various alloys.

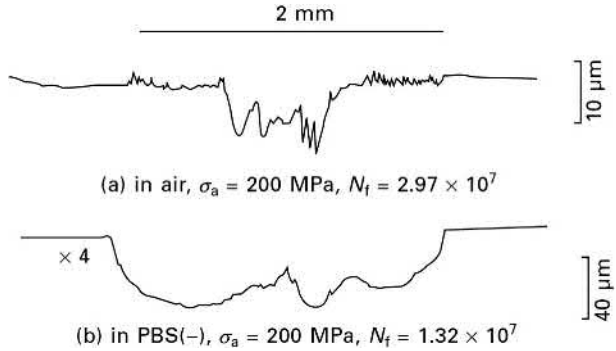


Fig. 6.21 Cross-sectional profiles of fretted surface for Co-Cr alloy.
Maruyama, N., Kobayashi, T., Nakazawa, K., Sumita, M., Sato, M., 1999. Fatigue and fretting fatigue behaviour of Ni free Co-Cr alloy in a pseudo-body fluid. J. Jpn. Soc. Biomater. 17, 172–179, in courtesy of Japanese Society for Biomaterials.

simulated body fluid, not by a design based on the required durable years or the fatigue strength. Another method for improving the fretting fatigue characteristics is to provide compressive residual stress by shot-peening treatment.

6.8 Effect of pH level on fatigue strength in simulated body fluid

The pH level which affects corrosion of metallic materials is generally 7–7.35 in the living body. However, as mentioned in Section 6.2, the pH level drops to 5.2 due to inflammation or foreign body reaction when an implant is inserted into the body (Hench and Ethridge, 1975). The following describes the effect of pH level on fatigue strength of 316L stainless steel (Maruyama et al., 2011).

Generally, dilute HCl solution is used to control the pH level of the solution. However, it is better to control the pH level of the simulated body fluid without changing the chloride ion content which attacks the oxide film of steels. Therefore, fatigue tests are carried out in a 0.9% (154 mol/m^3) NaCl-containing citric phosphate buffer solution (CPBS) with three pH levels, that is, 5.0, 6.0, and 7.5. The three pH levels of CPBS are obtained by changing the volume ratio of 100 mol/m^3 citric acid to 200 mol/m^3 Na_2HPO_4 from 0.08/0.92 to 0.48/0.52.

Fig. 6.22 shows effect of pH level on the S-N relationship in CPBS for SUS316L stainless steel. Here, the dissolved O content is controlled with 4% O_2/N_2 gas bubbling. The fatigue strength at 10^7 cycles decreases from 205 to 160 MPa when the environment is changed from air to CPBS of pH 7.5. The fatigue strength in CPBS tends to decrease with decrease in pH from 7.5 to 5.0 even in the high-cycle region, where the fatigue strength in air reaches the fatigue limit. The pH level clearly affects the fatigue strength of biomaterials.

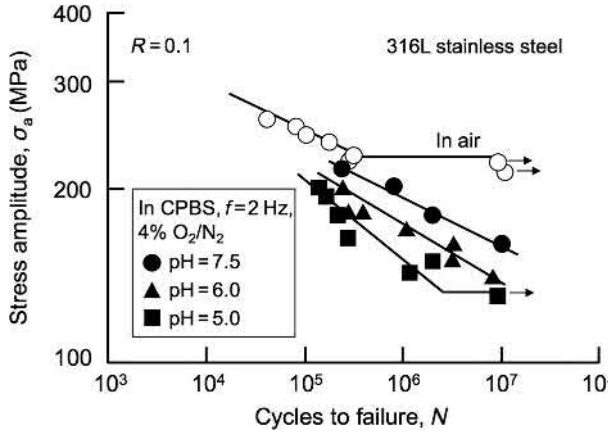


Fig. 6.22 Effect of pH level on S-N curve of SUS316L stainless steel in CPBS (Maruyama et al., 2011).

6.9 New fatigue test for metallic biomaterials

The living body contains a large amount of amino acids and proteins. The materials implanted in the body are forced into contact with various cells and textures such as macrophage immune cells. Conventional corrosion fatigue tests for biomaterials have used a simulated body fluid such as normal saline, PBS(−), etc. Today, however, it is known that macrophage produces the active O that accelerates corrosion of metallic materials through foreign body reaction immediately after insertion of the device, and the environment is more severe than in the conventional simulated body fluids (ASTM Standard F1801-97, 1997). Actually, Hayashi et al. reported that for a cold-worked SUS316 stainless steel, the fatigue strength (maximum stress) at 5×10^6 cycles in air, in normal saline, and in horse blood serum was approximately 850 MPa and the fatigue strength in the rabbit shinbone at 5×10^6 cycles was approximately 700 MPa, which is about 150 MPa lower than the former values (Hayasi et al., 1985).

Maruyama and coworkers developed a system for fatigue tests in a living cell environment similar to that of the living body, instead of the conventional simulated body fluids (Maruyama et al., 2006). As shown in Fig. 6.23, a specimen with cells attached on the surface is inserted into a cell culture chamber kept at 27°C and fatigue properties are measured over a long period by conducting cell culture through the circulation of a culture fluid bubbled by an O and carbon dioxide gas mixture. The S-N curve of a SUS316L stainless steel in a macrophage culture environment obtained by this system is shown in Fig. 6.24. As shown in Figs. 6.14 and 6.24, the fatigue strength of the SUS316L stainless steel does not change in air, PBS(−), or in an osteoblast cell L929 culture environment. However, the fatigue strength in a macrophage culture environment is lowered by approximately 30 MPa in the high-cycle region. As

described in Section 6.6, this shows that different factors affect the metallic biomaterial in the living body environment and in the simulated body fluids.

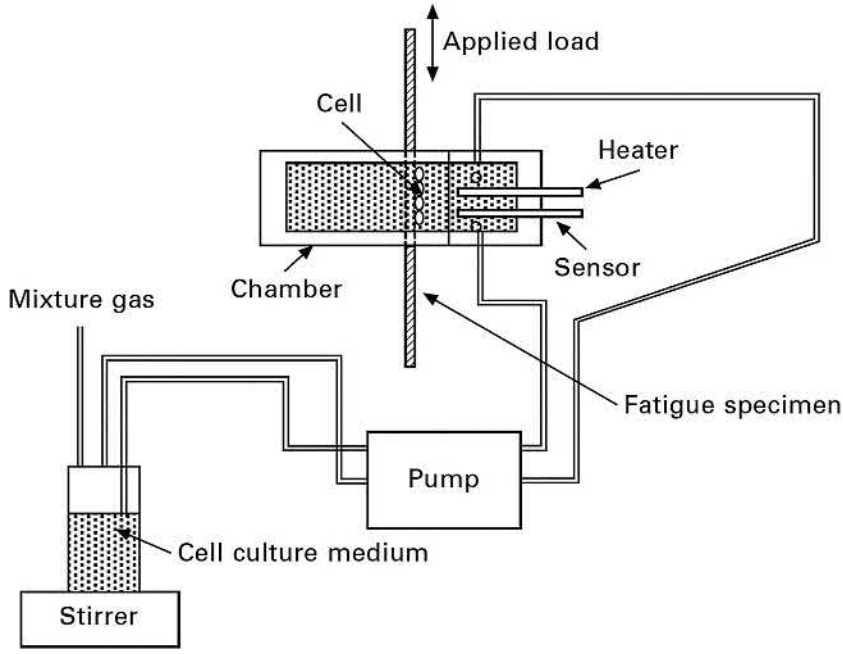


Fig. 6.23 Schematic diagram of cell culture system for fatigue test.

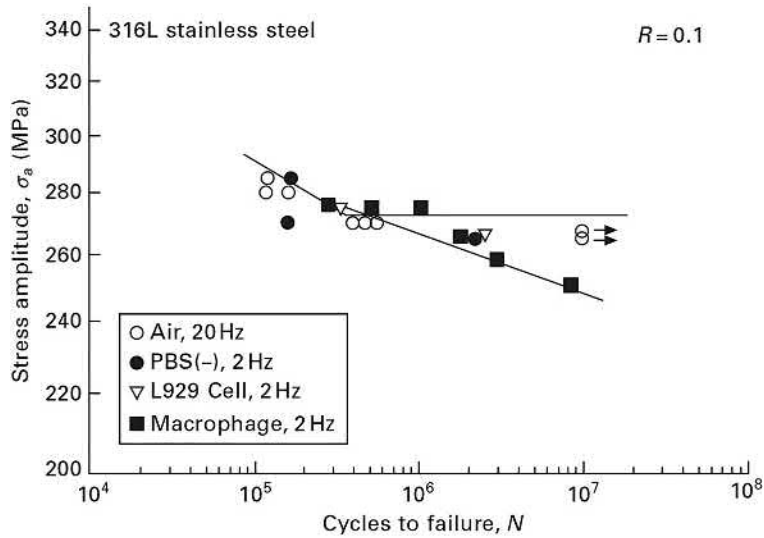


Fig. 6.24 S-N curves of 316L stainless steel in various types of environments.

Acknowledgment

The author is greatly indebted to The Iron and Steel Institute of Japan, Japanese Society for Biomaterials and The Japan Institute of Metals for providing the figures.

References

ASTM Standard F1801-97, 1997. Standard Practice for Corrosion Fatigue Testing of Metallic Implant Materials.

ASTM Standard F897-84, 2002. Standard Test Method for Measuring Fretting Corrosion of Osteosynthesis Plates and Screws.

Hayasi, H., Sasada, T., Morita, M., Tsukamoto, Y., Nishi, H., 1985. Tensile fatigue test of metallic materials in living body. Biomaterials 3, 143–149.

Hench, L.L., Ethridge, E.C., 1975. Biomaterials—the interfacial problem. Adv. Biomed. Eng. 5, 35–150.

Klesnil, M., Lukas, P., 1984. Fatigue of Metallic Materials. (Japanese Translation by Araki, T. and Horibe, S.). Yokendo.

Maruyama, N., Sumita, M., Nakazawa, K., 1990. Fretting fatigue strength analysis of Ti-6Al-4V in air. Tetsu-to-Hagane 76, 262–269.

Maruyama, N., Kobayashi, T., Sumita, M., 1995. Fretting fatigue strength of a Ti-6AI-4V alloy in a pseudo-body-fluid and quantitative analysis of the substances in the fluids. J. Jpn. Soc. Biomater. 13, 14–20.

Maruyama, N., Kobayashi, T., Nakazawa, K., Sumita, M., Sato, M., 1999. Fatigue and fretting fatigue behaviour of Ni free Co-Cr alloy in a pseudo-body fluid. J. Jpn. Soc. Biomater. 17, 172–179.

Maruyama, N., Nakazawa, K., Sumita, M., Sato, M., 2000. Effect of stress frequency on fatigue and fretting life for commercially pure Ti and Ti-6AI-4V alloy in pseudo-body fluid. J. Jpn. Soc. Biomater. 18, 17–23.

Maruyama, N., Yamamoto, A., Kohyama, Y., Hiromoto, S., Nakamura, M., 2006. Fatigue properties of SUS316L stainless steel in a macrophage culture environment. In: Japanese Society for Biomaterials, the 28th Conference, Proceedings.

Maruyama, N., Mori, D., Hiromoto, S., Kanazawa, K., Nakamura, M., 2011. Fatigue strength of 316L-type stainless steel in simulated body fluids. Corros. Sci. 53, 2222–2227.

Maruyama, N., Hiromoto, S., Akiyama, E., Nakamura, M., 2013. Fretting fatigue behavior of Ni-free high-N stainless steel in simulated body fluid. Sci. Technol. Adv. Mater. 14, 025002.

Mu, Y., Kobayashi, T., Sumita, M., Yamamoto, A., Hanawa, T., 2000. Metal ion release from Ti with active O species generated by rat macrophages in vitro. J. Biomed. Mater. Res. 49, 238–243.

Nakazawa, K., Sumita, M., Maruyama, N., 1992. Effect of contact pressure on fretting fatigue of high strength steel and Ti alloy. In: Standardization of Fretting Fatigue Test Methods and Equipment, ASTM STP 1159, pp. 115–125.

Nakazawa, K., Sumita, M., Maruyama, N., 1999. Fatigue and fretting fatigue of austenitic and ferritic stainless steels in pseudo-body fluid. J. Jpn. Inst. Metals 63, 1600–1608.

Nishioka, I., Hirakawa, K., 1969. Fundamental investigation of fretting fatigue, Part 5: The effect relative slip amplitude. Bull. JSME 52, 692–697.

Sasada, T., Tsukamoto, Y., Mabuchi, K., 1988. Biotribology—Friction and Lubrication of Joints. Sangyo Tosho, pp. 123–137.

Waterhouse, R.B., 1984. Fretting Corrosion (Japanese Translation by J. Sato). Yokendo, p. 191.

Yamamoto, A., Kobayashi, T., Maruyama, N., Nakazawa, K., Sumita, M., 1995. Fretting fatigue properties of Ti-GAL-4V alloy in pseudo-body fluid and evaluation of biocompatibility by cell culture method. J. Jpn. Inst. Metals 59, 463–470.

Tribology and tribocorrosion testing and analysis of metallic biomaterials

7

Y. Yan
University of Leeds, Leeds, United Kingdom

7.1 Introduction to tribology-related testing

Tribology is defined as the science and technology of interacting surfaces in relative motion. It includes the study and application of the principles of friction, lubrication, and wear. The phenomenon of tribology has been realized for thousands of years. In 1966, the well-known "Jost Report" was released to the British government. Since then, the word "tribology" has been widely used and research on this area has been greatly explored. Tribology has become an interdisciplinary area. It is linked with materials, chemistry, physics, and even biology.

For materials used in biomedical devices, if there are relative motions involved with interfaces, tribology contact is present. From orthopedic implants to dental implants to ophthalmic devices, wear and friction of materials are of major importance, together with biocompatibility. The ultimate goals for such devices are to last longer and be safe to use. However, in vivo tests are normally too complicated. Various tribological testing methods and apparatus have been invented to study metallic or nonmetallic materials in vitro. In this chapter, different testing methods are discussed. Those used to evaluate materials' tribological properties are considered in Section 7.2. For metallic materials, corrosion is also of major concern, especially for those materials under tribological contact. Section 7.3 presents new research on interactions of tribology and corrosion, namely tribocorrosion. After testing, materials always undergo analysis to determine the damage and resulting mechanisms. A brief introduction to the most commonly used surface analysis techniques is included in Section 7.4. Comments on future trends in tribology and tribocorrosion testing are presented in the last part of this chapter.

7.2 General testing methods for tribological properties

In order to increase the service life, to provide reliable performance, and to reduce cost and maintenance, wear tests are used to provide data and engineering information for specific applications, for instance, biomedical devices. Wear tests can help to improve material selection and the design of devices. The mechanisms of tribology are complex. The nature of the applications is different. There is no single or universal testing

Metals for Biomedical Devices. https://doi.org/10.1016/B978-0-08-102666-3.00007-9
© 2019 Elsevier Ltd. All rights reserved.

method for tribology. In a tribological system, wear, friction, and lubrication form a triangle of important factors. Hence, the tribology test selection and use are key aspects in the overall consideration of wear testing. A recent survey by the National Physical Laboratory (Gee and Owen-Jones, 1998) in the United Kingdom identified over 400 wear testing standards in use around the world. A review by the American Society of Lubrication Engineers in 1973 identified 300 tests that were in use in various test laboratories (ASM, 1992). However, many of these tests are slight variations on others, and the true number of tests available is probably <100. Therefore, the question is what method or methods should be chosen for a particular problem.

7.2.1 Types of wear

Failures can generally be reduced but this requires an understanding and identification of wear mechanisms involved. Researchers can find useful information and data from handbooks and guidebooks. This is an area where experience is particularly valuable. However, previous experience may not be adequate to tackle the specific problem encountered. It will then be necessary to obtain a basic knowledge of the wear performance of different materials when subjected to different types of wear. This can be achieved by carrying out comparative and controlled wear tests in laboratories. The various types of wear tests that are available therefore need to be reviewed, and matched to the various guidance on the selection of tests where they are likely to give valid information on the relative wear performance of various materials in practical applications.

Wear is progressive damage to a surface caused by relative motion with respect to another substance (ASM, 1992). One key point is that wear is damage and it is not limited to loss of material from a surface. Sometimes it is a change in the geometry or dimension or cracks in a surface. The main types of wear are shown in Table 7.1 and detail is described in the following paragraphs.

Wear mechanisms can be identified by the appearance of the worn surface and the nature of the application (Williams, 1994). However, in a tribology situation, it is normally not a simple wear process. More than one mechanism can be present in a particular application.

7.2.2 Selection of wear testing

The type of wear test is chosen in the laboratory to simulate the real conditions for tribological problems. The focus is to select a design that can achieve not only a good material selection but also general engineering information. Fig. 7.1 summarizes the configuration of different test setups.

Fig. 7.1A is a pin-on-plate configuration. It can provide either a plane-on-plane contact or a point-on-plane contact. Normally, a point-on-plane contact is chosen to have an accurate alignment of the pin, which has a spherical end. A ball-on-plate configuration is shown in Fig. 7.1B. It has a point-on-plane contact. Fig. 7.1C shows a cylinder-on-plane test. The contact is line-on-plane. A pin on a rotating disk configuration is shown in Fig. 7.1D, where the wear surface is a ring shape. The difference is

Table 7.1 Types of wear mechanisms

Type of wear	Cause and behavior mechanism
Abrasive wear	Abrasive wear is caused by hard particles trapped between moving surfaces, which results in grooves, scratches, or indentations on a surface
Adhesive wear	When two surfaces come into contact, they adhere to one another at localized sites. As they move relatively, wear occurs by one surface pulling the material out of the other surfaces at these sites. Transferred materials can be seen on surfaces
Fretting	Fretting occurs when there are small oscillatory movements between two surfaces
Erosion	Erosion involves the removal of material from the surface by impact of a liquid or a stream of hard particles
Cavitation	Cavitation can be seen as a type of erosion. However, it arises from the intense local impact of the collapse of vapor bubbles onto the surface
Corrosive wear	When the tribological contacts are in a corrosive environment, both chemical/electrochemical and tribology are the controlling factors. The growth and removal of oxide layers/tribofilm controls the wear rate
Thermal wear	Material can be removed due to the result of local transient heating or recreated surface temperature
Fatigue	Fatigue can lead to the loss of material then failure when cracks in the surface join together. Cracks can occur due to high local contact stress

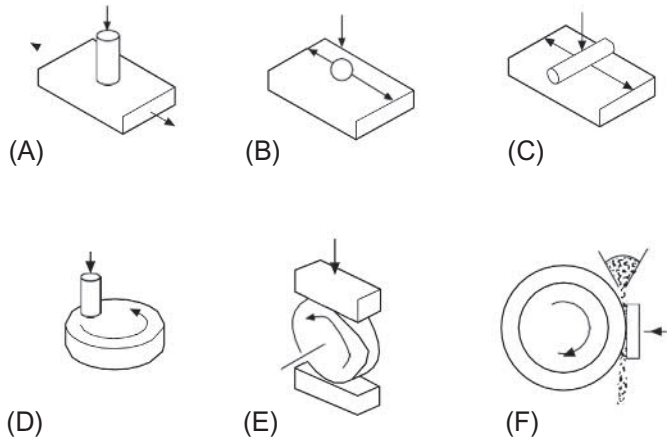


Fig. 7.1 Configuration of various test setups (A) pin-on-plate, (B) ball-on-plate, (C) cylinder on plate, (D) pin on rotating disk, (E) block on rotating wheel, and (F) abrasive with plate on rotating wheel.

Table 7.2 Parameters to be considered for wear tests

Parameter/ condition	Example
Materials	Metals (Ti and Ti alloys, Co alloys, stainless steel, etc.), nonmetallic (ceramics, bioglass, polymer, etc.)
Lubrication	Blood, serum, synovial fluid, saliva, physiological saline (0.9% NaCl), etc.
Geometry	Point-on-plane, plane-on-plane, ball-on-socket, etc.
Motion	Unidirectional reciprocation, multidirectional, fretting (nano-, micro-motion), rotation, etc.
Loading	Value of load (body weight, etc.), constant loading, cyclic loading, etc.
Environment	Corrosive, temperature (36–37°C), etc.

that it involves two directional movement. A rolling and sliding motion is achieved in Fig. 7.1E. The wheel disk rotates with a stationary plate or a reciprocating plate. Fig. 7.1F presents tests of abrasive wear caused by particles. The plate is held against a rotating wheel with a feed of loose abrasive to the interface.

Before the decision of which wear test is made, several conditions and parameters should be considered. A summary for biomedical wear testing is shown in Table 7.2.

Because of the simplicity of wear tests, they can provide very general reference data for an evaluation of materials and environmental conditions for an application. However, they are only a simulation of the real application. The critical point is to choose a similar configuration that is a reasonable representation of the practical situation. The most important objective in a test is to reproduce the dominant wear mechanism (Neale and Gee, 2000).

7.2.3 Friction

Friction is the force resisting the relative motion of two surfaces in contact or a surface in contact with a fluid. When contacting surfaces move relative to each other, the friction between the two surfaces converts kinetic energy into thermal energy or heat. A widely used parameter to characterize friction is the friction coefficient (or the coefficient of friction). It is a dimensionless scalar value (μ) used to describe the ratio of the frictional force between two surfaces (F_f) and the force applied on them (F_n). It is explained in Eq. 7.1:

$$F_f = \mu F_n \tag{7.1}$$

In a sliding and/or rolling wear situation, it is generally desirable to measure or monitor frictional behavior during the test. The correlation of frictional changes with wear behavior frequently provides useful information regarding mechanisms and modeling. There are two categories for friction: (a) static friction—when two objects are not moving relative to each other, and (b) kinetic friction (dynamic friction)—when

Table 7.3 Typical friction coefficients for various materials

Combination	Friction coefficient
Steel on steel (dry)	0.4–0.7
Steel on steel (water)	0.2–0.4
Steel on steel (oil)	0.1–0.3
Wood on steel (dry)	0.2–0.6
Rubber on steel (dry)	0.4–0.7
Rubber on steel (water)	0.3–0.9
Contact lenses (hydrated)	0.05–0.1
Synovial joint	0.001–0.05

two objects are moving relative to each other (Loomis, 1985). In this chapter, the friction referred to is dynamic friction. Table 7.3 shows typical friction coefficients under dry and lubricated conditions. Friction can relate to the comfort or otherwise of biomedical devices, such as contact lenses. Low friction is also desirable for orthopedic joint implants. The squeaking of hip prostheses may be associated with vibration caused by high frictional forces (Bayer, 2004; Hutchings, 1992). In tribological tests, friction force is always measured by transducers or load cells then divided by the normal applied load to obtain the friction coefficient.

7.2.4 Lubrication and lubricant

Lubrication regime is defined by the lambda ratio (l). The lambda ratio is the minimum film thickness (h_{min}) in relation to the composite surface roughness (R_{a1} and R_{a2}):

$$\lambda = \frac{h_{min}}{\sqrt{R_{a1}^2 + R_{a2}^2}} \tag{7.2}$$

Stribeck (Stachowiak and Batchelor, 2001) demonstrated that the coefficient of friction is directly proportional to the viscosity of the lubricant and the difference in speed of the contact surfaces; and inversely proportional to the pressure that is exerted on the contact surfaces. Fig. 7.2 shows the Stribeck curve, which is the friction coefficient against the bearing number: $\mu w/p$ (lubricant viscosity (h), speed (w), and contact pressure (p)). There are three regimes as defined from the Stribeck diagram: boundary lubrication, mixed lubrication, and hydrodynamic lubrication.

At lambda ratio values lower than 1, it is conventionally supposed that asperity interaction becomes more severe and that the shear properties of the films on the solid surfaces, whether formed by adsorption or reaction, become significant. This regime is called boundary lubrication. In the boundary lubrication regime, the physical properties of the bulk lubricant (such as density and viscosity) are not as important as the chemical properties of the lubricant and the properties of the surfaces in contact. In animal or human joints and some hip replacements, the lubrication regime is in

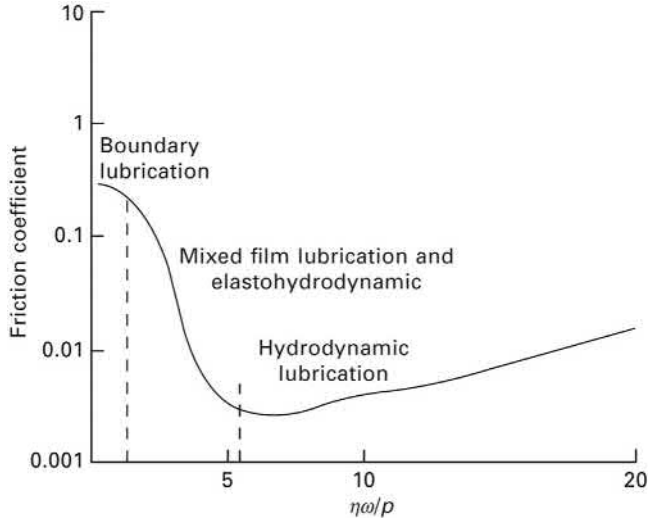


Fig. 7.2 Friction coefficient as a function of the bearing number.

boundary lubrication (Jin et al., 2000; Totten and Liang, 2004). However, for other hip replacements, the lubrication regime can be mixed lubrication (Jin et al., 1997). Therefore, the boundary and mixed lubrication regimes are of primary importance in joint tribology.

If the lambda ratio is very much greater than unity, so that the film is thick, then the traction or friction force will be a function of the bulk rheological properties of the lubricant under the appropriate operating conditions of load, temperature, shear rate, and so on. The influence of the surface roughness will be negligible. This regime is called full film lubrication or hydrodynamic lubrication. Full film lubrication is the most desirable form of lubrication. In this case the surfaces are not in contact so the resistance to their tangential motion, friction force, is dependent primarily on the viscosity of the lubricant (Stachowiak and Batchelor, 2001). Also, since in theory there is essentially no contact between surfaces, no wear should occur.

When the film thickness and the surface roughness are of comparable dimensions ($1 < l < 5$), then the traction will still be determined by the bulk properties of the lubricant but the local contact conditions of asperity interaction will need to be considered (Stachowiak and Batchelor, 2001). Since the lubrication is a mix of full film lubrication and some asperity contact, the regime is called the mixed lubrication regime. On further decreasing the speed and at very high specific loads, full film lubrication is difficult to maintain and, despite the presence of micro elastohydrodynamic-lubrication (EHL), there will be some mechanical interactions between opposing surface asperities. In this regime, the lubricant film provides partial separation (Totten and Liang, 2004). The contact load is shared between the contacting asperities and the film when mixed lubrication prevails.

Table 7.4 Quality profile of bovine serum (Harlan SERA-LAB, pH = 7.2–7.4)

Element	Quality profile	Element	Quality profile
Sodium	140 mmol/L	AST	32 U/L
Potassium	8.0 mmol/L	ALT	12 U/L
Glucose	6.7 mmol/L	LDH	809 U/L
Urea	6.4 mmol/L	Amylase	33 U/L
Total protein	61.83 g/L	Triglyceride	0.88 mmol/L
Albumin	32 g/L	Cholesterol	1.8 mmol/L
Calcium	1.97 mmol/L	Magnesium	1.22 mmol/L
Phosphate	3.02 mmol/L	Iron	19 μmol/L
Total bilirubin	7 μmol/L	Immunoglobulins	8.2 g/L

As shown in Table 7.2, several lubricants can be used in simulation wear tests, depending on the application. For contact lenses, physiological saline solution is normally employed. For dental implants, both sodium chloride solution (0.9%) and saliva solution are used. Serum and synovial fluid are studied in joint prostheses application. Table 7.4 shows the normal composition of bovine serum, which may be used in the same tests. Apart from the lubricants mentioned above, wear tests and corrosion tests are also carried out in other solutions, such as Ringer's solution containing sodium, potassium, calcium, and chloride ions.

7.3 Tribocorrosion testing

Tribocorrosion is defined as the chemical/electrochemical and mechanical processes leading to a degradation of material under tribological contacts in a corrosive environment (Landolt et al., 2001; Mischler et al., 1999). It is an irreversible transformation. Material degradation due to the combination of mechanical and electrochemical processes may occur under a variety of conditions. A sliding movement between two surfaces under two-body or three-body (i.e., with debris) contact is a common cause of tribocorrosion. With micro-motion involved, fretting-corrosion is a special type of tribocorrosion. Tribocorrosion is also observed in ball bearings under rolling contact. Particle impact or impingement can also result in a combined mechanical, chemical, electrochemical attack of material.

The selection of metals in biomedical devices aims to choose materials that have very high corrosion resistance. A stable passive film on the metallic material surface can protect it from corrosion attack. Under mechanical relative movement, oxide films on passive metals can be locally or even completely destroyed. Accelerated corrosion has been found by different studies (Landolt et al., 2001; Rossi et al., 2000). It is generally believed that wear will enhance corrosion rate.

An electrochemical approach offers opportunities to control the surface chemistry of the material under tribological contact, as described in the next subsections. The

current change can be monitored by holding a certain potential. The fundamental work suggests that the passive film plays an important role on mechanical degradation.

7.3.1 Bench tests

A new material combination has to undergo stringent wear testing before being adopted as fit for use in manufacturing prosthetic joints. Simple configuration wear testing has been used extensively as an ideal method for screening novel materials, and comparing them with existing ones, for use in joint replacements, prior to more complex joint simulator tests. At a fractional cost of a full simulator wear test, the reciprocating ball-on-plate apparatus has enabled better control of the individual tribological variables, leading to a better understanding of how these tribological factors independently influence the wear mechanisms and corrosion behavior. These simple tests also provide important information about the relative wear and wear-corrosion performance of bearing materials.

An integrated three-electrode cell can be used to determine electrochemical behavior under tribological contacts (Fig. 7.3). These three electrodes are:

- working electrode (WE): the specimen
- reference electrode (RE): an Ag/AgCl electrode
- counter electrode (CE): a platinum wire/mesh.

Some electrochemical techniques can be performed to understand the complex tribocorrosion behaviors.

7.3.1.1 The free corrosion potential measurement

At the free corrosion potential (E_{corr}), the anodic reaction rate is equal to the cathodic reaction rate and so there is no net current flow to or from the electrode. The value of E_{corr} is often used to give a qualitative indication of the corrosion regime (active or

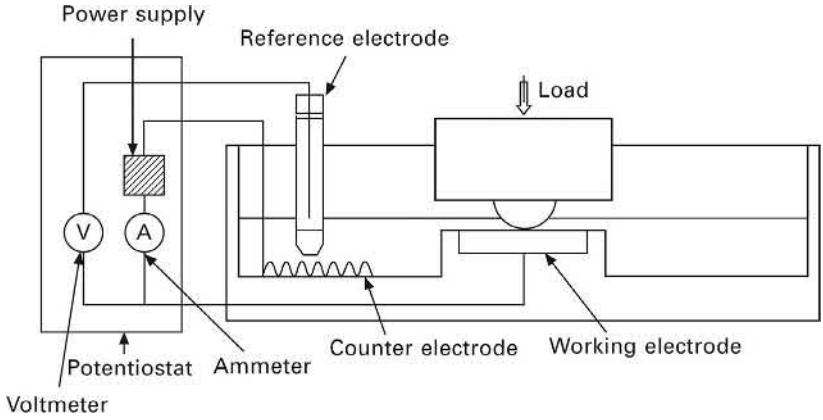


Fig. 7.3 Schematic representation of integrated three-electrode cell.

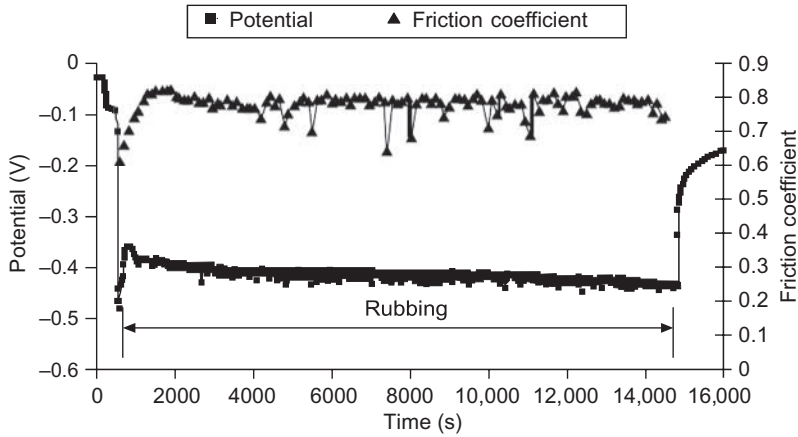


Fig. 7.4 Open circuit potential as a function of sliding time for a Co-Cr-Mo alloy in serum at 37°C.

passive) in which a material resides. It can provide a useful way to differentiate conditions of *active* corrosion from *passive* conditions. In such a study (Yan et al., 2006a), measurement of E_{corr} was used to assess (a) how the action of a sliding counterface, against a passive alloy affects the passivity of the alloy, and (b) how the material "recovers" once the sliding wear ceases and passivity is re-established. In this work, E_{corr} was monitored under static conditions, under the action of sliding wear, and once sliding wear ceased, as the material passivity was re-established (Fig. 7.4).

7.3.1.2 Anodic polarization scans

In anodic polarization tests, the rate of metal dissolution (anodic) processes can be determined. In one study (Yan et al., 2006b), the key purpose was to monitor the extent of passivity of the surface. This was done by using a standard three-electrode cell and a computer-controlled potentiostat to shift (at a rate of 15 mV/min) the potential of the working electrode (WE) from the free corrosion potential, E_{corr}, in the positive direction. This leads to the WE (sample) becoming a net anode, and by analyzing the rate of charge transfer as a function of potential, the corrosion behavior can be evaluated. The overpotential (the shift from E_{corr}) is the driving force for passivity breakdown and the magnitude of the breakdown potential (E_b), defined as the potential where the current in the three-electrode cell increases rapidly, gives a measure of the resistance of the passive film to localized corrosion initiation. For passive materials, the current will stay very low in the passive region, normally <10 μA/cm^2, because of the protective passive film. For active materials, where there is no protective film formed on the surface, the current will increase immediately on shifting the potential from E_{corr} (Fig. 7.5).

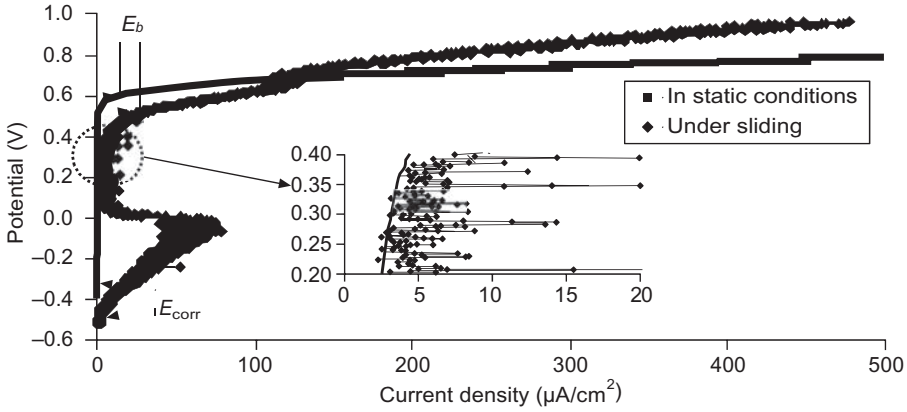


Fig. 7.5 Anodic polarization curves for a Co-Cr-Mo alloy in serum in static and under sliding condition at 37°C.

7.3.1.3 Linear polarization resistance tests

A linear polarization resistance (LPR) test is a corrosion rate monitoring method and it can give an indication of the corrosion resistance of materials in an aqueous environment (Yan et al., 2006c). LPR tests are performed both in the static condition and under reciprocating motion. With the material under sliding conditions, LPR tests are conducted every hour for up to 8 hours. In LPR tests, potential is shifted from 50 mV below E_{corr} (more negative than E_{corr}) to 50 mV more positive than E_{corr}. Current flow between the specimen and the counter electrode is monitored. A linear relationship of potential and current values can be observed. The value of $\Delta E/\Delta i$ is calculated (Fig. 7.6).

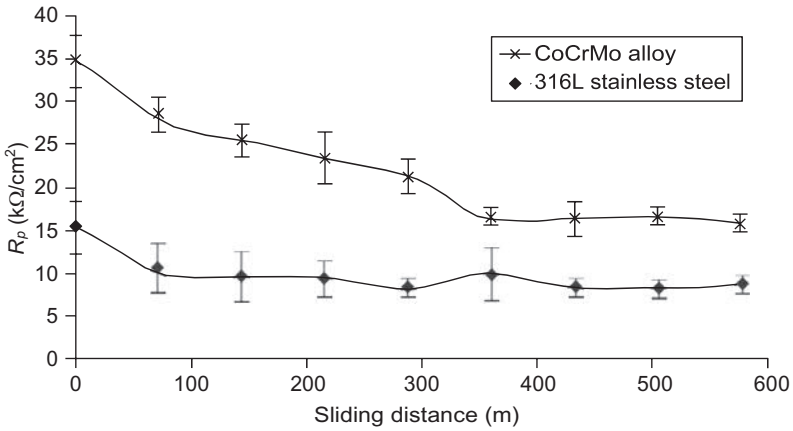


Fig. 7.6 Corrosion resistance for a Co-Cr-Mo alloy and SUS 316L stainless steel in serum under sliding condition at 37°C.

7.3.1.4 Cathodic protection

One of the main aims of work is to establish the extent of interactions between wear and corrosion processes. The most effective means of achieving isolation of the *wear* component of degradation is to completely stop any charge transfer (corrosion) at the working electrode surface. Cathodic protection (CP), by the impressed current method, is a widely used technique to control corrosion and sliding wear tests under CP have enabled the wear material loss to be determined (Yan et al., 2006c). The applied potential used can be 0.8 V (Ag/AgCl), chosen to be more negative than the equilibrium electrode potential for the Co/Co^{2+} reaction yet sufficiently noble enough to prevent hydrogen-evolution at the surface, which would inevitably affect the wear process. Pourbaix *E*-pH diagrams can assist to choose an appropriate potential value to be applied.

7.3.1.5 Quantification of corrosion-related damage

To date, there have been a few studies that attempted to quantify the contributions of material degradation (T) due to corrosion, wear, and their interactions in a bio-tribocorrosion environment where active biological solutions or saline solutions are used (Barril et al., 2004; Yan et al., 2006a). This can be done by considering Eq. 7.3, which allows the quantities of corrosion, wear, and corrosion-wear to be analyzed.

$$T = W + C' + S \tag{7.3}$$

where W is the material loss in the absence of corrosion, which was measured by applying CP. C' is the material loss due to electrochemical processes (corrosion) in the absence of wear. The synergy S includes two components which are:

- the effect of wear on corrosion (C_w) and
- the corrosion effect on wear (W_c).

Corrosion-related damage ($C' + S$) can therefore be assessed. It should be remembered that this is not only the corrosion rate—it is the damage that corrosion processes do when wear–corrosion processes occur in parallel. Hence it is referred to as *corrosion-related damage* rather than corrosion damage.

7.3.2 Simulator studies

For orthopedic implants, their movement and loading conditions are much more complicated than in bench tests. The latter provide an initial validation and view of the combination and contribution of tribological contacts and corrosion reactions. More realistic simulators have been used to determine the wear rate for hip/knee prostheses.

The phenomena of running-in state and steady state have been recognized in many applications when wear is presented (Dowson et al., 2004a). Many authors have been studying metal-on-metal (MoM) total hip replacements' wear behavior in vivo and in vitro. Two distinct wear phases were discernible for MoM joints. A running-in (or bedding-in, wearing-in) stage, followed by a lower wear rate steady-state stage

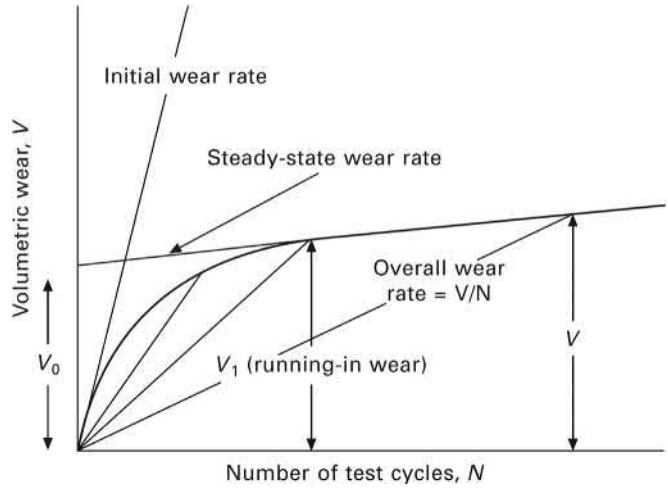


Fig. 7.7 Basic features of volumetric wear for joint simulator tests (Dowson et al., 2004a).

(Dowson et al., 2004b) (Fig. 7.7). The length of the running-in state varies depending on the different simulators and geometry of contacts (pin-on-plate, ball-on-plate etc.) from thousands of cycles up to about 1 million cycles (Dowson, 1998; Katti, 2004; Stemp et al., 2003). Generally, after 1 million cycles in vitro and 1 year in vivo, implants are considered to reach a steady state. Small wear debris particles are created mostly in the running-in phase and cause abrasive wear. From clinical examinations for the first few days after implantation of MoM joints, metal ions were found to increase dramatically. The metal ion levels then stabilized (Dowson et al., 2004b; Lemons and Lucas, 1986), which is possibly related to the biphasic (running-in and steady-state) wear phenomena and the saturation of metal ions in the body. As shown in Fig. 7.8, from the clinical wear factor, a stable wear factor was reached

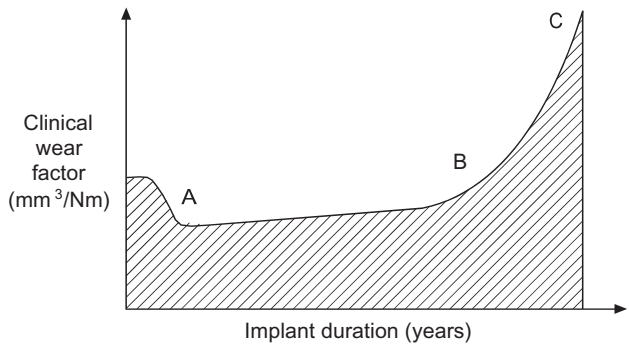


Fig. 7.8 Clinical wear rate for total hip replacements.

in region A to B after the initial relatively high wear rate (before A). It is considered that a running-in process is present before point A, as mentioned previously, the duration being about 1 year. Then the wear dramatically accelerated (region B to C) due to the failure of devices.

Several parameters are used to quantify or evaluate material wear. Material total weight or volume loss is the most common one. The depth or width of the wear scar is also used. However, those values show no association with testing conditions. Wear factor (k) has been suggested as more appropriate. It is proportional with total wear and applied load and sliding distance. The calculation is shown in Eq. (7.4):

$$k = \frac{\text{Wear volume}}{\text{Applied load} \times \text{sliding distance}} \left(\frac{\text{mm}^3}{\text{Nm}}\right) \tag{7.4}$$

Fig. 7.9 shows the force change during a cycle of walking. A peak load of more than four times bodyweight was obtained when the action of heel strike was made. Two phases in the human hip joint are classified during a normal walking cycle. In the stance phase, the hip joint carries a very high load and the relative movement in the joint (between femoral head and socket) is small. In the swing phase, even though the load on the joint is lower than in the stance phase, the movement of the joint is greater. Some authors believe that the material degradation (wear) progresses severely in this phase (Dowson and Jin, 2006). For the Leeds hip simulators (Fig. 7.10), load is applied on the femoral head as shown in Fig. 7.11. It is very similar to the walking cycles shown in Fig. 7.9.

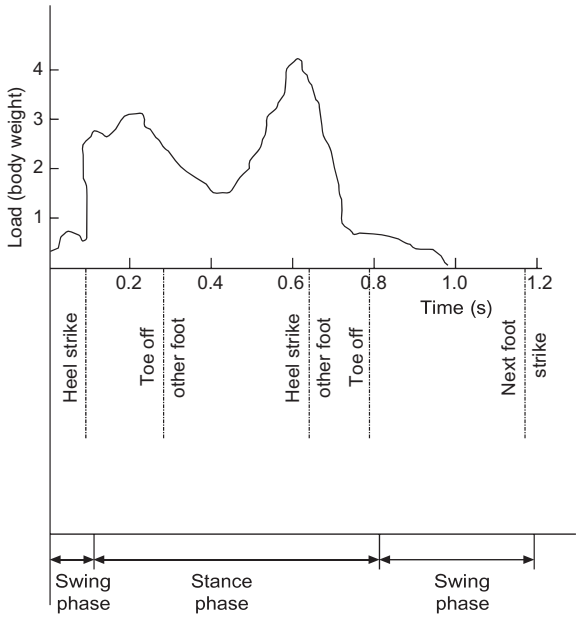


Fig. 7.9 Hip joint force during one cycle of walking.

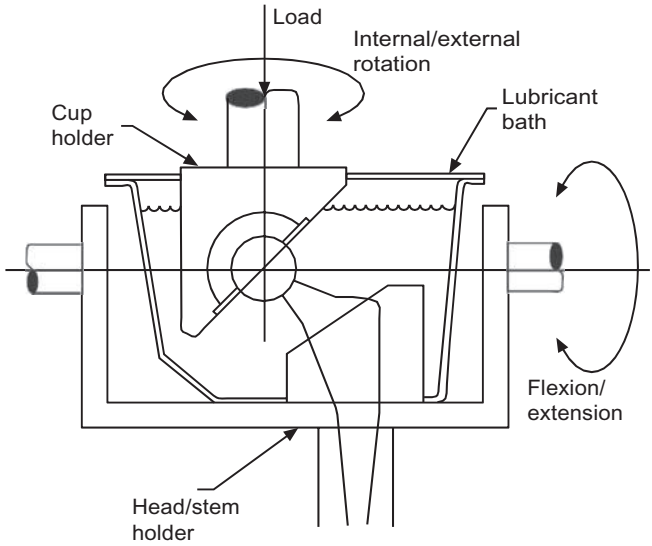


Fig. 7.10 Schematic diagram for a Leeds hip simulator.

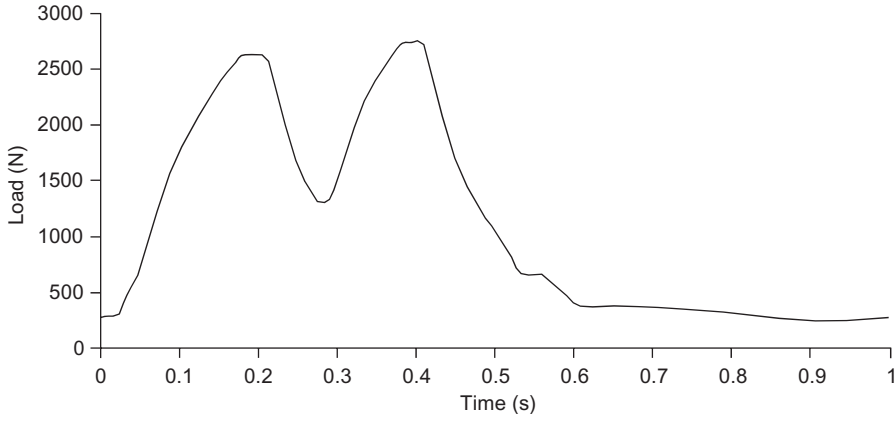


Fig. 7.11 Load profile applied in hip simulators.

7.4 Surface analysis for tribology and tribocorrosion properties

In order to understand the mechanisms and behavior of materials' surfaces after wear tests, surface analysis techniques have been widely used. Over the years, an enormous number of techniques have been developed to probe different aspects of the physics and chemistry of surfaces. It is obvious that the surface properties of solids are

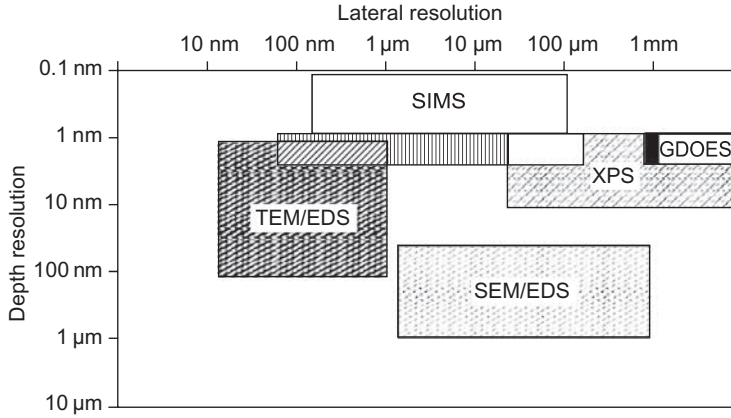


Fig. 7.12 Comparison of various surface analysis techniques for their lateral resolution and depth resolution.

influenced to a large extent by the solid state properties of the material. After wear testing, normally there is a thin film that covers the worn area, namely a tribofilm. The thickness of the tribofilm differs over various applications and conditions. The goal of applying surface analysis is to determine the properties of the tribofilm.

For the examination conditions, surface analysis techniques can be divided in to: (a) vacuum system (including high vacuum and ultra-high vacuum), and (b) normal air pressure condition. For surfaces' properties, there are two categories: (a) physical properties, and (b) chemical properties. To obtain the chemical composition or structure detail of surfaces, most of the techniques require the surfaces to be bombarded with photons, electrons, or ions. Those techniques normally need to be operated under a vacuum condition. However, for Raman spectroscopy (RS) and Fourier transform infrared spectroscopy (FTIR), samples do not need to be placed in a vacuum chamber. Techniques for determining surfaces' mechanical properties, appearance, or topography can be used in normal laboratory conditions, such as nano-indentation, atomic force microscopy (AFM), ellipsometry, etc. To choose which analysis technique(s) to use, the basic principles of those technique(s) need to be known prior to the sample examination. The detection limits, advantages, and disadvantages of different methods should be considered. Fig. 7.12 shows the lateral and depth resolution for some surface analysis techniques. In this section, some commonly used surface analysis techniques are introduced.

7.4.1 Scanning electron microscopy (SEM)

Scanning electron microscopy (SEM) images the sample surface by scanning it with a high-energy beam of electrons in a raster scan pattern. The primary electron beam, which is produced under high vacuum, is scanned across the surface of a specimen.

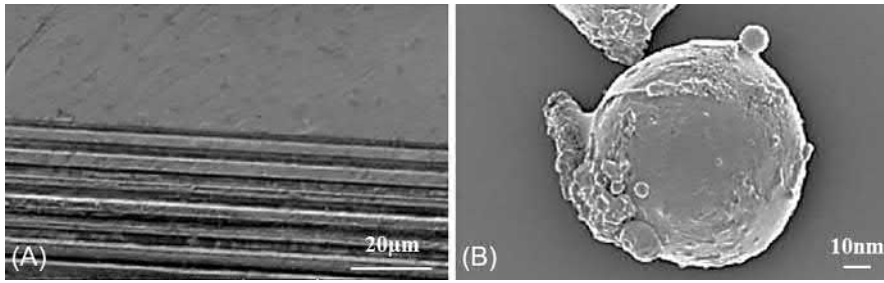


Fig. 7.13 SEM images for (A) wear scar on a Co-Cr-Mo alloy and (B) a nanometallic particle.

When the electrons strike the specimen, a variation of the signal produces an image of the surface, or its elemental composition together with energy dispersive X-rays (EDX). An SEM image is shown in Fig. 7.13A. Clear grooves can be seen at the bottom half of the image. This indicates debris generated by tribological contacts trapped in the contact. They scratch the sample surface, which results in wear. Several functions have been developed with the principles of SEM to gain a better understanding of material surfaces. Back scattered electrons (BSE) are beam electrons that are reflected from the sample by elastic scattering. BSE images can provide information about the distribution of different elements in the sample according to their atomic number. Field emission guns SEM (FEG SEM) enable a higher resolution and magnification, which is widely used in nanotechnology and biomedical fields. Fig. 7.13B shows a nanoparticle from FEG SEM. One of the latest innovations in SEM is environmental scanning electron microscopy (ESEM). It differs from conventional SEM in two crucial aspects. Firstly, it allows the introduction of a gaseous environment in the specimen chamber although the electron gun is kept under the standard SEM high vacuum. Secondly, nonconductive samples, such as fibers, wood, polymer, etc. do not need to be coated with a carbon or metallic layer, as is the case with conventional SEM.

7.4.2 X-ray photoelectron spectroscopy (XPS)

X-ray photoelectron spectroscopy (XPS) is a powerful technique widely used for surface analysis of materials. In one particular machine (Beamson et al., 1990), a high-power monochromatized Al K_a X-ray source ($hv = 1486.6$ eV), high transmission electron optics and multichannel detector are employed. Using this machine, *survey scans* and more detailed *region scans* were run at 300 eV pass energy and 0.8 mm slit width. Although X-rays penetrate to a depth of several micrometres, ejected photoelectrons generally come from only the first several nanometres of material. In XPS, the photon is absorbed by an atom in a molecule or solid, leading to ionization and the emission of a core (inner shell) electron. The binding energy (BE) is taken to be a direct measure of the energy required to remove the electron from its initial level to the vacuum level. In order to assess the variation of composition as a function of

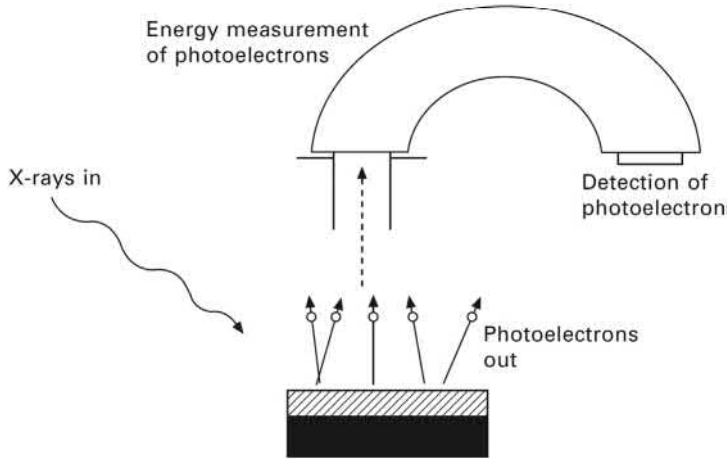


Fig. 7.14 Schematic representation of XPS.

depth, the samples were subjected to argon-ion bombardment for various periods of time. A schematic diagram of XPS is shown in Fig. 7.14.

The high X-ray power rotating anode has a maximum power rating of 8 kW, a factor of thirteen higher than the typical power of 600 W for a conventional fixed anode source. A large, seven crystal, double focusing monochromator focuses the X-ray onto an area 6 mm by 0.3 mm. The beam line is then focused in the middle of the wear scar in an area of 400 μm by 300 μm. The Al K_a (1486.7 eV) line profile has a "full width at half maximum" (FWHM) of 0.26 eV, a factor of three narrower than for an unmonochromated Al K_a source. The computer-controlled lens system has two modes of operation: a high transmission mode for optimum acceptance of photoelectrons and an imaging mode for high spatial resolution with <50 μm lateral resolution. The detection system consists of a 300 mm radius hemispherical analyzer and a multichannel detector. This gives an overall instrument resolution of 0.3 eV minimum.

In typical XPS analysis, a survey scan (Fig. 7.15A) is obtained first in order to identify elements present, and then the long scans (Fig. 7.15B) of the selected peaks are obtained in order to determine a more comprehensive picture of the chemical composition.

7.4.3 White light interferometry (WLI)

White light interferometry (WLI) is a powerful technique for noncontact measurement of surface topography at high vertical and moderate lateral resolution. The Phase Shifting Interference (PSI) mode was used and the resolution for this mode is 0.3 nm. The Wyko machine has a range of objectives from $2\times$ to $50\times$ and has an additional zoom from 0.5 to $2\times$ called the field-of-view (FOV) objective.

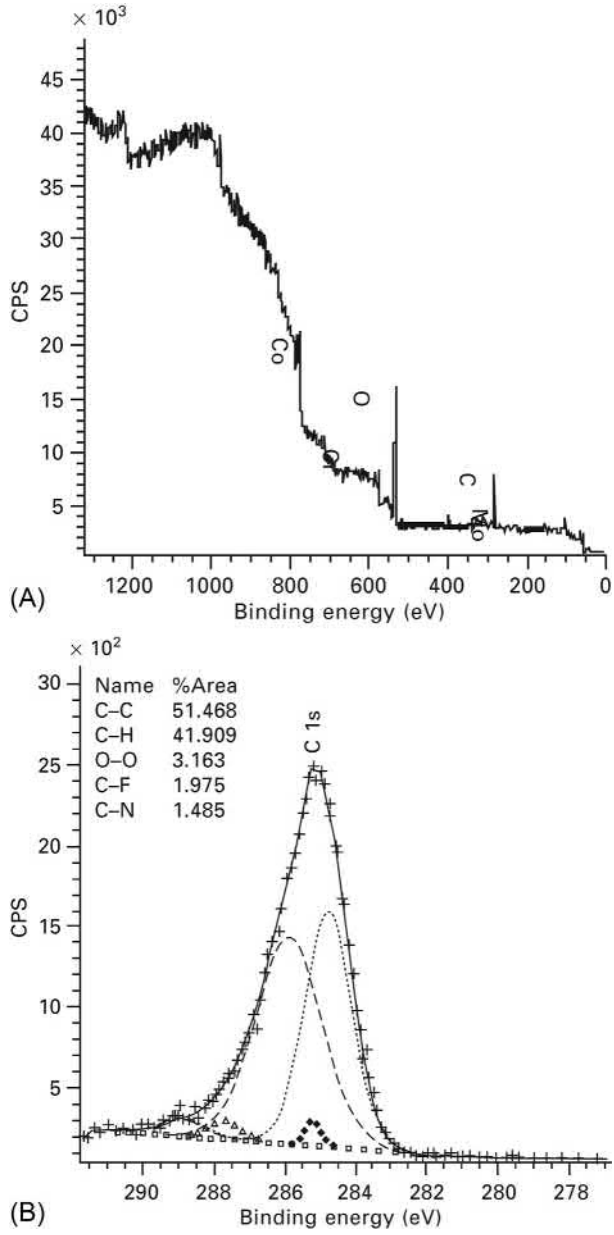


Fig. 7.15 XPS spectra for the tribofilm on a Co-Cr-Mo alloy in serum (A) survey scan and (B) long scan.

7.4.4 Atomic force microscopy (AFM)

Atomic force microscopy (AFM) is in the family of scanning probe microscopy (SPM). It is very useful to study properties of material from the atomic to the micron level. AFM consists of a microscale cantilever with a sharp tip (probe) at its end that

is used to scan the specimen surface. Fig. 7.16 shows a schematic diagram of AFM. It is ideally suited to the investigation of topographical structure (having high resolution) along with local surface properties such as local stiffness and adhesion. AFM normally has three imaging modes: (a) contact mode, (b) noncontact mode, and (c) intermittent contact or tapping mode (Vickerman, 1997; O'Connor, 2003). During scanning in the contact mode, a constant bend in the cantilever is maintained. In the noncontact mode, the cantilever oscillates just above the specimen. The tip–specimen separation and the oscillation amplitude are in the order of 1–10 nm, which is the main difference to the tapping mode, where the oscillation amplitude of the tip is in the range of 20 nm to 200 nm. The tapping mode is very useful for soft surfaces, especially biological samples. Fig. 7.17 shows images under contact mode for tribofilm on a Co-Cr-Mo alloy.

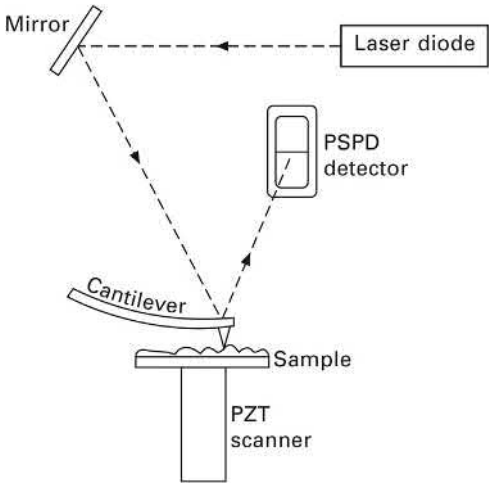


Fig. 7.16 Schematic diagram of AFM.

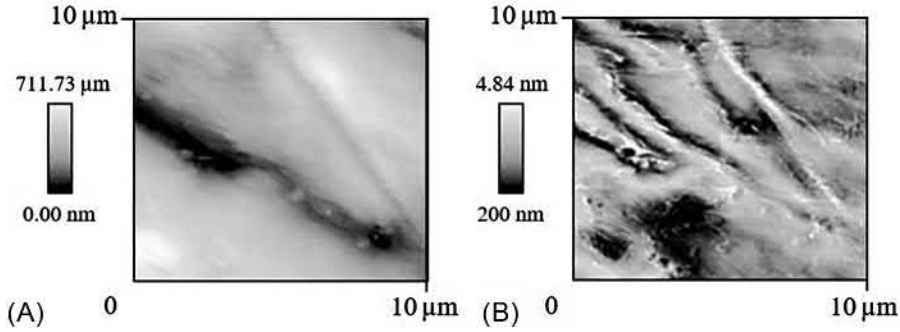


Fig. 7.17 Typical AFM image of a Co-Cr-Mo alloy surface. (A) Topography and (B) lateral force.

7.4.5 Mass spectroscopy

Surface mass spectroscopy techniques consist of measuring the masses of secondary ions that are ejected, in a process known as sputtering, from the surface of a specimen when a primary beam of energetic particles bombards it. This results in the emission of a range of secondary particles, including positively and negatively charged ions. The secondary ions can provide unique information about the chemistry of the surface from which they originated. It is common practice to use electron spectroscopy in combination with surface mass spectroscopy to characterize the surface chemistry of an unknown specimen. The main methods of surface mass spectroscopy are: secondary ion mass spectroscopy (SIMS), laser ionization mass spectrometry (LIMA), and sputtered neural mass spectrometry (SNMS). SIMS is by far the most commonly used surface spectroscopic technique. It has three basic modes: (a) static SEM—used for submonolayer elemental analysis, (b) dynamic SIMS—used for obtaining compositional information as a function of depth below the surface, and (c) imaging SIMS—used for spatially resolved elemental analysis (Briggs and Seah, 1990; Vickerman, 1997). A typical SIMS spectrum is shown in Fig. 7.18.

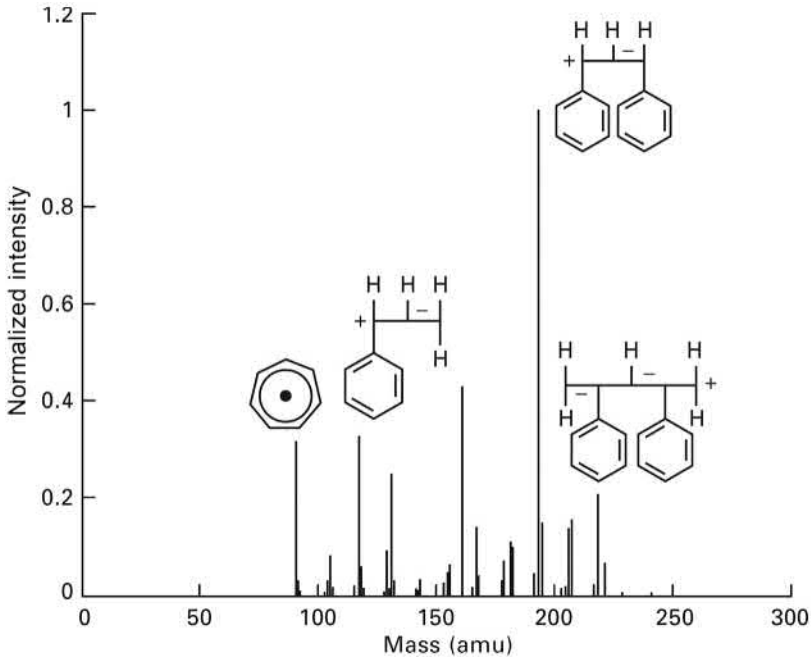


Fig. 7.18 A typical SIMS spectra.

7.5 Future trends

Wear testing methods have been developed for hundreds of years. However, with the fast development of materials and exploration of applications, some possible trends can be summarized as follows:

- In situ*, on line wear testing*: Wear tests will be integrated with surface analysis techniques, which will provide real time wear properties—how the tribofilm forms under various conditions and environments. More information will therefore be obtained from a single wear test, such as temperature, contact resistance, corrosion resistance, lubrication film properties, chemical structure changes, etc.
- *Modeling*: General property modeling, where basic mechanical properties are linked to wear behavior (yield strength, work hardening, ductility, fracture toughness, etc.) will be developed. This is another approach to understanding tribological behavior. Wear tests will provide a database for future modeling of different materials and conditions.
- *Micro- and nano-tribology*: This involves assemblies of atoms and molecules having at least one nano-scale dimension. Four areas at present relate to nano-tribology: probes, structure, processes, and simulation of tribological systems. Testing methods need to go smaller and smaller.
- *Coatings*: It is clear that coatings have huge potential to reduce wear and friction in a large range of applications and can provide solutions where lubricants cannot be used.
- *Specific wear testing*: More individual wear testing techniques will be developed as well as the documented standards. The family of wear testing standards will grow. Unique ways to test unique systems will be developed and invented.

References

ASM, 1992. Metals handbook. In: Friction, Lubrication and Wear Technology. vol. 18. ASM International.

Barril, S., Mischler, S., Landolt, D., 2004. Influence of fretting regimes on the tribocorrosion behaviour of Ti6A14V in 0.9 wt.% sodium chloride solution. Wear 256, 963–972.

Bayer, R., 2004. Mechanical Wear Fundamentals and Testing. Marcel Dekker, Inc.

Beamson, G., Briggs, D., Davies, S.F., Fletcher, I.W., Clark, D.T., Howard, J., Gelius, U., Wannberg, B., Balzer, P., 1990. Performance and application of the scienta ESCA300 spectrometer. In: Surface Interface Analysis. vol.15. pp. 541–549.

Briggs, D., Seah, M.P., 1990. Practical Surface Analysis. John Wiley.

Dowson, D., 1998. History of Tribology. Professional Engineering Publishing, London.

Dowson, D., Hardaker, C., Flett, M., Isaac, G.H., 2004a. A hip joint simulator study of the performance of metal-on-metal joints Part I: the role of materials. Arthroplasty 19, 118–123.

Dowson, D., Hardaker, C., Flett, M., Isaac, G.H., 2004b. A hip joint simulator study of the performance of metal-on-metal joints part II: design. Arthroplasty 19, 124–130.

Dowson, D., Jin, Z.M., 2006. Metal-on-metal hip joint tribology. Proc. Inst. Mech. Eng. H Eng. Med. 220, 107–118.

Gee, M.G., Owen-Jones, S., 1998. Wear testing methods and their relevance to industrial wear problems. NPL Rep. CMMT(A)92.

Hutchings, I.M., 1992. Tribology: Friction and Wear of Engineering Materials. Edward Arnold, London.
Jin, Z.M., Dowson, D., Fisher, J., 1997. Analysis of fluid film lubrication in artificial hip joint replacements with surfaces of high elastic modulus. Proc. Inst. Mech. Eng. H J. Eng. Med. 211, 247–256.
Jin, Z.M., Firkins, P., Farrar, R., Fisher, J., 2000. Analysis and modelling of wear of cobalt-chrome alloys in a pin-on-plate test for a metal-on-metal total hip replacement. Proc. Inst. Mech. Eng. H 214, 559–568.
Katti, K.S., 2004. Biomaterials in total joint replacement. Colloids Surf. 39, 133–142.
Landolt, D., Mischler, S., Stemp, M., 2001. Electrochemical methods in tribocorrosion: a critical appraisal. Electrochim. Acta 46, 3913–3929.
Lemons, J.E., Lucas, L.C., 1986. Properties of biomaterials. Arthroplasty 1, 143–147.
Loomis, W.R., 1985. New Directions in Lubrication, Materials, Wear and Surface Interaction. Noyes Publications.
Mischler, S., Spiegel, A., Landolt, D., 1999. The role of passive oxide film on the degradation of steel in tribocorrosion systems. Wear 225–229, 1078–1087.
Neale, M.J., Gee, M., 2000. Guide to Wear Problems and Testing for Industry. Professional Engineering Publishing.
O'Connor, D.J., 2003. Surface Analysis Methods in Materials Science. 31 Springer.
Rossi, S., Fedrizzi, L., Deflorian, F., Zen, M. (Eds.), 2000. Wear-corrosion of nitrided steel: corrosion potential monitoring to evaluate the effect of test parameters. Mater. Corros. 51, 552–556.
Stachowiak, G.W., Batchelor, A.W., 2001. Engineering Tribology. Heinemann, Woburn, Butterworth.
Stemp, M., Mischler, S., Landolt, D., 2003. The effect of mechanical and electrochemical parameters on the tribocorrosion rate of stainless steel in sulphuric acid. Wear 255, 466–475.
Totten, G.E., Liang, H., 2004. Mechanical Tribology. Marcel Dekker, Inc, New York.
Vickerman, J.C., 1997. Surface analysis: The Principal Techniques. John Wiley & Sons.
Williams, J.A., 1994. Engineering Triblogy. Oxford Science Publication.
Yan, Y., Neville, A., Dowson, D., 2006a. Understanding the role of corrosion in the degradation of metal-on-metal implants. Proc. Inst. Mech. Eng. H J. Eng. Med. 220, 173–180.
Yan, Y., Neville, A., Dowson, D., Williams, S., 2006b. Tribocorrosion in implants—assessing high carbon and low carbon Co–Cr–Mo alloys by *in-situ* electrochemical measurements. Tribol. Int. 39, 1509–1517.
Yan, Y., Neville, A., Dowson, D., 2006c. Biotribocorrosion—An appraisal of the time dependence of wear and corrosion interactions—part I: the role of corrosion. J. Phys. D. Appl. Phys. 39, 3200–3205.

Biocompatibility and fabrication of in situ bioceramic coating

8

C. Cui*, Mitsuo Niinomi†,‡,§,¶
*Hebei University of Technology, Tianjin, China, †Tohoku University, Sendai, Japan, ‡Osaka University, Osaka, Japan, §Nagoya University, Nagoya Japan, ¶Meijo University, Nagoya, Japan

8.1 Introduction

As biomaterials, Ti and its alloys are superior to many materials such as stainless steel, pyrolytic carbon (C), and so on, in terms of mechanical properties and biocompatibility. Ti and its alloys are widely used in biomedical devices and components, especially as hard tissue replacements as well as in cardiac and cardiovascular applications, because of their desirable properties, such as relatively low Young's modulus, good fatigue strength, formability, machinability, corrosion resistance, and biocompatibility. However, Ti and its alloys cannot meet all of the clinical requirements of biomedical devices. Therefore, in order to improve the biological, chemical, and mechanical properties, surface modification is often performed. This chapter reviews the various surface modification technologies pertaining to Ti and its alloys including mechanical treatment, thermal spraying, sol-gel, chemical and electrochemical treatment, and ion implantation from the perspective of biomedical engineering. Recent work has shown that the wear resistance, corrosion resistance, and biological properties of Ti and its alloys can be improved selectively using appropriate surface treatment techniques while the desirable bulk attributes of the materials are retained. Proper surface treatment expands the use of Ti and its alloys in the biomedical fields. Some recent applications are also discussed in this chapter.

8.2 Ti and its alloys

Titanium (Ti) is one of the transition elements in Group iV and Period 4 of Mendeleev's Periodic Table. It has an atomic number of 22 and an atomic weight of 47.9. Being a transition element, Ti has an incompletely filled d shell in its electronic structure (Ogden, 1961). Some basic physical properties of pure Ti are summarized in Table 8.1. The incomplete shell enables Ti to form solid solutions with most substitutional elements having a size factor within 20%. in the elemental form. Ti has a high melting point (1668°C) and possesses a hexagonal, closely packed crystal structure (hcp: crystal structure of α-phase) up to a temperature of 882.5°C. Ti transforms into a body-centered cubic structure (bcc: crystal structure of β-phase) above this temperature (Collings, 1984). Ti alloys may be classified as α, near-α, α + β, near-β,

Metals for Biomedical Devices. https://doi.org/10.1016/B978-0-08-102666-3.00008-0
© 2019 Elsevier Ltd. All rights reserved.

Table 8.1 Summary of physical properties of unalloyed Ti

Property	Value
Atomic number	22
Atomic weight (g/mol)	47.9
Crystal structure	
Alpha	Hexagonal, closely packed
c (Å)	4.6832 ± 0.0004
a (Å)	2.9504 ± 0.0004
Beta	Cubic, body centered
a (Å)	3.28 ± 0.003
Density (g cm^{-3})	4.54
Coefficient of thermal expansion, *a*,	8.4 ∞ 10^{-6}
at 20°C (K^{-1}) Thermal conductivity (W/(m K))	19.2
Melting temperature (°C)	1668
Boiling temperature (°C)	3260
Transformation temperature (°C)	882.5
Electrical resistivity	
High purity (μ Ω cm)	42
Commercial purity (μ Ω cm)	55
Modulus elasticity *a*, (GPa)	105
Yield strength *a*, (MPa)	692
Ultimate strength *a*, (MPa)	785

metastable β, or stable β-type alloys depending upon the room temperature microstructure (Polmear, 1981). In this regard, alloying elements for Ti fall into three categories: (i) α-stabilizers, such as aluminum (Al), oxygen (O), nitrogen (N), and carbon (C); (ii) β-stabilizers, such as molybdenum (Mo), vanadium (V), niobium (Nb), and tantalum (Ta) (isomorphous), iron (Fe), tungsten (W), chromium (Cr), silicon (Si), cobalt (Co), manganese (Mn), and hydrogen (H) (eutectoid); (iii) neutrals, such as zirconium (Zr). The α and near-α Ti alloys exhibit superior corrosion resistance to the α + β alloys but have limited low temperature strength. In contrast, the α + β alloys exhibit higher strength due to the presence of both the α- and β- phases. The properties of the materials depend on the composition, relative proportions of the α and β phases, thermal treatment, and thermo-mechanical processing conditions.

The β alloys offer the unique characteristic of low elastic modulus and superior corrosion resistance to the α and α + β alloys (Bania, 1993; Schutz, 1993). The Ti-nickel (Ni) alloy is a stoichiometric compound of Ti and Ni. The equiatomic intermetallic compound TiNi exhibits the shape memory phenomenon that allows for the spontaneous recovery of shape after being subjected to macroscopic deformation higher than its elastic limit. Shape recovery may occur after heating or after release of loads. TiNi shape memory alloy with 55 wt% of Ni and 45 wt% of Ti is often called NiTiNOL (Ni for Ni, Ti for Ti, and NOL for Naval Ordnance Laboratory, the place where Buehler and co-workers discovered this alloy). Research activities on the

application of TiNi shape memory alloys to medicine began in the late 1960s to take advantage of their unique shape memory properties. For example, tailored compressive fixation of bone fragments, and anchoring of implants and dentures to living tissues can be more easily achieved with TiNi alloys (although Ni is poisonous to the human body if there is no coating on the alloy). In addition, flexible TiNi stents are increasingly used in surgical treatments involving constricted arteries, recurrent urethral obstructions, biliary obstructions, and malignant esophageal stenosis.

8.3 Biomedical applications and development of Ti and its alloys

Earlier applications of Ti in medical, surgical, and dental devices were based on post-World War II advances in manufacturing processes as a result of the more stringent requirements demanded by the aerospace and military industry. Increased use of Ti and its alloys as biomaterials stems from their low Young's modulus, superior biocompatibility, and better corrosion resistance when compared to more conventional stainless steels and Co-based alloys. These attractive properties were the driving force for the early introduction of α (commercially pure Ti: cpTi) and (α + β)-type (Ti-6Al-4 V) alloys, as well as the more recent development of modern Ti-based alloys and orthopedic metastable β-type Ti alloys. Applications of Ti and its alloys can be classified according to their biomedical functionalities.

8.3.1 Hard tissue replacements

A schematic diagram of hard tissues in the human body is shown in Fig. 8.1. Hard tissues are often damaged due to accidents, aging, and other causes. It is a common practice to surgically substitute the damaged hard tissues with artificial replacements. Depending on the regions in which the implants are inserted and the functions to be provided, the requirements of the endoprosthetic materials are different.

Because of the aforementioned desirable properties, Ti and its alloys are widely used as hard tissue replacements in artificial bones, joints, and dental implants. As a hard tissue replacement, the low elasticity of Ti and its alloys is generally viewed as a biomechanical advantage because the lower elasticity results in less stress shielding. One of the most common applications of Ti and its alloys is artificial hip joints that consist of an articulating bearing (femoral head and cup) and stem, as depicted in Fig. 8.2. The articulating bearings must be positioned in such a way that they can reproduce the natural movement inside the hip joints whereas secure positioning of the femoral head in relation to the other components of the joint is achieved using the stem. The hip stem is anchored permanently to the intramedullary canal of the femur. The cup, which is the articulating partner of the femoral head, is used for fixation by reaming out the natural acetabulum to fit the design. Ti and its alloys are also often used in knee joint replacements, which consist of a femoral component, tibial component, and patella.

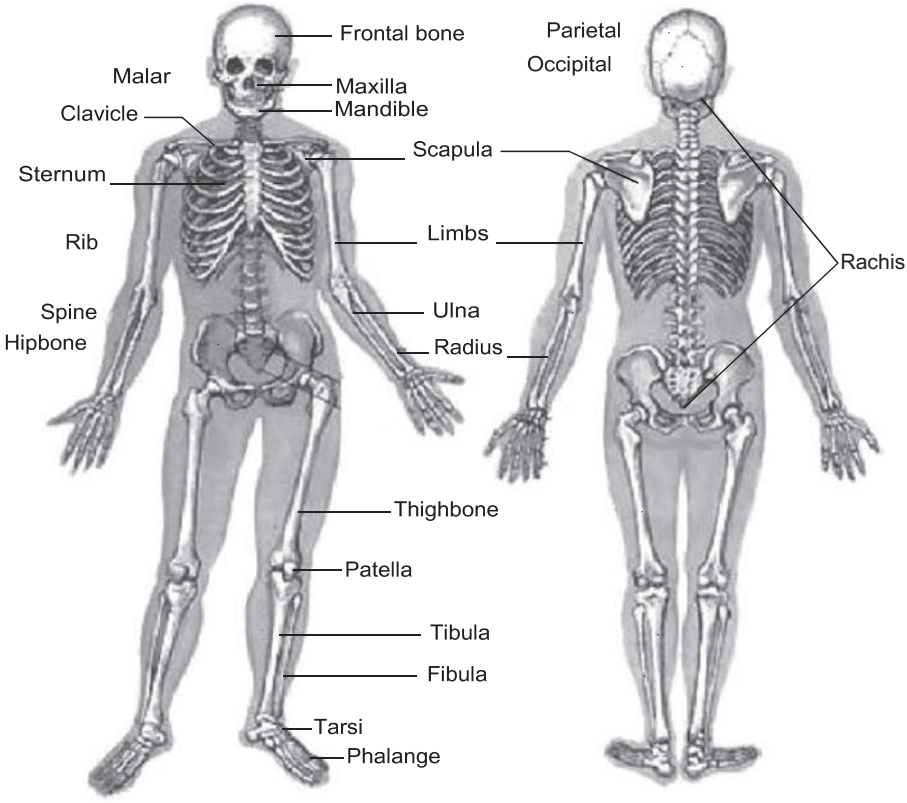


Fig. 8.1 Schematic diagram of hard tissues in human body.

Ti and its alloys are common in dental implants, which can be classified as subperiosteal, transosteal, and endosseous according to their position and shape. Subperiosteal implants consist of a custom-cast framework resting on the bone surface beneath the mucoperiosteum. The prosthesis is secured on posts or abutments that penetrate the mucosa into the oral cavity. Transosteal implants can be placed only in the frontal lower jaw while endosseous implants can be placed in both the upper and lower jaws via a mucoperiosteal incision. They are the most commonly used implant types and can be used in almost any situation as single implants to replace one missing tooth as well as in cases of partial and total edentulism. The most commonly used endosseous implants are root-forming analogs.

Fig. 8.3 shows one of the more popular designs—a screw-shaped artificial tooth. Most dental implants are placed according to the "osseointegration" concept, which allows dental implants to fuse with bones. Surface modification technologies, such as grist blast, chemical etching, and plasma spraying are often utilized to improve the osseointegration ability of Ti dental implants. For endosseous implant fixation in bones, such as in the case of artificial hip and knee joints, two methods are currently

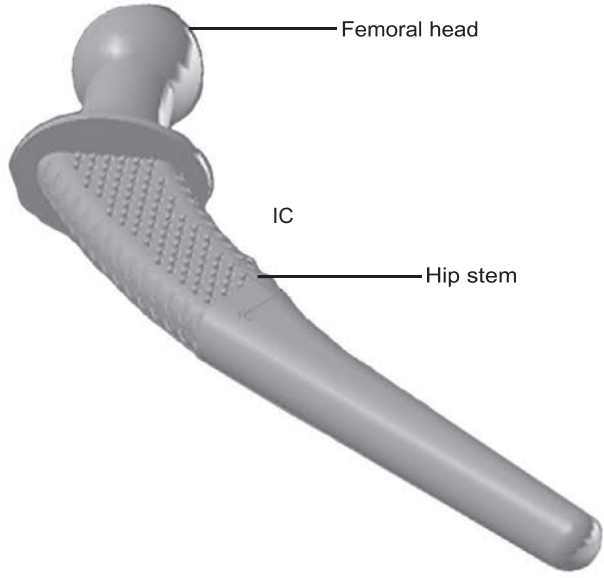


Fig. 8.2 Schematic diagram of artificial hip joint.

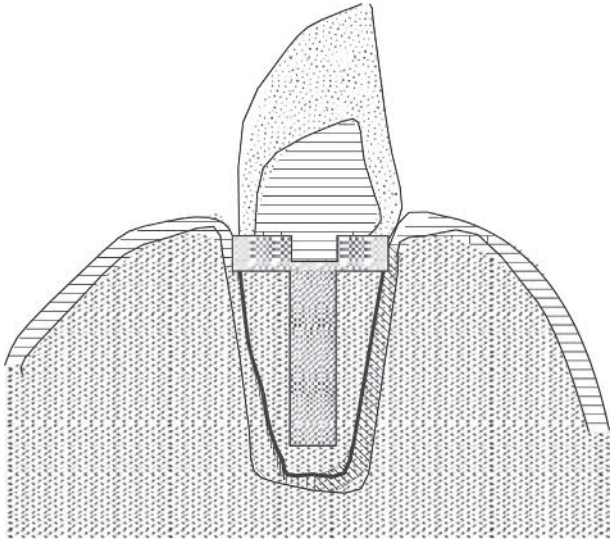


Fig. 8.3 Schematic diagram of screw-shaped artificial tooth.

employed. One is bone cement fixation and the other is cementless implantation. Consequently, prostheses can be classified into cemented and cementless prostheses in accordance with the fixation methods in bone tissues. The requirements that are related to the properties and design of the prostheses depend closely on the type of

anchoring in the human body. For cemented prostheses, the components are fixed to the bony implant bed employing bone cement based on poly(methylmethacrylate) (PMMA). The cement is usually prepared at the time of the surgery and applied with the aid of a syringe to the bony implant bed after blood and medullary fat have been removed. Penetrating into the cancellous bone structure, the cement hardens within a few minutes due to an exothermal reaction. This leads to a continuous cement mantle that is well anchored in the bone and lies closely against the implant (Morscher, 1995). With regard to bone cement fixation, apart from the risk of necrotic damage to the living bone by the heat liberated during polymerization of the cement, the lifetime of a cemented endoprosthesis depends on the durability of the cement as well as its tensile bond strength on the implant surface. Failure begins with loosening at the interface accompanied by micro-movements between the metal and the cement, consequently initiating the formation of metal particles and release of metal ions. Due to its poor mechanical properties, cement is branded as the weak point in the fixation, as exemplified by the growing number of cases involving loosening of cemented prostheses since the late 1970s, regardless of prosthesis design (Jones and Hungerford, 1987). Anchoring of the prosthesis directly to the living bone is one of the solutions and the driving force for further developments. In comparison with cementing, direct cementless anchoring of the prosthesis to the bone through osseointegration is a more recent technique. Cementless prostheses with the optimal surface structure and composition to enable osseointegration can produce lasting mechanical interlocking between the implant and bone (Bobyn et al., 1980; Dowson and Wright, 1981; Howie, 1990; Jast, 1993; Long and Rack, 1998). Rough surfaces, porous coatings, and surfaces with osteoconductivity and osteoinductivity in body fluids have been shown to be good surfaces for osseointegration. Depending on the desired anchorage in the bone, partial osseointegration of the prosthetic components may be considered the best option. In such cases, the design is divided into functional zones that are optimized according to their individual functions. For a proximal anchored hip prosthesis stem, the solution may require the provision of a proximal surface that can osseointegrate with the bone.

In order to avoid adverse tissue reactions arising from hard tissue replacements, a bioinert material, which is stable in the human body and does not react with body fluids and tissues, is preferred. Bioinert materials are generally encapsulated after implantation into the living body by fibrous tissues that isolate them from the surrounding bone. Some bioactive materials, such as hydroxyapatite and bioactive glasses are increasingly used as hard tissue replacements to improve the bonding between implants and bone tissues because the materials can bond to living bones without the formation of fibrous tissues by creating a bone-like apatite layer on their surface after implantation. Apatite formation is currently believed to be the main requirement for the bone-bonding ability of materials. In this respect, Ti with its native surface oxide is known to be bioinert, but it is difficult to achieve good chemical bonding with bones and form new bones on its surface at the early stage after implantation. Hence, Ti and its alloys do not meet all the requirements of an “ideal” material. In addition, longer human life expectancy and younger patients requiring implants have driven biomedical research from original implant concerns, such as material strength,

infection, and short-term rejection to a consideration of more long-term material limitations; for instance, wear, fatigue strength, and long-term biocompatibility. The current trend is to use surface modification technologies to address a number of these ever-increasing clinical demands, and the various issues are discussed later in this chapter.

8.3.2 Cardiac and cardiovascular applications

Ti and its alloys are common in cardiovascular implants because of their unique properties. Early application examples were prosthetic heart valves, protective cases in pacemakers, artificial hearts, and circulatory devices. Recently, the use of shape memory TiNi alloy (NiTiNOL) in intravascular devices, such as stents and occlusion coils, has received considerable attention. The advantages of Ti cardiovascular applications are that Ti is strong, inert, and nonmagnetic. It also produces few artifacts under magnetic resonance imaging (MRI), which is a very powerful diagnostic tool. A disadvantage is that it is not sufficiently radio-opaque in finer structures. In artificial heart and circulatory assist devices, the materials are used both in the mechanical components of the pump and as a blood-contacting surface. Artificial hearts made entirely of Ti have, in general, not been very successful, clinically, mainly due to problems with blood-clotting occurring on the device surface (Rintoul et al., 1993).

Many types of prosthetic heart valves have been used clinically. The ring and struts are made of Ti or its alloys while the disk is made of pyrolytic C. Around the ring is a sewing ring made of knitted Teflon (PTFE) cloth, where the sutures anchoring the prosthesis to the heart are placed. The metals in the prosthetic heart valves are often coated with a thin C film to enhance blood compatibility. At present, stents (Fig. 8.4) are commonly used in the treatment of cardiovascular disease. They dilate and keep narrowed blood vessels open. Stents are usually mounted on balloon catheters or folded inside special delivery catheters. TiNi alloy is one of the most common materials used in vascular stents due to its special shape memory effects. Because of inevitable damage to the vessel wall in connection with placement of the stent and possible rejection by the body, there is always a risk of thrombotic occlusion of the stented vessel segment. Therefore, it is necessary to improve the antithrombogenic properties of stents.

Commercially pure Ti and Ti alloys are preferred for dental and orthopedic implants or prostheses because of their corrosion resistance, biocompatibility, durability, and strength. However, being bioinert, the integration of such implants in bone was not good. To achieve improved osseointegration, there have been many efforts to modify the composition and topography of the implant surface. Recently, the anodic oxidation treatment of Ti has attracted a great deal of attention (Ogden, 1961; Collings, 1984; Polmear, 1981; Bania, 1993; Schutz, 1993). Park et al. reported that an anodized Ti implant appeared to have higher removal torque values and higher percentages in both the bone-to-implant contact and the bone area in the threads than the machined implant (Collings, 1984). Meanwhile, calcium phosphate is commonly applied to metallic implants as a coating material for fast fixation and firm implant-bone attachment on account of its demonstrated bioactive and

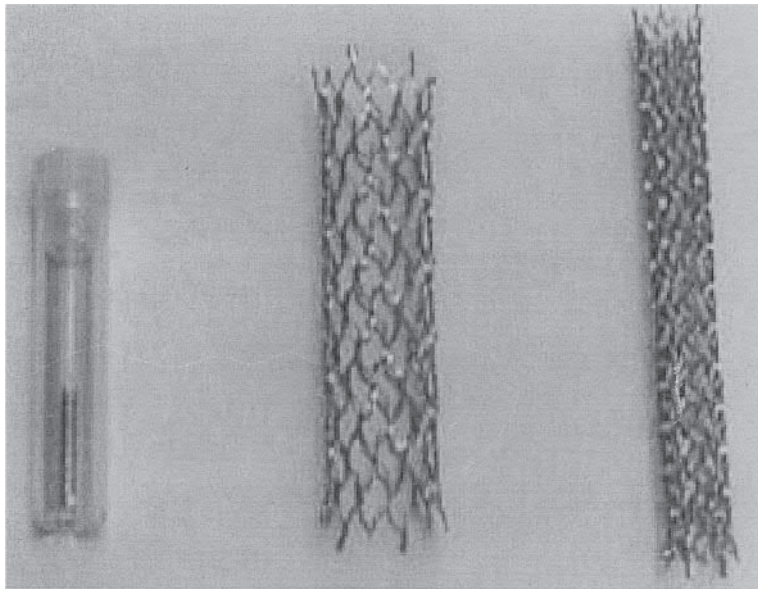


Fig. 8.4 Stents commonly used in the treatment of cardiovascular disease.

osteoconductive properties. Recently, various Ca/P ratios of thin calcium phosphate films were formed by electron beam evaporation: The films had an excellent bonding strength and showed different dissolution behaviors, depending on the calcium (Ca)/phosphorous (P) ratio (Morscher, 1995; Jones and Hungerford, 1987; Bobyn et al., 1980). Concerning the stability of the coatings, much effort has been devoted to determine the immersion behavior of calcium phosphate coatings in solutions with ionic composition similar to the inorganic fraction of blood plasma, such as phosphate buffered saline (PBS) solution, Hank's balanced salt solution (HBSS) (Howie, 1990; Jast, 1993), and Kokubo's simulated body fluid (SBF) (Jast, 1993; Long and Rack 1998). These in vitro studies are important as they could give some indication of the in vivo behavior of the coating. Especially, thin coating layers are of interest. Consequently, these tests are practiced as a first stage to assess the bioactivity of a potential biomaterial through the formation of a bonelike apatite layer (Rintoul et al., 1993; Williams, 2001; Textor et al., 2001). The addition of certain biologically active proteins with biomaterial will improve the bioactivity of the material. Some proteins and, in particular, growth factors, have been shown to be potent osteogenic inductors. Basic fibroblast growth factor (BFGF) is one of several well-characterized growth factors that has crucial properties in bone formation processes (Boehm, 1971). Therefore, the association of BFGF with carriers would be promising in orthopedic and dental fields. So far, different scaffolds including hydroxyapatite (HA), beta-tricalcium phosphate (β-TCP), and biodegradable polymers have been used as the carrier of BFGF (Schindler, 1990; Parfitt, 1976; Hendrich, 1985; Parks, 1965).

In a recent study (Cui et al., 2005), many methods for making a bioceramic coating and calcium phosphate deposition film with an excellent biocompatibility were tested on the surfaces of Ti and its alloy. Some of main methods used are introduced as follows.

8.4 Biocompatibility and fabrication of in situ synthesized bioceramic coatings on Ti alloys

8.4.1 *In situ synthesized potassium titanate/Ti alloys as biomedical materials*

Using an in situ dry mixed calcination synthetic method, Cui et al. (2003) prepared a $K_2Ti_6O_{13}$ coating layer with a heat expansion coefficient close to that of the matrix and a good mechanical character. Cui et al. (2003) used $TiAl_x$ Zr_y Sn_z Nb alloys as matrix materials and $K_2CO_3 + TiO_2$ as the original material for coating. The bonding of coating and matrix was improved in this study. Cui et al. (2005) studied the surface pattern, phase composition, bonding strength, and bioactivity of the coating. The Ti alloys were produced by vacuum induction smelting furnace or nonconsumable vacuum arc smelting furnace, respectively. The structure, composition, and property of the Ti alloys were analyzed. The matrix was badly contaminated by C and O in the graphite crucible or the CaO coating crucible. The contents of C and TiC particles were high in the Ti alloys. Using the CaO coating crucible reduced the C contamination of the Ti alloys. But the O contamination at high temperatures made it impossible to fabricate the Ti alloys with normal properties. Then the structural character of as-cast Ti alloy produced by the nonconsumable vacuum arc smelting furnace was studied. The effects of the addition alloying elements on the structure and the asymmetry law of the addition elements were also analyzed.

The processing technique of potassium titanate ($K_2O{\cdot}6TiO_2$) was established in the author's laboratory. Effects of K_2CO_3/TiO_2 ratio and reaction temperature on the growth of the $K_2O{\cdot}6TiO_2$ whisker were analyzed. The results showed that: when the K_2CO_3/TiO_2 ratio was about 1:5.5–1:6, a high quality and high productivity potassium titanate whisker was synthesized by the calcination method at applicable reaction temperatures. The diameter of the whisker was about 0.1–0.3 μm and the length to diameter ratio was about 100–200. According to the processing technique of the whisker, potassium titanate coating was synthesized in situ on the surface of the Ti alloy. The coating was made up of potassium titanate whiskers in an orientation perpendicular to the surface of the matrix. The coating thickness was about 2–3 μm. The action of the surface oxidized layer on the surface of the matrix in the in situ synthesis reaction was also studied. The effect of the reaction was that solid and liquid were the main phases and the gas phase escaped synchronously with the potassium titanate whisker's growth in orientation.

Surface micropore Ti had been fabricated, based on the principle that the growth stress and thermal stress between the high-temperature oxidized layer and the base material resulted in a physical lamination, which was surface bio-activated through

an acid-alkali two-step method, followed by the formation and surface bio-activation reaction of the micropore Ti. It was indicated that the orientation and shape of the micropore was related to the structure of the matrix and that a gel film was formed on the surface after the bio-activation treatment. It was found that the deposition layer, after simulation body fluid (SBF) solution cultivation, was composed of honey-*comb*-liked polygonal cell-shaped elements, which were constructed of randomly arranged graticule-like nanometer loops with a Ca to P atomic ratio, (Ca)/(P) of 1.61:1, akin to that of HA and human bones. An analysis of the deposition mechanics suggested that the deposition of Ca and P in the liquid phase was attributed to the bioactivity of the micropore Ti surface and the ion over-saturation environment of the SBF solution.

The biological activity of the $K_2O{\cdot}6TiO_2$ coating is closely related to its specific structure and physicochemical properties, as was discovered in the research. It should be noted that the activated TiO_2 surface can physically and chemically adsorb a quantity of OH and H_2O to form Ti-OH on the surface; and that it also can act as the bioactive base for apatite heterogeneous nucleation under biological conditions, when the pores in the coating can accelerate the diffusion of the organic small molecules through the oxide networks at room temperature to form strong chemical bonds with their functional groups. For example, organic small molecules containing COOH, OH, NH_2, C═O, or phosphoric acid functional groups can be fixed in this processing. Therefore, the excellent biological activity of $K_2O{\cdot}6TiO_2$ coatings is mainly attributed to their major ingredient TiO_2. Additionally, the $K_2O{\cdot}6TiO_2$ possesses excellent water compatibility, is stable under certain acid-alkali conditions, and its dispersion pH value in water is comparable to that of SBF. Therefore, $K_2O{\cdot}6TiO_2$ will influence the body fluid environment less in implants. Therefore, the application of $K_2O{\cdot}6TiO_2$ bioactive coatings in clinical implants and reparations is viable.

An SBF cultivation experiment was used to evaluate the biological activity of $K_2O{\cdot}6TiO_2$ functional coating. The surface properties, together with the influence of the tunnel structure of $K_2O{\cdot}6TiO_2$ crystal's ability to induce Ca/P to deposit in the liquid phase, was examined in our studies. The discovery of phenomena of the molecule self-assembling Ca/P nanometer whiskers on the $K_2O{\cdot}6TiO_2$ functional coating during SBF cultivation was very rewarding. During research on the low-temperature deformation of in situ Ti-matrix composite materials, it was found that there were the textures of $\{10\bar{1}0\}\langle 11\bar{2}0\rangle$ and $(0002) < 11\bar{2}0 >$. When deformation occurred at higher temperature, multislip systems were operating and, moreover, the texture $\{11\bar{2}1\}$ appeared. When the temperature was higher than the recrystallization temperature, the texture was obscured.

8.4.2 Fabrication and biocompatibility of nano-TiO_2/Ti alloys as biomedical materials

As biomedical materials, Ti and its alloys are superior to many materials such as stainless steel, pyrolytic C, and so on, in terms of mechanical properties and biocompatibility. However, the biocompatibility of Ti and its alloys is still not sufficient for prolonged clinical use. Hence, the development of surface modification is a necessity

for the biomedical community. Ti with a biocompatible coating such as HA has been successfully studied in recent years (Kamitakahara et al., 2003; Rønold and Ellingsen, 2002; Wang et al., 1993; Klein et al., 1994; Tsui et al., 1998; Korkusuz and Uluoglu, 1999). Ti alloys are used for dental and orthopedic implants for their superior compatibility, which is attributed to the oxide film formed on their surface (Kamitakahara et al., 2003; Rønold and Ellingsen, 2002). Surface modification recently became active in the field of implants, such as hydroxyapatite coating by plasma spraying or electrophoretic deposition (Wang et al., 1993; Klein et al., 1994; Tsui et al., 1998), electrochemical deposition of Ca phosphates, basification treatment, sol-gel and anodized dielectric film (Korkusuz et al., 1999; Wang et al., 1993; Haman et al., 1995; Kyeck and Remer, 1999; Singh et al., 1996; Ong et al., 1991; Dasarathy et al., 1996; Wolke et al., 1994; Yamashita et al., 1996; Montenero et al., 2000; Haddow et al., 1998; Jillavenkatesa and Condrate Sr, 1998; Hero et al., 1994). In this research, nanometer Ti dioxide powder was adopted as the raw material to embed Ti alloys and sinter. In this way, a new biomaterial, a nano-TiO_2 biocompatible coating on the surface of Ti alloys, was fabricated successfully. The method is a simple and adaptable technique for surface modification of Ti alloys.

Ti-2Zr-2Nb alloy ingots were made in a 25 kg vacuum induction furnace by melting and casting. The ingots were machined into many specimens with a size of 20 mm × 20 mm × 8 mm. Before sintering, specimens were polished and then rinsed with distilled water and acetone, subsequently degreased with hydrofluoric acid (5%), washed with absolute alcohol, and dried. Nanometer Ti dioxide powders were prepared by hydrolysis of Ti-tetrabutoxide with ethanol. The particle size of TiO2 powder in the anatase structure was generally between 5 and 10 nm (Fig. 8.5). Ti alloy specimens were embedded in nanometer TiO_2 powders, sintered at 600°C for 1 h, and annealed at 500°C for 6 h.

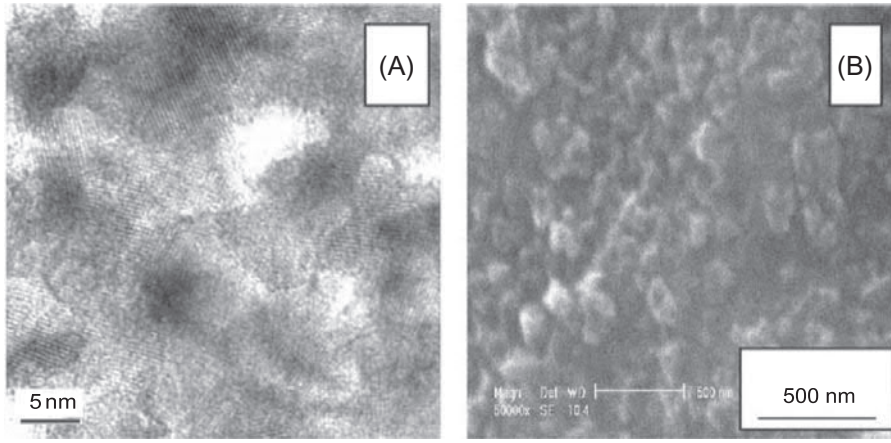


Fig. 8.5 (A) HREM image and (B) SEM micrograph of nano-TiO_2 synthesized particles.

The preparation of the nano-TiO_2/Ti dioxide, powders by hydrolysis of Ti-tetrabutoxide with ethanol included two processes: hydrolyzation and aggregation. Under favorable conditions, the exchanges take place as follows:

$$Ti(OC_4H_9)_4 + 4H_2O = Ti(OH)_4 + 4C_4H_9OH \quad (8.1)$$

$$Ti(OH)_4 = TiO_2(s) + 2H_2O \quad (8.2)$$

The Ti dioxide powder was examined by X-ray diffraction and TEM, and the result showed that the particle size was mainly between 5 and 10 nm. Using this kind of nanometer Ti dioxide powders, Ti alloy specimens were clad with TiO_2 and sintered at temperatures from 500°C to 950°C for 1 h (the temperature interval was 50°C). When the sintering temperature was low, such as at around 500°C, the oxide film was too thin to form a coating; when the temperature was high (800°C), the TiO_2 particles tended to grow, so the coating was not of a nanometer structure. The optimal sintering temperature was fixed at 600°C for 1 h.

The microstructure of the surface of the sintered specimen was examined with a Philips Tacnai F20 high resolution transmission microscopy (HREM) and Philips XL30 TMP scanning electron microscopy (SEM). X-ray diffraction (XRD) with the high-low temperature appurtenance was used to study the phase composition of the sintered coating on the surface of the Ti alloy. The specimens were cultivated in SBF to test biocompatibility and bioactivity. Measurements of ion consistency of SBF and blood plasma were also performed with an XD685 electrolyte analyzing system. Table 8.2 gives the ion consistency of the SBF and blood plasma.

Fig. 8.5 shows a high-resolution electron microscopy (HREM) (Fig. 8.5A) and a scanning electron microscopy (SEM) (Fig. 8.5B) image of the synthesized nano-TiO_2 particles of the coating. It is indicated by Fig. 8.5A that the particle diameter of TiO_2 particles is about 50–90 nm. The oxide film is a very thin (<10 μm) anatase-type TiO_2 (analyzed by XRD, as shown in Fig. 8.6). The Ti surface is oxidized easily in the air when the temperature is <500°C. Because of the Ti dioxide powder on the surface, the noncrystal layer grows more easily by the diffusion of O. There is a very thin TiO_2 film with a thickness of 3–5 nm on the surface of the Ti alloy before the nanometer TiO_2 powder coating is formed, and this thin TiO_2 film belongs to the two-dimension nanometer material. The interface between this thin TiO_2 film and the embedded nanometer TiO_2 particles can disappear because both grow a larger crystal

Table 8.2 Ion consistency of simulated body fluid and blood plasma

	Na^+	K^+	Ca^{2+}	Mg^{2+}	HCO_3^-	Cl^-	HPO_4^{2-}	SO_4^{2-}
Blood plasma	142.0	5.0	2.5	1.5	27.0	103.0	1.0	0.5
SBF	142.0	5.0	2.5	1.5	4.2	148.5	1.0	0.5

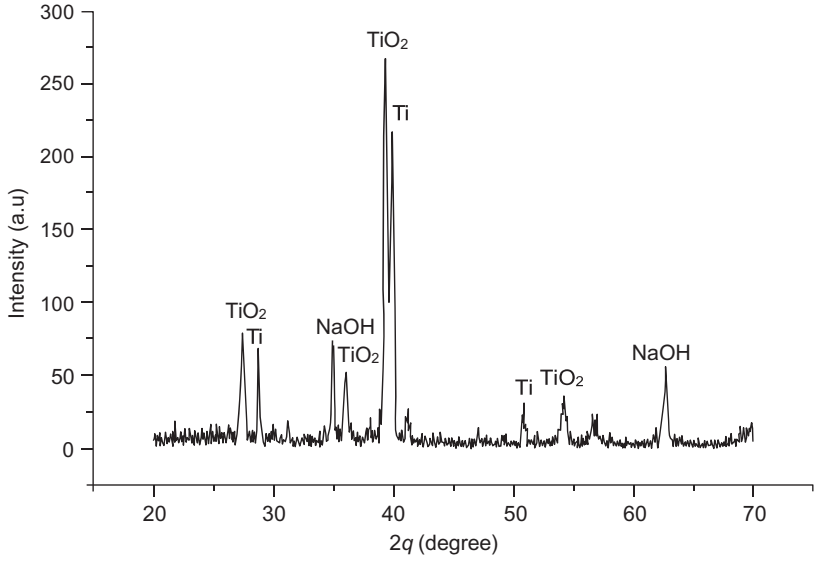


Fig. 8.6 XRD pattern of nanometer TiO_2 coating.

grain with a thickness of 50–90 nm during the sintering processing. So, the coating and substrate are well knit. At the same time, the temperature is not high and this can prevent particles from growing. However, the particle size will be 4–6 μm if the specimens are enwrapped by ordinary commercial Ti dioxide powders.

Theoretically speaking, nanometer materials possess much better characteristics than ordinary materials. To test the biocompatibility of nano-TiO_2/Ti alloys, we dipped the materials in SBF to cultivate the Ca/P layer, and Table 8.2 shows the ion consistency of SBF and blood plasma. After seven days, the specimens were taken out of the SBF, washed, and the surface morphology observed (Fig. 8.7). From Fig. 8.7

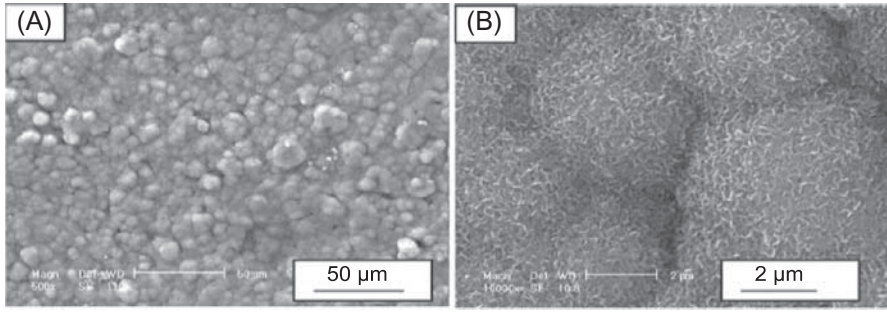


Fig. 8.7 Surface morphology of nanometer TiO_2 coating after immersion in SBF for seven days and annealed under vacuum at 500°C for 6 h: SEM micrographs of (A) low-fold and (B) high-fold amplifications.

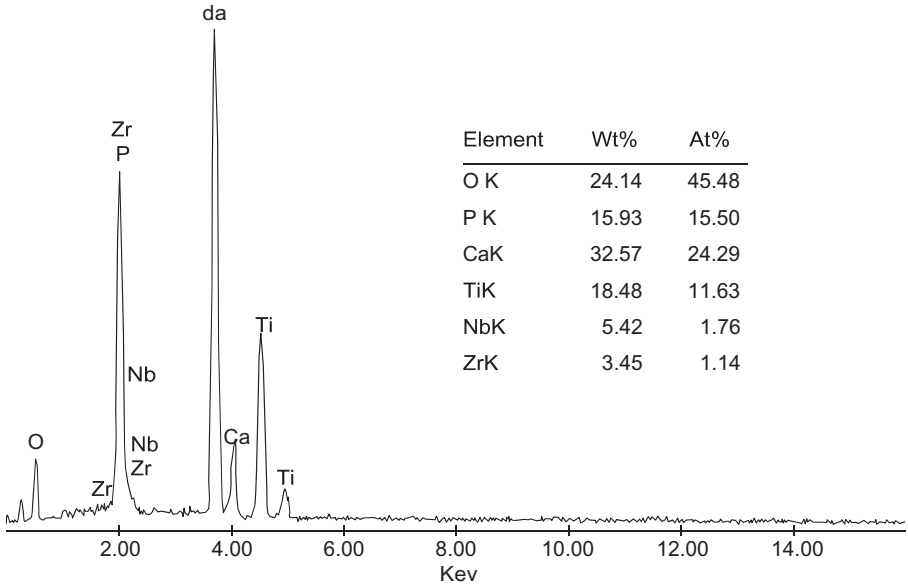


Fig. 8.8 Element analysis of EDS for the layer of nanometerTiO_2.

we can see that the Ca phosphates were deposited on the surface of specimens. The Ca/P deposition layer consisted of cystiform polygons made up with irregular nanometer circles, similar to honeycomb. The energy spectrum (Fig. 8.8) shows that the Ca/P atomic ratio is about 1.6:1, which is very similar to that of HA and human bone. It can be concluded that nanometer TiO_2/Ti alloys possesses favorable biocompatibility.

The presence of the significant interface between nano-TiO_2 particles and the Ti alloy matrix represents excellent biocompatibility and bioactivity. So, Ca phosphates can be easily deposited on the surface of nano-TiO_2 particles. Since TiO_2 is a ceramic phase with a high melting temperature, the interface of nano-TiO_2/Ti alloys is very stable at room temperature and elevated temperatures. Analogous to the tailoring of these films through control of pH and electrochemical cell potential (Kilpadi et al., 1998; Ask et al., 1988–1989; Pham et al., 1997), the interaction between nano-TiO_2 particles and the Ti matrix during annealing causes variations in the stable oxide forms. Previous studies have specifically noted the potential toxicological benefits of low V oxide content of Ti implant materials (Kilpadi et al., 1998; Ask et al., 1988–1989), and hence the impact of the oxides evolved during heat treatment and the related topic of diffusive behavior deserve significant attention.

Phase transformations occurring in TiO_2 particles and Ti alloy are independent of both the crystal lattice and the physical, chemical, and mechanical properties. Formation of the oxide phases of other elements such as Zr and Nb diffused into Ti requires the removal of the outer layers from cast and forged Ti products following annealing treatments, which is very difficult, so the oxides of Zr and Nb cannot be found by

XRD, as shown in Fig. 8.6. Based on physical metallurgy, Zr and Nb existing in the solid solution state can prevent severe decrease in fatigue and fracture resistance (Donachie, 1998). Taken independently, the results suggest that heat treatment under vacuum eliminates the formation of oxides for other elements in Ti alloys at the interface; however, the desired biomaterial structure has no pure nano-TiO_2 particles on the surface of the Ti alloy. Therefore, the nano-TiO_2/Ti alloy biomedical material can be fabricated using the process whereby Ti alloys are embedded by nanometer Ti dioxide powders and sintered in the high temperature furnace. TEM observation has indicated that the particle size of TiO_2 is mainly 50 –90 nm. The coating layer prepared by nanometer Ti oxide powders possesses excellent biocompatibility. It is indicated by cultivation tests in SBF that Ca phosphates are deposited on the specimen surface, and the Ca/P atomic ratio is about 1.6:1, which is similar to that of HA and human bone.

8.4.3 Fabrication mechanism and characteristics of surface micro-porous Ti as biomaterials

This section deals with the chemical fabrication technique of surface micro-porous Ti. The pure Ti clad with potassium titanate whiskers was calcined for a short time, then rapidly cooled, and then the surface micro-porous Ti was achieved. The degree of surface roughness of the Ti samples was about 3–5 μm, and this kind of surface micro-porous Ti can be used as an excellent implanting biomaterial with good biocompatibility and bioactivity. The surface microstructure of the micro-porous Ti was observed and analyzed using SEM, EDS, XPS, and XRD, and the chemical formation mechanism of the surface micro-porous Ti biomaterial has been discussed in this chapter.

As hard-tissue implants, Ti matrix biomaterials are some of the first selected among all metal materials. Although Ti and its alloys have excellent biocompatibility and mechanical properties, their surfaces are still bio-inert. At present, the surface modification has become a main research field of Ti matrix biomedical materials to improve further matrix materials' biocompatibility and bioactivity (Cui et al., 2003; David and Buddy, 2002). Hydroxyapatite (HA), as a kind of bioactive coating material, has been widely studied; implants with plasma spray HA coating have been used in clinical orthopedics (Brown et al., 1994; McPherson et al., 1995; Cheang and Khor, 1996). Because of its low bonding strength between coating and matrix, the HA coatings often peel off from the matrix, which leads to a failure of the implants.

In order to increase the bonding strength at the interface of bioactive coating/matrix, surface micro-porous Ti was prepared by in situ reaction processing. For the fabrication process, pure Ti clad with potassium titanate whiskers was calcined for a short time; this kind of surface can combine firmly with the bioactive coating. The surface, micro-porous with a homogeneous distribution of micro-apertures, is obviously different from those morphologies obtained by other modification technologies. This fabrication process has several merits, such as low cost, simple fabrication processing, and short preparation cycle.

The samples of surface micro-porous Ti were made in three steps, as follows;

(i) The first step was the preparation of the samples and their pretreatment. The sponge Ti as raw material was melted and cast into pure Ti ingots in the nonself-waste vacuum electrical arc furnace, and the ingots forged into bar shapes. The forged Ti bars were machined into 10 mm × 10 mm × 2 mm experimental samples using a SPARK FW1 electric spark line incising machine. Then the samples were burnished using a series of sand papers, such as No. 280, No. 400, No. 600, and cleaned in acetone by an ultrasonic cleaner for 15 min. Then these samples were eroded in 10% HF liquid for a short time. Finally, they were placed into distilled water to be ultrasonically cleaned.

(ii) The second step was selecting potassium titanate whiskers with perfect length-diameter ratios as cladding powders.

(iii) The third step was embedding pure Ti samples in potassium titanate whisker powders that were mixed with acetone liquid; these were placed into a KSY12-16 program controlling furnace and heated at the rate of 5°C/min, sintered at 800–900°C for a short time, and finally cooled rapidly. A peeling layer can be wholly peeled off from the Ti matrix at the time the surface micro-porous Ti was obtained.

The microstructure of the surface micro-pores and of the peeling layer was examined with a Philips XL30 TMP scanning electron microscopy (SEM) and with an energy dispersive X-ray spectrometer (EDS). PHI 4300 X-ray photoelectron spectrum (XPS) and Philips X'pert TMD X-ray diffraction (XRD) were used to study the surface elements and the phase composition of the peeling layer.

Fig. 8.9A shows the cross-section microstructures of the titania oxided layer obtained by conventional physical delaminating of the oxide layer on the surface of a Ti matrix. It is clear that the titania layer is made up of two sublayers, which contain coarse grains of TiO_2 and fine grains of TiO_2. The layer of fine grains is between the Ti matrix and the coarse grains. Fig. 8.9B shows the surface morphology of the Ti matrix after the conventional physical delaminating. Compared with general oxidation delaminating of Ti (Fig. 8.9B), Fig. 8.10 shows various morphologies of the porous surface Ti. It is obvious that these surface structures are markedly different.

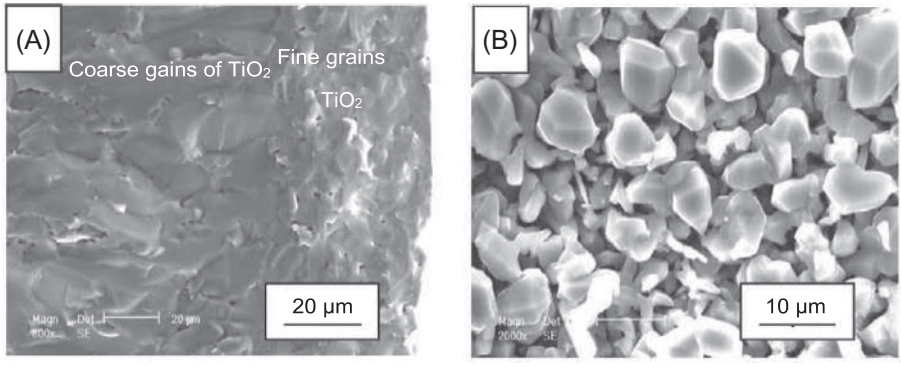


Fig. 8.9 SEM micrographs of titania layers after conventional physical delaminating: (A) cross-section and (B) surface morphology of titania.

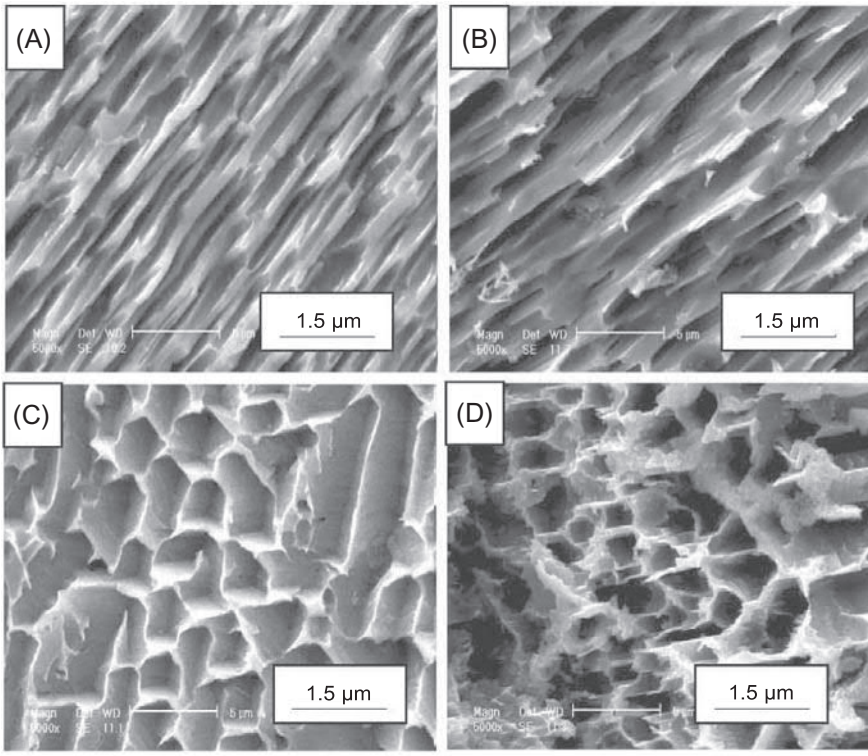


Fig. 8.10 Various morphologies of surfaces of porous surface Ti: (A) porous barrette surface, (B) porous sandwich surface, (C) porous pit surface, and (D) porous hollow surface.

Thus it can be seen that the cladding layer of potassium titanate whiskers and the peeling layer, together flake away from the Ti matrix after the pure Ti cladded with the potassium titanate whiskers has been calcined for a short time, and then rapidly cooled. Finally, a micro-porous structure on the surface of the Ti sample is obtained. The morphologies of the surface porous Ti were various with the change of parameters of processing, as shown in Fig. 8.10A–D.

In this study, it was found that the cross-section microstructures of the peeling layer that made the surface micro-porous Ti (Figs. 8.11 and 8.12) were also different from those of the titania layer after conventional physical delaminating (Fig. 8.9A). Besides coarse grain TiO_2 and fine grain TiO_2, a directional layer grew on the fine grain TiO_2 and a layer of black powder was synthesized between the directional growing layer and the Ti matrix.

Using XPS analysis (Fig. 8.13A), it was affirmed that the layer of black powder was TiO_2, because the Ti2p1 (binding energy) was 458.54 eV, which was near to 458.5 eV of TiO_2. As shown in Fig. 8.13B, the phase compositions of the interior of the peeling layer were analyzed by XRD. The results of the analysis indicated that the directional growing layer was composed of TiO_2, TiO, $KTi_8O_{16.5}$, $K_2Ti_8O_{17}$, and $K_2Ti_6O_{13}$.

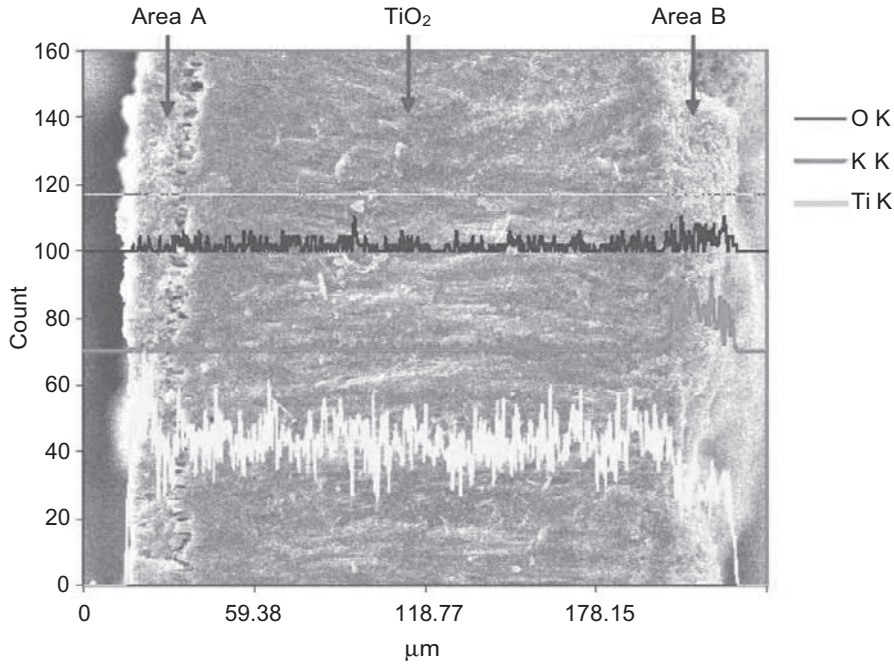


Fig. 8.11 SEM micrograph of cross-section and element linear distribution diagram of the peeling layer.

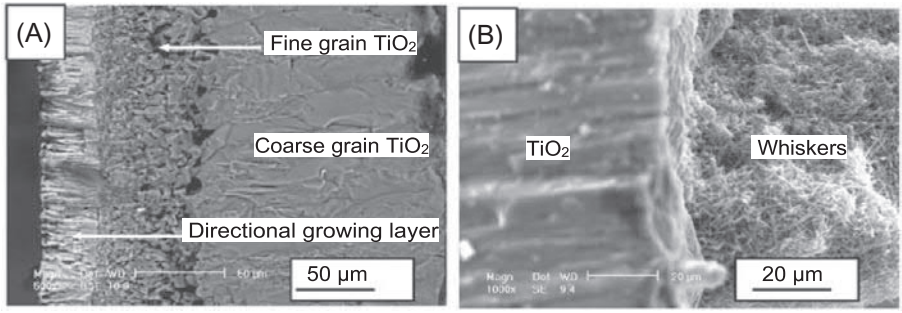


Fig. 8.12 High magnification SEM images of areas (A) A and (B) B in Fig. 8.11.

Based on an analysis of the microstructure of the peeling layer described above, it is possible to discuss the formation mechanism of the surface micro-porous Ti. The process of micro-porous Ti formation includes chemical and physical delaminating. A diffusion reaction results in chemical delaminating, and chemical delaminating is transformed into a physical delaminating during the processing where potassium titanate whiskers are calcined on the Ti matrix. Under the common action of growing

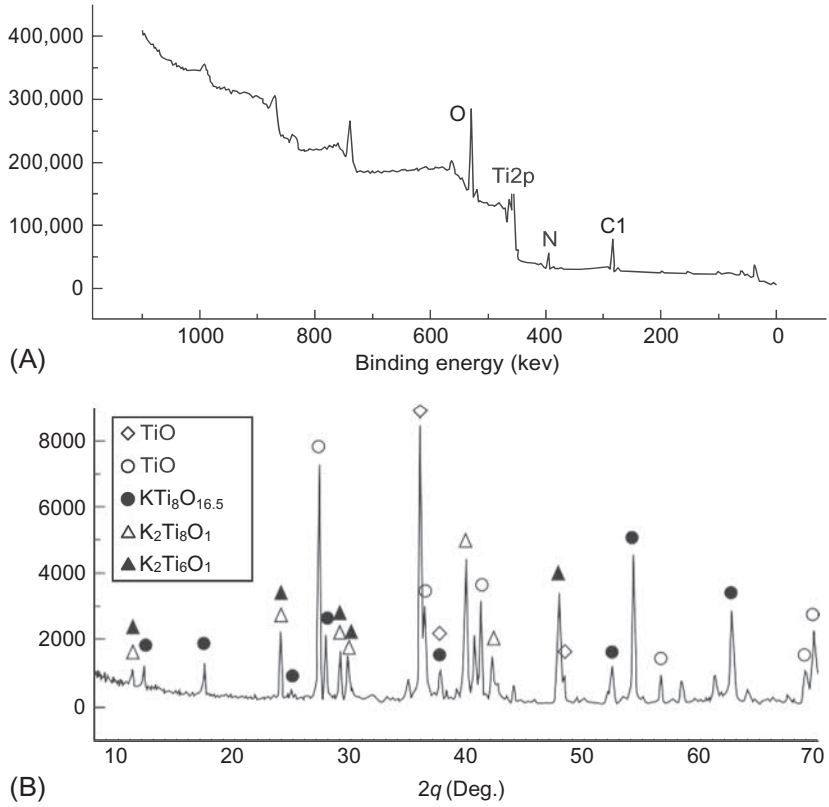


Fig. 8.13 (A) XPS and (B) XRD profiles of the peeling layer with black powders.

stress and heat stress on the interface between the reacted layer and Ti matrix, the exterior reacted layer is separated from the Ti matrix.

It is obvious that the cladding of potassium titanate whiskers has an intense effect on the substructures of the peeling layer.

During the process of heating, for Ti is an active metal, a thin layer of TiO_2 firstly forms on the surface of the Ti matrix. Along with an increase of temperature, the reactions of potassium titanate in the cladding powders and TiO_2 are as follows:

$$K_2Ti_6O_{13} + 2TiO_2 = K_2Ti_8O_{17} \tag{8.3}$$

$$(1/2)K_2Ti_6O_{13} + 5TiO_2 = KTi_8O_{16.5} \tag{8.4}$$

$$K_2Ti_4O_9 + 2TiO_2 = K_2Ti_6O_{13} \tag{8.5}$$

$K_2Ti_8O_{17}$, $KTi_8O_{16.5}$, $K_2Ti_6O_{13}$, and TiO_2 form a chemical delaminating. At the same time, the diffusion of Ti ions and O atoms continues at all times. During the diffusion of the ions in this system, the radius of the Ti ion is an important parameter. Here,

$R(Ti^{2+}) = 0.086$ nm, $R(Ti^{3+}) = 0.067$ nm, $R(Ti^{4+}) = 0.053$ nm, $R(K^{+}) = 0.133$ nm, $R(O^{-}) = 0.093$ nm, and $R(O^{2-}) = 0.21$ nm. Because the radii of metal ions are less than that of O atoms, the moving space of metal ions is bigger. Therefore, the TiO_2 formed during the in situ reaction grows on the outer surface of the front chemical delaminating. During the process of subsequent heat and preservation, $K_2Ti_8O_{17}$, $KTi_8O_{16.5}$, and $K_2Ti_6O_{13}$ whiskers grow up in virtue of outer TiO_2 and occur in directional growth between the TiO_2 and Ti matrix, which is consistent with references (Cui et al., 2005; Venezuela et al., 1999; Cahn, 2001; Currey, 2001; He and Antonelli, 2001). The thicker the outer TiO_2 is, the more difficult it is for the O atoms to diffuse in, so the entering diffusing O atoms and the Ti ions diffusing out are transformed into Ti-rich oxide (TiO) among the $K_2Ti_8O_{17}$, $KTi_8O_{16.5}$, $K_2Ti_6O_{13}$, and TiO_2. Furthermore, we find that the interface between the fine grain TiO_2 and the directional growing layer is distinct and bonding firmly, as shown in Fig. 8.12A. This is because the fine grain TiO_2 takes part in the reaction to synthesize potassium titanate whiskers. Noticeably, a thin layer of black TiO_2 powder comes into being between the Ti matrix and the directional growing layer, but the formation of this layer of black powder still needs to be further investigated. Due to the uncompacted black powder, the bonding force between the directional growing layer and the Ti matrix is less than that between the fine grain TiO_2 and coarse grain TiO_2 (Tierney and Kim, 1993; Velev et al., 1999; Jiang et al., 2001; Erlebacher et al., 2001; Bukaluk, 2001; Qu et al., 2001), which leads to a physical delaminating on the interface of the former. So, the microcosmic characters of the surface micro-pores are directly determined by the morphology and size of the potassium titanate whiskers in the directional growing layer. Therefore, the potassium titanate whiskers cladding the pure Ti have a great effect on the substructure of the peeling layer, which is different from that of the titania layer after conventional chemical and physical delaminating (Liang and Zhou, 2003; Koubo and Takadama, 2006; Sul and Johansson, 2001; Xuebin and Chuanxian, 2000; Cui et al., 2005; Bu and Cui, 2007). The phase composition of the directional growth layer on the surface microporous Ti is made up of $K_2Ti_8O_{17}$, $KTi_8O_{16.5}$, $K_2Ti_6O_{13}$, and TiO_2.

8.4.4 Fabrication and biocompatibility of nano-$K_2(Ti_8O_{17})/TiO_2$ bioceramic composite coating on the surface of Ti

A $K_2(Ti_8O_{17})/TiO_2$ composite bioceramic coating on the surface of Ti was prepared successfully using an in situ electrochemical technique. During immersion in a simulated body liquid, the surface morphology, microstructure, composition-of-phases, and bioactivity of the coating were evaluated. The test results indicated that the $K_2(Ti_8O_{17})/TiO_2$ bioceramic composite coating had good biocompatibility and bioactivity.

As biomedical materials, Ti and its alloys are superior to many other materials in several attributes, including biocompatibility and corrosion resistance, and have mechanical properties similar to those of bone. So, they have broad application in hard tissue repair and replacement. However, Ti and its alloys are bio-inert because of the compact passivation layer on the surface. This means that the Ca and P cannot be

deposited on the surface after implantation in bodies, and the combination between the implant and the bone is only mechanical. But the surface bioactivity can be improved by surface treatment. After the treatment, a bioactive layer can be formed on the surface of Ti and its alloys. The common methods can be classified in physics, chemistry, and electrochemistry. Each method has its advantages and disadvantages. Compared to the physical method, the chemical method operates easily and can form a homogeneous layer. But its efficiency is low (Liang and Zhou, 2003). The electrochemical method not only has the advantages of the chemical method but also a high efficiency.

In this research, we fabricated a $K_2(Ti_8O_{17})/TiO_2$ composite bioceramic coating on a Ti surface using the electrochemical method, and the surface topography, microstructure, composition-of-phases, and the bioactivity of the coating were analyzed and evaluated.

The pure Ti was machined into many specimens with a size of 10 mm × 10 mm × 1 mm. Then the specimens were milled using sand paper with screen mesh 240, 400, and 600 ordinally, and rinsed with acetone, absolute alcohol and distilled water, and subsequently dried. The specimens were used as the electrodes, and 0.5 mol/L K_2CO_3 electrolyte was prepared. A voltage of 20 V was applied for 20 min. After this step a TiO_2 layer was formed on the surface of the anode. Then, the electrodes were put into 3 mol/L hot KOH electrolyte for 30 min and given a current density at 2 mA/cm^2. Finally the nano-$K_2(Ti_8O_{17})$ layer was synthesized in situ on the surface of the TiO_2 layer. In order to evaluate the bioactivity of the $K_2(Ti_8O_{17})$, the specimen was immersed in SBF (Koubo and Takadama, 2006). Using the Philips XL30W/TMP SEM, Edax Phoenix EDS, Philips Tecnai-F20 TEM, and Rigaku XRD, the surface topography, microstructure, and composition-of-phases of the surface coating were analyzed.

8.4.4.1 Nano-TiO_2 layer synthesized by anode oxidation on the surface of Ti matrix

After the first treatment in the K_2CO_3 electrolyte, a blue film was obtained on the anode. The thickness of the film was about 70 nm (Sul and Johansson, 2001). The SEM micrographs show that there were many even depressions. The TEM electron diffraction indicated the film was rutile TiO_2. From the structure and the misty diffraction ring shown in Fig. 8.14, we can conclude that the TiO_2 film was nano-structured and the crystal was not fine. In other words, the film on the surface of the Ti matrix was composed of nano-particles and was amorphous TiO_2.

The reaction at the anode/electrolyte interface is:

$$\mathrm{Ti} = \mathrm{Ti}^{4+} + 4\mathrm{e} \tag{8.6}$$

$$\begin{aligned}\mathrm{Ti}^{4+}(\mathrm{ox}) + 4\mathrm{H_2O}(\mathrm{aq}) &= \mathrm{Ti(OH)_4(ox)} + 2\mathrm{H_2} \\ &= \mathrm{TiO_{2-x}(OH)_{2x}} + (2-x)\mathrm{H_2O}\end{aligned} \tag{8.7}$$

After drying, the gelatinous $TiO_{2-x}(OH)_{2x}$ changed to TiO_2.

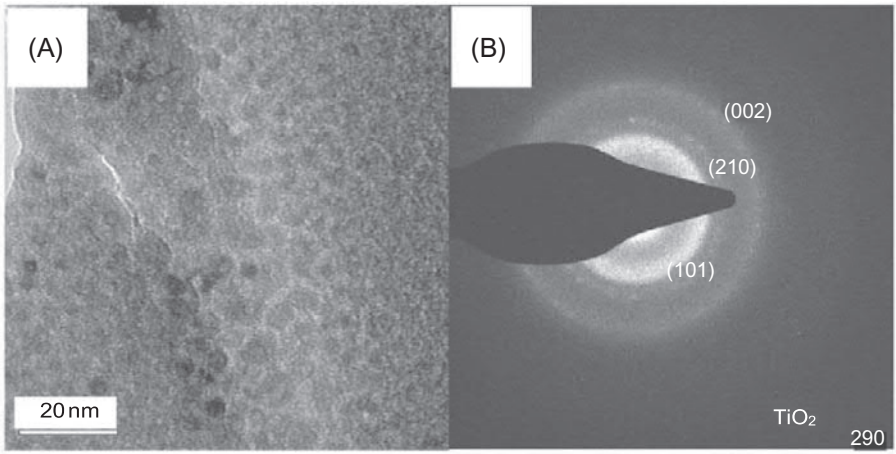


Fig. 8.14 (A) TEM micrograph and (B) diffraction pattern of TiO_2.

8.4.4.2 *Preparation by an in situ electrochemical technique*

At the second step, the electrodes were put into 3 mol/L hot KOH electrolyte for 30 min with a current density at 2 mA/cm^2. After that the new coating was observed and tested. Fig. 8.15 shows that after the treatment, a layer of $K_2(Ti_8O_{17})$ with a nanocrystalline grain appeared on the sample. The XRD result (Fig. 8.16) indicated that this film was even and simplex. Based on the observation of the diffraction halation in Fig. 8.14B and the diffraction peaks at small angles ($2\theta < 30°$), it can be inferred that some amorphous phases are present.

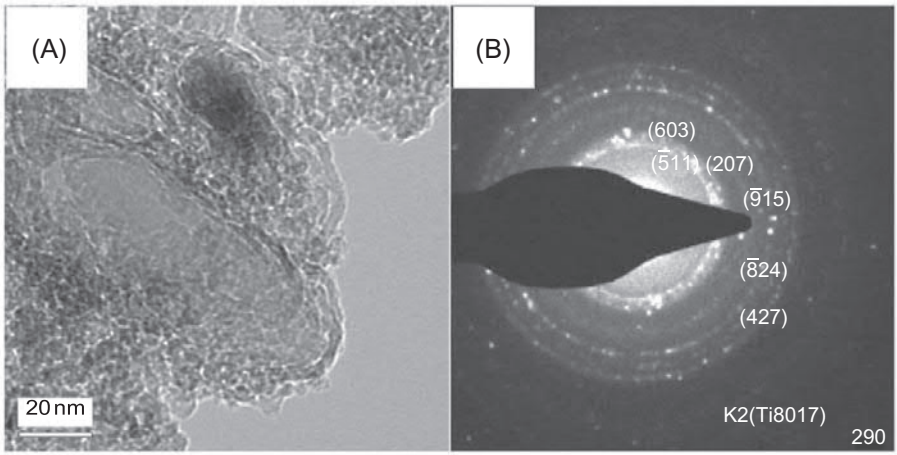


Fig. 8.15 (A) TEM micrograph and (B) diffraction pattern (B) of the surface structure after posttreatment.

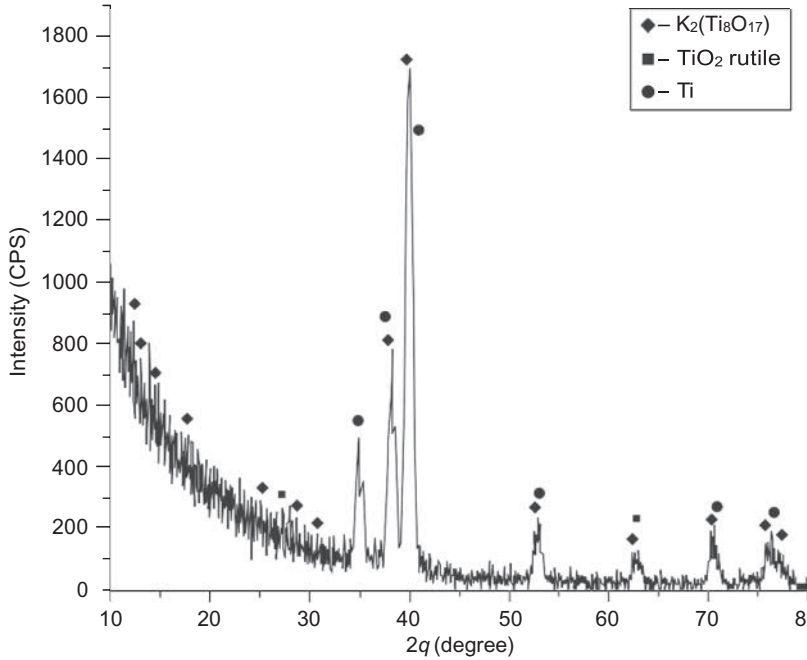


Fig. 8.16 XRD pattern of the surface coating after electrochemical treatment.

Fig. 8.17 shows the schematic structure of the double layer at the anode/electrolyte interface. The OH^- was concentrated near the anode. The TiO_2 formed in the first step reacted with the OH^-, so a gelatinous $Ti(OH)_4$ layer was obtained. Subsequently this united with K^+ and become $K_2Ti_8O_{17}$.

The electrode reaction is:

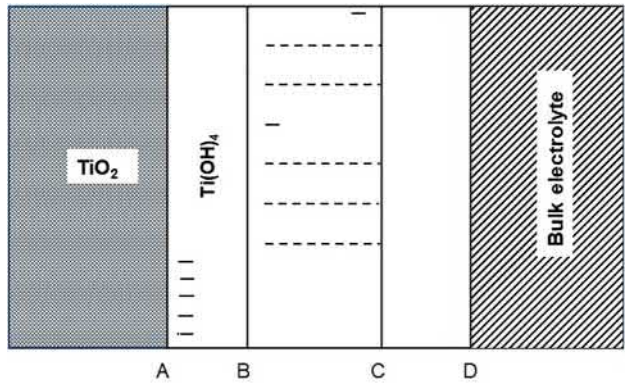
$$\text{Anode}: TiO_2 + 4\,OH^- = Ti(OH)_4 + O_2{}^{\uparrow} + 4e \tag{8.8}$$

$$\text{Cathode}: 2H^+ + 2e = H_2{}^{\uparrow} \tag{8.9}$$

Therefore, the total electrode reaction is:

$$8TiO_2 + 6OH^- + 4H^+ + 2K^+ = K_2Ti_8O_{17} + O_2{}^{\uparrow} + 2H_2{}^{\uparrow} + 3H_2O \tag{8.10}$$

Fig. 8.18 shows the SEM micrographs of the $K_2(Ti_8O_{17})$ coating surface. The appearance of this coating is an even and distinct reticular formation. The structure increased the roughness of the surface, and therefore the superficial area. All of these offered sites for bone growth. Thereby, the combination between implant and bone was enhanced.



A: $TiO_2/Ti(OH)_4$ interface
B-C: Defect layer of cations
C: Gradient line of concentration distribution
C-D: Balance layer of concentration distribution
+: K+
–: OH–

Fig. 8.17 Schematic structure of electrical double layer at anode/electrolyte interface.

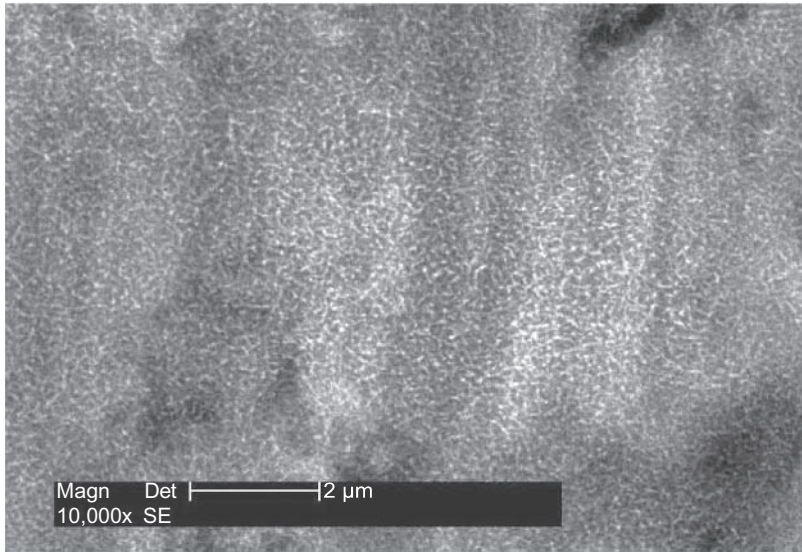


Fig. 8.18 SEM micrograph of $K_2(Ti_8O_{17})$ coating.

8.4.4.3 SBF cultivation

In order to evaluate the bioactivity of the $K_2(Ti_8O_{17})/TiO_2$ composite coating, the samples were dipped in 36.5°C SBF for given periods. After three days, some flocculent sediments and some sheet phases (Fig. 8.19A) appeared on the coating. Seven

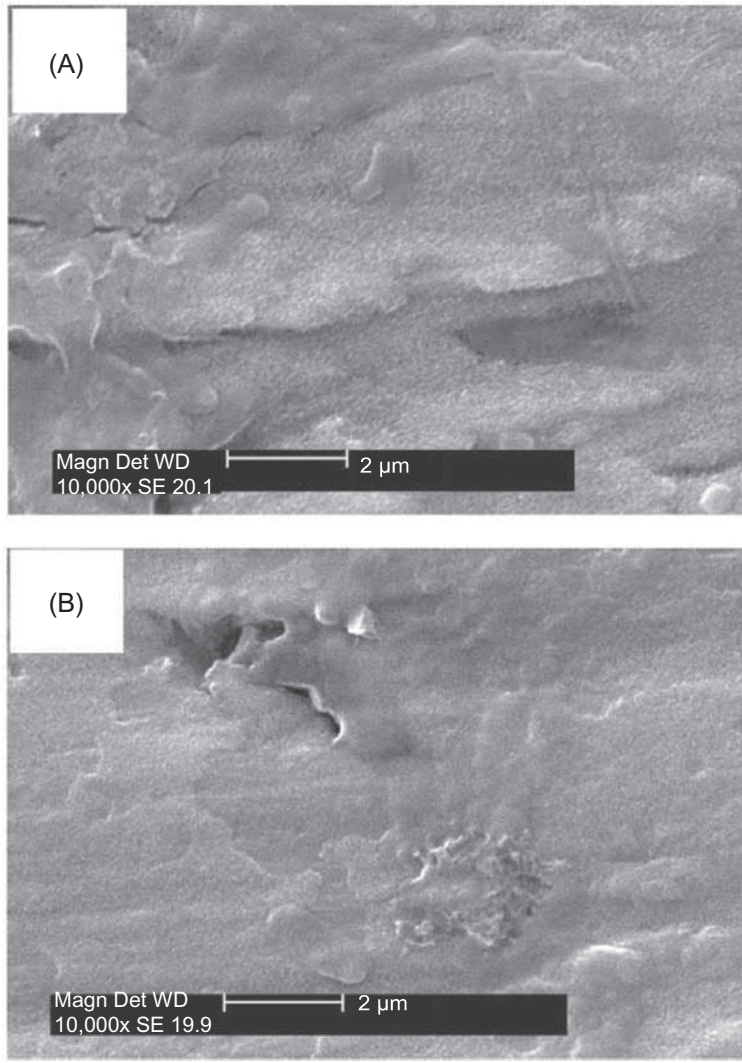


Fig. 8.19 SEM micrographs of surfaces of $K_2(Ti_8O_{17})$ coating dipped in SBF.

days later, there were more distinct changes. The clear reticular formation was covered completely by the sheet phases (Fig. 8.19B). The EDS result (Fig. 8.20) shows that the phase contained Ca, P, O and the ratio of Ca to P was about 1.67:1, which is similar to that of bones (Zheng and Ding, 2000).

The structure of $K_2(Ti_8O_{17})$ is shown in Fig. 8.21. In its structure, the coordination number of the Ti is six and the TiO_6 octahedrons connect with each other at the edge and the corner to form a concatenate tunnel structure. The K^+ is inside the tunnel isolating it from the environment so that it had no chemical activity. The TiO_6 became electronegative, so the Ca^{2+} was adsorbed by the Coulomb force and could attract the

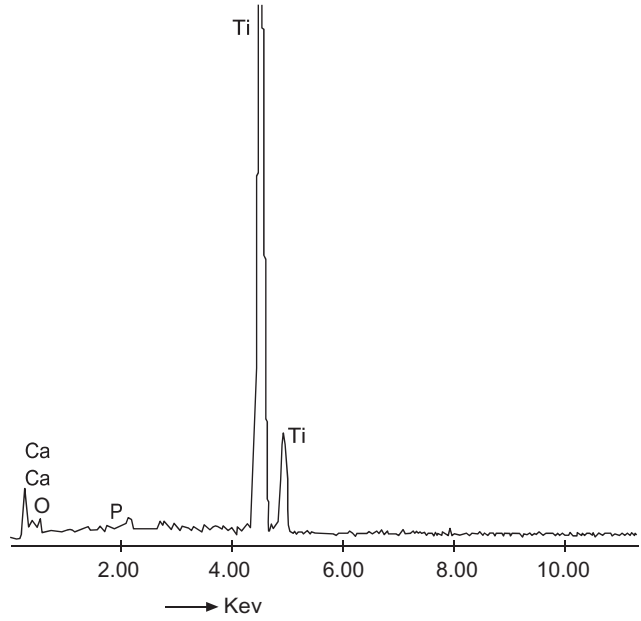
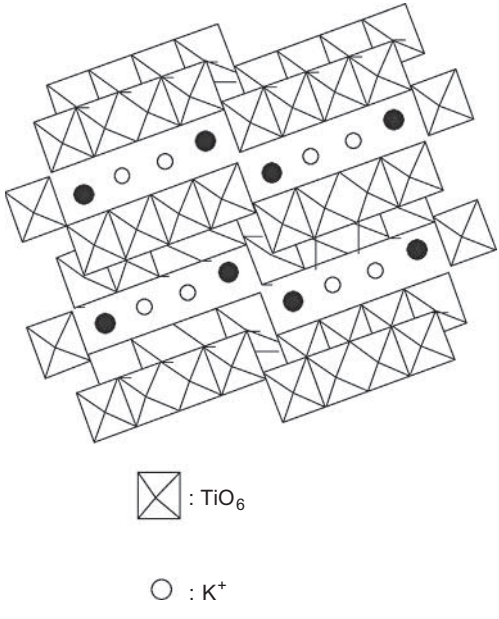


Fig. 8.20 EDX spectra of Ti samples dipped in SBF.

Fig. 8.21 Crystal structure of $K_2(Ti_8O_{17})$.



HPO_4^{2-}. Therefore the Ca and P were supersaturated near the surface and it was propitious to deposit the Ca and P. In addition, the reticular formation of the $K_2(Ti_8O_{17})$ increased the roughness, so that offered more nucleant points for the Ca and P sedimentation. The deposited layer appeared in a short time. This layer of Ca and P made the $K_2(Ti_8O_{17})$ coating better suited to stimulate the growth of bones and combine the bone with the implant—the coating has fine biocompatibility and bioactivity.

Therefore, a $K_2(Ti_8O_{17})/TiO_2$ bioceramic composite coating with a microstructure of nano-crystalline grain, amorphous on the surface, can be prepared successfully on Ti using an in situ electrochemical technique. The appearance of this composite coating is an even and distinct reticular formation. A layer of phosphate with a Ca/P ratio similar to that of bone was deposited on the surface after the SBF cultivation in a given time. The test of SBF cultivation indicated that the $K_2(Ti_8O_{17})/TiO_2$ bioceramic composite coating has adequate biocompatibility and bioactivity.

Acknowledgments

This work was supported by the programs of the Natural Science Foundation of China (Project No. 50271024), The Natural Science Foundation of Tianjin (Project No. 05YFZJC02200), and the Natural Science Foundation of Hebei Province (Project No. E2006000025).

References

Ask, M., Lausmaa, J., Kasemo, B., 1988–1989. Appl. Surf. Sci. 35, 283.
Bania, P.J., 1993. In: Eylon, D., Boyer, R.R., Koss, D.A. (Eds.), Titanium Alloys in the 1990s. The Mineral, Metals & Materials Society, Warrendale, PA, pp. 3–14.
Bobyn, J.D., Pilliar, R.M., Cameron, H.U., Weatherly, G.C., 1980. Clin. Orthop. 150, 263.
Boehm, H.P., 1971. Discuss. Faraday 52, 264.
Brown, S., Turner, J., Reiter, H., 1994. J. Mater. Sci. 5, 756.
Bu, S., Cui, C., Liu, X., Bai, L., 2007. J. Sol-Gel Sci. Technol. 43, 151.
Bukaluk, A., 2001. Appl. Surf. Sci. 175–176, 790.
Cahn, R.W., 2001. Nature 410, 643.
Cheang, P., Khor, K.A., 1996. Biomaterials 17, 537.
Collings, E.W., 1984. In: Gegel, H.L. (Ed.), The Physical Metallurgy of Titanium Alloys. ASM Series in Metal Processing, Edward Arnold Publications, Cleveland, Metals Park, OH.
Cui, C., Shen, Y., Xu, Y., Li, Y., Wang, R., Wang, X., Wang, C., 2003. Rare Met. Mater. Eng. 32, 627.
Cui, C., Liu, H., Li, Y., Sun, J., Wang, R., Liu, S., Greer, A.L., 2005. Mater. Lett. 59, 3144.
Currey, J., 2001. Nature 414, 699.
Dasarathy, H., Riley, C., Coble, H.D., Lacefield, W.R., Maybee, G., 1996. J. Biomed. Mater. Res. 31, 81.
David, G.C., Buddy, D.R., 2002. Surf. Sci. 500, 28.
Donachie, M.J., 1998. Titanium: A Technical Guide. American Society for Testing and Materials, Philadelphia, PA, pp. 29–34.
Dowson, D., Wright, V., 1981. In: Dowson, D., Wright, V. (Eds.), Introduction to the Biomechanics of Joints and Joint Replacement. Mechanical Engineering Publications, London.

Erlebacher, J., Aziz, M.J., Karma, A., Dimitrov, N., Sieradzki, K., 2001. Nature 410, 4.
Haddow, D.B., James, P.F., Van, N.R., 1998. J. Sol-Gel Sci. Technol. 13, 261.
Haman, J.D., Boulware, A.A., Lucas, L.C., Crawmer, D.E., 1995. J. Thermal Spray Technol. 4, 179.
He, X., Antonelli, D., 2001. Angew. Chem. Int. Ed. 41, 214.
Hendrich, V.E., 1985. Rep. Prog. Phys. 48, 1481.
Hero, H., Wie, L., Jorgensen, R.B., Ruyter, I.E., 1994. J. Biomed. Mater. Res. 28, 343.
Howie, D.W., 1990. In: Older, M.W.J. (Ed.), Implant-Bone Interface. Springer, London.
Jast, M., 1993. J. Appl. Biomater. 4, 273.
Jiang, P., Bertone, J.F., Colvin, V.L., 2001. Science 291, 453.
Jillavenkatesa, A., Condrate Sr, R.A., 1998. J. Mater. Sci. 33, 4111.
Jones, L.C., Hungerford, D.S., 1987. Clin. Orthop. 225, 192.
Kamitakahara, M., Kawashita, M., Miyata, N., Kokubo, T., Nakamura, T., 2003. Biomaterials. 24(1357).
Kilpadi, D.V., Raikar, G.N., Liu, J., Lemons, E., Vohra, Y., Gregory, J.C., 1998. J. Biomed. Mater. Res. 40, 646.
Klein, C.P.A.T., Wolke, J.G.C., de BlieckñHogervorst, J.M.A., de Groot, K., 1994. J. Biomed. Mater. Res. 28, 909.
Korkusuz, F., Uluoglu, O., 1999. Bull. Hosp. Jt Dis. 58, 86.
Koubo, T., Takadama, H., 2006. Biomaterials 27, 2907.
Kyeck, S., Remer, P., 1999. Mater. Sci. Forum 308 (311), 368.
Liang, F., Zhou, L., 2003. Rare Met. Mater. Eng. 32, 241.
Long, M., Rack, H.J., 1998. Biomaterials 19, 1621.
McPherson, R., Gane, N., Bastow, T., 1995. J. Mater. Sci. 6, 327.
Montenero, A., Gnappi, G., Ferrari, F., Cesari, M., Salvioli, E., Mattogno, L., Kaciuli, S., Fini, M., 2000. J. Mater. Sci. 35, 2791.
Morscher, E., 1995. Endoprosthetics. Springer, Berlin, Germany.
Ogden, H.R., 1961. In: Clifford, A.H. (Ed.), Rare Metals Handbook. Reinhold Publishing Corporation, Chapman & Hall Ltd., London, UK, pp. 559–579.
Ong, J.L., Harris, L.A., Lucas, L.C., Lacefield, W.R., Rigney, D., 1991. J. Am. Ceram. Soc. 74, 2301.
Parfitt, G.D., 1976. Progress in Surface and Membrane Science. vol. 11. Academic Press, New York, p. 181.
Parks, G.A., 1965. Chem. Rev. 65, 177.
Pham, M.T., Zyganow, I., Matz, W., Reuther, H., Ostwald, S., Richte, R.E., Wieser, E., 1997. Thin Solid Films 310, 251.
Polmear, J.J., 1981. Titanium alloys. In: Light Alloys. Edward Arnold Publications, London (Chapter 6).
Qu, H., Zhou, L., Wei, H., 2001. Chinese J. Nonferr. Metal. 11, 398.
Rintoul, T.C., Bulter, K.C., Thomas, D.C., Carriker, J.W., Maher, T.R., Kiraly, R.J., Massiello, A., Himely, S.C., Chen, J.F., Fukamachi, K., 1993. ASAIO J. 39, 168.
Rønold, H.J., Ellingsen, J.E., 2002. Biomaterials 23, 4211.
Schindler, P.W., 1990. Rev. Mineral. 23, 281.
Schutz, R.W., 1993. In: Eylon, D., Boyer, R.R., Koss, D.A. (Eds.), Beta Titanium Alloys in the 1990s. The Mineral, Metals & Materials Society, Warrendale, PA, pp. 75–91.
Singh, R.K., Qian, F., Damodaran, R., Moudgil, S., 1996. Mater. Manuf. Process. 11, 481.
Sul, Y.-T., Johansson, C.B., 2001. Med. Eng. Phys. 23, 329.
Textor, M., Sittig, C., Frauchiger, V., Tosatti, S., Brunette, D.M., 2001. In: Brunette, D.M., Tengvall, P., Textor, M., Thomsen, P. (Eds.), Titanium in Medicine. Springer, Berlin, Berlin, Germany, pp. 171–230.

Tierney, M.J., Kim, H.O.L., 1993. Anal. Chem. 65, 3435.
Tsui, Y.C., Doyle, C., Clyne, T.W., 1998. Biomaterials 19, 2031.
Velev, O.D., Tessier, P.M., Lenhoff, A.M., Kaler, E.W., 1999. Nature 140, 548.
Venezuela, J.P., Tersoff, J.A., Floro, E., Chason, D.M., 1999. Nature 397, 678.
Wang, B.C., Chang, E., Yang, C.Y., Tu, D., Tsai, C.H., 1993. Surf. Coat. Technol. 58, 107.
Williams, D.F., 2001. In: Brunette, D.M., Tengvall, P., Textor, M., Thomsen, P. (Eds.), Titanium in Medicine. Springer, Berlin, Germany, pp. 13–24.
Wolke, J.G.C., van Dijk, K., Schaeken, H.G., de Groot, K., Tansen, J.A., 1994. J. Biomed. Mater. Res. 28, 1477.
Xuebin, Z., Chuanxian, D., 2000. Plasma sprayed HA/ZrO_2 composite coating. J. Inorg. Mater. 15, 341.
Yamashita, K., Yagi, T., Umegaki, T., 1996. J. Am. Ceram. Soc. 79, 3313.

Biodegradable magnesium alloys

9

Amir Dehghanghadikolaei[*], *Hamdy Ibrahim*[†], *Amirhesam Amerinatanzi*[‡], *Mohammad Elahinia*[‡]

*School of Mechanical, Industrial and Manufacturing Engineering, Oregon State University, Corvallis, OR, United States, †Mechanical Engineering Department, The University of Tennessee at Chattanooga, Chattanooga, TN, United States, ‡Dynamic and Smart Systems Laboratory, Mechanical Industrial and Manufacturing Engineering Department, The University of Toledo, Toledo, OH, United States

9.1 Introduction

Magnesium (Mg) has a resorbable nature in the body, which means that its corrosion byproducts can be excreted or integrated through natural metabolic processes (Seitz et al., 2014). The biodegradation nature of Mg and its alloys makes them very attractive for various biomedical applications when the permanent existence of the biomedical device is not desired (e.g., bone fixation hardware and stents). For instance, a good alternative for the current stiff bone fixation hardware could be biodegradable fixation hardware made of an Mg alloy that provides the bone with sufficient support during the healing period and disappears gradually (Manivasagam and Suwas, 2014). In terms of Mg use for cardiovascular applications, transluminal technologies have developed a bioresorbable Mg-based vascular closure device called "Velox CD " that is CE-approved (Ibrahim et al., 2017a). Other bioresorbable Mg-based products and applications include ureteral stents (Lock et al., 2014) and coronary scaffold (Biotronik Dream) (Campos et al., 2013; New BIOTRONIK DREAMS, 2013). It should be mentioned that the history of bio-applications of Mg goes back more than a century ago, where Mg wires were used as a ligature for bleeding vessels (Witte, 2010).

Many polymeric biodegradable materials such as polyglycolic acid (PGA), poly-L-lactic acid (PLLA), thermoplastic starch, and polycaprolactone (PCL) have been introduced for bone fixation applications as they offer excellent biocompatibility, but their applications are mostly limited to low stress-bearing parts due to their low mechanical strength (Ibrahim et al., 2014, 2018a; Mehanny et al., 2012, 2016; Hermawan, 2012; Elsayed et al., 2012). From the metallic fixations, Mg alloys have recently been the center of attention thanks to their higher strength compared to biodegradable polymers, bioresorbability, biocompatibility, and low stiffness (close to the bone) (Seitz et al., 2014; Andani et al., 2014; Ibrahim et al., 2018b). Compared to titanium (Ti) and polymer fixations that are used clinically, Mg implants offer a higher osseointegration, bone-implant contact, and implant stability (Castellani et al., 2011; Tan et al., 2014). However, Mg suffers from many undesirable characteristics that prevent it from being the superior biodegradable fixation material.

Metals for Biomedical Devices. https://doi.org/10.1016/B978-0-08-102666-3.00009-2
© 2019 Elsevier Ltd. All rights reserved.

These deficiencies include low strength, fast degradation rate, and biocompatibility concerns of the Mg alloys after adding alloying elements in order to improve their mechanical and corrosion properties (Ibrahim et al., 2017a). Proper mechanical and corrosion properties could be designed by extensive studies involving both in vivo and in vitro tests along with finite element analysis (FEA) (Taljanovic et al., 2003; Nassiri et al., 2012). Other mechanical properties such as fatigue, creep, and stress relaxation are in the next order of importance and should also be considered. In addition, corrosion products would be released inside the human body and the proposed elemental ratio in Mg alloys should be in a way that does not exceed the permitted values of these products (Taljanovic et al., 2003; Sankara Narayanan et al., 2014). Biodegradable and metallic fixations that are patient-specified could reduce operating costs and time while providing better results in healing and treatment. Additive Manufacturing (AM) gives a high flexibility during the fabricating processes to control geometry, density, mechanical properties, and even corrosion properties of the resorbable fixation devices (Andani et al., 2014). To this end, suitable alloying, fabrication, and post-fabrication processes (i.e., casting, heat treatments, and coatings) are required. Once proper mechanical and corrosion characteristics are established in an alloy, enabling tools such as FEA can be used to design a biodegradable Mg-based device.

9.2 Mg alloys

Pure Mg has many advantages that qualify it as a biomaterial for various biomedical applications. However, pure Mg cannot satisfy all the clinical requirements for various biomedical applications such as internal fixation hardware. This can be attributed to its low mechanical strength and undesirable fast corrosion rates. Precipitate hardening, grain refinement, and solid solution strengthening are the main alloying methods that can be used to improve the mechanical and corrosion properties of Mg (Bamberger and Dehm, 2008). A significant variety of elements (aluminum (Al), zinc (Zn), calcium (Ca), zirconium (Zr), silicon (Si), and Rare Earth (RE) elements) could be added to form solid solutions with Mg. This wide range of alloying elements is due to the atomic diameter (0.320 nm) and the hexagonal-closed-packed (HCP) structure of Mg (Kirkland and Birbilis, 2014). Mg alloys have been extensively investigated in numerous studies for their microstructural, biocompatibility, corrosion, and mechanical properties, in vitro and in vivo. Mg-Ca, Mg-RE, Mg-Zn, and Mg-Zr are some of the most investigated Mg-based alloys (Bakhsheshi-Rad et al., 2014; Bornapour et al., 2014; Tan et al., 2013; Zhang et al., 2010a; Gu et al., 2009; Saha et al., 2015).

Alloying elements have different biocompatibility natures. As an example, Cd and Pb are known to be toxic elements alloyed with Mg but Ca, strontium (Sr), Zr, manganese (Mn), and Zn, alone or alloyed with Mg, are biocompatible (Kirkland et al., 2011; Li et al., 2008; Chen et al., 2014). Once considered safe, Al was found to cause allergic reactions and hepatotoxicity (Luckey and Venugopal, 1977; Domingo, 1995) with the potential of causing Alzheimers (Flaten, 2001). It may also cause muscle fiber damage (Cases, 2005). The same problem arose with the RE elements such as yttrium

(Y), as an alloying element, that was related to severe hepatoxicity (Bruce et al., 1963; Hirano et al., 1993). It is important to mention that the presence of impurities such as iron (Fe), nickel (Ni), beryllium (Be), and copper (Cu) inside the Mg matrix increases the corrosion rate of the alloy while deteriorating the strength of the Mg alloy (Lee et al., 2009; Poinern et al., 2012).

Mg-Ca, Mg-Zn, and Mg-Zn-Ca are some examples of Mg alloys made of nontoxic elements due to the nutritive nature of the Ca and Zn elements (Chen et al., 2014; Kirkland and Birbilis, 2014). For instance, Mg-Ca has low cost, low density (1.55 g/cm^3), and the added benefit of released Mg and Ca ions during bone healing. This has made Mg-Ca suitable for orthopedic fixation applications (Chen et al., 2014). Furthermore, Ca strengthens the Mg alloy and refines the grain structure (Kirkland and Birbilis, 2014). Also, based on in vitro and in vivo studies, Mg-Ca has shown formation of a mixture of $Mg(OH)_2$ and hydroxyapatite on Mg-Ca parts followed by formation of bone on this surface after 3 months of implantation (Li et al., 2008). However, uncoated Mg-Ca bone fixations are vulnerable to the physiological environment and degrade quickly (Tan et al., 2013). Li et al. reported a corrosion resistance enhancement by decreasing the proportion of Mg_2Ca in the alloy (Li et al., 2008). As a result, the Mg-Ca alloys with >1 wt% Ca do not perform adequately in the physiological conditions, i.e., it degrades rapidly and the amount of released Ca content surpasses the permitted values (Li et al., 2008; Kirkland and Birbilis, 2014). On the other hand, Zn is involved in cellular metabolism and supports the immune system of the human body (Zhang et al., 2010a; Witte et al., 2008). Due to Mg-Zn intermetallic compound formation and refining the grain size, the same as Ca, addition of Zn to the Mg matrix improves strength (Mezbahul-Islam et al., 2014; Ghosh et al., 2012). In addition, the Zn content lowers the destructive corrosion effect of impurities such as Fe and Ni (Bakhsheshi-Rad et al., 2014). In a study, Koç et al. (2015) showed that the corrosion and mechanical properties of the Mg-Zn alloys have improved with Zn content up to 3 wt%. With desirable antibacterial, mechanical, and corrosion properties, ternary alloys have introduced better alternatives compared to binary Mg alloys and pure Mg itself (Song et al., 2013; Zhao et al., 2014). Various phases could be available on the grain boundaries of Mg-rich alloys that result in various degradation and mechanical properties. In the case of the ternary Mg-Zn-Ca alloys, the most important factor is the Zn/Ca atomic ratio (Ibrahim et al., 2017b). When the atomic ratio of Zn/Ca is in the range of 1.1–1.4, the eutectic phase of α-Mg + Mg_2Ca + $Ca_2Mg_6Zn_3$ forms (Ibrahim et al., 2017a; Farahany et al., 2012; Bakhsheshi-Rad et al., 2012; Zhang and Yang, 2008; Larionova et al., 2001; Jardim et al., 2002). Larionova et al. (2001) showed that in rapidly solidified alloys, this atomic ratio changes the interplanar distances. The presence of the $Ca_2Mg_6Zn_3$ phase causes a higher corrosion rate while offering enhanced mechanical properties. In addition, more hydroxyapatite and corrosion byproduct brucite ($Mg(OH)_2$) form on the surface (Li et al., 2008; Bakhsheshi-Rad et al., 2012). Significant corrosion resistance improvement was reported by adding >1 wt % Zn to the Mg-0.5 wt% Ca and the Mg-1 wt% Ca alloys (Bakhsheshi-Rad et al., 2012; Du et al., 2011; Rad et al., 2012) while at higher values of 2–3 wt%, a reduction in corrosion resistance with significant deterioration above 5 wt% was reported (Kirkland et al., 2011; Bakhsheshi-Rad et al., 2012; Du et al., 2011; Cha et al., 2013).

Adding more elements, such as Mn and Zr, to the composition of the Mg alloys could result in changing insoluble metallic impurities into harmless intermetallic phases (e.g., AlMnFe phase in Mg-Al alloys) that improves the performance of resorbable and biocompatible bone fixation devices (Kirkland and Birbilis, 2014; Zhang et al., 2009). In a study on the effect of addition of Mn, Bakhsheshi-Rad et al. (2014) found that the corrosion resistance and mechanical properties of Mg-2wt%Ca-2wt%Zn and the Mg-2wt.%Ca-4wt.%Zn alloys were improved by adding 0.5 wt.% Mn with a significant decrease in the grain size. As a result of smaller grain size, a smoother surface would be provided that reduces pitting and increases corrosion resistance. In order to investigate biocompatibility of quaternary alloys, Qu et al. (2015) implanted an Mg-Zn-Ca-Y alloy as a bone fixation with a composition of Mg-2.0 wt.%Zn-0.5 wt.%Ca-1.0 wt.%Y in rabbits. They observed low levels of macrophages and lymphocytes around the tissue during the first week with mild inflammatory cells, which decreased after 2–4 weeks and vanished after 12 weeks. In addition, a thin fibrous membrane, which maintained the U.S. ASTM-F4 implant requirements (<30 μm), was observed around the implants. The other finding of this study was mentioned as enhanced mechanical properties and corrosion resistance after adding the Mn, Zr, and Y contents to the basic ternary alloy.

Compared to conventional Mg-Zn-Ca, the Mg-Zn-Ca bulk metallic glasses (BMGs) have been introduced as a replacement biodegradable fixation material with significantly higher corrosion resistance and strength (Zhao et al., 2014; Gu et al., 2010). In contrast to crystalline atomic structure of cast alloys, Mg-Zn-Ca BMGs have an amorphous structure (Zberg et al., 2009) that is the result of rapid cooling, which does not let the crystalline phases nucleate and expand. This rapid cooling causes a glass transition resulting in a glass structure (Zberg et al., 2009; Cao et al., 2012). Zberg et al. (2009) indicated that, compared to crystalline cast alloys, amorphous Mg-Zn-Ca BMGs have less (H) evolution and good tissue compatibility followed by wound-healing signs. The mechanical properties of such BMGs are very high compared to conventional cast Mg alloys. For example, the tensile strength and elongation percent of the $(60 + x)$Mg-$(35\text{-}x)$Zn-(5)Ca BMG are 675–894 MPa and <4%, respectively. The disadvantage of these materials is the limited available time prior to crystallization and especially in smaller thicknesses and geometries (Zhao et al., 2014; Zberg et al., 2009; Gu et al., 2005), which results in difficulty in creating several complex biomedical devices such as stents and bone implants made of Mg-Zn-Ca BMGs.

9.3 Manufacturing of Mg alloys

Mg alloys can be produced by different methods that are selected based on shape, desired properties, desired components, dimensions, number of production batch, and the ability to cast an alloy (Kaiser and Kainer, 2003; Mordike and Ebert, 2001). However, the majority of Mg alloys, up to 98%, are produced by conventional casting (Luo, 2013) while the rest of the processes such as spray deposition, in situ processing, liquid infiltration, and disintegrated melt deposition occur in the remaining 2% (Gupta and Meenashisundaram, 2015; Dehghan Ghadikolaei and

Vahdati, 2015). Due to its inherent reactivity, Mg, especially when in powder form, is prone to rapid ignition. One way to reduce the oxidization is to use inert gas-controlled facilities during the fabrication process (Bakhsheshi-Rad et al., 2014; Zhang et al., 2010a; Chen et al., 2014). This section provides a brief description of the most applicable processes to fabricate Mg parts in the desired shape, size, and chemical composition.

9.3.1 Mg alloy casting

Casting is the easiest and the most applicable metal casting method for Mg and its alloys due to various advantages such as low cost, reasonable precision, and high production rate (Mordike and Ebert, 2001; Avedesian and Baker, 1999). In addition, the chemical composition of the Mg alloy can be controlled precisely and all elements melt completely prior to or during the casting process. However, most of the cast medical devices need further processing to achieve the final shape and properties before implantation (Bamberger and Dehm, 2008; Cha et al., 2013; Nie and Muddle, 1997; Oh-Ishi et al., 2009; Yue et al., 2004). Since the conventional casting process requires many post-processes, researchers have introduced many modified casting processes under controlled environments such as semi-solid casting, ablation casting, low pressure casting, high pressure die casting (HPDC), squeeze casting, and lost foam casting (Zhiqiang, 1998; Ghomashchi and Vikhrov, 2000). HPDC is the dominant casting method for Mg alloy parts and it is performed in two categories known as hot or cold chamber die casting (Luo, 2013). Advantages of HPDCs are represented in the precise geometry, the ability to fabricate thin walls and small/complex parts, the high production rate, and the high surface quality. The main disadvantages of HPDCs are the limited alloy compositions available for die casting, difficulty of complex part heat treatment, and inevitable trapping of air inside the mold cavity (Mordike and Ebert, 2001; Luo et al., 1995; Luo and Pekguleryuz, 1994; Inoue et al., 1992). In the hot chamber die-casting method, the melt stays in an atmosphere-controlled crucible prior to molding. At the time of need, the hydraulic arms will inject the melt into the mold cavity. The crucible stage is designed to minimize contact with contaminating materials and the atmosphere to prevent the formation of any undesired phases (Vinarcik, 2002). In the cold chamber die-casting, molten Mg is led into a shot cylinder by a pump followed by a ladling process. In the next step, the shots are injected into the mold cavity and stay under pressure until the solidification is completed. In the cold chamber casting, contact between the melt and the mold material is minimized and the slugs can be removed prior to pouring the shots. In addition, contact with air is minimized and due to the fast injection rate, fabricating larger parts would be cost-effective (Vinarcik, 2002; Nehan and Maloney, 1996).

In another casting method, the casting is performed under a low pressure and the process is called low pressure casting (LPC). In LPC, a hydraulic arm pushes the surface of the melt inside a container that results in a low-pressure injection of the melt into the mold cavities. Since the injection is performed from the bottom of the mold and a vent is designed at the top of the mold, there is no trapped air inside the mold, which allows the fabrication of hollow parts (Fu et al., 2008). However, this method is

incapable of fabricating thin walls, below 3 mm thickness (Dahle et al., 2001). Another common casting method used for Mg alloys is gravity casting. Gravity casting is usually performed in sand or silicate-based materials and sometimes in permanent metallic molds (Luo and Pekguleryuz, 1994). The advantage of the gravity casting is that there is no limitation on the size of the cast parts and it has been used to fabricate Mg parts up to 1400 kg. However, the sand mold reacts with the melt prior to solidification and makes the outer layer of the parts rough and inclusion-laden (Avedesian and Baker, 1999). The solution to this problem could be using permanent molding including metallic molds or sand molds covered with specifically designed resins. However, these molds are not flexible to the variation of shapes although they provide precise long-term dimension control and high surface quality (Luo, 2013; Luo et al., 2010; Gutman et al., 1997). Fig. 9.1 represents schematic illustration of these three processes.

9.3.2 Machining

Almost all the conventional and advanced machining processes such as milling, turning, deburring, and advanced finishing processes can be performed on Mg and its alloys to achieve the desired shape and size while enhancing the surface quality. The surface finish has a significant effect on the corrosion performance of Mg alloys as it indicates whether the surface has sharp peaks and valleys or straight smooth surfaces (Denkena and Lucas, 2007; Ghoreishi et al., 2018; Dehghanghadikolaei et al., 2018a). For instance, and for bone implant applications, Höh et al. (2009) reported that a higher surface finish offers the best bone integration relative to the rougher surfaces and it results in an improved pitting corrosion resistance. In another study, Yue et al. (2004) investigated the effect of four machining process including single point diamond turning (SPDT), wire electric discharge machining (WEDM), polishing, and grinding on the changes in Mg ZM51/SiC corrosion behavior. As they reported, the higher surface finish improved the corrosion resistance of the composite in an in vitro experiment.

9.3.3 AM

The very first efforts on additive manufacturing (AM) of Mg and its alloys utilized the selective laser melting (SLM) method (Ng et al., 2010). In SLM, a high-power laser beam diffuses the powder particles together based on the computer-aided design (CAD) slice provided in the machine processing unit (Ma et al., 2017). This fusing and bonding process takes place in a layer-by-layer nature (Bremen et al., 2012; Amerinatanzi et al., 2016). Since Mg powders have a high oxygen affinity compared to a bulk of Mg, the powder handling becomes challenging through the AM of Mg alloys. In addition, the small difference between Mg melting point and vaporization point of 650°C and 1090°C, respectively, causes another challenge in powder production and handling processes (Holland, 2012). Also, the melt of Mg has a low dynamic viscosity, which may cause spatter of the melt pool and cause porosity in the fabricated parts. Thus, this low viscosity creates a flow of molten Mg in the melting tracks

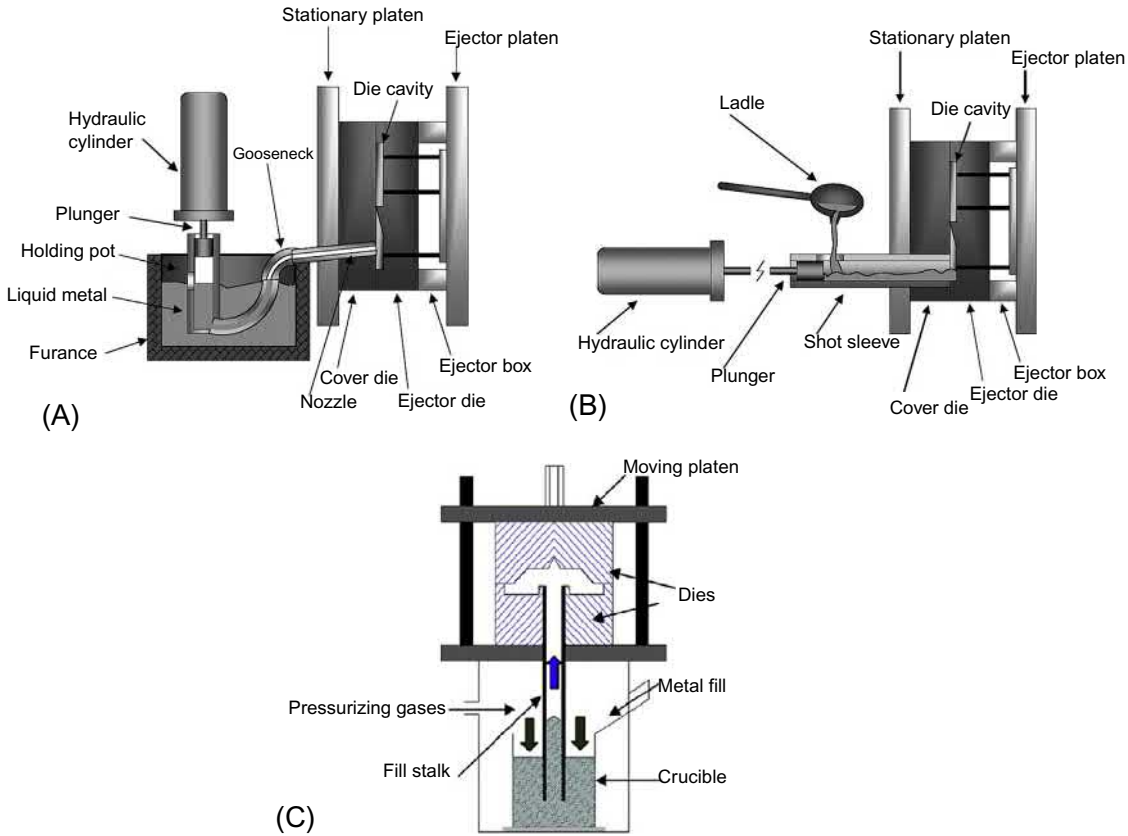


Fig. 9.1 Schematic illustration of (A) hot chamber die casting, (B) cold chamber die casting (Vinarcik, 2002), and (C) low pressure casting (Fu et al., 2008).

and brings a new difficulty to the AM process of Mg and its alloys (Leong, 1998). As a result, the laser power density and scanning speed are the key factors to be selected wisely in order to prevent excessive loss of dynamic viscosity. The other adverse characteristic of AM of Mg alloys could be powder balling during the process due to the small difference of melting and vaporization points. It has also been reported that the vapor of Mg in the chamber of the AM machine deposits on the surface of the solidified materials (Nölke, 2013; Zhang et al., 2012; Giesekel et al., 2013). In order to resolve this problem, it has been suggested to increase the pressure of the chamber to the range of 3 bar, as depicted in Fig. 9.2. Then the difference of the melting and vaporization point would be increased from 440°C to 570°C (Askeland and Phulé, 2003). In a study conducted in the Fraunhofer Institute for Laser Technology (ILT), the researchers followed the same procedure and succeeded to additively manufacture AZ91 Mg alloy with a density of above 99%. However, the challenge in this process was maintaining the oxygen content of the inert gas below 10 ppm (Fraunhofer Institute for Laser Technology ILT, 2014). Roland et al. (2015) and Matena et al. (2015) successfully fabricated porous Mg structures using the SLM technique with the highest resolution of 600 μm.

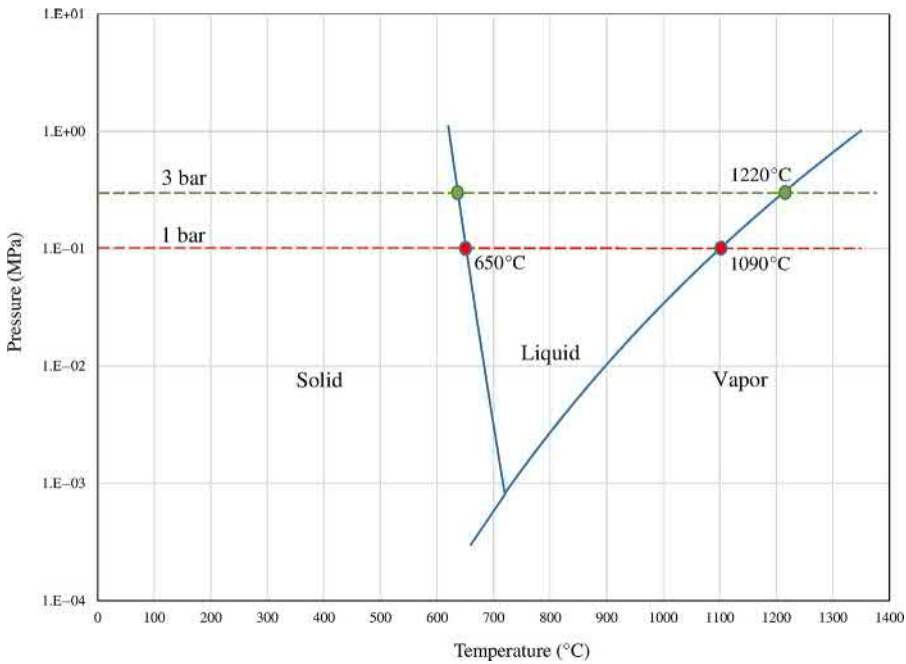


Fig. 9.2 Schematic unary phase diagram for pure magnesium, showing the melting and vaporization points and their difference at two proposed pressure levels of 1 and 3 bar that increases the difference between the melting and vaporization points from 440°C to 570°C (Ibrahim et al., 2017a; Holland, 2012; Askeland and Phulé, 2003).

9.4 Corrosion of Mg alloys

As a naturally resorbable element, Mg corrodes inside the human body and releases its byproducts through natural metabolic processes (Seitz et al., 2014). However, Mg is highly prone to galvanic corrosion that corrodes the material in SBF with high rates of corrosion potential and H evolution up to −2.027 V and 56.5 mL/cm^2/day, respectively (Bakhsheshi-Rad et al., 2014; Chen et al., 2014). Mg dissolves in pH values below 11.5 and as the body fluid pH is in the range of 7.3–7.4, the corrosion takes place continuously until complete degradation of Mg. $Mg(OH)_2$ is one of the byproducts of Mg corrosion that prevents corrosion in pH values higher than 11.5 but in the case of circulating body fluid, this will not hinder the corrosion process (Grunde, 2010). The overall reaction consumes H^+ and produces OH^- from the medium, leading to an increase in the pH value (Manivasagam and Suwas, 2014; Kirkland et al., 2012; Witte et al., 2005; Agha et al., 2016). Mg is known as a reliable biocompatible material in bio-applications; however, it suffers from low corrosion resistance. Based on the Puorbiax diagram presented in Fig. 9.3, Mg is less noble than most metals by showing a low standard electrode potential (−2.72 V) compared to the H electrode potential (−2.37 V at zero and at 25°C) (Grunde, 2010). This means that

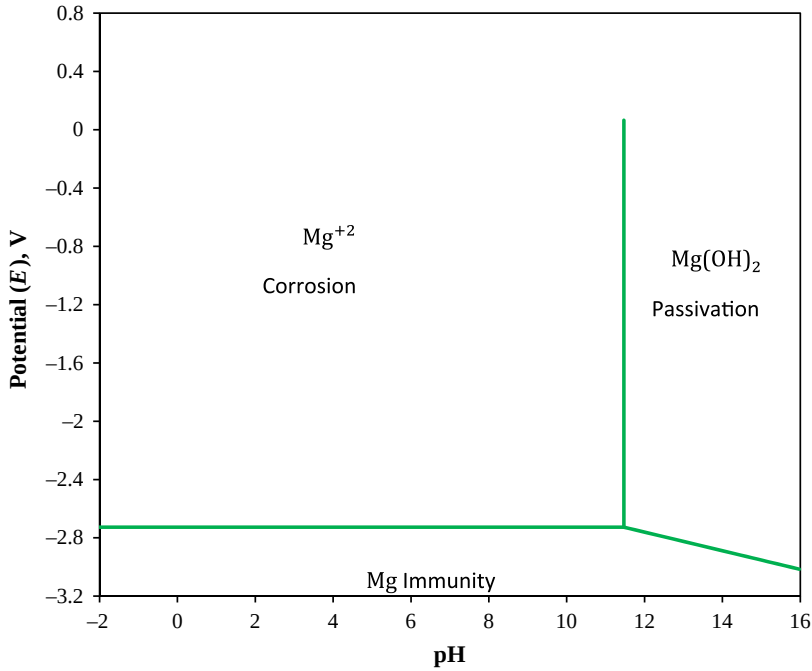


Fig. 9.3 Pourbaix diagram of Mg presenting dependency of Mg corrosion, passivation, and immunity regions (Pourbaix, 1974).

Mg is most prone to galvanic corrosion, which is the key factor in selection, adjustment, and modification of Mg alloys.

The Mg corrosion products in a physiological environment are mainly hydroxyl (OH) groups, Mg ions, and hydrogen gas (H_2). A quick reaction between the Mg ions and the hydroxyl groups produces a layer of magnesium hydroxide $Mg(OH)_2$ on the surface (Manivasagam and Suwas, 2014; Kirkland et al., 2012; Witte et al., 2005; Agha et al., 2016). For every 1 mg of Mg, 1 mL of H_2 is released during the corrosion process. These gases may become trapped within the body tissue at the surgical site, forming gas pockets leading to potential tissue separation and delayed bone healing (Remennik et al., 2011). In addition, the evolution of H may cause H absorption in the Mg device or implant, which deteriorates the mechanical properties of the Mg fixation hardware with a H cracking or a brittle fracture (Manivasagam and Suwas, 2014). The nature of Mg corrosion inside body fluids is a dynamic interface that emerges mostly at the early stages of corrosion process due to the increase of pH, Mg and/or Ca containing corrosive products, and H emission (Xin et al., 2010; Wu et al., 2013).

9.4.1 Galvanic corrosion

As discussed above, Mg has a low corrosion potential and this makes it susceptible to corrosion. Galvanic corrosion is a metallic degradation process that occurs while there is a potential difference between two contacting metals. This process is more severe in the cathode area (Poinern et al., 2012). Galvanic corrosion takes place through two different mechanisms: internal and external galvanic corrosions. The internal mechanism happens due to the cathodic impurities and metallic phases inside the Mg matrix while the external mechanism takes place when Mg is in contact with a nobler metal. These two mechanisms are shown in Fig. 9.4. In the case of pure Mg, impurities such as Fe, Cu, or Ni have a major impact on corrosion since they have low solubility inside the Mg matrix and they might form micro galvanic cells and attach to the matrix from the inside (Hanawalt et al., 1942). This effect shows the importance of having low impurity level in pure Mg. Generally, impurity elements cause more damage than the intended alloying elements. However, the alloying elements will not harm the Mg matrix compared to the impurities since they are in higher H overvoltage and lower potential difference between anodic and cathodic regions (Song and Atrens, 1999).

9.4.2 Stress corrosion and stress corrosion cracking

Mg alloys are promising biomaterials for various load-bearing applications such as bone fixation hardware. Fig. 9.5 shows another mechanism of Mg alloy corrosion known as stress corrosion cracking (SCC) that may cause a sudden failure of the material. Pure Mg does not experience SCC while the alloying elements of Al and Zn increase the stress corrosion susceptibility of the alloy (Atrens et al., 2011a). SCCs can take place through inter-granular and/or trans-granular mechanisms, which are dependent on the alloy's composition, microstructure, and the working environment (Swann, 1963; Winzer et al., 2008). The former occurs continuously near grain

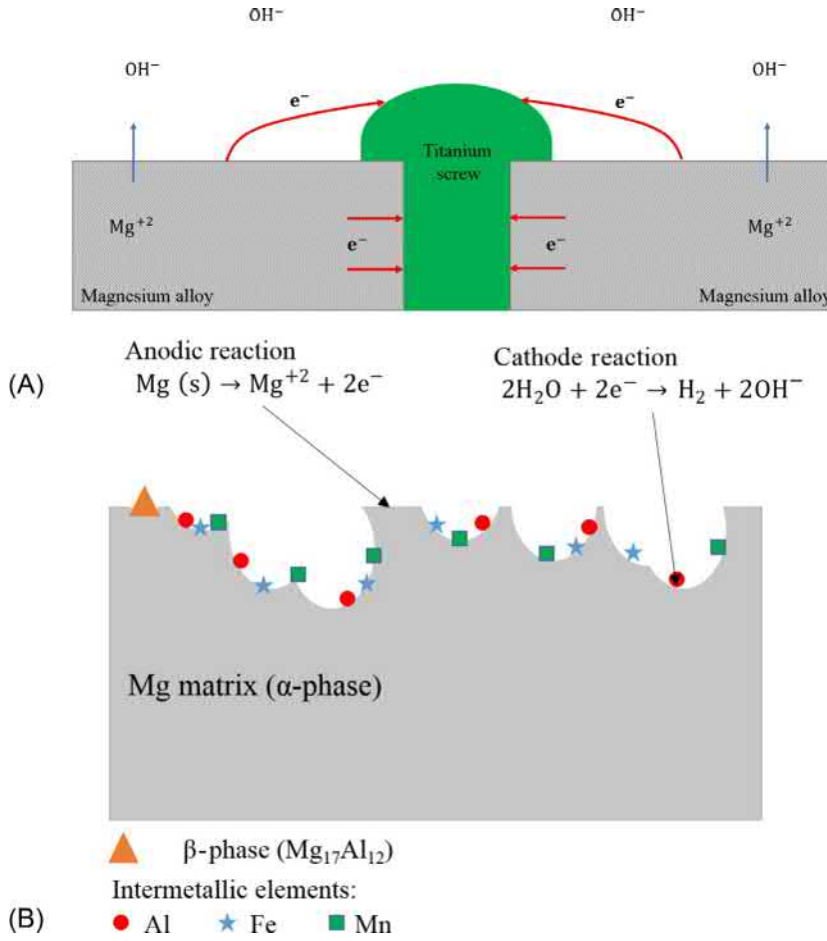


Fig. 9.4 (A) The external galvanic corrosion and (B) internal galvanic corrosion.

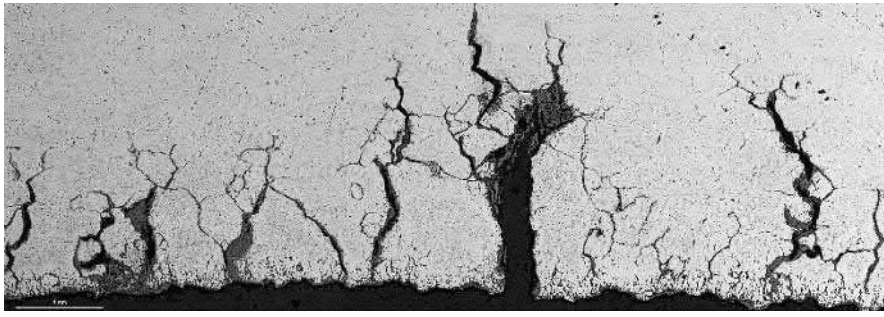


Fig. 9.5 Stress corrosion cracking on Mg-1.2Zn-0.5Ca (Winzer et al., 2005).

boundaries and has an electrochemical nature. The anodic dissolution of the matrix happens at the grain boundaries. After this type of corrosion, an applied force or stress breaks the material structure (Atrens et al., 2011b). The latter is divided into two mechanisms and is the cause of failure and fracture in most Mg alloys. The two mechanisms of trans-granular mechanism are known as dissolution and brittle cracks caused by cleavage propagation. In the first mechanism, local corrosion rates will increase and dissolution accelerates (Atrens et al., 2011a). In the second mechanism, the brittle fractures occur due to the micro-cracks on the surface and mostly the surface of these types contain ridges (Grunde, 2010).

9.4.3 Pitting corrosion

Pitting corrosion in general is the effect of losing the surface oxide layer that acts as a protective layer and is a localized corrosion mechanism. Due to the presence of corrosion products, it is difficult to observe pitting corrosion. The other destructive effect of this corrosion mechanism is that it grows locally and inward to the metallic matrix (Verstraeten et al., 2008). In the case of pitting corrosion, if the impurity level is high and the localized corrosion zone penetrates enough to reach these zones, an additional corrosion mechanism of galvanic corrosion forms that will accelerate the degradation of the material (Ambat et al., 2000; Liu and Schlesinger, 2009). As pitting corrosion is highly aggressive, when it starts, based on the depth of penetration, it might cause a stress corrosion crack, as well. Thus, after a shorter period of time, relative to the other mechanisms of degradation, an Mg-based biomedical device collapses, even under normal loading conditions. In addition, having a localized nature, pitting corrosion can cause stress concentration points that reduce the mechanical properties and load-bearing capacity of the implant (Zeng et al., 2008). Fig. 9.6 shows a typical pitting corrosion mechanism.

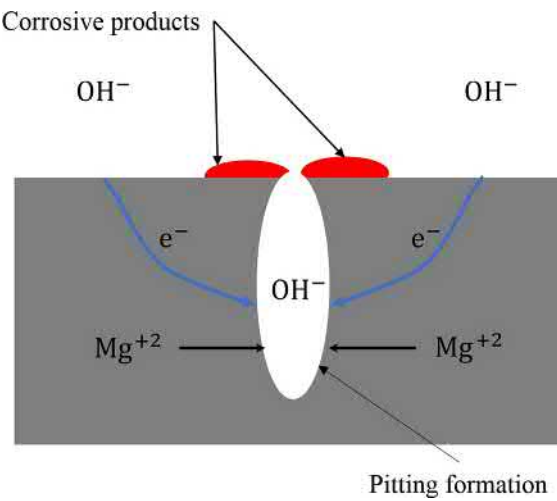


Fig. 9.6 Pitting corrosion of Mg alloys (Poinern et al., 2012).

9.5 Biocompatibility of Mg alloys

Cytotoxicity tests can reveal the short-term biocompatibility properties of Mg-based alloys. In addition, animal testing might be a solid indicator for both short- and long-term biocompatibility properties of Mg alloys. However, many studies did not dedicate their research to the in vitro and in vivo toxicity tests prior to designing Mg-based fixation hardware. The lack of evidence and data on this topic causes uncertainty on many proposed alloying and coating compositions and methods and their bio-safety for short- and long-term applications. The alloying elements in Mg alloys have different biocompatibility properties. Many of these elements are toxic in nature such as cadmium (Cd), lead (Pb), and some other heavy metals and the alloying process does not alter their toxicity properties. Fortunately, many of the other elements are available that showed a reliable biocompatibility, at least in the initial experiments. These elements are strontium (Sr), lithium (Li), Zr, Si, and RE elements. However, these elements need further research to reveal reliable results and conclusions for long-term applications (Gu et al., 2009, 2012). Many researchers have undertaken studies on the short-term effects of these alloying elements. As an example, the effect of addition of 0.5 wt% Sr to an Mg-1wt%Ca alloy after an in vitro cytotoxicity test on a mouse was investigated and it was reported that it showed low overall toxicity (Berglund et al., 2012). In addition, another positive effect of adding alloying elements was reported to achieve a higher bone mineral content (BMC) and bone mineral density (BMD) by adding Zr to the Mg alloys. This in vivo test showed that improved osteointegrative properties would be achieved as an effect of the added alloying element of Zr. Also, it has been reported that a bone forming ability was improved by observing an increase in serum alkaline phosphatase level (ALP) activity in animals (Li et al., 2012). Gu et al. (2009) conducted in vitro cytotoxicity and hemocompatibility tests on nine binary Mg-1X (wt%) alloys with Al, Ag, indium (In), Mn, Si, Sn, Y, Zn, and Zr alloying elements. The only group that did not demonstrate any reduction in adhered platelets and hemolysis was reported to be the pure Mg control group. Also, Mg-1Al, Mg-1Sn, and Mg-1Zn were the only groups that did not undergo a significant reduction in cell viability to fibroblasts (L-929 and NIH3T3) and osteoblasts (MC3T3-E1).

Being among the essential nutrients in the human body, it has been reported that Mg, Ca, Zn, and Mn did not show any toxicity (Cha et al., 2013; Zhang et al., 2010b). However, the daily dosage of the mentioned elements should not pass the standard values in order to not cause any toxic effects. As an example, excessive Mn and Zn in the human body may cause neurotoxicity and may hinder bone development (Chen et al., 2014; Witte et al., 2008; Zheng et al., 2014). In an investigation, Zhang et al. (2010a) studied the in vitro and in vivo biocompatibility of a 6% Zn content binary Mg-Zn alloy and reported that no signs of toxicity were observed in L-929 cells. The other important factor to consider prior to designing an Mg alloy is the metallic ion release properties. Corrosion happens to metallic implants and devices exposed to the physiological environment of the human body and as a result, changes the pH in the adjacent tissues. This change of pH has a negative effect on the neighboring cell viability and disturbs the normal behavior. In general, controlling the corrosion rate and properties will enhance the life of the fixation hardware while

maintaining the device in the reliable range of biocompatibility and cytotoxicity. Another important factor defining the corrosion properties of the material could be the location of the device or implant inside the human body. Most of the toxicity caused by these materials is local and would not spread out easily unless it was close to main blood vessels or a critical organ.

9.6 Coating of Mg alloys

Coating in general increases the corrosion resistance of materials, especially the ones exposed to a physiological environment, and Mg alloys are not an exception (Kirkland and Birbilis, 2014; Wu et al., 2013; Shadanbaz and Dias, 2012; Krishna and Sundararajan, 2014). The coating layer for biomedical applications should be biocompatible with sufficient corrosion resistance to maintain the mechanical properties of the Mg alloys during implantation. The most common coating methods for Mg alloys are divided into three categories: substrate-involving coatings, nonsubstrate-involving coatings, and composite coatings (Wu et al., 2013; Dehghanghadikolaei et al., 2018b). Examples of substrate-involving coatings are micro-arc oxidation (MAO), alkaline oxidation, and fluoridation. The MAO process is also known as micro plasma oxidation (MPO) and plasma electrolytic oxidation (PEO). This coating technique is one of the most popular processes among researchers and has been investigated in many studies. One of the unique characteristics of the MAO process is the formation of a hard-protective layer on the surface of the coated Mg alloy. A typical MAO coating layer is made of MgO and other ceramic compounds, depending on the nature of the used electrolyte in the process (Malayoglu et al., 2010; Dehghanghadikolaei, 2018).

For the nonsubstrate involving coatings, calcium phosphate (Ca/P) containing coating layers such as HA and tricalcium phosphate (TCP) have been used in order to enhance the bone ingrowth and biocompatibility. In addition, these coating layers could be used for drug delivery purposes and release a designed dose of drugs, such as antibiotics, as they corrode. Nonsubstrate-involving coatings also utilize biodegradable polymers such as dichloromethane (DCM), polylactic acid (PLLA), poly lactic-*co*-glycolic acid (PLGA), and polycaprolactone (PCL) (Wu et al., 2013; Li et al., 2010; Xu and Yamamoto, 2012; Wong et al., 2010). PLGA coating is known to enhance corrosion properties and improve cell adhesion (Li et al., 2010).

9.7 Corrosion modeling

Finite element analysis (FEA) can be used to simulate and calculate stress and strain distribution in a biomedical device. In the case of bone fixation hardware, this type of analysis can help predict the possibility of bone fracture, fatigue, and the safety of the implant (Nassiri et al., 2012). It is also very useful for developing patient-specific biodegradable medical devices. The general goal of this type of specific design is to reduce costs, time, and complexity of the surgery while reducing the hospitalization time. In a study, Lethaus et al. (2014) compared 17 patients who underwent patient-specific implantation with 16 other patients that underwent conventional surgeries.

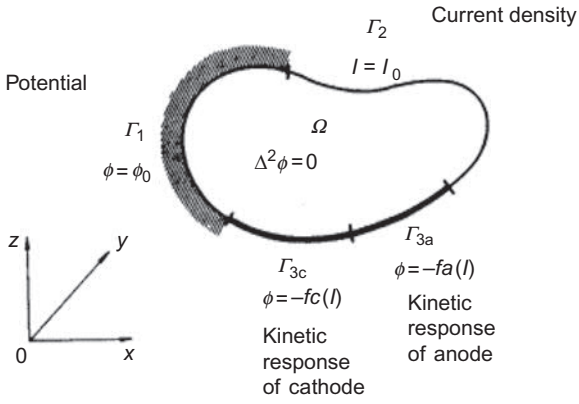


Fig. 9.7 BEM boundary conditions and equations (Jia et al., 2006).

They claimed that the surgery complexity, costs, time, and hospitalization time was significantly lower compared to the second group. To date, only a few researchers have studied modeling of biodegradable alloys (Grogan et al., 2012; Petrini et al., 2004; Zunino et al., 2009; Murr et al., 2011; Morlacchi and Migliavacca, 2013; Ding et al., 2014; Gonzalez and Nuno, 2016). The FEA approaches can be categorized as boundary element method (BEM), and continuum damage mechanics (CDM).

9.7.1 Boundary element modeling (BEM)

BEM is known to be used for solving linear partial differential equations. BEM has been used to model the biodegradation of Mg alloys from a galvanic corrosion point of view. Shi et al. (2012) utilized BEM to predict in vitro galvanic corrosion of coupled Mg-carbon steel structures in a 3.5% NaCl solution. In other studies, Jia et al. (2006) implemented BEM to predict the galvanic corrosion current density of an AZ91D alloy connected to steel. They have included the effect of geometry variables in their model by Laplacian and mathematical equations. Based on their report, for this specific case, BEM can predict and calculate the galvanic corrosion current density distribution and this distribution is proved to be in an acceptable range for the selected couple structure (Jia et al., 2004, 2006, 2007). The disadvantage of the BEM technique is that it is unable to consider the movement of the corrosion interface. However, some research reports such as Deshpande (2010), Xiao and Chaudhuri (2011), Onishi et al. (2012), and Sun et al. (2013) utilized finite element meshing to track the movement of the pitting and galvanic corrosion but they claimed that it would be difficult to predict and run the model for complex 3D components. Fig. 9.7 shows the BEM boundary conditions and equations.

9.7.2 Continuum damage mechanics (CDM)

Lemaitre et al. (Lemaitre and Desmorat, 2005; Lippmann and Lemaitre, 1996) proposed the CDM technique to overcome the issues related to the BEM technique. In the proposed model, as shown in Eq. (9.1), they used a formula that calculates the effective stress ($\overline{\sigma}_{ij}$) considering stress tensor (σ_{ij}) and scalar damage parameter

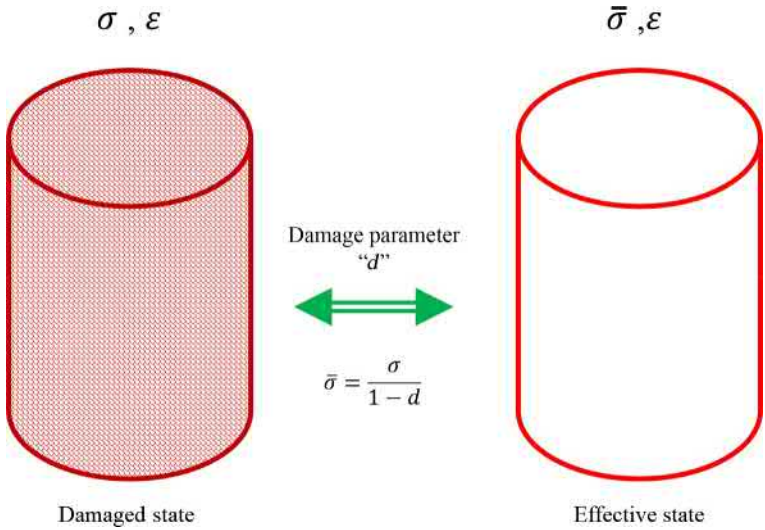


Fig. 9.8 Schematic CDM technique steps and variables.

(d). In a study, Wenman et al. (2008) chose random numbers of d between 0 and 1. Finite element deletion removed a portion of the component after each time increment until the effective stress was larger than the defined damage threshold. After each time increment, the stress field of the removed portion updates itself and takes another d value to run the next iteration. This loop continues until the degradation meets the defined levels. In addition, a higher resolution of meshing results in a more precise prediction but experimental verification of the results arise required to calibrate the damage parameter "d" (Grogan et al., 2013). Fig. 9.8 represents the schematic depiction of the CDM technique, variables, and formulation.

$$\overline{\sigma}_{ij} = \frac{\sigma_{ij}}{1-d} \tag{9.1}$$

In another study Grogan et al. (2011) proposed a new phenomenological corrosion prediction model in a finite element framework to predict corrosion behavior of an AZ31 alloy. This model utilizes uniform corrosion and pitting corrosion that cause uniform and non-uniform breakdown of the component, respectively. They have calibrated their parameters based on mass loss data out of immersion tests and a tensile test data-set. Gastaldi et al. (2011) proposed a phenomenological FE model to predict both uniform and stress corrosion processes on ZK60, ZM21, AZ31, AZ61, and AZ80 alloys. In order to take into account the effect of stress corrosion, they implemented the damage law for stainless steel proposed by da Costa-Mattos et al. (2008). In another study, Oppeel (2015) enhanced the model by Gastaldi et al. (2011) to predict pitting and stress corrosion at the same time. Up to now, the most comprehensive Mg corrosion model was proposed by Oppeel (2015), which takes into account both pitting and stress corrosion. There are several issues associated with their model. Table 9.1 notes advantages and disadvantages of phenomenological corrosion models

Table 9.1 Overview of corrosion modeling frameworks applicable to biodegradable alloys

Group	Alloy	Approach	Corrosion model	Limitations
Grogan et al. (2011)	AZ31	CDM	$-d = d_P$	– Ψ factor is considered 1, so three pitting parameters (K_u, γ, and β) are only tuned – Tuning technique is used for calibration – The pitting corrosion model is used to reproduce experiments of stress corrosion
Gastaldi et al. (2011)	AZ31 ZK60 ZM21 AZ61 AZ80	CDM	$-d = d_u + d_{SC}$	– Pitting corrosion is not considered – Only one parameter K_u is used since the uniform model is considered rather than pitting model – Tuning technique is used for calibration – The experimental data of immersion testing is mistakenly used to find three stress parameters (δ_{sc}, S, and R)
Debusschere et al. (2012)		CDM	$d = d_P + d_{SC}$	– Neither the pitting parameter nor stress parameters are calculated
Oppeel (2015)	AZ31	CDM	$-d = d_P + d_{SC}$	– Tuning technique is used for calibration – The experimental data of tensile loading after a certain level of corrosion is mistakenly used to find three stress parameters (δ_{sc}, S, and R)

Table 9.2 The calibrated parameters by different groups in literature

Parameter	Description	Grogan et al. (2011)	Gastaldi et al. (2011)	Oppeel (2015)
γ (−)	Shape factor in PDF function	0.2	–	0.2
Ψ (−)	Scale factor in PDF function	1	–	1
β (−)	Scaling parameter controlling pitting growth acceleration	0.8	–	0.5
K_u (h^{-1})	Kinetic parameter	0.00042	0.00500	0.00650
d_{SC}	Stress-driven damage in compression	–	0.07	0.067
S ($mm^2h^{-0.5}N^{-1}$)	Kinetics factor of the stress corrosion process-dependency to pH	–	0.007	0.003
R (−)	Kinetics factor of the stress corrosion process-dependency to temperature	–	2	2
Tuning method	–	Trial and error	Trial and error	Trial and error

in an FE framework using the CDM approach and Table 9.2 summarizes a data-set reported by different authors in literature for the corrosion model parameters.

References

Agha, N.A., et al., 2016. Magnesium degradation influenced by buffering salts in concentrations typical of in vitro and in vivo models. Mater. Sci. Eng. C 58, 817–825.

Ambat, R., Aung, N.N., Zhou, W., 2000. Evaluation of microstructural effects on corrosion behaviour of AZ91D magnesium alloy. Corros. Sci. 42 (8), 1433–1455.

Amerinatanzi, A., et al., 2016. The effect of porosity type on the mechanical performance of porous niti bone implants. In: ASME 2016 Conference on Smart Materials, Adaptive Structures and Intelligent Systems. American Society of Mechanical Engineers.

Andani, M.T., et al., 2014. Metals for bone implants. Part 1. Powder metallurgy and implant rendering. Acta Biomater. 10 (10), 4058–4070.

Askeland, D.R., Phulé, P.P., 2003. The Science and Engineering of Materials. Springer, Stamford.

Atrens, A., Winzer, N., Dietzel, W., 2011a. Stress corrosion cracking of magnesium alloys. Adv. Eng. Mater. 13 (1–2), 11–18.

Atrens, A., et al., 2011b. Stress corrosion cracking (SCC) of magnesium (Mg) alloys. In: Corrosion of Magnesium Alloys. Elsevier, Cambridge, pp. 299–364.

Avedesian, M.M., Baker, H., 1999. ASM Specialty Handbook: Magnesium and Magnesium Alloys. ASM International, Materials Park, OH, p. 15.

Bakhsheshi-Rad, H., et al., 2012. Relationship between the corrosion behavior and the thermal characteristics and microstructure of Mg–0.5 Ca–xZn alloys. Corros. Sci. 64, 184–197.
Bakhsheshi-Rad, H., et al., 2014. Mechanical and bio-corrosion properties of quaternary Mg–Ca–Mn–Zn alloys compared with binary Mg–Ca alloys. Mater. Des. 53, 283–292.
Bamberger, M., Dehm, G., 2008. Trends in the development of new Mg alloys. Annu. Rev. Mater. Res. 38, 505–533.
Berglund, I.S., et al., 2012. Synthesis and characterization of Mg-Ca-Sr alloys for biodegradable orthopedic implant applications. J. Biomed. Mater. Res. B Appl. Biomater. 100 (6), 1524–1534.
Bornapour, M., et al., 2014. Magnesium implant alloy with low levels of strontium and calcium: the third element effect and phase selection improve bio-corrosion resistance and mechanical performance. Mater. Sci. Eng. C 35, 267–282.
Bremen, S., Meiners, W., Diatlov, A., 2012. Selective laser melting. Laser Tech. J. 9 (2), 33–38.
Bruce, D.W., Hietbrink, B.E., DuBois, K.P., 1963. The acute mammalian toxicity of rare earth nitrates and oxides. Toxicol. Appl. Pharmacol. 5 (6), 750–759.
Campos, C.M., et al., 2013. Bioresorbable drug-eluting magnesium-alloy scaffold for treatment of coronary artery disease. Int. J. Mol. Sci. 14 (12), 24492–24500.
Cao, J., et al., 2012. Ca–Mg–Zn bulk metallic glasses as bioresorbable metals. Acta Biomater. 8 (6), 2375–2383.
Cases, N., 2005. Macrophagic myofasciitis associated with vaccine-derived aluminium. Med. J. Aust. 183 (3), 145–146.
Castellani, C., et al., 2011. Bone–implant interface strength and osseointegration: biodegradable magnesium alloy versus standard titanium control. Acta Biomater. 7 (1), 432–440.
Cha, P.-R., et al., 2013. Biodegradability engineering of biodegradable Mg alloys: tailoring the electrochemical properties and microstructure of constituent phases. Sci. Rep. 3.
Chen, Y., et al., 2014. Recent advances on the development of magnesium alloys for biodegradable implants. Acta Biomater. 10 (11), 4561–4573.
da Costa-Mattos, H., Bastos, I., Gomes, J., 2008. A simple model for slow strain rate and constant load corrosion tests of austenitic stainless steel in acid aqueous solution containing sodium chloride. Corros. Sci. 50 (10), 2858–2866.
Dahle, A.K., et al., 2001. Development of the as-cast microstructure in magnesium–aluminium alloys. J. Light. Met. 1 (1), 61–72.
Debusschere, N., et al., 2012. Modeling of coated biodegradable stents. In: ASME 2012 Summer Bioengineering Conference. American Society of Mechanical Engineers.
Dehghan Ghadikolaei, A., Vahdati, M., 2015. Experimental study on the effect of finishing parameters on surface roughness in magneto-rheological abrasive flow finishing process. Proc. Inst. Mech. Eng. B J. Eng. Manuf. 229 (9), 1517–1524.
Dehghanghadikolaei, A., 2018. Enhance Its Corrosion Behavior of Additively Manufactured NiTi by Micro-Arc Oxidation Coating in Mechanical, Manufacturing and Industrial Engineering. The University of Toledo. The University of Toledo.
Dehghanghadikolaei, A., et al., 2018a. Abrasive machining techniques for biomedical device applications. Juniper Online J. Mater. Sci. 5, 1–11. 1.
Dehghanghadikolaei, A., Ansary, J., Ghoreishi, R., 2018b. Sol-gel process applications: a mini-review. Proc. Nat. Res. Soc. 2 (1), 02008.
Denkena, B., Lucas, A., 2007. Biocompatible magnesium alloys as absorbable implant materials–adjusted surface and subsurface properties by machining processes. CIRP Ann. Manuf. Technol. 56 (1), 113–116.
Deshpande, K.B., 2010. Validated numerical modelling of galvanic corrosion for couples: magnesium alloy (AE44)–mild steel and AE44–aluminium alloy (AA6063) in brine solution. Corros. Sci. 52 (10), 3514–3522.

Ding, J., et al., 2014. Finite element analysis on bending fretting fatigue of 316L stainless steel considering ratchetting and cyclic hardening. Int. J. Mech. Sci. 86, 26–33.
Domingo, J.L., 1995. Reproductive and developmental toxicity of aluminum: a review. Neurotoxicol. Teratol. 17 (4), 515–521.
Du, H., et al., 2011. Effects of Zn on the microstructure, mechanical property and bio-corrosion property of Mg–3Ca alloys for biomedical application. Mater. Chem. Phys. 125 (3), 568–575.
Elsayed, H., et al., 2012. Influence of flax fibers on properties of starch-based composites. In: ASME 2012 International Mechanical Engineering Congress and Exposition. American Society of Mechanical Engineers.
Farahany, S., et al., 2012. In-situ thermal analysis and macroscopical characterization of Mg–xCa and Mg–0.5 Ca–xZn alloy systems. Thermochim. Acta 527, 180–189.
Flaten, T.P., 2001. Aluminium as a risk factor in Alzheimer's disease, with emphasis on drinking water. Brain Res. Bull. 55 (2), 187–196.
Fraunhofer Institute for Laser Technology ILT, 2014. Selective Laser Melting of Magnesium Alloys. [cited 2014 16 Dec]; Available from: http://www.ilt.fraunhofer.de/en/publication-and-press/annual-report/2012/annual-report-2012-p88.html.
Fu, P., et al., 2008. Low-pressure die casting of magnesium alloy AM50: response to process parameters. J. Mater. Process. Technol. 205 (1), 224–234.
Gastaldi, D., et al., 2011. Continuum damage model for bioresorbable magnesium alloy devices—application to coronary stents. J. Mech. Behav. Biomed. Mater. 4 (3), 352–365.
Ghomashchi, M., Vikhrov, A., 2000. Squeeze casting: an overview. J. Mater. Process. Technol. 101 (1–3), 1–9.
Ghoreishi, R., Roohi, A.H., Ghadikolaei, A.D., 2018. Analysis of the influence of cutting parameters on surface roughness and cutting forces in high speed face milling of Al/SiC MMC. Mater. Res. Express 5 (8), 086521.
Ghosh, P., Mezbahul-Islam, M., Medraj, M., 2012. Critical assessment and thermodynamic modeling of Mg–zn, Mg–sn, Sn–Zn and Mg–Sn–Zn systems. Calphad 36, 28–43.
Giesekel, M., et al., 2013. Selective laser melting of magnesium and magnesium alloys. In: Magnesium Technology 2013, Springer, pp. 65–68.
Gonzalez, F.J.Q., Nuno, N., 2016. Finite element modeling of manufacturing irregularities of porous materials. Biomater. Biomech. Bioeng. 3 (1), 1–14.
Grogan, J., et al., 2011. A corrosion model for bioabsorbable metallic stents. Acta Biomater. 7 (9), 3523–3533.
Grogan, J.A., Leen, S.B., McHugh, P.E., 2012. Comparing coronary stent material performance on a common geometric platform through simulated bench testing. J. Mech. Behav. Biomed. Mater. 12, 129–138.
Grogan, J.A., Leen, S.B., McHugh, P.E., 2013. Optimizing the design of a bioabsorbable metal stent using computer simulation methods. Biomaterials 34 (33), 8049–8060.
Grunde, P., 2010. Biodegradable Magnesium Alloys for Osteosynthesis: Alloy Development and Surface Modifications. ETH Zurich, Zurich.
Gu, X., et al., 2005. Mg–Ca–Zn bulk metallic glasses with high strength and significant ductility. J. Mater. Res. 20 (08), 1935–1938.
Gu, X., et al., 2009. In vitro corrosion and biocompatibility of binary magnesium alloys. Biomaterials 30 (4), 484–498.
Gu, X., et al., 2010. Corrosion of, and cellular responses to Mg–Zn–Ca bulk metallic glasses. Biomaterials 31 (6), 1093–1103.
Gu, X., et al., 2012. In vitro and in vivo studies on a Mg–Sr binary alloy system developed as a new kind of biodegradable metal. Acta Biomater. 8 (6), 2360–2374.

Gupta, M., Meenashisundaram, G.K., 2015. Insight into Designing Biocompatible Magnesium Alloys and Composites: Processing, Mechanical and Corrosion Characteristics. Springer, Singapore.
Gutman, E., et al., 1997. Influence of technological parameters of permanent mold casting and die casting on creep and strength of Mg alloy AZ91D. Mater. Sci. Eng. A 234, 880–883.
Hanawalt, J., Nelson, C., Peloubet, J., 1942. Corrosion studies of magnesium and its alloys. Trans. AIME 147, 273–299.
Hermawan, H., 2012. Biodegradable metals: state of the art. In: Biodegradable Metals. Springer, Berlin, Heidelberg, pp. 13–22.
Hirano, S., et al., 1993. Metabolism and toxicity of intravenously injected yttrium chloride in rats. Toxicol. Appl. Pharmacol. 121 (2), 224–232.
Höh, N.V.D., et al., 2009. Influence of different surface machining treatments of magnesium-based resorbable implants on the degradation behavior in rabbits. Adv. Eng. Mater. 11 (5), B47–B54.
Holland, L., 2012. Vacuum Manual. Springer Science & Business Media, London.
Ibrahim, H., et al., 2014. Characteristics of starch-based biodegradable composites reinforced with date palm and flax fibers. Carbohydr. Polym. 101, 11–19.
Ibrahim, H., et al., 2017a. Resorbable bone fixation alloys, forming, and post-fabrication treatments. Mater. Sci. Eng. C 70, 870–888.
Ibrahim, H., et al., 2017b. Microstructural, mechanical and corrosion characteristics of heat-treated Mg-1.2 Zn-0.5 Ca (wt%) alloy for use as resorbable bone fixation material. J. Mech. Behav. Biomed. Mater. 69, 203–212.
Ibrahim, H., et al., 2018a. A comparative study on the mechanical and biodegradation characteristics of starch-based composites reinforced with different lignocellulosic fibers. J. Polym. Environ. 26 (6), 2434–2447.
Ibrahim, H., et al., 2018b. In vitro corrosion assessment of additively manufactured porous NiTi structures for bone fixation applications. Metals 8 (3), 164.
Inoue, A., et al., 1992. Mg–Cu–Y bulk amorphous alloys with high tensile strength produced by a high-pressure die casting method. Mater. Trans. JIM 33 (10), 937–945.
Jardim, P.M., Solórzano, G., Sande, J.B.V., 2002. Precipitate crystal structure determination in melt spun Mg-1.5 wt% Ca-6wt% Zn alloy. Microsc. Microanal. 8 (06), 487–496.
Jia, J., et al., 2004. Evaluation of the BEASY program using linear and piecewise linear approaches for the boundary conditions. Mater. Corros. 55 (11), 845–852.
Jia, J.X., Song, G., Atrens, A., 2006. Influence of geometry on galvanic corrosion of AZ91D coupled to steel. Corros. Sci. 48 (8), 2133–2153.
Jia, J.X., Song, G., Atrens, A., 2007. Experimental measurement and computer simulation of galvanic corrosion of magnesium coupled to steel. Adv. Eng. Mater. 9 (1–2), 65–74.
Kaiser, F., Kainer, K., 2003. Magnesium Alloys and Technology. John Wiley & Sons-VCH, Weinheim.
Kirkland, N.T., Birbilis, N., 2014. Magnesium Biomaterials: Design, Testing, and Best Practice. Magnesium Biomaterials. Springer, Cham.
Kirkland, N.T., et al., 2011. Performance-driven design of biocompatible Mg alloys. JOM 63 (6), 28–34.
Kirkland, N., Birbilis, N., Staiger, M., 2012. Assessing the corrosion of biodegradable magnesium implants: a critical review of current methodologies and their limitations. Acta Biomater. 8 (3), 925–936.
Koç, E., et al., 2015. Influence of zinc on the microstructure, mechanical properties and in vitro corrosion behavior of magnesium–zinc binary alloys. J. Alloys Compd. 648, 291–296.

Krishna, L.R., Sundararajan, G., 2014. Aqueous corrosion behavior of micro arc oxidation (MAO)-coated magnesium alloys: a critical review. JOM 66 (6), 1045–1060.
Larionova, T.V., Park, W.-W., You, B.-S., 2001. A ternary phase observed in rapidly solidified Mg–Ca–Zn alloys. Scr. Mater. 45 (1), 7–12.
Lee, J.-Y., et al., 2009. Effects of impurities on the biodegradation behavior of pure magnesium. Met. Mater. Int. 15 (6), 955–961.
Lemaitre, J., Desmorat, R., 2005. Engineering Damage Mechanics: Ductile, Creep, Fatigue and Brittle Failures. Springer Science & Business Media, Berlin.
Leong, K., 1998. Laser Beam Welding of Any Metal. Argonne National Lab., Argonne, IL, US.
Lethaus, B., et al., 2014. Interval cranioplasty with patient-specific implants and autogenous bone grafts–success and cost analysis. J. Cranio-Maxillofac. Surg. 42 (8), 1948–1951.
Li, Z., et al., 2008. The development of binary Mg–Ca alloys for use as biodegradable materials within bone. Biomaterials 29 (10), 1329–1344.
Li, J., et al., 2010. In vitro degradation and cell attachment of a PLGA coated biodegradable Mg–6Zn based alloy. J. Mater. Sci. 45 (22), 6038–6045.
Li, Y., et al., 2012. Mg–Zr–Sr alloys as biodegradable implant materials. Acta Biomater. 8 (8), 3177–3188.
Lippmann, H., Lemaitre, J., 1996. A Course on Damage Mechanics. Springer, Berlin Heidelberg: Berlin.
Liu, L., Schlesinger, M., 2009. Corrosion of magnesium and its alloys. Corros. Sci. 51 (8), 1733–1737.
Lock, J.Y., et al., 2014. Degradation and antibacterial properties of magnesium alloys in artificial urine for potential resorbable ureteral stent applications. J. Biomed. Mater. Res. A 102 (3), 781–792.
Luckey, T., Venugopal, B., 1977. Metal Toxicity in Mammals. Volume 1. Physiologic and Chemical Basis for Metal Toxicity. Metal Toxicity in Mammals. vol. 1. Plenum Press, New York, London.
Luo, A.A., 2013. Magnesium casting technology for structural applications. J. Magnes. Alloys 1 (1), 2–22.
Luo, A., Pekguleryuz, M., 1994. Cast magnesium alloys for elevated temperature applications. J. Mater. Sci. 29 (20), 5259–5271.
Luo, A., et al., 1995. Magnesium castings for automotive applications. JOM 47 (7), 28–31.
Luo, A.A., Sachdev, A.K., Powell, B.R., 2010. Advanced casting technologies for lightweight automotive applications. China Foundry 7 (4), 463–469.
Ma, C., et al., 2017. Improving surface finish and wear resistance of additive manufactured nickel-titanium by ultrasonic nano-crystal surface modification. J. Mater. Process. Technol. 249, 433–440.
Malayoglu, U., Tekin, K.C., Shrestha, S., 2010. Influence of post-treatment on the corrosion resistance of PEO coated AM50B and AM60B Mg alloys. Surf. Coat. Technol. 205 (6), 1793–1798.
Manivasagam, G., Suwas, S., 2014. Biodegradable Mg and Mg based alloys for biomedical implants. Mater. Sci. Technol. 30 (5), 515–520.
Matena, J., et al., 2015. Comparison of selective laser melted titanium and magnesium implants coated with PCL. Int. J. Mol. Sci. 16 (6), 13287–13301.
Mehanny, S., et al., 2012. Fabrication and characterization of starch based bagasse fiber composite. In: ASME 2012 International Mechanical Engineering Congress and Exposition. American Society of Mechanical Engineers.
Mehanny, S., et al., 2016. High-content lignocellulosic fibers reinforcing starch-based biodegradable composites: properties and applications. In: Composites from Renewable and Sustainable Materials. InTech, London, pp. 45–64.

Mezbahul-Islam, M., Mostafa, A.O., Medraj, M., 2014. Essential magnesium alloys binary phase diagrams and their thermochemical data. J. Mater. 2014.
Mordike, B., Ebert, T., 2001. Magnesium: properties—applications—potential. Mater. Sci. Eng. A 302 (1), 37–45.
Morlacchi, S., Migliavacca, F., 2013. Modeling stented coronary arteries: where we are, where to go. Ann. Biomed. Eng. 41 (7), 1428–1444.
Murr, L.E., et al., 2011. Microstructural architecture, microstructures, and mechanical properties for a nickel-base superalloy fabricated by electron beam melting. Metall. Mater. Trans. A 42 (11), 3491–3508.
Nassiri, M., MacDonald, B., O'Byrne, J.M., 2012. Locking compression plate breakage and fracture non-union: a finite element study of three patient-specific cases. Eur. J. Orthop. Surg. Traumatol. 22 (4), 275–281.
Nehan, M., Maloney, R., 1996. Magnesium AM60B Instrument Panel Structure for Crashworthiness FMVSS 204 and 208 Compliance. SAE. Technical Paper.
New BIOTRONIK DREAMS, 2013. Bioabsorbable Metal Drug Eluting Coronary Scaffold in First Patient. [cited 2016 14 May]; Available from: http://www.medgadget.com/2013/10/biotronik-dreams.html.
Ng, C., et al., 2010. Layer manufacturing of magnesium and its alloy structures for future applications. Virtual Phys. Prototyp. 5 (1), 13–19.
Nie, J., Muddle, B., 1997. Precipitation hardening of Mg-Ca (-Zn) alloys. Scr. Mater. 37 (10), 1475–1481.
Nölke, C., 2013. A cure in 3D. In: The Trumpf Laser Magazine. Laser-Community, Hannover, Germany, p. 5.
Oh-Ishi, K., et al., 2009. Age-hardening response of Mg–0.3 at.% Ca alloys with different Zn contents. Mater. Sci. Eng. A 526 (1), 177–184.
Onishi, Y., et al., 2012. Numerical method for time-dependent localized corrosion analysis with moving boundaries by combining the finite volume method and voxel method. Corros. Sci. 63, 210–224.
Oppeel, A., 2015. Experimental characterisation and finite element modeling of biodegradable magnesium stents. In: Engineering and Architecture. Universiteit Ghent, Ghent.
Petrini, L., et al., 2004. Numerical investigation of the intravascular coronary stent flexibility. J. Biomech. 37 (4), 495–501.
Poinern, G.E.J., Brundavanam, S., Fawcett, D., 2012. Biomedical magnesium alloys: a review of material properties, surface modifications and potential as a biodegradable orthopaedic implant. Am. J. Biomed. Eng. 2 (6), 218–240.
Pourbaix, M., 1974. Atlas of Electrochemical Equilibria in Aqueous Solutions. National Assoc. Corrosion Engineers, Houston.
Qu, Y., et al., 2015. Evaluation of a new Mg–Zn–Ca–Y alloy for biomedical application. J. Mater. Sci. Mater. Med. 26 (1), 1–7.
Rad, B., et al., 2012. Characterization and corrosion behavior of biodegradable Mg-Ca and Mg-Ca-Zn implant alloys. In: Applied Mechanics and Materials. Trans Tech Publ.
Remennik, S., et al., 2011. New, fast corroding high ductility Mg–Bi–Ca and Mg–Bi–Si alloys, with no clinically observable gas formation in bone implants. Mater. Sci. Eng. B 176 (20), 1653–1659.
Roland, L., et al., 2015. Poly-ε-caprolactone coated and functionalized porous titanium and magnesium implants for enhancing angiogenesis in critically sized bone defects. Int. J. Mol. Sci. 17 (1), 1.
Saha, P., et al., 2015. Effects of grain refinement on the biocorrosion and in vitro bioactivity of magnesium. Mater. Sci. Eng. C 57, 294–303.

Sankara Narayanan, T., Park, I.S., Lee, M.H., 2014. Strategies to improve the corrosion resistance of microarc oxidation (MAO) coated magnesium alloys for degradable implants: prospects and challenges. Prog. Mater. Sci. 60, 1–71.
Seitz, J.M., et al., 2014. Magnesium degradation products: effects on tissue and human metabolism. J. Biomed. Mater. Res. A 102 (10), 3744–3753.
Shadanbaz, S., Dias, G.J., 2012. Calcium phosphate coatings on magnesium alloys for biomedical applications: a review. Acta Biomater. 8 (1), 20–30.
Shi, Z., Jia, J.X., Atrens, A., 2012. Galvanostatic anodic polarisation curves and galvanic corrosion of high purity Mg in 3.5% NaCl saturated with Mg (OH) 2. Corros. Sci. 60, 296–308.
Song, G.L., Atrens, A., 1999. Corrosion mechanisms of magnesium alloys. Adv. Eng. Mater. 1 (1), 11–33.
Song, Y., Shan, D., Han, E.-H., 2013. A novel biodegradable nicotinic acid/calcium phosphate composite coating on Mg–3Zn alloy. Mater. Sci. Eng. C 33 (1), 78–84.
Sun, W., et al., 2013. An arbitrary Lagrangian–Eulerian model for studying the influences of corrosion product deposition on bimetallic corrosion. J. Solid State Electrochem. 17 (3), 829–840.
Swann, P., 1963. Dislocation substructure vs transgranular stress corrosion susceptibility of single phase alloys. Corrosion 19 (3), 102t–114t.
Taljanovic, M.S., et al., 2003. Fracture fixation 1. Radiographics 23 (6), 1569–1590.
Tan, L., et al., 2013. Biodegradable materials for bone repairs: a review. J. Mater. Sci. Technol. 29 (6), 503–513.
Tan, L., et al., 2014. Loss of mechanical properties in vivo and bone–implant interface strength of AZ31B magnesium alloy screws with Si-containing coating. Acta Biomater. 10 (5), 2333–2340.
Verstraeten, S.V., Aimo, L., Oteiza, P.I., 2008. Aluminium and lead: molecular mechanisms of brain toxicity. Arch. Toxicol. 82 (11), 789–802.
Vinarcik, E.J., 2002. High Integrity Die Casting Processes. John Wiley & Sons, New York.
Wenman, M., et al., 2008. A finite-element computational model of chloride-induced transgranular stress-corrosion cracking of austenitic stainless steel. Acta Mater. 56 (16), 4125–4136.
Winzer, N., et al., 2005. A critical review of the stress corrosion cracking (SCC) of magnesium alloys. Adv. Eng. Mater. 7 (8), 659–693.
Winzer, N., et al., 2008. Comparison of the linearly increasing stress test and the constant extension rate test in the evaluation of transgranular stress corrosion cracking of magnesium. Mater. Sci. Eng. A 472 (1–2), 97–106.
Witte, F., 2010. The history of biodegradable magnesium implants: a review. Acta Biomater. 6 (5), 1680–1692.
Witte, F., et al., 2005. In vivo corrosion of four magnesium alloys and the associated bone response. Biomaterials 26 (17), 3557–3563.
Witte, F., et al., 2008. Degradable biomaterials based on magnesium corrosion. Curr. Opinion Solid State Mater. Sci. 12 (5), 63–72.
Wong, H.M., et al., 2010. A biodegradable polymer-based coating to control the performance of magnesium alloy orthopaedic implants. Biomaterials 31 (8), 2084–2096.
Wu, G., Ibrahim, J.M., Chu, P.K., 2013. Surface design of biodegradable magnesium alloys—a review. Surf. Coat. Technol. 233, 2–12.
Xiao, J., Chaudhuri, S., 2011. Predictive modeling of localized corrosion: an application to aluminum alloys. Electrochim. Acta 56 (16), 5630–5641.

Xin, Y., Hu, T., Chu, P.K., 2010. Influence of test solutions on in vitro studies of biomedical magnesium alloys. J. Electrochem. Soc. 157 (7), C238–C243.
Xu, L., Yamamoto, A., 2012. Characteristics and cytocompatibility of biodegradable polymer film on magnesium by spin coating. Colloids Surf. B: Biointerfaces 93, 67–74.
Yue, T., Yan, L., Man, H., 2004. The effect of machined surface condition on the corrosion behavior of magnesium ZM51/SiC composite. Mater. Manuf. Process. 19 (2), 123–138.
Zberg, B., Uggowitzer, P.J., Löffler, J.F., 2009. MgZnCa glasses without clinically observable hydrogen evolution for biodegradable implants. Nat. Mater. 8 (11), 887–891.
Zeng, R., et al., 2008. Progress and challenge for magnesium alloys as biomaterials. Adv. Eng. Mater. 10 (8), B3–B14.
Zhang, E., Yang, L., 2008. Microstructure, mechanical properties and bio-corrosion properties of Mg–Zn–Mn–Ca alloy for biomedical application. Mater. Sci. Eng. A 497 (1), 111–118.
Zhang, E., et al., 2009. Microstructure, mechanical and corrosion properties and biocompatibility of Mg–Zn–Mn alloys for biomedical application. Mater. Sci. Eng. C 29 (3), 987–993.
Zhang, S., et al., 2010a. Research on an Mg–Zn alloy as a degradable biomaterial. Acta Biomater. 6 (2), 626–640.
Zhang, E., et al., 2010b. Microstructure, mechanical properties and bio-corrosion properties of Mg–Si (–Ca, Zn) alloy for biomedical application. Acta Biomater. 6 (5), 1756–1762.
Zhang, B., Liao, H., Coddet, C., 2012. Effects of processing parameters on properties of selective laser melting Mg–9% Al powder mixture. Mater. Des. 34, 753–758.
Zhao, Y., et al., 2014. High strength Mg–Zn–Ca alloys prepared by atomization and hot pressing process. Mater. Lett. 118, 55–58.
Zheng, Y., Gu, X., Witte, F., 2014. Biodegradable metals. Mater. Sci. Eng. R. Rep. 77, 1–34.
Zhiqiang, S.H.Z.M.G., 1998. Overview and prospect of semi solid casting. Spec. Cast. Nonferrous Alloys 5, 1–9.
Zunino, P., et al., 2009. Numerical simulation of drug eluting coronary stents: mechanics, fluid dynamics and drug release. Comput. Methods Appl. Mech. Eng. 198 (45), 3633–3644.

Part Three

Processing metals for biomedical applications

Forging of metals and alloys for biomedical applications

10

Margam Chandrasekaran
Wise Consultants and Services Pte Ltd, Singapore, Singapore

10.1 Introduction

Metallic materials have been long used in medical devices which can be broadly divided in to implantable and nonimplantable devices. Properties of implantable materials are of interest for both the biomedical engineer and the surgeon as it needs to meet certain requirements besides being biocompatible and bioinert to physiological environment. The most common metallic materials that are used include titanium (Ti) and its Alloys, cobalt (Co)-chromium (Cr) alloys, stainless steels (SS), and special alloys such as nickel (Ni)-Ti. Much of the properties of the end products such as implant and fixation materials are governed by the manufacturing method used and have a significant impact on the application design. Conventional methods of fabrication used were casting and machining to shape. While some of the above materials are heat treatable to arrive at the desired property, certain materials such as 316L SS (316L) pose restrictions as they are nonheat treatable. In such cases, work hardening using cold working overcomes the limitations associated with other conventional methods of fabrication especially in terms of properties achievable. Besides the above, there are many examples of wrought alloys of Co-Cr or Ti which are forged to achieve desired properties in the final product. The current chapter focuses on the fundamentals of forging of metallic materials and typical forging methodology used for metals and alloys used in biomedical applications.

10.2 Fundamentals of forging and typical forging process applied to metals and alloys for biomedical applications

Forging is a process in which the work piece is shaped by compressive forces applied through various dies and tools. It is one of the oldest metalworking operations. Most forgings require a set of dies and a press or a forging hammer.

Unlike other metal forming operations, which generally produce continuous plates, sheets, strip, or various structural cross sections, forging is predominantly used to produce discrete parts. Forging can be broadly classified based on few factors such as temperature; tools used for forging operation die design in forging; machine used

Metals for Biomedical Devices. https://doi.org/10.1016/B978-0-08-102666-3.00010-9
© 2019 Elsevier Ltd. All rights reserved.

for forging, etc. However, the most common classification is based on temperature and the Die Design (Lange et al., 1985).

10.2.1 Cold and hot forging

Cold forging is an operation done normally at room temperature or near room temperature. Metallurgically, any forging operation done below the recovery temperature ($0.2T_m$, where T_m is the melting point of the material) of the material is termed as cold forging. Since there is no recovery from residual stresses from forging operation, it results in a work hardening effect. On the other hand, hot forging is done at elevated temperatures, typically $>0.4T_m$. Deformation at these temperatures reduces the flow stress making the metal or alloy easier to shape and are less likely to fracture. The temperature of operation is above the recrystallization temperature of the material (usually between $0.4T_m$ and $0.6T_m$) which eliminates strain-hardening effect. The intermediate temperatures of operation (i.e., between $0.2T_m$ and $0.4T_m$) is usually termed as warm forging. Despite the three classifications based on temperature, the terminology of warm forging is seldom used. Hot forging besides eliminating the strain hardening has many advantages that include:

- decrease in yield strength and hence lower flow stress facilitating easier plastic deformation at low loads,
- increased ductility,
- increase in temperature also reduces chemical inhomogeneities,
- closure or elimination of pores during operation.

Hot forging on the other hand has disadvantages such as:

- poor surface finish and dimensional control,
- oxidation or undesirable reactions between the material and surrounding atmosphere, etc.

On the contrary, cold forging has certain advantages such as:

- better surface finish and dimensional control,
- increase in strength due to work hardening,
- minimum contamination.

Despite these advantages, cold forging suffers from disadvantages such as:

- higher yield strength and hence higher loads for deformation,
- poor ductility compared with hot forging,
- intermediate annealing may be required to address work hardening,
- residual stresses may be produced,
- may result in texture formation (www.farinia.com, Lange et al., 1985; Degarm et al., 2003).

10.2.2 Hot die and isothermal forging

One of the major problems associated with hot forging is the high temperatures associated, which generally requires special materials that can withstand the temperatures with a judicial compromise on the strength. However, in most forging, the die material is kept at a lower temperature compared with the forging temperature of the

workpiece. A general problem associated with such a setup is the heat transfer from the workpiece to the die surfaces causing thermal gradients in the workpiece. The cooler areas closer to the die surfaces undergo less plastic flow than in the hotter core areas, so that plastic flow is not uniform. The nonuniform plastic flow is caused by die chilling. In conventional forging practice, dies for steel forgings are heated to a maximum temperature range of 150–300°C, depending on equipment, to reduce the effects of die chilling. Another way to reduce the die chilling effect is to use lubricants that can form as thermal barrier between the workpiece and the die surfaces. Die chilling can also be reduced or eliminated by heating the dies nearer to the actual forging temperature or maintaining the die at the same temperature as that of the workpiece. The process can be classified as hot die forging when the temperature of the die is closer to the forging temperature while maintaining the die at the same temperature as that of workpiece is termed as isothermal forging (Altan et al., 2005; Lange et al., 1985).

In general, most wrought implant materials such as alloys of Ti and Ni are forged in the range of 925–1260°C. Conventionally, Ti and its alloys are hot forged as isothermal forging of these alloys requires special tooling materials, such as Ni-based superalloys and molybdenum (Mo) alloys for dies, and lubricants that can perform adequately at these temperatures. Special attention to the surrounding atmosphere is also important, such as the use of an inert gas or vacuum to protect both the dies and the work piece from oxidation.

Hot die and isothermal forging offer advantages and disadvantages. The primary advantages are closer forging tolerances resulting in reduced machining and material costs, a reduction in the number of preforming and blocking operations resulting in reduced processing and tooling costs, the use of slow ram speeds resulting in lower forging pressures, and the use of smaller machines. Secondary operations such as machining could pose challenges in some of the materials used in medical implants such as Ti and its alloys (Hong et al., 2001; Ezugwu and Wang, 1997).

The primary disadvantages are the requirements for more expensive die materials, uniform and controllable die heating systems, and an inert atmosphere or vacuum around the dies and workpiece to avoid oxidation of the dies. The typical production rates are very low to permit proper die filling at the low forging pressures.

10.2.3 Warm forging

Forging operations typically carried out between the recovery temperature of the material and that of recrystallization temperatures ($0.2T_m$–$0.4T_m$) are normally termed as warm forging. This type of forging is preferred where the strength and other properties need to be either maintained within tolerable limits, but not substantially high over the initial value. Warm forging has a number of cost-saving advantages over cold or hot forging methods. Compared with cold forging, warm forging has the potential advantages of reduced tooling loads, reduced press loads, increased ductility, elimination of need to anneal prior to forging, and favorable as-forged properties that can eliminate heat treatment. On the other hand, the temperatures used for warm forging are lower than that of hot forging operation thus saving on energy costs as well as eliminating the need for special tools that are required in hot forging operation.

This type of metalworking is limited to temperature ranges of 0.2–0.4 times the melting point of the respective material/alloy system. The operation produces a tolerable surface finish with slightly lower energy requirement. It also normally does not require annealing in intermediate stages of forging. In practice, the recrystallization or recover temperatures will get altered with pretreatment, alloying additions, and other factors. Due to this, the recrystallization or recovery temperatures gets lowered or altered and usually the recovery temperatures are very close to room temperature. A classical example of this is aluminum (Al). A commercially pure Al will have a recrystallization temperature of 200–300°C whereas the same Al when it is zone refined can have a recrystallization temperature of −50°C making room temperature processing as hot working condition. So generally any small increase in temperatures from room temperatures may bring the temperatures within the warm forging regime. So generally for practical purposes, the terminology of cold forging or cold forming is used when the operations are done at room temperature (Callister, 1994; Lange et al., 1985).

Another major classification of forging is based on the die design and includes open-die forging, closed-die forging, and flash-less forging. Medical implants are normally closed-die forged to shape (Lange et al., 1985; Altan et al., 2005).

In the open-die forging shown in Fig. 10.1A, the die or punch carries the impression of the product and the material is allowed to flow under the action of a compressive load from the punch in the cavity. However, this type of forging is limited to shapes that are simple.

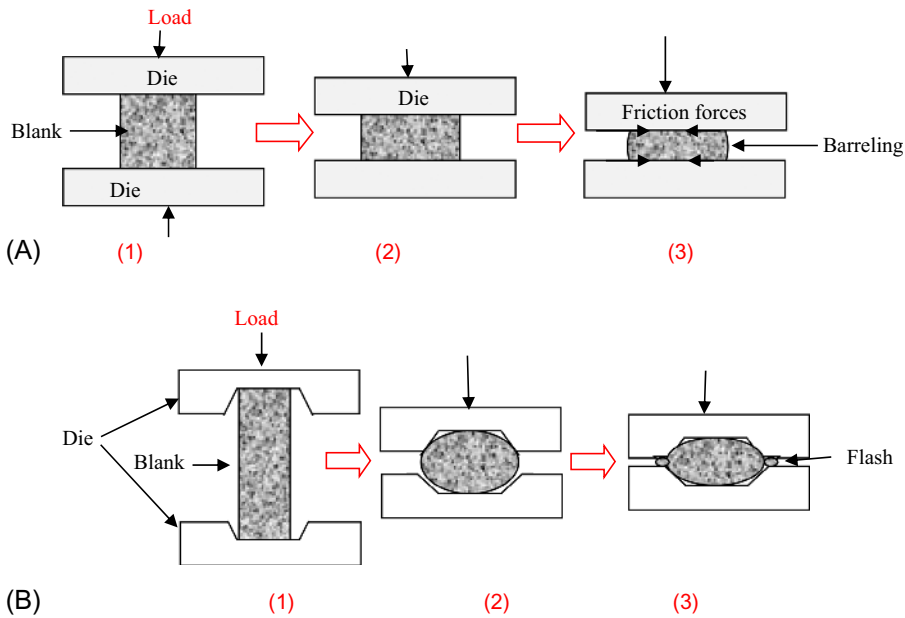


Fig. 10.1 Schematic illustrations of open-die forging and closed-die forging processes. (A) Open-die forging and (B) closed-die forging.

The closed-die forging shown in Fig. 10.1B, however, has the forging impression on both the die and punch with a land for flash material to flow. The material is allowed to flow into the cavities of punch and die to form the required shape. This also results in production of a flash. The volume of the material used in this type of forging is similar to the final volume of the product with some tolerance. Most medical implants are produced using the closed-die forging followed by a finishing operation.

10.3 Properties for forgeability

The most important property that is required for good forgeability is the plasticity in the material, which governs the deformation and flow stress of the material.

The stress experienced by a work piece can be represented by the following equation:

$$\sigma = K\varepsilon^{n}\hat{\varepsilon}^{m}T^{t}G^{g} \tag{10.1}$$

where K is a constant depending on the material, ε is the strain, "n" is the strain-hardening exponent, $\hat{\varepsilon}$ is the strain rate, m is the strain rate sensitivity index (strain rate sensitivity index) of the material, T is the temperature, t is the rate of change of temperature with deformation, G is the grain size, and g is the rate of change of grain size during deformation.

It can be clearly seen as the strain-hardening exponent or strain rate sensitivity increases the flow stress increases substantially. In other words, forgeability of the material is a function of strain, strain rate, temperature, and deformation rate is already included in strain rate. Besides this various other factors do influence the flow stress and hence the forgeability. They include, surface texture, plastic anisotropy, billet size, and temperature/preprocessing history of the billet. Strain rate sensitivity plays a critical role in superplastic forming. In practical, forging flow stress calculations, strain rate sensitivity, rate of change of temperature, and rate of change of grain size during deformation are considered negligible. The constitutive equation becomes to be as follows:

$$\sigma = K\varepsilon^{n} \tag{10.2}$$

The crystal structure of implant material chosen plays a significant role in the forgeability of the material as the flow stress depends on the slip systems present. Both SS and Co-Cr alloys exhibit FCC (face centered cubic) structure while Ti exhibits polymorphism of two different crystal structures at room and elevated temperature. The room temperature phase often referred to as α-Ti has a HCP (hexagonally close packed) which has only 3 systems active at room temperature while the high temperature beta phase exhibits BCC (body centered cubic) structure, which has 48 slip systems (Callister, 1994). The number of active slip systems in the alloy has a direct effect on forgeability by affecting the flow stress of the material. Typically, alloy systems

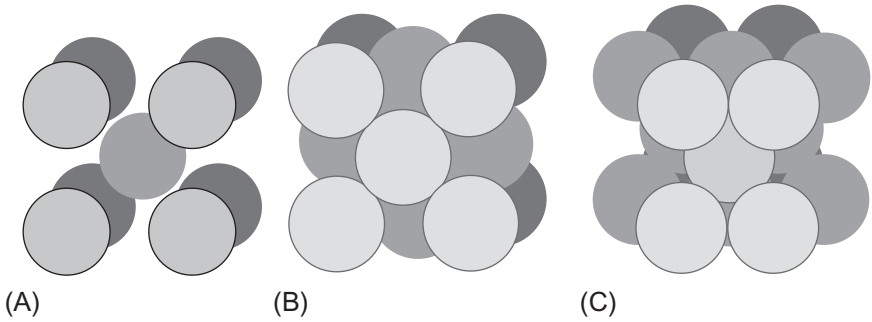


Fig. 10.2 Schematic illustration of crystal structure in a unit cell in common implant materials: (A) BCC (β-Ti), (B) FCC (SS and Co-Cr alloys), and (C) HCP (α-Ti).

having HCP structure is most difficult to forge followed by FCC and then BCC crystal structure. Thus, for forging a alloy with HCP structure, it is imperative to activate more slip systems by increasing the temperature to make the alloy forgeable and thus the forging temperature of Ti alloy systems vary from 800°C to 1200°C (El-Domiaty, 1992) while those of Co-Cr alloys and SS require temperatures of 1100–1300°C (Lippard and Kennedy, 1999; Bunea et al., 2003; Bhat, 2002; Kramer, 2000). Fig. 10.2 shows typical crystal structures observed in common implant materials.

10.4 Microstructural developments and its consequence on properties

Forging results in metal that is stronger than cast or machined metal parts. This is due to the grain flow caused through forging. As the metal is pounded the grains deform to follow the shape of the part, and thus the grains are unbroken throughout the part. Some modern parts take advantage of this for a high strength-to-weight ratio.

Many metals are forged cold, but iron (Fe) and its alloys are almost always forged hot. This is for two reasons: first, if work hardening is allowed to progress, hard materials such as iron and steel would become extremely difficult to work with; secondly, steel can be strengthened by other means than cold-working, thus it is more economical to hot forge and then heat-treat. Alloys that are amenable to precipitation hardening, such as most alloys of Al and Ti are also hot forged and then hardened. Similarly Co-Cr is hot forged while it is preferable to perform cold working of surgical grade of SS as strengthening is achieved by cold working. Other materials must be strengthened by the forging process itself.

As highlighted above, one of the factors deciding the strength of the forged components is the microstructural changes occurring during the forging operation. Hence, the forging temperatures selected becomes critical as it will decide the final strength and modulus of the material. Modulus becomes important from the aspect of stress shielding effects of most implant materials. The closer the modulus is to the bone modulus, better would be functional behavior. Stress shielding is one of perennial

problem not only in orthopedic implants, but, in general, in most biomedical implants where biomechanics plays a vital role in the body function. It could range from mastication in dentistry to functional integration of implants in orthopedics. Besides stress shielding, other properties such as cracking resistance, fatigue resistance, and wear behavior becomes critical depending on the application. While these aspects control the functional performance, there are other complications such as probable contaminations from environment during hot working of materials. Being a medical device, the regulatory controls on this aspect becomes important. Section 10.9 highlights some of the standardization initiatives both on the grade of the material and forging process controls. Similar control applies to other processing methods such as casting or machining as well.

Hot forging of Ti alloys for biomedical applications are usually carried out near the recrytallization temperatures, but when the temperature difference between those selected for forging and recrystallization is higher, the changes in microstructure affects the properties. Similarly, preheating of billet prior to forging temperature also has an effect on the microstructure and properties (Dziubińska et al., 2017, Semlitsch, 1987; Imam and Fraker, 1996, Kramer, 2000; El-Domiaty, 1992), Higher the preheat temperature, the microstructural changes and effective final properties would be closer to the standard. So it becomes important to control the process with standardization of parameters to arrive at implants with consistent and repeatable properties.

10.5 Forging of metals and alloys for biomedical applications

10.5.1 Forging of Ti and its alloys

The use of Ti and its alloys in clinical applications dates back to early 1950s owing to its excellent corrosion resistance, biocompatibility, and high strength to weight ratio. However, the processing of Ti and its alloys has been a major challenge owing to its high reactivity at elevated temperatures. Conventional method of processing includes vacuum casting followed by machining. Machining of Ti and its alloys is a major challenge due to its poor thermal conductivity necessitating the use of high-speed machining with a suitable coolant to prevent galling (Hong et al., 2001; Ezugwu and Wang, 1997). On the other hand, deforming Ti and its alloys (forging) to the required shape followed by finish machining is difficult owing to Ti being highly strain rate sensitive. Moreover, Ti and its alloys exhibit polymorphism and the allotropic transformation occurs at 882.5°C for pure Ti and this temperature varies with the alloying additions. The alloying additions can be either an α or β stabilizer depending on whether they increase or decrease the transformation temperatures. The α/β stabilizer can be classified as either isomorphous or eutectoid stabilizers depending on the crystal structure of the additive (Imam and Fraker, 1996). The eutectoid stabilizers result in transformation of β phase in to α with the corresponding alloying element on slow cooling. Hence in order to retain the β phase at room temperature quenching is preferred. The main difference between isomorphous and eutectoid stabilizers are that the alloy

system when slowly cooled from its β transformation temperature does not cause change of phase to α plus others. Hence, for eutectoid stabilizers, it is recommended that the alloy be quenched from its beta transformation temperature to retain partial beta phase on cooling. Vanadium (V) and molybdenum (Mo) are typical examples of isomorphous beta stabilizers while Fe, Cr, and silicon (Si) are eutectoid beta stabilizers. Similarly, most commonly used alloying element—Al is an α stabilizer. Pure β phase alloy can be rolled to about 90% reduction in thickness. α and near-α Ti are not heat treatable/weldable and have limited formability at room temperature. α-β or β titanium alloys have reasonably a good formability (Imam and Fraker, 1996). α or near α alloys are strengthened by inducing cold work or plastic deformation. Various grades of Ti and its alloys are being used in implants which include commercially pure Ti in dental implants and maxillofacial applications to the specific alloy systems such as Ti-6Al-4V in hip and knee prosthesis, trauma for fixation devices and implants (Freese et al., 2001). Commercially pure Ti offers excellent corrosion resistance and biocompatibility, but is restricted by its lower strength and poor wear properties. The microstructure of Ti has considerable effect on the deformation behavior and work hardening rate of Ti. This property is exploited in strengthening Ti and its alloys as well as for deformation processing of Ti and its alloys (Forging). The most commonly used Ti alloy (example Ti-6Al-4V) has an α + β structure. The flow stress of the alloy is very high at room temperature causing poor formability but on the other hand lesser contamination as the billet is maintained at room temperature. Raising the temperature of Ti and its alloys induces oxygen (O) and hydrogen (H) contamination affecting the deformation despite the increase in number of active slip systems. Thus, the deformation needs to be carried out at temperatures close to β transformation temperature (transus) activating more slip planes. Ti offers excellent corrosion resistance at room temperature as a thin tenacious layer titanium dioxide forms at room temperatures on its surface. This layer protects from Ti surface from further propagation of corrosion. However, Ti is highly oxidative above 600°C since; the stable Ti oxides film normally formed at room temperatures is broken exposing nascent Ti surface increasing the rate of oxidation. Thus, the deformation of Ti and its alloys near β transus temperature needs to be carried out in a controlled environment in an inert atmosphere to minimize or eliminate the oxidation increasing the processing cost. Ti and its alloys are forged at temperatures ranging from 900°C to 1200°C depending on the grade of pure Ti or the alloying additions used. The deformation behaviors of Ti and its alloys are much dependent on the phases present at the deformation or hot working temperature. Typically in an α-β system, the deformation is controlled by either α or β phase depending on the temperature selected for the hot working temperature. To improve properties such as wear resistance, surface modifications such as ion nitriding or coating is used. Some of the typical alloys which are used include Ti-6Al-4V, Ti-5Al-2.5Fe, Ti-6Al-7 niobium (Nb) (Semlitsch, 1987). Ti alloys also exhibit superplasticity (elongations ranging from 200% to 2000%) if it meets certain criteria such as fine grain size and a suitable grain refiner. Recent developments are directed toward application of superplastic forming for fabricating to dental implants. Typical flow stress of Ti alloys are above 400 MPa at room temperature, but drops to $<$50 MPa at about 900–1100°C. Moreover, Ti and its alloys work harden easily

necessitating intermediate annealing steps before final shape is arrived when it is either cold worked or warm forged (El-Domiaty, 1992; Oliveira et al., 1998; Hu and Dean, 2001; Ma et al., 2006).

Ti alloys form a good choice for permanent implant, due to high corrosion resistance (due to spontaneous self-passivation, or development of oxide surface layer). Most Ti alloys for implant are typically fabricated by combined forging and annealing. Despite the fact that young's modulus of common Ti alloy used for implants (Ti-6Al-4V) is the lowest of the materials of choice, that is, Co-Cr or SS and is $\approx$50% or lower than SS and Co-Cr alloys, thus reducing the stress shielding but the modulus of Ti alloy is still $\sim$6 times that of bone and this is critical especially in wrought (forged) alloys as mechanical properties are better than the cast alloys. Major disadvantage includes reduced fatigue life due to presence of stress concentrations and high wear rates. Table 10.1 gives typical properties of most commonly used Ti alloys for implant applications and Figure 10.3 depicts a schematic representation of typical hot forging and isothermal forging methods used for Ti alloys.

10.5.2 Forging of Co-Cr alloys

The use of wrought Co-Cr alloys in clinical applications goes back to early 1950s replacing the cast components owing to better mechanical properties such as fatigue life and strength. Despite the fact that there are many Co-based biomaterials, two main alloys namely, cast Co-Cr alloys and wrought Co-Cr alloys are used. Co-Cr alloy has an austenitic structure (FCC), which is stabilized by the presence of Ni, Fe and manganese (Mn) thus avoiding the change of crystal structure of BCT (body centered tetragonal) which is difficult to process. The presence of Ni improves the forgeability of wrought Co-Cr alloys. From biocompatibility perspective, Co, Cr, and Ni are not preferred as individual ions such as Ni and Co have been found to cause allergy, while Cr is toxic (Bunea et al., 2003). Though wrought Co-Cr alloy as such does not cause any toxicity, the elution of metal ions is a serious concern of which Ni is carcinogenic. Thus, from biocompatibility perspective, the Ni content needs to be reduced or

Table 10.1 Typical properties of commonly used Ti and its alloys in implants (Freese et al., 2001; Semlitsch, 1987; Kramer, 2000).

Material	ISO code	Ultimate tensile strength (MPa)	Elongation to failure (%)
Grade-1	5832-2	240	24
Grade-2	5832-2	345	20
Grade-3	5832-2	450	18
Grade-4	5832-2	550	15
Ti-6A-l4V	5832-3	860	10
Ti-6Al-7Nb	5832-11	900	10

Table consolidated from different references.

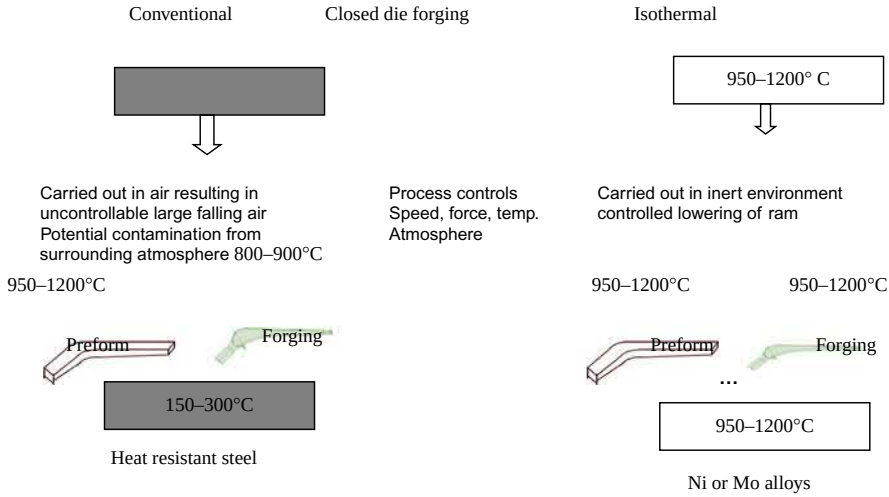


Fig. 10.3 Schematic illustrations of typical hot forging and isothermal forging of Ti alloy.

eliminated to avoid the toxicity issue. This results in a contradicting situation wherein the removal of Ni will affect the workability of the material similar to what is experienced in SS (Chiba et al., 2005). Wrought Co-Cr alloys are hot forged and intermediate annealing may be required before arriving at the final shape. Due to the difficulty associated with machining of Co-Cr alloys, it's preferable to perform a closed-die forging operation to minimize the finish machining. Forging of Co-Cr alloys normally requires sophisticated press with heat resistant tooling since it is difficult to work at lower temperatures and isothermal or hot forging is desired with intermediate annealing process (Mishra et al., 1999; Lippard and Kennedy, 1999; Hiriomoto et al., 2005).

The metallurgy for Co-Cr alloys is identical to the Co-based superalloys and solid solution strengthening is produced by the presence of alloying elements. Formation of carbides also increases the strength. Therefore, the carbides should be minimized in order to have working of wrought alloys. The order of C content is about one-fifths compared to the casting alloys. In addition to this, reduction of Cr content contributes to enhanced workability of Co-Cr alloys. Recommended practice is to heat treat Co-Cr alloys within 900–1150°C before hot working such as forging in done. By controlling the forging ratio, the microstructure of Co-Cr alloys can be controlled to obtain good fatigue strength and wear resistance. The forging of Co-Cr alloys is carried out in a similar manner as that of titanium except for the change in the working temperature which varies typically from 1150°C to 1300°C (Chyouhwu et al., 2014; Lippard and Kennedy, 1999; Immarigeon et al., 1984; Okazaki, 2008).

Co-Cr-Mo alloy forms a good choice for permanent implant, due to high corrosion resistance. Generally cast parts have poorer mechanical properties than 316L SS and the mechanical strength is enhanced by forging or hot isostatic pressing,

Table 10.2 Typical properties of Co-Cr alloys for use in implants.

Material	ASTM code	Yield strength (MPa)	Ultimate tensile strength (MPa)	Ultimate elongation (%)	Hardness (HRC)	Bending strength (MPa)
Cast	F75	450	655	8	NA	300
Forged	F799	827	1172	12	35	600
Wrought and Annealed	F1537	517	897	20	25	
Wrought and hot worked	F1537	700	1000	12	28	
Wrought and warm worked	F1537	827	1172	12	35	
Annealed	F562		800	40		
Annealed	F563	276	600	50		
Cold worked	F562		1200	10		
Cold worked	F563		1310	12		

Table consolidated from different references.

which reduces grain size and concentration of defects. The typical disadvantages include high cost and limitations on component complexity (Bunea et al., 2003). The Table 10.2 consolidated from different references and standards, gives typical properties of the most common Co-Cr alloys used in biomedical implants.

10.5.3 Forging of stainless steel

SS are generally preferred for short-term implants where the implant can be removed within 1–2 years. SS materials which are used in implants are normally not heat treatable and thus much of their mechanical properties are tailored by performing cold work. They find use in components such as bone screws, plates, and other temporary fixation devices. SS used for implants are austenitic and have good formability. The typical hot working temperatures are around 1100–1250°C. Rapid cooling on completion of hot working is not required in case of implant materials such as 316L since there will be no detrimental precipitation of carbides. Precipitation of carbides affects the corrosion resistance and ductility (Kramer, 2000; Bhat, 2002; Davis, 2003; Altan et al., 2005). The Table 10.3 consolidated from different references gives typical properties of surgical grade SS used in medical implants.

Table 10.3 Typical properties of SS for use in implants.

Material	ASTM code	Yield strength (MPa)	Ultimate tensile strength (MPa)	Ultimate elongation (%)
DIN 17443	5832-1		490–690	40
REX 734	5832-9		740	35
In development	P2000		980	55
316L		205	515	40
DIN 17443 CW			860	12
REX 734 CW			1060	12
In development CW			1200	12
316L CW		690	860	12

CW, cold worked.
Table consolidated and based on various standards and supplier information.

10.5.4 Forging of shape memory alloys

Shape memory alloys are used in applications such as osteosynthesis plates and dental braces. They derive the name due to its property to remember the prior shape even if it undergoes significant deformation. One such shape memory alloy used in implants is Nitinol (Ni-Ti Alloy). Nitinol undergoes forging and rolling at elevated temperatures after the ingot is produced. Typical hot working temperatures are around 800–900°C where the workability of the material is good with minimal surface oxidation. Hot working processes improve the mechanical properties of Nitinol by adjusting its microstructure. Following hot working Ni-Ti alloy is cold worked and heat treated to obtain the final dimensions with desired properties. Ni-Ti alloy undergoes rapid work hardening, thus necessitating multiple reductions with intermediate annealing steps at 600–800°C until the final shape and size are obtained. Major problem associated with Ni-Ti alloy forming is the spring back. Thus, Ni-Ti alloy forging requires over deformation in order to release the stress to achieve the desired shape. Another option to counter act the spring back is to subject the part to heat treatment under constraint (Filip, 2001; Prymark et al., 2005; Elahinia et al., 2012).

10.5.5 Cold forming for miscellaneous applications

Hot forming or hot forging is most commonly used in processing of wrought alloys for medical applications. However, there are few applications where cold forming is preferred and used due to the inherent advantages listed above such as better surface finish and dimensional control, Increase in strength due to work hardening, minimal contamination, etc. The advantages of cold forming become very useful especially when small parts with precision are required. In addition to the above, it comes handy while processing precious biocompatible materials such as gold (Au), which are very difficult to process using a machining or hot forming as it can result in deformities or too sticky for machining. Cold forming is very useful in such cases where secondary

processing needs to be minimized or eliminated for the above reasons. In other words, cold forming would be able to deliver products, which are precise in tolerances with minimal or no secondary processing and ensure consistency of the batch. Most common devices that are processed using a cold forming include precision fasteners, housing for devices such as hearing aid devices, and sensor components besides dental implants (www.stsintelli.com, https://www.sussexwire.com/docs/SussexWire-MDB-article-20140507.pdf).

10.6 Die materials and die design for forging

10.6.1 Die materials

Hot work die steels are the most commonly used in forging dies for working in the temperatures of 350–650°C. The hot work die steels usually contain carbide-forming elements such as Cr, tungsten (W), and molybdenum (Mo). These alloying elements induce formation of carbides that induce hardening with high resistance to softening.

10.6.2 Factors in the selection of die materials

For hot forging the die material should possess the following properties:

(i) uniform hardenability
(ii) good abrasion resistance
(iii) high hardness
(iv) toughness
(v) good mechanical and thermal fatigue strength

Besides the selection of the die material, it is imperative that the die design takes into account properties such as metal flow, and minimal losses into flash. Thus, die design for multistage forging and corresponding preformed designs are critical for obtaining defect free forging. Thus, both the preform die design and preform shaping in workpieces are critical to obtain a successful and economic forging. Therefore, the preform shaping is done either by machining or by open-die forging until the required shape for final closed-die forging operation is achieved. The preform shaping operation has to be carefully selected in order to avoid stress concentration or nonuniform stress distribution in the preform. This will affect the flow stress of the material in different regions and thus the plasticity. Recent development in the field of modeling helps to overcome the limitations of conventional trial and error methods to obtain optimum preform designs and die designs. Finite element modeling helps to identify nonuniform stress states that arise due to different processing methodologies and optimize the preprocessing conditions and the die design for preprocessing.

For Isothermal forging, the die material should possess the following properties.

1. good mechanical and fatigue strengths at elevated temperature,
2. good abrasion resistance, and
3. hot hardness and toughness.

Isothermal forging are typically carried out between 900°C and 1100°C depending on the material being forged and die steel materials do not meet strength criterion at elevated temperatures. Thus, isothermal forging necessitates the use of Ni superalloys and Mo alloys for the die. One of the major problems associated with hot die forging and isothermal forging is the poor tool life as opposed to cold forging which also contributes to economics of forging (Lange et al., 1985; Davis, 1998; Altan et al., 2005).

10.7 Powder metallurgy forging of metals and alloys for biomedical applications

Powder metallurgy (PM) forging is a process whereby a sintered powder metal part is forged using a conventional closed-die forging to attain the final shape. One of the recent developments in the field of medical implants is production of porous metallic implants using the above-mentioned process using Co-based alloys or Ti-based alloys. This type of forging is preferred especially for improving the osteo-integration of the implant as well as to address the limitations associated with conventional wrought alloys such as limited plasticity and high flow stress. Especially isothermal forging of Ti and Co-based alloys require expensive special tooling materials such as Ni-based superalloys and Mo alloys for dies and use of expensive lubricants. Moreover, use of PM process to produce the preform required for final close die forging contributes to the cost advantage thereby improving the economics of forging of such alloys (Mareka et al., 2015).

10.8 Superplastic forming

Superplasticity is a property exhibited by materials like Ti-6Al-4V wherein the material can be deformed beyond their usual strain limits. Usually when a material is exhibiting superplasticity, strains over 200% is sustained without failure. When the grain size is controlled and deformation is attempted at a very low strain rate, there is practically insignificant strain-hardening effect on the material which permits elongation beyond 200%. Superplastic forming has been mainly attempted in dental implants especially oral maxillofacial implants due to its significant advantage over forging. The flow stresses are very low compared to forging and so large deformations can be achieved with insignificantly low stress, which can be achieved with gas pressures. Currently, superplastic forming is limited to cranial and oral maxillofacial implants. However, the potential for expanding to other medical devices due to their advantages such as low die cost, ability to form complex shapes with reduced spring back, and customization of implants becomes possible with superplastic forming. Current application of superplastic forming is limited to dental implants but has potential to expand further (Lee, 2007).

Constituent equation for superplasticity will follow the flow stress equation (10.1).

However, the effect of all the other terms such as ϵ, T, and G will be negligible. Especially the strain-hardening exponent will be zero ($n = 0$) above the recrystallization temperature. Therefore, effective equation will reduce to as following equation:

$$\sigma = K\hat{\epsilon}^m \tag{10.3}$$

Therefore, the deformation is dependent on strain rate and it is intentionally kept low so that forming can be achieved at low flow stresses.

10.9 Standards for selection and forging of biomedical materials

One of the key factors for medical devices is the regulatory control so that the device fabricated is safe. The main driver for quality management systems in medical devices is to keep the device safe and effective for use. As seen from foregoing discussions, there are certain degree of variability in terms of contamination and other concerns with different types of forming, that is, cold or hot forming. Therefore, standards development organizations (SDO) have been working on various methods of control measures that can be used to minimize contamination and also ensure consistency of the process. SDO's such as ISO and ASTM have developed base standards both for selection of the most commonly used materials for process control and consistency in properties (www.iso.com, www.astm.org).

Some of the example baseline standards have been included below for reference purposes

1. ISO 15374:1998(en) Implants for surgery—Requirements for production of forgings
2. ISO 5832-7:2016 Characteristics of, and corresponding test methods for, forgeable and cold-formed cobalt-chromium-nickel-molybdenum-iron alloy for use in the manufacture of surgical implants.
3. ASTM-F620 › Standard Specification for Titanium Alloy Forgings for Surgical Implants in the Alpha Plus Beta Condition
4. ASTM-F1091 › Standard Specification for Wrought Cobalt-20Chromium-15Tungsten-10Nickel Alloy Surgical Fixation Wire (UNS R30605)
5. ASTM-F1295 › Standard Specification for Wrought Titanium-6Aluminum-7Niobium Alloy for Surgical Implant Applications (UNS R56700)
6. ASTM-F1314 › Standard Specification for Wrought Nitrogen Strengthened 22 Chromium-13 Nickel-5 Manganese-2.5 Molybdenum Stainless Steel Alloy Bar and Wire for Surgical Implants (UNS S20910)
7. ASTM-F961—Standard Specification for 35Cobalt-35Nickel-20Chromium-10Molybdenum Alloy Forgings for Surgical Implants (UNS R30035)
8. ASTM-F621—Standard Specification for Stainless Steel Forgings for Surgical Implants
9. ASTM-F562—Standard Specification for Wrought 35Cobalt-35Nickel-20Chromium-10Molybdenum Alloy for Surgical Implant Applications (UNS R30035)

10.10 Summary

Artificial implants should possess certain properties such as good dimensional tolerance, ability to be modified during surgery to fit the patient, high fracture toughness, good fatigue resistance, comparable strength, and modulus close to that of bone, and high wear resistance besides regular requirements of tissue, biocompatibility, high purity, and reproducibility. Thus, processing plays a vital role as some of the properties such as strength, modulus, fracture toughness, and fatigue resistance are adjusted during the processing. Besides this, the need for anisotropic elastic properties similar to bone in an important criterion and is solely dependent on processing methodology. Forging of metals and alloys for biomedical applications have an important place in the fabrication methodologies adopted. Forging improves the strength that is critical in certain applications. However, on the other hand, forging has certain limitations with respect to fatigue properties which are affected by strength and hardness of the material. Typically, higher the strength and hardness, the resistance to fatigue is higher, but may fail catastrophically as crack propagation is faster. This becomes critical as the type of forging adopted decides the surface finish and strength. The surface finish plays a vital role in crack initiation, which is affected by the forging process. This becomes especially critical in Ti and its alloys, which also have poor wear properties. Thus it may be necessary to subject the metal and alloys for a secondary processing to improve the surface properties such as finish machining or coating. On the other hand, materials, which are difficult to strengthen by heat treatment, can be strengthened by cold working. Recent developments such as powder forging technology or superplastic forming applied medical devices overcome limitation of using expensive tooling for production of preforms and also offers some advantages. However, these processes cannot completely replace the conventional methods such as forging or machining or casting. Moreover medical devices are reliant on conventional methods as a change in processing methods is a long process to prove the said change is as safe and effective as the original method. The controls for manufacturing and distribution of medical devices are more stringent than other industries. Thus a deviation from the approved process becomes very challenging. On the commercial benefits of forging, despite the advantage of forging such as improved strength where heat treatment is a challenge, the cost benefit and economics of forging over the other methods of fabrication need to be evaluated before designing the process to be adopted.

References

Altan, T., Ngaile, G., Shen, G., 2005. Cold and Hot Forging Fundamentals and Applications. ASM International, Materials Park, OH.

Bhat, S.V., 2002. Biomaterials. Kluwer Academic Publishers, Dordrecht.

Bunea, D., Bojin, D., Zamfir, S., Miculescu, F., Miculescu, M., 2003. Experimental researches concerning the Co-Cr-Mo alloys implantology. Eur. Cell. Mater. 5 (1), 53–54.

Callister Jr., W.D., 1994. Materials Science and Engineering, third ed. John Wiley & Sons Inc., Hoboken, NJ.

Chiba, A., Kumagai, K., Takeda, H., Nomura, N., Naoyuki, 2005. Mechanical properties of forged low Ni and C-containing Co-Cr-Mo biomedical implant alloy. Mater. Sci. Forum 475–479 (3), 2317–2322.

Chyouhwu, H., Chen, H.S., Sainbuyan, N., Hsiung, J.C., Lee, J.M, 2014. Analysis of the hot forging parameters of CCM alloy for medical device. Life Sci. J. 11 (11), 732–736.

Davis, J.R., 1998. Forging, Metals Handbook Desk, first ed. ASM International, Materials Park, OH.

Davis, J.R., 2003. Handbook of Materials for Medical Devices. ASM International, Materials Park, OH.

Degarm, E.P., Black, J.T., Kohser, R.A., Ronald, A., 2003. Materials and Processes in Manufacturing, ninth ed. John Wiley & Sons, Hoboken, NJ.

Dziubińska, A., Majerski, K., Winiarski, G., 2017. Investigation of the effect of forging temperature on the microstructure of grade 5 titanium ELI. Adv. Sci. Technol. Res. J. 11 (4), 147–158.

Elahinia, M.H., Hashemi, M., Tabesh, M., Bhaduri, S.B., 2012. Manufacturing and processing of NiTi implants: a review. Prog. Mater. Sci. 57, 911–946.

El-Domiaty, A., 1992. The effect of strain, strain rate and temperature on forgeability of TI-6AL-4V alloy. J. Mater. Process. Technol. 32, 243–251.

Ezugwu, E.O., Wang, Z.M., 1997. Titanium alloys and their machinability—a review. J. Mater. Process. Technol. 68, 262–274.

Filip, P., 2001. Titanium nickel shape memory alloys in medical applications. In: Brunette, D.M., Tengvall, P., Textor, M., Thomsen, P. (Eds.), Titanium in Medicine, Material Science, Surface Science, Engineering, Biological Responses and Medical Applications. Springer, Berlin, pp. 53–86.

Freese, H.L., Volas, M.G., Wood, J.R., 2001. Metallurgy and technological properties of titanium and, titanium alloys. In: Brunette, D.M., Tengvall, P., Textor, M., Thomsen, P. (Eds.), Titanium in Medicine, Material Science, Surface Science, Engineering, Biological Responses and Medical Applications. Springer, Berlin, pp. 25–52.

Hiriomoto, S., Onoderab, E., Chiba, A., Asami, K., Hanawa, T., 2005. Microstructure and corrosion behaviour in biological environments of the new forged low-Ni Co–Cr–Mo alloys. Biomaterials 26, 4912–4923.

Hong, S.Y., Markus, I., Jeong, W., 2001. New cooling approach and tool life improvement in cryogenic machining of titanium alloy Ti-6Al-4V. Int. J. Mach. Tool Manu. 41, 2245–2260.

Hu, Z.M., Dean, T.A., 2001. Aspects of forging titanium alloys and the production of blade forms. J. Mater. Process. Technol. 111, 10–19.

Imam, M.A., Fraker, A.C., 1996. Titanium alloys as implant materials. In: Brown, S.A., Lemons, J.E. (Eds.), Medical Applications of Titanium and Its Alloys, The Materials and Biological Issues. ASTM STP 1272. American Society for Testing and Materials, West Conshohocken, PA, pp. 3–16.

Immarigeon, J.P., Krishna, R., Wallace, W., 1984. Microstructural changes during isothermal forging of Co-Cr-Mo alloy. Metall. Trans. A. 15 (2), 339–345.

Kramer, K.H., 2000. Implants for surgery. In: Stallforth, H., Revell, P. (Eds.), EUROMAT, Materials for Medical Engineering. In: vol. 2. John Wiley & Sons, Canada, Ltd, Hoboken, NJ, pp. 9–29.

Lange, K., Pohlandi, K., Raghupathi, P.S., Saniter, J.D., Wolfgang, S., 1985. Schey, J.A., Weinmann, K.A., Widera, G.E.O. (Eds.), Handbook of Metal Forming. Columbus, OH, McGraw-Hill.

Lee, T.D, 2007. The Process of Using Superplastic Forming to Create Medical Components (Master's thesis). University of Kentucky, p. 489.
Lippard, H.E., Kennedy, R.L., 1999. Process metallurgy of wrought Co-Cr-Mo alloys. In: Disegi, J.A., Kennedy, R.L., Pilliar, R. (Eds.), Cobalt Based Alloys for Biomedical Applications. ASTM STP 1365. American Society for Testing and Materials, West Conshohocken, PA, pp. 98–107.
Ma, F., Lu, W., Qin, J., Zhang, D., 2006. Microstructure evolution of near-alpha titanium alloys during thermomechanical processing. Mater. Sci. Eng. A 416, 59–65.
Mareka, I., Nováka, P., Mlynára, J., Voitcha, D., Kubatíkb, T.F., Málekc, J., 2015. Powder metallurgy preparation of Co-based alloys for biomedical applications. Acta Phys. Pol. A 128 (4), 597–601.
Mishra, A.K., Hamby, M.A., Kaiser, W.B., 1999. Metallurgy, microstructure and mechanical properties of new grade cobalt chromium alloy before and after porous coating. In: -Disegi, J.A., Kennedy, R.L., Pilliar, R. (Eds.), Cobalt Based Alloys for Biomedical Applications. ASTM STP 1365. American Society for Testing and Materials, West Conshohocken, PA, pp. 71–88.
Okazaki, Y., 2008. Effects of heat treatment and hot forging on microstructure and mechanical properties of Co-Cr-Mo alloy for surgicaliImplants. Mater. Trans. 49 (4), 817–823.
Oliveira, V., Chaves, R.R., Bertazzoli, R., Caram, R., 1998. Preparation and characterization of Ti-Al-Nb alloys for orthopedic implants. Braz. J. Chem. Eng. 15 (4), 326–333.
Prymark, O., Bogdanski, D., Köller, M., Esenwein, S.A., Muhr, G., Beckmann, F., Donath, T., Assad, M., Epple, M., 2005. Morphological characterization and in vitro biocompatibility of a porous nickel titanium alloy. Biomaterials 26, 5801–5807.
Semlitsch, M., 1987. Titanium alloys for hip joint replacements. Clin. Mater. 2, 1–13.

Further reading

http://stsintelli.com/resources/medical-applications.html.
http://www.iso.org.
https://www.astm.org.
https://www.azom.com/article.aspx?ArticleID=7156.
https://www.farinia.com/forge/cold-forging/cold-forging-vs-hot-forging-considerations-benefits-and-drawbacks.
Kardish, T., 2014. Where component design functionality and cost reduction converge: cold and hot forging fundamentals and applications: white paper. In: Medical Design Briefs. https://www.sussexwire.com/docs/SussexWire-MDB-article-20140507.pdf.
Peterson, C.D., Hillberry, B.M., Heck, D.A., 1988. Component wear of total knee prostheses using Ti- 6Al-4V, titanium nitride coated Ti-6Al-4V, and cobalt-chromium-molybdenum femoral components. J. Biomed. Mater. Res. 22, 887–903.

Casting

11

Mitsuo Niinomi
Tohoku University, Sendai, Japan, Osaka University, Osaka, Japan, Nagoya University, Nagoya, Japan, Meijo University, Nagoya, Japan

11.1 Introduction

Casting is a near-net-shape processing, which effectively reduce the cost of products. Precision casting is very effective at fabricating products with complex shape, particularly dental and biomedical prostheses such as crowns, inlays, bridges, and dentures that are made by dental precision casting.

Titanium (Ti) and its alloys have gained much attention in the fabrication of biomedical prostheses such as stems of artificial hip joints, bone plates, etc. They are also popularly used to fabricate dental prostheses because they are not only nontoxic, but also allergen-free, which aids patients, who tend to suffer from allergies.

Castings suffer from casting defects such as pores and shrinkages, and coarse microstructures, which lead to low ductility and low fatigue strength. Therefore, improvement in the mechanical properties of castings is necessary.

This chapter discusses dental precision casting, casting process and mold materials, dental casting alloys, mechanical properties of cast biocompatible Ti alloys and required improvements, and alloy design for lowering the melting point of biocompatible Ti alloys used for casting.

11.2 Casting process and mold materials

Gas melting using gas such as (city gas + air), (propane gas + air), (city gas + oxygen (O) gas), (propane gas + air gas), (O gas + acetylene gas), and [O gas + hydrogen (H) gas], high-frequency induction melting, arc melting, and electric resistance melting are generally used for dental casting. High-frequency induction melting and arc melting are advantageous for melting high-temperature material such as Ti and its alloys.

Fig. 11.1 shows the complete profile of an arc melting dental casting machine, its internal chamber, and control panel. The LEVICAST method (Demukai and Tsushima, 2005), which is a process constituted of combination of levitation melting and counter-gravity low-pressure casting, schematically shown in Fig. 11.2, can be used to cast implants such as stems of artificial hip joints, as shown in Fig. 11.3. Such implants are made of Ti-29Ti (Nb)-13tantalum (Ta)-4.6zirconium (Zr) referred to as TNTZ (Kuroda et al., 1998). The TNTZ will be discussed in detail in a latter section. Using the LEVICAST system, cold crucible levitation melting (CCLM), which is

Metals for Biomedical Devices. https://doi.org/10.1016/B978-0-08-102666-3.00011-0
© 2019 Elsevier Ltd. All rights reserved.



Fig. 11.1 (A) Whole profile of dental precision casting machine (height 139 cm × width 39 cm × depth 70 cm), and (B) inside of chamber and control panel.

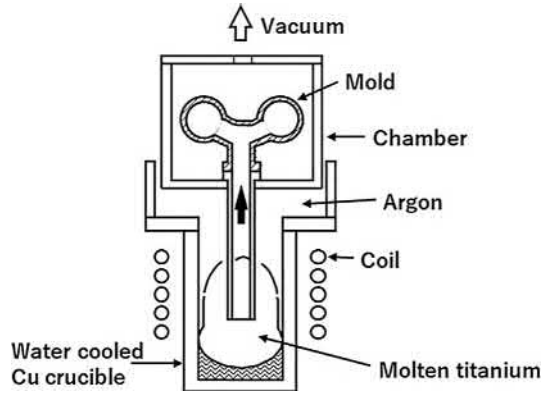


Fig. 11.2 Schematic drawing of LEVICAST process.

generally used for melting a large amount of high-temperature metallic materials such as Ti and its alloys (see Fig. 11.4), has been modified to melt and cast small-sized dental prostheses made of Ti alloys (Morita et al., 2000).

The precision casting method is predominantly used to fabricate dental prostheses and medical implants. A schematic illustration of the dental precision casting process used to create dental prostheses such as crowns is shown in Fig. 11.5 (Niinomi, 2001). In this process, wax patterns are used to make the product cavity. Investment materials, that is, mold materials, should be selected correctly. Popular mold materials for



Fig. 11.3 Cast stem of artificial hip joint made of TNTZ by LVICAST method.

dental precision casting using Ti and its alloys are silica (SiO_2)-, alumina (Al_2O_3)-, or magnesia (MgO)-based. Zirconia (Zr_2O_3)-, yttria (Y_2O_3)-, and calcia (CaO)-based mold materials, which are often used for industrial precision casting with Ti and its alloys, are also used. SiO_2- and Al_2O_3-based mold materials generally contain phosphate as a binding agent, which show high reactivity with Ti melt (Niinomi et al., 2001).

To select the appropriate mold materials for casting, standard free energy changes of formation of oxides, as shown in Fig. 11.6, which is called as Ellingham diagram (Ellingham, 1994), should be referred to. A balanced consideration of the stability of the oxide and its cost is crucial in the final selection of the most suitable oxide for the mold material.

The TNTZ was developed for biomedical applications by the author's group (Kuroda et al., 1998). The melt of TNTZ reacts with general mold materials for Ti

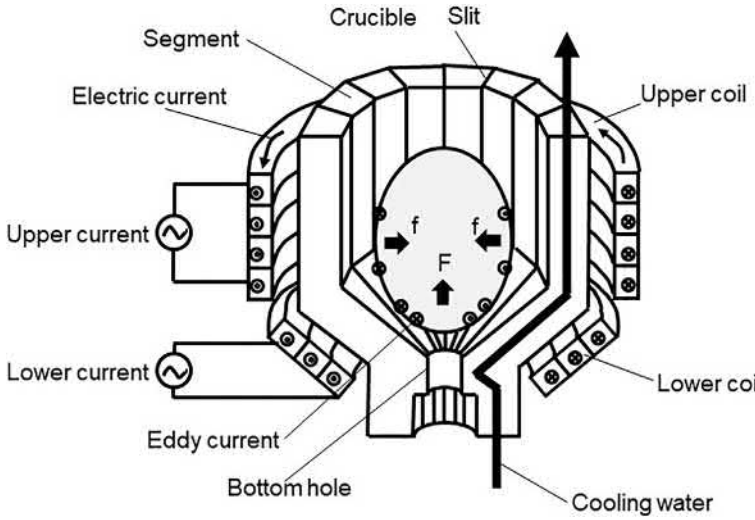


Fig. 11.4 Cold crucible levitation melting (CCLM) process.

and its alloys because the melting point of TNTZ is higher than that of Ti alloys such as Ti-6aluminum (Al)-4vanadium (V) ELI (extra low interstitial) or Ti-6Al-4V, which are conventionally used for biomedical applications (as stated in the following section).

Fig. 11.6 shows that as per the standard free energy changes for the formation of oxides, CaO is suitable for casting TNTZ because it is very stable and inexpensive although it is difficult to treat. However, dental prostheses made using TNTZ, such as dental crowns have been successfully fabricated using the duplex CaO coating molds made of CaO particles. The particle size is controlled using mixed CaO particles of fine and coarse sizes, as shown in Fig. 11.7 (Tsutsumi et al., 2010). Fig. 11.8 (Takeuchi et al., 2005) shows schematic drawing of the cross section of the duplex calcia mold. Fig. 11.9 (Takeuchi et al., 2005) shows photographs of the dental crown cast by duplex CaO coating mold.

11.3 Dental casting alloys

Dental casting alloys are commonly used to fabricate dental prostheses such as crowns, inlays, bridges, and dentures as prosthodontic treatments for missing teeth. These alloys are typically gold (Au), silver (Ag), and nickel-chromium (Ni-Cr) or cobalt-chromium (Co-Cr) alloys. Ti and its alloys are also used for fabricating cast dental prostheses when patients suffer a high risk of allergy problems. Artificial dental roots for reconstructing failed teeth are sometimes cast using Ti and its alloys.

The dental casting alloys exhibiting suitable mechanical properties, such as excellent corrosion resistance, nontoxicity, and casting performance, allow their use in dental prostheses.

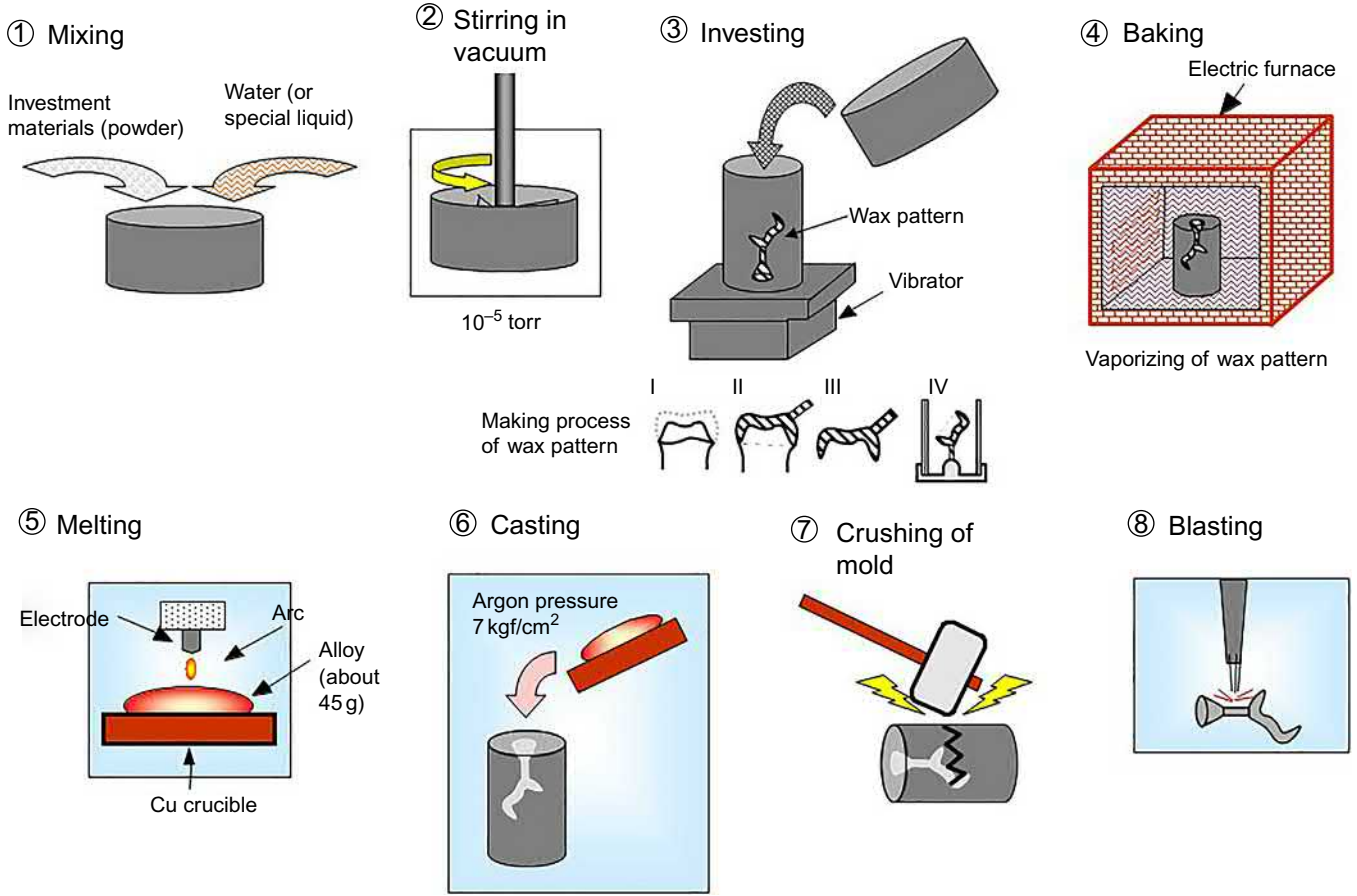


Fig. 11.5 Schematic illustration of dental precision casting method.

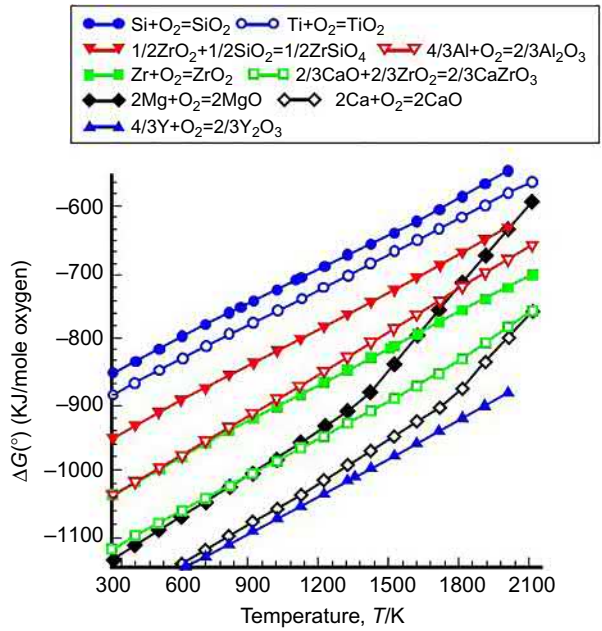


Fig. 11.6 Standard free energy change of the formation of oxides.

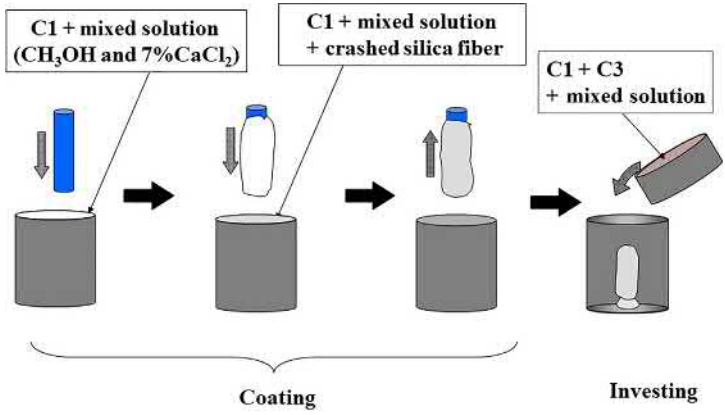


Fig. 11.7 Schematic drawing of coating process: C1 and C3 are fine and coarse calcia particles, respectively.

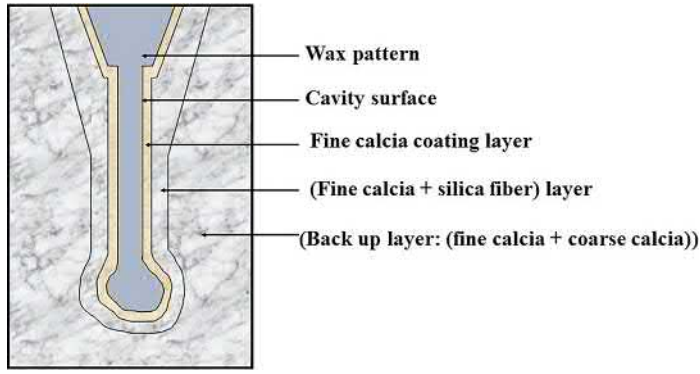


Fig. 11.8 Schematic drawing of cross section of duplex calcia coating mold.



Fig. 11.9 Dental product (crown) made by duplex calcia coating mold.

11.3.1 High precious metals (Au alloys)

Dental casting Au alloys comprise Au, Ag, and copper (Cu), and contain at least 60% Au and 75% [Au + platinum (Pt) group metals (Pt, palladium (Pd))] by mass. They are classified into four types according to the amount of precious metals contained and mechanical properties. Table 11.1 (Takada, 2010) lists their chemical compositions. Types 1, 2, and 3 comprise the Au-Ag-Cu alloys and type 4 the Au-Pt alloy for dental casting. The amount of Cu, which lowers the melting point and improves hardness and strength, increases from type 1 to 4. The addition of Pt and Pd increases the strength and elastic modulus. A small amount of zinc (Zn) or iridium (Ir) is also added to Au alloys. Zn inhibits oxidation, but decreases corrosion resistance. Ir effectively refines the microstructure.

11.3.2 Low precious metals (Ag alloys)

Dental casting Ag alloys were developed to reduce the cost entailed in using dental Au alloys. Therefore, their mechanical properties are similar to those of Au alloys of types 3 and 4. The main elements in Ag alloys are Ag, Pd, and Cu (Ag-Pd-Cu-Au alloys) and a small amount of Zn is also used. They must contain at least 12% Au, 20% Pd, and 40% Ag by mass.

Table 11.1 Composition of Au alloys by type

Gold alloy	Composition range (mass%)					
	Au	Ag	Cu	Pt	Pd	Zn
Type 1	80.2–95.8	2.4–12.0	1.6–6.2	0–1.0	0–3.6	0–1.2
Type 2	73.0–83.0	6.9–14.5	5.8–10.5	0–4.2	0–5.6	0–1.4
Type 3	71.0–79.8	5.2–13.4	7.1–12.6	0–7.5	0–6.5	0–2.0
Type 4	62.4–71.9	8.0–17.4	8.6–15.4	0.2–8.2	0–10.1	0–2.7

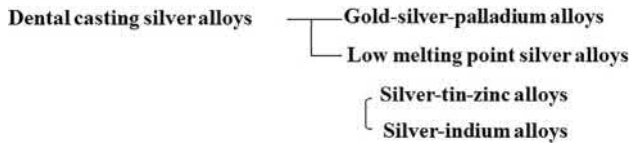


Fig. 11.10 Types of dental casting Ag alloys.

Low-melting point Ag alloys also exist, namely silver-tin-zinc (Ag-Sn-Zn) (type 1) and silver-indium (Ag-In) (type 2) alloys. Both alloys contain at least 60% Ag by mass and have a melting point below 1273 K.

Dental casting Ag alloys are summarized in Fig. 11.10 (Takada, 2010).

11.3.3 Ti and its alloys

Pure Ti and Ti-6Al-4V are most widely used for fabricating dental and medical prostheses. Table 11.2 presents Ti and its alloys used for casting and their chemical compositions as per ASTM standard B367 (ASTM B367, 2017). Other Ti alloys used for casting and their chemical compositions are listed in Tables 11.3 and 11.4 (Eylon et al., 1990; Niinomi, 2001).

Casting dental Ti alloys are commonly diverted from general structural Ti alloys. Representative dental casting Ti alloys reported are listed in Table 11.5 (Niinomi, 2001) along with their mechanical properties. The usage of Ti-6Al-7niobium (Nb), which is modified Ti-6Al-4 V by replacing harmful V with nonharmful Nb, is spreading gradually in the dental field. The use of TNTZ and Ti-15Zr-Nb-Ta, which were originally developed for biomedical applications, for dental casting has been investigated. Ti-5Al-13Ta (Doi et al., 1998) and Ti-40Zr (Niinomi et al., 2001) were developed for dental casting. Since the high melting points of Ti alloys are one cause of the high reactivity of the Ti melt with mold materials, it is necessary to lower alloy melting points. For this purpose, elements with a melting point lower than that of Ti and large solid solubility are effective as alloy elements, because they are expected to improve the mechanical properties. Examples include Cr, manganese (Mn), Pd. Zr, and Co (Niinomi et al., 2001).

11.3.4 Other dental casting alloys

Other dental casting alloys include nonprecious alloys such as Co-Cr alloys and Ni-Cr alloys.

Dental casting Co-Cr alloys are composed of 40%–70% Co, 20%–30% Cr, 0%–20% Ni, and 0%–10% molybdenum (Mo) by mass and have mechanical properties equivalent to ISO22674 type 5 (ISO 22674, 2016). The use of these alloys is indicative when heavy loads are applied, and strong rigidity is required, such as in the case of plate denture metal frames and clasps.

Table 11.2 Sorts and chemical compositions of casting Ti alloys registered in ASTMA B367 (mass %)

Alloy	N max	C max	H max	Fe max	O max	Al	V	Sn	Pd	Other each element	Total other elements
C-2	0.05	0.10	0.015	0.20	0.40	–	–	–	–	0.10	0.40
C-3	0.05	0.10	0.015	0.25	0.40	–	–	–	–	0.10	0.40
C-5	0.05	0.10	0.015	0.40	0.25	5.5–6.7	3.5–4.5	–	–	0.10	0.40
C-6	0.05	0.10	0.015	0.50	0.20	4.00–6.00	–	2.0–3.0	–	0.10	0.40
Ti-Pd7B	0.05	0.10	0.015	0.20	0.40	–	–	–	0.12 min	0.10	0.40
Ti-Pd8A	0.05	0.10	0.015	0.25	0.40	–	–	–	0.12 min	0.10	0.40
Ti-Pd16	0.03	0.10	0.0150	0.30	0.18	–	–	–	0.04–0.08	0.10	0.40
Ti-Pd17	0.03	0.10	0.015	0.20	0.25	–	–	–	0.04–0.08	0.10	0.40
Ti-Pd18	0.05	0.10	0.015	0.25	0.15	2.5–3.5	2.0–3.0	–	0.04–0.08	0.10	0.40

Table 11.3 Other casting Ti alloys and their chemical compositions (mass %)

Alloy	O	N	C	H	Al	Fe	V	Cr	Sn	Mo	Nb	Zr	Si
Ti-6Al-4V ELI	0.11	0.015	0.03	0.006	6	0.10	4	–	–	–	–	–	–
Ti-6Al-2Sn-4Zr-2Mo	0.10	0.010	0.03	0.006	6	0.15	–	–	2	2	–	4	–
Ti-6Al-2Sn-4Zr-6Mo	0.10	0.010	0.03	0.006	6	0.15	–	–	2	6	–	4	–
Ti-5Al-2.5Sn	0.16	0.015	0.03	0.006	5	0.2	–	–	2.5	–	–	–	–
Ti-3Al-8 V-6Cr-4Zr-4Mo (Beta–C)	0.10	0.015	0.03	0.006	3.5	0.2	8.5	6	–	4	–	4	–
Ti-15 V-3Al-3Cr-3Sn (Ti-15-3)	0.12	0.015	0.03	0.006	3.0	0.2	15	3	3	–	–	–	–
Ti-1100	0.07	0.015	0.04	0.006	6.0	0.02	–	–	2.75	0.4	–	4.0	0.45
IMI-834	0.10	0.015	0.06	0.006	5.8	0.02	–	–	4.0	0.5	0.7	3.5	0.35

Table 11.4 Mechanical properties of other casting Ti alloys

Alloy	Yield stress, MPa	Tensile strength, MPa	Elongation, %	Reduction of area, %
Ti-6Al-4V ELI	758	827	13	22
Ti-6Al-2Sn-4Zr-2Mo Annealed	910	1006	10	21
Ti-6Al-2Sn-4Zr-6Mo Beta STA	1269	1345	1	1
Ti-3Al-8 V-6Cr-4Zr-4Mo Beta STA	1241	1330	7	12
Ti-15 V-3Al-3Cr-3Sn Beta STA	1200	1275	6	12
Ti-1100 Beta STA	848	938	11	20
IMI-834 Beta STA	952	1069	5	8

Table 11.5 Ti alloys for dental applications and their mechanical properties

Alloy	Process	Tensile strength (MPa)	Yield strength (MPa)	Elongation (%)	Vickers hardness
1. Ti-20Cr-0.2Si	Casting	874	669	6	318
2. Ti-25Pd-5Cr	Casting	880	659	5	261
3. Ti-13Cu-4.5Ni	Casting	703		2.1	
4. Ti-6Al-4 V	Casting	976	847	5.1	
5. Ti-6Al-4 V	Super plastic forming	954	729	10	346
6. Ti-6Al-7Nb	Casting	933	817	7.1	
7. Ti-Ni	Casting	470		8	190

Dental casting Ni-Cr alloys are commonly composed of 68%–89% Ni and 11.9%–26.3% Cr by mass, but it is desirable that they contain at least 10% Cr and over 90% (Cr + Ni) by mass, as well as small amounts of other elements such as Mo, beryllium (Be), silicon (Si), iron (Fe), Mn, Cu, and tungsten (W). Mo improves corrosion resistance (Sousa et al., 2014). It is a refractory metal that oxidizes slowly, but the oxide produced (e.g., MoO_3) is volatilized easily if the temperature exceeds 700 °C (Dootz et al., 1993). It is important to add Cr and Mo to an alloy to increase its corrosion resistance, because Cr and Mo improve the surface passivation. As an alloying element, Cr can increase resistance to corrosion, oxidation, and staining; in other words, it increases the surface stability due to the formation of Cr oxide (Cr_2O_3) (Bergman et al., 1980; Horath, 1995; Liu et al., 2010; Viswanathan and Choe, 2010).

11.4 Mechanical properties and their improvement in cast biocompatible Ti alloys

Microstructures of cast dental metallic materials are, in general, much coarser than those of wrought ones and have cast defects such as pores and shrinkages. To diminish pores or shrinkages, hot isostatic pressing (HIP) is effective although the microstructure remains still coarse. In order to refine the microstructures of cast (α + β)-type Ti alloys such as Ti-6Al-4V and Ti-6Al-7Nb, thermochemical processing (TCP), which is schematically shown in Fig. 11.11 (Niinomi et al., 1995), is employed. In TCP, the hydrogenation treatment for H absorption is carried out below β transus temperature in H gas atmosphere. The hydrogenation treatment ensures that the amount of H reaches approximately 1% by mass. Then, the solution treatment (ST) is carried out, followed by dehydrogenation treatment under high vacuum. The final H content is equivalent to or slightly lower than that before conducting TCP because hydrogenation and dehydrogenation are reversible. Fig. 11.12 (Akahori et al., 2000) shows scanning electron microscopy (SEM) micrographs of Ti-6Al-4V in (A) hot isostatic pressing (as-HIPped) conditions and (B) after hydrogenation and dehydrogenation processing. The microstructure of cast Ti-6Al-4V subjected to TCP is much finer than that subjected to HIP only. Fig. 11.13 (Akahori et al., 2000) shows the tensile properties of as-HIPped cast Ti-6Al-7Nb, and HIPped cast Ti-6Al-7Nb with TCP. The strength (tensile strength and 0.2% proof stress) of HIPed cast Ti-6Al-7Nb is greater than that of HIPped cast Ti-6Al-7Nb with TCP whereas the elongation of the former is smaller. Fig. 11.14 (Akahori et al., 2000) shows fatigue strength via S-N curves of as-HIPped cast Ti-6Al-7Nb and HIPped cast Ti-6Al-7Nb with TCP. The fatigue strength of HIPped cast Ti-6Al-7Nb increases significantly due to TCP.

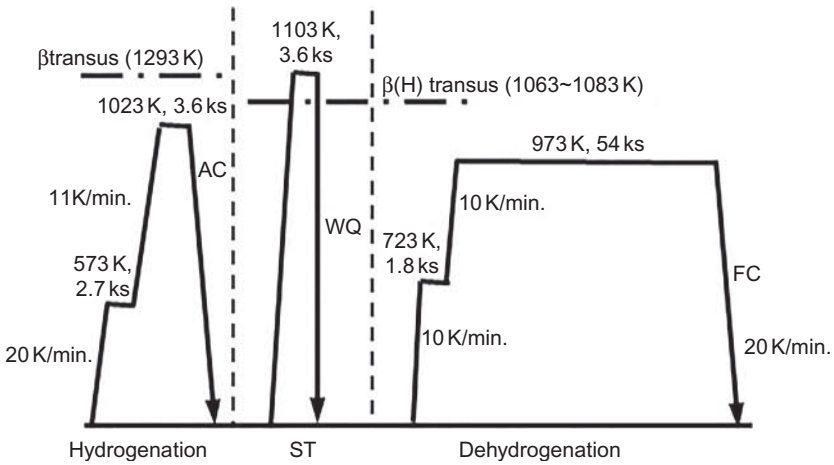


Fig. 11.11 Schematic drawings of thermochemical processing (TCP).

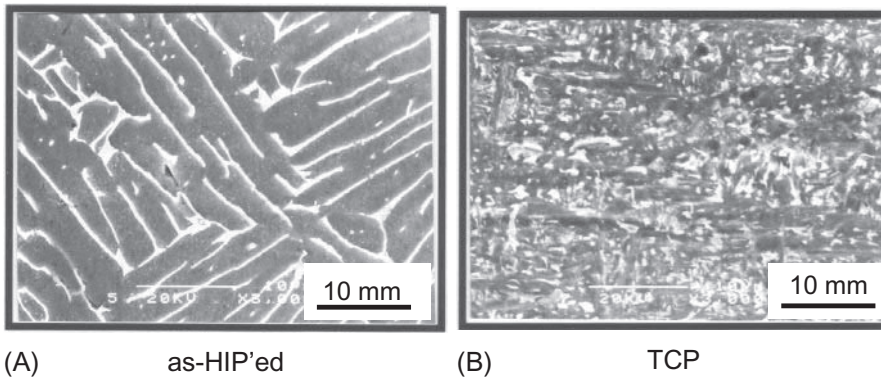


Fig. 11.12 SEM micrographs of (A) as-HIPped cast Ti-6Al-7Nb and (B) Ti-HIPped cast Ti-6Al-7Nb conducted with TCP.

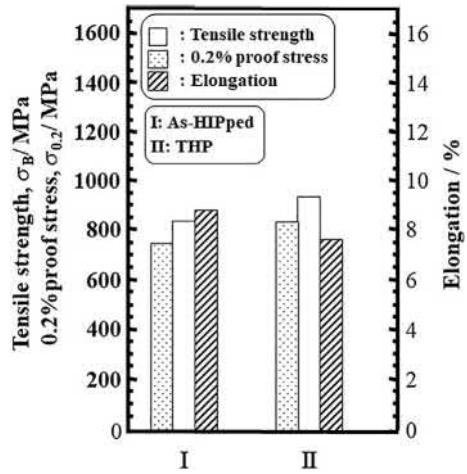


Fig. 11.13 Tensile strength, 0.2% proof stress and elongation of (I): as-HIPped cast Ti-6Al-7Nb and (II): HIPped cast Ti-6Al-7Nb conducted with TCP.

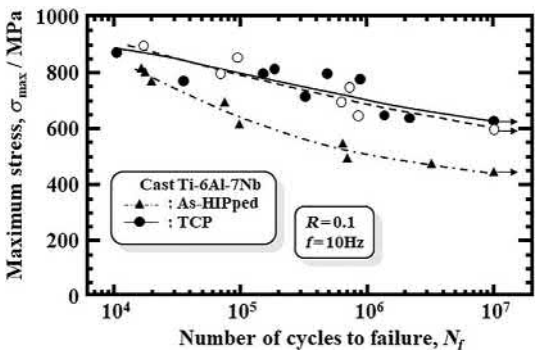


Fig. 11.14 S-N curves of as-HIPped cast Ti-6Al-7Nb, and HIPped cast Ti-6Al-7Nb conducted with TCP.

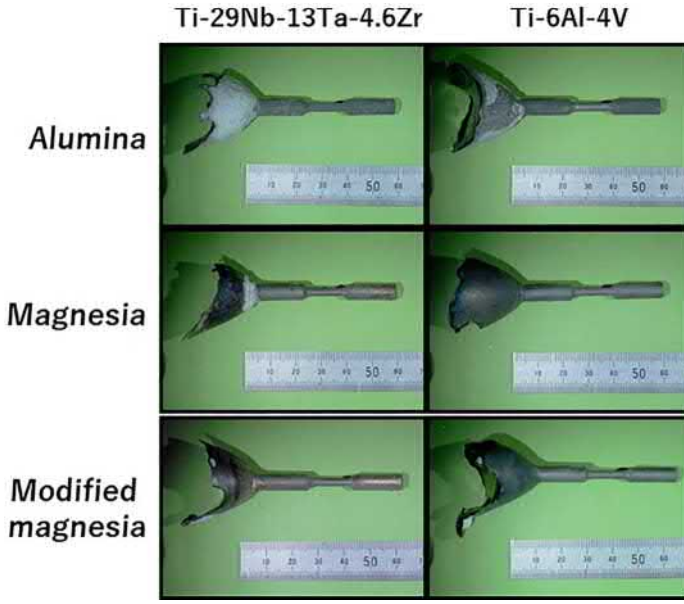


Fig. 11.15 Appearances of as-blasted cast tensile specimens of Ti-29Nb-13Ta-4.6Zr and Ti-6Al-4 V using each investment material.

The mechanical properties of dental cast Ti alloys significantly depend on the mold materials. As stated above, Al_2O_3- and MgO-based mold materials are used for dental casting of Ti and its alloys. However, ordinary mold materials require modification when used with Ti alloys with high melting points such as TNTZ. The TNTZ was cast using Al_2O_3- and MgO-based mold materials, and modified MgO-based material where the SiO_2-based expansion agent and Al_2O_3 were removed. Fig. 11.15 (Niinomi et al., 2004). shows the appearances of as-blasted cast tensile specimens of TNTZ and Ti-6Al-4 V ELI using Al_2O_3- and MgO-based mold materials as well as modified MgO-based material. The appearances of both alloys cast using alumina-base mold material are very poor in surface gloss. The appearance of Ti-6Al-4V ELI cast using MgO-based mold material and modified MgO-based mold material exhibits excellent and nearly similar surface gloss. The appearance of TNTZ cast using MgO-based mold material exhibits poor surface gloss, but the TNTZ cast using modified MgO-based mold material exhibits excellent surface gloss. The mechanical properties of TNTZ cast using MgO-based mold material and modified MgO-based mold material are nearly the same, and better than those of the cast TNTZ using Al_2O_3-based mold material.

The mechanical properties and surface appearance of TNTZ cast using CaO-based mold material were reported to be better than those of TNTZ cast using MgO-based mold material. Fig. 11.16 (Tsutsumi et al., 2010) shows the volume fractions of casting defects, including pores and shrinkage observed on the fracture surfaces of TNTZ

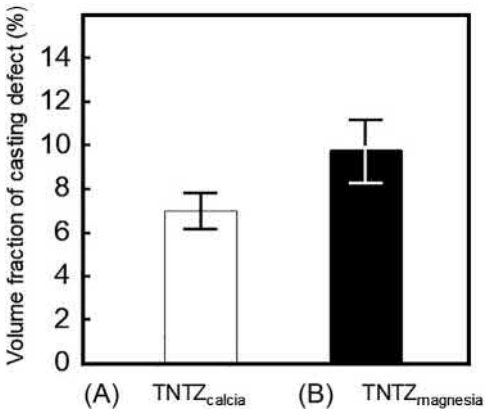


Fig. 11.16 Volume fractions of casting defects tensile facture surfaces of (A) $TNTZ_{calcia}$ and (B) $TNTZ_{magnesia}$.

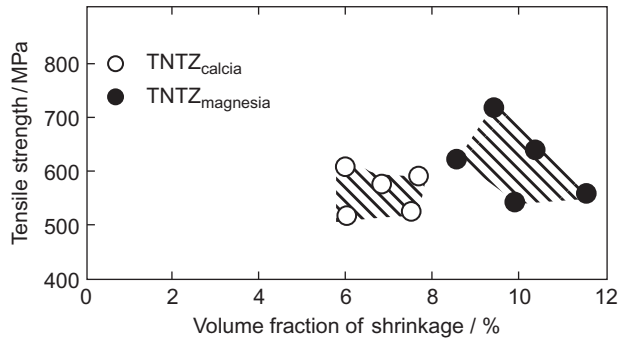


Fig. 11.17 Relationships between tensile strength and volume fraction of casting defects on cross sections of $TNTZ_{calcia}$ and $TNTZ_{magnesia}$.

cast using CaO-based mold material ($TNTZ_{calcia}$) and MgO-based mold material ($TNTZ_{magnesia}$) after tensile tests. The volume fraction of $TNTZ_{calcia}$ is less than that of $TNTZ_{magnesia}$. The relationships between the tensile strength and the volume fraction of casting defects on the cross section of $TNTZ_{calcia}$ and $TNTZ_{magnesia}$ are shown in Fig. 11.17 (Tsutsumi et al., 2010). The tensile strength of $TNTZ_{magnesia}$ decreases with an increase in the volume fraction of casting defects, but that of $TNTZ_{calcia}$ is nearly constant under the same scenario. $TNTZ_{calcia}$ exhibits a lower volume fraction and lower size of defects than those of $TNTZ_{magnesia}$. The tensile strength of $TNTZ_{calcia}$ is slightly less than that of $TNTZ_{magnesia}$. The fatigue strength, shown by S-N curves, is shown in Fig. 11.18 (Tsutsumi et al., 2010) along with that of forged TNTZ subjected to ST. The fatigue strength of both $TNTZ_{calcia}$ and $TNTZ_{magnesia}$ is lower than that of forged TNTZ subjected to ST because of casting defects and the coarse microstructure. However, the fatigue strength of $TNTZ_{calcia}$ is slightly greater than that of $TNTZ_{magnesia}$.

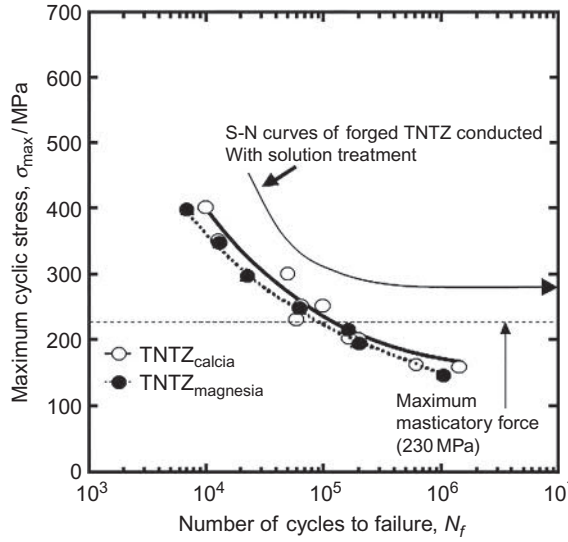


Fig. 11.18 S-N curves of $TNTZ_{calcia}$, $TNTZ_{magnesia}$, and forged TNTZ solutionized at 1063 K for 3.6 ks obtained from fatigue tests.

11.5 Alloy designs for lowering the melting point of biocompatible Ti alloys for casting

The melting point of Ti alloys is generally high. Therefore, the reactivity of Ti melt with molding materials is very high. Thus, the O existed in mold materials diffuses into the cast Ti alloys, leading to the formation of α-case and an area with high dissolved O near the surface of the cast. These factors are responsible for the brittle nature of Ti alloys cast in such conditions. In order to reduce the reactivity of Ti alloy melt with mold materials, it is important to lower the melting point or select a mold material with high stability. In addition, Ti alloys exhibiting high melting points for biomedical prostheses can be used for fabricating dental casting prostheses. Highly stable mold material is typically difficult to treat and expensive, as stated above. Lowering the melting point of Ti alloys is discussed below.

The TNTZ may be used for dental casting, but its melting point is approximately 2300 K. CaO mold is suitable for casting TNTZ, as stated above, but CaO-based mold material is relatively difficult to treat and is also relatively costly. Therefore, the melting point of TNTZ can be lowered by omitting the high-melting point element, Ta; controlling the amounts of the main alloying elements, namely, Nb and Zr; and by adding small amounts of Fe, Cr, and Si. The compositions of the alloys are finalized using the d-electron alloy design method, where the proportions of d-orbital energy level (Md) and bond order (Bo) values in the alloys are nearly equal to those in TNTZ. The so-designed modified TNTZ alloys were Ti-29Nb-15Zr-1.5Fe, Ti-29Nb-10Zr-0.5Si, Ti-29Nb-18Zr-2Cr-0.5Si, Ti-29Nb-10Zr-0.5Cr-0.5Fe, and Ti-29Nb-13Zr-2Cr. Fig. 11.19 (Akahori et al., 2005) shows their cooling curves. The melting point of each alloy is lower than that of TNTZ, and Ti-29Nb-13Zr-2Cr exhibits the lowest melting point among all the alloys. Fig. 11.20 (Akahori et al., 2005) shows the

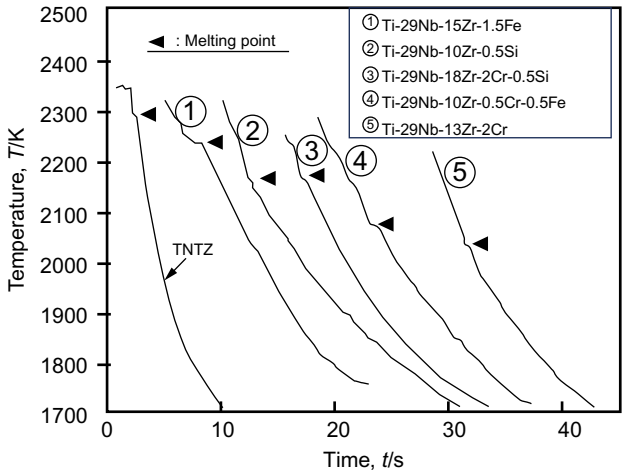


Fig. 11.19 Cooling curves of various designed Ti alloys and TNTZ.

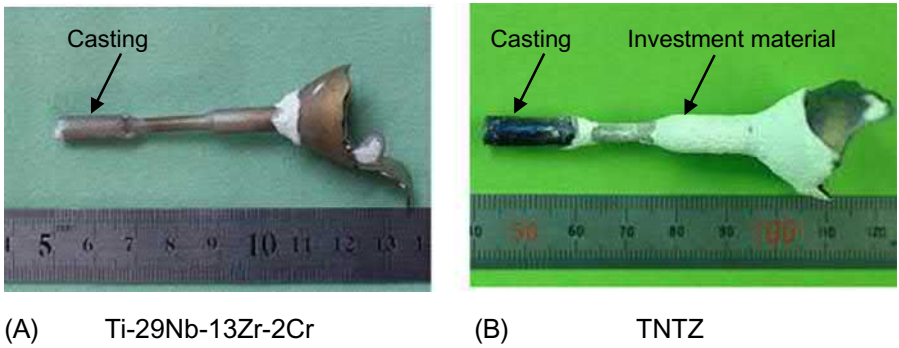


Fig. 11.20 Appearances of cast tensile specimens of (A) Ti-29Nb-13Zr-2Cr and (B) TNTZ.

appearances of the as-cast tensile specimens of (A) Ti-29Nb-13Zr-2Cr and (B) TNTZ cast using a modified MgO-based mold material. The removability of the mold material for Ti-29Nb-13Zr-2Cr is better than that for TNTZ. The same trend was reported for the other designed alloys. Fig. 11.21 (Akahori et al., 2005) shows Vickers hardness of various designed Ti alloys and TNTZ as a function of distance from the surface of specimen. The Vickers hardness of each alloy becomes nearly constant at approximately 200 μm from the surface, but that of TNTZ is higher than that of all the designed alloys up to approximately 100 μm from the surface. Therefore, the reactivity of the melt of each designed alloy can be judged to be lower than that of TNTZ. Average volume fractions of casting defects of various designed Ti alloys and TNTZ in cross sections of the tensile test specimens are shown in Fig. 11.22. The average volume fractions of casting Ti-29Nb-18Zr-2Cr-0.5Si, Ti-29Nb-10Zr-0.5Cr-0.5Fe,

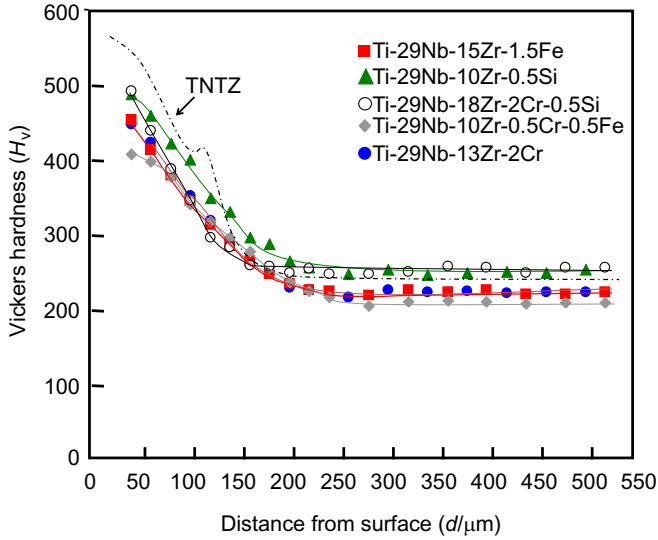


Fig. 11.21 Vickers hardness of various designed Ti alloys and TNTZ as a function of distance from surface of specimen.

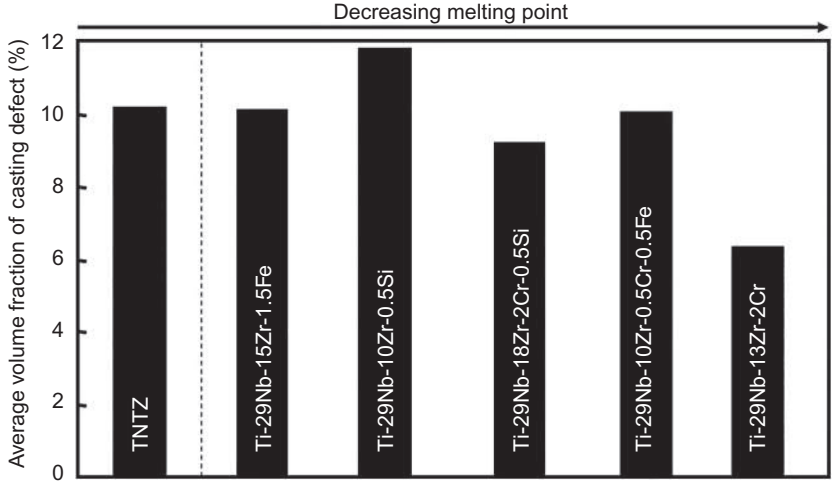


Fig. 11.22 Average volume fractions of casting defects of various designed Ti alloys and TNTZ in cross sections of tensile test specimens.

and Ti-29Nb-13Zr-2Cr are less than that of TNTZ. The mechanical properties of casting designed alloys are shown in Fig. 11.23 (Akahori et al., 2005). Casting Ti-29Nb-10Zr-0.5Cr-0.5Fe and Ti-29Nb-13Zr-2Cr exhibit good balance of strength and elongation.

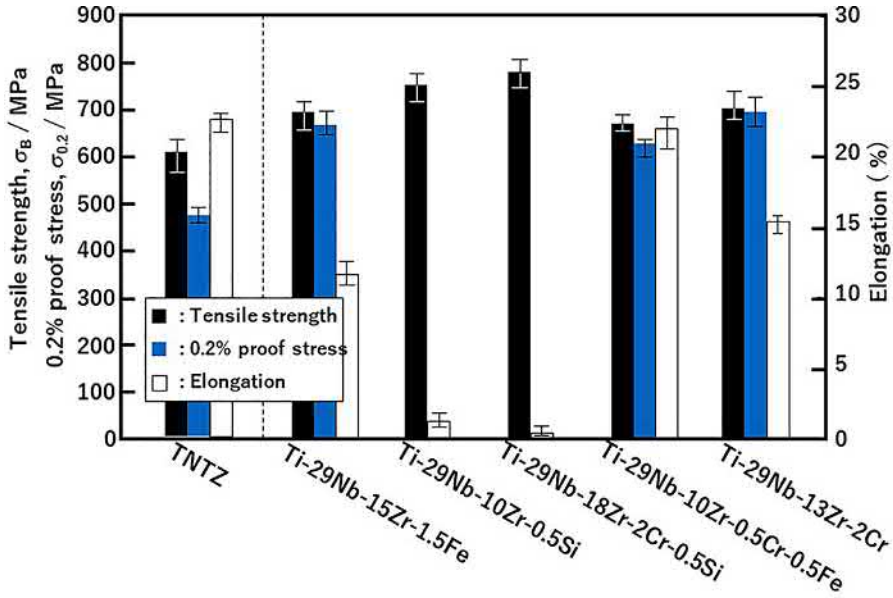


Fig. 11.23 Tensile properties of various designed Ti alloys and TNTZ.

11.6 Summary

Precision casting retains its importance, particularly in the fabrication of dental prostheses although machining processes using computer-aided design (CAD) and computer-aided manufacturing are achieving increasing attentions. To ensure continued usage in the biomedical and dental field, particularly for the fabrication of prostheses, the precision casting process using Ti and its alloys requires modifications in terms of improving the mold materials, casting process, and mechanical properties of castings.

References

Akahori, T., Niinomi, M., Ishohama, R., Suzuki, A., 2000. Effect of thermochemical treatment on mechanical properties of cast Ti-6Al-7Nb alloy for dental applications. J. Jpn. Inst. Metal. Mater. 64, 895–902.

Akahori, T., Niinomi, M., Harada, M., Takeda, J., Toda, H., Katsura, S., Takeuchi, T., Fukui, H., 2005. Mechanical properties and cyto-toxicity of newly designed β type Ti alloys for dental applications. J. Jpn. Metal. Mater. 69, 96–102.

ASTM B367-13, 2017. Standard Specification for Titanium and Titanium Alloy Castings. West Conshohocken, PA, USA.

Bergman, M., Band, B., Söremark, R., 1980. Tissue accumulation of nickel released due to electrochemical corrosion of non-precious dental casting alloy. J. Oral Rehabil. 7, 325–330.

Demukai, N., Tsushima, K.-I., 2005. Development of a new type titanium casting technology: LEVICAST process. J. Adv. Mater.-Covina 37, 12–16.
Doi, H., Yoneyama, T., Kobayashi, E., Hamanaka, H., 1998. Mechanical properties and corrosion resistance of Ti- 5Al-13Ta alloy castings. Jpn. Soc. Dental Mater. Devices 17, 47–52.
Dootz, E.R., Koran, A., Craig, R.G., 1993. Physical property comparison of 11 soft denture lining materials as a function of accelerated aging. J. Prosthet. Dent. 69, 114–119.
Ellingham, H.J.T., 1994. Transactions and communications. J. Soc. Chem. Ind. 63, 125.
Eylon, D., Newman, J.R., Torne, J.K., 1990. Metals Handbook, tenth ed. 2, ASM International, Almere, Netherlands, p. 634.
Horath, L., 1995. Fundamentals of Materials Science for Technologists: Properties, Testing and Laboratory Exercises. Prentice Hall Inc., New Jersey, USA.
ISO 22674, 2016. Dentistry—Metallic Materials for Fixed and Removable Restorations and Appliances. Geneva Switzerland.
Kuroda, D., Niinomi, M., Morinaga, M., Kato, Y., Yashiro, T., 1998. Design and mechanical properties of new beta type titanium alloys for implant materials. Mater. Sci. Eng. A 243, 244–249.
Liu, Y., Wang, Z., Gao, B., Zhao, X., Lin, X., Wu, J., 2010. Evaluation of mechanical properties and porcelain bonded strength of nickel–chromium dental alloy fabricated by laser rapid forming. Lasers Med. Sci. 25, 799–804.
Morita, A., Fukui, H., Tadano, H., Hayashi, S., Hasegawa, J., Niinomi, M., 2000. Alloying titanium and tantalum by cold crucible levitation melting (CCLM) furnace. Mater. Sci. Eng. A 280, 208–213.
Niinomi, M., 2001. Casting of titanium and its alloys. J. Jpn. Foundry Eng. Soc. 73, 784–790.
Niinomi, M., Gong, B., Kobayashi, T., Oyabu, Y., Toriyama, O., 1995. Fracture characteristics of Ti-6Al-4V and Ti-5Al-2.5Fe with refined microstructure using hydrogen. Metall. Mater. Trans. A 26, 1141–1151.
Niinomi, M., Fukui, H., Takeuchi, T., Katsura, S., 2001. Dental precision casting of titanium and its alloys. J. Jpn. Foundry Eng. Soc. 73, 798–804.
Niinomi, M., Akahori, T., Manabe, T., Takeuchi, T., Katsura, S., Fukui, H., Suzuki, A., 2004. Tensile properties and surface reaction layer of biomaterial, Ti-29Nb-13Ta-4.6Zr, cast by dental precision casting process using various investment materials. Testu-to Hagane 90, 154–161.
Sousa, L.L., Silva, J.W., Sampaio, N.A.S., Nakazato, R.Z., Acciari, H.A., Codaro, E.N., 2014. Corrosion process development of a Ni-Cr-Mo alloy used in dental prothesis. Int. J. Eng. Res. Dev. 10, 70–76.
Takada, Y., 2010. 4.5 Precious alloys. In: Hanawa, T. (Ed.), Metals for Medicine. Jpn Inst. Metal. Mater., Sendai, Japan, pp. 117–133.
Takeuchi, T., Niinomi, M., Akahori, T., Katsura, S., Fukui, S., 2005. Development of dental precision casting technology for high biocompatible and functional titanium alloys. Materia Japan 44, 68–70.
Tsutsumi, H., Niinomi, M., Akahori, T., Nakai, M., Takeuchi, T., Katsura, S., 2010. Mechanical properties of a β-type titanium alloy for biomedical applications cast using a calcia mold. Mater. Trans. 51, 136–142.
Viswanathan, S.S., Choe, H.C., 2010. Preferential dissolution behaviour in Ni-Cr dental cast alloy. Bull. Mater. Sci. 33, 463–468.

Further reading

Okazaki, Y., 2002. Implant applications of highly corrosion-resistant Ti-15Zr-4Nb-4Ta alloy. Mater. Trans. 43, 2936–2942.

Additive manufacturing (AM)

12

Mohammadreza Namatollahi[*], *Ahmadreza Jahadakbar*[*], *Mohammad Javad Mahtabi*[*,†], *Mohammad Elahinia*[*]
*Dynamic and Smart Systems Laboratory, Mechanical Industrial and Manufacturing Engineering Department, The University of Toledo, Toledo, OH, United States, †Department of Mechanical Engineering, University of Tennessee at Chattanooga, Chattanooga, TN, United States

12.1 Introduction

Additive manufacturing (AM), also known as three-dimensional (3D) printing and rapid prototyping, is the technology of making solid objects through layer-by-layer addition of material based on a computer-aided design (CAD). Before the invention of AM, most of the metallic parts, including medical implants, were fabricated using traditional processes such as forging, investment casting, hot rolling, and machining. The AM is a powerful and flexible fabrication technique that has gained significant popularity in various applications, from aerospace to biomedical industries. In recent years, AM techniques have been developed to a level that they can realize fabrication of parts with desired functionality. In medical devices, AM can be of great interest due to a high demand for custom-made (i.e., patient-specific) medical devices and biomedical implants with complex geometries. Moreover, the precision of the final product is very important in medical parts.

The process of developing a medical device using AM techniques involves various steps, as illustrated in Fig. 12.1. After determining the requirement from AM, imaging and scanning may be needed to determine the geometry of the part that is to be fabricated, unless a completely new design is needed. This imaging and scanning can be performed using advanced techniques, such as computed tomography (CT scan). Based on the imaging followed by necessary customizations, a 3D model needs to be constructed as the input to the computer program that controls the 3D printer. Sometimes, more advanced computer simulation, such as finite element analysis (FEA), is needed of the designed model to assess the biomechanical properties or to design a surgery planning. Then, the 3D geometry will be sliced using a computer program to be used by a 3D printing software and manufacturing/processing parameters are assigned for the fabrication. The processing parameters depend on the method of AM and include laser power, laser scanning speed, layer thickness, scanning pattern, hatch spacing (i.e., distance between two adjacent passes of laser). After fabrication, based on the "indications for use" of the fabricated part, different regulatory approvals and tests are required to evaluate the biological considerations including biocompatibility, cleaning, and sterility.

Metals for Biomedical Devices. https://doi.org/10.1016/B978-0-08-102666-3.00012-2
© 2019 Elsevier Ltd. All rights reserved.

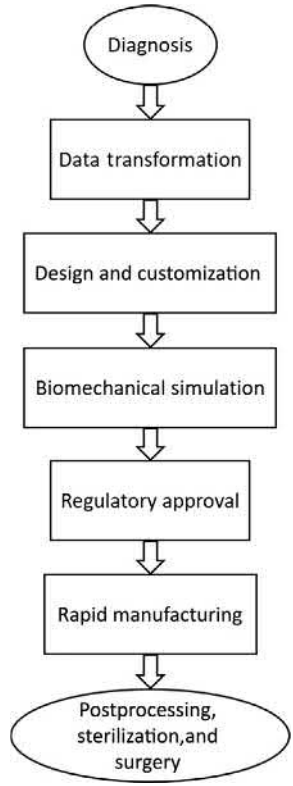


Fig. 12.1 Process of design and fabrication of AM medical devices (Javaid and Haleem, 2017).

In this chapter, various methods of AM, which have been used to fabricate metallic medical devices, are introduced followed by the advantages and limitations of AM. Next, different applications that can benefit from AM are introduced and some examples are provided. Statistics about the AM medical industry and the associated market are also provided. Biological considerations for a successful use of AM for medical devices are discussed next. Finally, a case study is presented on an additively manufactured bone fixation plate made of NiTi alloys.

12.2 AM techniques for medical devices

Several AM technologies have been developed in the past two decades for free-form fabrication of different materials: stereolithography for photocurable resins, laminated object manufacturing for any material in sheet form, material jetting for polymers and waxes, binder jetting, material extrusion and powder bed fusion for various materials, to name a few. Among the AM techniques, selective laser melting (SLM), direct energy deposition (DED), and electron beam melting (EBM) are the most common

techniques for the fabrication of metallic medical parts. In all of these methods, first a 3D CAD of the product is needed. As mentioned before, the CAD model can be designed or prepared based on the data from 3D scanners or CT scans. Then the CAD file will be sliced into subsequent two-dimensional (2D) layers using appropriate software. Finally, the desired part is printed layer by layer using one of the aforementioned techniques. A brief description of each technology will be discussed in the following sections.

12.2.1 Selective laser melting

The SLM is a laser powder bed fusion (LPBF) technique that uses a laser beam to melt a powder bed selectively. For SLM AM of metals, the material should be in the form of fine powder. The powder can be generated from an ingot using various techniques, such as gas atomization or plasma atomization techniques. Fig. 12.2 shows a schematic illustration of an SLM AM process. To start the fabrication, this fine powder is deposited on a substrate using a roller or scraper. The thickness of the powder layer is usually 20–100 μm. Then a laser beam melts the desired 2D cross section of the first layer (selective melting), based on the sliced CAD file, resulting in melting and fusing of those areas. Afterwards, the substrate moves down by the thickness of each layer, which is set by the user, and a new layer of powder is deposited. This layer-by-layer process will continue until the part is completely fabricated.

Laser power, scanning speed, hatch spacing, and powder bed layer thickness are some of the most important parameters that are involved in SLM process. These parameters need to be optimized, for each material, to achieve a successful fabrication. The process parameters directly affect the microstructure, density, mechanical behavior, strength, and surface quality of the final product. Due to high reactivity of materials

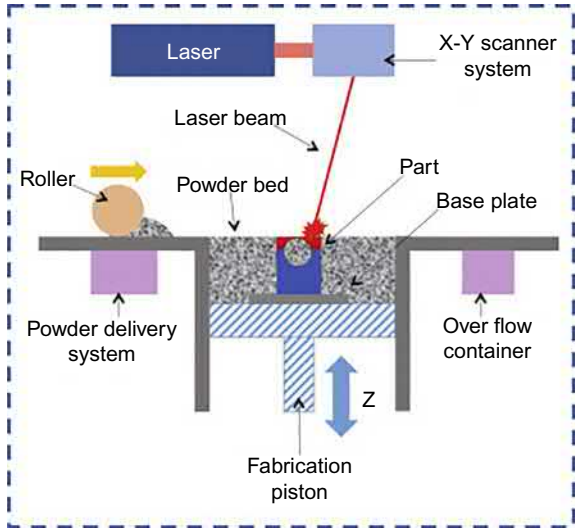


Fig. 12.2 Schematic illustration of an SLM AM process (Shamsaei et al., 2015).

in high temperatures, usually the SLM process is carried out in an inert atmosphere, such as argon, to lower the impurity pick-up level and produce medical grade products. The SLM enables the fabrication of metallic parts with excellent mechanical properties, because of the characteristics of grain refinement, extended solid solubility, chemical homogeneity, and reduction in quantity and size of phase segregation.

12.2.2 Direct energy deposition

The direct laser deposition (DLD) is another type of metal AM method in which instead of having a powder bed, the powder is selectively deposited and simultaneously melted by a laser beam, resulting in a molten pool on the substrate. The laser/deposition head and/or the substrate can travel in space directions, demonstrating the ability to fabricate 3D objects. Fig. 12.3 schematically demonstrates the DED AM technique. As shown in this figure, the powder spray nozzles are located next to the laser and can move with laser, if needed. The number of the nozzles may vary from machine to machine and a DED machine can be equipped with single or multiple nozzles. The most important process parameters in this method that need to be optimized are laser-substrate relative velocity (traverse speed), laser power and beam diameter, hatch spacing, powder feeding rate, and scanning strategy. Thanks to the control flexibilities of the laser beam and powder deposition, DED can be used to repair existing parts or add new structures to the currently fabricated parts.

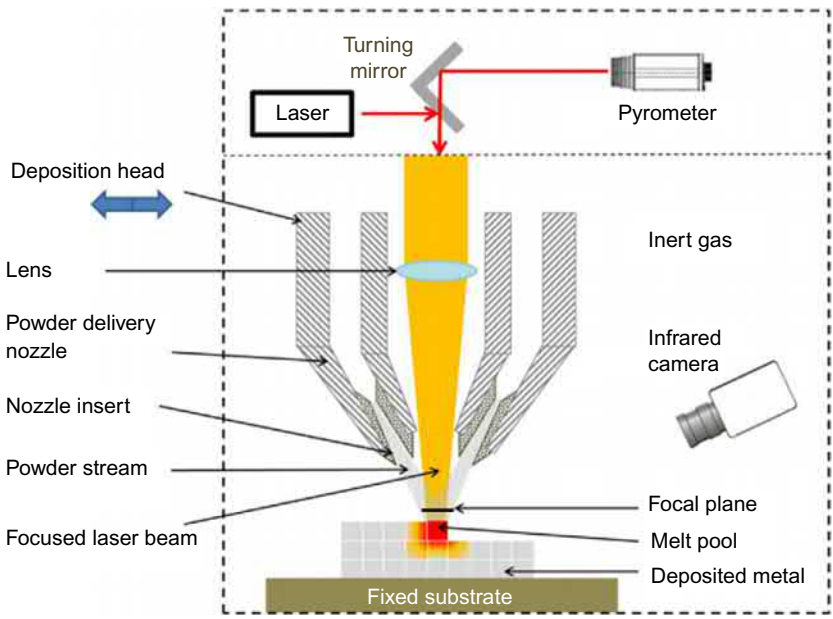


Fig. 12.3 Schematic illustration of direct energy deposition (DED) additive manufacturing technique (Shamsaei et al., 2015).

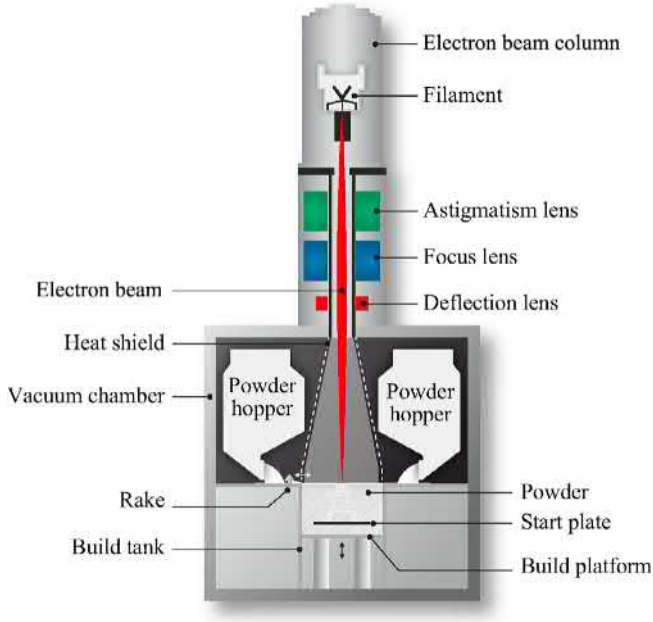


Fig. 12.4 Electron beam melting schematics (Galati and Iuliano, 2018).

12.2.3 Electron beam melting

Fig. 12.4 shows the features of EBM technique. The heat source in EBM is an electron beam that melts the powder. Similar to SLM the EBM parts are fabricated layer by layer but in a high vacuum chamber, which makes this method suitable for highly reactive materials, such as titanium (Ti) and alloys. Another advantage of EBM over other AM techniques is that the process occurs at temperatures as high as 1000°C resulting in low residual stresses during fabrication and eliminating the need of post heat treatment.

A comparison between capabilities and resulting properties of biomedical components fabricated via different AM techniques, explained above, is presented in Table 12.1 Also, Table 12.2 provides a summary of the laser type, fabrication resolution, and the type of materials that can be used in each of the discussed AM techniques.

12.3 Advantages, limitations, and challenges of AM

Similar to any other fabrication technique, there are advantages and challenges associated with using AM in medical devices. In this sections some of the main advantages and challenges associated with these technologies are discussed, which may help in making a decision in using AM for certain medical applications.

Table 12.1 Comparison between the various AM techniques for fabricating biomedical components (Trevisan et al., 2017).

Method	Component	Mechanical properties	Ref.
SLM	Porous Ti-6Al-4V scaffolds	E = 3.7–6.7 Pa UCS = 145–164 MPa	Wieding et al. (2012)
DED	Porous Ti-6Al-4V structures	E = 7–60 GPa YS = 471–809 MPa	Bandyopadhyay et al. (2010)
DED	Porous Ti structures	E = 2.6–44 GPa YS = 24–463 MPa	Xue et al. (2007)
EBM	Compact and porous Ti-6Al-4V structures	E = 3.9–12.9 GPa YS = 49.6–107.5 MPa UCS = 127.1–148.4 MPa	Ponader et al. (2009)
EBM	Porous Ti-6Al-4V implant	E = 14.5–38.5 GPa YS = 138–194 MPa UCS = 163–286 MPa	Li et al. (2012)

E, modulus of elasticity; *UCS*, ultimate compressive stress; *YS*, yield stress.

Table 12.2 Common materials, resolution, and laser type for each of the mentioned powder-based metal AM methods (Shayesteh Moghaddam et al., 2017).

Method	Common materials	Resolution	Laser type
SLM	Stainless steels, aluminum (Al), copper (Cu), iron (Fe), cobalt (Co)-chrome (CR), Ti, Ni-based alloy, and a mixture of different types of particles (Fe, Ni, Cu, and Fe_3P) (Abe et al., 2001; Childs et al., 2005; Kruth et al., 2004)	20 μm (Ravari et al., 2015)	Nd:YAG (Delgado et al., 2012)
DED	Steel alloys, stainless steel, tool steel, Al, bronze, Co-Cr, (Fe, Ni)-TiC composites and Ti (Xiao and Zhang, 2007)	20 μm (Hänninen, 2001)	CO_2 (Zhu et al., 2003), Fiber (Schleifenbaum et al., 2010)
EBM	Ti, Ti-6Al-4V, Ti Grade 2, Co-Cr	N/A	N/A

12.3.1 Advantages of AM

The advantages of AM in medical device industry originate from both the needs of the medical industry—such as complex geometries, patient-to-patient variation, high required precision, etc.—as well as the capabilities of AM, such as flexibility in geometry and fabrication of complex geometries, such as porous lattice structures, that conventional methods are unable to make. Using AM, completely customized parts can be fabricated that can be very advantageous for medical devices, where the device may vary from patient to patient. Moreover, the use of different materials to fabricate medical devices and parts is easily possible in AM, as long as the material can be produced

to a form that can be used by AM machines. For an optimized AM process, very little postfabrication treatment is needed.

For AM, a 3D model of the final product is generated in a computer before fabrication. This provides the opportunity of virtually assessing the appropriateness of the product and its match with the final implantation with the anatomy of the patient. In such cases, modifications can be made to the product quickly, before making the device. Finally, because of all these characteristics, AM of medical devices has a noticeably shorter supply-chain lead time and, in general, lower production cost.

12.3.2 Challenges of AM

Although AM technologies are advantageous in making medical devices, there are challenges toward achieving a successful fabrication with desired functional and structural properties. Indeed, first time fabrication of parts with a material could be challenging until a set of appropriate processing parameters (e.g., laser power, scanning speed, etc., in a laser-based manufacturing) could be determined. This procedure adds to the lead time and cost of fabrication in an AM process. On the other hand, since AM is in its early stages of development, there are a lot of uncertainties on the effects of various factors, such as shape and size of the part, on the properties of the fabricated parts. Understanding and tailoring the influence of various fabrication parameters on the mechanical properties of the part requires extensive research. This also requires regulations for fabricating and characterizing AM parts to ensure consistency of fabrications using different machines and at different fabrication sites.

Dimensional accuracy of the AM parts is another challenge with fabricating metallic medical devices especially for miniature components. In addition, providing an acceptable surface quality of the fabricated part, to eliminate postfabrication modifications, requires a lot of work and may not be possible for most materials and geometries at the current state of metal AM. Finally, durability of the fabricated AM parts is still the main challenge toward using these parts for medical applications, as majority of the real-world applications involve cyclic loading applied to these components. At the current state of AM, imperfections such as voids and impurities are inevitable in a fabricated AM component. Moreover, surface finish of the as-fabricated AM parts shows rough features. All these fabrication imperfections contribute to the fatigue failure of the AM devices and reduce their durability (Bagheri et al., 2018; Mahtabi et al., 2015a; Yadollahi et al., 2018).

12.4 Applications of AM in medical devices

The applications of AM in various industries has grown rapidly during the past decade. Especially in medical industry, these applications range from educational aspects to fabrication of final medical devices and implants (Javaid and Haleem, 2017; Tuomi et al., 2014; Zadpoor and Malda, 2017). While applications of AM in biomedical applications can be categorized based on different perspectives, some of the major application of AM in medical devices are discussed in this section.



Fig. 12.5 A prototype forceps fabricated using additive manufacturing (Kontio et al., 2012).

12.4.1 Tools, guides, and instruments for medical devices

One of the applications of AM technology in medical devices is to fabricate tools and instruments to improve the effectiveness of a medical procedure or surgery. The main advantage of AM for this type of application is that the complete process from design to fabrication can be done at once and the production process is much faster and more consistent. AM drill guides (Bibb et al., 2009; Labadie et al., 2008), oral appliances (Salmi et al., 2013), and surgical instruments/guides (Kontio et al., 2012) are examples of such applications. Fig. 12.5 shows an example of the additively manufactured tools and instruments. Using AM, instruments can be made for a specific operation—which are not available in the market—to meet the especial needs of the operation. As the devices and instruments for this type of application are in direct contact with body fluids and tissues for a limited time, one important consideration is that the material used for this type of application must be sterilizable, but does not need to be implantable (Tuomi et al., 2014).

12.4.2 Prosthesis and orthotics

The AM has been also used in orthotic and prosthetic applications. Similar to other applications, these applications benefit from the capability of AM in creating customized parts. Moreover, for prosthetic devices, AM enables fabricating functionally tuned devices by matching the dimensions of the device. For such applications, multimaterial technologies that are able to print colorful materials, which are not necessarily metals, are very advantageous. An additively manufactured prosthetic hand is shown in Fig. 12.6.

12.4.3 Customized implants

Freedom in form is the main advantage of AM for fabricating customized, patient-specific implants. Using this capability, implants can be fabricated to match the anatomy of a patient. Examples of implants that are fabricated using various AM techniques are presented in Fig. 12.7 Implant applications of AM are so advanced that

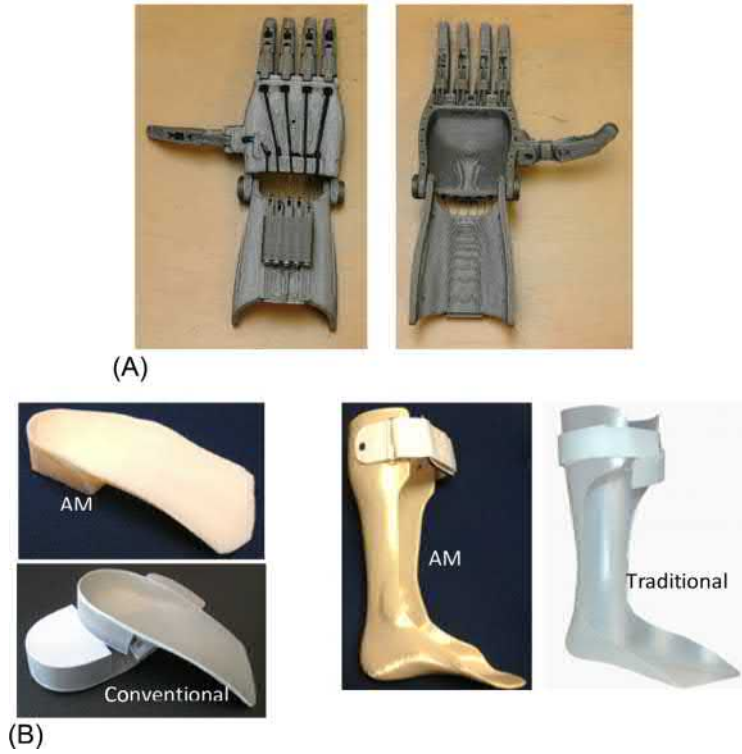


Fig. 12.6 Examples of AM orthotic and prosthetic parts: (A) Prosthetic hand (Burn et al., 2016), (B) foot orthosis (left) and ankle-foot orthosis (right) (Chen et al., 2016).

there are already companies that offer patient-specific AM implants following the procedure explained in Section 12.2. In addition, complex geometries such as lattice structures with intentional porous structures can be fabricated using different AM techniques. Examples of such lattice structures are shown in Fig. 12.7B. The lattice structures can be designed to meet different requirements, such as matching the mechanical properties of the implant to the biological tissue, and preventing some postimplantation issues, such as stress shielding. The porous structure of the implants also provides the potential for growth of tissue during healing, as well as osseointegration. The AM was used to fabricate artificial teeth as well (Liang et al., 2018) (Fig. 12.7C).

12.4.4 Education and training

Another important use of AM is its use for educational and training purposes, as well as for communicating with patients. In addition, 3D reconstruction of the devices and physical parts (Zadpoor and Malda, 2017; Spottiswoode et al., 2013; Zein Nizar et al., 2013) using an AM can be very helpful for planning complex surgeries. The

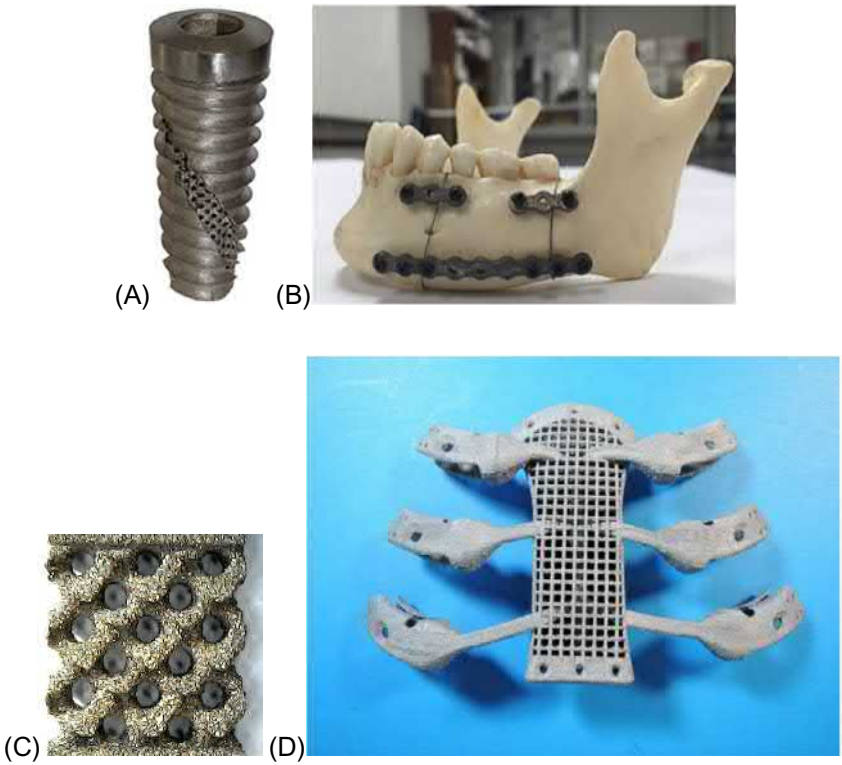


Fig. 12.7 Examples of medical implants fabricated by AM techniques: (A) Ti alloy dental implant (Obaton et al., 2017), (B) NiTi bone fixation plate, (C) lattice structure of NiTi fabricated by SLM technique, and (D) as-fabricated titanium sternum/rib implant made by EBM technique (Thompson, 2018).

capabilities of AM can also help evaluate the implantation procedure and the match between patient's anatomy and the medical device. The AM parts can be fabricated to represent human anatomy and for educating new surgeons and medical students by providing a more realistic environment. Multimaterial printing can be very helpful in this type of application by providing colorful fabricated objects.

12.4.5 Drug delivery

In 2015, food and drug administration (FDA) approved drug products fabricated by AM (Goyanes et al., 2016), indicating the great potential of AM for drug delivery devices in the solid form (Zadpoor and Malda, 2017). The main AM techniques that can be used for this type of application are binder jetting techniques, material extrusion, and material jetting. Using an AM, the drug release profile can be controlled by

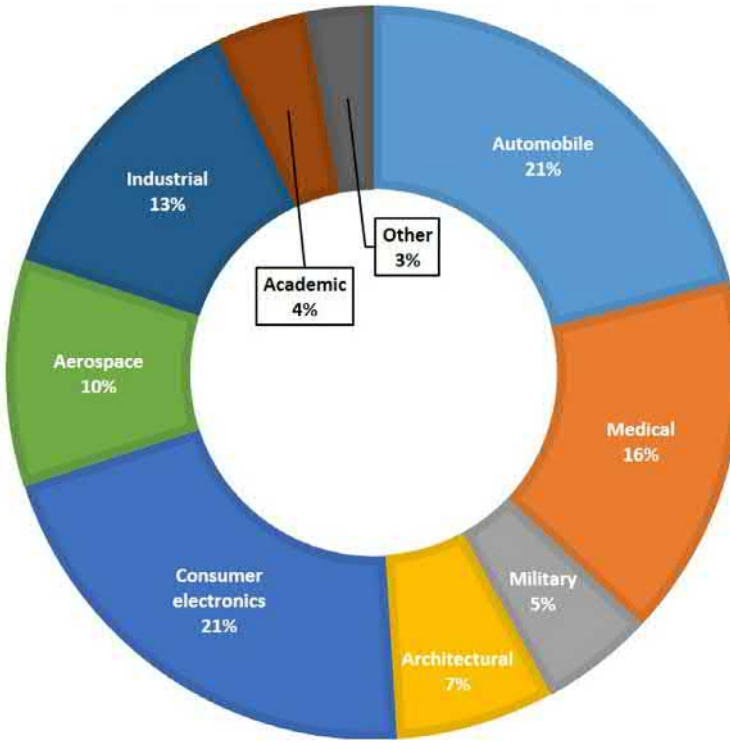


Fig. 12.8 Revenue split of AM equipment customers (Europe, 2015).

adjusting the shape of the device. Moreover, spatial distribution of the active agent in the device can also be designed in AM devices to have more control over the release profile. Another advantage of AM for drug delivery devices is the capability of fabricating multidrug materials into a single delivery device.

12.5 Market and statistics

The AM market is one of the world's fastest growing markets with a predicted market value of $10.8 billion by 2021. Fig. 12.8 shows the revenue of AM medical devices (Europe, 2015). It can be seen that the most rapid growth is in automotive, electronics, and medical industries.

Furthermore, considering very broad and generic applications as well as increasing number of accidents causing injuries and diseases there are demands in the market for faster AM of medical devices. The advantage of designing patient-specific devices is,

another reason toward additively manufactured medical devices in the market, to such an extent that it is estimated that in the near future AM will be used for 80% of the implants. Reports show that a total market of approximately $1.5 billion is anticipated for AM of medical devices by 2026 (Liang et al., 2018).

12.6 Biological considerations and biocompatibility of AM parts

12.6.1 Biological consideration

Technological advancement and availability of AM methods have led to increased investment and use by medical device industry. In December 2017, the United States FDA issued a comprehensive guidance for industry and FDA staff on "Technical Considerations for Additive Manufactured Medical Devices" (Food and Drug Administration, 2017). Beside other technical and mechanical considerations, this FDA document introduces and discusses all the parameters and conditions for the AM process that can affect the biocompatibility of the fabricated parts. While different AM techniques have been used in medical device industry, according to FDA—in addition to biocompatibility—other critical considerations, including cleaning and sterility, must be evaluated for AM medical devices. In general, achieving adequate cleaning, sterility, and biocompatibility is a major concern for different methods of AM and can be a limiting factor for the fabrication of specific geometries and materials. For instance, porous or internally complex devices must be carefully designed and processed due to the challenging procedure of cleaning and sterilization of these parts. In this section first we discuss the general aspects of biological considerations of AM devices, including cleaning, sterility, and biocompatibility, and then as an example, the biological consideration of additively manufactured Ti-6Al-4V will be discussed in more detail.

For all methods of AM fabrication, each of the process parameters including the raw material, building atmosphere, energy input properties, as well as any postfabrication treatments may significantly affect the biological properties of the final part. The first item to consider is the material composition of the final AM part after postfabrication treatments. Process parameters such as the energy input and the existing elements in the build chamber may cause unexpected chemical reactions, which may adversely affect the biocompatibility of the fabricated parts. If this is the case, the content and build atmosphere properties (i.e., temperature, humidity, etc.) of the AM process must be controlled and monitored during the fabrication. In some cases, an inert gas such as argon is fed into the built chamber to decrease the oxygen level to specific levels to prevent the oxidation of the main material. Postfabrication processing, especially heat treatment, may have the same effect and cause the formation of a nonbiocompatible element.

Although AM facilitates the creation of devices with complex geometries, such as components with engineered porosity, internal voids or cavities that may not exist in traditional manufacturing methods, are currently inevitable in AM products.

Therefore, one should also consider the increased difficulty in removing manufacturing material residues (cleaning) and in the sterilization due to the likelihood of increased surface area, generation of extensive tortuous pathways, and creation of internal voids with limited or no access. In cases where the residual materials could have an adverse effect on the biological aspect of the fabricated part, the manufacturer must establish and maintain procedures for the use and removal of such residual manufacturing material to ensure that it is removed or limited to an amount that does affect the part's features. For complex AM fabricated geometries, it should be mentioned that since many end-user facilities may not have access to equipment or materials required to implement specific cleaning procedures, only devices that are sufficiently clean of residual manufacturing materials should be provided to the end user.

To evaluate the biocompatibility of the final finished devices, the same procedure as in conventional devices must be considered. For any medical device, FDA suggests to evaluate the biocompatibility as described in the guidance "Use of International Standard ISO-10993, 'Biological Evaluation of Medical Devices Part 1: Evaluation and Testing within a Risk Management Process'" (Anand, 2000). Based on the FDA document, the first step for the assessment of the biocompatibility is the risk management for biocompatibility evaluations. One should identify and asset the potential risks based on the application of the medical device. For instance, a medical device that is in temporary contact with skin needs different types of evaluations compared to a permanent cardiovascular implant. After the risk assessment, a series of required tests should be designed and reported. These tests could be one or a couple of biocompatibility tests including, cytotoxicity, sensitization, hemocompatibility, pyrogenicity, implantation, genotoxicity, carcinogenicity, reproductive and developmental toxicity, and degradation assessments.

12.6.2 Biocompatibility of AM Ti and its alloys

Ti and its alloys are among the most well-known biocompatible metals that can be fabricated via AM. In general, in addition to the biocompatibility, bioadhesion, biofunctionality, and corrosion resistance are the other important properties for biomedical applications. The biocompatibility of Ti is mainly due to its low electrical conductivity, which contributes to the electrochemical oxidation of Ti leading to the formation of a thin passive oxide layer on its surface (Quinn and Armstrong, 1978). This oxide layer creates a high resistance to corrosion. In addition, this protective oxide layer remains at pH values of the human body (Schiff et al., 2002). In this section, as an example, some of the studies on biocompatibility of AM Ti and its alloys are discussed in more details.

Commercially pure Ti (CP-Ti) and Ti-6Al-4V are the most well-known compositions for the fabrication of Ti implants. The American Society for Testing and Materials (ASTM F67-06, 2006) specifies CP-Ti and Ti-6Al-4V as grade 1–5. Grades 1–4 are unalloyed CP-Ti and grade 5 is the Ti-6Al-4V alloy (ASTM F136-08, 2008). Table 12.3 summarizes the mechanical properties and different grades of Ti based on ASTM standards F67 and F136 (ASTM F67-06, 2006, 2008). The first step to

Table 12.3 Selected mechanical requirements properties for an implantable Ti Bar (Elias et al., 2008).

Material	Specification	Tensile strength (MPa)	0.2% proof stress (MPa)	Elongation (%)	Elastic modulus (GPa)
CP-Ti	ASTM F67 Grade 1	240	170	24	103–107
CP-Ti	ASTM F67 Grade 2	345	275	20	109–107
CP-Ti	ASTM F67 Grade 3	450	380	18	103–107
CP-Ti	ASTM F67 Grade 4	550	483	15	103–107
Ti-6Al-4V	ASTM F67 Grade 5	860	795	10	114–120

fabricate a biocompatible Ti is to reach to the standard mechanical properties based on the standards.

In addition to the mechanical properties, the chemical composition of the fabricated part must fulfill some standard requirements. ASTM and ISO have recently published new standards (ISO 22068-14, 2014; ASTM F3001-14, 2014; ASTM F2924-14, 2014; ASTM 2885-11, 2011) for additively layered manufactured (ALM) Ti parts, which are summarized in Table 12.4. These standards also include the minimum mechanical properties of the fabricated parts via ALM and is summarized in Table 12.5.

Following the mechanical properties and chemical composition, *in vitro* and in vivo studies have been performed on the AM fabricated Ti parts that verify the biocompatibility and reliability of this material. These studies used cultured fibroblasts

Table 12.4 Chemical composition requirements for ALM Ti according to ASTM standards.

Specification	Chemical composition (wt%)							
	Al	V	Fe	C	N	O	H	Y
ASTM F2885 Grade 5	5.5–6.75	3.5–4.5	<0.30	<0.08	<0.05	<0.20	<0.015	<0.005
ASTM F2924 ALM Ti-6Al-4V	5.5–6.5	3.5–4.5	<0.3	<0.08	<0.05	<0.20	<0.015	–
ASTM F3001 ALM Ti-6Al-4V	5.5–6.5	3.5–4.5	<0.25	<0.08	<0.05	<0.13	<0.012	<0.005

Table 12.5 Mechanical properties of ALM Ti-6Al-4V.

Material	Specification	Tensile strength	0.2% proof stress	Elongation (%)	Reduction of area
Ti-6Al-4V	ASTM F2885 Grade 5	780	680	10	15
ALM Ti-6Al-4V	ASTM F2924 ALM Ti-6Al-4V	895	825	10	15
ALM Ti-6Al-4V	ASTM F3001 ALM Ti-6Al-4V (ELI) Tensile	860	795	8	25

and osteoblasts in the observation of cell responses to surfaces and also human and animal subjects. Table 12.6 summarizes the processing methods, test types, and general findings of these studies.

12.7 Case study: Stiffness-matched bone fixation plates for mandibular reconstruction surgery

Mandibular segmental defects usually happen due to tumors, cancers, radiation therapy, and trauma. The standard of care for the treatment of a segmental defect starts with resectioning the defected region and using a bone graft (i.e., a healthy piece of bone harvested from patient's own body, such as fibula) to fill the resected region. As a part of this procedure, mechanical fixations including metallic bone plates and screws are used to immobilize the pieces of bone, and to facilitate and expedite the healing process (Fig. 12.9A) (Shayesteh Moghaddam et al., 2016). Conventionally, these bone plates are made of Ti-6Al-4V alloys. Although biocompatible Ti-6Al-4V bone plates provide enough immobilization immediately after the surgery, they may cause major complexities when the bones heal. Due to the high stiffness of Ti-6Al-4V in comparison to cortical bones, the load and stress distribution on the surrounding bones is affected in a way that a major portion of the loads are carried by the fixation plates instead of the bones. This reduced level of stress, which is also called stress shielding, leads to bone resorption and eventually failure of the surgery based on the bone remodeling phenomena (Mertens et al., 2014). The existence of bone resorption due to stress shielding can be clearly seen in the hip implant, thanks to X-ray images, in Fig. 12.9B. As it can be seen in this figure, the surrounding bones, especially on the top right portion of the hip implant, are darker in comparison with the healthy case that shows the bone resorption due to the stress-shielding effect.

One solution to prevent this failure is to remove the bone plates after the bone-healing period in a secondary surgery. Although removing the bone plates could

Table 12.6 Summary of AM processing methods and findings.

Method	Alloy	Biocompatibility test	Cell line/ implantation	General findings
EBM	Ti-6Al-4V	In vitro	Human fetal osteoblasts (hFOB 1.19)	Reduced cell proliferation in highly rough surfaces (ASTM F136-13, 2013)
EBM	Ti-6Al-4V	In vivo	Frontal skull of domestic pig	More bone contact in more porous samples (Ponader et al., 2009)
EBM	Ti-6Al-4V	In vivo	Rabbit femur and tibia	As-EBM implant response comparable to machined (Thomsen et al., 2008)
EBM	Ti-6Al-4V	In vitro	Human adipose-derived adult stem cells (hASC)	Increased proliferation on porous compared to polished and unpolished EBM discs (Haslauer et al., 2010)
EBM	Ti-6Al-4V	In vitro and in vivo	Osteoblasts extracted from Calvaria of rabbits, Calvaria of rabbits	Proliferation in porous EBM Ti-6Al-4V implants matched coated implants (Li et al., 2012)
EBM	Ti-6Al-4V	In vivo	Sheep	High bone-implant contact in porous implant (Palmquist et al., 2011)
DMLS	Ti-6Al-4V	In vitro	Human osteoblasts cells (HOB)	Cultured cells attached and proliferated on SLM substrates (Hollander et al., 2003)
DMLS	Unspecified	In vitro and in vivo	BMP-7 transduced human gingival Fibroblasts	In vitro and in vivo test data showing substantial bone ingrowth (Hollister et al., 2005)
DMLS	Ti-6Al-4V	In vivo	Human anterior mandible, minipig mandibular	Peri-implant bone in close contact with the surface of the implant (Mangano et al., 2010)

Table 12.6 Continued

Method	Alloy	Biocompatibility test	Cell line/ implantation	General findings
DMLS	Ti-6Al-4V	In vitro	Human osteoblasts human	Osteoblasts well-spread and with multiple contact points (Warnke et al., 2008)
LENS	CP-Ti	In vitro	Human osteoblast cells (OPC1)	Cells well spread on porous Ti (Xue et al., 2007)
LENS	Ti-6Al-4V	In vivo	Male Sprague-Dawley rats	Increase in calcium (bone) within implant pores (Bandyopadhyay et al., 2010)
Modified FDM	CP-Ti	In vitro	L929 mouse fibroblast	Excellent bone cell attachment and proliferation (Wiria et al., 2010)



Fig. 12.9 (A) Schematic illustration of a mandibular reconstruction (Jahadakbar et al., 2016) and (B) the effect of stress shielding and bone resorption (Engh et al., 1987).

prevent the risk of failure, extra cost and risk of the second surgery, and the increased recovery time are the main side effects of this solution (Boyd et al., 2012). Recently, patient-specific, stiffness-matched bone plates have been introduced to prevent the stress-shielding phenomenon and to eliminate the need for a second surgery (Jahadakbar et al., 2016). These bone plates are made of Ni-Ti alloy (NiTi or Nitinol), designed based on medical images of the patient (CT scans or X-rays), and are fabricated via AM. The stiffness-matching option minimizes the stress shielding on the

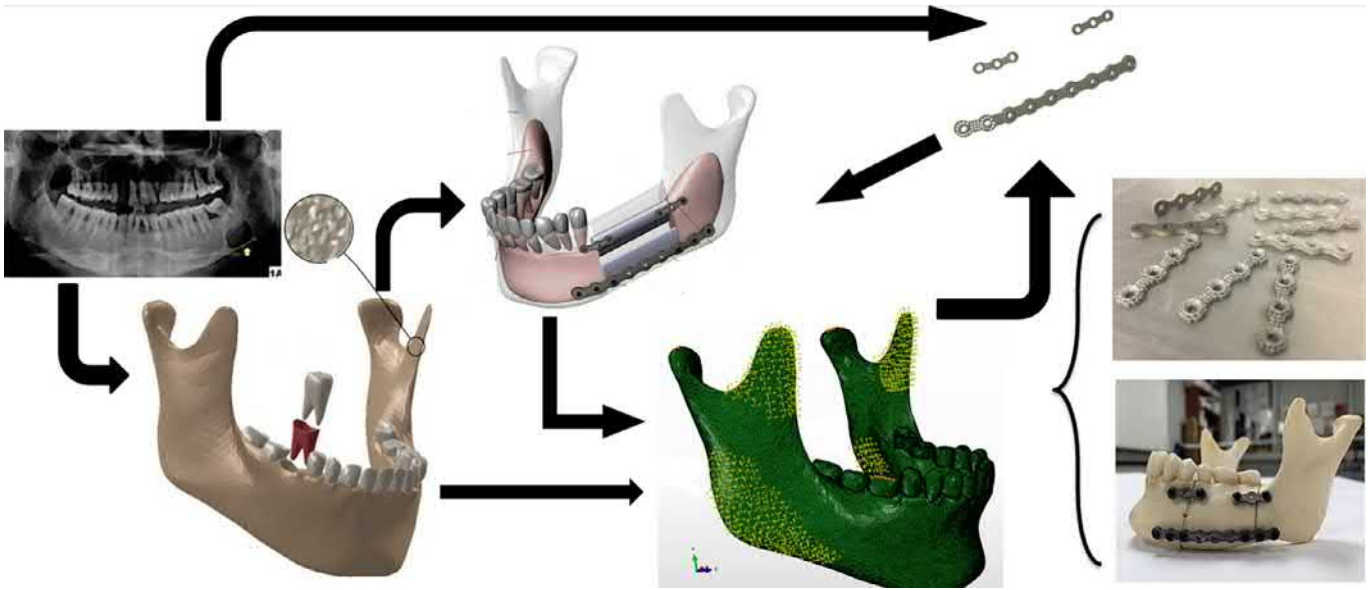


Fig. 12.10 The process of design and fabrication of patient-specific, stiffness-matched mandibular bone fixation plates.

surrounding bone and prevent bone resorption. Therefore, there is no need to remove the bone plates with a second surgery.

It is worth noting that NiTi, which is the base material for this next generation of bone plates, is a biocompatible shape memory alloy with unique features such as superelasticity and high fatigue life at large levels of strains, which make it a great candidate for biomedical implants (Mahtabi et al., 2015b,c; Mahtabi and Shamsaei, 2017). Due to the high thermomechanical sensitivity of this alloy, the conventional methods of fabrication such as machining and forging are very challenging for this material (Elahinia et al., 2012). Due to these manufacturing limitations, in the past NiTi was only available in the form of wire, rod, tube, and sheet. Recently, AM has been used for successful fabrication of this alloy with almost no limitations directly from CAD files (Elahinia et al., 2016). The mechanical properties and biological properties of the AM fabricated NiTi have been compared with conventionally fabricated NiTi and confirmed the successful fabrication of this alloy via SLM technique (Habijan et al., 2013; Haberland et al., 2012; Ibrahim et al., 2018).

Fig. 12.10 shows a general schematic of the process of AM of mandibular fixation plate. The design of these bone plates starts with CT-scan data of the patient's mandible. Based on the CT-scan data, first a 3D CAD model of the patient's mandible is created. Then in a virtual process the defected region is resected and replaced with a double barrel fibula graft. Following this step, the general geometry of the required bone plates is designed. Then the reconstructed mandible along with the bone plates and screws are transferred to a finite element (FE) software and modeled. In a series of simulations, using the CT-scan data, the required stiffness of the bone plates is calculated. Next, specific levels and types of porosity are assigned to the bone plates to modulate the final stiffness of the bone plates to the required level. Finally the CAD file of the patient-specific, stiffness-matched bone plates are designed based the patient's anatomy and FE simulations is used for AM (Jahadakbar et al., 2016).

References

Abe, F., Osakada, K., Shiomi, M., Uematsu, K., Matsumoto, M., 2001. The manufacturing of hard tools from metallic powders by selective laser melting. J. Mater. Process. Technol. 111 (1–3), 210–213.

Anand, V.P., 2000. Biocompatibility safety assessment of medical devices: FDA/ISO and Japanese standards. Med. Device Diagn. Ind. 22 (1), 206–219.

ASTM 2885-11, 2011. Standard Specification for Metal Injection Molded Titanium-6Aluminum-4Vanadium Components for Surgical Implant Applications. ASTM International, West Conshohocken, PA.

ASTM F136-08, 2008. Standard Specification for Wrought Titanium-6 Aluminum-4 Vanadium ELI (Extra Low Interstitial) Alloy for Surgical Implant Applications (UNS R56401). ASTM International, West Conshohocken, PA.

ASTM F136-13, 2013. Standard Specification for Wrought Titanium-6 Aluminum-4 Vanadium ELI (Extra Low Interstitial) Alloy for Surgical Implant Applications (UNS R56401). ASTM International, West Conshohocken, PA.

ASTM F2924-14, 2014. Standard Specification for Additive Manufacturing Titanium-6 Aluminum-4 Vanadium ELI with Powder Bed Fusion. ASTM International, West Conshohocken, PA.
ASTM F3001-14, 2014. Standard Specification for Additive Manufacturing Titanium-6 Aluminum-4 Vanadium ELI (Extra Low Interstitial) with Powder Bed Fusion. ASTM International, West Conshohocken, PA.
ASTM F67-06, 2006. Standard Specification for Unalloyed Titanium, for Surgical Implant Applications (UNS R50250, UNS R50400, UNS R50550, UNS R50700). ASTM International, West Conshohocken, PA.
Bagheri, A., Mahtabi, M.J., Shamsaei, N., 2018. Fatigue behavior and cyclic deformation of additive manufactured NiTi. J. Mater. Process. Technol. 252, 440–453.
Bandyopadhyay, A., Espana, F., Balla, V.K., Bose, S., Ohgami, Y., Davies, N.M., 2010. Influence of porosity on mechanical properties and in vivo response of Ti6Al4V implants. Acta Biomater. 6 (4), 1640–1648.
Bibb, R., Bocca, A., Eggbeer, D., Evans, P., Sugar, A., 2009. Rapid manufacture of custom-fitting surgical guides. Rapid Prototyp. J. 15 (5), 346–354.
Boyd, T.G., Huber, K.M., Verbist, D.E., Bumpous, J.M., Wilhelmi, B.J., 2012. CASE REPORT removal of exposed titanium reconstruction plate after mandibular reconstruction with a free fibula osteocutaneous flap with large surgical pin cutters: a case report and literature review. Eplasty 12, e42.
Burn, M.B., Ta, A., Gogola, G.R., 2016. Three-dimensional printing of prosthetic hands for children. J. Hand Surg. Am. 41 (5), e103–e109.
Chen, R.K., Jin, Y.-a., Wensman, J., Shih, A., 2016. Additive manufacturing of custom orthoses and prostheses—a review. Addit. Manuf. 12, 77–89.
Childs, T., Hauser, C., Badrossamay, M., 2005. Selective laser sintering (melting) of stainless and tool steel powders: experiments and modelling. Proc. Inst. Mech. Eng. B J. Eng. Manuf. 219 (4), 339–357.
Delgado, J., Ciurana, J., Rodríguez, C.A., 2012. Influence of process parameters on part quality and mechanical properties for DMLS and SLM with iron-based materials. Int. J. Adv. Manuf. Technol. 60 (5–8), 601–610.
Elahinia, M.H., Hashemi, M., Tabesh, M., Bhaduri, S.B., 2012. Manufacturing and processing of NiTi implants: a review. Prog. Mater. Sci. 57, 911–946.
Elahinia, M., Shayesteh Moghaddam, N., Taheri Andani, M., Amerinatanzi, A., Bimber, B.A., Hamilton, R.F., 2016. Fabrication of NiTi through additive manufacturing: a review. Prog. Mater. Sci. 83, 630–663.
Elias, C.N., Lima, J.H.C., Valiev, R., Meyers, M.A., 2008. Biomedical applications of titanium and its alloys. JOM 60 (3), 46–49.
Engh, C., Bobyn, J., Glassman, A., 1987. Porous-coated hip replacement. The factors governing bone ingrowth, stress shielding, and clinical results. J. Bone Joint Surg. Br. 69-B (1), 45–55.
Europe, M., 2015. An Overview of the Additive Manufacturing Market and Its Role on the Advances in Medical, Bioprinting and Drug Discovery. Medtec Europe.
Food and Drug Administration, 2017. Technical Considerations for Additive Manufactured Medical Devices. Food and Drug Administration.
Galati, M., Iuliano, L., 2018. A literature review of powder-based electron beam melting focusing on numerical simulations. Addit. Manuf. 19, 1–20.
Goyanes, A., Det-Amornrat, U., Wang, J., Basit, A.W., Gaisford, S., 2016. 3D scanning and 3D printing as innovative technologies for fabricating personalized topical drug delivery systems. J. Control. Release 234, 41–48.

Haberland, C., Meier, H., Frenzel, J., 2012. On the Properties of Ni-Rich NiTi Shape Memory Parts Produced by Selective Laser Melting. pp. 97–104.

Habijan, T., Haberland, C., Meier, H., Frenzel, J., Wittsiepe, J., Wuwer, C., Greulich, C., Schildhauer, T.A., Köller, M., 2013. The biocompatibility of dense and porous Nickel–Titanium produced by selective laser melting. Mater. Sci. Eng. C 33 (1), 419–426.

Hänninen, J., 2001. DMLS moves from rapid tooling to rapid manufacturing. Met. Powder Rep. 56 (9), 24–29.

Haslauer, C.M., Springer, J.C., Harrysson, O.L.A., Loboa, E.G., Monteiro-Riviere, N.A., Marcellin-Little, D.J., 2010. *In vitro* biocompatibility of titanium alloy discs made using direct metal fabrication. Med. Eng. Phys. 32 (6), 645–652.

Hollander, D.A., Wirtz, T., von Walter, M., Linker, R., Schultheis, A., Paar, O., 2003. Development of individual three-dimensional bone substitutes using "Selective LaserMelting" Eur. J. Trauma 29 (4), 228–234.

Hollister, S.J., Lin, C.Y., Saito, E., Lin, C.Y., Schek, R.D., Taboas, J.M., Williams, J.M., Partee, B., Flanagan, C.L., Diggs, A., Wilke, E.N., Van Lenthe, G.H., Müller, R., Wirtz, T., Das, S., Feinberg, S.E., Krebsbach, P.H., 2005. Engineering craniofacial scaffolds. Orthod. Craniofac. Res. 8 (3), 162–173.

Ibrahim, H., Jahadakbar, A., Dehghan, A., Moghaddam, S.N., Amerinatanzi, A., Elahinia, M., 2018. *In vitro* corrosion assessment of additively manufactured porous NiTi structures for bone fixation applications. Metals 8 (3), 164.

ISO 22068-14, 2014. Sintered-Metal Injection-Molded Materials—Specifications. International Organisation for Standardisation ISO, Geneva.

Jahadakbar, A., Shayesteh Moghaddam, N., Amerinatanzi, A., Dean, D., Karaca, E.H., Elahinia, M., 2016. finite element simulation and additive manufacturing of stiffness-matched NiTi fixation hardware for mandibular reconstruction surgery. Bioengineering 3 (4), 36.

Javaid, M., Haleem, A., 2017. Additive manufacturing applications in medical cases: a literature based review. Alex. J. Med. https://doi.org/10.1016/j.ajme.2017.09.003.

Kontio, R., Björkstr, R., Salmi, M., Paloheimo, M., Paloheimo, K.-S., Tuomi, J., Mäkitie, A.A., 2012. Designing and additive manufacturing a prototype for a novel instrument for mandible fracture reduction. Surgery 3 (2), 2–4.

Kruth, J.-P., Froyen, L., Van Vaerenbergh, J., Mercelis, P., Rombouts, M., Lauwers, B., 2004. Selective laser melting of iron-based powder. J. Mater. Process. Technol. 149 (1–3), 616–622.

Labadie, R.F., Noble, J.H., Dawant, B.M., Balachandran, R., Majdani, O., Fitzpatrick, J.M., 2008. Clinical validation of percutaneous cochlear implant surgery: initial report. Laryngoscope 118 (6), 1031–1039.

Li, X., Feng, Y.-F., Wang, C.-T., Li, G.-C., Lei, W., Zhang, Z.-Y., Wang, L., 2012. Evaluation of biological properties of electron beam melted Ti6Al4V implant with biomimetic coating *in vitro* and in vivo. PLoS One 7 (12), e52049.

Liang, X., Liao, W., Cai, H., Jiang, S., Chen, S., 2018. 3D-printed artificial teeth: accuracy and application in root canal therapy. J. Biomed. Nanotechnol. 14 (8), 1477–1485.

Mahtabi, M.J., Shamsaei, N., 2017. Fatigue modeling for superelastic NiTi considering cyclic deformation and load ratio effects. Shape Mem. Superelasticity 3, 250–263.

Mahtabi, M.J., Shamsaei, N., Mitchell, M.R., 2015a. Fatigue of Nitinol: the state-of-the-art and ongoing challenges. J. Mech. Behav. Biomed. Mater. 50, 228–254.

Mahtabi, M.J., Shamsaei, N., Elahinia, M.H., 2015b. Fatigue of shape memory alloys. In: Shape Memory Alloy Actuators. John Wiley & Sons, Ltd., pp. 155–190.

Mahtabi, M.J., Shamsaei, N., Rutherford, B., 2015c. Mean strain effects on the fatigue behavior of superelastic Nitinol alloys: an experimental investigation. Procedia Eng. 133, 646–654.

Mangano, C., Piattelli, A., d'Avila, S., Iezzi, G., Mangano, F., Onuma, T., Shibli, J.A., 2010. Early human bone response to laser metal sintering surface topography: a histologic report. J. Oral Implantol. 36 (2), 91–96.

Mertens, C., Decker, C., Engel, M., Sander, A., Hoffmann, J., Freier, K., 2014. Early bone resorption of free microvascular reanastomized bone grafts for mandibular reconstruction—a comparison of iliac crest and fibula grafts. J. Craniomaxillofac. Surg. 42 (5), e217–e223.

Obaton, A.F., Fain, J., Djemaï, M., Meinel, D., Léonard, F., Mahé, E., Lécuelle, B., Fouchet, J.J., Bruno, G., 2017. In vivo XCT bone characterization of lattice structured implants fabricated by additive manufacturing. Heliyon 3 (8), e00374.

Palmquist, A., Snis, A., Emanuelsson, L., Browne, M., Thomsen, P., 2011. Long-term biocompatibility and osseointegration of electron beam melted, free-form–fabricated solid and porous titanium alloy: experimental studies in sheep. J. Biomater. Appl. 27 (8), 1003–1016.

Ponader, S., von Wilmowsky, C., Widenmayer, M., Lutz, R., Heinl, P., Körner, C., Singer Robert, F., Nkenke, E., Neukam Friedrich, W., Schlegel Karl, A., 2009. In vivo performance of selective electron beam-melted Ti-6Al-4V structures. J. Biomed. Mater. Res. A 92A (1), 56–62.

Quinn, R.K., Armstrong, N.R., 1978. Electrochemical and surface analytical characterization of titanium and titanium hydride thin film electrode oxidation. J. Electrochem. Soc. 125 (11), 1790–1796.

Ravari, M.K., Kadkhodaei, M., Ghaei, A., 2015. A microplane constitutive model for shape memory alloys considering tension–compression asymmetry. Smart Mater. Struct.. 24 (7). 075016.

Salmi, M., Paloheimo, K.-S., Tuomi, J., Ingman, T., Mäkitie, A., 2013. A digital process for additive manufacturing of occlusal splints: a clinical pilot study. J. R. Soc. Interface 10 (84), 20130203.

Schiff, N., Grosgogeat, B., Lissac, M., Dalard, F., 2002. Influence of fluoride content and pH on the corrosion resistance of titanium and its alloys. Biomaterials 23 (9), 1995–2002.

Schleifenbaum, H., Meiners, W., Wissenbach, K., Hinke, C., 2010. Individualized production by means of high power Selective Laser Melting. CIRP J. Manuf. Sci. Technol. 2 (3), 161–169.

Shamsaei, N., Yadollahi, A., Bian, L., Thompson, S.M., 2015. An overview of direct laser deposition for additive manufacturing; Part II: Mechanical behavior, process parameter optimization and control. Addit. Manuf. 8, 12–35.

Shayesteh Moghaddam, N., Jahadakbar, A., Amerinatanzi, A., Elahinia, M., Miller, M., Dean, D., 2016. Metallic fixation of mandibular segmental defects: graft immobilization and orofacial functional maintenance. Plast. Reconstr. Surg. Glob. Open 4 (9), e858.

Shayesteh Moghaddam, N., Jahadakbar, A., Amerinatanzi, A., Elahinia, M., 2017. Recent advances in laser-based additive manufacturing. In: Bian, L., Shamsaei, N., Usher, J. (Eds.), Laser-Based Additive Manufacturing of Metal Parts: Modeling, Optimization, and Control of Mechanical Properties. CRC Press.

Spottiswoode, B.S., van den Heever, D.J., Chang, Y., Engelhardt, S., Du Plessis, S., Nicolls, F., Hartzenberg, H.B., Gretschel, A., 2013. Preoperative three-dimensional model creation of magnetic resonance brain images as a tool to assist neurosurgical planning. Stereotact. Funct. Neurosurg. 91 (3), 162–169.

Thompson, R.G., 2018. Anatomics 3D-printed titanium implants from head to heel. In: Froes, F.-H., Qian, M. (Eds.), Titanium in Medical and Dental Applications. Woodhead Publishing, pp. 225–237 (Chapter 3.2).

Thomsen, P., Malmström, J., Emanuelsson, L., René, M., Snis, A., 2008. Electron beam-melted, free-form-fabricated titanium alloy implants: material surface characterization and early bone response in rabbits. J. Biomed. Mater. Res. B Appl. Biomater. 90B (1), 35–44.

Trevisan, F., Calignano, F., Aversa, A., Marchese, G., Lombardi, M., Biamino, S., Ugues, D., Manfredi, D., 2017. Additive manufacturing of titanium alloys in the biomedical field: processes, properties and applications. J. Appl. Biomater. Funct. Mater. 16 (2), 57–67.

Tuomi, J., Paloheimo, K.-S., Vehviläinen, J., Björkstrand, R., Salmi, M., Huotilainen, E., Kontio, R., Rouse, S., Gibson, I., Mäkitie, A.A., 2014. A novel classification and online platform for planning and documentation of medical applications of additive manufacturing. Surg. Innov. 21 (6), 553–559.

Warnke, P.H., Douglas, T., Wollny, P., Sherry, E., Steiner, M., Galonska, S., Becker, S.T., Springer, I.N., Wiltfang, J., Sivananthan, S., 2008. Rapid prototyping: porous titanium alloy scaffolds produced by selective laser melting for bone tissue engineering. Tissue Eng. Part C Methods 15 (2), 115–124.

Wieding, J., Jonitz, A., Bader, R., 2012. The effect of structural design on mechanical properties and cellular response of additive manufactured titanium scaffolds. Materials 5 (8), 1336–1347.

Wiria, F.E., Shyan, J.Y.M., Lim, P.N., Wen, F.G.C., Yeo, J.F., Cao, T., 2010. Printing of Titanium implant prototype. Mater. Des. 31, S101–S105.

Xiao, B., Zhang, Y., 2007. Laser sintering of metal powders on top of sintered layers under multiple-line laser scanning. J. Phys. D Appl. Phys. 40 (21), 6725.

Xue, W., Krishna, B.V., Bandyopadhyay, A., Bose, S., 2007. Processing and biocompatibility evaluation of laser processed porous titanium. Acta Biomater. 3 (6), 1007–1018.

Yadollahi, A., Mahtabi, M.J., Khalili, A., Doude, H.R., Newman, J.C., 2018. Fatigue life prediction of additively manufactured material: effects of surface roughness, defect size, and shape. Fatigue Fract. Eng. Mater. Struct. 41 (7), 1602–1614.

Zadpoor, A.A., Malda, J., 2017. Additive manufacturing of biomaterials, tissues, and organs. Ann. Biomed. Eng. 45 (1), 1–11.

Zein Nizar, N., Hanouneh Ibrahim, A., Bishop Paul, D., Samaan, M., Eghtesad, B., Quintini, C., Miller, C., Yerian, L., Klatte, R., 2013. Three-dimensional print of a liver for preoperative planning in living donor liver transplantation. Liver Transpl. 19 (12), 1304–1310.

Zhu, H., Lu, L., Fuh, J., 2003. Development and characterization of direct laser sintering Cu-based metal powder. J. Mater. Process. Technol. 140 (1–3), 314–317.

Surface treatment

13

C. Moseke*, U. Gbureck†
*Mittelhessen University of Applied Sciences, Giessen, Germany,
†University of Würzburg, Würzburg, Germany

13.1 Introduction

Biomaterials for medical implants comprise a variety of metallic, polymeric, and ceramic materials, which may be utilized as single materials or as parts of material compounds. These materials are being chosen with respect to specific requirements of the application site, regarding functional properties, biocompatibility, and longevity of the designated medical implant. However, different application sites not only provide different challenges to the mechanical properties of the implant material but ambient conditions—that is, the presence and composition of extracellular fluids and blood as well as the interaction of the medical devices with soft and hard tissues—may also vary significantly.

While the mechanical behavior of a medical implant, particularly in load-bearing applications like total arthroplasty, is mainly governed by the mechanical properties of the bulk material, its interaction with the surrounding biological system arises from the particular properties of the material surface. These surface properties can be specific mechanical structures or topographies, surface hardness, different electronic modifications, and chemical functionalities attained by the attachment of specific chemical species like ions, biomacromolecules, or molecule fractions.

The first and most important aim of any surface treatment with respect to the modification of the afore-mentioned properties is to improve the biocompatibility of the medical device. In a modern sense, the term biocompatibility means much more than the bare tolerance of the foreign object in the biological system, it is rather an application-dependent optimization of the functional interaction between medical implant and the application site, which consists of a biomechanical part on one hand (e.g., the muscular-skeletal system) and the soft or hard host tissue on the other.

One frequently occurring complication of implant surgery is septic loosening as a result of bacterial infection, which may be caused by intrusion of bacteria into the surgical wound or by blood transport. Many surface treatment techniques aim to achieve antimicrobial properties of the implant, which are ideally being maintained for a long time after the implantation of the material. Antimicrobial surface modifications comprise various strategies like local drug delivery (e.g., by inserting antibiotics into the implant surface), coupling of biochemically active molecules to the surface by suitable spacer molecules, and surface coating with antibacterial inorganic films (e.g., silver and copper).

Metals for Biomedical Devices. https://doi.org/10.1016/B978-0-08-102666-3.00013-4
© 2019 Elsevier Ltd. All rights reserved.

Besides the requirements of the biological system to the surface properties of a medical implant, any surface modification must meet certain demands of the surgical environment; sterilizability, storability, and easy operability are aspects concerning the daily routine of the surgeon, and hence are equally important as the in situ performance of the implant. Furthermore, the insertion of an implant into the body—particularly into hard tissue—often involves shear or frictional forces affecting the implant surface; hence, mechanical stability is a crucial parameter for the successful implantation and the optimal long-term performance of the medical device and its surface-based functionality.

In order to meet all of the abovementioned requirements to medical implants, highly interdisciplinary and competent communication among clinicians, biologists, physicists, chemists, and material scientists is mandatory. Promising strategies for the development of biomaterials, regarding all relevant aspects from the basics of material fabrication to the therapeutic needs of the medical patient, must by all means involve all scientific disciplines, being consolidated in the interdisciplinary field of bioengineering.

13.2 Surface structuring

The fabrication of specifically structured surface topographies as a means to control and trigger biological reactions of adjacent host tissue is a frequently addressed subject of current biomaterial research, which has already found its way into diverse applications. It is well known that particularly cells respond to certain surface topographies: groove-like structures on the micron scale, for example, encourage eukaryotic cells to migrate and to grow in elongated shape alongside these grooved patterns (Elter et al., 2009; Scheideler et al., 2003), which may have advantageous effects on the directed secretion of extracellular matrix and hence the reduced formation of scar tissue during the healing process of an implant (Wang et al., 2000). However, the topographic influence of surfaces on cell adhesion is not limited to dimensions which are characteristic for the morphology of the cell body; even nano-scaled surface structuring can have a significant influence on cell orientation (Monsees et al., 2005) as well as on specific cellular functions, like extracellular matrix (ECM) secretion, proliferation, and cell metabolism (Martines et al., 2004; Dalby et al., 2004). A more complicated situation arises, when micro- and nanostructure are superimposed; nevertheless, particularly this form of surface topography represents a most promising approach in order to mimic the morphology of naturally mineralized tissue (Tan and Saltzman, 2004). In orthopedics, the ambitious aim of the respective research efforts among others is the significant improvement in the osseointegrative properties of implant surfaces, which is the most important prerequisite for accelerated implant healing and the restoration of the load-carrying ability of the locomotor system at an early stage of the postsurgical treatment. However, in other applications the requirements to cell-adhesive properties may be significantly different; for example, in the case of vascular stents the surface must strictly avoid the adhesion of endothelial

cells, in order to be suitable for the application in direct contact to flowing blood (Bedair et al., 2017).

Also bacterial adhesion to orthopedic implants is noticeably connected with the chemical and physical properties of the substrate surface; however, the significance of the topographical influence appears to be strongly dependent on the dimensional scale of the respective structure (Hou et al., 2011). Furthermore, it was found that the adhesion of microorganisms and the formation of biofilms apparently are being favored on more irregularly patterned surface topographies (Katsikogianni and Missirlis, 2004), while a plain increase in surface roughness leads to increasing surface energy and reduced contact angles and hence reduces bacterial adhesion (Colon et al., 2006). This applies particularly to the surface of the most prominent biomaterial titanium (Ti), which by itself does not provide significant antibacterial activity (Leonhardt and Dahlén, 1995).

The choice of an appropriate surface treatment for the material of a specific medical device has to consider several important aspects: the mechanical parameters of the bulk material and its surface, the design of the implant and its manufacturing process, the surgical technique being applied for the implantation, and certainly also the medical condition of the patient and his desired postsurgical activity. The most frequent applications of surface-treated materials can be found in maxillofacial and orthopedic surgery, where the dominating aspect is the mechanical stability of the implant-tissue interface, and also in technical therapeutics within the cardiovascular system or in contact with parts of the central nervous system. For a long time, the material of choice for such applications has been stainless steel of the 316L type, but in the last few years other materials like cobalt (Co)-chromium (Cr) alloys, commercially pure Ti of different grades as well as its alpha and beta alloys have been given preference, mainly because of their better biocompatibility and higher resistance against corrosion (Jurczyk, 2013). In general, metallic materials have highly advantageous properties regarding ductility and fatigue strength, as compared to, for example, polymer-based materials. Particularly Ti-based biomaterials—as well as pure metal or as alloys—provide additional properties, which make them the most promising materials for many medical applications. The unique biocompatibility of Ti arises from the so-called passivation layer, a thin film of oxide that forms spontaneously, in air as well as in aqueous solutions, and is highly resistant against aggressive chemical environment. However, the mechanical stability of this passivation layer is rather low, and its shear resistance could be easily overcome by the mechanical forces occurring during the insertion of the implant or its function in a load-bearing application (Jauch et al., 2011). This makes Ti one of the most prominent candidates for surface treatment procedures, which can provide the biocompatible implant surface with the required stability against wear and tear.

Modifications of metallic biomaterial surfaces lead to a vast expansion of the application range, which comprise among others the prevention of metal ions from the substrate, the formation of barrier layers, the fabrication of low-frictional, hemocompatible, nonthrombogenic surfaces, and so on. In addition to that, metallic surfaces can be equipped with a variety of bioactive coatings in order to promote specific cell responses and hence improve the in vivo performance of the modified

implant (Surmenev et al., 2014). Such coatings mostly consist of calcium phosphates like hydroxyapatite (HA), brushite, and so on, and also degradable compounds like magnesium phosphates, which may serve as short-term drug-delivery systems in critical situations of the host bone tissue (Meininger et al., 2016). Coatings can be deposited on bulk material surfaces as well as on Ti wires and meshes for tissue engineering scaffolds (Hirota et al., 2012). Suitable coating techniques comprise physical and chemical vapor deposition (PVD resp. CVD) methods as well as plasma spray, sol-gel techniques, and electrochemical coating methods.

Without the restriction of validity, but regarding the limited thematic frame, this chapter will mostly emphasize on physical and chemical methods for surface structuring and coating modifications.

13.3 Physical modifications

Basically, physical modifications of material surfaces can be divided into subtractive and additive techniques, or more specifically the mechanical/physical removal of surface material and the deposition of functional coatings. Mechanical surface structuring of surgical implant materials may be achieved by machining, sandblasting, or liquid jet application, whereby macro- or micro-structured, uniformly shaped or even quasifractal topographies can be achieved. When sandblasting techniques are being applied to biomaterial surfaces, it is crucial to avoid the contamination of the implant with foreign species, hence the sandblasting medium has to be chosen with care. In the case of corundum blasting, for example, aluminum oxide can be detected in the treated metal surface in noticeable amounts, which may have detrimental effects on the in vivo performance of the implant. This problem can be overcome by coating the corundum grains with more biocompatible materials like Ti oxide or HA. Thus, not only the surface contamination with unwanted species is significantly reduced, but also the material is being surface-structured and provided with a beneficial ceramic coating in the same process (Gbureck et al., 2003).

Irregular surfaces with random topographies with dimensions in the nanometer range can also be manufactured by means of plasma etching techniques (Minati et al., 2017; Yang et al., 2010). The material surface is being exposed to a highly ionized gas in a vacuum chamber, where various surface reactions may take place, depending on the choice of the process gas: inert gases will mainly cause an impact of kinetic energy on the substrate surface, which leads to the removal of single particles or reordering processes in the surface near crystal lattice, while reactive gases can form reaction products with the surface. With suitable process parameters reactive gases like oxygen can be introduced into the lattice structure of metallic biomaterials (oxygen diffusion hardening), whereby the mechanical surface properties can be significantly improved without affecting the biocompatibility (Schmitz et al., 2013).

Many biomaterial applications may require a regular, nonrandom-shaped topography with defined dimensions in the micron or submicron range of the substrate surface. Several diverse methods have been discussed in literature, which can be utilized to achieve this goal.

In electron beam lithography (EBL) the solubility of an electrosensitive film is locally modified, in order to achieve selective removal of the film by subsequent chemical treatment (Dial, 1998). Photolithography works with a quite similar technical principle, but utilizes light as the surface-ablative energy source. In comparison to EBL, this reduces the dimensions of the topographic features that can be fabricated, but on the other hand it is much faster. Complex structures in the range of few nanometers can be produced by scanning probe lithography (SPL), either by direct mechanical carving of the substrate (Müller et al., 2004) or alternatively by means of an oxide mask deposited via tunnel current and subsequent reactive ion etching (RIE) (Avouris et al., 1997). All aforementioned techniques have in common that the structuring of the surface occurs by the ablative removal of substrate material.

An alternative approach could consist in providing the biomaterial surface with functionalized coatings, which may be structured either during the deposition process itself or afterwards in a suitable secondary treatment.

The application of PVD techniques in the field of medical engineering includes among others the surface hardening of metallic materials, particularly in order to increase the resistance against abrasion, resp. to reduce the release of nanosized wear particles (Pizzoferrato, 2009). Frequently used coating materials for this purpose are Ti and titanium nitride (TiN). Due to its favorable mechanical properties like wear resistance, low friction coefficient, and good thermal stability, TiN is being applied, for example, as coating for heavily stressed tools, increases evidently the corrosion resistance of steel and Cr-Co alloys (Zuo et al., 2015), and shows antimicrobial activity against several bacteria strains (*Staphylococcus aureus*, *Staphylococcus epidermidis*, *Staphylococcus mutans*, and *Pseudomonas aeruginosa*) (Zhao et al., 2009).

Particularly low-temperature PVD techniques involving the vaporization of the coating material by means of magnetron sputtering have been reported as promising methods for the specific fabrication of surface topographies with antimicrobial potential, as they require high reproducibility of the film morphology on low dimensional scales (Lüdecke et al., 2013).

In summary, it can be stated that in comparison to ablative structuring techniques considerable advantages of the PVD technique consist in the possibility of physicochemical functionalization and functional structuring of the resulting coatings with only one instrument-based method on one hand and a significant expansion of the spectrum of usable substrate materials on the other. Suitable surface topographies can even be utilized for the immobilization of additional functional chemicals or even biomolecules, which provides possibilities to equip material surfaces with physical, chemical, and biological functionalization on different dimensional scales at the same time (see Image 13.1).

A very unique method to fabricate functional nanotopographies on metallic biomaterial surfaces is the electrochemical technique of anodic oxidation, which is capable of producing ordered nanotubular structures on the surface of transition metals. In brief, polished surfaces of refractory metals like Ti, tantalum (Ta), niobium (Nb), etc. (or any alloys of these) are immersed in suitable electrolytes (e.g., aqueous acidic solutions or polyethylene glycol, often supplemented with fluoric acid or fluoride salts) and connected to high positive voltages. Thus, metal oxide layers develop in

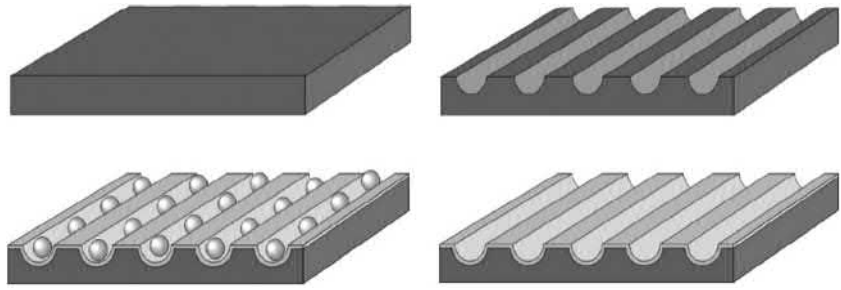


Image 13.1 Surface modifications of biomaterial surfaces: Different application sites and desired functions may require surface structuring, physical or chemical modification, coating, or equipment with chemical or biochemical functional species.

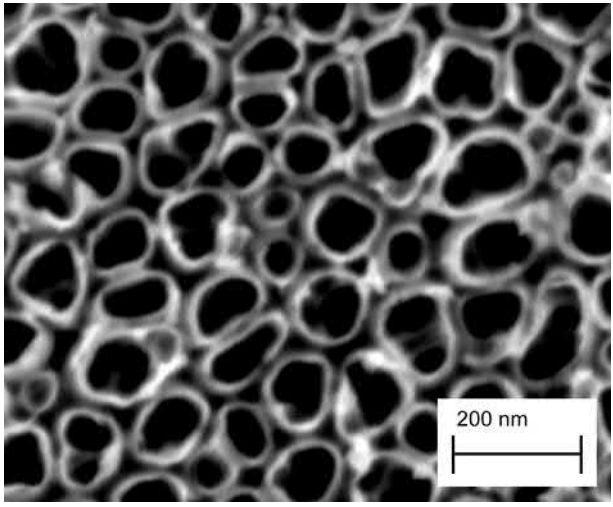


Image 13.2 Titania (TiO_2) nanotubes, formed by anodization in fluoride-containing polyethylene glycol electrolyte. The tubes are self-standing structures with well-separated walls of only a few nanometers thickness.

a manner of self-organized structure formation, consisting of long oxide tubes with varying diameters and a high aspect ratio (see Image 13.2) (Grimes, 2007).

An obvious application of such nanotubes can be found in drug-delivery systems for locus-specific medication. It has been found that Ti oxide nanotubes can be loaded with significant amounts of antibiotics or metal ions, which were then released into physiological media for many months in therapeutically relevant doses (Moseke et al., 2012; Losic et al., 2015). Recently studies have been conducted, in which such nanotube structures could even be fabricated in thin layers of refractory metals, previously deposited on various, even nonconductive substrates. Thus, the range of possible applications for drug-loaded nanotube arrays can be significantly enhanced.

Furthermore, the variation in anodization parameters, namely the applied voltages and the composition of the applied electrolyte permit the fabrication of nanotubes with a wide range of different parameters and hence nanostructured surfaces with very specific effects on various cell types and microorganisms (Gao et al., 2014; Lü et al., 2015). When alloys are used instead of pure refractory metals, the different metallic components will contribute to the formation of multimodal size distributions of the resulting nanotubes (Moseke et al., 2013). On this basis, multifunctional nanotube arrays could be developed, which selectively promote the desired adhesion of cells on one hand and inhibit the adhesion of unwanted microbial species on the other.

13.4 Chemical modifications

Chemical modification of implant metal surfaces includes a wide range of methods such as electrochemically assisted deposition (ECAD) of calcium phosphate (Gao et al., 2018), surface activation by alkali treatment to induce CaP crystallization in vivo (Jonášová et al., 2002), sol-gel derived oxide coatings (Chai et al., 2010) with the additional possibility of a covalent binding of biomolecules via amino, carboxylic, or methacrylate moieties (Dubruel et al., 2006) or the application of thin polyethylene glycol (PEG) layers to prevent unspecific protein adsorption (Hansson et al., 2005).

Since many metals are used within the skeletal system in direct contact with bone, the surface modification with calcium phosphates (similar to plasma spray HA coatings) is frequently utilized to achieve a direct bonding to bone (Dorozhkin, 2010). Here, the ECAD method is a versatile tool, since it enables modification with a broad range of different crystalline phases. The basic principle of the method is based on the pH-dependent solubility of the different CaP phases. When the metal substrate is placed as a cathode in an acidic calcium- and phosphate-containing electrolyte, hydrogen gas is formed at the surface of the metal due to proton discharge. This leads to a local increase in pH near the electrode, which in turn decreases CaP solubility and results in the formation of a crystalline coating at the surface. The method is technically relatively simple as compared to plasma spraying; however, the achievable coating thickness is smaller (several microns) and adhesion is likely lower. Nevertheless, a great advantage is the possibility to produce not only HA coatings, but also hydrated phases such as brushite (Blanda et al., 2016), struvite (Meininger et al., 2016), or portlandite (Moseke et al., 2009) by variation of the electrolyte composition and the coating parameters (temperature, current density). In addition, the method can be applied to a wide range of metallic substrates such as Ti alloys (Popa et al., 2011), stainless steel (Blanda et al., 2016), or even magnesium (alloys) (Zhang et al., 2016). This is possible, since the metal serves as cathode and hence its oxidation in the aqueous electrolyte is prevented. It has been demonstrated that further ionic modifications of the coatings with Sr^{2+}, Cu^{2+}, Zn^{2+}, Mg^{2+}, and Ag^{+} are possible (Bir et al., 2012; Fu et al., 2016; Furko et al., 2016; Lee et al., 2018; Wolf-Brandstetter et al., 2014), which are beneficial to direct the biological response to the coating (e.g., osseointegration, angiogenesis, antimicrobial activity).

CaP coatings on metals can be also formed by a biomimetic approach. Here, the metal surface is activated in a first step by treatment with NaOH, which results in the formation of a surface sodium titanate layer (Jonášová et al., 2002). Similar to the above-described ECAD, this layer results in a significant increase in the pH of an aqueous solution leading to CaP crystallization at the surface. This has been demonstrated in vitro by using simulated body fluid (Müller et al., 2007), however, CaP crystallization will also take place in vivo, as demonstrated by von Wilmowsky et al. and hence leads to an improved osseointegration of Ti implants (von Wilmowsky et al., 2008).

Sol-gel derived oxide coatings on implant metals are obtained by using alkoxides of various metals such as silicon, Ti, zirconium (Zr), or Nb as precursors. The aim of such coatings is mainly to protect the substrate from corrosion or to improve the bonding ability of the host tissue (Saranya et al., 2017; Carradò et al., 2017). Compared to metal oxide coatings produced by CVD, sol-gel processing offers a couple of advantages such as lower costs, a lower processing temperature, and the possibility to produce nanoporous coatings following supercritical drying of the surface applied gels (Saranya et al., 2017). The latter may be utilized as drug reservoirs with both a high loading capacity and a strongly retarded release due to the high specific surface area and small pore sizes of such coatings (Zhang et al., 2014; Gultepe et al., 2010; Harmankaya et al., 2013).

The sol-gel process can also be used to achieve a covalent binding of bioactive molecules to metal surfaces by using bifunctional silanes with mostly amine functionalities (Tack et al., 2015). For this purpose, the siliane is firstly prehydrolyzed with small amounts of water for sol formation and then applied to the surface, for example, by dip coating. Afterwards, bioactives are coupled to the free amino groups following the activation of carboxylic groups (of the bioactive) with carbodiimides (Tebbe et al., 2007). The result is a direct covalent bonding of bioactives to the metal surface, for example, collagen type I to stainless steel (Müller et al., 2005), BMP-2 to Ti (Chatzinikolaidou et al., 2010) or fibronectin (Scheideler et al., 2007). This above-described reaction procedure requires the presence of carboxylic groups within the bioactives for successful chemical coupling. In case that such groups are not present, alternatively epoxy-modified silanes can be used as reported by Pitt et al. (2004). The authors modified a stainless steel surface with an epoxysilane, which was converted to an aldehyde functional group followed by covalent binding of hyaluronan to minimize platelet adhesion from plasma.

In contrast to surface modification of metals for the application in bone replacement, the implantation of materials into the blood system (e.g., as cardiovascular stents or heart valves) requires a nonadhesive surface which does not initiate blood clotting or support neointimal cell proliferation. Here, coating strategies are based on either creating highly hydrophilic (Pan et al., 2014) or strong hydrophobic (Hoshikawa et al., 2012) surface properties to prevent unwanted adhesion of proteins or platelets or by covalent binding of anticoagulative drugs such as heparin (Li et al., 2011). This can be achieved, for example, by hydrophilic PEG coatings to prevent adsorption of biomolecules and platelets (Hansson et al., 2005; Pan et al., 2014) or by modification with methyltriethoxysilane (Hoshikawa et al., 2012). Such surface

modifications usually follow the same coating strategy via the sol-gel processing route using mainly amino-functionalized silanes as described above. However, although many studies have demonstrated the general functionality of such modifications in vitro and in vivo, clinical data regarding a long-term benefit for the patient are still missing.

13.5 Summary

Surface modification techniques can significantly improve the long-term in vivo performance of biomedical implants as well as provide them with certain biological functions. The judgement of the suitability of a certain treatment has to consider various aspects, namely the specific properties of the chosen substrate material, the biological environment of the respective application site, that is, the biological hard or soft tissue adjacent to the implant surface as well as the composition of the involved body fluids, and the particular medical situation of the patient. This chapter places the emphasis on physical and chemical routes for surface treatment. Physical methods comprised the fabrication of surface topographies with different scales (macro, micro, and nano), surface treatment with PVD techniques, and the fabrication of nanotube arrays for the application as drug delivery systems, while the subchapter about chemical modification deals with methods to change the chemical surface properties as well as chemical routes for the deposition of functional coatings on metallic substrates.

References

Avouris, P., Hertel, T., Martel, R., 1997. Atomic force microscope tip-induced local oxidation of silicon. Kinetics, mechanism, and nanofabrication. Appl. Phys. Lett. 71 (2), 285–287.

Bedair, T.M., ElNaggar, M.A., Joung, Y.K., Han, D.K., 2017. Recent advances to accelerate re-endothelialization for vascular stents. J. Tissue Eng. 8, 1–14.

Bir, F., Khireddine, H., Touati, A., Sidane, D., Yala, S., Oudadesse, H., 2012. Electrochemical depositions of fluorohydroxyapatite doped by Cu2+, Zn2+, Ag+ on stainless steel substrates. Appl. Surf. Sci. 258 (18), 7021–7030.

Blanda, G., Brucato, V., Pavia, F.C., Greco, S., Piazza, S., Sunseri, C., Inguanta, R., 2016. Galvanic deposition and characterization of brushite/hydroxyapatite coatings on 316L stainless steel. Mater. Sci. Eng. C Mater. Biol. Appl. 64, 93–101.

Carradò, A., Perrin-Schmitt, F., Le, Q.V., Giraudel, M., Fischer, C., Koenig, G., Jacomine, L., Behr, L., Chalom, A., Fiette, L., Morlet, A., Pourroy, G., 2017. Nanoporous hydroxyapatite/sodium titanate bilayer on titanium implants for improved osteointegration. Dent. Mater. 33 (3), 321–332.

Chai, F., Ochsenbein, A., Traisnel, M., Busch, R., Breme, J., Hildebrand, H.F., 2010. Improving endothelial cell adhesion and proliferation on titanium by sol-gel derived oxide coating. J. Biomed. Mater. Res. A 92 (2), 754–765.

Chatzinikolaidou, M., Lichtinger, T.K., Müller, R.T., Jennissen, H.P., 2010. Peri-implant reactivity and osteoinductive potential of immobilized rhBMP-2 on titanium carriers. Acta Biomater. 6 (11), 4405–4421.

Colon, G., Ward, B.C., Webster, T.J., 2006. Increased osteoblast and decreased *Staphylococcus epidermidis* functions on nanophase ZnO and TiO2. J. Biomed. Mater. Res. A 78 (3), 595–604.

Dalby, M.J., Riehle, M.O., Johnstone, H., Affrossman, S., Curtis, A.S.G., 2004. Investigating the limits of filopodial sensing. A brief report using SEM to image the interaction between 10 nm high nano-topography and fibroblast filopodia. Cell Biol. Int. 28 (3), 229–236.

Dial, O., 1998. Fabrication of high-density nanostructures by electron beam lithography. J. Vac. Sci. Technol., B: Microelectron. Nanometer Struct. 16 (6), 3887–3890.

Dorozhkin, S.V., 2010. Bioceramics of calcium orthophosphates. Biomaterials 31 (7), 1465–1485.

Dubruel, P., Vanderleyden, E., Bergadà, M., de Paepe, I., Chen, H., Kuypers, S., Luyten, J., Schrooten, J., van Hoorebeke, L., Schacht, E., 2006. Comparative study of silanisation reactions for the biofunctionalisation of Ti-surfaces. Surf. Sci. 600 (12), 2562–2571.

Elter, P., Sickel, F., Ewald, A., 2009. Nanoscaled periodic surface structures of medical stainless steel and their effect on osteoblast cells. Acta Biomater. 5 (5), 1468–1473.

Fu, C., Zhang, X., Savino, K., Gabrys, P., Gao, Y., Chaimayo, W., Miller, B.L., Yates, M.Z., 2016. Antimicrobial silver-hydroxyapatite composite coatings through two-stage electrochemical synthesis. Surf. Coat. Technol. 301, 13–19.

Furko, M., Jiang, Y., Wilkins, T., Balázsi, C., 2016. Development and characterization of silver and zinc doped bioceramic layer on metallic implant materials for orthopedic application. Ceram. Int. 42 (4), 4924–4931.

Gao, A., Hang, R., Huang, X., Zhao, L., Zhang, X., Wang, L., Tang, B., Ma, S., Chu, P.K., 2014. The effects of titania nanotubes with embedded silver oxide nanoparticles on bacteria and osteoblasts. Biomaterials 35 (13), 4223–4235.

Gao, A., Hang, R., Bai, L., Tang, B., Chu, P.K., 2018. Electrochemical surface engineering of titanium-based alloys for biomedical application. Electrochim. Acta 271, 699–718.

Gbureck, U., Masten, A., Probst, J., Thull, R., 2003. Tribochemical structuring and coating of implant metal surfaces with titanium oxide and hydroxyapatite layers. Mater. Sci. Eng. C 23 (3), 461–465.

Grimes, C.A., 2007. Synthesis and application of highly ordered arrays of TiO2 nanotubes. J. Mater. Chem. 17 (15), 1451.

Gultepe, E., Nagesha, D., Sridhar, S., Amiji, M., 2010. Nanoporous inorganic membranes or coatings for sustained drug delivery in implantable devices. Adv. Drug Deliv. Rev. 62 (3), 305–315.

Hansson, K.M., Tosatti, S., Isaksson, J., Wetterö, J., Textor, M., Lindahl, T.L., Tengvall, P., 2005. Whole blood coagulation on protein adsorption-resistant PEG and peptide functionalised PEG-coated titanium surfaces. Biomaterials 26 (8), 861–872.

Harmankaya, N., Karlsson, J., Palmquist, A., Halvarsson, M., Igawa, K., Andersson, M., Tengvall, P., 2013. Raloxifene and alendronate containing thin mesoporous titanium oxide films improve implant fixation to bone. Acta Biomater. 9 (6), 7064–7073.

Hirota, M., Hayakawa, T., Yoshinari, M., Ametani, A., Shima, T., Monden, Y., Ozawa, T., Sato, M., Koyama, C., Tamai, N., Iwai, T., Tohnai, I., 2012. Hydroxyapatite coating for titanium fibre mesh scaffold enhances osteoblast activity and bone tissue formation. Int. J. Oral Maxillofac. Surg. 41 (10), 1304–1309.

Hoshikawa, Y., Onoki, T., Akao, M., Akatsu, T., Tanabe, Y., Yasuda, E., 2012. Blood compatibility and tissue responsiveness on simple and durable methylsiloxane coating. Mater. Sci. Eng. C Mater. Biol. Appl. 32 (6), 1627–1631.

Hou, S., Gu, H., Smith, C., Ren, D., 2011. Microtopographic patterns affect *Escherichia coli* biofilm formation on poly(dimethylsiloxane) surfaces. Langmuir 27 (6), 2686–2691.

Jauch, S.Y., Huber, G., Hoenig, E., Baxmann, M., Grupp, T.M., Morlock, M.M., 2011. Influence of material coupling and assembly condition on the magnitude of micromotion at the stem-neck interface of a modular hip endoprosthesis. J. Biomech. 44 (9), 1747–1751.

Jonášová, L., Müller, F.A., Helebrant, A., Strnad, J., Greil, P., 2002. Hydroxyapatite formation on alkali-treated titanium with different content of Na+ in the surface layer. Biomaterials 23 (15), 3095–3101.

Jurczyk, M., 2013. Bionanomaterials for Dental Applications. Pan Stanford Publishing, Singapore.

Katsikogianni, M., Missirlis, Y.F., 2004. Concise review of mechanisms of bacterial adhesion to biomaterials and of techniques used in estimating bacteria-material interactions. Eur. Cell. Mater. 8, 37–57.

Lee, K., Ko, Y.-M., Choe, H.-C., 2018. Electrochemical deposition of hydroxyapatite substituted with magnesium and strontium on Ti-6Al-4V alloy. J. Nanosci. Nanotechnol. 18 (2), 1449–1452.

Leonhardt, Å., Dahlén, G., 1995. Effect of titanium on selected oral bacterial species in vitro. Eur. J. Oral Sci. 103 (6), 382–387.

Li, G., Yang, P., Liao, Y., Huang, N., 2011. Tailoring of the titanium surface by immobilization of heparin/fibronectin complexes for improving blood compatibility and endothelialization. An in vitro study. Biomacromolecules 12 (4), 1155–1168.

Losic, D., Aw, M.S., Santos, A., Gulati, K., Bariana, M., 2015. Titania nanotube arrays for local drug delivery. Recent advances and perspectives. Expert Opin. Drug Deliv. 12 (1), 103–127.

Lü, W.L., Wang, N., Gao, P., Li, C.Y., Zhao, H.S., Zhang, Z.T., 2015. Effects of anodic titanium dioxide nanotubes of different diameters on macrophage secretion and expression of cytokines and chemokines. Cell Prolif. 48 (1), 95–104.

Lüdecke, C., Bossert, J., Roth, M., Jandt, K.D., 2013. Physical vapor deposited titanium thin films for biomedical applications. Reproducibility of nanoscale surface roughness and microbial adhesion properties. Appl. Surf. Sci. 280, 578–589.

Martines, E., McGhee, K., Wilkinson, C., Curtis, A., 2004. A parallel-plate flow chamber to study initial cell adhesion on a nanofeatured surface. IEEE Trans. Nanobioscience 3 (2), 90–95.

Meininger, M., Wolf-Brandstetter, C., Zerweck, J., Wenninger, F., Gbureck, U., Groll, J., Moseke, C., 2016. Electrochemically assisted deposition of strontium modified magnesium phosphate on titanium surfaces. Mater. Sci. Eng. C 67, 65–71.

Minati, L., Migliaresi, C., Lunelli, L., Viero, G., Dalla Serra, M., Speranza, G., 2017. Plasma assisted surface treatments of biomaterials. Biophys. Chem. 229, 151–164.

Monsees, T.K., Barth, K., Tippelt, S., Heidel, K., Gorbunov, A., Pompe, W., Funk, R.H.W., 2005. Effects of different titanium alloys and nanosize surface patterning on adhesion, differentiation, and orientation of osteoblast-like cells. Cells Tissues Organs 180 (2), 81–95.

Moseke, C., Braun, W., Ewald, A., 2009. Electrochemically deposited Ca(OH)2 coatings as a bactericidal and osteointegrative modification of Ti implants. Adv. Eng. Mater. 11 (3), B1–B6.

Moseke, C., Hage, F., Vorndran, E., Gbureck, U., 2012. TiO2 nanotube arrays deposited on Ti substrate by anodic oxidation and their potential as a long-term drug delivery system for antimicrobial agents. Appl. Surf. Sci. 258 (14), 5399–5404.

Moseke, C., Lehmann, C., Schmitz, T., Reinert, F., Groll, J., Gbureck, U., 2013. Nanostructuring of refractory metal surfaces by electrochemical oxidation. Nb and the binary systems Ti-Ta and Nb-Ta. Curr. Nanosci. 9 (1), 132–138.

Müller, M., Fiedler, T., Gröger, R., Koch, T., Walheim, S., Obermair, C., Schimmel, T., 2004. Controlled structuring of mica surfaces with the tip of an atomic force microscope by mechanically induced local etching. Surf. Interface Anal. 36 (2), 189–192.

Müller, R., Abke, J., Schnell, E., Macionczyk, F., Gbureck, U., Mehrl, R., Ruszczak, Z., Kujat, R., Englert, C., Nerlich, M., Angele, P., 2005. Surface engineering of stainless steel materials by covalent collagen immobilization to improve implant biocompatibility. Biomaterials 26 (34), 6962–6972.

Müller, F.A., Müller, L., Caillard, D., Conforto, E., 2007. Carbonate substitution and preferred growth orientation of biomimetic apatites. Key Eng. Mater. 330–332, 725–728.

Pan, C.-J., Hou, Y.-H., Zhang, B.-B., Dong, Y.-X., Ding, H.-Y., 2014. Blood compatibility and interaction with endothelial cells of titanium modified by sequential immobilization of poly (ethylene glycol) and heparin. J. Mater. Chem. B 2 (7), 892–902.

Pitt, W.G., Morris, R.N., Mason, M.L., Hall, M.W., Luo, Y., Prestwich, G.D., 2004. Attachment of hyaluronan to metallic surfaces. J. Biomed. Mater. Res. A 68 (1), 95–106.

Pizzoferrato, A., 2009. Evaluation of the tissue response to the wear products of the hip joint endo-arthroprosthesis. Biomater. Med. Devices Artif. Organs 7 (2), 257–262.

Popa, M.V., Moreno, J.M.C., Popa, M., Vasilescu, E., Drob, P., Vasilescu, C., Drob, S.I., 2011. Electrochemical deposition of bioactive coatings on Ti and Ti–6Al–4V surfaces. Surf. Coat. Technol. 205 (20), 4776–4783.

Saranya, K., Thirupathi Kumara Raja, S., Subhasree, R.S., Gnanamani, A., Das, S.K., Rajendran, N., 2017. Fabrication of nanoporous sodium niobate coating on 316L SS for orthopaedics. Ceram. Int. 43 (15), 11569–11579.

Scheideler, L., Geis-Gerstorfer, J., Kern, D., Pfeiffer, F., Rupp, F., Weber, H., Wolburg, H., 2003. Investigation of cell reactions to microstructured implant surfaces. Mater. Sci. Eng. C 23 (3), 455–459.

Scheideler, L., Rupp, F., Wendel, H.P., Sathe, S., Geis-Gerstorfer, J., 2007. Photocoupling of fibronectin to titanium surfaces influences keratinocyte adhesion, pellicle formation and thrombogenicity. Dent. Mater. 23 (4), 469–478.

Schmitz, T., Hertl, C., Werner, E., Gbureck, U., Groll, J., Moseke, C., 2013. Oxygen diffusion hardening of tantalum coatings on cp-titanium for biomedical applications. Surf. Coat. Technol. 216, 46–51.

Surmenev, R.A., Surmeneva, M.A., Ivanova, A.A., 2014. Significance of calcium phosphate coatings for the enhancement of new bone osteogenesis—a review. Acta Biomater. 10 (2), 557–579.

Tack, L., Schickle, K., Böke, F., Fischer, H., 2015. Immobilization of specific proteins to titanium surface using self-assembled monolayer technique. Dent. Mater. 31 (10), 1169–1179.

Tan, J., Saltzman, W.M., 2004. Biomaterials with hierarchically defined micro- and nanoscale structure. Biomaterials 25 (17), 3593–3601.

Tebbe, D., Thull, R., Gbureck, U., 2007. Influence of spacer length on heparin coupling efficiency and fibrinogen adsorption of modified titanium surfaces. Biomed. Eng. Online 6, 31–38.

von Wilmowsky, C., Müller, L., Lutz, R., Lohbauer, U., Rupp, F., Neukam, F.W., Nkenke, E., Schlegel, K.A., Müller, F.A., 2008. Osseointegration of chemically modified titanium surfaces. An in vivo study. Adv. Eng. Mater. 10 (12), B61–B66.

Wang, J.H.-C., Grood, E.S., Florer, J., Wenstrup, R., 2000. Alignment and proliferation of MC3T3-E1 osteoblasts in microgrooved silicone substrata subjected to cyclic stretching. J. Biomech. 33 (6), 729–735.

Wolf-Brandstetter, C., Oswald, S., Bierbaum, S., Wiesmann, H.-P., Scharnweber, D., 2014. Influence of pulse ratio on codeposition of copper species with calcium phosphate coatings on titanium by means of electrochemically assisted deposition. J. Biomed. Mater. Res. B Appl. Biomater. 102 (1), 160–172.

Yang, J., Cui, F.-z., Lee, I.S., Wang, X., 2010. Plasma surface modification of magnesium alloy for biomedical application. Surf. Coat. Technol. 205, S182–S187.

Zhang, Y., He, F., Sun, Z., Li, L., Huang, Y., 2014. Controlled delivery of dexamethasone from TiO2 film with nanoporous structure on Ti–25Nb–3Mo–2Sn–3Zr biomedical alloy without polymeric carrier. Mater. Lett. 128, 384–387.

Zhang, C., Cai, C., Liu, X., Wang, J., 2016. Calcium phosphate coatings prepared by electrochemical deposition on fluoride-treated magnesium alloy. Rare Metal Mater. Eng. 45 (8), 2116–2122.

Zhao, L., Chu, P.K., Zhang, Y., Wu, Z., 2009. Antibacterial coatings on titanium implants. J. Biomed. Mater. Res. B Appl. Biomater. 91 (1), 470–480.

Zuo, J., Xie, Y., Zhang, J., Wei, Q., Zhou, B., Luo, J., Wang, Y., Yu, Z.M., Tang, Z.G., 2015. TiN coated stainless steel bracket. Tribological, corrosion resistance, biocompatibility and mechanical performance. Surf. Coat. Technol. 277, 227–233.

Coatings for metallic biomaterials

14

Toshihiro Kasuga
Division of Advanced Ceramics, Nagoya Institute of Technology, Nagoya, Japan

14.1 Introduction

The high-performance biomaterials for replacing damaged hard tissues, such as artificial joints, bone fillers, dental implants, and so on, are in high demand among the aged people. Metallic biomaterials with biological safety, such as stainless steel, cobalt (Co)-based alloys, titanium (Ti) and its alloys, are reasonable for replacing hard tissues at load-bearing sections. Ti and its alloys are especially widely used as orthopedic and dental implants because of their excellent biocompatibility. Much attention has been paid to β-type Ti alloys because they have high mechanical strength with low modulus of elasticity. One of the attractive metals is β-type Ti alloys, which contain elements sufficiently tolerated by living tissues, such as niobium (Nb), tantalum (Ta), and zirconium (Zr) (Niinomi, 2003; Kuroda et al., 1998). A Ti-29Nb-13Ta-4.6Zr (denoted by TNTZ) alloy, which has been suggested as one of the best materials designed, shows a high tensile strength of ~1 GPa and low Young's modulus of 60–80 GPa. Although Ti and its alloys do not make a chemical bond with living bone, they can adhere to it with almost no fibrous tissues.

Calcium phosphate ceramics such as hydroxyapatite ($Ca_{10}(PO_4)_6(OH)_2$: HA) and β-tricalcium phosphate (β-$Ca_3(PO_4)_2$: β-TCP) exhibit bioactivity, which is the ability to make a bond chemically with natural bone tissues (Hench, 1992). Some glasses and glass-ceramics are also well known as bioactive materials. Some portions in artificial substitutes for hard tissue may require bioactivity. Bioactive surface modification is, in general, applied to Ti and its alloys to further improve their bio-functionality, including osteoconductivity. The bioactive ceramic coatings prepared using various processes have been investigated so far and some materials are clinically used as biomaterials for dental and surgical implants.

In this chapter, some bio-functional coatings on metals are briefly reviewed.

14.2 Calcium phosphate ceramic coatings

Implants coated with calcium phosphates such as HA and β-TCP have been widely used in orthopedics and dentistry. The cementless fixation technique combines the mechanical strength, ductility, and ease of fabrication with bioactivity. Since much earlier, calcium phosphate coatings have been applied by a variety of methods, such

Metals for Biomedical Devices. https://doi.org/10.1016/B978-0-08-102666-3.00014-6
© 2019 Elsevier Ltd. All rights reserved.

as dip-coating (Li et al., 1996), electrophoretic deposition (EPD) (Ducheyne et al., 1986), plasma spraying (Lacefield, 1993), ion-beam sputtering (Ong and Lucas, 1994), flame spraying (Berndt et al., 1990), wet-process coating, and so on. In this section, some recent possible coatings are briefly discussed.

14.2.1 Thermal sprayed coatings

Thermal spraying employs a plasma/ionized gas or fuel/oxygen (O) gas to melt the ceramic particles and subsequently to carry them onto the surface of substrates. Two important properties of thermal sprayed coatings are: (i) bonding strength between the calcium phosphate layer and the metallic substrate, and (ii) dissolution behavior in body fluid. Residual stress arises at the interface between the metallic substrate and the coating layer due to the large difference in their thermal expansions. Amorphous calcium phosphate tends to dissolve rapidly in body fluid: coatings with low crystallinity rapidly become weak and may induce inflammatory responses. A relatively high bonding strength on Ti or its alloys was reported by Tsui et al. (1998); the values were in the range of 20–40 MPa after optimization of coating properties. The crystallinity of HA in their coating layers was relatively high (83%–94%). Their high crystallinity was very important for the long-term benefit of the coated implants.

A radio-frequency thermal plasma spraying (rf-TPS) method was developed to obtain strong bonding between the HA coating and Ti substrate, employing an HA/Ti composite coating (Inagaki et al., 2003). The HA/Ti composite coatings were prepared by controlling the starting composition using two microfeeders, which fed the HA and Ti powders at an accurate rate. The starting powders were fed so as to form the coated layer with a compositional gradient from a Ti-rich phase at the bottom to an HA-rich at the top. The composition of plasma gas played an important role in improving the bonding strength of the coatings. Rf-TPS with nitrogen (N)-containing plasma gas induced the formation of the coatings with excellent bonding to the Ti substrate (the tensile bonding strength of 65 MPa). The microstructure of the interface between deposited Ti particles in the coatings was significantly influenced by plasma gas composition during rf-TPS. By rf-TPS with N- or O-containing plasma gas, Ti nitride or Ti oxide was formed in the deposited Ti particles, respectively. The bonding of the composite coatings on the Ti substrate was suggested to be influenced by microstructure at the interface between Ti particles.

Surgical Site Infection (SSI) is one of the complications in artificial joint replacement surgery, and its treatment is often not easy. About 50% of the infecting organisms are Methichillin-resistant *Staphylococcus aureus* (MRSA) and methicillin-resistant *Staphylococcus epidermidis* (MRSE). The SSI associated with the surgery, which is called "implant related infection" or "peri-prosthetic joint infection", is known to be linked to the formation of biofilm and it has a serious influence on the outbreak and severity of infectious disease. Antibacterial drugs don't work well on bacteria in biofilms, and the treatment of SSI is difficult due to an increase in drug-resistant bacteria such as MRSA and MRSE.

A silver (Ag)-containing calcium phosphate (CP) coating has been prepared using frame spraying to reduce the incidence of SSI in total hip arthroplasty (THA) (Noda et al., 2009). A mixture of 97% HA and 3% Ag_2O powders (in wt%) was

flame-sprayed on metallic Ti using an acetylene torch to be coated with a compositionally homogeneous amorphous calcium phosphate layer of ~40 μm thickness (denoted by Ag-CP coating, hereafter). As shown in Fig. 14.1A and B, a typical surface structure of thermal spraying was obtained. Energy dispersive x-ray spectrometry (EDX) showed that the content of Ag_2O in the sprayed layer was reduced to ~0.3%. However, its calcium (Ca)/phosphate (P) ratio was almost unchanged from the nominal composition. The amount of Ag^+ ions dissolved from the Ag-CP coating in fetal bovine serum (FBS) was 78 ppb after 1 h of soaking and 260–330 ppb after 24–48 h, respectively; Ag^+ ion dissolution at an initial stage would be important for preventing SSI (Noda et al., 2009).

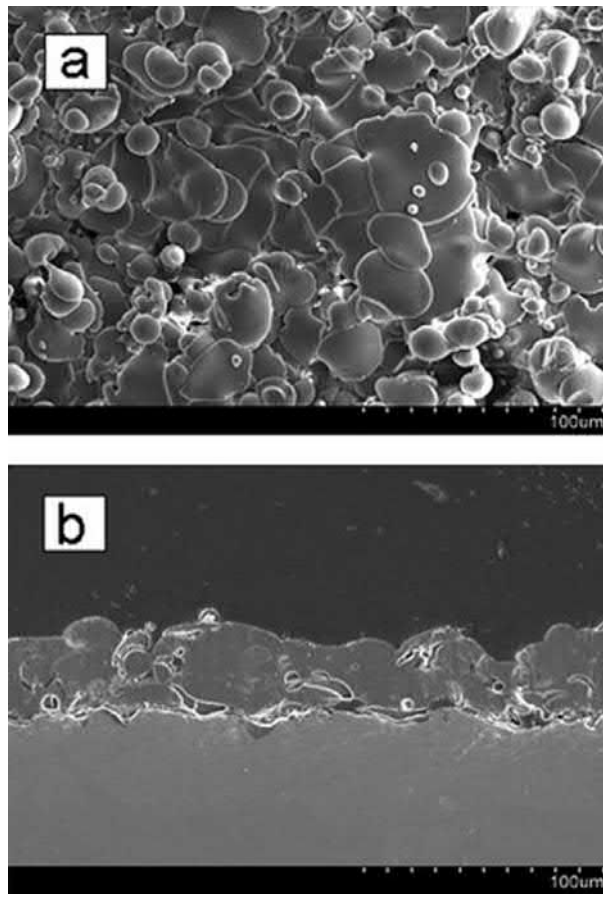


Fig. 14.1 Scanning electron microscopic (SEM) images of (A) surface and (B) cross-section of Ag-CP coating. No silver-related particles were observed.
Reprinted from Noda, I., Miyaji, F., Ando, Y., Miyamoto, H., Shimazaki, T., Yonekura, Y., Miyazaki, M., Mawatari, M., Hotokebuchi, T., 2009. Development of novel thermal splayed antibacterial coating and evaluation of release properties of silver ions. J. Biomed. Mater. Res. B Appl. Biomater. 89B, 456–465. Copyright 2008, with permission from Wiley.

After phosphate buffer solution (PBS) containing 10^2 CFU of MRSA was injected in a hole drilled into the tibial medullary cavity of 10-week-old Sprague-Dawley rats, Ag-CP coating and conventional CP flame-sprayed coating (denoted by CP coating, hereafter) samples were implanted and closed. After 24, 48, and 72 h, the tibia including the implant was dissected out and then crushed and ultrasonically irrigated with PBS. The dilution of this PBS was incubated on agar plates at 37°C and the number of inoculated viable cells was calculated (a dilution plate method). It was confirmed that the number of bacteria in the case of Ag-CP coating was significantly smaller ($P < .02$) than that in the case of CP coating (Akiyama et al., 2013). The silver amounts in the serum of artificial joint replacement surgery using Ag-CP coating showed a maximum value at day 14 postoperatively (average value ~1.4 ng/mL), and then they gradually decreased. During the experimental period, no troubles caused by argyria were observed; high safety was indicated (Eto et al., 2016).

Osteoconductivity of the Ag-CP and CP coatings was evaluated in tibia models using rats and rabbits. Newly formed bone was observed on the surface layer of both the samples, and there was no significant difference between them. Both of them were concluded to have excellent osteoconductivity. The Ag-CP coating is emphasized to be a great coating technology for the formation of functional surface with both osteoconductivity and antibacterial activity. The coating has obtained the clearance of Japanese Ministry of Health, Labor and Welfare in 2016 for femoral stem and acetabular cup of THA.

14.2.2 Thin film coatings

Physical vapor deposition (PVD) is one of the most promising methods to obtain thin, uniform, and dense CP coatings on metallic substrates. Radiofrequency (rf) magnetron sputtering has been used widely for coatings of thin films with excellent bonding to the substrates and has been applied to the coatings of CP films on commercially pure Ti (cpTi) (Yoshinari et al., 1997; Wolke et al., 2003) and Ti alloys (van Dijk et al., 1995), and the method has a great advantage in that the coatings can be achieved at relatively low temperatures. That is, no degradation in the mechanical properties of the metallic substrates occurs.

Narushima et al. (2005) prepared CP films on cpTi substrates by rf magnetron sputtering using a hot-pressed, dense β-TCP target. The resulting films were dense and uniform with a smooth surface, consisting of amorphous CP and/or oxyapatite phases (Fig. 14.2; Ueda et al., 2007). The bonding strengths between the coating and the cpTi substrate were estimated to be >60 MPa. When the film was soaked in Hank's balanced salt solution (HBSS) or PBS, the dissolved amount of Ca^{2+} ions from amorphous coatings was significantly larger than that from oxyapatite coatings. Animal test using beagle dogs showed that cpTi coated with the CP film was fixed rapidly and strongly with bone (Narushima et al., 2007; Ueda et al., 2007).

CpTi with a sputtered HA thin layer was developed as dental implants in Japan. Animal tests using canine mandibles for 28 weeks showed excellent bone-to-implant contact (BIC) by scanning electron microscopic analysis: the values of HA-sputtered implants showed larger (98.1%), in comparison with those of machined implants

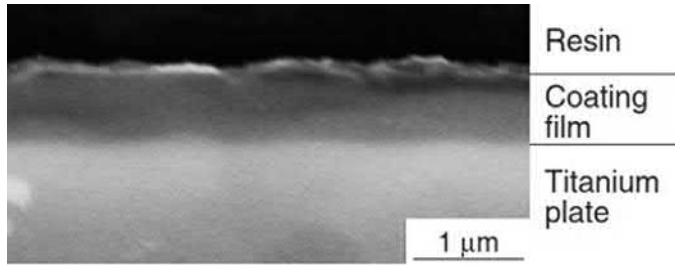


Fig. 14.2 Cross-sectional SEM image of calcium phosphate film on a cpTi plate prepared by rf magnetron sputtering.
Reprinted from Ueda, K., Narushima, T., Goto, T., Katsube, T., Nakagawa, H., Kawamura, H., Katsube, T., 2007. Evaluation of calcium phosphate coating films on titanium fabricated using RF magnetron sputtering. Mater. Trans. 48, 307–312. Copyright 2007, with permission from The Japan Institute of Metals.

(without HA-coatings) (70.4%) (Madi et al., 2016). The HA coating layer was almost completely dissolved. By evaluating the type and dimensions of bone defects after progressive peri-implantitis in dogs, peri-implant defects around the HA-sputtered implants were smaller than those around plasma-sprayed HA-coated implants (Madi et al., 2014). The dental implant system using HA-sputtered cpTi has been commercialized in Japan since 2010.

Chemical vapor deposition (CVD) also has great advantages in the preparation of CP thin films coated strongly onto metallic substrates, because of high deposition rates with excellent microstructure controllability. Some reports have been published on the preparation of β-$Ca_2P_2O_7$ film (Allen et al., 1996) and its conversion to β-TCP phase by postheat treatment. A few works on the direct preparation of bioactive CP films such as HA or β-TCP have been reported so far (Darr et al., 2004; Sato et al., 2007a).

Bioactive CP films have been prepared on cpTi substrates by metal-organic chemical vapor deposition (MOCVD) using bis-dipivaloylmetanato-calcium ($Ca(dpm)_2$) and tryphenyl phosphate ($(C_6H_5O)_3PO$) precursors (Sato et al., 2007a). A dense HA film was prepared by controlling Ca/P atomic ratio and substrate temperature at 700–800°C. The resulting HA film showed (002) preferred orientation parallel to the substrate surface. The film can be deposited at high rates of 4–6 nm/s. HA formed in HBSS at 37°C within 6 h on the HA film. The film on cpTi was expected to show excellent bioactivity.

Tsutsumi et al. (2010) prepared a polycrystalline HA film on a TNTZ surface using MOCVD by controlling the heating temperature, as shown in Fig. 14.3. The thickness of the HA film on TNTZ could be varied by 1–7 μm with the deposition time. An α-phase precipitated in the TNTZ matrix after heating the substrate during the deposition process, and the mechanical properties of HA-coated TNTZ were improved by maintaining its low Young's modulus. MOCVD would be one of the most effective methods for HA coating on TNTZ.

Calcium titanate ($CaTiO_3$) film has also been investigated as one of the promising bioactive coatings, using a sputtering (Asami et al., 2007) or CVD (Sato et al., 2007b)

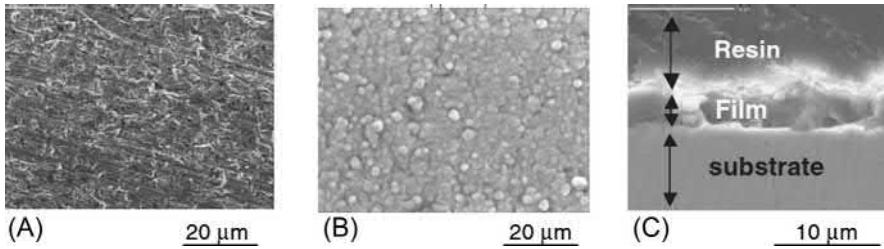


Fig. 14.3 SEM images of surfaces of (A) TNTZ, (B) surface, and (C) cross-section of HA coated on TNTZ using MOCVD. HA deposited on TNTZ had a dense granular microstructure and its grain diameter was ~2 μm.
Reprinted from Tsutsumi, H., Niinomi, M., Nakai, M., Gozawa, T., Akahori, T., Saito, K., Tu, R., Goto, T., 2010, Fabrication of hydroxyapatite film on Ti-29Nb-13Ta-4.6Zr using a MOCVD technique, Mater. Trans. 51, 2277–2283. Copyright 2010, with permission from The Japan Institute of Metals.

method. HA formed on the film after soaking in HBSS for 3–7 days. It was proposed that the $CaTiO_3$ film would firstly dissolve into the solution to locally increase Ca^{2+} ion concentration, where PO_4^{3-} ions could be attracted and reacted with Ca^{2+} ions, resulting in the formation of HA.

14.2.3 Apatite coatings using wet-processing

At the interface between bioactive ceramics and bone in living body, an apatite layer can be often seen: the ceramics bond to living bone through the apatite layer (Kitsugi et al., 1986), which consists of a hydroxycarbonate apatite (HCA) with small crystallites and defective structure, precipitated by incorporating carbonate anions from body fluid within amorphous CP phase. HCA has a similar composition and structure to bone. The apatite layer can form on the ceramics, metals, and polymers when they are soaked in simulated body fluid (SBF) with ion concentrations nearly equal to those of human blood plasma (Kokubo and Takadama, 2006). Two indispensable conditions needed for the HCA formation on materials using SBF are: (i) the existence of surface functional groups that induce the nucleation of apatite (e.g., Si-OH, Ti-OH, Nb-OH, Ta-OH, COOH, and PO_4H_2 groups), and (ii) the increase in the supersaturation concerning apatite around the surface of the materials.

Metallic Ti and its alloys are generally covered with a passive layer of Ti oxide. Since the surface of the layer includes the Ti-OH group, there exists the possibility of HCA formation. However, relatively high supersaturation concerning HCA is usually needed around the surface. To increase the supersaturation in SBF, a large amount of Ca^{2+} ions should be supplied. For example, soluble Ca carbonate (vaterite) was expected to supply both Ca^{2+} and carbonate ions when soaked in SBF: the supersaturation concerning HCA increased in SBF and rapid HCA-formation occurred (Hashimoto et al., 2007). However, the mechanically adhesive strength of the HCA layer on metallic substrates might be weak.

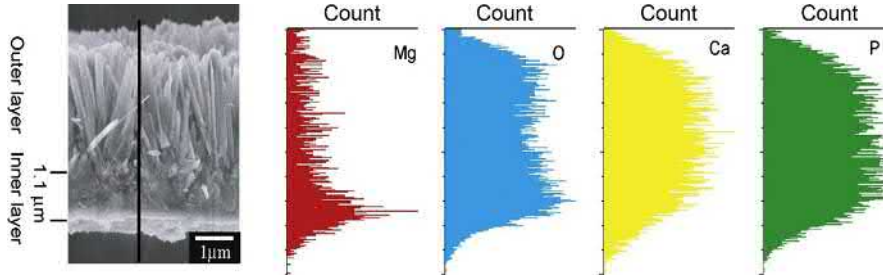


Fig. 14.4 Cross-sectional SEM and element distribution images of HA-coating on Mg prepared by a chemical solution deposition method at pH 8.9. The sample was scratched off from the substrate. A thin $Mg(OH)_2$ layer formed at the bottom of the coating. The intensity of Ca and P distribution was almost constant in the outer HA-layer packed densely.
Reprinted from Tomozawa, M., Hiromoto, S., 2011b. Microstructure of hydroxyapatite- and octacalcium phosphate-coatings formed on magnesium by a hydrothermal treatment at various pH values. Acta Mater. 59, 355–363. Copyright 2010, with permission from Elsevier.

Metallic Mg or its alloys have been investigated as a biodegradable material for applications in medical implants such as vascular stents. In application to orthopedic devices such as fracture fixation materials and artificial bones, there exists a serious issue with Mg corrosion, which proceeds faster than healing of the diseased area. Therefore, in order to suppress the corrosion of the Mg or its alloys, a chemical solution deposition method for developing well-crystallized CP coatings on them, has been reported (Hiromoto and Yamamoto, 2009).

An HA coating was prepared by soaking in $C_{10}H_{12}CaN_2$-Na_2O_8 (Ca-EDTA) - KH_2PO_4 (their concentration: 0.25 mol L^{-1}) adjusted to pH 9–12 at 90°C for 2 h. The coating showed a double-layer structure, consisting of a continuous inner layer of ~1 μm thickness and an outer layer of rod-shaped HA crystals grown on the inner layer to a length of ~4 μm, as shown in Fig. 14.4. Almost no nanopores were observed in the inner layer, and the coating was dense at its micrometer level (Tomozawa and Hiromoto, 2011a). From the anodic polarization curve of HA-coated or noncoated pure Mg in 3.5 mass% NaCl *aq*., it was shown that the cathode current density of the coated sample was much smaller than that of the noncoated one (Tomozawa and Hiromoto, 2011b). It has been shown that the corrosion of Mg or its alloys could be suppressed drastically by the dense HA coating.

14.2.4 Calcium phosphate glass-ceramic coatings

Since glass-based materials can be allowed some latitude in choice of composition, they have a significant advantage in that they are controllable to improve their physico-chemical properties and microstructures after their crystallization to attain sufficient performance as biomaterials. Silicate-based glass and glass-ceramics such as Bioglass and Cerabone A-W are well-known as bioactive materials (Hench, 1992).

In some types of glass, anionic groups can be connected through a cation, which should usually be a network modifier, to form the glassy state; such glass types are called "invert glasses". Kasuga (2005) reported silicate-free invert glass with compositions of high CaO and low P_2O_5 contents; the glass consisted of PO_4^{3-} (orthophosphate) and/or $P_2O_7^{4-}$ (pyrophosphate) groups without PO_3^- (metaphosphate) group, and the phosphate groups were connected through Ca^{2+} ions. The proposed mother composition was 60CaO-30P_2O_5-3TiO_2-7Na_2O (in mol%, denoted by PIG hereafter). It is usually difficult to obtain glass with Ca/P > 0.75 in the binary system, but they can be prepared with small amounts of TiO_2 and Na_2O. TiO_2 addition into phosphate glass improved their glass-forming ability and chemical durability. The structural role of TiO_2 in the CP invert glass was clarified by spectroscopic analysis and molecular dynamics simulation (Maeda et al., 2017).

PIG was pulverized to <10 μm in diameter (the average size; 1.0–1.5 μm) The glass powder slurry was dip-coated onto a sandblasted TNTZ and then dried. Then the substrate with the glass powder layer was heated in air at 800°C for 1 h and cooled to room temperature. Due to sintering of the glass powder, a layer with ~10 μm thickness was formed on TNTZ. Many pores of several micrometers in size were seen. There existed a reaction zone of 2–4 μm in thickness between the glass-ceramic layer and the substrate. The reaction layer was spontaneously developed on TNTZ by heating in air to relax the thermal stress generated in the coating layer and the substrate, resulting in the formation of the strong joint. The coating layer in the sample consisted predominantly of β-$Ca_3(PO_4)_2$ (β-TCP) phase with trace amounts of β-$Ca_2P_2O_7$ (β-CPP) and TiO_2 (rutile phase) crystalline phases.

The tensile bonding strength of the glass-ceramic layer on TNTZ was estimated to be ~26 MPa. The fracture occurs in the glass-ceramic layer with porosity; the bonding strength at the interface layer between TNTZ and the glass-ceramic was higher than the tensile strength of the glass-ceramic (Kasuga et al., 2012). The oxidized layer at the TNTZ surface was estimated to be <0.5 μm in depth. This thin oxidized layer worked to form the strong bond to PIG glass-ceramic.

Aging treatment of TNTZ at ~400°C is effective for increasing its hardness, modulus of elasticity, and strength (Niinomi et al., 2002). This improvement is due to the precipitation of ω-phases in the matrix β-phase during the aging. After the glass-ceramic-coated TNTZ was heat-treated for aging, tensile bonding strength of the sample with the coating layer of 5 μm thickness was not degraded, while that of 20 μm thickness was degraded due to the generation of microcracks, which originated from the formation of ω-phase, at the interface between the layer and the substrate (Niinomi et al., 2003; Akahori et al., 2005).

The coated samples were machined for fatigue tests according to ISO1099-75 specifications (Li et al., 2004). No delaminations of the coating were observed during the fatigue test. The fatigue resistance of the samples was improved due to an increase in resistance to fatigue crack initiation caused by the formation of the α-phase during heating for the coating and the precipitation of the ω-phase from the substrate during the slow cooling. In addition, aging at 400°C for 72 h greatly increased fatigue limit of the coated TNTZ and effectively relieved the detrimental effect of sandblasting on fatigue properties.

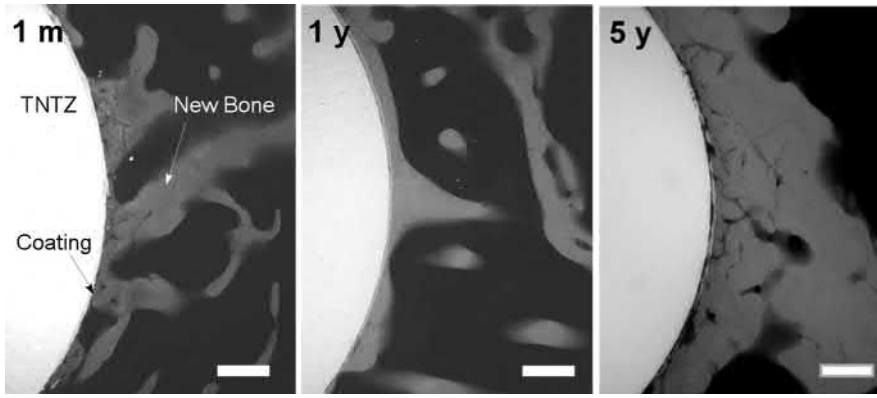


Fig. 14.5 Contact microradiographs around the glass-ceramic-coated TNTZ rods (5 mmϕ) implanted into femurs of Japanese rabbits after 1 month, 1 year, and 5 years. The scale bar indicates 50 μm.
Reprinted from Kasuga, T., Hattori, T., Niinomi, M., 2012. Phosphate glasses and glass-ceramics for biomedical applications. Phosphorous Res. Bull. 26, 008–015. Copyright 2012, with permission from Japanese Association of Inorganic Phosphorus Chemistry.

A rod-shaped sample of 5 mm diameter × 10 mm length was implanted into the femur of a Japanese rabbit. The sample was autoclaved in water at 121°C for 1 h. Fig. 14.5 shows contact microradiographs (CMR) after 1 month, 1 year, and 5 years of implantation. No significant change in the thickness of the glass-ceramic coating layer after the implantation could be seen. The observation showed new bone formation around the autoclaved glass-ceramic-coated TNTZ after 1 month of implantation and the bone tissue showed direct contact with implants. After 1 year and 5 years of implantation, the glass-ceramic-coating was surrounded by maturated bone tissue and had bonded directly with them. When the samples were sliced and polished for the observation after 1 year of implantation, no crack occurred between the coating and bone and also between the coating and TNTZ. This result shows excellent bioactivity of the PIG glass-ceramic coating on TNTZ (Kasuga et al., 2012).

14.3 Bioactive surface prepared by chemical treatments

Bioactive surface modifications described in this section might not be included in the category of coatings on metallic substrates. However, they are briefly reviewed, since they are very important, practical techniques for preparing bioactive surfaces on metallic substrates.

14.3.1 Chemical treatment with a concentrated alkaline solution

Ti and its alloys react with alkaline aqueous solutions. The reacted surface consists of negatively charged $HTiO_3^-$•nH_2O, which incorporates alkaline ions. Kokubo et al. prepared amorphous sodium titanate on cpTi by soaking the metal in an aqueous NaOH

solution of 5 *M* at 60°C for 24 h and subsequent heating at 600°C for 1 h. A surface consisting of a porous layer was obtained. The sodium titanate phase was integrated with the metal substrate through a graded structure within a depth of 1.5 μm from the surface. When the treated sample was soaked in SBF, HCA formed on the porous sodium titanate layer. Since the HCA showed a graded structure, it achieved a tight adhesion to the metal substrate (tensile bonding strength; >30 MPa). When Ti alloys, such as Ti-6Al-4V, Ti-6Al-2Nb-Ta and Ti-15Mo-5Zr-3Al, were treated with NaOH and subsequent heating, they also formed sodium titanate phase, which was free of the alloying components. These treatments had no negative impact on the strength under tensile loading nor fatigue strength under cyclic loading of the metals in saline solution (Kokubo et al., 2009).

The treated Ti metal and its alloys have been investigated in some animal models. When a cylindrical rod of the treated cpTi was implanted into the intramedullar canal of a rabbit femur, apatite formed on its surface within 3 weeks and it was completely covered with bone within 12 weeks. The rectangular sample implanted into a rabbit tibia formed an HCA layer on its surface and bonded to bone through the layer after 8 weeks. Surface modified Ti and its alloys started to be clinically used as artificial hip joints since 2007.

Modification of a TNTZ surface using this type of treatment was also examined; HCA-forming ability was lower on the surface of alkali-treated TNTZ than that on the alkali-treated cp-Ti (Akahori et al., 2007). The HCA-forming ability might be affected due to the existence of the sodium niobate film, which was considered to delay the exchange between the Na^+ and H_3O^+ ions.

The surface modification technique to induce bioactivity can also be applied to tantalum (Ta) metal with excellent fracture toughness and malleability (Miyazaki et al., 2000). Typical treatment conditions were subjected to NaOH *aq* of 0.5 *M* at 60°C for 24 h and subsequently heated at 300°C. After the treatment, amorphous sodium tantalate phase formed on its surface. Since Na^+ ions in the phase on Ta were exchanged with the H_3O^+ ions in SBF to form Ta-OH groups for inducing apatite nucleation, HCA formed on the treated Ta. This metal also formed apatite in the living body, and bonded tightly to bone through the apatite layer (Kato et al., 2000).

14.3.2 Surface modification by micro-arc oxidation and chemical treatment

Since metallic Zr and its alloys show excellent physico-chemical properties similar to Ti and small artifact effect in MRI, they are expected to perform well as new biomaterials. It is known that Ti and its alloys show high biocompatibility close to bioactivity, in comparison with other metallic materials, and have a potential to form CPs on their surface in the living body (Fujibayashi et al., 2003). On the other hand, no CP formation occurs on the surface of Zr due to its high chemical stability (Tsutsumi et al., 2009). This might be an issue to be solved for devices requiring early bone adhesion.

Ha et al. (2011) investigated the modification of the Zr surface using a micro-arc oxidization (MAO) method (Rocchi et al., 2003). When the MAO treatment for 10 min was performed to Zr in an aqueous solution containing calcium glycerophosphate and magnesium acetate, a porous ZrO_2 layer of ~5 μm thickness formed on its surface. Subsequently, when the sample was chemically treated with sulfuric acid or sodium hydroxide, some changes at its surface, such as enhancement of oxidation and increase in the amount of hydroxy groups, occurred. When they were soaked in HBSS for 12 d at 37°C, they were completely covered with a thick layer of HCA. On the other hand, Zr treated with only MAO (without the chemical treatments) showed no HCA formation. The biocompatibility of the Zr surface can be improved effectively by combining a MAO method with some chemical treatments.

14.4 Summary

This chapter has briefly reviewed some surface modifications on metallic biomaterials, based on ceramics. Some directions, such as antibacterial hydroxyapatite coatings using thermal spraying and strongly bonded, thin film coatings consisting of a CP phase using rf-magnetron sputtering or MOCVD, have been developed. A bioactive coating using CP glass for harmonizing β-type TNTZ might be one of the most significant items for various biomedical applications. In order to suppress the corrosion of the Mg or its alloys, well-crystallized CP coatings have been prepared by a chemical solution deposition method. Surface modification by alkali-treatment is one of the most useful methods for preparing bioactive surfaces. The "bioactive Ti" has high reliability for long-term use, since the bioactive ceramic phase is integrated with metallic Ti. The bioinert surface of Zr can be converted into a bioactive one by combining a MAO method with chemical treatments.

Surface-modification of metallic biomaterials may make new progress for the next generation through the integration with bioresorbable polymers or biological substances such as proteins and/or cells. Although not shown in this chapter, the coatings of polymers on metallic materials are very attractive. Hanawa and his colleagues have reported that segmented polyurethane (SPU) was coated on Ti or TNTZ with a silane coupling agent (mercaptopropyltrimethoxysilane: γ-MPS) (Sakamoto et al., 2007; Hieda et al., 2014). It has been reported that SPU coating could inhibit blood platelet adhesion and biofilm formation (Tanaka et al., 2010) and that immobilization of RGD peptide on SPU could enhance bone formation (Oya et al., 2009). In future, this is expected to develop into metallic biomaterials to which various bio-functional molecules are manipulated.

References

Akahori, T., Niinomi, M., Koyanagi, Y., Kasuga, T., Toda, H., Fukui, H., Ogawa, M., 2005. Mechanical properties of biocompatible beta-type titanium alloy coated with calcium phosphate invert glass-ceramic layer. Mater. Trans. 46, 1564–1569.

Akahori, T., Niinomi, M., Nakai, M., Fukuda, H., Fukui, H., Ogawa, M., 2007. Bioactive ceramic surface modification of β-type Ti-Nb-Ta-Zr system alloy by alkali solution treatment. Mater. Trans. 48, 293–300.

Akiyama, T., Miyamoto, H., Yonekura, Y., Tsukamoto, M., Ando, Y., Noda, I., Sonohata, M., Mawatari, M., 2013. Silver oxide-containing hydroxyapatite coating has in vivo antibacterial activity in the rat tibia. J. Orthop. Res. 31, 1195–1200.

Allen, G.C., Ciliberto, E., Fragala, I., Spoto, G., 1996. Surface and bulk study of calcium phosphate bioceramics obtained by metal organic chemical vapor deposition. Nucl. Instrum. Methods Phys. Res. B 116, 457–460.

Asami, K., Saito, K., Ohtsu, N., Nagata, S., Hanawa, T., 2007. Titanium-implanted $CaTiO_3$ films and their changes in Hanks' solution. Surf. Interface Anal. 35, 483–488.

Berndt, C.C., Haddad, G.N., Farmer, A.J.D., 1990. Thermal spraying for bioceramic applications. Mater. Sci. Forum 14, 161–173.

Darr, J.A., Guo, Z.X., Raman, V., Bououdina, M., Rehman, V., 2004. Metal organic chemical vapour deposition (MOCVD) of bone mineral like carbonated hydroxyapatite coatings. Chem. Commun. 62, 455–460.

van Dijk, K., Schaeken, H.G., Wolke, J.C.G., Maree, C.H.M., Habraken, F.H.P.M., Verhoeven, J., Jansen, J.A., 1995. Influence of discharge power level on the properties of hydroxyapatite films deposited on Ti-6A1-4V with RF magnetron sputtering. J. Biomed. Mater. Res. 29, 269–276.

Ducheyne, P., Raemdonck, W.V., Heughebaert, J.C., Heughebaert, M., 1986. Structural analysis of hydroxyapatite coating on titanium. Biomaterials 7, 97–103.

Eto, S., Kawano, S., Someya, S., Miyamoto, H., Sonohata, M., Mawatari, M., 2016. First clinical experience with thermal-sprayed silver oxide-containing hydroxyapatite coating implant. J. Arthroplasty 31, 1498–1503.

Fujibayashi, S., Neo, M., Kim, H.M., Kokubo, T., Nakamura, T., 2003. A comparative study between in vivo bone ingrowth and in vitro apatite formation on Na_2O-CaO-SiO_2 glasses. BiomateriaIs 24, 1349–1356.

Ha, J.Y., Tsutsumi, Y., Doi, H., Nomura, N., Kim, K.H., Hanawa, T., 2011. Enhancement of calcium phosphate formation on zirconium by micro-arc oxidation and chemical treatments. Surf. Coat. Technol. 205, 4948–4955.

Hashimoto, T., Obata, A., Kasuga, T., 2007. Preparation of silicon-containing apatite coating on titanium. Arch. BioCeram. Res. 7, 133–136 (Proc. Asian BioCeram. 2007).

Hench, L.L., 1992. Bioceramics: from concept to clinic. J. Am. Ceram. Soc. 74, 1487–1510.

Hieda, J., Niinomi, M., Nakai, M., Cho, K., Mohri, T., Hanawa, T., 2014. Adhesive strength of medical polymer on anodic oxide nanostructures fabricated on biomedical β-type titanium alloy. Mater. Sci. Eng. C 36, 244–252.

Hiromoto, S., Yamamoto, A., 2009. High corrosion resistance of magnesium coated with hydroxyapatite directly synthesized in an aqueous solution. Electrochim. Acta 54, 7085–7093.

Inagaki, M., Yokogawa, Y., Kameyama, T., 2003. Bond strength and microstructure of radio-frequency thermal plasma sprayed hydroxyapatite/titanium composite coatings. Key Eng. Mater. 240–242, 99–102.

Kasuga, T., 2005. Bioactive calcium pyrophosphate glasses and glass-ceramics. Acta Biomater. 1, 55–64.

Kasuga, T., Hattori, T., Niinomi, M., 2012. Phosphate glasses and glass-ceramics for biomedical applications. Phosphorous Res. Bull. 26, 008–015.

Kato, H., Nakamura, T., Nishiguchi, S., Matsusue, Y., Kobayashi, M., Miyazaki, T., Kim, H.-M., Kokubo, T., 2000. Bonding of alkali- and heat-treated tantalum implant to bone. J. Biomed. Mater. Res. 53, 28–35.

Kitsugi, T., Yamamuro, T., Nakamura, T., Higashi, S., Kotani, Y., Hyakuna, K., Ito, S., Kokubo, T., Takagi, M., Shibuya, T., 1986. Bone bonding behavior of three kinds of apatite containing glass ceramics. J. Biomed. Mater. Res. 20, 1295–1307.

Kokubo, T., Takadama, H., 2006. How useful is SBF in predicting in vivo bone bioactivity? Biomaterials 27, 2907–2915.

Kokubo, T., Matsushita, T., Takadama, H., Kizuki, T., 2009. Development of bioactive materials based on surface chemistry. J. Eur. Ceram. Soc. 29, 1267–1274.

Kuroda, D., Niinomi, M., Morinaga, M., Kato, Y., Yashiro, T., 1998. Design and mechanical properties of new β type titanium alloys for implant materials. Mater. Sci. Eng. A 243, 244–249.

Lacefield, W.R., 1993. Hydroxylapatite coatings (Chapter 12). In: An Introduction to Bioceramics. World Scientific, Singapore, pp. 223–238.

Li, T.T., Lee, J.H., Kobayashi, T., Aoki, H., 1996. Hydroxyapatite coating by dipping method, and bone bonding strength. J. Mater. Sci. Mater. Med. 7, 355–357.

Li, S.J., Niinomi, M., Akahori, T., Kasuga, T., Yang, R., Hao, Y.L., 2004. Fatigue characteristics of bioactive glass-ceramic-coated Ti–29Nb–13Ta–4.6Zr for biomedical application. Biomaterials 25, 3369–3378.

Madi, M., Zakaria, O., Kasugai, S., 2014. Coated vs uncoated implants: bone defect configurations after progressive peri-implantitis in dogs. J. Oral Implantol. 40, 661–669.

Madi, M., Zakaria, O., Ichinose, S., Kasugai, S., 2016. Effect of induced periimplantitis on dental implants with and without ultrathin hydroxyapatite coating. Implant. Dent. 25, 39–46.

Maeda, H., Tamura, T., Kasuga, T., 2017. Experimental and theoretical investigation of the structural role of titanium oxide in $CaO-P_2O_5-TiO_2$ invert glass. J. Phys. Chem. B 121, 5433–5438.

Miyazaki, T., Kim, H.M., Miyaji, F., Kokubo, T., Nakamura, T., 2000. Bioactive tantalum metal prepared by NaOH treatment. J. Biomed. Mater. Res. 50, 35–42.

Narushima, T., Ueda, K., Goto, T., Masumoto, H., Katsube, T., Kawamura, H., Ouchi, C., Iguchi, Y., 2005. Preparation of calcium phosphate films by radiofrequency magnetron sputtering. Mater. Trans. 46, 2246–2252.

Narushima, T., Ueda, K., Goto, T., Katsube, T., Ouchi, C., Iguchi, Y., 2007. Calcium phosphate films coated on titanium by RF magnetron sputtering for medical applications. Mater. Sci. Forum 539–543, 551–556.

Niinomi, M., 2003. Cyto-toxicity and fatigue performance of low rigidity titanium alloy, Ti-29Nb-13Ta-4.6Zr, for biomedical applications and healthcare goods. Biomaterials 24, 2673–2683.

Niinomi, M., Hattori, T., Morikawa, K., Kasuga, T., Suzuki, A., Fukui, H., Niwa, S., 2002. Development of low rigidity β-type titanium alloy for biomedical applications. Mater. Trans. 43, 2970–2977.

Niinomi, M., Akahori, T., Yamaguchi, T., Kasuga, T., Fukui, H., Suzuki, A., 2003. Ageing characteristics and mechanical properties of Ti-29Nb-13Ta-4.6Zr coated with calcium phosphate glass-ceramic for biomedical applications. J. Jpn. Inst. Metals 67, 604–613.

Noda, I., Miyaji, F., Ando, Y., Miyamoto, H., Shimazaki, T., Yonekura, Y., Miyazaki, M., Mawatari, M., Hotokebuchi, T., 2009. Development of novel thermal splayed antibacterial coating and evaluation of release properties of silver ions. J. Biomed. Mater. Res. B Appl. Biomater. 89B, 456–465.

Ong, J.L., Lucas, L.C., 1994. Post-deposition heat treatments for ion beam sputter deposited calcium phosphate coatings. Biomaterials 15, 337–341.

Oya, K., Tanaka, Y., Saito, H., Kurashima, K., Nogi, K., Tsutsumi, H., Doi, H., Nomura, N., Hanawa, T., 2009. Calcification by MC3T3-E1 cells on RGD peptide immobilized on titanium through electrodeposited PEG. Biomaterials 30, 1281–1286.

Rocchi, A., Martignori, M., Gottlow, J., 2003. Immediate loading of Brånemark system® TiUnite™ and machined-surface implants in the posterior mandible: a randomized open- ended clinical trial. Clin. lmplant. Dent. Relat. Res. 5, 57–63.

Sakamoto, H., Doi, H., Kobayashi, I., Yoneyama, T., Suzuki, S., Hanawa, T., 2007. Structure and strength at the bonding interface of a titanium-segmented polyurethane composite through 3-(trimethoxysilyl) propyl methacrylate for artificial organs. J. Biomed. Mater. Res. A 82, 52–61.

Sato, M., Tu, R., Goto, T., Ueda, K., Narushima, T., 2007a. Hydroxyapatite formation on calcium phosphate coated titanium. Mater. Sci. Forum 561–565, 1513–1516.

Sato, M., Tu, R., Goto, T., Ueda, K., Narushima, T., 2007b. Hydroxyapatite formation on $CaTiO_3$ film prepared by metal-organic chemical vapor deposition. Mater. Trans. 48, 1505–1510.

Tanaka, Y., Matin, K., Gyo, M., Okada, A., Tsutsumi, Y., Doi, H., Nomura, N., Tagami, J., Hanawa, T., 2010. Effects of electrodeposited poly(ethylene glycol) on biofilm adherence to titanbium. J. Biomed. Mater. Res. A 95, 1105–1113.

Tomozawa, M., Hiromoto, S., 2011a. Growth mechanism of hydroxyapatite-coatings formed on pure magnesium and corrosion behavior of the coated magnesium. Appl. Surf. Sci. 257, 8253–8257.

Tomozawa, M., Hiromoto, S., 2011b. Microstructure of hydroxyapatite- and octacalcium phosphate-coatings formed on magnesium by a hydrothermal treatment at various pH values. Acta Mater. 59, 355–363.

Tsui, Y.C., Doyle, C., Clyne, T.W., 1998. Plasma sprayed hydroxyapatite coatings on titanium substrates, part 1: mechanical properties and residual stress levels. Biomaterials 19, 2015–2029.

Tsutsumi, Y., Nishimura, D., Doi, H., Nomura, N., Hanawa, T., 2009. Difference in surface reactions between titanium and zirconium in Hanks' solution to elucidate mechanism of calcium phosphate formation on titanium using XPS and cathodic polarization. Mater. Sci. Eng. C 29, 1702–1708.

Tsutsumi, H., Niinomi, M., Nakai, M., Gozawa, T., Akahori, T., Saito, K., Tu, R., Goto, T., 2010. Fabrication of hydroxyapatite film on Ti-29Nb-13Ta-4.6Zr using a MOCVD technique. Mater. Trans. 51, 2277–2283.

Ueda, K., Narushima, T., Goto, T., Katsube, T., Nakagawa, H., Kawamura, H., Katsube, T., 2007. Evaluation of calcium phosphate coating films on titanium fabricated using RF magnetron sputtering. Mater. Trans. 48, 307–312.

Wolke, J.G.C., JPCM, v.d.W., Schaeken, H.G., Jansen, J.A., 2003. In vivo dissolution behavior of various RF magnetron-sputtered Ca-P coatings on roughened titanium implants. Biomaterials 24, 2623–2629.

Yoshinari, M., Hayakawa, T., Wolke, J.G.C., Nemoto, K., Jansen, J.A., 1997. Influence of rapid heating with infrared radiation on RF magnetron-sputtered calcium phosphate coatings. J. Biomed. Mater. Res. 37, 60–67.

Bioinspired functionalization of metal surfaces with polymers

15

Kazuhiko Ishihara, Bohan Cheng
The University of Tokyo, Tokyo, Japan

15.1 Introduction

Metal substrates are being used as biomaterials for preparing medical devices including implantable artificial organs and in hard-tissue prostheses. Metal biomaterials have excellent mechanical properties, but due to their lack of sufficient surface functionalities such as biocompatibility and binding ability for bioactive molecules, these biomaterials require some sort of pharmaceutical treatment before being applied as metallic implantable medical devices. One of the methods for improving the surface biocompatibility of a metal substrate is to modify it with biocompatible materials such as ceramics or polymers. Various methodologies for ceramic coatings on metal substrates have been reported, and some of these coated substrates are being used clinically (Aktuğ et al., 2017; Asri et al., 2017; Habibovic et al., 2002; Rasouli et al., 2018; Watanabe et al., 2017).

Because of their functionality and easy processability, polymers are also used as implantable medical devices and artificial organs, and particularly, to achieve an effective surface modification of metal substrates (Fig. 15.1). However, a good bonding between the metal and polymer at the interface is important to stabilize the polymer layer. Using silane chemistry is suitable to achieve this goal, because alkoxysilane compounds can react with the metal oxide layer formed on the surface of the metal substrate (Amano et al., 2010). Recently, biomimetic reactions using dopamine derivatives have been reported (Kaushik et al., 2015; Kuang and Messersmith, 2012; Maier and Butler, 2017). This is a spontaneous reaction that takes place under very mild conditions and can be applied to metals, as well as ceramics and certain polymer substrates. Thus, dopamine derivatives can form an intermediate layer between the polymer and the metal substrate, due to the presence of various functional groups. Moreover, a significant progress has been achieved in polymer chemistry, so that the regulation of polymer chain length, distribution of molecular weight, and terminal functional groups can be realized during the polymerization process (Chen et al., 2008; Friis et al., 2016; Inoue et al., 2018; Zeng et al., 2015). Therefore, the development of new surface modification strategies to form a polymer brush layer on metal substrates has attracted significant attention. Generally, the polymer brush layer has a uniform thickness on the nanometer scale and has a high density of polymer chains with reactive terminal functional groups, which easily enable multifunctionality on the metal substrate; some examples of such polymer layers are shown in Table 15.1.

Metals for Biomedical Devices. https://doi.org/10.1016/B978-0-08-102666-3.00015-8
© 2019 Elsevier Ltd. All rights reserved.

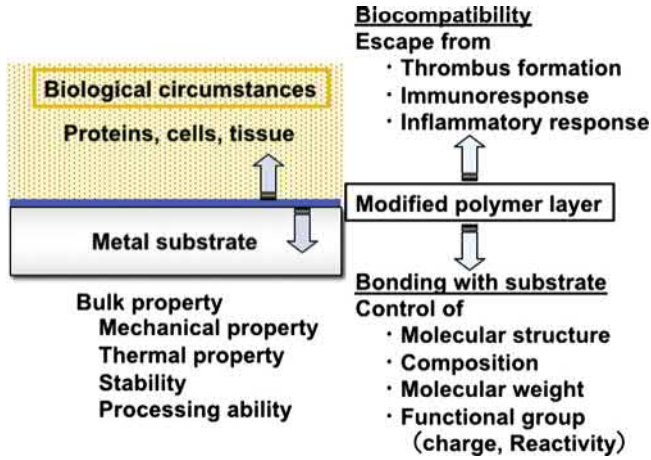


Fig. 15.1 Surface modification with polymers on metal substrate.

In this chapter, we present an overview of polymer brush layers and their integration onto metals through biomimetic chemistry (Fig. 15.2). The evaluation of biocompatibility of the composite materials from the point of view of platelet and fibroblast adhesion on the 2-methacryloyloxyethyl phosphorylcholine (MPC) polymer-modified surface are also described.

15.2 Phospholipid polymers providing biocompatible surfaces on metal substrates

15.2.1 Basic concept for the construction of a cell membrane-like structure

A classical method of surface modification of metal substrates is by using poly(ethylene glycol) (PEG) (Hoffman, 2016). Several approaches to PEG application have been examined and these in general, are found to function well. However, some studies have claimed that protein adsorption results from a conformational change in the protein, and platelet adhesion occurs on PEG-modified surfaces. Another serious problem with PEG is the degradation of the PEG chain by oxidation reaction under biological conditions, which may occur due to instability of the PEG-modified layer. Oxygen radicals formed by activated cells can easily attack the ether bond in the PEG chain, generating a peroxide linkage, which can immediately decompose, thus shortening the chain length and reducing the grafting density of PEG chains. Thus, PEG-modified surfaces can be applied only in single-use blood-contacting devices.

To find appropriate substitutes for PEG, the development of new polymers has been investigated, using strategies based on the mimicking a simple component present on the extracellular surfaces of the phospholipid bilayer that forms the matrix of cell membranes, which is the phosphorylcholine (PC) group of phosphatidylcholine

Table 15.1 Polymer-modified metal substrate for developing medical devices

Metal	Polymer	Surface modification process	Functionality	Application	Reference
Co-Cr alloy	Polyethylene	Physical adhesion	Lubrication	Joint prosthesis	LaBerge et al. (1990)
Co-Cr-Mo alloy	2-Methacryloyloxyethyl phosphorylcholine (MPC) polymers	Physical adhesion, surface reaction, and surface grafting	Lubrication	Joint prosthesis	Kyomoto et al. (2010)
Co-Cr alloy	Poly(2-hydroxyethyl methacrylate)/poly(D,L-lactic acid)	Atom transfer radical polymerization (ATRP) and ring opening polymerization	Sustained release of bioactive reagent	Drug eluting stent	Bedair et al. (2014)
Co-Cr-Mo alloy	Chitosan/casein phosphopeptides	3-Aminopropyl triethoxysilane (APTES) treatment and layer-by-layer deposition	Bone induction	Orthopedic implants	Qin et al. (2015)
Co-Cr alloy	Poly(L-lactic acid)	Dopamine treatment and ATRP	Sustained release of bioactive reagent	Drug eluting stent	Bedair et al. (2016)
SUS 316L stainless steel, Ti alloy and Co-Cr-Mo alloy	Poly(D,L-lactic acid)	Physical adhesion	Allergological characteristics	Orthopedic implants	Gollwitzer et al. (2005)
TiO_2	Poly(L-lysine)-grafted-poly(ethylene glycol)	Physical adsorption	Reduction of adsorption of plasma and ECM proteins	Orthopedic and dental implant	Harris et al. (2004)
Ti	MPC polymer	Dip coating/ physical adhesion	Thromboresistance	Cardiovascular devices	Snyder et al. (2007)
Ti	Poly(methacrylic acid)/ silk sericin	ATRP	Osteoblast adhesion	Orthopedic implants	Zhang et al. (2008)

Continued

Table 15.1 Continued

Metal	Polymer	Surface modification process	Functionality	Application	Reference
Ti alloy	MPC polymer	Physical adhesion and layer-by-layer deposition	Cell adhesion resistance	Orthopedic implants	Choi et al. (2008)
Ti-6Al-4V	MPC polymer	Reaction with APTES and reaction with the polymer	Thromboresistance	Cardiovascular devices	Ye et al. (2009a)
Ti	Hyaluronic acid/ chitosan	Physical adsorption and layer-by-layer processing	Reduction of bacteria adhesion	Orthopedic implant	Chua et al. (2008)
Ti-6Al-4V	MPC polymer	plasma-induced grafting	Thromboresistance	Cardiovascular devices	Ye et al. (2009b)
Ti-6Al-4V	Poly(allyl amine)	Plasma polymerization	Induction of cell adhesion	Orthopedic implants	Finke et al. (2014)
Ti-6Al-4V	Poly(allyl amine), poly(ethylenediamine)	Plasma polymerization	Osseointegration	Orthopedic implants	Gabler et al. (2014)
Ti	Chitosan/bone morphogenetic protein-2	APTES treatment and glutaraldehyde reaction	Osteoinduction	Orthopedic implants	Han et al. (2014)
Ti-6Al-4V	MPC polymer	Self-polymerization of dopamine and ATRP	Thromboresistance	Cardiovascular devices	Ma et al. (2015)
Ti alloy (Ti-6Al-4V)	Poly(L-lysine)/ hyaluronic acid	Ionic adsorption and layer-by-layer processing	Osseointegration	Orthopedic implant	Guillot et al. (2016)
Ti	Polycaprolactone/ polyethylene glycol + lysozyme	Dip coating, physical adsorption	Infection resistance	Orthopedic implant	Visan et al. (2017)

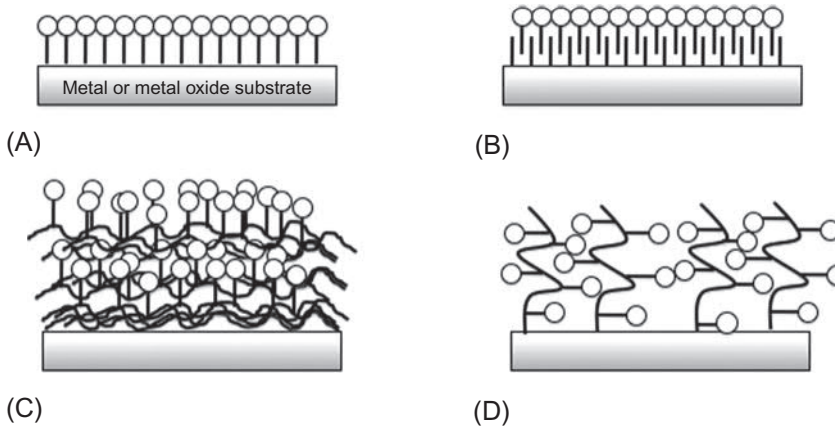


Fig. 15.2 Various surface modification processes: (A) Direct bonding of phospholipid molecules, (B) self-assembly of phospholipid molecules, (C) integration of phospholipid polymers, and (D) grafting of phospholipid polymers.

and sphingomyelin. The PC group, typical of phospholipid head groups present on the external surface of cells, is electrically neutral containing a zwitterionic head group and is inert in coagulation assays; some methods used in surface modification are described in Fig. 15.2. The first one is by directly attaching phospholipid derivatives on the metal surface (Fig. 15.2A). While being a very convenient procedure, this method requires the introduction of a specific functional group into the phospholipid molecules. The second method is the formation of a monolayer of phospholipid molecules on the metal surface based by self-assembly (Fig. 15.2B). The metal surface is modified with alkyl groups using silane chemistry, following which, phospholipid molecules are deposited onto the surface to form a self-assemble monolayer through physical molecular interactions. This procedure leads to a very good surface coverage of phospholipids, but the monolayer has insufficient stability and poor mechanical properties. The third and fourth methods illustrated in Fig. 15.2C and D provide very stable and functionally good surfaces; these two methods will be described in detail in this chapter. To prepare a highly stable functional surface, polymers with PC group have been synthesized and used for surface modification of the substrate (Ishihara, 2019; Lewis, 2000; Iwasaki and Ishihara, 2005, 2012; Monge et al., 2011).

15.2.2 Molecular design of MPC polymers

Ishihara and Nakabayashi developed the polymer biomaterial, which is a phospholipid polymer containing MPC units (Fig. 15.3). In the first report, Ishihara considered a new process for the synthesis and purification of MPC, where sufficient yield and purity were obtained (Ishihara et al., 1990). This result opened the way to prepare MPC polymers with various other alkyl methacrylates and styrene, and to precisely evaluate their biocompatibility (Ueda et al., 1992). Currently, MPC and several

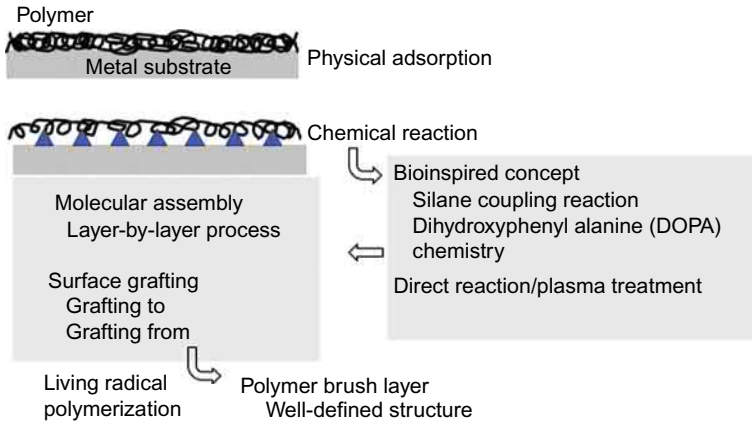


Fig. 15.3 Interfacial design between polymer layer and metal substrate.

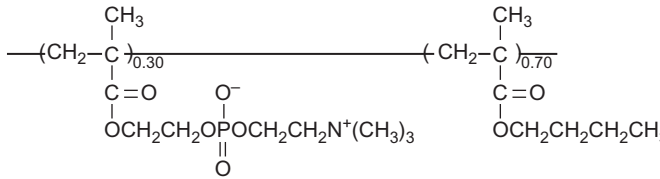


Fig. 15.4 Chemical structure of typical MPC polymer, PMB30.

MPC polymers are commercially available worldwide. Among MPC polymers, PMB30, which is a poly[MPC-*co*-*n*-butyl methacrylate (BMA)] with a MPC unit-mole fraction of 0.30, was the first such compound to be evaluated as a blood-compatible polymer (Fig. 15.4). PMB30 has been approved since 2012 by the Food and Drug Administration (FDA) in the United States under the Master Access File as LIPIDURE-CM5206. The solubility of the MPC polymer strongly depends on its molecular structure, the composition of the MPC and other monomer units, and its molecular weight. The homopolymer, poly(MPC) easily dissolves in water and alcohol; however, high molecular weight (*Mw*) PMB30 ($Mw > 5.0 \times 10^6$), is insoluble in water and soluble in ethanol. The introduction of other monomer units can change the solubility of MPC polymers, which means that it is very easy to design a MPC polymer structure to adapt to a substrate to be modified. These polymerization characteristics are very important to obtain a suitable MPC polymer for use as a biomaterial. The MPC polymer has also been prepared with other polymer architectures such as *block*-type copolymers and *graft*-type copolymers by conventional radical polymerization and advanced living radical polymerization techniques (Asanuma et al., 2013; Liu et al., 2014). Functional MPC polymer is useful for surface modification and can convert block- and graft-type copolymers.

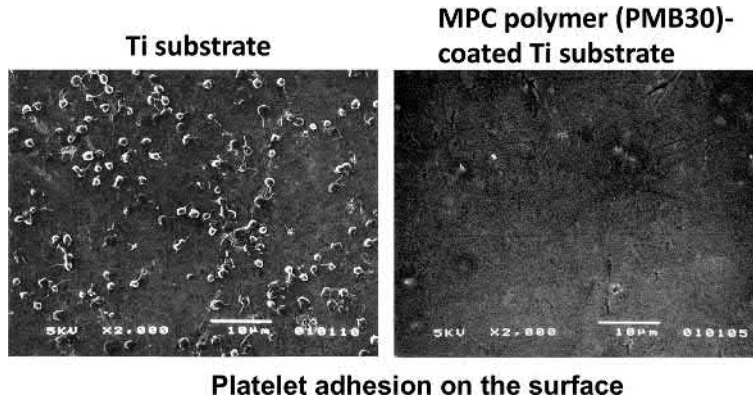


Fig. 15.5 SEM image of TI substrate and that coated with PMB30 after contact of platelet-rich-plasma for 1 h.

15.2.3 Biocompatibility and antithrombogenicity of MPC polymers

Excellent antithrombogenic properties were observed when MPC polymers were in contact with blood components (Ishihara et al., 1992; Jamiolkowski et al., 2015, 2016). Fig. 15.5 shows the scanning electron microscopy (SEM) images of a titanium surface coated with the PMB30, following contact with platelet-rich plasma (PRP). The titanium (Ti) substrates were immersed in an ethanolic solution containing 0.5 wt% PMB30 and dried under atmosphere. The substrates were then contacted with PRP for 1 h. It is seen that many platelets adhere to the surface of the Ti surface and are significantly deformed, but no cell adhesion can be found on the surface after being coated with PMB30. Moreover, in the presence of PMB30, when contacted with whole human blood without an anticoagulant, blood coagulation was completely suppressed and a very clean surface was maintained. These results clearly show that MPC polymers have excellent antithrombogenic properties and the MPC moieties in the polymers play an important role in their antithrombogenicity.

Protein adsorption is one of the most important properties that determine the biocompatibility of materials. In general, proteins adsorb on a surface within a few minutes of the material coming into contact with body fluids such as blood, plasma, or tears. Protein adsorption on MPC polymers from human plasma, as determined by radioimmunoassay and an immunogold-colloid labeling technique, showed that the amount of adsorbed protein was quite small and decreased with increase in the number of MPC moieties (Ishihara et al., 1991). The proteins present on the surfaces of the poly(BMA) and PMB30 that were in contact with plasma, were then determined by radioimmunoassay. The major components of plasma proteins such as albumin, fibrinogen, and γ-globulin, along with other minor components, were observed on the surfaces of all the materials tested. The observed resistance to protein adsorption was attributed to the unique hydration state of the PC group at the interface. It was revealed that hydrophobic hydration is mainly observed around the PC group, which

leads to a weak interaction with proteins. Thus, proteins attached to the MPC polymer surface detach easily and no significant conformational change occurs (Ishihara et al., 1998, 2017).

15.2.4 Performance of MPC polymer on medical devices

In view of the above-mentioned characteristics, MPC polymers are being used as coating materials on various medical devices including cardiovascular stents (Whelan et al., 2000; Lewis and Stratford, 2002), drug-eluting stents (Lewis et al., 2004; Abizaid et al., 2007; Gershlick et al., 2007), oxygenators (Myers et al., 2003; Newland et al., 2012), and catheters (Gobeil et al., 2002). In the case of stents, the metal surface is covered with a self-curable MPC polymer to prevent initial thrombus formation during implantation into the blood vessel. The surface inhibits any cell adhesion during the first stage, after which, the stent is embedded into the blood vessel wall. The coating layer also functions as a drug reservoir wherefrom, sustained drug release can be achieved. It is expected that the next generation of stents will be the drug-eluting type, which will prevent excess bioreactions at the interface between the stent and the blood vessel.

A ventricular assist device (VAD) was made from a titanium Ti alloy, whose surface was modified with PMB30 (Snyder et al., 2007; Kitano and Iwasaki, 2018); PMB30 can be physically coated on the surface and a stable polymer coating layer is obtained by a simple dip-coating method from a solution of PMB30 in ethanol. The performance of the PMB30 layer in preventing thrombus formation was good and remained so for >823 days in animal tests without any anticoagulant treatment. Following long-term mechanical movement test of the pump and in vivo animal tests, the first clinical implantation of EVAHEART was successfully performed in a pilot study on 18 patients, in May 2005. After obtaining permission for its production and ensuring cost coverage by the National Health Insurance since March 2011 in Japan, >160 patients have been supplied with EVAHEART as of December 2017.

15.3 Biomimetic attachment of polymer on metal surface

To obtain a facile adhesion of organic compounds to a metal substrate, mussel-inspired chemistry has been developed (Lee et al., 2007; Park et al., 2013; Sobocinski et al., 2014; Madhurakkat Perikamana et al., 2015). Mussels possess extraordinary capabilities of rapid and permanent adhesion to all types of wet inorganic and organic surfaces in aqueous environment. Such adhesive properties rely on the exhaustive repeat unit of the 3,4-dihydroxy-L-phenylalanine (DOPA) moiety found in the foot protein of mussels. The oxidation of the DOPA moiety in these proteins can dramatically reduce its strength of its adhesion to metals. Mussel-inspired chemistry can be applied to the surface modification of substrates by polymers. When a polymer with 3,4-dihydroxy phenyl (DHP) groups is in contact with a metal substrate, a thin polymer film can spontaneously deposit on the surface.

The MPC polymer *co*ntaining the DHP group, poly(MPC-co-methacrylic acid-co-3,4-dihydroxyphenylethyl methacrylamide) (PMDP) is obtained by a polymeric reaction and used to coat the Ti substrate (Yao et al., 2011). To prepare the PMDP-Ti substrate, the Ti substrate is simply dipped in the PMDP aqueous solution at the room temperature for 10 s, and then dried. The presence of DHP group in PMDP is confirmed by the appearance of an IR absorbance peak at 1553 cm^{-1}, attributed to the aromatic ring of the DHP group. The presence of peaks due to DHP group even after rinsing for 1 month confirms the strong adhesion of PMDP to the Ti substrate.

Platelets adhesion and activation are the two main indicators to evaluate the blood compatibility of materials. A lot of platelets adhered to both Ti and SUS 316L stainless steel (SUS) substrates; morphological analysis showed that adherent platelets aggregated and spread through a pseudopodium network as shown in Fig. 15.6. On the Ti substrate treated with the PMDP, a small number of individual platelets with spherical shape without pseudopods, are observed. In addition, a significant reduction in the amount of plasma proteins adsorbed on the Ti substrate is observed after treatment with the PMDP. These results reveal that modification with the PMDP provides a very easy and effective procedure to improve blood compatibility on the Ti substrate and SUS substrates, which has great potential in medical application.

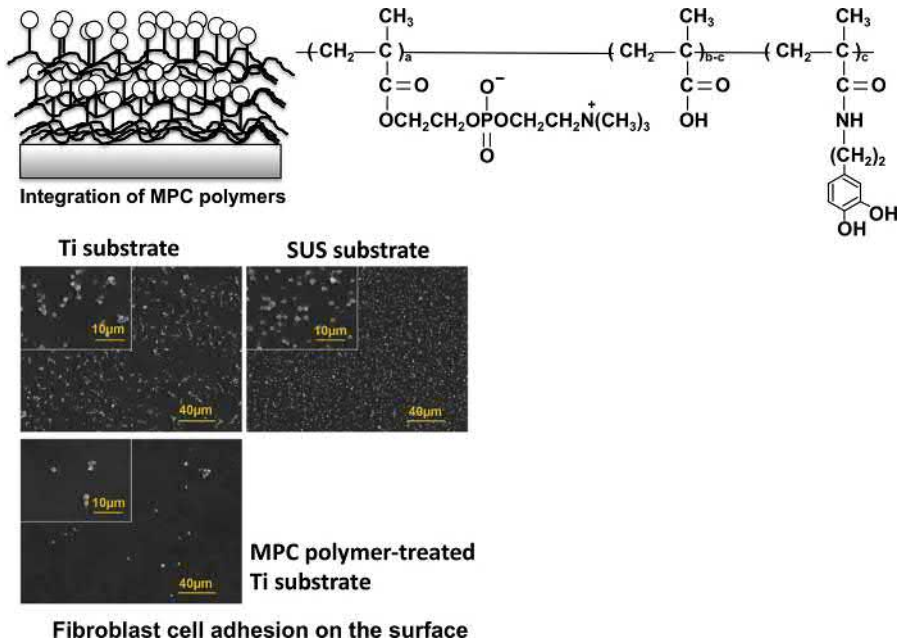


Fig. 15.6 Chemical structure of MPC polymer bearing DHP unit (PMDP), and SEM images of original Ti substrate, that treated by the MPC polymer, and SUS 316L stainless steel (SUS) substrate after culturing fibroblast cells.

15.4 Surface grafting of MPC polymer on Ti substrates

15.4.1 "Grafting to" method for binding MPC polymer onto Ti substrate

The covalent attachment of organosilanes has proved to be a simple and versatile method to tailor the physical properties such as wettability, adhesion, and surface activity, in solids. Self-assembled monolayers (SAMs) have been widely used to study biofouling of material surfaces (Sigal et al., 1998). Several functionalized SAMs on metal have been prepared and the effects of surface chemistry on protein adsorption and cell adhesion have been discussed. Among these, the modification of a Ti surface with MPC polymers using a monolayer of organosilanes as the binding layer has been considered. Iwasaki investigated the surface modification of a Ti alloy using a well-defined MPC polymer by a "grafting to" method (Iwasaki and Saito, 2003), where the MPC polymer with a reactive terminal was synthesized, after which, the polymer terminal group reacted with a reactive group of a SAM layer on the Ti substrate. Using this approach, the controlled immobilization of an end-functional MPC polymer with a vinyl dimethysilane (VDMS) monolayer, was achieved on a Ti substrate. A chemical reaction occurred between the vinyl groups immobilized on the surface and the amino group in the terminal part of the polymer, leading to grafting of the polymer. The introduction of vinyl groups onto solid surfaces is made possible by varying the functionalities of the surface and improving the adhesion between polymers and inorganic materials. Generally, amino group-terminated poly(MPC) chains are used for such modification. The surface density of poly(MPC) on the Ti may can also be controlled by changing the surface density of the VDMS layer and the adsorption of proteins on the graft surface was monitored by X-ray photoelectron spectroscopy (XPS) analysis, where nitrogen (N) attributed to the amino acid residue or peptide bond in the protein was monitored during the adsorption of protein. The N/Ti ratio on the surface after contact with serum albumin increased for the first few minutes. A high intensity for the nitrogen signal was observed on the untreated Ti and VDMS surfaces due to adsorbed albumin. In contrast, albumin adsorption was reduced on the PMPC-modified surfaces. In the case of the MPC polymer, a controlled modification of the Ti substrate with poly(MPC) was carried out by depositing a VDMS monolayer. The effect of grafting the MPC polymer on resistance to plasma protein adsorption was also clarified. Using organosilane monolayers as binding layers, a precise modification of the surface with a polymer, using the "grafting to" method, is made possible.

15.4.2 "Grafting from" method for binding MPC polymer onto a Ti substrate

The advanced radical polymerization process, or living radical polymerization, is an efficient method to obtain well-defined polymers, where both the molecular weight and its distribution are regulated, and the terminal groups of the polymer chains can also be tailored. This process has been generalized to carry out surface-initiated

living radical polymerization to obtain polymer chains directly from surfaces of substrates. Specifically, a highly dense polymer brush structure can be formed via surface-initiated atom transfer radical polymerization (SI-ATRP). The polymer brush structure is presently the only candidate structure that can provide a polymer layer with well-controlled properties on the substrate, since the SI-ATRP technique facilitates control of the chemical and three-dimensional (3D) structure of the polymer layers and allows independent modulation of these parameters. The merits of this technique include: (1) the wide variety of monomer species (hereafter termed monomer selection) that can be used in the process, (2) a good control of the polymer layer thickness can be achieved by regulating the molecular weight of the polymer chains, (3) controlling graft density is possible by modulating the surface density of the initiator groups, and (4) the possibility to introduce terminal functional groups. In the SI-ATRP process, the first step is the introduction of an ATRP initiator on the surface. Initiators are usually, silane compounds, as described in several publications. The other option is to use a polymeric macroinitiator with many initiator units in one polymer chain, and one that can bind stably on the substrate. After activation of the substrate by plasma treatment or acid etching, a covalent bond is formed between the ATRP initiator and the substrate. On the other hand, a much easier procedure has been developed using biomimetic DOPA chemistry (Ma et al., 2015). Once DOPA is adsorbed on the surface by molecular interactions, it polymerizes by spontaneous oxidation and finally, a highly chemically cross-linked DOPA layer is generated, which provides hydroxy and amine groups on the substrate. This chemical reaction is performed in order to introduce the ATRP initiators. The ATRP of MPC in an aqueous solution proceeds efficiently and a polymer brush structure is fabricated on the Ti substrate. Cell adhesion is lower on the surface of poly(MPC)-grafted Ti substrate as compared with those on the Ti substrate, and SUS 316L stainless steel substrates (Yao et al., 2012). Even though currently the results are not entirely satisfactory, this procedure is considered to be a candidate method to improve blood compatibility of Ti substrates.

15.5 MPC polymer assembly on Ti alloy

Modifications of biomaterial surfaces have a long history in implantology and form a major area of research. Ever since its introduction by Decher (1997), the process of building up organic multilayer films through layer-by-layer (LbL) self-assembly has attracted a great deal of attention and allows the formation of interpolymer complexes through the deposition of oppositely charged polyelectrolytes. The LbL method is renowned for being a convenient, versatile, and efficient technique for the generation of biologically active surfaces. Furthermore, various important techniques have been introduced to promote the formation of multilayers by the LbL method, such as electrostatic interaction (Ren et al., 2006), hydrogen bonding (Sukhishvili and Granick, 2002), and covalent bonding (Brynda and Houska, 1996).

Phenylboronic acid is known to rapidly form a cyclic boronic complex when reacted with cis-diols (Yan et al., 2004) such as carbohydrates, and certain polymers such as poly(vinyl alcohol) (PVA). It is synthesized using a new water-soluble MPC

polymer, poly(MPC-*co*-BMA-co-4-vinyl phenylboronic acid) (PMBV) (Konno and Ishihara, 2007; Oda et al., 2013, 2015). The interpolymer complexation of a polymer made from boronic acid with PVA has been reported to form a hydrogel due to covalent linkage in both the constituent polymers. It is expected that using the LbL deposition method, PMBV and PVA can be combined to produce a polymer hydrogel multilayer bonded to the Ti alloy (Choi et al., 2008; Gao et al., 2013). By constructing a multilayered hydrogel on the Ti alloy surface, the surface may become even more biocompatible, and moreover, the hydrogel layer could have a functional stage for the sustained release of biologically active molecules.

The surface modification process is described in Fig. 15.7, a monolayer of octadecylsilane (ODS) was prepared on the Ti alloy substrate by immersion in octadecyltoriethoxysilane solution. The ODS-treated Ti alloy substrates were then coated with an aqueous solution of photoreactive PVA with phenylazide groups as photoreactive groups to the alkyl group of the ODS moieties, to obtain a PVA-modified Ti alloy substrate. Next, PMBV is coated from an aqueous solution, on the PVA-modified Ti alloy substrate. A multilayer is formed by alternately dipping for 10 min, the Ti alloy substrates with bonded photoreactive PVA into the PMBV

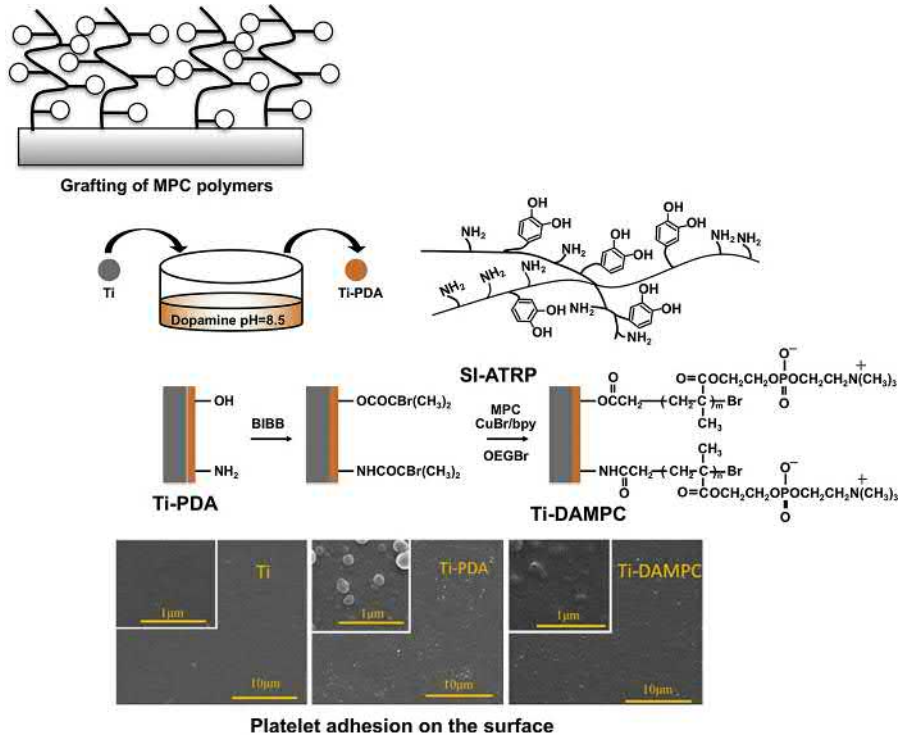


Fig. 15.7 Biomimetic procedure for grafting of poly(MPC) chains by surface-initiated atom transfer polymerization and various Ti alloy substrates after contacting platelet-rich-plasma for 1 h.

and PVA solutions, followed by rinsing with distilled water for 1 min. Six layers (three bilayers), terminating with a layer of PMBV, were obtained by the LbL method. The thickness of the PMBV/PVA hydrogel increased exponentially as a function of the number *n* of deposited layers. The final thickness of the PMBV/PVA multilayers was in the range of 6–8 μm.

For the PMBV/PVA systems, the observed tendency is the exponential increase in thickness of the multilayered hydrogel with the number of layers during the build-up process. This phenomenon may be attributed to the diffusion behavior of the outermost polymer layers, PMBV and PVA. Moreover, the thickness and weight of the multilayered hydrogels of PMBV/PVA depend on the polymer concentration. This means that both PVA and PMBV (which contain hydrophilic PC groups), attract water molecules. Contact angle data also support the hydrophilic property of these polymers.

The morphological aspects of L929 cells grown on the differently loaded multilayered hydrogel coatings were evaluated using SEM (Fig. 15.8). As usual, the adhesion and proliferation of L929 cells was observed during a 1-day culture both on plain Ti alloy and that modified with photoreactive PVA substrates. However, apparent differences in cell morphology were found on PMBV and PVA, when compared to that on the Ti alloy substrate and photoreactive PVA-modified substrate. The number of L929 cells that adhered to the PMBV and PVA surfaces was significantly lower than that on the Ti alloy substrate and photoreactive PVA. Moreover, the L929 cells did not preserve their normal spindle-like shape, but exhibited circular, round shapes.

Cellular behavior is an important factor in evaluating the biocompatibility of a biomaterial. Cell morphology images revealed that Ti alloy and photoreactive PVA surfaces permitted adhesion, spreading, and migration of L929 cells to a degree that PVA and PMBV surfaces did not. The adhesion of cells to surfaces is dependent on the adsorption of highly adhesive proteins such as fibronectin and vitronectin, which link

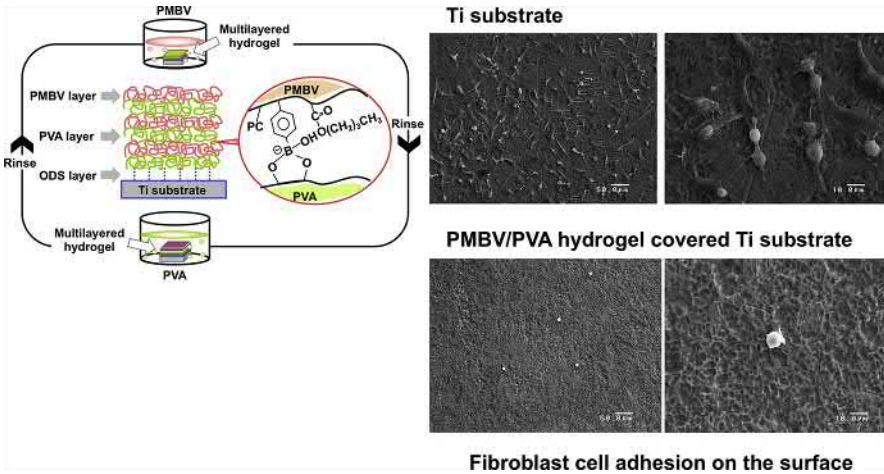


Fig. 15.8 Fabrication of MPC polymer hydrogel layer on Ti alloy surface by layer-by-layer process and SEM image of the substrates after culturing fibroblast cells.

the cells to the surface of the biomaterial. They can reduce the adhesion of cells, including fibroblasts, platelets, and macrophages. The MPC polymer-hybridized Ti alloy substrates and multilayered hydrogels offer the possibility for the preparation of blood-contacting materials via the incorporation of an outermost layer of PMBV, which inhibits the adsorption of proteins and the adhesion of cells. Also, the PMBV/PVA multilayered hydrogel can function as a reserve for bioactive molecules such as drugs and proteins (Gao et al., 2013). Thus, the Ti alloy substrate incorporated with bioactive molecules can pave the way to new type of hybrid functional biomaterials.

15.6 Future perspectives

In addition to implantable medical devices, metal biomaterials are needed for the fabrication of other related bio-devices such as nano-needles, nanoparticles, and nanowires. The principal characteristics of metal biomaterials are their very good mechanical properties and easy processability; however, their surface biocompatibility is low, and needs to be improved. Conventionally, surface modification has been performed using strategies such as surface coating with bioceramics and biocompatible polymers. Polymers are potentially interesting alternatives to provide surface functionality to metal biomaterials. Therefore, a greater focus is required on metal/polymer hybrid-type materials. From this point of view, controlling the interaction between the metal and polymer layer will be important to obtain a stable and high-performance metal/polymer hybrid. In this chapter, we have described several examples of how to modify a metal surface using a phospholipid polymer. In these cases, surface modification occurred only in a very thin surface layer and did not affect the innated mechanical properties of the metal biomaterial. Other functions based on a hydrogel-like structure, such as the controlled release of bioactive molecules, super-hydrophilicity, and excellent lubrication properties, could also be realized in this hybrid structure. The recent progress in bioscience has led to the availability of many biomolecules with high bioactive functions. When proteins that activate or induce tissues are incorporated into the polymer layer formed on metal biomaterials, these proteins can be slowly released from the polymer layer. Thus, the formation new tissue can take place, and as a result, a tight adhesion of the metal biomaterials to the tissue may be achieved.

Metal-on-metal bearings have been used principally due to their very low long-term clinical wear rate. A survey of the relevant literature has shown that researchers working in the field of orthopedics are in general agreement with the fact that that metal-on-metal bearings wear clinically at a rate of 1–5 mm^3/year, which is 10–100 times lower than the typical wear rate for a conventional metal-on-ultrahigh molecular weight polyethylene (UHMWPE) bearing couple. However, even in metal-on-metal bearings, aseptic loosening induced by wear particles and metallosis remains a serious issue in revision surgeries. In addition to metallosis, electrochemical corrosion and carcinogenesis occurring due to the dissemination of wear particles to other parts of the body have been reported. The sizes of wear particles in metal-on-metal bearings vary in the wide range between 6 and 5 mm. Nanometer-sized metallic wear

debris is more easily digested by cells, bound into proteins, and/or dissolved into body fluids than the larger UHMWPE wear debris. Several improvements to the bearing materials and surface modifications of the metal have been attempted to reduce such wear particles. Surface modifications of the metal surface with hydrophilic polymers may be suitable for reducing wear due to the formation of a thin water layer at the interface between the metal bearings. Kyomoto et al. carried out fundamental experiments to prepare a highly lubricious metal bearing material in which, the biocompatible MPC polymer was grafted onto the surface of the Co-Cr-Mo alloy (Kyomoto et al., 2007, 2009, 2010). The excellent functions of the MPC polymer-modified Co-Cr-Mo alloy could serve to hinder of the activation of cell systems by the wear particles and thus prevent aseptic loosening and metallosis. In view of its greatly superior lubrication properties and biological advantages, the metal/polymer hybrid is expected to have great potential as a candidate bearing material for the next-generation artificial hip joints. Such hybrids can be beneficial in preventing many of the problems observed at the interface between medical devices and tissues.

15.7 Summary

In this chapter, the fabrication of well-controlled polymer layers on metal substrates has been described. A phospholipid polymer (MPC polymer) platform was constructed on the metal substrate to simulate a cell membrane structure, and functionalized. MPC polymer chains were reacted or grafted onto the surface of the Ti by chemical reactions, including biomimetic DOPA chemistry; the surface density and thickness of the MPC polymer could be controlled. The second surface modification method consisted of the construction of a multilayered polymer on a Ti alloy substrate via LbL self-assembly deposition. The MPC polymer platform on the metal substrates reduced the adhesion and morphology of cells when compared to untreated substrates. It was thus concluded that the formation of an artificial cell membrane structure by the MPC polymer was effective in improving the biocompatibility of Ti-based medical devices.

Acknowledgment

The authors express their gratitude to Dr. Kyoko Fukazawa at the University of Tokyo, for her help in preparing the manuscript.

References

Abizaid, A., Popma, J.J., Tanajura, L.F., Hattori, K., Solberg, B., Larracas, C., Feres, F., Costa Jde Jr., R., Schwartz, L.B., 2007. Clinical and angiographic results of percutaneous coronary revascularization using a trilayer stainless steel-tantalum-stainless steel phosphorylcholine-coated stent: the TriMaxx trial. Catheter. Cardiovasc. Interv. 70, 914–919.

Aktuğ, S.L., Durdu, S., Yalçın, E., Çavuşoğlu, K., Usta, M., 2017. Bioactivity and biocompatibility of hydroxyapatite-based bioceramic coatings on zirconium by plasma electrolytic oxidation. Mater. Sci. Eng. C Mater. Biol. Appl. 71, 1020–1027. https://doi.org/10.1016/j.msec.2016.11.012.

Amano, D., Ueda, T., Sugiyama, T., Takemoto, S., Oda, Y., Sakurai, K., 2010. Improved brushing durability of titanium dioxide coating on polymethylmethacrylate substrate by prior treatment with acryloxypropyl trimethoxysilane-based agent for denture application. Dent. Mater. J. 29, 97–103.

Asanuma, Y., Inoue, Y., Yusa, S., Ishihara, K., 2013. Hybridization of poly(2-methacryloyloxyethyl phosphorylcholine-block-2-ethylhexyl methacrylate) with segmented polyurethane for reducing thrombogenicity. Colloids Surf. B Biointerfaces 108, 239–245. https://doi.org/10.1016/j.colsurfb.2013.02.042.

Asri, R.I.M., Harun, W.S.W., Samykano, M., Lah, N.A.C., Ghani, S.A.C., Tarlochan, F., Raza, M.R., 2017. Corrosion and surface modification on biocompatible metals: a review. Mater. Sci. Eng. C Mater. Biol. Appl. 77, 1261–1274. https://doi.org/10.1016/j.msec.2017.04.102.

Bedair, T.M., Cho, Y., Joung, Y.K., Han, D.K., 2014. Biodegradable polymer brush as nanocoupled interface for improving the durability of polymer coating on metal surface. Colloids Surf. B Biointerfaces 122, 808–817.

Bedair, T.M., Kang, S.N., Joung, Y.K., Han, D.K., 2016. A promising approach for improving the coating stability and in vivo performance of biodegradable polymer-coated sirolimus-eluting stent. J. Biomed. Nanotechnol. 12, 2015–2028.

Brynda, E., Houska, M., 1996. Interactions of proteins with polyelectrolytes at solid/liquid interfaces: sequential adsorption of albumin and heparin. J. Colloid Interface Sci. 183, 18–25. https://doi.org/10.1006/jcis.1996.0514.

Chen, R., Zhu, S., Maclaughlin, S., 2008. Grafting acrylic polymers from flat nickel and copper surfaces by surface-initiated atom transfer radical polymerization. Langmuir 24, 6889–6896. https://doi.org/10.1021/la800171h.

Choi, J., Matsuno, R., Konno, T., Takai, M., Ishihara, K., 2008. Surface immobilization of biocompatible phospholipid polymer multilayered hydrogel on titanium alloy. Colloids Surf. B Biointerfaces 67, 216–223. https://doi.org/10.1016/j.colsurfb.2008.08.025.

Chua, P.H., Neoh, K.G., Kang, E.T., Wang, W., 2008. Surface functionalization of titanium with hyaluronic acid/chitosan polyelectrolyte multilayers and RGD for promoting osteoblast functions and inhibiting bacterial adhesion. Biomaterials 29, 1412–1421.

Decher, G., 1997. Fuzzy nanoassemblies: toward layered polymeric multicomposites. Science 277, 1232–1237. https://doi.org/10.1126/science.277.5330.1232.

Finke, B., Rebl, H., Hempel, F., Schäfer, J., Liefeith, K., Weltmann, K.D., Nebe, J.B., 2014. Aging of plasma-polymerized allylamine nanofilms and the maintenance of their cell adhesion capacity. Langmuir 30, 13914– – 13924. https://doi.org/10.1021/la5019778.

Friis, J.E., Brøns, K., Salmi, Z., Shimizu, K., Subbiahdoss, G., Holm, A.H., Santos, O., Pedersen, S.U., Meyer, R.L., Daasbjerg, K., Iruthayaraj, J., 2016. Hydrophilic polymer brush layers on stainless steel using multilayered ATRP initiator layer. ACS Appl. Mater. Interfaces 8, 30616–30627.

Gabler, C., Zietz, C., Göhler, R., Fritsche, A., Lindner, T., Haenle, M., Finke, B., Meichsner, J., Lenz, S., Frerich, B., Lüthen, F., Nebe, J.B., Bader, R., 2014. Evaluation of osseointegration of titanium alloyed implants modified by plasma polymerization. Int. J. Mol. Sci. 15, 2454–2464.

Gao, B., Konno, T., Ishihara, K., 2013. A simple procedure for the preparation of precise spatial multicellular phospholipid polymer hydrogels. Colloids Surf. B Biointerfaces 108, 345–351. https://doi.org/10.1016/j.colsurfb.2013.02.022.

Gershlick, A., Kandzari, D.E., Leon, M.B., Wijns, W., Meredith, I.T., Fajadet, J., Popma, J.J., Fitzgerald, P.J., Kuntz, R.E., Endeavor Investigators, 2007. Zotarolimus-eluting stents in patients with native coronary artery disease: clinical and angiographic outcomes in 1,317 patients. Am. J. Cardiol. 100, 45M–55M.

Gobeil, F., Juneau, C., Plante, S., 2002. Thrombus formation on guide wires during routine PTCA procedures: a scanning electron microscopic evaluation. Can. J. Cardiol. 18, 263–269.

Gollwitzer, H., Thomas, P., Diehl, P., Steinhauser, E., Summer, B., Barnstorf, S., Gerdesmeyer, L., Mittelmeier, W., Stemberger, A., 2005. Biomechanical and allergological characteristics of a biodegradable poly(D,L-lactic acid) coating for orthopaedic implants. J. Orthop. Res. 23, 802–809.

Guillot, R., Pignot-Paintrand, I., Lavaud, J., Decambron, A., Bourgeois, E., Josserand, V., Logeart-Avramoglou, D., Viguier, E., Picart, C., 2016. Assessment of a polyelectrolyte multilayer film coating loaded with BMP-2 on titanium and PEEK implants in the rabbit femoral condyle. Acta Biomater. 36, 310–322.

Habibovic, P., Barrère, F., Blitterswijk, C.A., Groot, K., XLayrolle, P., 2002. Biomimetic hydroxyapatite coating on metal implants. J. Am. Ceram. Soc. 85, 517–522. https://doi.org/10.1111/j.1151-2916.2002.tb00126.x.

Han, L., Lin, H., Lu, X., Zhi, W., Wang, K.F., Meng, F.Z., Jiang, O., 2014. BMP2-encapsulated chitosan coatings on functionalized Ti surfaces and their performance in vitro and in vivo. Mater. Sci. Eng. C Mater. Biol. Appl. 40, 1–8. https://doi.org/10.1016/j.msec.2014.03.043.

Harris, L.G., Tosatti, S., Wieland, M., Textor, M., Richards, R.G., 2004. *Staphylococcus aureus* adhesion to titanium oxide surfaces coated with non-functionalized and peptide-functionalized poly(L-lysine)-grafted-poly(ethylene glycol) copolymers. Biomaterials 25, 4135–4148.

Hoffman, A.S., 2016. The early days of PEG and PEGylation (1970s-1990s). Acta Biomater. 40, 1–5. https://doi.org/10.1016/j.actbio.2016.05.029.

Inoue, Y., Onodera, Y., Ishihara, K., 2018. Initial cell adhesion onto a phospholipid polymer brush surface modified with a terminal cell adhesion peptide. ACS Appl. Mater. Interfaces 10, 15250–15257. https://doi.org/10.1021/acsami.8b01906.

Ishihara, K., 2019. Blood compatible surfaces with phosphorylcholine-based polymers for cardiovascular medical devices. *Langmuir*. 35, 1778–1787.

Ishihara, K., Ueda, T., Nakabayashi, N., 1990. Preparation of phospholipid polymers and their properties as hydrogel membrane. Polym. J. 22, 355–360. https://doi.org/10.1295/polymj.22.355.

Ishihara, K., Nomura, H., Mihara, T., Kurita, K., Iwasaki, Y., Nakabayashi, N., 1998. Why do phospholipid polymer reduce protein adsorption. J. Biomed. Mater. Res. 39, 323–330 https://doi.org/10.1002/(SICI)1097-4636(199802)39:2<323::AID-JBM21>3.0.CO;2-C.

Ishihara, K., Ziats, N.P., Tierney, B.P., Nakabayashi, N., Anderson, J.M., 1991. Protein adsorption from human plasma is reduced on phospholipid polymers. J. Biomed. Mater. Res. 25, 1397–1407. https://doi.org/10.1002/jbm.820251107.

Ishihara, K., Oshida, H., Endo, Y., Ueda, T., Watanabe, A., Nakabayashi, N., 1992. Hemocompatibility of human whole blood on polymers with a phospholipid polar group and its mechanism. J. Biomed. Mater. Res. 26, 1543–1552. https://doi.org/10.1002/jbm.820261202.

Ishihara, K., Mu, M., Konno, T., Inoue, Y., Fukazawa, K., 2017. The unique hydration state of poly(2-methacryloyloxyethyl phosphorylcholine). J. Biomater. Sci. Polym. Ed. 28, 884–899. https://doi.org/10.1080/09205063.2017.1298278.

Iwasaki, Y., Ishihara, K., 2005. Phosphorylcholine-containing polymers for biomedical applications. Anal. Bioanal. Chem. 381, 534–546. https://doi.org/10.1007/s00216-004-2805-9.

Iwasaki, Y., Ishihara, K., 2012. Cell membrane-inspired phospholipid polymers for developing medical devices with excellent biointerfaces. Sci. Technol. Adv. Mater. 13064101https://doi.org/10.1088/1468-6996/13/6/064101.

Iwasaki, Y., Saito, N., 2003. Immobilization of phosphorylcholine polymers to Ti-supported vinyldimethylsilyl monolayers and reduction of albumin adsorption. Colloids Surf. B. Biointerfaces 32, 77–84. https://doi.org/10.1016/S0927-7765(03)00147-4.

Jamiolkowski, M.A., Woolley, J.R., Kameneva, M.V., Antaki, J.F., Wagner, W.R., 2015. Real time visualization and characterization of platelet deposition under flow onto clinically relevant opaque surfaces. J. Biomed. Mater. Res. A 103, 1303–1311. https://doi.org/10.1002/jbm.a.35202.

Jamiolkowski, M.A., Pedersen, D.D., Wu, W.T., Antaki, J.F., Wagner, W.R., 2016. Visualization and analysis of biomaterial-centered thrombus formation within a defined crevice under flow. Biomaterials 96, 72–83. https://doi.org/10.1016/j.biomaterials.2016.04.022.

Kaushik, N.K., Kaushik, N., Pardeshi, S., Sharma, J.G., Lee, S.H., Choi, E.H., 2015. Biomedical and clinical importance of mussel-inspired polymers and materials. Mar. Drugs 13, 6792–6817. https://doi.org/10.3390/md13116792.

Kitano, T., Iwasaki, K., 2018. Long-term durability test for the left ventricular assist system EVAHEART under the physiologic pulsatile load. ASAIO J. 64, 168–174.

Konno, T., Ishihara, K., 2007. Tamporal and spatially controllable cell encapsulation using a water-soluble phospholipid polymer with phenylboronic acid moiety. Biomaterials 28, 1770–1777. https://doi.org/10.1016/j.biomaterials.2006.12.017.

Kuang, J., Messersmith, P.B., 2012. Universal surface-initiated polymerization of antifouling zwitterionic brushes using a mussel-mimetic peptide initiator. Langmuir 28, 7258–7266. https://doi.org/10.1021/la300738e.

Kyomoto, M., Iwasaki, Y., Moro, T., Konno, T., Miyaji, F., Kawaguchi, H., Takatori, Y., Nakamura, K., Ishihara, K., 2007. High lubricious surface of cobalt-chromium-molybdenum alloy prepared by grafting poly(2-methacryloyloxyethyl phosphorylcholine). Biomaterials 28, 3121–3130.

Kyomoto, M., Moro, T., Iwasaki, Y., Miyaji, F., Kawaguchi, H., Takatori, Y., Nakamura, K., Ishihara, K., 2009. Superlubricious surface mimicking articular cartilage by grafting poly (2-methacryloyloxyethyl phosphorylcholine) on orthopaedic metal bearings. J. Biomed. Mater. Res. A 91, 730–741. https://doi.org/10.1002/jbm.a.32280.

Kyomoto, M., Moro, T., Saiga, K., Miyaji, F., Kawaguchi, H., Takatori, Y., Nakamura, K., Ishihara, K., 2010. Lubricity and stability of poly(2-methacryloyloxyethyl phosphorylcholine) polymer layer on Co-Cr-Mo surface for hemi-arthroplasty to prevent degeneration of articular cartilage. Biomaterials 31, 658–668. https://doi.org/10.1016/j.biomaterials.2009.09.083.

LaBerge, M., Drouin, G., Gélinas, C., Champagne, B., Bobyn, J.D., 1990. Adherence of HDPE powder coating on Co-Cr surfaces: effect of substrate preparation and gas sterilization. J. Biomed. Mater. Res. 24, 1427–1438.

Lee, H., Dellatore, S.M., Miller, W.M., Messersmith, P.B., 2007. Mussel-inspired surface chemistry for multifunctional coatings. Science 318, 426–430.

Lewis, A.L., 2000. Phosphorylcholine-based polymers and their use in the prevention of biofouling. Colloids Surf. B. Biointerfaces 18, 261–275.

Lewis, A.L., Stratford, P.W., 2002. Phosphorylcholine-coated stents. J. Long-Term Eff. Med. Implants 12, 231–250.

Lewis, A.L., Willis, S.L., Small, S.A., Hunt, S.R., O'byrne, V., Stratford, P.W., 2004. Drug loading and elution from a phosphorylcholine polymer-coated coronary stent does not affect long-term stability of the coating in vivo. Biomed. Mater. Eng. 14, 355–370.

Liu, Y., Inoue, Y., Mahara, A., Kakinoki, S., Yamaoka, T., Ishihara, K., 2014. Durable modification of segmented polyurethane for elastic blood-contacting devices by graft-type 2-methacryloyloxyethyl phosphorylcholine copolymer. J. Biomater. Sci. Polym. Ed. 25, 1514–1529. https://doi.org/10.1080/09205063.2014.920172.

Ma, Y., Yang, P., Li, J., Li, S., Li, P., Zhao, Y., Huang, N., 2015. Immobilization of poly(MPC) brushes onto titanium surface by combining dopamine self-polymerization and ATRP: preparation, characterization and evaluation of hemocompatibility in vitro. Appl. Surf. Sci. 349, 445–451. https://doi.org/10.1016/j.apsusc.2015.05.035.

Madhurakkat Perikamana, S.K., Lee, J., Lee, Y.B., Shin, Y.M., Lee, E.J., Mikos, A.G., Shin, H., 2015. Materials from mussel-inspired chemistry for cell and tissue engineering applications. Biomacromolecules 16, 2541–2555. https://doi.org/10.1021/acs.biomac.5b00852.

Maier, G.P., Butler, A., 2017. Siderophores and mussel foot proteins: the role of catechol, cations, and metal coordination in surface adhesion. J. Biol. Inorg. Chem. 22, 739–749. https://doi.org/10.1007/s00775-017-1451-6.

Monge, S., Canniccioni, B., Graillot, A., Robin, J.J., 2011. Phosphorus-containing polymers: a great opportunity for the biomedical field. Biomacromolecules 12, 1973–1982. https://doi.org/10.1021/bm2004803.

Myers, G.J., Johnstone, D.R., Swyer, W.J., McTeer, S., Maxwell, S.L., Squires, C., Ditmore, S.N., Power, C.V., Mitchell, L.B., Ditmore, J.E., Aniuk, L.D., Hirsch, G.M., Buth, K.J., 2003. Evaluation of mimesys phosphorylcholine (PC)-coated oxygenators during cardiopulmonary bypass in adults. J. Extra Corpor. Technol. 35, 6–12.

Newland, R.F., Baker, R.A., Sanderson, A.J., Tuble, S.C., Tully, P.J., 2012. Oxygenator safety evaluation: a focus on connection grip strength and arterial temperature measurement accuracy. J. Extra Corpor. Technol. 44, 53–59.

Oda, H., Konno, T., Ishihara, K., 2013. The use of the mechanical microenvironment of phospholipid polymer hydrogels to control cell behavior. Biomaterials 34, 5891–5896. https://doi.org/10.1016/j.biomaterials.2013.04.015.

Oda, H., Konno, T., Ishihara, K., 2015. Efficient differentiation of stem cells encapsulated in a cytocompatible phospholipid polymer hydrogel with tunable physical properties. Biomaterials 56, 86–91. https://doi.org/10.1016/j.biomaterials.2015.03.051.

Park, J.Y., Kim, J.S., Nam, Y.S., 2013. Mussel-inspired modification of dextran for protein-resistant coatings of titanium oxide. Carbohydr. Polym. 97, 753–757. https://doi.org/10.1016/j.carbpol.2013.05.064.23911511.

Qin, L., Dong, H., Mu, Z., Zhang, Y., Dong, G., 2015. Guangneng donga, preparation and bioactive properties of chitosan and casein phosphopeptides composite coatings for orthopedic implants. Carbohydr. Polym. 133, 236–244.

Rasouli, R., Barhoum, A., Uludag, H., 2018. A review of nanostructured surfaces and materials for dental implants: surface coating, patterning and functionalization for improved performance. Biomater. Sci. 6, 1312–1338. https:/doi.org/10.1039/c8bm00021b.

Ren, K., Ji, J., Shen, J., 2006. Construction and enzymatic degradation of multilayered poly-l-lysine/DNA films. Biomaterials 27, 1152–1159. https://doi.org/10.1016/j.biomaterials.2005.07.021.

Sigal, G.B., Mrksics, M., Whitesides, G.M., 1998. Effect of surface wettability on the adsorption of proteins and detergents. J. Am. Chem. Soc. 120, 3464–3473. https://doi.org/10.1021/ja970819l.

Snyder, A.T., Tsukui, H., Kihara, S., Akimoto, T., Litwak, K.N., Yamazaki, K., Kameneva, M.V., Yamazaki, K., Wagner, W.R., 2007. Preclinical biocompatibility assessment of the EVAHEART ventricular assist device: coating comparison and platelet activation. J. Biomed. Mater. Res. A 81, 85–92. https://doi.org/10.1002/jbm.a.31006.

Sobocinski, J., Laure, W., Taha, M., Courcot, E., Chai, F., Simon, N., Addad, A., Martel, B., Haulon, S., Woisel, P., Blanchemain, N., Lyskawa, J., 2014. Mussel inspired coating of a biocompatible cyclodextrin based polymer onto CoCr vascular stents. ACS Appl. Mater. Interfaces 6, 3575–3586. https://doi.org/10.1021/am405774v.

Sukhishvili, S.A., Granick, S., 2002. Layered, erasable polymer multilayers formed by hydrogen-bonded sequential self-assembly. Macromolecules 35, 301–310. https://doi.org/10.1021/ma011346c.

Ueda, T., Oshida, H., Kurita, K., Ishihara, K., Nakabayashi, N., 1992. Preparation of 2-methacryloyloxyethyl phosphorylcholine copolymers with alkyl methacrylate and their blood compatibility. Polym. J. 24, 1259–1269. https://doi.org/10.1295/polymj.24.1259.

Visan, A., Cristescu, R., Stefan, N., Miroiu, M., Nita, C., Mihailescu, I.N., Socol, G., Socol, N., Florica, C., Rasoga, O., Zgura, I., Sima, L.E., Chiritoiu, M., Chifiriuc, M.C., Holban, A.M., 2017. Antimicrobial polycaprolactone/polyethylene glycol embedded lysozyme coatings of Ti implants for osteoblast functional properties in tissue engineering. Appl. Surf. Sci. 417, 234–243.

Watanabe, S., Kashiwagi, R., Matsumoto, M., 2017. Alternate spray-coating for the direct fabrication of hydroxyapatite films without crystal growth step in solution. J. Oleo Sci. 66, 279–284. https://doi.org/10.5650/jos.ess16142.

Whelan, D.M., van der Giessen, W.J., Krabbendam, S.C., van Vliet, E.A., Verdouw, P.D., Serruys, P.W., van Beusekom, H.M., 2000. Biocompatibility of phosphorylcholine coated stents in normal porcine coronary arteries. Heart 83, 338–345. https://doi.org/10.1136/heart.83.3.338.

Yan, J., Springsteen, G., Deeter, S., Wang, B., 2004. The relationship among pK_a, pH, and binding constants in the interactions between boronic acids and diols—it is not as simple as it appears. Tetrahedron 60, 11205–11209. https://doi.org/10.1016/j.tet.2004.08.051.

Yao, Y., Fukazawa, K., Huang, N., Ishihara, K., 2011. Effects of 3,4-dihydrophenyl groups in water-soluble phospholipid polymer on stable surface modification of titanium alloy. Colloids Surf. B Biointerfaces 88, 215–220. https://doi.org/10.1016/j.colsurfb.2011.06.034.

Yao, Y., Fukazawa, K., Ma, W., Ishihara, K., Huang, N., 2012. Platelet adhesion-resistance of titanium substrate with mussel-inspired adhesive polymer bearing phosphorylcholine group. Appl. Surf. Sci. 258, 5418–5423. https://doi.org/10.1016/j.apsusc.2012.02.027.

Ye, S.H., Johnson Jr., C.A., Woolley, J.R., Snyder, T.A., Gamble, L.J., Wagner, W.R., 2009a. Covalent surface modification of a titanium alloy with a phosphorylcholine-containing copolymer for reduced thrombogenicity in cardiovascular devices. J. Biomed. Mater. Res. A 91, 18–28. https://doi.org/10.1002/jbm.a.32184.

Ye, S.H., Johnson Jr., C.A., Woolley, J.R., Oh, H.I., Gamble, L.J., Ishihara, K., Wagner, W.R., 2009b. Surface modification of a titanium alloy with a phospholipid polymer prepared by a plasma-induced grafting technique to improve surface thromboresistance. Colloids Surf. B Biointerfaces 74, 96–102. https://doi.org/10.1016/j.colsurfb.2009.06.032.

Zhang, F., Zhang, Z., Zhu, X., Kang, E.T., Neoh, K.G., 2008. Silk-functionalized titanium surfaces for enhancing osteoblast functions and reducing bacterial adhesion. Biomaterials 29, 4751–4759.

Zeng, G., Ogaki, R., Meyer, R.L., 2015. Non-proteinaceous bacterial adhesins challenge the antifouling properties of polymer brush coatings. Acta Biomater. 24, 64–73. https://doi.org/10.1016/j.actbio.2015.05.037.

Further reading

Chuang, T.W., Lin, D.T., Lin, F.H., 2008. Immobilization of $NaIO_4$-treated heparin on PEG-modified 316L SS surface for high anti-thrombin-III binding. J. Biomed. Mater. Res. A 86, 648–661.

Kawabe, A., Nakagawa, I., Kanno, Z., Tsutsumi, Y., Hanawa, T., Ono, T., 2014. Evaluation of biofilm formation in the presence of saliva on poly(ethylene glycol)deposited titanium. Dent. Mater. J. 33, 638–647. https://doi.org/10.4012/dmj.2014-025.

Lewis, F., Cloutier, M., Chevallier, P., Turgeon, S., Pireaux, J.J., Tatoulian, M., Mantovani, D., 2011. Influence of the 316 L stainless steel interface on the stability and barrier properties of plasma fluorocarbon films. ACS Appl. Mater. Interfaces 3, 2323–2331.

Sterilization and cleaning of metallic biomaterials

16

S. Lerouge
Ecole de Technologie Supérieure (ETS), Montreal, QC, Canada

16.1 Introduction

Sterilization is an important step in manufacturing implants or biomedical devices to prevent the spread of infection. Failures in adequate sterilization of medical devices (MDs) result in significant institutional costs related to patient nosocomial infections and mortality/morbidity concerns. It is important to consider sterilization issues and requirements at the earliest stages of development of any new MDs, to ensure that the final product can be sterilized effectively and safely, with the most cost-effective and environment-friendly procedures. Except for the rare instances when sterilization can take place where the sterile products are to be used, MDs must be packaged to preserve their sterility during storage, handling, and transport. The majority of sterile MDs are terminally sterilized—that is, they are sterilized already packaged. If reusable, the device must sustain several cycles of cleaning and sterilization in clinical settings.

In the following section, the main concepts of sterilization will be defined, such as sterilization efficiency and safety, which are the two most important aspects to consider when choosing a biomaterial, designing the device, and choosing the packaging and sterilization technique. When deciding on a sterilization method, one of the first considerations should be product compatibility. All type of materials can be degraded to some extent by one or more sterilization processes. Sterilization can also leave toxic products that may impair device biocompatibility. For these reasons, functional and biocompatibility testing for the US Food and Drug Administration (FDA) or European Community (EC) approval must be performed on the final packaged and sterilized products.

An overview of the main sterilization processes and more recent alternatives will be presented in Sections 16.3 and 16.4, with emphasis on their main advantages and limitations. The most widely used MD sterilization technologies are gamma and electron beam irradiation, hot steam, and ethylene oxide (EO). Alternatives include low-temperature hydrogen peroxide gas plasma (LTHPGP), vapor-phase hydrogen peroxide, ozone, liquid peracetic acid, X-rays, and chlorine dioxide. Although this book focuses on metallic implants, which are resistant to heat and are little prone to damage by sterilization processes, it should be kept in mind that many metallic devices nowadays include small polymeric parts (adhesives, interconnectors, liners, protective layers, and so on) and are packaged with materials that may be sensitive to high temperatures and radiation.

Metals for Biomedical Devices. https://doi.org/10.1016/B978-0-08-102666-3.00016-X
© 2019 Elsevier Ltd. All rights reserved.

In Section 16.5, prion and endotoxin deactivation will be briefly discussed, as this represents an important challenge due to their high resistance to sterilization techniques. Cleaning methods will be presented in Section 16.6. Finally, Section 16.7 will briefly present the many regulations and standards related to sterilization and will propose other useful sources of information.

16.2 Concepts and definitions

16.2.1 Sterilization efficiency

Sterilization efficiency is defined as the ability to remove or destroy all forms of microbial life, including viruses, bacteria, and fungi, in the vegetative state or as spores (Crow, 1993). Since absolute sterility cannot be verified, the statistical definition of sterility is used in practice, by using the Security Assurance Level (SAL), defined as 'the probability of a single viable microorganism occurring in or on a product after sterilization.' The worldwide accepted definition of sterility of MDs is defined as the chance of finding a viable organism in or on a MD to be, at most, 1 in 1,000,000 or a SAL of, at most, 10^{-6} (Block, 2000).

16.2.2 Sterilization vs disinfection

It is important to distinguish sterilization from disinfection, which does not ensure the same security level and does not necessarily inactivate all forms of microorganisms—bacterial spores for instance. The choice between sterilization and disinfection must be done according to the risk of spreading infection. Thus, according to the Spaulding Classification (Spaulding, 1972), sterilization is required for all critical MDs, that is, those intended to be used in contact with sterile tissues, and is recommended for semi-critical devices, for example, those intended to be in contact with mucous tissues or breached tissues, such as endoscopes. A high level of disinfection is, however, acceptable for the latter (Spaulding, 1972).

Sterilization should not be confused with cleaning, which is defined as the removal of all foreign material (dust, soil, and organic debris). Yet, cleaning devices are an important step before sterilization, especially in healthcare centers, since it has been demonstrated that it is more difficult to sterilize devices where microorganisms hide behind proteineous or greasy matter.

16.2.3 Sterilization validation

Sterilization validation studies must document that the product attains the required SAL after exposure to the proposed process. In the industry, sterilization validation is evaluated by determining the typical bioburden (type and number of viable microorganisms on the implant just prior to sterilization) after the manufacturing process and using fractional-run sterilization studies to determine the rate of killing. In a

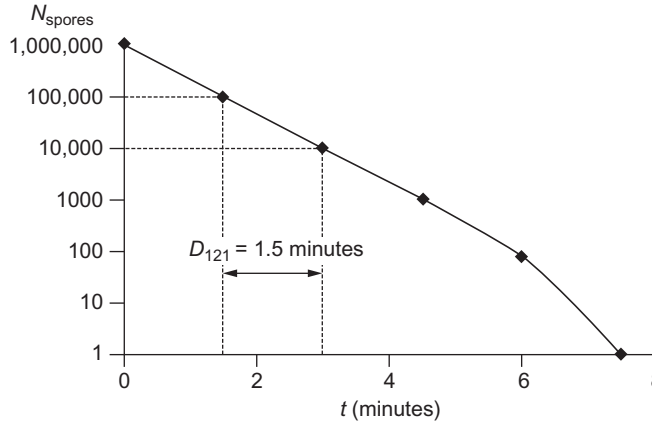


Fig. 16.1 A typical deactivation curve of bacterial spores during steam sterilization, which allow to calculate the *D*-value (D_{121}) as the time required to decrease spores' number from 90% at 121°C.

fractional sterilization run, product samples (in packages) are exposed to various fractions of the desired sterilization process or dose. The number of survival microorganisms is reported graphically on a semilogarithmic scale to extrapolate the exposure time or dose required to achieve a 10^{-6} SAL (Fig. 16.1). A security factor is then generally applied.

As seen in Fig. 16.1, microbial inactivation does not follow a linear curve but generally a logarithmic or first-order rate function. At a certain temperature (here 121°C), the same exposure time is required to decrease the number of microorganisms from 10^6 to 10^5 as from 10^2 to 10^1. This exposure time (or dose, in the case of radiation sterilization) required to inactivate 90% of the microorganism burden is called the *D*-value (the decimal reduction time) and is very useful in calculating the exposure time required to achieve SAL from a known bioburden. Such a parameter does, however, not exist for every sterilization process.

Validation studies must be done on product samples prepared under actual manufacturing conditions and exposed to the sterilization process under its final packaging configuration. Device geometry (small lumen or cavities) can be of concern when sterilization agents have limited penetration. More details about sterilization process validation can be found in the specific ISO documents standards (ISO17665-1:2006; ISO11135:2014; ISO11137-3:2017).

It is important to differentiate between industrial sterilization and resterilization of reusable devices achieved in healthcare centers. In the latter cases, the bioburden cannot be easily determined since it can be influenced by several factors and a more drastic sterilization called 'overcharge' sterilization is, therefore, generally used, considering an initial microbial charge of 10^6 per device. Moreover, cleanliness is another important parameter for reusable devices, and this must be taken into account when designing the device, to avoid unreachable cavities.

Even once the process has been validated, its efficiency must be verified on each sterilization load. With an increasing number of sterilization processes, product release can be based on the dosimetric release, parametric control, or process control. As discussed later, monitoring the delivered radiation dose is sufficient to allow product release after gamma sterilization. In contrast, EO process control is more complex since several parameters such as EO concentration, humidity rate, time, temperature, and vacuum/pressure influence process efficiency. In many cases, monitoring sterilization efficiency requires biological indicators (BIs) containing bacterial endospores. While conventional BIs require 24–48 h spore incubation before reading results and releasing sterilized products, a new generation of BI, using spore-associated enzymes, is now able to detect sterilization failure in only a few hours (Albert et al., 1998; McCormick et al., 2003; Rutala et al., 1996; Leventon, 2002; Rutala and Weber, 2001; Setlow et al., 2016).

Finally, an expiration date must be labeled on sterilized products given that packaging materials cannot indefinitely prevent recontamination with microorganisms. The time allowed between sterilization and clinical use mostly depends on the type of packaging material used. For costly single-use devices such as implants, manufacturers should take this matter into account to avoid withdrawal of unused and expired sterilized products from the market.

16.2.4 Sterilization safety

Safety of sterilization is a broad term including concerns for patients, sterilization personnel, and the environment. The first concern with the choice of a sterilization process is the demonstration that the product is compatible with the sterilization process; the integrity of the product and of the packaging which maintains its sterility after the process must be demonstrated since most sterilization conditions can degrade materials. This could lead to a significant loss of functionality or biocompatibility of the device. For instance, toxic residues or by-products may be formed on devices during sterilization. It is then essential to ensure that patient exposure to these residuals stays below safe limits. Metallic biomaterials are generally resistant to most processes but packaging materials are often polymers and most new devices now incorporate also small amounts of polymeric compounds, which are more sensitive to sterilization conditions. Moreover, metallic reusable devices can also be damaged by multiple sterilization exposures such as corrosion of carbon steels after steam sterilization. These issues will be specifically addressed when discussing each sterilization process. One should also be aware of the possible direct harm of the sterilization process toward manufacturing personnel and the environment, as will be discussed in the EO sterilization section. National or international regulations may also lead to progressive proscription of a sterilization method with time, as has already been done for chlorofluorocarbon gas (CFC), an ozone-layer depletion agent commonly used to stabilize EO, now forbidden in EO sterilizers (Jorkasky, 1993).

16.3 Main sterilization methods for biomaterials; advantages and limitations

16.3.1 Overview of sterilization processes

Gamma or electron beam radiation and EO are still the main industrial sterilization processes of MDs but several other processes, such as moist heat (steam autoclave), dry heat, and, more recently, LTHPGP, ozone, or peracetic acid are available and are increasingly used in healthcare facilities. Process principles and inactivation mechanisms, as well as main advantages and disadvantages, of each of these processes will be described in the following section. Main parameters, as well as advantages and disadvantages are reviewed in Table 16.1.

Table 16.1 Parameters, advantages and limitations of the main sterilization processes

Technique	Main parameters	Advantages	Limitations
Steam (autoclave)	121–134°C, 5–20 min Gravity High humidity level	**Simple, safe, rapid, and efficient** Good penetrability Easy to monitor No toxic residues Can sterilize liquids Low cost	**High temperature** and moisture Incompatible with many thermosensitive polymers. Metals may corrode Need breathable packaging
	Options: Flash autoclave 134°C, 3–6 min in vacuum with steam pulses)	Rapid	Limited to unpackaged product—sterility not conserved. For rapid reprocessing in the surgical room only.
	"Low-temperature" steam (110–115°C, 35–40 min)	Allow sterilization of more heat sensitive materials	Longer exposure Efficiency subject to some controversy
Dry heat	160–170°C 1–2 h	Generally avoid metal corrosion	Longer exposure than steam
Gamma radiations	10–40 kGy (most common 25 kGy) Ambient temperature A few hours	Low temperature **Excellent penetrability, efficiency, and reliability** Dosimetric release Large product volumes—terminally packaged	Isotope containment requires costly facilities for safety reasons **→ Only available in a few industrial centers** Alteration of many polymers (ionization

Continued

Table 16.1 Continued

Technique	Main parameters	Advantages	Limitations
		products Cost effective **Compatible with many materials** No residues Environmentally safe, except for the disposal of radioactive waste	leading to polymer chain scission or cross-linking; maximal dose strongly dependent on the polymer chemistry
Electron-beam	11–40 kGy	Very rapid (Seconds/min) More material compatibility than gamma rays	Less penetration than gamma Industrial sterilization
Ethylene oxide (EO)	25–65°C (generally 55°C) High humidity EO: 400–1500 mg/L 2–4 h + aeration	**Low-temperature** **Compatible with most materials** Efficiency, relatively good penetrability	**Long cycle and safety risks** EO toxicity and carcinogenicity: Safety risks for sterilization personnel and patients Toxic EO residues and reaction products in polymers: requires aeration EO release now restricted in many countries →Decreasing use in hospital centers
Hydrogen peroxide gas sterilization (Sterrad, V-Pro maX, etc.)	Hydrogen peroxide gas (± plasma)	**Low temperature** **Low toxicity of H_2O_2 compared to EO** H_2O_2 residues rapidly eliminated, especially in Sterrad due to plasma	Possible material alteration due to oxidation Not compatible with papers (cellulose) Small loads Care must be taken to choose the right cycle depending on the load Number of MD validated for reprocessing is still limited (relatively new technology)

16.3.2 Radiation sterilization

Radiation sterilization is still the main industrial sterilization process for single-use MDs. Sterilization processes using radiation include gamma rays, electron-beam process, and, more recently, X-rays. All ionize molecules but via different processes, which affects their practical application to sterilization. Gamma rays from a cobalt (Co) or cesium (Cs) isotope source are by far the most popular and widespread agent for MD (Block, 2000; Booth, 2001). A ^{137}Cs source is generally used for the irradiation of blood and insect sterilization, ^{60}Co for medical devices.

16.3.2.1 Gamma radiation

Gamma rays emitted by ^{60}Co source have an energy of about 1.2 MeV and are highly penetrating, thus allowing sterilization of large amounts of densely packaged materials but requiring highly specialized facilities to protect workers from radiation. Fig. 16.2 presents a typical industrial ^{60}Co irradiator, where the radioisotope is contained in sealed 'pencils' around which medical products are moved. Gamma radiation requires bulky shielding for the safety of the operators; it also requires storage of the radioisotope, which continuously emits gamma rays. A water-filled pool is, therefore, used to immerse the source when personnel require to enter the radiation cell. For safety reason, gamma-ray sterilization cannot be performed in clinical facilities and takes place only in a few industrial centers. This is one of the reason why about 65% of sterilization of MD is outsourced by contract service providers (Parsons, 2012).

Gamma rays cause ionization of key cellular components, especially nucleic acids, which results in the death of microorganisms (Hutchinson, 1961). DNA is also altered by oxidoreduction reactions due to water radiolysis into H^+ and OH^- radicals

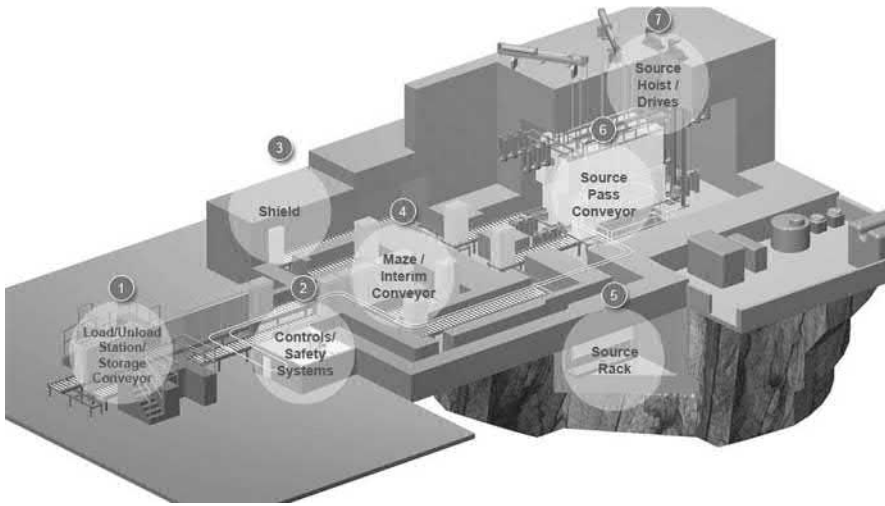


Fig. 16.2 An industrial gamma sterilization irradiator
From Nordion.

under ionizing radiations. These radiations are highly effective in killing microorganisms, but they do not have sufficient energy to impart radioactivity to the sterilized material.

Gamma sterilization is performed at ambient temperature and allows sterilization of temperature-sensitive material. The high penetrability of gamma rays permits large sterilization loads and reliability, even in complex geometries and densely packaged materials. Other benefits include precise dosing, rapid processing, uniform dose distribution, and FDA dosimetric release. This last point means that control of the dose of radiation delivered to the product (by dosimeters placed in containers, read after the process) is sufficient to ensure efficiency. It allows elimination of sterility tests using BI and permits immediate availability of product after processing, both of these allowing cost savings. The most commonly validated dose used to sterilize MDs is 25 kGy (kilograys). While steam and EO sterilization require packages that are permeable to the gases and vapors, radiation sterilization is compatible with nonbreathable packaging. This allows for a wider selection of materials of choice for the package.

Gamma radiation is compatible with many materials, including all metallic alloys which are very stable to radiation. While all polymers are affected in some degree by ionizing radiation, many have a natural tolerance for sterilizing radiation doses of up to and beyond 50 kGy, with the notable exceptions of acetal, unstabilized polypropylene (PP), and polytetrafluoroethylene (PTFE or Teflon) (Fig. 16.3). Polymer irradiation can lead to molecular-chain cross-linking or scission, and possible alteration of mechanical properties (Bruck and Mueller, 1988; Collier et al., 1996; Nair, 1995; Plester, 1970; Premnath et al., 1996; Yagoubi et al., 1997; Ries et al., 1996). While polymers with cyclic groups such as polystyrene (PS) are highly resistant to radiation, others such as PTFE, nylon, acetal, and cyanoacrylates have high radiation sensitivity (Kowalski and Morrissey, 2004; Morrissey and Ratner, 1998). More complete data on various polymers' compatibility with radiation can be found in other books (Massey, 2005; Hill, 1998; Rogers, 2005; Rogers, 2012b). Most bioresorbable polymers are also too sensitive to radiation to be sterilized by this process. It has also been shown than gamma radiation provides an environment conducive to the oxidation of UHMWPE used in load-bearing joints. Gamma sterilization processes in inert environments (argon, nitrogen, or vacuum) instead of ambient air are now commonly used to reduce oxidation and improve wear resistance of UHMWPE for such applications. Color change is common in PVC, PC, PS, ABS, and acrylics, before any physical change can be detected. Irradiated polymers (such as polyurethanes) can also be the source of strong odors. For more sensitive polymers, the first and most significant change in mechanical properties is the loss of elongation to break. This is due to molecular shortening by scission and is one reason to start with high molecular weight materials. It should be noted that gamma compatibility is less an issue than before since suppliers have introduced a variety of radiation-compatible materials that are now being specified by device manufacturers.

While ideal for the sterilization of many single-use devices, gamma radiation is not very appropriate for resterilization of MDs. Reasons are that this method cannot be performed in clinical settings and that repeated irradiation may cause important damage to polymers.

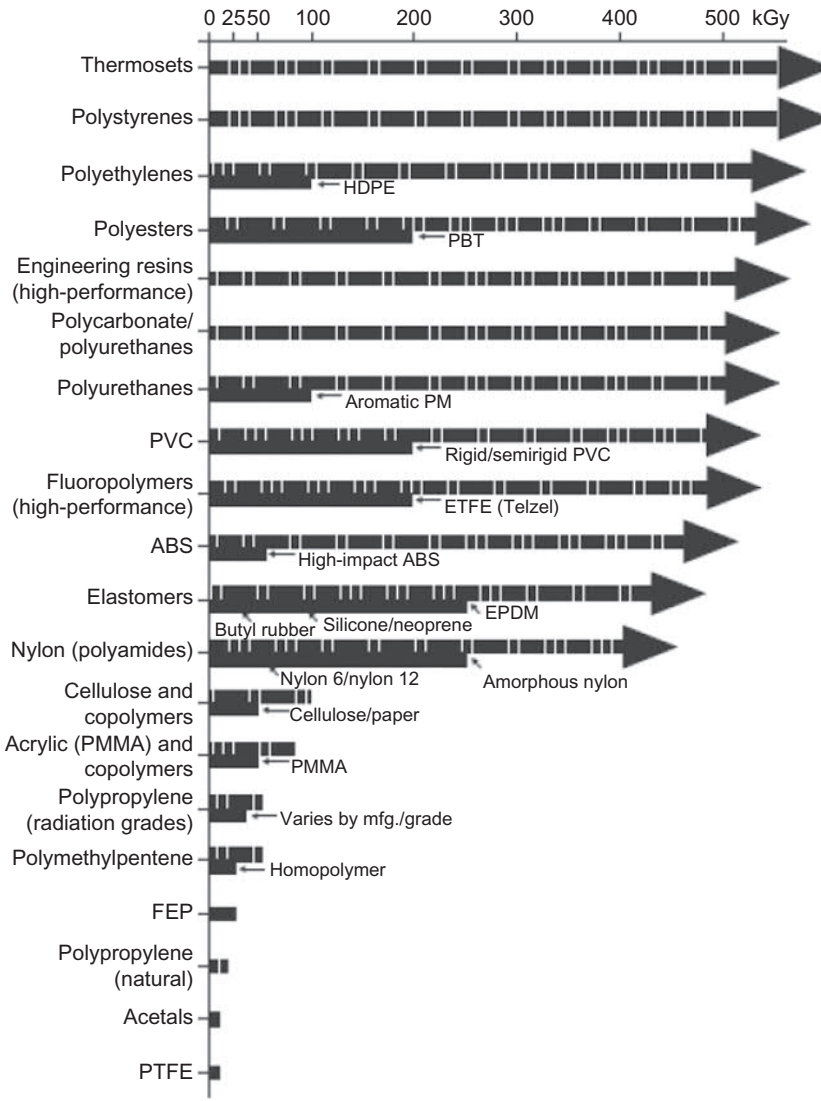


Fig. 16.3 Relative stability of medical polymer families after radiation sterilization, indicating the dose at which elongation decreases by 25%.
Reprinted with permission from Medical Device and Diagnostic Industry 'Radiation Sterilization-Polymer Materials Selection for Radiation-sterilized Products,' Feb 2000. Copyright ©2000 Canon communications LLC.

16.3.2.2 Electron beam, X-ray, and ultraviolet light radiation

Electron beam (e-beam) processing is commonly used for industrial MD sterilization (Reich et al., 2005; Block, 2000). In this process, high-energy electrons are machine generated using an accelerator. The electron energy is then higher than with gamma

rays (between 4 and 6 MeV) (Massey, 2005; Woo and Sandford, 2002). While these installations must also be installed in a concrete room to contain electrons, they use an on-off technology (no radiation is emitted once the accelerator is turned off and personnel can then safely enter the sterilization room) which decrease costs and enables in-house facilities.

Due to the higher dose rate, less exposure time is needed and thereby potential degradation of polymers is reduced, making e-beam compatible with more materials than gamma radiation. It can degrade rubber and PP but these materials now come in grades that are e-beam compatible. The process can also be harmful to electronic components or batteries. The main limitations of electron beam processing are, however, the much lower penetration of electrons compared to either gamma or X-rays, and the shadowing effect, which make this method unsuitable for thick or densely package products, and more risky for devices with complex geometries. Penetration of electrons is directly related to their kinetic energy and to the acceleration voltage used.

X-ray sterilization is growing as a result of recent increases in the beam power ratings of industrial electron accelerators, which can generate intense X-ray beams. X-rays are more penetrating than e-beams, but less than gamma rays. They are more costly than gamma processes but will decrease exposure times, require less shielding and shorten turnaround times. A first X-ray sterilization facilities has been open in Switzerland in 2012 (Parsons, 2012) and several electron beam facilities in Europe, Japan, and North America are already equipped for both electron beam and X-ray sterilization (Stichelbaut et al., 2007) (ISO/ASTM 51608:201502).

Both electron beam and X-rays have a wide range of polymer compatibility compared to gamma. All radiation-based sterilization techniques have some limitations due to oxidation effects. The readers are referred to an excellent comparison between industrial sterilization technologies (including gamma, electron beam, and X-rays) to get a more complete list of pros and cons of each technology (White paper, 2017).

In contrast, ultraviolet (UV) light radiation has very low penetrability and is limited to the treatment of surfaces. UV irradiation by germicidal lamps is routinely used to sterilize the interiors of biological hoods between uses, but is ineffective in shaded areas, including areas under dirt.

16.3.3 Moist and dry heat sterilization

16.3.3.1 Steam sterilization

Steam sterilization has limited industrial application but is very commonly used in healthcare facilities. A steam sterilizer, also known as an 'autoclave,' uses saturated steam at 121–134°C. A typically standard for steam sterilization is achieved by exposure to a temperature of 121°C at a pressure of 15 psi for 15–30 min (Block, 2000). Since inactivation is even more efficient when the temperature increases, an exposure time of 10 min at 121°C may be compared to a 150 min at 111°C or 3 min at 132–134°C (Rogers, 2012a).

Steam sterilization steps are loading, air removal, heat up, exposure, cool down, and drying. To insure reliability of this sterilization method, the critical factors are:

(i) proper temperature and time and (ii) the complete replacement of the air with steam (i.e., no entrapment of air). Some autoclaves use a precycle vacuum to remove air prior to steam introduction. Others utilize a steam-activated exhaust valve that remains open during the replacement of air by live steam until the steam triggers the valve to close. To ensure efficient sterilization, all joined or mated-surface instruments should be opened (Rogers, 2012a).

Moist heat sterilization kills microorganisms by destroying structural and metabolic components essential to their replication. The coagulation of essential enzymes and the disruption of proteins and lipids are the main lethal events (Kowalski and Morrissey, 2004). The advantage of wet heat is a better heat transfer to, and into, the cell, resulting in needing an overall shorter exposure time and a lower temperature (Block, 2000).

Steam sterilization has many advantages. It is a simple, rapid, effective, safe, environment-friendly, and low-cost sterilization method. It yields little waste (entropy is its only by-product). Monitoring physical parameters (moisture, temperature, time, etc.) can be used to ensure efficiency of sterilization, although BIs are still commonly used in several countries. It can also sterilize liquids. It is, therefore, commonly used in healthcare centers for the sterilization of reusable metallic devices and instruments, hospital linen, various solutions, etc.

Its main limitation is clearly that it is incompatible with many materials. Steam sterilization damages most polymers. It can also cause corrosion of some metallic devices, in particular high carbon steels used for surgical and dental instruments, and cause unprotected cutting edges to dull. Moisture also can adversely affect electronics. To avoid this, it is of utmost importance to clean and thoroughly dry the instruments before sterilizing by autoclave. One way to reduce progressive corrosion of carbon steel instruments is to dip them in an anticorrosive solution prior to autoclaving (Stach et al., 1995; Holmlund, 1965). In surgical trays, contact between instruments of dissimilar metals should be avoided to prevent galvanic corrosion.

Damage on polymers can vary from a little oxidation to complete distortion and melting, depending on the polymer composition and properties. It is not possible here to do a complete review of polymers regarding steam sterilization. More information can be found in books (Rogers, 2012a, b). It is important to mention that some polymers can be safely sterilized by steam. This is the case of PP, PTFE, aromatic polyurethanes, nylons, Tyvec, polycarbonate, cellulose (papers), etc. Others will undergo mild to severe changes. Steam sterilization of certain polyurethanes may result in a toxic hydrolytic by-product, dimethyl aniline (Shintani, 1995). The number of plastic materials capable of being steam sterilized will vary considerably with the selected temperature of sterilization. To accommodate more heat-sensitive polymers, there is trend toward heat sterilization at lower temperature, in combination with other agents (e.g., acids to modify pH) and takes place at 110–115°C, but for much longer time than at 121°C. This so-called ‘low-temperature’ steam sterilization is yet still subject to controversy. In contrast, fewer materials can be sterilized by flash sterilization, which uses higher temperatures (134°C, 3–6 min in vacuum with steam pulses). Flash sterilization, also called immediate-use steam sterilization, is sometimes used in operating rooms when a surgical instrument or device is needed urgently (Carlo, 2007), but it is not recommended for implants.

16.3.3.2 Dry heat sterilization

To avoid metallic corrosion, dry heat sterilization can be used as an alternative, but it is less efficient than wet heat and requires longer times and/or higher temperatures. In order to accomplish the same effect with dry heat in an oven, the temperature needs to be increased to 140°C for 3 h or 160–170°C (320–338°F) for 1 or 2 h (Block, 2000; Kowalski and Morrissey, 2004). Dry heat can sterilize some electrical components without damaging them, and it can sterilize metals without producing corrosion. It is not often used in the MD industry, except for silicon prosthesis, thermoresistant powder, and drug-device combination (Rogers, 2012a; Chapter 2).

16.3.4 EO gas sterilization

EO gas sterilization has been widely used in the biomedical industry as well as in healthcare centers, especially for temperature-sensitive materials. However, due to potential hazards of EO to patients, staff, and the environment, its use in healthcare centers is decreasing and may even be banned in several countries within a few years or decades. But it remains a sterilant of choice for industrial sterilization of many MD containing thermolabile plastic, elastomeric polymers, and electronic parts (Mendes et al., 2012).

EO gas (Fig. 16.4) is an alkylating agent that reacts with the cellular constituents of organisms, such as nucleic acid and functional proteins, including enzymes, which leads to consequent denaturation. The addition of alkyl groups to proteins, DNA, and RNA in microorganisms prevents normal cellular metabolism and the ability to reproduce, which render microorganisms nonviable. EO sterilization takes place in a sterilization chamber under vacuum to prevent EO leakage outflow. Gas concentration, moisture level (between 30% and 80%), and temperature (between 40°C and 55°C) must be carefully controlled throughout the process (around 2 h) to ensure efficiency. This process is preceded by a preconditioning phase during which time the products are heated and humidified (humidity is synergistic for EO inactivation of spores), and followed by an aeration phase to remove EO residues.

The main advantages of this low-temperature chemical sterilization process are its effectiveness, its reliability, and more especially its compatibility with most materials, including all metals, ceramics, and most polymers. A few polymers can be, however, altered by this alkylating agent.

Unfortunately, EO gas has also been shown to be toxic, hemolytic, and mutagenic, and is classified as a potential carcinogen (A2). The United States Occupational Safety and Health Administration (USOSHA) permissible exposure limit is 1 part per million over an 8-h shift. Safety procedures must be taken to prevent exposure of personnel to EO, especially since this gas is odorless. Toxic EO residues or by-products (ethylene

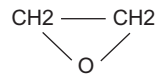


Fig. 16.4 Ethylene oxide molecule.

chlorohydrin, and the less toxic ethylene glycol) can also stay on MDs and desorb during their clinical use (Page, 1993). Regulations and ISO10993 standards (ISO10993-7, 2008) have been created to ensure that those resides remain below the safety limit. The aeration phase which must follow the sterilization process can last only a few hours for metallic devices but up to several weeks for some polymers that easily absorb EO and slowly desorb it (Handlos, 1980). This time period can be significantly shorter when using the new generation EO sterilizers designed to allow aeration within the sterilization chamber. An EO sterilization cycle duration is typically of thus 12 h to several days. While this is not a big issue for industrial sterilization, it requires hospital centers to buy several batches of similar devices to ensure their availability.

Another safety concern is that EO is flammable and highly explosive. Mixed with air at a ratio of at least 3% EO gas forms an explosive mixture. Commonly used to stabilize EO in the past, CFC gas is now forbidden by regulations due to the ozone depleting nature of CFCs. Hydrochlorofluorocarbons (HCFC) with smaller ozone depletion potential will also very soon be banned. Many industrial sterilization settings now use 100% EO, which requires intrinsically explosion-safe equipment and instrumentation. EO can be mixed with CO_2, but this requires a high-pressure process. In industrial settings, pure EO is increasingly combined with nitrogen inert gas to avoid contact with O_2 and risk of explosion.

Finally, due to EO toxicity, several counties such as Canada, Europe, and the United States have introduced regulations to limit the amount of EO released in the atmosphere (Environment Canada, 2005). Catalytic converters (converting EO in CO_2 and water) are a solution for industrial centers but healthcare centers tend to abandon this technique. This situation requires a safe alternative to EO for reprocessing heat-sensitive MDs.

16.4 Alternative sterilization methods

The main low-temperature alternatives to EO include LTHPGP sterilization, vaporized hydrogen peroxide (VHP), ozone, chlorine dioxide, and immersion into liquids such as peracetic acid or formaldehyde solution.

16.4.1 LTHPGP sterilization

LTHPGP sterilization, marketed under the trade name Sterrad [Advanced Sterilization Products (ASP), Johnson and Johnson, Irvine, CA] is the widespread novel technology in North America and Europe. This process combines an oxidative chemical phase (VHP, a strong antimicrobial agent), followed by low-temperature plasma. The five phases or stages of the LTHPGP sterilization process consist of vacuum, H_2O_2 injection, diffusion, plasma, and vent (Fig. 16.5) (Rutala et al., 1999). Briefly, after vacuum and diffusion of H_2O_2, an electromagnetic field is created in which the hydrogen peroxide vapor breaks apart, producing a low-temperature plasma cloud, a partially ionized gas that contains UV light and free radicals. Following the reaction, the activated

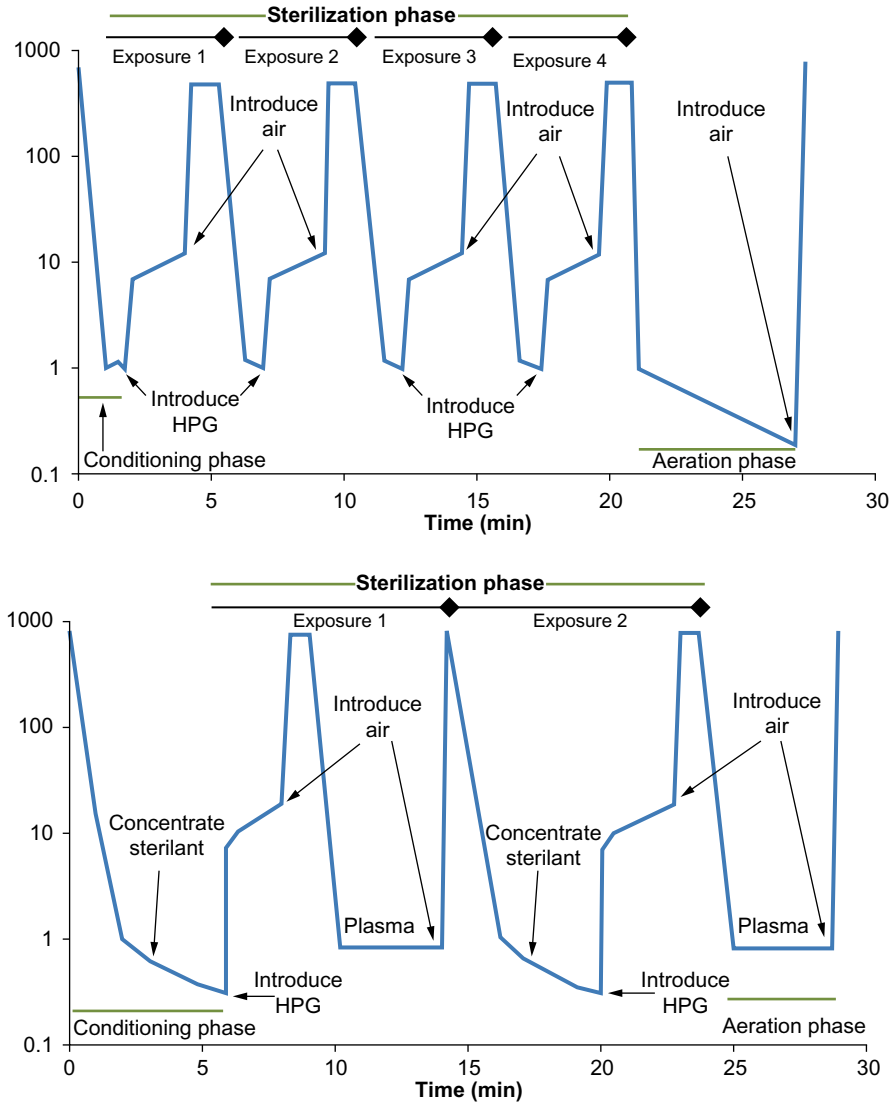


Fig. 16.5 Process diagram of two hydrogen peroxide gas sterilizers: STERRAD 100 NX (Advanced Sterilization Products, Johnson and Johnson) and V-Pro maX (from STERIS) (HPG: hydrogen peroxide gas).
Source: Nancy A. Robinson, phD and Randal W. Eveland, phD, Using HPG sterilization for heat-sensitive devices, https://www.hpnonline.com/ce/pdfs/1501cetest.pdf, with permission from STERIS.

components lose their high energy and recombine to form oxygen and water. Although most inactivation efficiency is provided by the chemical phase, gas plasma can further kill microorganisms and helps in eliminating H_2O_2 residues (Lerouge et al., 2002). All the process is done at temperatures below 55°C.

The first Sterrad system was cleared in 1993 as an alternative to EO and has known wide success with several thousand systems in clinical facilities. In several countries, it has become the most common low-temperature alternative to EO in healthcare centers. The newest system (Sterrad100NX) offers a standard cycle of 47 min, an express cycle of 24 min for rigid endoscopes and batteries, and a 60 min cycle for flexible endoscopes.

Sterrad sterilization is an interesting technology since it is a fast, low-temperature process, in which chemical active species disappear practically immediately after the plasma power is turned off; by-products are water vapor and oxygen. It is, therefore, potentially safer for healthcare workers, patients and for the environment, and this eliminates the need for aeration or ventilation. In hospital centers, the quick instrument turnaround decreases the need for duplicate inventories and associated costs. Moreover, as discussed later, the latest Sterrad technology has been shown able to destroy prions (Rutala and Weber, 2013). Sterrad systems' efficiency and safety have been tested on hundreds of devices from many different manufacturers.

However, the technology has also limitations. The main one is the limited penetrability of vaporized and plasma reactive species into the innermost areas, lumens, and packaging materials. This limits the size of each sterilization load, and impairs the efficiency for some devices, especially those with small diameter/length ratio of lumens. Failure of the process is also quite common. Sterrad sterilization systems and operation are relatively expensive. Finally, material damage, especially to polymers, can be induced by oxidative species (Lerouge et al., 2000a). Little is known about this issue compared to the numerous data acquired regarding alterations by radiation or heat sterilization. Polyacetal and nylons may have limited life. Paper, cellulose, and linen absorb H_2O_2 and cannot be processed by this technique.

More generally, low-pressure plasmas have been shown to kill microorganisms very rapidly (Lerouge et al., 2000b); other sterilization processes based on the gas plasma processes are under development (Kylian et al., 2006, 2008; Baxter et al., 2005; Halfmann et al., 2007). It is a promising technology in that it acts rapidly, does not leave toxic residuals on processed parts or in the exhaust gas, and the temperature of a substrate usually does not exceed 60°C. This field is rapidly moving forwards, for sterilization as well as for cleaning processes.

16.4.2 Vaporized hydrogen peroxide

Another interesting alternative to EO is simply VPH, without plasma, as the V-PRO maX Low Temperature Sterilization System (Steris) (Fig. 16.5).

This technology is designed with three sterilization cycles to efficiently sterilize a variety of instrument types, including one for flexible scopes. It can process loads up to 50 lb., and there is less risks of avorted cycles due to humidity, but higher risks of H_2O_2 residues since there is no plasma process to retrieve them at the end of the cycle. VPH can also be interesting to multiple sterilization of laparoscopic instruments (Scharf et al., 2018).

Finally, since the active agent is the same than LTHPGP sterilization, the limitations in terms of materials are similar. Thus, the technology cannot be used for liquid,

linens, powders, or any cellulose materials. It requires synthetic packaging (PP) and there is still limited materials compatibility data (Rutala and Weber, 2013).

VPH is presently spreading out in hospital centers, as replacement of EO.

16.4.3 Ozone sterilization

After being used for decades in water decontamination (Dufresne et al., 2008; Murphy, 2006), Ozone (O_3) has also been proposed for sterilization of MD. Ozone is an oxidative gas, which quickly and effectively deactivates microorganisms by denaturing cell membranes. It can be created in an enclosed ozone generator by passing oxygen through an electrical field that converts the oxygen (O_2) into O_3. The main advantages of ozone sterilization are low temperature (temperature range of 30–36° C), safe and easy use, and the absence of toxic by-products or residues. Moreover, since operation requires only water, oxygen, and electricity, operation costs are low.

However, O_3 is a very strong oxidizer. Moreover, the humidity within the sterilization chamber is high, a factor that may cause natural rubber and some plastics to degrade. Metals may also corrode using this technique. Ozone sterilization, therefore, led to damage a lot of materials. Therefore, the ozone sterilizer for MDs developed by TSO3 (Québec, Canada) has now being replaced by STERIZONE, a sterilizer using a mixture of ozone and hydrogen peroxide.

SterizoneVP is designed to sterilize all your low-temperature sterilizable devices, including some of the most complex and sensitive devices like the multichanneled endoscopes such as duodenoscopes, gastroscopes, and colonoscopes. It was cleared in Canada in 2015, but not for implants or devices intended to be in contact with the human body for more than 24 h.

16.4.4 Other sterilization techniques

Other sterilization techniques for healthcare centers are under decline or in development. For example, low-temperature steam and formaldehyde (LTSF) (ISO 25424:2009) used in European countries (the United Kingdom, Sweden, Holland, and Germany) instead of EO (Rogers, 2006). It shares many characteristics of steam sterilization but at lower compatible temperatures (65–85°C). Formaldehyde is, however, toxic and a potential carcinogen. Gaseous formaldehyde has been around for many years but is used less than it was previously because of toxicity, odor, and carcinogenicity. It is still used in several countries, mainly in Asia.

Another available alternative for chemical sterilization is chlorine dioxide gas (ClO_2), an oxidative gas, which is best efficient at temperatures ranging from 25°C to 30°C (Kowalski and Morrissey, 2004). The process has been shown to be effective for the sterilization of medical products. It is relatively rapid (1.5–3 h) in duration, and there is little or no need for poststerilization. However, this strong oxidative gas also requires prehumidification and may corrode some materials.

Liquid sterilization, consisting of immersing devices in peracetic acid or glutaraldehyde-based solution, is also commonly used for reusable endoscopes but should be considered as a high-level disinfection owing to the efficiency limits and

the inability to conserve sterility after sterilization (Rutala et al., 1998). The YSTEM 1E Liquid Chemical Sterilant Processing System (Steris) uses a liquid peracetic acid solution with a proprietary anticorrosion formulation to reprocess metallic endoscopes, cameras, or other long lumen instruments. The main limitation with liquid chemical sterilants is that the MD cannot be wrapped during processing; therefore, it is impossible to maintain sterility following processing and during storage (Rutala and Weber, 2013; Rutala and Weber, 2016). Moreover, to limit the duration of the treatment, the process often lead to disinfection instead of real sterilization.

Chemical liquid sterilant (glutaraldehyde, peracetic acid, liquid hydrogen peroxide, etc.) are reserved to heat-sensitive critical and semicritical patient care items that can be immersed (Rutala and Weber, 2013; FDA, 2012).

Therefore, while irradiation and EO are still widely used in industry, healthcare centers are still looking for the ideal technique to replace EO as standard procedure for heal-sensitive material, and there is a large variety and turnover of chemical sterilization techniques. Pulsed high-intensity light sterilization and microwave sterilization have also been the subject of a number of patents, but without commercial systems at this time.

At the standard temperature (121°C), steam remains the shorter process in healthcare centers, with about 30 min (including all steps), compared to 1–6 h for dry heat, ~15 h for EO, 24–60 min for Sterrad, and 42–55 min for hydrogen peroxide (Rutala and Weber, 2013).

16.5 New challenges for sterilization

16.5.1 Prions

Healthcare resterilization is challenged by the risk of transmission of prions (short for proteinaceous infectious particle). Stanley Pruisner, winner of the Nobel Prize in Physiology or Medicine in 1997, determined that a prion is neither bacterial nor fungal nor viral, and contains no genetic material. It is a protein that occurs normally in a harmless form but can fold into an aberrant shape, able to self-replicate and to be the agent of infection in a variety of degenerative brain diseases, such as Creutzfeldt-Jakob disease (CJD), fatal familial insomnia, an unusual form of hereditary dementia known as Gertsmann-Straeussler-Scheinker disease, or the well-known bovine spongiform encephalopathy (BSE) in animals (Prusiner, 1995; Rosenberg, 1997).

Prions have been shown to be transmissible via several routes, including transplantation and contaminated medical products. They are notoriously resistant to processes known to inactivate bacteria, spores, and viruses (Steelman, 1999; Taylor, 2000; Zobeley et al., 1999). None of the conventional sterilization procedures has been shown to be completely efficient. Since these diseases are progressive and cannot be diagnosed efficiently, preventing their transmission is a real challenge. To prevent accidental transmission of CJD, various decontamination procedures have been adopted for reusable MDs in contact with high-risk tissues, such as instruments for brain, spinal cord, and eye surgeries. For patients with known or suspected CJD, it

is even recommended to discard instruments used for surgery, since no proven technique is available.

Thus, the World Health Organization (WHO) recommend incineration of prion-contaminated surgical instruments but, since MD can be very costly, they assembled several options with what prion-contaminated surgical instruments could be decontaminated, cleaned, and terminally reprocessed with a reasonable margin of safety. Promising results showed elimination of detectable levels of infectivity after using an alkaline cleaner followed by autoclaving (Fichet et al., 2004; Lawson et al., 2007; Lemmer et al., 2008). One of the recommended procedure by the WHO is immersion in NaOH 1 N or sodium hypochlorite NaOCL, 1 N, followed by steam sterilization for 30 min or 1 h at 121°C (Sehulster, 2012). However, most materials do not sustain such aggressive conditions.

In addition to steam (Rogers, 2012a), oxidative sterilization techniques showed an effect against prions, for example, enzymatic cleaning preparation in conjunction with gaseous hydrogen peroxide (Fichet et al., 2007) and LTHPGP (Rogez-Kreuz et al., 2009). Gaseous hydrogen peroxide decreased the infectivity of prions and/or the level of the protease-resistant form of the prion protein on different surface materials. However, the efficiency of this treatment depended strongly on the concentration of hydrogen peroxide and the delivery system used in MDs, because these effects were more pronounced for the new generation of Sterrad technology. The SterradNX sterilizer was found to be efficient (Rogez-Kreuz et al., 2009). In contrast to the gas form, liquid peroxide was not effective. Despite these interesting results, the WHO still recommend incineration of contaminated instruments. For instruments used on patients at risk, in particular all instruments used in brain and eye surgery, such sterilization procedure may be an option. Indeed, the diagnostic of such degenerative diseases may take years, which renders the risk assessment difficult.

16.5.2 Endotoxins

Endotoxins are another challenge for sterilization. Endotoxins are lipopolysaccharides found in the cell wall of gram-negative bacteria, which can induce inflammation and fever as an immune response in higher organisms. This is particularly true if endotoxins enter the blood stream. It can lead to anaphylactic shock and death of patients. A particular attention must, therefore, be taken with liquids (such water), which can contains an important load of bacteria and therefore, of endotoxins released when water is sterilized. Endotoxins can also be present on 'sterile' biomedical devices since sterilization processes do not remove microorganisms but simply deactivate them or partly destroy them. This risk has been illustrated in rare but serious clinical cases (Cookson et al., 1997). They are highly resistant to sterilization processes. Presently, the only procedure recommended by the United States Pharmacopeia (USP) is dry heat at 250°C during 30 min, or 180°C during 3 h, which is completely impractical for polymeric, and even metallic materials (Cookson et al., 1997; Nakata, 1993). Despite some studies showing the potential for depyrogenization of oxidative process such as LTHPGP or other plasma techniques (Kylian et al., 2006; Tessarolo et al., 2006), none of these processes have been recognized as fully efficient.

16.6 Cleaning

Surface cleaning is also an important manufacturing step, not only useful to decrease the bioburden (living organisms) before sterilization but also to eliminate contaminants originating from manufacturing processes, such as cutting or polishing fluids and particles, mold release agents, polymer processing aids, airborne contamination, etc. These can negatively impact on device biocompatibility and further processing, such as coating adhesion or bonding between two surfaces and corrosion resistance.

Conventional cleaning methods generally employ wet chemical techniques, such as the use of an aqueous surfactant solution with/without acids or organic solvents to dissolve and eliminate contaminant. Ultrasound can also be used as adjunct. However, these methods have several limitations, for example, aqueous surfactants may leave residues, even after several rinses. Organic solvents can also leave toxic residues and may degrade polymeric devices. Low-temperature plasma processes have a high potential for these kinds of applications and several processes have been patented. Plasma reactive species (UV and VUV emissions, oxygen or hydrogen radicals, etc.) are known to be able to etch surfaces without altering bulk properties and can remove contaminants. As mentioned, protein removal is also an important issue in a clinical setting, for reusable devices, since protein adsorbed on the device surface may alter its biocompatibility and prevent efficient resterilization. The use of plasma discharge for these applications is also under investigation (Kylian et al., 2008). Ozone is another possible process for surface cleaning by oxidizing surface dirt.

16.7 Standards and other sources of further information

Many regulations and standards provided by nongovernmental international organizations (e.g., the International Organization for Standardization, ISO (ISO/TC 198, Sterilization of Healthcare Products), or the EC for Normalization, CEN (CEN/TC 204, Sterilization of Medical Devices)), pharmaceutical compendiums, private organizations [such as the Association for the Advancement of Medical Instrumentation (AAMI)], and governmental agencies (e.g., US FDA) have been developed regarding sterilization issues, such as safety, validation, and evaluation of toxic residues (Reich et al., 2005). In the United States, the FDA is responsible for approving sterilization methods. In the United Kingdom, it is the Department of Health Sciences. Concerning standards, an attempt to harmonize some of the AAMI and CEN standards has resulted in many ISO standards, which are too numerous to describe in this chapter. Briefly, the main standards are ISO 11134 for industrial moist heat sterilization, ISO 11135 for EO, and ISO 11137 for radiation sterilization, which includes the use of X-rays as the sterilization agent. Standards regarding biological and chemical indicators are ISO11138 and 11140, respectively. An interesting although nonexhaustive description of standards is provided in Sterilization of Polymer Healthcare Products (Rogers, 2005; Chapter 2, Table 2.2). The reader can also refer directly to the ISO. More information on sterilization can also be found in books focused on sterilization (Lerouge and Simmons 2012; Block, 2000; Booth, 2001).

16.8 Summary

Sterilization is an important and problematic step that should be considered as early as possible in the design of any new MD intended for use in contact with sterile tissues, mucous membranes, or breached skin, in order to save money, time, and trouble. There is no singular sterilization method that is compatible with all healthcare products including drugs, polymers, devices, and materials, because of the severity of a process to meet the sterilization criteria and definitions. An ideal sterilization method (i) should be efficient and highly reliable (this can be achieved when the sterilant is highly penetrating and can be homogeneously distributed within the load); (ii) should be able to deactivate prions and endotoxins; (iii) should be easy to monitor, by checking that the required physical or chemical conditions were achieved within each package; (iv) should be easy, cheap, and safe to operate; (v) should be safe for patients and not leave any toxic residues on biomedical devices or in the environment; and (vi) should be compatible with all materials. As discussed, metallic alloys are generally compatible with most sterilization processes. However, devices are getting smaller and more fragile, with complex geometries, and often include polymeric compounds (such as coatings or adhesives) that require low-heat sterilization processes. The increasing use of drugs or biological products with synthetic materials, for example, in coated stents or tissue engineering applications, is also challenging.

The growing importance of polymers, on the one hand and the hazardous nature of EO on the other hand, has led to the development of novel sterilization methods, especially for healthcare centers. However, these have their own limitations. Therefore, no ideal sterilization technique presently exists. The parameters and effects of different sterilization methods must thus be evaluated and reviewed before selecting the best method for each application. As discussed earlier, a high variation of resistance to sterilization techniques is observed in biomaterials, particularly for polymers. It is recommended, when possible, to choose materials that are compatible with radiations. Manufacturers should take advantage of the new medical-grade materials compatible with radiation sterilization. In the case of reusable devices, their design should take into account that they must be cleaned and dried before they can be resterilized and that other sterilization methods than radiation will be used. Materials that are compatible with steam sterilization should then be favored when possible. Devices should be designed to avoid regions sealed off from the cleaning or sterilization process or allow the device to be disassembled to expose all parts. The efficiency and safety of sterilization will have to be demonstrated before device approval. Due to the increasing number and complexity of regulations and standards, many industrial manufacturers are going to outside contract sterilization.

References

Albert, H., Davies, D.J., Woodson, L.P., Soper, C.J., 1998. Biological indicators for steam sterilization: characterization of a rapid biological indicator utilizing Bacillus stearothermophilus spore-associated alpha-glucosidase enzyme. J. Appl. Microbiol. 85 (5), 865–874.

Baxter, H.C., Campbell, G.A., Whittaker, A.G., Jones, A.C., Aitken, A., Simpson, A.H., Casey, M., Bountiff, L., Gibbard, L., Baxter, R.L., 2005. Elimination of transmissible spongiform encephalopathy infectivity and decontamination of surgical instruments by using radio-frequency gas-plasma treatment. J. Gen. Virol. 86, 2393–2399.

Block, S.S., 2000. Disinfection, Sterilization and Preservation, fifth ed. Lippincott Williams & Wilkins.

Booth, A., 2001. Sterilization Validation and Routine Operation Handbook: Radiation. Technomics Publishing Company.

Bruck, S.D., Mueller, E.P., 1988. Radiation sterilization of polymeric implant materials. J. Biomed. Mater. Res. 22, 133–144.

Carlo, A., 2007. The new era of flash sterilization. Aorn J. 86, 58–68. quiz 69–72.

Collier, J.P., Sutula, L.C., Currier, B.H., Currier, J.H., Wooding, R.E., Williams, I.R., Farber, K.B., Mayor, M.B., 1996. Overview of polyethylene as a bearing material: Comparison of sterilization methods. Clin. Orthop. Relat. Res., 76–86.

Cookson, S.T., Nora Jr., J.J., Kithas, J.A., Arduino, M.J., Bond, W.W., Miller, P.H., Monahan, J., Hoffman, R.E., Curiel, T., Kaufman, D., Groves, B.M., Jarvis, W.R., 1997. Pyrogenic reactions in patients undergoing cardiac catheterization associated with contaminated glass medicine cups. Catheter. Cardiovasc. Diagn. 42, 12–18.

Crow, S., 1993. Sterilization processes. meeting the demands of today's health care technology. Nurs. Clin. North Am. 28, 687–695.

Dufresne, S., Leblond, H., Chaunet, M., 2008. Relationship between lumen diameter and length sterilized in the 125L ozone sterilizer. Am. J. Infect. Control 36, 2917.

Environment Canada, 2005. Guidelines for the reduction of ethylene oxide releases from sterilisation applications. In: C.D.O.T, (Ed.), Environment. Government of Canada, Ottawa.

FDA (Food and Drug Administration). FDA-Cleared Sterilant And High-Level Disinfectants With General Claims for Processing Reusable Medical and Dental Devices-March 2009. Available from: http://www.fda.gov/cdrh/ode/germlab.html. Accessed December 15, 2012.

Fichet, G., Antloga, K., Comoy, E., Deslys, J.P., McDonnell, G., 2007. Prion inactivation using a new gaseous hydrogen peroxide sterilisation process. J. Hosp. Infect. 67, 278–286.

Fichet, G., Comoy, E., Duval, C., Antloga, K., Dehen, C., Charbonnier, A., McDonnell, G., Brown, P., Lasmezas, C.I., Deslys, J.P., 2004. Novel methods for disinfection of prion-contaminated medical devices. Lancet 364, 521–526.

Halfmann, H., Bibinov, N., Wunderlich, J., Awakowicz, P., 2007. A double inductively coupled plasma for sterilization of medical devices. J. Phys. D. Appl. Phys. 40, 4145–4154.

Handlos, V., 1980. Kinetics of the aeration of ethylene oxide sterilized plastics. Biomaterials 1, 149–157.

Hill, D., 1998. Design Engineering of Biomaterial for Medical Devices. John Wiley, Chichester.

Holmlund, L.G., 1965. Steam corrosion and inhibition in autoclave sterilization of dental and surgical steel materials. Biotechnol. Bioeng. 7, 177–198.

Hutchinson, F., 1961. Molecular basis for action of ionizing radiations. Science 134, 533–538.

Jorkasky, J., 1993. Special considerations for ethylene oxide: chlorofluorocarbons (CFCs). In: -Morrissey, R.F., Phillips, G.B. (Eds.), Sterilization Technology: A Practical Guide for Manufacturers and Users of Health Care Products. Van Nostrand reinhold.

Kowalski, J.B., Morrissey, R.F., 2004. Sterilization of implants. In: Ratner, B.D., Hoffman, A.S., Schoen, F.J., Lemons, J.E. (Eds.), Biomaterials Science: An Introduction to Materials in Medicine. Academic Press.

Kylian, O., Rauscher, H., Gilliland, D., Bretagnol, F., Rossi, F., 2008. Removal of model proteins by means of low-pressure inductively coupled plasma discharge. J. Phys. D. Appl. Phys. 41, 8.

Kylian, O.H., Hasiwa, M., Rossi, F., 2006. Plasma based De-pyrogenization. Plasma Process. Polym. 3 (3), 272–275.

Lawson, V.A., Stewart, J.D., Masters, C.L., 2007. Enzymatic detergent treatment protocol that reduces protease-resistant prion protein load and infectivity from surgical-steel monofilaments contaminated with a human-derived prion strain. J. Gen. Virol. 88, 2905–2914.

Lemmer, K., Mielke, M., Kratzel, C., Joncic, M., Oezel, M., Pauli, G., Beekes, M., 2008. Decontamination of surgical instruments from prions. II. In vivo findings with a model system for testing the removal of scrapie infectivity from steel surfaces. J. Gen. Virol. 89, 348–358.

Lerouge, S., Guignot, C., Tabrizian, M., Ferrier, D., Yagoubi, N., Yahia, L., 2000a. Plasma-based sterilization: effect on surface and bulk properties and hydrolytic stability of reprocessed polyurethane electrophysiology catheters. J. Biomed. Mater. Res. 52, 774–782.

Lerouge, S., Wertheimer, M.R., Marchand, R., Tabrizian, M., Yahia, L., 2000b. Effect of gas composition on spore mortality and etching during low-pressure plasma sterilization. J. Biomed. Mater. Res. 51, 128–135.

Lerouge, S., Tabrizian, M., Wertheimer, M.R., Marchand, R., Yahia, L., 2002. Safety of plasma-based sterilization: surface modifications of polymeric medical devices induced by Sterrad and Plazlyte processes. Biomed. Mater. Eng. 12, 3–13.

Lerouge, S., Simmons, A., 2012. Sterilisation of Biomaterials and Medical Devices. Woodhead Publishing Series in Biomaterials #46, 352 p. ISBN: 978–1–84569-932-1.

Leventon, W., 2002. Medical Device Sterilization: What Manufacturers Need to Know. MD&DI. Sept., p 52.

Massey, L., 2005. The Effects of Sterilization Methods on Plastics and Elastomers. William Andrew Publishing/Plastics Design Library PDL.

Mendes, G.C., Brandao, T.R.S., Silva, C.L.M., 2012. Ethylene oxide sterilization of healthcare products. In: Lerouge, S., Simmons, A. (Eds.), Sterilisation of Biomaterials and Medical Devices. Woodhead Publishing series in Biomaterials #46, pp. 71–95 Chap 4.

McCormick, P., Finocchario, C., Manchester, R., Glasgow, L., Costanzo, S., 2003. Qualification of a rapid readout biological indicator with moist heat sterilization. PDA J. Pharm. Sci. Technol. 57, 25–31.

Morrissey, F., Ratner, B.D., 1998. Sterilization. In: Hill, C.H. (Ed.), Design Engineering of Biomaterials for Medical Use. John Wiley, Chichester.

Murphy, L., 2006. Ozone—the latest advance in sterilization of medical devices. Can. Oper. Room Nurs. J. 24, 28, 30–2, 37–8.

Nair, P.D., 1995. Currently practised sterilization methods—some inadvertent consequences. J. Biomater. Appl. 10, 121–135.

Nakata, T., 1993. Destruction of typical endotoxins by dry heat as determined using LAL assay and pyrogen assay. J. Parenter. Sci. Technol. 47, 258–264.

Page, B.F.J., 1993. Special considerations of ethylene oxide: product residues. In: Morrissey, R.-F., Phillips, G.B. (Eds.), Sterlization Technology: A Practical Guide for Manufacturers and Users of Health Care Products. Van Nostrand reinhold, New York.

Parsons, B.J., 2012. Sterilisation of healthcare products by ionising radiations: principles and standards. In: Lerouge, S., Simmons, A. (Eds.), Sterilisation of Biomaterials and Medical Devices. Woodhead Publishing series in Biomaterials #46, pp. 56–69 (Chapter 3).

Plester, D.W., 1970. The effects of sterilising processes on plastics. Biomed. Eng. 5, 443–447.

Premnath, V., Harris, W.H., Jasty, M., Merrill, E.W., 1996. Gamma sterilization of UHMWPE articular implants: an analysis of the oxidation problem. Biomaterials 17, 1741–1753.

Prusiner, S.B., 1995. The prion diseases. Sci. Am. 272 (48–51), 54–57.
Reich, R.S., Schneider, P.M., Kinsley, C., 2005. Global Sterilization: Making the Standards Standard. MD&DI, p. 78. March.
Ries, M.D., Weaver, K., Rose, R.M., Gunther, J., Sauer, W., Beals, N., 1996. Fatigue strength of polyethylene after sterilization by gamma irradiation or ethylene oxide. Clin. Orthop. Relat. Res. 87–95.
Rogers, W., 2005. Sterilisation of Polymer Healthcare Products. Smithers rapra.
Rogers, W., 2006. Steam: Uses and Challenges for Device Sterilization. MD&DI, p. 80. March.
Rogers, W., 2012a. Steam and dry heat sterilization of biomaterials and medical devices. In: -Lerouge, S., Simmons, A. (Eds.), Sterilisation of Biomaterials and Medical Devices. Woodhead publishing series in biomaterials #46, pp. 20–54 (Chapter 2).
Rogers, W., 2012b. Sterilisation techniques for polymers. In: Lerouge, S., Simmons, E. (Eds.), Sterilisation of Biomaterials and Medical Devices. Woodhead publishing series in biomaterials #46, pp. 151–211. Chap 7.
Rogez-Kreuz, C., Yousfi, R., Soufflet, C., Quadrio, I., Yan, Z.X., Huyot, V., Aubenque, C., Destrez, P., Roth, K., Roberts, C., Favero, M., Clayette, P., 2009. Inactivation of animal and human prions by hydrogen peroxide gas plasma sterilization. Infect. Control Hosp. Epidemiol. 30 (8), 769–777.
Rosenberg, R.N., 1997. Nobel prize in physiology or medicine for 1997 awarded to Stanley B. Prusiner, MD. Arch. Neurol. 54, 1456.
Rutala, W.A., Gergen, M.F., Weber, D.J., 1998. Comparative evaluation of the sporicidal activity of new low-temperature sterilization technologies: ethylene oxide, two plasma sterilization systems, and liquid peracetic acid. Am. J. Infect. Control 26, 393–398.
Rutala, W.A., Gergen, M.F., Weber, D.J., 1999. Sporicidal activity of a new low- temperature sterilization technology: the Sterrad 50 sterilizer. Infect. Control Hosp. Epidemiol. 20, 514–516.
Rutala, W.A., Jones, S.M., Weber, D.J., 1996. Comparison of a rapid readout biological indicator for steam sterilization with four conventional biological indicators and five chemical indicators. Infect. Control Hosp. Epidemiol. 17, 423–428.
Rutala, W.A., Weber, D.J., 2001. New disinfection and sterilization methods. Emerg. Infect. Dis. 7, 348–353.
Rutala, W.A., Weber, D.J., 2013. Disinfection and sterilization: an overview. Am. J. Infect. Control 41 (5), S2–S5.
Rutala, W.A., Weber, D.J., 2016. Disinfection and sterilization in health care facilities: an overview and current issues. Infect. Dis. Clin. N. Am. 30 (3), 609–637.
Scharf, V.F., Dent, B., Jacob, M.E., Moore, B., 2018. Efficacy of vaporized hydrogen peroxide for repeated sterilization of a single-use single-incision laparoscopic surgery port. Vet. Surg. https://doi.org/10.1111/vsu.12905. 2018 May 17.
Sehulster, D., 2012. Prions and endotoxins: reprocessing strategies for reusable medical devices. In: Lerouge, S., Simmons, A. (Eds.), Sterilisation of Biomaterials and Medical Devices. Woodhead publishing series in biomaterials #46 (Chapter 10).
Setlow, B., Korza, G., Setlow, P., 2016. Analysis of alpha-glucosidase enzyme activity used in a rapid test for steam sterilization assurance. J. Appl. Microbiol. 120 (5), 1326–1335.
Shintani, H., 1995. Formation and elution of toxic compounds from sterilized medical products: methylenedianiline formation in polyurethane. J. Biomater. Appl. 10, 23–58.
Spaulding, E.H., 1972. Chemical disinfection and antisepsis in the hospital. J. Hosp. Res. 9, 5–31.
Stach, D.J., Cross-Poline, G.N., Newman, S.M., Tilliss, T.S., 1995. Effect of repeated sterilization and ultrasonic cleaning on curet blades. J. Dent. Hyg. 69, 31–39.

Steelman, V.M., 1999. Prion diseases—An evidence-based protocol for infection control. Aorn J. 69. 946–54, 956–67 passim; quiz 968–76.

Stichelbaut, F., Bol, J.L., Cleland, M.R., et al., 2007. A high performance X-ray system for medical device irradiation. Radiat. Phys. Chem. 76, 1775–1778.

Taylor, D.M., 2000. inactivation of transmissible degenerative encephalopathy agents: a review. Vet. J. 159, 10–17.

Tessarolo, F., Caola, I., Nollo, G., Antolini, R., Guarrera, G.M., Caciagli, P., 2006. Efficiency in endotoxin removal by a reprocessing protocol for electrophysiology catheters based on hydrogen peroxide plasma sterilization. Int. J. Hyg. Environ. Health 209, 557–565.

White paper (2017) A Comparison of Gamma, E-beam, X-ray and Ethylene Oxide Technologies for the Industrial Sterilization of Medical Devices and Healthcare Products, AUGUST 31, 2017 White paper. http://iiaglobal.com/wp-content/uploads/2017/10/White-Paper-Comparison-Gamma-Eb-Xray-and-EO-for-Sterilisation.pdf.

Woo, L., Sandford, C.L., 2002. Comparison of electron beam irradiation with gamma processing for medical packaging materials. Radiat. Phys. Chem. 63, 845–850.

Yagoubi, N.B., Boucherie, P., Ferrier, D., 1997. Radiosterilization and steam autoclaving sterilization effects on phosphite antioxidant stability. Nucl. Instrum. Methods Phys. Res., Sect. B 131, 398–404.

Zobeley, E., Flechsig, E., Cozzio, A., Enari, M., Weissmann, C., 1999. Infectivity of scrapie prions bound to a stainless steel surface. Mol. Med. 5, 240–243.

Part Four

Specific applications of metals for biomedical devices

Orthopedic applications of metallic biomaterials

17

T. Matsushita[*], *H. Takahashi*[†]
*Chubu University, Kasugai, Japan, †Teijin-Nakashima Medical Corp., Okayama, Japan

17.1 Introduction

Human beings are able to walk and pickup things because our joints move smoothly. If a bone is broken in an accident, we cannot move at all. If arthritis is growing worse, one suffers from pain and it becomes uncomfortable to walk. Bone fractures can be stabilized by performing a surgical operation using metallic plates and screws. Sometimes, tubular and stick-type metal pieces, such as intramedullary nails and γ-nails are used to treat a subtrochanteric fracture.

Joint replacement is performed for severe cases of articular diseases. As bones and joints are necessary to bear our body weight and make movement possible, materials used for orthopedic surgery must have high strength, toughness, and wear resistance. Therefore, metallic biomaterials are unavoidably employed as implant materials with a combination of ceramics and polymer materials. Fig. 17.1 shows examples of metallic implants used for replacing various skeletal site structures.

Typical metallic materials for orthopedic applications include of stainless steel, cobalt (Co)-chromium (Cr)-molybdenum (Mo) alloy, and pure titanium (Ti) and its alloys. These materials were originally developed for industrial uses, then were later utilized for clinical applications. Since metallic implants are exposed to a strong corrosive environment inside the body, metallic ions are released. The living body itself already contains almost all of the metallic elements. If the amount of any metal in the body exceeds a certain level, these elements become toxic. Therefore, metallic biomaterials have been altered so as to be compatible with the living body based on the clinical experience over a long period. Table 17.1 provides examples of new alloys that have been developed from the perspective of solving shortcomings.

Over the past 10 years, the mechanical characteristics of metallic biomaterials have been substantially improved and new manufacturing processes such as additive manufacturing (AM) have been developed and made available to prepare medical devices of complex structures that are difficult to fabricate using conventional processes. The newer implants have been designed so as to allow simple, less invasive surgical procedures. Examples of applications of these metallic biomaterials to orthopedic surgery will be introduced in this chapter.

Metals for Biomedical Devices. https://doi.org/10.1016/B978-0-08-102666-3.00017-1
© 2019 Elsevier Ltd. All rights reserved.

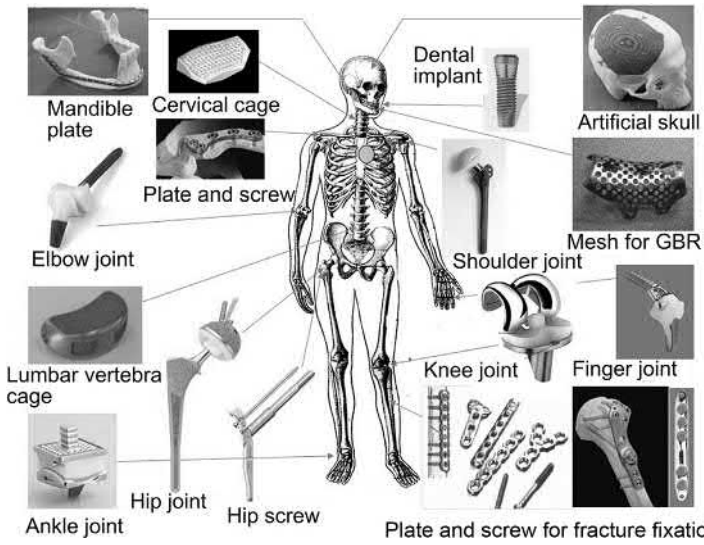


Fig. 17.1 Various implants made of metallic biomaterials.
With permissions from Kyocera Corp., Teijin-Nakashima Medical Corp., and Mizuho Co., Ltd.

Table 17.1 Development of metallic biomaterials

Materials	Subjects	Examples of alloys
Stainless steel	Corrosion resistance ⇒ **reducing C content** Skin allergy ⇒ **Ni free**	Fe-18Cr-8Ni-0.03C Fe-18Cr-12Ni-2.5Mo-0.03C Fe-23Cr-2Mo-1.4N
Co-Cr-Mo alloy	Wear resistance, high strength and Ni allergy	Co-29Cr-6Mo
Ti-alloy	Cyto-toxity ⇒ **V free** High strength and low elasticity ⇒ **β-alloy** High biocompatibility	Ti-6Al-7Nb Ti-6Al-2Nb-1Ta-0.8Mo Ti-15Mo-5Zr-3Al Ti-12Mo-6Zr-2Fe Ti-35Nb-4Sn Ti-15Zr-4Nb-4Ta Ti-29Nb-13Ta-4.6Zr

17.2 Total hip replacement

17.2.1 Materials for total hip replacement

A hip joint consists of a sphere and a socket. It allows the joint to be mobile in every direction with low friction and is extremely important for human movement. Approximately 60 years have passed since the modern artificial hip joint system began to be

used clinically. This technique became widespread after an artificial hip prosthesis was developed by Charnley during the 1960s (Charnley, 1970). Hip arthroplasty alleviates pain and improves function such that the patient is able to walk and thus enjoy an improved quality of life. Numerous people all over the world have benefited from hip replacement arthroplasty. Artificial hip joints can ordinarily serve for 20 years or more after surgery (Ilchmann et al., 1998; Mending et al., 2000; Caton and Prudhon, 2011).

Of course the effective lifespan of a prosthesis depends on the activity of the specific patient, but it is also affected by the materials constituting the artificial joint. Recently, advanced materials have been used in order to increase the lifetime to over 30 years. This requires (i) avoidance of materials associated with inflammation or cancer, (ii) high strength and ductility, (iii) early fixation and long-term stability, as well as (iv) reduced wear debris on the sliding surfaces. These requirements will be discussed in detail below.

Fig. 17.2 illustrates a typical example of an artificial hip joint. The stem is fixed to the femur. The stem needs to have high fatigue strength because it is loaded with more than three times the patient's body weight. Historically, stainless steel consisting of iron, chromium, and nickel was at first used due to the corrosion resistance provided by chromium. However, since this material was unable to bear high stress and had a risk of causing skin allergy, a Co-Cr-Mo alloy was adopted due to its higher strength and corrosion resistance. Cast material was initially used. Since this did not have sufficient strength, elements such as tungsten (W) and nickel (Ni) were added to enhance the plastic deformability of the alloy during hot forging. Recently, thanks to the improvement of materials processing technology, the Co-Cr-Mo alloys shown in Table 17.1 have been used. Ti, which has a high biocompatibility, has also proven to be useful as a metallic biomaterial.

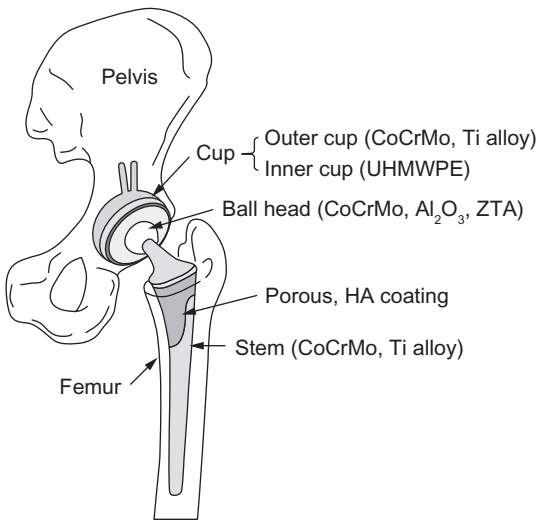


Fig. 17.2 Structure of artificial total hip joint.

Ti-6 aluminum (Al)-4 vanadium (V) alloy is a particularly versatile material having high mechanical strength in conjunction with corrosion resistance. Due to the concern about vanadium's cytotoxicity, the Ti alloys shown in Table 17.1 are applied clinically as V-free alloys, such as the alloys Ti-6Al-7niobium (Nb) and Ti-15Mo-5Zr-3Al. Subsequently, Ti alloys composed of elements harmless to the human body, such as tantalum (Ta), Nb, zirconium (Zr), and tin (Sn), for example, Ti-15Zr-4Nb-4Ta, Ti-29Nb-13Ta-4.6Zr, and Ti-35Nb-4Sn, have been developed (Okazaki et al., 1998; Kuroda et al., 1998; Matsumoto et al., 2005) and used for the stem and cup of hip joints as well as spinal fixation devices (Niinomi, 2012). Many kinds of metallic materials for prostheses have been developed, in fact, too many to be practically used. It is very important that a newly developed alloy strikes a balance between the merit of the new function and the material price.

There are two ways to integrate the stem and cup with bone. The first method is to use bone cement made of polymethyl methacrylate (PMMA). Numerous studies have indicated outcomes which showed the effects of the bone cement thickness, surface roughness of the stem, and the implant materials combination on clinical results. Furthermore, as bone cement using PMMA does not adhere to bone, bioactive bone cements have been investigated to strengthen bone bonding with the metallic material (Shinzato et al., 2001). The other method is to apply bioactive treatment to the implant surface, directly binding the bone and the implant. These two methods will be described later in more detail.

Wear debris, which is produced on the sliding surfaces of the ball head and the acetabular cup in artificial hip joints, can cause significant inflammation and pain, and has been a serious concern since the first use of Charnley's hip replacement. It leads to osteolysis around the implant. In order to suppress the generation of wear debris, certain novel materials have been developed. High-density polyethylene (HDPE) was first used for the acetabular cup. Then, ultra high molecular weight polyethylene (UHMWPE) came into use to improve the performance of the cup. Over the past two decades, cross-linked UHMWPE (HXLPE) cups have been reported to be advantageous for decreasing wear debris in combination with mirror-finished ball heads made of Co-Cr-Mo alloy or alumina ceramic and the lowering of the wear debris has been verified clinically (Kurtz et al., 2017).

Oxidation of cross-linked UHMWPE decreases its mechanical properties and results in an increase in wear debris due to the residual free radicals trapped inside. To prevent oxidation, UHMWPE containing vitamin E as an antioxidant has been developed (Tomita et al., 1999) and shown to prolong the life of the UHMWPE liner and cup for knee and hip joints, respectively (Teramura et al., 2008; Tanaka et al., 2008). After extensive experiments, the optimum processing conditions such as the vitamin E concentration and radiation dose to make a UHMWPE block were determined. Then, the block is machined and irradiated with gamma rays to cross-link the polymer chains in order to achieve higher wear resistance (Oral et al., 2008a, b; Turner et al., 2015).

Furthermore, it has been experimentally shown that wear debris is markedly reduced in a cross-linked UHMWPE in which the surface was photo-polymerized by the 2-methacryloyloxyethyl phosphorylcholine (MPC) (Moro et al., 2004).

This material has been clinically used for the acetabular cup of total hip joints in Japan (Moro et al., 2017). A combination of a hard ball with a hard cup, such as ceramic on ceramic or metal-on-metal (MOM), is also effective in reducing wear debris. Alumina (Hamadouche et al., 2002), zirconia-toughened alumina (Massin et al., 2014; Kurtz et al., 2014), and Co-Cr-Mo alloy (Rieker and Kottig, 2002) are available for this articulation.

17.2.2 Femoral stem design

For total hip replacement arthroplasty, the material of the femoral stem and how the shape fits the patient's bone structure are important factors. Over the past two decades, with the ongoing development of material, surgical techniques, fixation methods, and the resulting decrease of wear debris between the head and the cup, stem design has shifted toward preserving muscles and ligaments in order to reduce the postoperative dislocation rate, resulting in early postoperative rehabilitation and improved activity of the patient (Harrison et al., 2010). A number of short-stem designs are available for this purpose (McTighe et al., 2014). In minimally invasive surgery, shorter stems with a rectangular cross-section or the anatomical shape shown in Fig. 17.3B and C, respectively, are easily inserted (Derar and Shahinpoor, 2015; Kim and Yoo, 2016), whereas the conventional stem type shown in Fig. 17.3A is used tightly fitted to the medullary canal.

Using short femoral stems is bone preserving, muscle sparing, and can even be used for anatomical correction, resulting in excellent long-term results. In young patients, a standard stem may be used instead of a longer revision stem even when re-replacement is required. In the future, it will be necessary to clinically confirm that

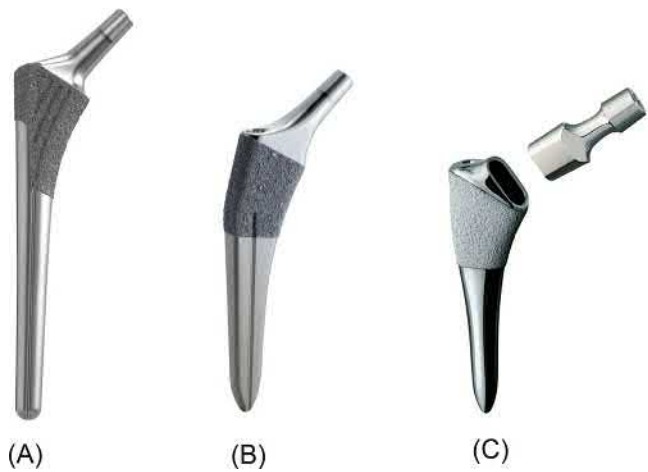


Fig. 17.3 Various types of femoral stems: (A) conventional type, (B) short type, and (C) anatomical type.
With permission from Kyocera corp.

fixation after surgery is done securely even if the stem length is shortened and to follow-up on the stability after the operation (Wittenberg et al., 2013).

In terms of material selection, the presence of metal ions released from the implants in the body is a concern (Dobbs and Minski, 1980; Hallab et al., 2001). Although Ti-6Al-4 V alloy is a well-known metallic biomaterial with superior properties, it contains vanadium (V) and thus exhibits cytotoxicity (Steinemann, 1980). To avoid this concern, Ti-6Al-7Nb (Semlitsh et al., 1985) and β-type alloy Ti-12Mo-6Zr-2iron (Fe) have been developed and clinically used as V-free Ti alloys. One of the authors and coworkers have applied the β-type alloy Ti-15Mo-5Zr-3Al to an artificial hip joint (Matsuda et al., 1997; Maehara et al., 2002). This alloy is biocompatible, as shown in Fig. 17.4 (Isama and Tsuchiya, 2002), and is registered in ISO as a metallic biomaterial. It possesses a tensile strength of 980 MPa and a fatigue strength of 600 MPa when annealed. With heat treatment strength as high as 1500 MPa with 14% elongation as well as higher corrosion resistance than Ti-6Al-4V can be achieved. The material's high strength allows a slender stem neck of 9 mm diameter, thus expanding the range of movement without impingement on the cup.

In the case of cementless artificial hip joints, the stem is generally exposed to high temperatures surface treatments to enhance bone-bonding ability. This treatment reduces the strength of β-type Ti and Ti-6Al-4V alloys. The author and coworkers have proposed Ti-6Al-2Nb-1Ta-0.8Mo as a biomaterial which contains no V and has good heat resistance (Anon., 1994). This alloy provides a high degree of corrosion resistance and superior biocompatibility. Its fatigue strength at room temperature after heat treatment up to 1000°C remains the same as that before heat treatment. This alloy was standardized in 2002 as JIS T 7401-3. In order to fabricate a porous layer on the surface of the stem and shell to attain bone ingrowth, Ti powders are plasma-sprayed and diffusion heat treated. If these heat treatments are applied to Ti-6Al-4 V alloy,

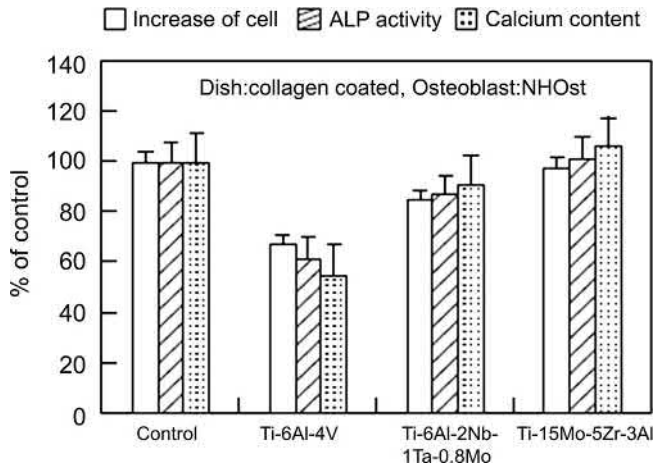


Fig. 17.4 Comparison of biocompatibility of vanadium-free titanium alloys with that of Ti-6Al-4V alloy.

however, the strength of the alloy is markedly reduced, so the stem loses its long life. This suggests that by using Ti-6Al-2Nb-1Ta-0.8Mo, it will be possible to design a stronger stem for cementless hip replacement.

Moreover, as the wear debris from the cross-linked UHMWPE acetabular cup is significantly reduced, the diameter of femoral head ball can be increased. According to the American Joint Replacement Registry data in 2016 (Anon., 2017), the femoral head/acetabular shell diameter combinations were 28 mm/42–46 mm, 32–34 mm/48–52 mm, and 36 mm/52–66 mm. A large diameter articulation has the advantages of lower wear and a lower risk of dislocation. Furthermore, this made it possible to achieve a wide range of motion without any impingement of the stem and cup. However, as the femoral head diameter increases, the wall thickness of the cup becomes thin, so it is necessary to pay attention to the clinical problems accompanying this feature (Girard, 2015).

On the other hand, when a large-diameter femoral head is used, the neck diameter needs to be thickened to withstand the high torque, and wear debris is generated due to the slippage between the stem neck and the femoral head. To overcome this problem, the neck taper of the femoral stem has been changed from a 10/12 taper to a 12/14 taper. As a result, the smaller sized neck of the stem is no longer needed.

The optimal design of the stem shape depends on the patient's bone structure, as well as clinical experience. This is the reason why a few hundred stem shape types have been developed throughout the world and many are supplied by manufacturers. Fig. 17.5 shows a cementless artificial hip joint designed using Ti-6Al-2Nb-1Ta-0.8Mo. The comparatively thin proximal portion of this stem is designed to preserve, the cancellous bone in the proximal portion of the femur as much as possible.

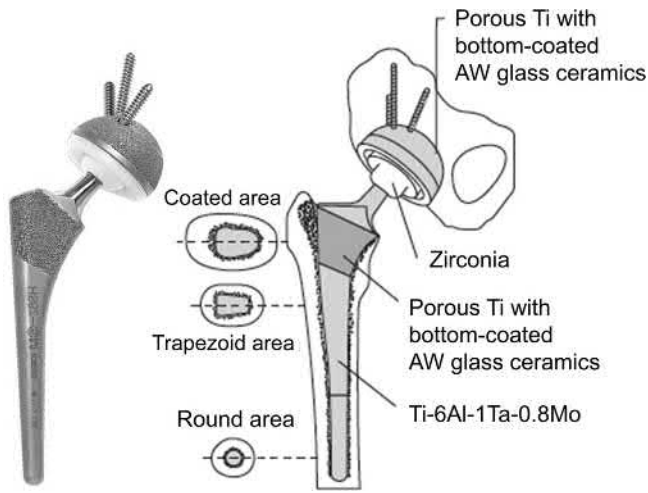


Fig. 17.5 Designs of cementless type artificial hip joint using Ti-6Al-2Nb-1Ta-0.8Mo alloy. Right: Originally designed with trapezoid area by Prof. Yamamuro, Left: Designed with straight back by Prof. Ninomiya.

As a result of the cancellous bone binding with the stem's porous surface, the force acting on the femoral head disperses into the femoral cortex to prevent stress concentration. The middle portion of the stem is designed with a trapezoidal cross section to prevent rotation of the stem. This part has a double-tapered shape, which is intended to support the load at the medial proximal position and secure fixation for extended periods. The clinical outcomes of this stem type have been excellent. However, rasping the double-tapered shape requires the surgeon to have a high skill level. Therefore, the double-tapered stem was changed to a straight shape as shown in Fig. 17.5 (left side) to secure easily drilling, with tapered reaming and rasping.

17.2.3 Cement fixation

With cemented fixation, bone cement penetrates the uneven bone surface formed by rasping to bind strongly with the bone. However, bone cement does not bind with the metallic implant (Barker et al., 2000). In the late 1970s, while an improved cement technique was introduced, early failure of cemented stem occurred and various causes such as poor cement technique, surface roughness, etc. were proposed (Barrack, 2000). Generally speaking, it is believed that a roughened surface is more effective in binding strongly at the stem-to-cement interface. In this condition, the strain in the stem and the cement is the same at the interface, and the cement is at a risk of fracture when the stress within the cement exceeds its strength. However, some researchers have reported that a polished surface produced better clinical performance since a subsidence of the stem generates compressive stress within the cement mantle (Collis and Mohler, 2002; Justin et al., 2006).

The thickness of the bone cement layer and its combination with the stem materials were examined to extend the life of fixation. It was found that, if the bone cement thickness too thin, it is responsible for failure; a thickness of around 2 mm is clinically preferable (Skinner et al., 2003). In terms of stem materials, Co-Cr-Mo alloy is reported to be preferable to Ti-6Al-4V (Issack et al., 2003). Otherwise, a Charnley-type stem made of Ti-15Mo-5Zr-3Al, introduced in the previous section, was used clinically by many surgeons. Its surface roughness was about Ra 0.3 μm, achieved by shot blasting, and the bone cement was 0.5 mm thick—the prosthesis showed favorable performance for over 10 years. This is attributed to the fact that the surface condition of the stem and its material are related to the friction with the bone cement.

A conventional cemented stem causes stress shielding at the proximal femur. A mirror-finished stem is advantageous for efficient load transmission from the stem to the bone by allowing subsidence of the stem when load is applied to the stem. If the cross section of the stem is given a triple taper, the subsidence of the stem creates compressive stress within the cement mantle and transmission of the load occurs at the proximal femur (Wroblewski et al., 2001). This prevents proximal femoral stress shielding, as is the case with cementless stems. Fig. 17.6 shows the difference in load transmission between a double and triple-tapered stem with a polished surface.

Bone cement made of polymethylmethacrylate (PMMA) is generally used for cement fixation in hip arthroplasty. However, it does not bond with bone, nor does it bond with metallic implants. As mentioned above, in order to increase the bonding

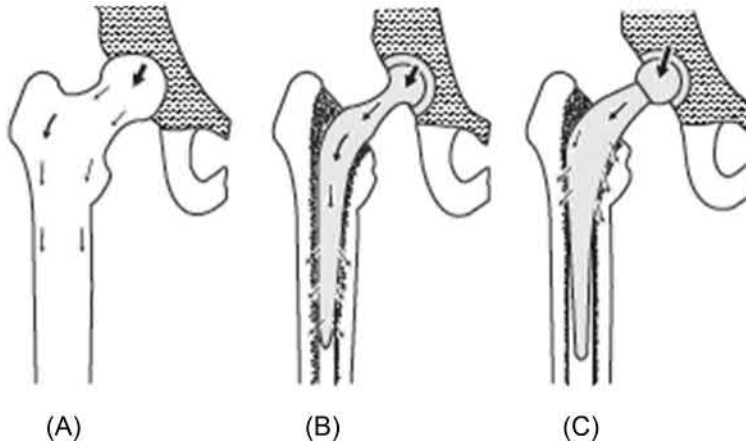


Fig. 17.6 Three types of load transmission patterns: (A) normal femur; load transmission through cortex, (B) conventional tapered stem; load transmission through the center axis and distal of stem, and (C) triple tapered stem; load transmission through proximal of stem.

force of the cement, the thickness of the cement layer, injection pressure, surface morphology of the implant, and irregularities on the bone side have been experimentally studied and were optimized clinically. Another approach is the use of bioactive bone cement. If the cement has bone bonding ability, the bonding force on the bone side will be increased and stable cement fixation will be realized. In addition, the use of bioactive bone cement may be a possible solution to problems associated with the use of PMMA bone cement in revision hip replacement (Ni et al., 2006).

When a bioactive glass is mixed into PMMA bone cement as a filler, it is necessary to choose the filler size to optimize the mechanical properties and osteoconductivity of the bone cement (Shinzato et al., 2001). When fine Ti particles are used as a bioactive filler mixed into PMMA powder, the composite material exhibits significantly higher bone-bonding strength than conventional PMMA bone cement, along with adequate mechanical strength and handling properties (Goto et al., 2008; Fukuda et al., 2011).

Since infection may occur in hip joint replacements using bone cement, releasing antibacterial ions from the implant surface is an effective way to suppress the infection (Price et al., 1996). For example, when the antibiotic gentamicin is contained in the bone cement, the gentamicin release can prevent infection when the joint is implanted in the body (Hendriks et al., 2005). In addition, if strontium (Sr) ions are included in bone cement, it is expected that Sr ions help promote bone growth (Ni et al., 2006).

17.2.4 Surface treatment for cementless fixation

In general, metallic biomaterials such as Ti and its alloys as well as Co-Cr-Mo alloy do not adhere to bone directly. One of the methods used to confer bone bonding on metallic implants is micro-texturing the implant surface by grit-blasting, acid etching and plasma spraying, etc. Another is to give the metallic implant surface micro- or

macroporous structures (Zhang et al., 2014). When metallic implants with porous surface layers are implanted or come into contact with bone, the bone grows into pores >50 μm in diameter (Pilliar, 1983), with an optimal range between 100 and 500 μm so as to be large enough to allow vascular infiltration and small enough to not impact the mechanical properties (Hulbert et al., 1972; Yamasaki and Sakai, 1992; Habibovic et al., 2006). This phenomenon has been applied to a femoral stem and an acetabular shell, and various kinds of design have been studied to achieve a cementless artificial hip joint that is to bind with the bone, using sintered beads, fiber mesh, and sprayed hydroxyapatite (HA).

Various surface treatment options are shown in Fig. 17.7. In the 1970s, a textured surface of the implant was expected to bring about strong fixation with the bone, but the clinical results were poor. Then, the implant surface was modified by a porous layer made of beads or fiber in the 1980s and fixation became stronger due to the bone ingrowth into the pores. For the stem, a porous layer formed along the whole circumference of the proximal stem generates a strong binding force with the bone and prevents stress shielding. It also prevents the invasion of wear debris to the interface, thus achieving favorable clinical performance. In the 1990s, a method for coating the roughened metal surface with HA was developed. This also achieved favorable clinical results (Coathap et al., 2001). When HA is plasma sprayed, the temperature during treatment reportedly becomes too high, deteriorating the bioactivity of the HA (Gross et al., 1998). To reduce deterioration, a HA flame-spray coating process has been developed and applied to stem and cup made of Ti-6Al-4 V (Fujisawa et al., 1995). The implants using this process are shown in Fig. 17.3.

The author and coworkers have used heat-resistant V-free Ti alloy, Ti-6Al-2Nb-1Ta-0.8Mo, to overcome the problem of decreasing strength up on heating. The plasma-sprayed porous layer had about 50% porosity, the pore diameter ranged from

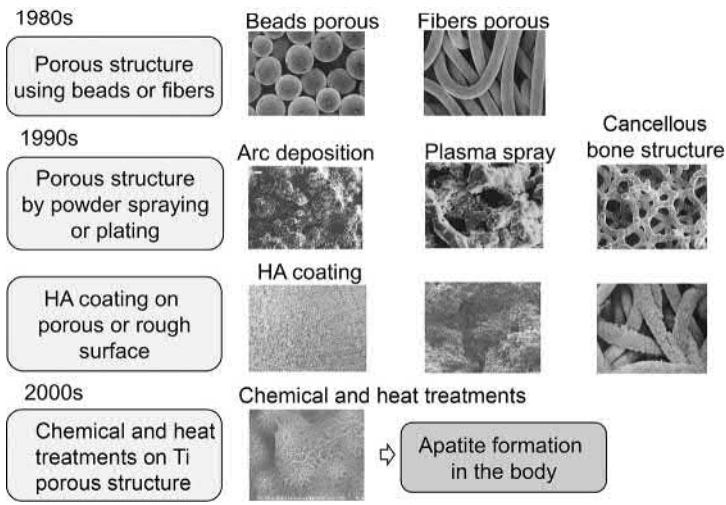


Fig. 17.7 Various surface treatments for both stem and cup in cementless hip joint.

200 to 400 μm and its tensile strength was 17 MPa. The tensile strength increased to 70 MPa after heat treatment at a temperature close to 1000°C under vacuum. This was followed by coating only the bottom areas of the Ti porous layer with apatite and wollastonite-containing glass ceramic (AWGC) to allow the bone to grow into the pores (Yamamuro and Takagi, 1991). An animal experiment verified that a high bonding strength with the bone could be obtained, and an artificial hip prosthesis employing this type of surface treatment is already commercialized in Japan.

Ti does not have any bone-bonding properties without surface treatment. In 1995, however, Prof. Kokubo invented a simple treating process to make Ti bioactive (Kokubo et al., 1996). In this process, a sodium titanate layer is formed by soaking Ti in NaOH solution at 60°C for 24 h and heating at 600°C for 1 h. The sodium titanate layer induces apatite formation on its surface when it is soaked in a simulated body fluid (SBF), which has ion concentrations (Na^+ 142.0, K^+ 5.0, Ca^{2+} 2.5, Mg^{2+} 1.5, Cl^- 147.8, HCO_3^- 4.2, HPO_4^{2-} 1.0, and SO_4^{2-} 0.5 mM) close to those of human blood plasma at 36.5°C, and the Ti binds with the living bone through the apatite layer. This novel method has been applied to a porous layer of Ti, plasma sprayed on the stem and cup. As shown in Fig. 17.8, a fine nanostructured network consisting of sodium titanate can be formed on the surface of the porous layer after the treatment. It is so bioactive that apatite grains precipitate and cover the entire surface of the treated Ti within a few days in SBF. Experiments also showed that when a porous body given such treatment is implanted in a dog's femur, rapid bone ingrowth is observed and that it has higher bonding strength than AWGC bottom coating (Nishiguchi et al., 2001). Based on these research findings, a clinical test on the artificial hip joint was conducted (Kawanabe et al., 2009) and 4 years after surgery, the system shows favorable

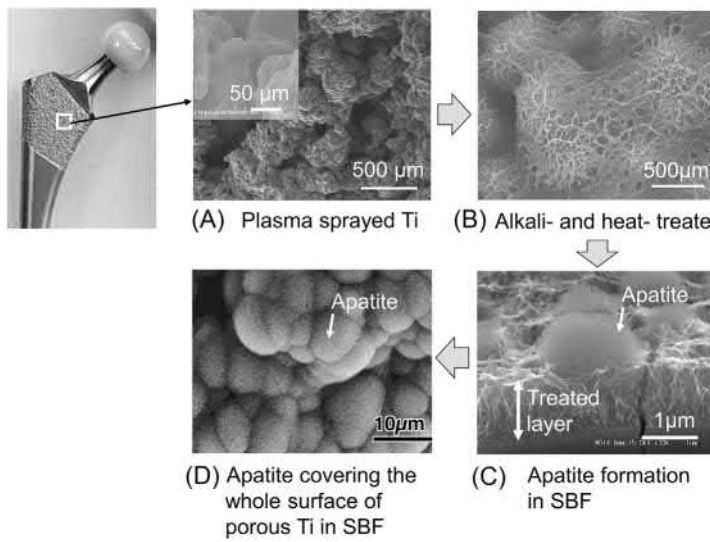


Fig. 17.8 Bioactivity of alkali- and heat-treated titanium porous layer plasma-sprayed on the stem.

clinical performance. In particular, bone ingrowth to the porous section was observed at an early stage and little to no thigh pain was reported. This NaOH- and heat-treated artificial hip joint has been used clinically in Japan since 2007 with an overall survival rate of 98% at 10 years after surgery (So et al., 2013).

In case of cementless total hip replacement, it is difficult to completely eliminate deep infection (Paxton et al., 2010; Gbejuade et al., 2015). When the device surface is coated with the antibiotic gentamicin, infection can be prevented by gentamicin release in the body (Neut et al., 2011). When coating with HA containing silver (Ag) oxide, the Ag ions elute in vivo, so it is possible to prevent bacterial infection such as methicillin-resistant *Staphylococcus aureus* (MRSA). Some modified methods have been developed, such as an electrochemical deposition of HA incorporating Ag (Ghani et al., 2012) and a method coating HA film coated with ionic silver via inositol hexaphosphate chelation based (Funao et al., 2016).

One practical approach is to spray a mixture of apatite powders and silver oxide particles on the surface of the devices (Akiyama et al., 2013). Ag ions will be subsequently released from the surface of the device, providing both bone bonding and antibacterial abilities. In a test in which samples spray coated with Ag-HA were embedded in rat tibia, antibacterial activity against MRSA was observed. An artificial hip joint treated with this method was developed in Japan in 2016 and is in clinical use.

A combined chemical and heat treatment was developed as another way to achieve metal ion release from the surface of medical devices. This method is called the alkali-calcium chloride-heat treatment method. It consists of the following steps: first, a substrate is soaked in a NaOH solution and then immersed in a mixed solution of a calcium chloride solution and a certain metal (M) chloride solution. The substrate is heated, followed by immersion in hot water (Kizuki et al., 2010). A sodium titanate-deficient calcium layer containing the metal (M) ion is formed on the Ti surface. When the device subjected to this treatment is implanted in the body, it is possible to achieve sustained release of the metal (M) ions in the body. For example, strontium (Sr) ions can be eluted from this implanted surface if $SrCl_2$ solution is used (Yamaguchi et al., 2014). It has been confirmed that early bone bonding to Ti was achieved by releasing strontium ions in rabbits (Okuzu et al., 2017). When Ga ions are released gradually from the device surface, antimicrobial properties and bone growth promoting effects are also exhibited (Yamaguchi et al., 2017).

These results show that it is possible to achieve the same effect as taking antibiotics by gradually releasing ions such as Sr, Mg, Ag, and Ga in the living body from the surface of a device, and such devices are expected to become available in the near future.

17.2.5 Joint bearing surface

Since the debut of Charnley's low-friction arthroplasty, polyethylene has been used for the acetabular cup. The wear debris generated by the friction between a polyethylene cup and a ball head induces aseptic loosening, so some way had to be developed to reduce the volume of wear debris. Table 17.2 shows the development in polyethylene and materials for the femoral head and cup since the 1960s as well as the pairings used in an effort to reduce wear debris.

Table 17.2 Combinations of acetabular cup and ball materials for artificial hip joint

Time	1960s			1980s		2000s		2020s
Cup and Ball head material	Polyethylene			Ultra high molecular weight PE (UHMWPE)				
				Hylamer	Cross-linked UHMWPE(HXLPE)			
								MPC grafted HXLPE
								Vitamin E-doped HXLPE
								Oxidized zirconium (Oxinium)
		Cobalt-chromium-molybdenum alloy						
					Zirconia	Alumina toughened zirconia		
				Alumina			Zirconia toughened alumina	
 Dia. (mm)	φ22	φ24	φ26	φ28	φ32	φ36	φ40～	
Articulation system (Cup/Ball head)	PE/SS		CoCrMo/CoCrMo					
		PE/CoCrMo		UHMWPE/CoCrMo		HXLPE/CoCrMo		MPC-HXLPE/CoCrMo
							HXLPE/Oxinium	
								VED-HXLPE/CoCrMo
			PE/Al_2O_3		UHMWPE/Al_2O_3		HXLPE/Al_2O_3	MPC-HXLPE/Al_2O_3
					UHMWPE/ZrO_2			
					Al_2O_3/Al_2O_3		ZTA/ZTA	MPC-HXLPE/ZTA

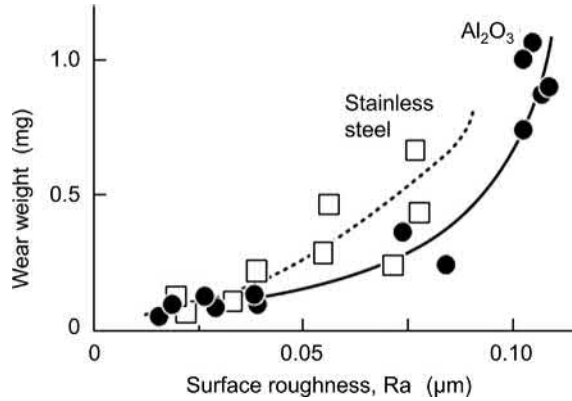


Fig. 17.9 Effect of surface roughness of ball head on wear weight of polyethylene cup at 10^6 cycles.
Reproduced from the table of Weightman and Light (1986).

One of the methods used to reduce wear debris is to polish the ball head to a smooth surface. As shown in Fig. 17.9, this is effective in decreasing the average surface roughness (Ra) to <0.02 μm (Weightman and Light, 1986). Thanks to advancements in the polishing technology, it is now possible to achieve a ball head surface roughness (Ra) of <0.01 μm. With metallic ball heads, however, it is difficult to maintain the ultra-mirror surface for long periods because of third-body wear debris. For example, the surface roughness was examined on 108 retrieved heads from 108 patients that were made from Co-Cr-Mo alloy and paired with conventional or highly cross-linked polyethylene. The average roughness value (Ra) was 0.18 ± 0.18 μm and the roughest femoral heads were correlated with recurrent dislocation and complete wear through the polyethylene liner. Their mean Ra was 0.56 μm (Ito et al., 2010).

Other methods include ceramicization of the metallic ball surface (Piconi et al., 2017). These include Ti nitride (TiN), Zr nitride (ZrN), Cr nitride (CrN), Zr dioxide (ZrO_2) coating on Zr-2.5Nb alloy and diamond-like carbon (DLC) coating, etc.

UHMWPE can be highly crystallized by applying high-pressure treatment (Hylamer) to enhance wear resistance. An in vitro wear test revealed only a small volume of wear debris, so it was expected to be a promising approach to suppressing wear debris. When used clinically, however, Hylamer produced a greater volume of wear debris than ordinary UHMWPE (Livingston et al., 1997; Iwase et al., 2003).

Acetabular cups made from cross-linked UHMWPE are predominantly used. γ-ray irradiation of approximately 25 kGy is a standard procedure in sterilizing medical products. During this process, however, free radicals are generated inside the polymer, and the material becomes partly cross-linked. During the 1970s, Oonishi et al. clinically adopted a HDPE cup irradiated with 1000 kGy of γ-rays and showed that it produced an extremely small volume of wear debris (Oonishi et al., 2001). However, because the irradiation dose is large, the polymer material becomes hard, with poor elasticity. When the γ-ray dose is lowered to 10–50 kGy, cross-linkage enhances the wear resistance while maintaining elasticity.

Currently, UHMWPE acetabular cups are heated to just below the melting point after irradiation and stored in nitrogen for longevity (Muruatoglu et al., 2001). Clinical data indicate smaller steady state femoral head penetration rates around

0.025 mm/year using a head made of Co-Cr-Mo alloy with a diameter of 28 mm together with highly cross-linked UHMWPE (HXPE) (McCalden et al., 2009; Whittaker et al., 2010; Howie, 2018). However, in vivo oxidation of cross-linked UHMWPE occurs due to residual free radicals that are trapped inside the material. HXPE with incorporated vitamin E showed better mechanical properties than conventional UHMWPE as well as improved wear resistance (Oral et al., 2008a, b; Turner et al., 2015). This was verified by clinical evaluation (Yamamoto et al., 2017).

Co-Cr-Mo MOM articulation has also been shown effective in reducing wear debris. This method was first attempted by McKee-Farrar. With subsequent improvements of metallic composition and superior polishing technology, this articulation method has been widely used in clinical applications. A hip resurfacing method in which the femoral head is covered with a hemispherical device made of Co-Cr-Mo alloy (MOM-type) was also used for patients with necrotized femoral heads. A lower wear rate of MOM was found in 231 retrieved articulations and the wear rate decreased to approximately 5 μm/year after a run-in period of approximately 1 year (Rieker and Kottig, 2002). On the other hand, there is a serious concern because Co and Cr ions released from the wear debris are present in the serum, even when the wear debris volume is small (Engh Jr et al., 2009; Posada et al., 2015; Munemoto et al., 2017).

A follow-up study postsurgery was performed to investigate the health effects of metallic ions released from the wear debris(Matharu et al., 2017). Whether the metallic ions generate cancer was also investigated. The results showed that the cancer incidence rates for male patients who had undergone hip replacement surgery were 6.2%, 4.8%, and 6.7%, respectively, when stemmed MOM, resurfacing MOM and other sliding surfaces were used. No particular problems were noted (Smith et al., 2012). Revisions due to adverse reactions to metal debris in various types of artificial hip joints have been reported; therefore, sufficient follow-up is required (Matharu et al., 2016).

The revision incidence over a period of 10 years after surgery using MOM devices supplied by six companies for hip resurfacing arthroplasty (HRA) was examined and the outcomes were compared with the results of total hip replacement (Seppanen et al., 2016). As a result, HRA showed good results until 4–5 years after surgery, but total hip arthroplasty (THA) was better after over 5 years. The Kaplan-Meier survival rate for the 10 years after surgery was 86% for HRA and 92% for THA. The main reasons for revision were aseptic loosening (40% of the total) in the case of HRA, whereas it was dislocation in THA. In addition, the revision rate of one company's device was particularly high, and this device is no longer in clinical use.

Alumina has a higher hardness than metal, so it can better maintain a mirror surface to reduce wear debris (Saikko et al., 1993; Dowson, 1995). The disadvantage of alumina is its brittleness that can lead to failure. Alumina on alumina articulation is also an attractive approach to reducing wear debris. Just as in the case of MOM, the generation of wear debris is low. Unfortunately, there are some complications with breakage, since alumina is a fragile material (Hasegawa et al., 2006; Lopes et al., 2012). In order to overcome this issue, smaller grain-sized alumina should be used and a combination of an alumina cup supported by a metallic shell, not a ceramic-polyethylene sandwich structure, should be adopted.

As zirconia is tougher than alumina, it would be expected to be suitable for the ball head. However, it causes a greater amount of wear debris than one made of alumina or Co-Cr-Mo alloy. This is attributed to the frictionally induced heat which is trapped inside the material because of the low heat conductivity of zirconia (Lu and McKellop, 1997) as well as the low-temperature phase transformation that may occur at temperatures close to 100°C under wet conditions. An effective method for suppressing zirconia's transformation is to add trace amounts of aluminum and to control the grain size. The manufacturing process must, therefore, be rigorously and thoroughly controlled.

In order to increase the toughness of alumina, an alumina matrix composite containing 10%–30% zirconia particles was developed. This alumina-zirconia composite (ZTA) showed improved wear characteristics (Lombardi Jr et al., 2010). As described in Table 17.3, ISO 6474 (Anon., 2010, 2012) requires high density solidification of highly pure alumina powder with a grain size of 2.5 μm or less together with four-points bending strength of at least 1000 MPa and biaxial bending strength of at least 600 MPa. ZTA has been adopted by artificial hip joint manufacturers all over the world for femoral heads and acetabular cups. Low abrasion and few cases of breakage have been reported (Kurtz et al., 2014).

Table 17.3 Limits for material properties of alumina ceramics by ISO standard

Revision year of the ISO standard		**1981**	**1994**	**2010**	**2012**
Types of alumina ceramic		**High purity alumina (ISO 6474-1:2010)**			**Zirconia-toughened alumina (ISO 6474-2:2012)**
Bulk density	($kg/m^3 \times 10^3$)	≧3.9	≧3.94	≧3.94	
Average relative bulk density	(%)				≧99
Basic material, Al_2O_3	(%)	≧99.5	≧99.5	≧99.7	60–90
$ZrO_2 + HfO_2$ (Amount of HfO_2 in ZrO_2)	(%)				10–90(≦5)
Sintering additive, MgO	(%)		MgO≦0.3	MgO≦0.2	≦10
Limit of impurities	(%)	≦0.1	≦0.1	≦0.1	≦0.2
Linear intercept grain size (μm)	Alumina Zirconia	≦7	≦4.5	≦2.5	≦1.5 ≦0.6
Mean four-points flexural strength	(MPa)	≧400	≧450	≧500	≧1000
Mean biaxial flexural strength	(MPa)		≧250	≧300	≧600

Recently, a new method for extending the longevity of a HXPE cup has been developed based on surface modifications using photo-induced graft polymerization, which is induced by ultraviolet irradiation onto the surface of a polymer cup soaked in an aqueous MPC (2-methacryloyloxyethyl phosphorylcholine) solution (Moro et al., 2004). After such treatment, brush-like structures of hydrophilic macromolecules are formed on the surface of the HXPE, as shown in Fig. 17.10, giving rise to hydration lubrication. Although the thickness varies depending on the treatment conditions, it is roughly 100 nm, and the surface layer is characterized by an extremely small water-contact angle (Kyomoto, 2009).

Fig. 17.11 shows the gravimetric wear in a hip joint simulation of HXPE cups with and without MPC grafting. The weight loss of the MPC-grafted cup is significantly less than that of the untreated cup. This effect was verified in long-term hip simulator

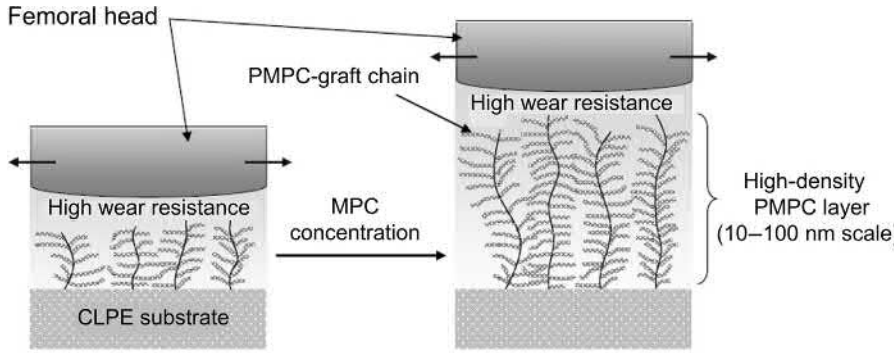


Fig. 17.10 Schematic illustration of the MPC-grafted layer with increasing MPC concentration (Kyomoto, 2009).

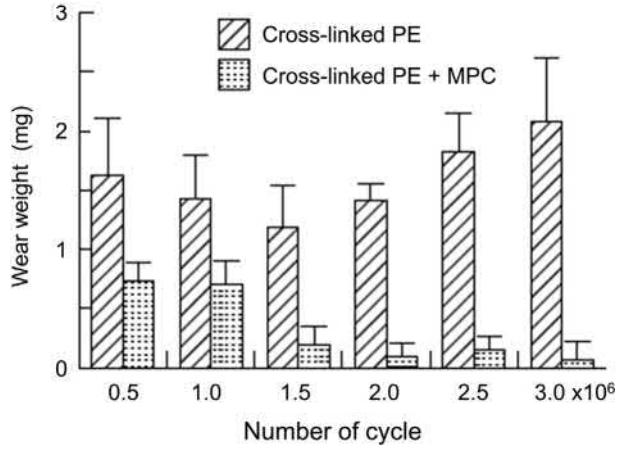


Fig. 17.11 Wear of MPC-grafted cross-linked UHMWPE cup in hip joint simulator compared with untreated cross-linked UHMWPE cup (Moro et al., 2004).

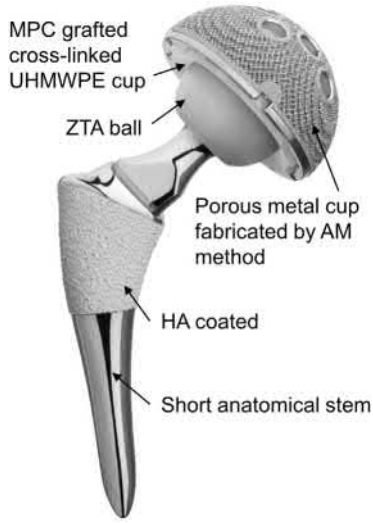


Fig. 17.12 Improved artificial hip joint composed of short anatomical stem with HA coating, ZTA ball-MPC grafted highly cross-linked polyethylene inner cup and porous metal cup fabricated using EBM method.
With permission from Kyocera Corp.

testing for 20×10^6 cycles (Moro et al., 2014). Based on these in vitro results, HXPE cups subjected to MPC treatment have been in clinical use in Japan. Three years after implantation, the wear of the HXPE cup was markedly reduced (Takatori et al., 2015). Fig. 17.12 shows an example of the latest improved artificial hip joint, which is composed of a ZTA femoral head ball and HXPE cup with MPC grafting as an articulating system, HA-coated short stem, and porous metal cup fabricated by electron beam melting (EBM) method.

17.3 Knee replacement

17.3.1 Various types of knee replacement

As a knee joint is indispensable to movement, it may not be possible to even walk due to the pain that arises from a disease of the knee joint. There are three types of medical treatments for knee joint disease. One of the options is total knee replacement, as shown in Fig. 17.13A, which can be an effective method for regaining function using a metallic component and polyethylene insert. However, the patient satisfaction is lower than in the case of total hip prosthesis replacement because in the current surgical technique both the anterior cruciate ligament (ACL) and posterior cruciate ligament (PCL) are removed, or only the ACL is surgically removed, despite the fact that these ligaments are necessary for stable movement of the knee joint.

When only "the inside" or "the outside" of the knee joint is damaged, partial knee replacement is an alternative procedure, in which the damaged side is replaced by

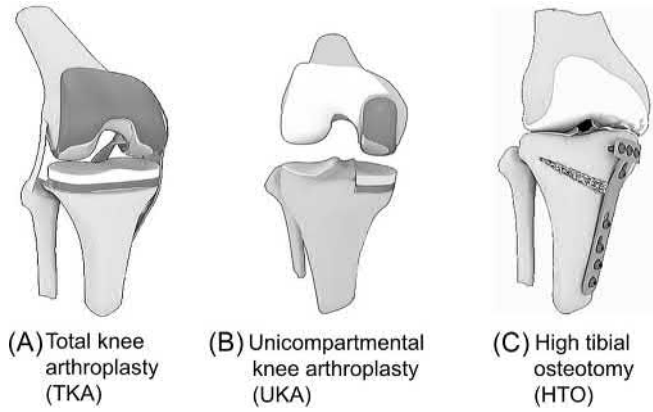


Fig. 17.13 Three types of medical treatments for knee joint disease.

artificial articulation composed of a metallic component and UHMWPE tray, as shown in Fig. 17.13B. This is known as unicompartmental knee arthroplasty (UKA). The damage often occurs on "the inside." A patient is more highly satisfied with UKA than with the TKA because UKA is less invasive and recovery after the procedure is faster. Clinical experience has shown that successful UKA acts more naturally. Furthermore, both fixed and mobile-bearing implants can yield excellent clinical outcomes >10 years, but tibial condylar fracture or wear of components sometimes occurs (Todd and Thomas, 2008).

Another surgical treatment of medial tibiofemoral osteoarthritis is high tibial osteotomy (HTO) (Sprenger and Doerzbacher, 2003; Amendola and Bonasia, 2009). When cartilage deformation occurs on one side of the tibial condyle, it can lead to O– or X-legs, resulting in one-sided stress on the knee joint. If the condition remains untreated for a long period of time, deformation or uneven wear of the articular cartilage occurs. To correct the lower limb alignment, HTO is performed. In this method, a wedge-shaped osteotomy is performed on the proximal part of the tibia, then the plate is fixed with screws, as shown in Fig. 17.13C. For early bone union in the osteotomy site, a bioactive ceramic substitute is used to fill the wedge-shaped space (Brosset et al., 2011). As a result, it is possible to return to work and play sports, since the joint surface is preserved. Rehabilitation is particularly important, because pain remains until the bone fusion in the wedge-shaped part is completed. The fixing plate is preferably as short and thin as possible, but at present, Ti alloy or Co-Cr-Mo alloy with a thickness of approximately 3 mm and a length of approximately 10 cm is used to maintain strong fixation.

17.3.2 Materials for knee replacement

Fig. 17.14 shows the structure of an artificial total knee joint forming the condyloid joint. It consists of a femoral component, a tibial component, and a patella. The majority of femoral components are made of Co-Cr-Mo alloys, but sometimes alumina or Ti alloys are used for patients with allergies to Co-Cr-Mo alloys. A femoral component

for UKA is made of Co-Cr-Mo alloy. In most cases, the tibial-side tray is made of Ti alloy and the insert is made of UHMWPE. The insert has grooves corresponding to the configurations of lateral and medial condyles. The tibial-side trays and inserts for UKA are made of the same materials as for femoral side. The patella, which is made of UHMWPE, slides on the surface of the femoral component. Similar to artificial hip joints, cemented and uncemented artificial knee joints are available. In addition, plates and screws made of Ti alloy are used for HTO.

17.3.3 Joint bearing surface

As the knee joint is a condyloid joint, rotation of lateral and medial condyles occurs in conjunction with sliding over the insert surface made of UHMWPE. This brings about the generation of wear debris. Considerable contact pressure is induced by the contact between the two condyles and the UHMWPE, and it is at a maximum slightly underneath the UHMWPE surface, causing delamination. If the UHMWPE insert is hard, a higher stress concentration is induced in the contact area between the insert and the femoral condyle, which makes it more likely for delamination to occur. Therefore, increasing the contact area between the UHMWPE and the femoral condyle may be advantageous for reducing the stress generated in the UHMWPE insert.

The addition of vitamin E to UHMWPE enables it to retain strength while remaining soft and flexible; which results in decreased wear debris (Tomita et al., 1999). According to an investigation of the effective vitamin E concentration and radiation dose on mechanical properties (Oral et al., 2008a, b), the cross-link density increases proportionally to the radiation dose and increases inversely proportional to the amount of vitamin E added. As these factors induce improved mechanical properties, HXPE with vitamin E may be advantageous under high stresses condition in total knee arthroplasty.

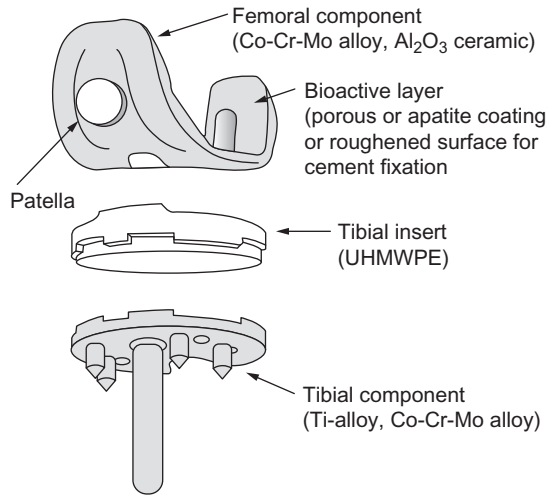


Fig. 17.14 Structure of an artificial total knee joint.

When a femoral component made of Co-Cr-Mo alloy slides over a UHMWPE surface, the roughness of the component surface determines the amount of wear on the UHMWPE. If a Ti alloy is used as a femoral component, the surface may be markedly scratched or damaged by a third body, such as fragments of bone cement, which accelerates the generation of wear debris. Although Co-Cr-Mo alloy is hard and its surface is mirror polished, roughening of condyles occurs clinically and thus UHMWPE wear increases. When a femoral component made of alumina is used, scratches are minimized and wear debris of UHMWPE is reduced, although a fracture of the alumina component may occur.

The above results suggest that a harder surface prevents scratches and provides low friction against UHMWPE. An oxidized Zr alloy femoral component was developed. It is made of wrought Zr alloy, Zr-2.5Nb, and its sliding surface is oxidized by thermal diffusion (Spector et al., 2001). The surface is coated with zirconia with a thickness of approximately 4 μm. This material is scratch resistant and provides low friction, while the toughness of femoral component is maintained due to the use of the wrought metallic alloy.

17.3.4 Design of knee joint with a large flexion angle

The knee joint has a sliding surface on the femorotibial side consisting of the femoral condyle and the tibial condyle, and on the patellofemoral side comprising the patella and the intercondylar fossa. Such an articulation has lower stability than the ball-and-socket in the artificial hip joint and creates articular movements with the support of ligaments and muscles. This movement is accompanied by rolling and sliding of the convex-shaped femoral condyle over the concave surface of the tibial condyle. In addition, the tibia rotates outwardly against the femur during flexion. This fact was recently taken into consideration when designing an artificial knee joint with a large flexion angle. Fig. 17.15 shows a novel total knee joint with the ball-and-socket joint in the mid-posterior portion of the femoral and tibial component. The surface 'A' is the same as that of the conventional femoral component. When the flexion angle exceeds 70 degrees, the hemispheric surface 'B' starts to work as a ball-and-socket joint to enlarge the flexion angle. This system allows a large flexion angle of around 140 degrees (Akagi et al., 2002).

The "mobile knee" realizes the natural movement of the knee described above. In this method, the UHMWPE insert can rotate around the pivot installed on the tray. As a result, the patient can bend the knee easily, even up to large flexion angles (Callaghan et al., 2001; Price et al., 2003). In employing the structure described above, it became possible to enlarge the area of contact between the femoral component and the UHMWPE insert, up to several times greater than conventional artificial knee articulation. The structure, moreover, helped to reduce the contact pressure induced in the UHMWPE insert and allowed stable articular movement. A concern with this method is that the dual sliding surfaces may produce an abundance of wear debris. It is, therefore, necessary to provide mirror finish on the surfaces of the tray and femoral component.

A third method is to design the shape of the femoral condyle to allow a movement similar to the natural human knee joint. Fig. 17.16 shows the shape of the femoral

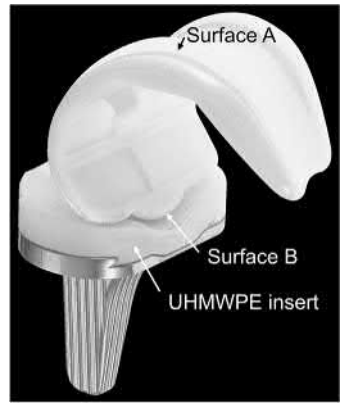


Fig. 17.15 Artificial knee joint with bisurface femoral component enlarging the flexion angle. The Femoral component cited here is made of a ceramic.
With permission from Kyocera Corp.

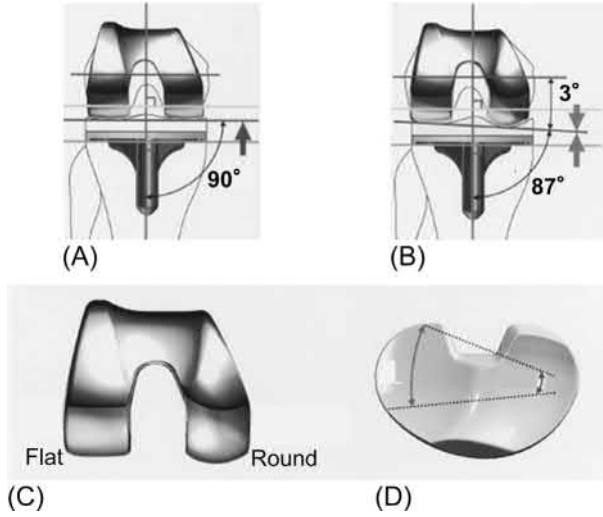


Fig. 17.16 New design of femoral component providing the anatomical motion of a natural knee: (A) conventional type of femoral component, (B) new type of femoral component; height difference of lateral and medial condyles, (C) asymmetrical shape of condyle, (D) external rotation of femoral component centering on medial condyle.
With permission from Teijin-Nakashima Medical Corp.

component and its movement opposite the UHMWPE insert. The lateral condyle of the femoral component is a flat surface, while the medial condyle is convex. There is a height difference of about 2 mm between the medial and lateral condyles. This design facilitates rotations centering on the medial condyle, making it possible to obtain a large flexion angle (Anon., 2009).

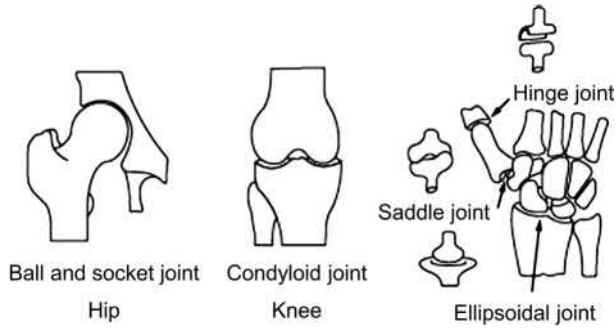


Fig. 17.17 Illustration of various types of diarthrodial joints.

17.4 Miscellaneous joint replacements

In addition to hip and knee joints, the human skeleton has numerous kinds of joints in the shoulder, elbow, wrist, and finger. These joints are suited to their functions, as shown in Fig. 17.17. Hip and shoulder joints are of the ball-and-socket type, enabling movements such as bending and rotating in all directions. The elbow joint, on the other hand, is a hinge type, whose primary movement is to bend in one direction. This movement may also be assisted by a slight rotation to increase the flexion angle. The wrist joint is a so-called 'oval joint' type, making two-way movements possible. The thumb has a saddle joint, allowing it to move in two directions.

Fig. 17.18 shows various kinds of artificial joints. The artificial shoulder joint (Fig. 17.18A) consists of a hemispheric head anchored to the tip of a stem and a socket. The stem is made of Ti alloy and its surface is coated with HA. The hemispheric head is made of either alumina or Co-Cr-Mo alloy and the socket is made of UHMWPE.

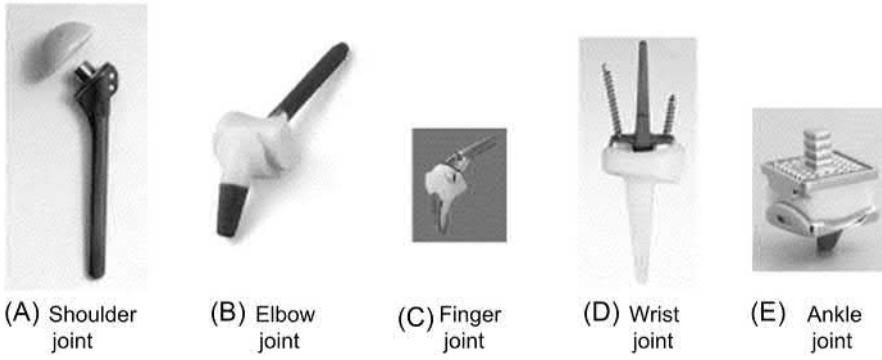


Fig. 17.18 Examples of various artificial joints: (A) shoulder joint, (B) elbow joint, (C) finger joint, (D) wrist joint, and (E) ankle joint.
Panel B: with permission from Kyocera Corp. Panel E: with permission from Teijin-Nakashima Medical Corp.

The artificial elbow joint (Fig. 17.18B) has a hinge-type sliding surface. On the humeral side, the stem, made of a Co-Cr-Mo alloy, is integrated with a drum-shaped cylinder. On the ulnar side, a receiver made of UHMWPE is attached to the tip of the Co-Cr-Mo alloy stem. Using this joint system, a flexion angle ranging from 0 to 100 degrees enables it to move together with a small relative rotation of both.

The artificial finger joint (Fig. 17.18C) has a structure resembling the artificial elbow joint. The sliding surfaces are comprised of Co-Cr-Mo alloy and UHMWPE. An example of an artificial wrist joint is shown in Fig. 17.18D. When a wrist joint loses its functions due to diseases such as rheumatoid arthritis, the joint is conventionally fixed with intramedullary nails and plates so as to be difficult to move. The patient's quality of life inevitably declines as a result. The new artificial wrist joint shown in Fig. 17.18D is characterized by having an egg-shaped sliding joint surface between the palm side and arm side components to allow movement in multiple directions. Fig. 17.18E shows an example of a total ankle joint system. The system consists of a talar component attached to the talus side, a socket holder attached to the tibial side, and a tibial socket made of UHMWPE. In this system, the metal portion is also made of Co-Cr-Mo alloy. The tibial socket is locked with the grooves of the socket holder; it allows back and forth movement and medial-lateral rotation up to an angle of 10 degrees without dislocation.

17.5 Implants for bone fracture fixation

17.5.1 Materials

Human bone tissue is a composite material consisting of apatite and collagen fibers, and has anisotropic properties. The strength and elasticity of cortical bone are at a maximum in the direction of the long bone axis, and at a minimum in the traverse direction. Because of these structural characteristics, bone tissue is very compression resistant, but weak against tension or torsion. If excessive force is applied to the arm or leg, the bone breaks. In cases of osteoporosis, the bone fractures easily. Implants for internal fixation have been used for over 100 years. In the past, many kinds of corrosion-resistant materials, such as stainless steel, were tried, and some were abandoned owing to problems due to corrosion or insufficient strength (Uhthoff et al., 2006).

At present, stainless steel and Ti alloys with an elastic modulus of 210 and 100 GPa, respectively, are considered to be promising materials. When a surgeon uses implants to repair bone fractures, the optimum implant is selected and the operation performed under conditions designed to promote bone healing. For example, when a bone fracture is repaired using highly stiff plates, stress shielding is caused by the big difference in the elastic modulus of the bone and metallic implant. As a result, the bone is resorbed. Furthermore, bone resorption due to bone remodeling occurs in the case of fracture fixation with bone plates (Ramakrishna et al., 2004). Thus, even in cases of simple plate fixation, the design must take into account plate rigidity, screw hole spacing, bone and plate contact conditions, etc. The plate size and shape also differ depending on the material used.

If the cross-sectional shape is the same, stainless steel has a higher rigidity than Ti alloy. Considering corrosion resistance and biocompatibility, however, Ti alloy is superior to stainless steel. Since Ti alloy characteristically has high bone affinity, a mirror-finished surface is advantageous compared to a rough surface to prevent binding of the bone to the implant.

17.5.2 Compression hip screws and nails

Compression hip screws (CHS) or compression hip Y -nails (CHY-nail), as shown in Fig. 17.19, are used in intertrochanteric fractures. The CHY-nail shown in Fig. 17.19 is similar to the γ nail in its basic structure except that a lag screw slides inside the lag screw supporter attached to an intramedullary nail. This structure enables the use of a shorter lag screw. Even if a lag screw slides during postoperative walking training, the end of the screw is held inside the lag screw supporter. The sliding screw, therefore, causes no subcutaneous irritations (Matsui et al., 2001). In the case of a CHS, the plate is fixed to the femur with a screw; and the lag screw to the femoral head through a barrel integrated to the plate. Since the fixed angle of the barrel (lag screw)-plate is determined by design (such as 125 degrees), the surgeon sometimes fails to join the intertrochanteric fracture, and a 'cutoff' of an internal lag screw from the femoral head may occur. A novel type of CHS has been developed to solve these problems. The angle can be continuously adjusted within a range of 125–145 degrees. Fig. 17.20 shows the structure and appearance of the novel CHS. The angle is adjusted by applying a cam-slide mechanism. After the lag screw is pierced into an appropriate location in the femoral head, the plate is closely fixed with screws onto the femur and the crossing angle is permanently set using a fixing screw (Nakayama et al., 2000).

17.5.3 Plates and screws

If a bone fracture occurs in the diaphysis, epiphysis, or metaphysis of the bone, it is repaired with a plate and screws. A plate needs to match the configuration of bone. In the case of a simple fracture of a long bone, a flat plate is set on the fractured site and fixed with a screw. In the case of a comminuted fracture, however, it is necessary to

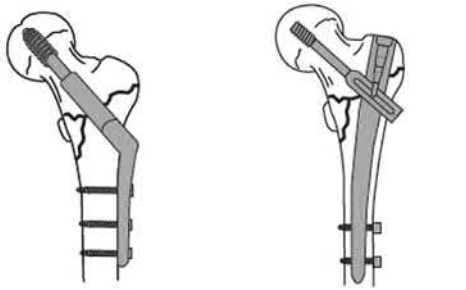


Fig. 17.19 Compression hip screw and hip Y-nail for intertrochanteric fracture.

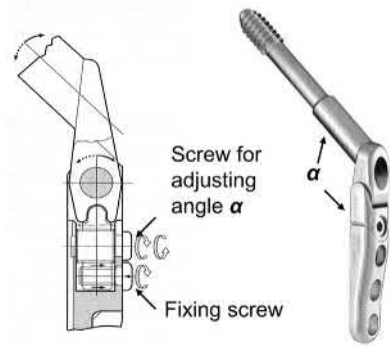


Fig. 17.20 A hip screw with cam-sliding mechanism to adjust angle α.

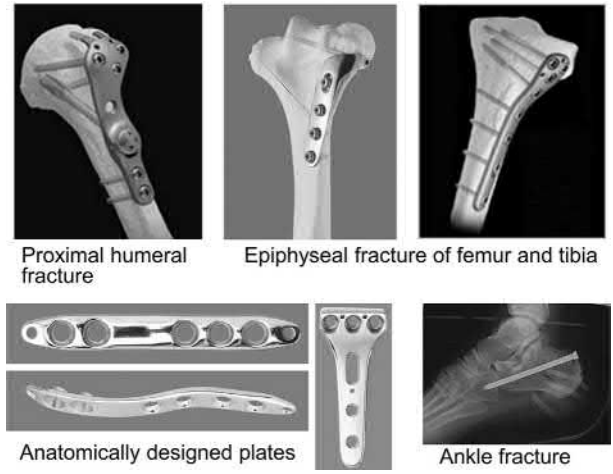


Fig. 17.21 Examples of plate and screw for fractures.
With permission from Teijin-Nakashima Medical Corp. and Mizuho Corp.

carefully gather the dispersed bone fragments and fix them. Multiple mini-plates may be used for the repair (Ikeda et al., 2003). To reconstruct the fractured bone's original shape, it may be necessary to fix it using an anatomically-shaped plate. Fig. 17.21 shows examples of various plates used for bone fractures. Recently, various kinds of plates have been developed for custom-made devices.

17.6 Orthopedic devices fabricated by AM

The conventional metallic devices described in the previous sections were manufactured using hot forging and subsequent machining. Recently, powder-bed type additive manufacturing (AM) method using a laser beam [selective laser melting

(SLM)] or an electron beam (EBM) have been progressively studied for practical applications because AM allows to fabricate patient- specific design at a reasonable cost. Since Hollander et al. showed that AM was applicable to medical device manufacturing (Hollander et al., 2006), experimental AM studies revealed the metallurgical and mechanical properties of pure Ti (Heinl et al., 2008), Ti-6Al-4V alloy (Murr et al., 2009), Co-Cr-Mo alloy (Sun et al., 2014), and stainless steel (Luecke and Slotwinski, 2014) achievable by AM. AM resembles casting at first glance, but the resulting structure is characterized by fine grains as if hot forged and heat treated and in general, the mechanical properties are similar to wrought material (Sames et al., 2016).

According to the reports in the literature, shapes that are difficult to obtain by conventional manufacturing methods have been fabricated by AM methods. For example, there are devices for repairing large pelvic defects (Colen et al., 2012; Wang et al., 2017), functional meshes and craniofacial reconstruction devices (Murr et al., 2010; Larosa et al., 2014), spinal cages (Spetzger et al., 2016; Matsushita et al., 2017; Wilcox et al., 2017) , various porous bodies with different structures (Pattanayak et al., 2011), a device for defining a mandibular defect (Mohammeda et al., 2016), and a personalized bone plate (Ma et al., 2017). Although AM is currently applied to custom-made devices, in the future they should be useful for manufacturing medical devices that are used in large quantities, such as artificial joints.

17.6.1 Properties of Ti fabricated by SLM

During metal powder AM, the powders repeatedly melt and coagulate several times, causing frequent recrystallization and resulting in fine crystals. One of the factors to optimize is the relative density of the product. Fig. 17.22 shows the relationship

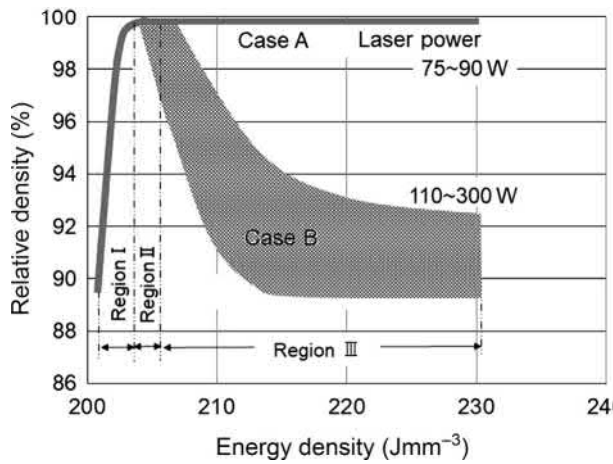


Fig. 17.22 Effect of supplied laser energy density on relative density of product fabricated by selective laser melting method (Material: commercially pure Ti, powder diameter ≦45 μm).

between input energy density and the resulting relative density when a laser beam is used as the heat source. The energy density E (J/mm^3) is given by the following equation:

$$E = P/(vHT) \tag{17.1}$$

where P (W) is the laser power, v (mm/s) is the scanning speed, H (mm) is the scanning pitch, and T (mm) is the powder layer thickness.

As shown in Fig. 17.22, the relative density increases in proportion to the supplied energy density and reaches a density of over 99.5% (region I). In this region, the process switches from a sintering state to a fusion state with increased energy input and the pores in the product decrease. After the maximum relative density is reached, it plateaus as the energy density increases (region II). When the supplied energy density increases, the relative density changes in two ways. The relative density remains either constant regardless of the energy density (case A in region III), or the relative density decreases with the increase in energy density (case B). Case A is observed when the laser power is as small as 75–90 W. Case B occurs as a result of melting with excessive energy of >110 W and solidification with pore formation by including the surrounding gas, which results in a spherical shape with a smooth surface.

The achievable relative density of commercially pure Ti rods prepared by SLM is in the range of 99.7%–99.9%. The tensile strength is 500–600 MPa with elongations of 22%–26%. These values satisfy JIS grade 3 or grade 4 standards even though the powder used is JIS grade 2. In addition, the microstructure shows recrystallized grains due to repeated melting and cooling cycles during manufacturing (Mori et al., 2016).

As the density of three-dimensional (3D)-printed pure Ti is in the range of 99.5%–100% the fatigue strength may decrease. A Ti rod with a diameter of 12 mm and a length of 80 mm was prepared by SLM using pure Ti powder (JIS grade 2) with particle sizes ≦45 μm in diameter and tensile and fatigue tests were conducted. The results are shown in Table 17.4

Materials fabricated with SLM exhibit a higher tensile strength than those of the conventional materials, which are annealed after hot forging. However, the fatigue strength is almost the same. In addition, although the material heated to 1300°C after SLM displayed almost the same tensile strength as conventionally processed materials, the SLM material exhibited a lower fatigue strength. The σ_F/σ_B ratio, where σ_F is the fatigue strength and σ_B is the tensile strength, is 0.69 for the SLM material;

Table 17.4 Comparison of fatigue strengths of commercially pure titanium bar with different processing histories

Processing route of specimens	Tensile strength σ_B (MPa)	Fatigue strength σ_F (MPa)	σ_F/σ_B
As-fabricated by SLM	500	342	0.684
SLM ➡ heated at 1300°C	390	270	0.692
Forging ➡ annealing	397	330	0.831

this value is <0.83 for conventional materials (Matsushita and Mori, 2018). This means that Ti material fabricated using SLM has a lower fatigue strength due to internal defects (Monroy et al., 2013; Kasperovich et al., 2016; Kabir and Richter, 2017), whereas the tensile strength and elongation are excellent. Improvement of fatigue strength is required in the future because devices are designed based on the fatigue strength design.

Fig. 17.23 shows the compressive strength of commercially pure Ti porous bodies with various pore structures fabricated by SLM (Matsushita et al., 2013). The compressive strength generally decreases with increasing porosity, but it is also affected by the pore structure. In addition, their strengths are higher than those of porous bodies prepared by space-holder sintering. This is a result of grain growth during sintering at a high temperature, whereas the crystal grain of the material fabricated by SLM is finer.

17.6.2 Orthopedic applications of medical devices fabricated by SLM

As described above, AM makes it possible to manufacture devices with complicated shapes and structures, that would be difficult to achieve with conventional manufacturing methods. A porous structure is essential to enhance bonding strength between device and bone due to bone ingrowth into pores. As mechanical behaviors of porous bodies are governed by pore architecture, pore volume, and porosity, these factors need to be controllable in the manufacturing process, preferably at a low manufacturing cost. AM is the most effective method for meeting these requirements. In order to promote bone growth into pores, the pore size is preferably in the range of 600–900 μm for additively manufactured bodies (Taniguchi et al., 2016). If porous bodies are made bioactive, bone invades the porous structure quickly and secures long-term stability (Takemoto et al., 2007).

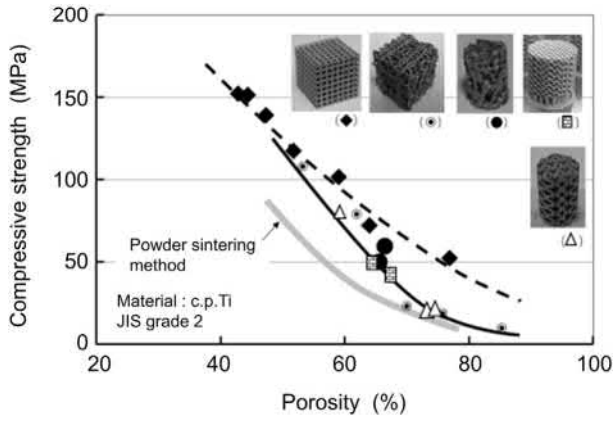


Fig. 17.23 Compressive strengths of porous titanium metal fabricated by SLM as a function of porosity for various porous structures.

On the other hand, stiffness reduction is essential for metallic devices. The elastic modulus of the metals used for orthopedic applications is in the range of 190–220 GPa for Co-Cr-Mo alloy and 316 L stainless steel, 50–120 GPa for Ti and its alloys, whereas that of cortical bone is 15–20 GPa. It is possible to decrease the elastic modulus to about 1/10 of that of the dense metallic material by adopting a porous structure, as well as by changing the relative porosity of the porous structure (Kumar et al., 2016).

17.6.2.1 Devices for large pelvic defects

One of the authors tried to fabricate an acetabular cup made of Ti-6Al-4V using EBM. A porous layer is formed on the outside of the acetabular cup in order to bond the cup to the acetabulum. Conventionally, the porous layer is created by sintering beads to the surface or plasma spraying (see Fig. 17.7). Recently, AM was adopted to fabricate the porous layer of the acetabular cup (Marin et al., 2010). Fig. 17.24 shows an example of this acetabular cup (Anon., 2015). The outside remains in its as-fabricated condition and the inside is machined after fabrication by EBM. Reduction of processing costs and quality stabilization will lead many companies to adopt AM.

AM has been used in various countries to prepare implants, which were difficult to manufacture by the conventional processes. The most noteworthy is the fabrication of a device enabling acetabulum reconstruction for patients who have lost hip joint function due to severe pelvic defects (Colen et al., 2012; Dwivedi et al., 2017). Patients who have undergone surgery using this device will be able to walk and enjoy an improved quality of life. Although this method is an innovative approach to the treatment of the hip joint, surgical treatment costs will rise, so there is a possibility that a balance between cost effectiveness may be required (Wyatt, 2015).

17.6.2.2 Device for lumbar and cervical interbody fusion

Surgical treatment of spinal interbody fusion is often performed by replacing the intervertebral disc in patients with degenerative unstable lumbar lesions. Conventionally, a simple cage made of Ti alloy has been used for lumbar interbody fusion. However, it



Fig. 17.24 Acetabular metal cup made of Ti-6Al-4 V alloy for artificial hip joint fabricated by EBM.
With permission from Teijin-Nakashima Medical Corp.

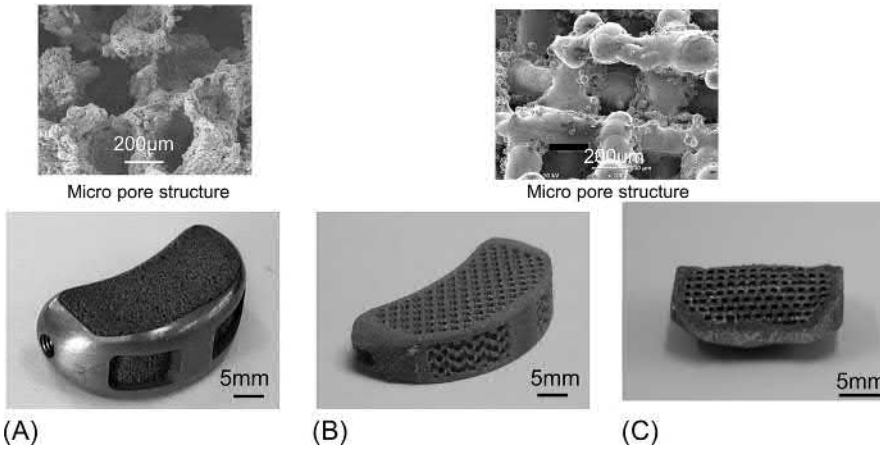


Fig. 17.25 Devices for lumbar interbody fusion fabricated by powder sintering and additive manufacturing methods using commercially pure titanium powders under 45 μm in diameter: (A) porous Ti spacer for lumber interbody fusion by powder sintering, (B) porous Ti spacer for lumbar interbody fusion by SLM, and (C) porous Ti spacer for patient specific cervical interbody fusion by SLM.

does not bond to the surrounding bone. In order to affix it to the surrounding bone, an autogenic bone graft is needed, which often leads to complications. The authors have attempted to fabricate a porous intervertebral spacer that does not require autogenic bone grafts. The fabrication methods used are powder sintering and SLM. The device is composed of a thin dense outer frame with a porous structure inside. They are shown in Fig. 17.25. Fig. 17.25A and B shows lumbar spine spacers processed by powder sintering and SLM, respectively. Fig. 17.25C shows a cervical spine spacer designed with patient-specific implant. In terms of the pore morphology, small irregularities appear to be formed on the cell wall when made by powder sintering while the cells are regularly lined up when made by SLM.

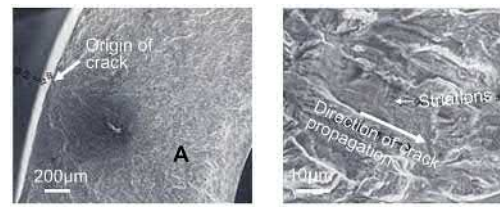
After fabricating the devices shown in Fig. 17.25A and C, they were subjected to chemical and heat treatments to induce bioactivity. Clinical trials were performed at Kyoto University Hospital, Japan, with five patients each and clinical assessment was based on the Japanese Orthopedic Association (JOA) pain evaluation questionnaire score. The safety and efficiency of bioactive Ti porous devices for lumbar and cervical interbody fusion were confirmed (Fujibayashi et al., 2011, 2018).

17.7 Failure of orthopedic implants

Orthopedic implants sometimes fail due to the large force acting on the bone and the implant (Barrack, 2000). When an implant fractures, the patient is operated on again to repair it and must tolerate excruciating pain once again. The JOA has investigated the failure of implants in orthopedic surgery in 1998 (Anon., 2000). The surveyed results

showed that breakage occurred in 1.39% of all surveyed cases, with 46% pertaining to artificial joints, 40% to fracture fixation devices, 13% to spinal fusions, and 1% to others. Failure of the implant is usually attributed to inappropriate selection of materials and inadequate design considerations. From the cases of artificial hip joint failures that occurred between 1992 and 2001, as surveyed by the FDA (US Food and Drug Administration), the sites of failure were investigated. It was found that in 52% of the cases breakage occurred in the stem, 20% in the inner cup, 14% in the ceramic ball head, 6% in the outer cup, and 8% in other components. Wear and tear were the main causes for failure of the inner cup, while the majority of the other failures was attributed to fatigue.

Fig. 17.26 shows a typical scanning electron microscopy (SEM) images of a fatigue failure in an intramedullary nail. This photograph reveals that a crack near the outer surface propagated due to repeated stress, as indicated by the striations. In general, fatigue is localized structural damage when an implant is subjected to cyclic loading. Therefore, fatigue life is influenced by various factors such as surface finish including notches, the microstructure of the metal subjected to heat treatment in manufacturing, residual stress, and over-loading after implantation. Taking these factors into consideration, the cause of fatigue can be classified into (i) design problems, (ii) manufacturing problems, and (iii) clinical problems, as shown in Table 17.5.



Origin of crack near the outer surface

Crack propagation through the wall observed at A

Fig. 17.26 SEM observation of fracture occurring in the intramedullary tube.

Table 17.5 Causes of fracture occurred in implants

Category	Major causes
Design	Insufficient strength (material selection)
	Inadequate microstructure
	Poor shape design, lack of assessment
	Prediction of lower working force
Manufacture	Surface defects (scar, crack, dent, etc.)
	Degradation caused by heat treatment
	Sharp edges and notches in machining
	Poor cleaning
Clinical operation and patient	Poor filling and fracture of bone cement
	Selection of unsuitable implant
	Large load on repaired bone before healing
	Violent movement of patient after operation

In order to prevent implant failure, prior evaluation based on various standards such as ISO, ASTM, and JIS is important. A variety of evaluation methods has been established, including fatigue tests of the femoral components, bending tests of plates and nails, and a twisting test for screws. Recently, it has become possible to use numerical simulations to predict the amount of stress that occurs in the implant. This method has advantages such as time and cost saving and prediction of the stress distribution generated inside the implant when boundary conditions are appropriately selected.

17.8 Summary

As described in this chapter, numerous implants made of metallic biomaterials have been developed in cooperation between surgeons and medical engineers for repairing tissues lost to disease. Generally, metallic implants release ions and generate wear debris, and sometimes fail because the implant is exposed to a high load, severe sliding motion, or highly corrosive environment. To avoid these problems and increase the lifetime of implants, biocompatible metals, ceramics, and polymers have been developed during the last five decades to meet orthopedic needs. However, these are not sufficient for the future because of the increasing number of patients due to aging population across the world and moreover, requirement of patient-specific treatment.

In the future, the demand for patient specific healthcare, including individually tailored medical devices, will increase. In order to meet this demand, medical devices need to be designed to match each patient and each disease, with the additional constraint that they must be supplied quickly and inexpensively. In addition, implant designs with appropriate shape and structure to fit the diseased site and with mechanical properties similar to living bone are becoming more important.

References

Akagi, M., Ueo, T., Takagi, H., Hamanishi, C., Nakamura, T., 2002. A mechanical comparison of two posterior-stabilizing designs: insall/burstein 2 knee and bisurface knee. J. Arthroplast. 17, 627–634. https://doi.org/10.1054/arth.2002.32694.

Akiyama, T., Miyamoto, H., Yonekura, Y., Tsukamoto, M., Ando, Y., Noda, I., Sonohata, M., Mawatari, M., 2013. Silver oxide-containing hydroxyapatite coating has in vivo antibacterial activity in the rat tibia. J. Orthop. Res. 31, 1195–1200. https://doi.org/10.1002/jor.22357.

Amendola, A., Bonasia, D.E., 2009. Results of high tibial osteotomy: review of the literature. Int. Orthop. 34 (2), 155–160. https://doi.org/10.1007/s00264-009-0889-8.

Anon, 1994. Materials properties handbook: titanium alloys. In: Boyer, R., Welsch, G., Collings, E.W. (Eds.), Materials Properties Handbook. ASM International, pp. 321–336.

Anon, 2000. Report of failure of implants. J. Jpn. Orthop. Assoc. 74, 525–534.

Anon, 2009. FINE Total Knee System. Catalog of Teijin-Nakashima Medical Corp.

Anon, 2010. ISO 6474-1, Implants for Surgery- Ceramic Materials-, Part 1: Ceramic Materials Based on High Purity Alumina.

Anon, 2012. ISO 6474-2, Implants for Surgery- Ceramic Materials-, Part 2: Composite Materials Based on High Purity Alumina Matrix With Zirconia Reinforcement.

Anon, 2015. GS Cup. Catalog of Teijin-Nakashima Medical Corp.

Anon, 2017. American Joint Replacement Registry, 2017 Annual Report Figures.

Barker, D.S., Wang, A.W., Yeo, M.F., Nawana, N.S., Brumby, S.A., Pearcy, M.J., Howie, D.W., 2000. The skeletal response to matt and polished cemented femoral stems. J. Bone Joint Surg. Br. 82 (8), 1182–1188.

Barrack, R.L., 2000. Early failure of modern cemented stems. J. Arthroplasty 15, 1036–1050. https://doi.org/10.1054/arth.2000.16498.

Brosset, T., Pasquier, G., Migaud, H., Gougeon, F., 2011. Opening wedge high tibial osteotomy performedwithout filling the defect but with locking plate fixation (TomoFix TM) and early weight-bearing: pospective evaluation of bone union, precision and maintenance of correction in 51 cases. Orthop. Traumatol. Surg. Res. 97, 705–711. https://doi.org/10.1016/j.otsr.2011.06.011.

Callaghan, J.J., Insall, J.N., Greenwald, A.S., Dennis, D.A., Komistek, R.D., Murray, D.W., Bourne, R.B., Rorabeck, C.H., Dorr, L.D., 2001. Mobile-bearing knee replacement- concept and results. Instr. Course Lect. 50, 431–449.

Caton, J., Prudhon, J.L., 2011. Over 25 years survival after Charnley's total hip arthroplasty. Int. Orthop. 35 (2), 185–188. https://doi.org/10.1007/s00264-010-1197-z.

Charnley, J., 1970. Total hip replacement by low-friction arthroplasty. Clin. Orthop. Relat. Res. 72, 7–21.

Coathap, M.J., Blunn, G.W., Flynn, N., Wiliams, C., Thomas, N.P., 2001. A comparison of bone remodeling around hydroxyapatite-coated, porous-coated and grit-blasted hip replacements retrieved at post-mortem. J. Bone Joint Surg. 83-B, 118–123.

Colen, S., Harake, R., De Haan, J., Mulier, M., 2012. A modified custom-made triflanged acetabular reconstruction ring (MCTARR) for revision hip arthroplasty with severe acetabular defects. Acta Orthop. Belg. 78, 71–75.

Collis, D.K., Mohler, C.G., 2002. Comparison of clinical outcomes in total hip arthroplasty using rough and polished cemented stems with essentially the same geometry. J. Bone Joint Surg. Am. 84 (4), 586–592.

Derar, H., Shahinpoor, M., 2015. Recent patents and designs on hip replacement prostheses. Open Biomed. Eng. J. 9, 92–102. https://doi.org/10.2174/1874120701509010092.

Dobbs, H.S., Minski, M.J., 1980. Metal ion release after total hip replacement. Biomaterials 1, 193–198.

Dowson, D., 1995. A comparative study of the performance of metallic and ceramic femoral head components in total replacement hip joints. Wear 190, 171–183.

Dwivedi, C., Gokhale, S., Khim, H.G., Oh, J.K., Shon, W.Y., 2017. Acetabular defect reconstruction with trabecular metal augments: Study with minimum one-year follow up. Hip Pelvis 29 (3), 168–175. https://doi.org/10.5371/hp.2017.29.3.168.

Engh Jr., C.A., MacDonald, S.J., Stritulanondha, S., Tompson, A., Naudie, D., Engh, C.A., 2009. Metal ion levels after metal-on-metal total hip arthroplasty: a randomized traial. Clin. Orthop. Relat. Res. 467, 101–110.

Fujibayashi, S., Takemoto, M., Neo, M., Matsushita, T., Kokubo, T., Doi, K., Ito, T., Shimizu, A., Takashi, N., 2011. A novel synthetic material for spinal fusion: a prospective clinical trial of porous bioactive titanium metal for lumbar interbody fusion. Eur. Spine J. 20, 1486–1495. https://doi.org/10.1007/s00586-011-1728-3.

Fujibayashi, S., Takemoto, M., Mori, S., Matsushita, T., 2018. Development of artificial bone using additive manufacturing technology. J. Jpn. Soc. Biomater. 36 (1), 52–57.

Fujisawa, A., Noda, I., Nishio, Y., Okimatsu, H., 1995. The development of new titanium arc-sprayed artificial joints. Mater. Sci. Eng. C 2, 151–157. https://doi.org/10.1016/0928-4931(95)00053-4.

Fukuda, C., Goto, K., Imamura, M., Neo, M., Nakamura, T., 2011. Bone bonding ability and handling properties of a titania–polymethylmethacrylate (PMMA) composite bioactive bone cement modified with a unique PMMA powder. Acta Biomater. 7, 3595–3600. https://doi.org/10.1016/j.actbio.2011.06.006.

Funao, H., Nagai, S., Sasaki, A., Hoshikawa, T., Tsuji, T., Okada, Y., Koyasu, S., Toyama, Y., Nakamura, M., Aizawa, M., Matsumoto, M., Ishii, K., 2016. A novel hydroxyapatite film coated with ionic silver via inositol hexaphosphate chelation prevents implant-associated infection. Sci. Rep. 17, 1–9. https://doi.org/10.1038/srep23238.

Gbejuade, H.O., Lovering, A.M., Webb, J.C., 2015. The role of microbial biofilms in prosthetic joint infections. Acta Orthop. 86 (2), 147–158. https://doi.org/10.3109/17453674.2014.966290.

Ghani, Y., Coathup, M.J., Hing, K.A., Blunn, G.W., 2012. Development of a hydroxyapatite coating containing silver for the prevention of peri-prosthetic infection. J. Orthop. Res. 30 (3), 356–363. https://doi.org/10.1002/jor.21543.

Girard, J., 2015. Femoral head diameter considerations for primary total hip arthroplasty. Orthop. Traumatol. Surg. Res. 101, S25–S29. https://doi.org/10.1016/j.otsr.2014.07.026.

Goto, K., Hashimoto, M., Takadama, H., Tamura, J., Fujibayashi, S., Kawanabe, K., Kokubo, T., Nakamura, T., 2008. Mechanical, setting, and biological properties of bone cements containing micron-sized titania particles. J. Mater. Sci. Mater. Med. 19, 1009–1016. https://doi.org/10.1007/s10856-007-3076-8.

Gross, K.A., Berndt, C.C., Herman, H., 1998. Amorphous phase formation in plasma-sprayed hydroxyapatite coatings. J. Biomed. Mater. Res. 39 (3), 407–414. https://doi.org/10.1002/(SICI)1097-4636(19980305)39:3%3C407::AID-JBM9%3E3.0.CO;2-N.

Habibovic, P., Sees, T.M., van den Doel, M.A., van Blitterswijk, C.A., de Groot, K., 2006. Osteoinduction by biomaterials-physicochemical and structural influences. J. Biomed. Mater. Res. A 77, 747–762. https://doi.org/10.1002/jbm.a.30712.

Hallab, N., Merritt, K., Jacobs, J., 2001. Metal sensitivity in patients with orthopaedic implants. J. Bone Joint Surg. Am. 83-A (3), 428–436.

Hamadouche, M., Boutin, P., Daussange, M.E., Sedel, L., 2002. Alumina-on-alumina total hip arthroplasty: a minimum 18.5-year follow-up study. J. Bone Joint Surg. Am. 84-A (1), 69–77.

Harrison, J., Keggi, J., Keppler, L., Kennon, R.T., McTghe, T., Van der Rijit, A., Turnbull, A., Woodgate, I., 2010. Design Rationale MSA™ Total HIP Stem Design (Muscle Sparinga Approach). Joint Implant Surgery & Research Foundation.

Hasegawa, M., Sudo, A., Uchida, A., 2006. Alumina ceramic on ceramic total hip replacement with a layered acetabular component. J. Bone Joint Surg. Br. 88, 877–882. https://doi.org/10.1302/0301-620X.88B7.17675.

Heinl, P., Körner, C., Singer, R.F., 2008. Selective electron beam melting of cellular titanium: mechanical properties. Adv. Eng. Mater. 10 (9), 882–888. https://doi.org/10.1002/adem.200800137.

Hendriks, J.G., Neut, D., Van Horn, J.R., Van der Mei, H.C., Busscher, H.J., 2005. Bacterial survival in the interfacial gap in gentamicin-loaded acrylic bone cements. J. Bone Joint Surg. Br. 87, 272–276.

Hollander, D.A., Walter, M.V., Wirtz, T., Sellei, R., Rohlfing, B.S., Paar, O., Erli, H.J., 2006. Structural, mechanical and in vitro characterization of individually structured Ti6Al4V

produced by direct laser forming. Biomaterials 27, 955–963. https://doi.org/10.1016/j.biomaterials.2005.07.041.

Howie, D., 2018. Larger articulations reduce dislocation and revision for dislocation without increased linear wear at ten-year follow-up in a randomized trial. In: Orthopaedic Proceedings. published on line: 21 Feb.

Hulbert, S.F., Morrison, S.J., Klawitter, J.J., 1972. Tissue reaction to three ceramics of porous and non-porous structures. J. Biomed. Mater. Res. 6, 347–374.

Ikeda, M., Yamashita, Y., Kamimoto, M., Oka, Y., 2003. Open reduction and internal fixation of comminuted fractures of radial head using low-profile mini-plates. J. Bone Joint Surg. Br. 85-B (7), 1040–1044.

Ilchmann, T., Markovic, L., Joshi, A., Hardinge, K., Murphy, J., Wingstrand, H., 1998. Migration and wear of long-term successful Charnley total hip replacement. J. Bone Joint Surg. Br. 80-B (3), 377–381.

Isama, K., Tsuchiya, K., 2002. Biocompatibility of titanium alloys. In: Proc. 24th Annual Meeting of Japanese Society for Biomaterials, p. 194.

Issack, P.S., Botero, H.G., Hibert, R.N., Bong, M.R., Stuchin, S.A., Zuckerman, J.D., DiCesare, P.E., 2003. Sixteen-year follow-up of the cemented spectron femoral stem for hip arthroplasty. J. Arthroplast. 18, 925–930.

Ito, H., Maloney, C.M., Crowninshield, R.D., Clohisy, J.C., McDonald, D.J., Maloney, W.J., 2010. In vivo femoral head damages and its effect on polyethylene wear. J. Arthroplasty 25 (2), 302–308. https://doi.org/10.1016/j.arth.2009.01.010.

Iwase, T., Warashina, H., Yamauchi, K., Sugiura, S., Hasegawa, Y., 2003. Early head penetration into cemented Hylamer ogee socket. J. Arthroplasty 18, 920–925.

Justin, J., Sherfey, D.O., Richard, W.M., 2006. Mid-term results of Exeter vs endurance cemented stems. J. Arthroplasty 21, 1118–1123. https://doi.org/10.1016/j.arth.2006.01.008.

Kabir, M.R., Richter, H., 2017. Modeling of processing-induced pore morphology in an additively-manufactured Ti-6Al-4V alloy. Materials 10, 145. https://doi.org/10.3390/ma10020145.

Kasperovich, G., Haubrich, J., Gussone, J., Requena, G., 2016. Correlation between porosity and processing parameters in TiAl6V4 produced by selective laser melting. Mater. Des. 105, 160–170. https://doi.org/10.1016/j.matdes.2016.05.070.

Kawanabe, K., Ise, K., Goto, K., Akiyama, H., Nakamura, T., Kaneuji, A., Sugimori, T., Matsumoto, T., 2009. A new cementless total hip arthroplasty with bioactive titanium porous-coating by alkaline and heat treatment: average 4.8-year results. J. Biomed. Mater. Res. B Appl. Biomater. 90B, 476–481. https://doi.org/10.1002/jbm.b.31309.

Kim, J.T., Yoo, J.J., 2016. Implant design in cementless hip arthroplasty. Hip Pelvis 28 (2), 65–75. https://doi.org/10.5371/hp.2016.28.2.65.

Kokubo, T., Miyaji, F., Kim, H.M., Nakamura, T., 1996. Spontaneous formation of bonelike apatite layer on chemically treated titanium metals. Am. Ceram. Soc. 79 (4), 1127–1129.

Kizuki, T., Takadama, H., Matsushita, T., Nakamura, T., Kokubo, T., 2010. Preparation of bioactive Ti metal surface enriched with calcium ions by chemical treatment. Acta Biomater. 6, 2836–2842. https://doi.org/10.1016/j.actbio.2010.01.007.

Kumar, A., Nune, K.C., Murr, L.E., Misra, R.D.K., 2016. Biocompatibility and mechanical behaviour of three-dimensional scaffolds for biomedical devices: process-structure-property paradigm. Int. Mater. Rev. 61 (1), 20–45. https://doi.org/10.1080/09506608.2015.1128310.

Kuroda, D., Niinomi, M., Morinaga, M., Kato, Y., Yashiro, T., 1998. Design and mechanical properties of β-type titanium alloys for implant materials. Mater. Sci. Eng. A 243, 244–249.

Kurtz, S.M., Kocagoz, S., Arnholt, C., Huet, R., Ueno, M., Walter, W.L., 2014. Advances in zirconia toughened alumina biomaterials for total joint replacement. J. Mech. Behav. Biomed. Mater. 31, 107–116. https://doi.org/10.1016/j.jmbbm.

Kurtz, S.M., Lau, E., Baykal, D., Springer, B.D., 2017. Outcomes of ceramic bearings after primary total hip arthroplasty in the medicare population. J. Arthroplast. 32. https://doi.org/10.1016/j.arth.2016.08.038 743e749.

Kyomoto, M., 2009. Design of Surface with Hydration Lubrication by Phospholipid Polymers for Extending Longevity of Artificial Joints, Doctorial Dissertation. The University of Tokyo.

Larosa, M.A., Jardini, A.L., de Carvallo, Z.C.A., Kharmandaaaayan, P., Calderoni, D.R., Filho, R.M., 2014. Microstructural and mechanical characterization of a custom-built implant manufactured in titanium alloy by direct metal laser sintering. Adv. Mech. Eng. 2014, 945819.

Livingston, B.J., Chemell, M.J., Spector, M., Poss, R., 1997. Complications of total hip arthroplasty associated with use of an acetabular component with Hylamer liner. J. Bone Joint Surg. Am. 79-A, 1080–1090.

Lombardi Jr., A.V., Berend, K.R., Seng, B.E., Clark, I.C., Adams, J.B., 2010. Delta ceramic-on-alumna ceramic articulation in primary THA. Clin. Orthop. Relat. Res. 468, 367–374.

Lopes, R., Philippeau, J.M., Passut, N., Gouin, F., 2012. High rate of ceramic sandwich liner fracture. Clin. Orthop. Relat. Res. 470, 1705–1710. https://doi.org/10.1007/s11999-012-2279-6.

Lu, Z., McKellop, H., 1997. Frictional heating of bearing materials tested in a hip joint wear simulator. Proc. Inst. Mech. Eng. 211 (Part H), 101–107.

Luecke, W.E., Slotwinski, 2014. Mechanical properties of austenitic stainless steel made by additive manufacturing. J. Res. Natl. Inst. Stand. Technol. 119, 398–418. https://doi.org/10.6028/jres.119.015.

Ma, L., Zhou, Y., Zhu, Y., Lin, Z., Chen, L., Zhang, Y., Xia, H., Mao, C., 2017. 3D printed personalized titanium plates improve clinical outcome in microwave ablation of bone tumors around the knee. Sci. Rep. 7, 7626. https://doi.org/10.1038/s41598-017-07243-3.

Maehara, K., Doi, K., Matsushita, T., Sasaki, Y., 2002. Application of vanadium-free titanium alloys to artificial hip joint. Mater. Trans. 43, 2936–2942.

Marin, E., Fusi, S., Pressacco, M., Paussa, L., Fedrizzi, L., 2010. Characterization of cellular solids in Ti6Al4V for orthopaedic implant applications: trabecular titanium. J. Mech. Behav. Biomed. Mater. 3 (5), 373–381. https://doi.org/10.1016/j.jmbbm.

Massin, P., Lopes, R., Masson, B., Mainard, D., 2014. Does Biolox® delta ceramic reduce the rate of component fractures in total hip replacement? Orthop. Traumatol. Surg. Res. 100 (6 Suppl), S317–S321. https://doi.org/10.1016/j.otsr.2014.05.010.

Matsui, T., Oota, Y., Saito, S., Ishii, J., Hasuike, N., 2001. 'Treatment of femoral neck fractures using compression hip Y(CHY)-nail: analysis of lag screw sliding' (Japanese). Orthop. Surg. 52, 768–771.

Matsumoto, H., Watanabe, S., Hanada, S., 2005. Beta TiNbSn alloys with low Young's modulus and high strength. Mater. Trans. 46, 1070–1078.

Matharu, G.S., Berryman, F., Judge, A., Reito, A., McConnell, J., Lainiala, O., Young, S., Eskelinen, A., Pandit, H.G., Murray, D.W., 2017. Blood metal ion thresholds to identify patients with metal-on-metal hip implantsat risk of adverse reactions to metal debris: An external multicenter validation study of Birmingham hip resurfacing and corail-pinnacle implants. J. Bone Joint Surg. Am. 99, 1532–1539. https://doi.org/10.2106/JBJS.16.01568.

Matharu, G., Pandit, H.G., Murray, D.W., Judge, A., 2016. Adverse reactions to metal debris occur with all types of hip replacement not just metal-on-metal hips: a restrospective obsevational study of 3340 revisions for adverse reactions to metal debris from the joint registry for England, Wales, Northern Ireland and the Isle of Man. BMC Musculoskelet. Disord. 17, 495. https://doi.org/10.1186/s12891-016-1329-8.

Matsuda, Y., Nakamura, T., Ido, K., Matsushita, T., Oka, M., 1997. Femoral component made of Ti-15Mo-5Zr-3Al alloy in total hip arthroplasty. J. Orthop. Sci. 2, 166–170.

Matsushita, T., Pattanayak, D.K., Takemoto, M., Fujibayashi, S., Nakamura, T., Sasaki, K., Kokubo, T., 2013. Compressive strength of porous titanium metal with thin cell wall prepared by selective laser melting. J. Jpn. Soc. Technol. Plast. 54 (630), 601–604.

Matsushita, T., Fujibayashi, S., Kokubo, T., 2017. Titanium foam for bone tissue engineering. In: Wen, C. (Ed.), Metallic Foam Bone-Processing, Modification and Characterizaiton and Properties. Woodhead Publishing, pp. 111–130.

Matsushita and Mori, 2018. Mechanical characteristics of titanium porous material and its medical applications. SOKEIZAI 59 (4), 2–7.

McTighe, T., Keggi, J., Stulberg, S.D., Keppler, L., Brazil, D., McPherson, E.J., 2014. Total hip stem classification system. JISRF Reconstr. Rev. 4 (2), 24–28.

McCalden, R.W., MacDonald, S.J., Rorabeck, C.H., Bourne, R.B., Chess, D.G., Charron, K.D., 2009. Wear rate of highly cross-linked polyethylene in total hip arthroplasty: A randomized controlled trial. J. Bone Joint Surg. Am. 91, 773–782. https://doi.org/10.2106/JBJS.H.00244.

Mending, J.B., Nassif, J.H., Ritter, M.A., 2000. Long-term survival the T-28 versus the TR-28 cemented total hip arthroplasties. J. Arthroplast. 15, 928–933.

Mohammeda, M.I., Fitzpatricka, A.P., Malyalab, S.K., Gibsona, I., 2016. Customised design and development of patient specific 3D printed whole mandible implant. In: Proceedings of the 26th Annual International Solid Freeform Fabrication Symposium—An Additive Manufacturing Conference.

Monroy, K., Delgado, J., Ciurana, J., 2013. Study of the pore formation on CoCrMo alloy by selective laser melting manufacturing process. Procedia Eng. 63, 361–369. https://doi.org/10.1016/j.proeng.2013.08.227.

Mori, S., Doi, K., Maruyama, S., Takeuchi, T., Hanami, K., Kitagaki, H., Terauchi, S., Matsushita, T., 2016. Effect of Particle Size on Quality Characteristics of Pure Titanium Using Metal Additive Manufacturing', PM 2016, Hamburug, Germany.

Moro, T., Takatori, Y., Ishihara, K., Konno, T., Takigawa, Y., Matsushita, T., Chung, U.-I., Nakamura, K., Kawaguchi, H., 2004. Surface grafting of artificial joints with a biocompatible polymer for preventing periprosthetic osteolysis. Nat. Mater. 3, 829–836. https://doi.org/10.1038/nmat1233.

Moro, T., Takatori, Y., Kyomoto, M., Ishihara, K., Hashimoto, M., Ito, H., Tanaka, T., Oshima, H., Tanaka, S., Kawaguchi, H., 2014. Long-term hip simulator testing of the artificial hip joint bearing surface graded with biocompatible phospholipid polymer. J. Orthop. Res. 32, 369–376. https://doi.org/10.1002/jor.22526.

Moro, T., Takatori, Y., Tanaka, S., Ishihara, K., Oda, H., Kim, Y.T., Umeyama, T., Fukatani, E., Ito, H., Kyomoto, M., Oshima, H., Tanaka, T., Kawaguchi, H., Nakamura, K., 2017. Clinical safety and wear resistance of the phospholipid polymer-grafted highly cross-linked polyethylene liner. J. Orthop. Res. 35, 2007–2016.

Munemoto, M., Grammatopoulos, G., Tanak, Y., Gibbons, M., Athanason, N.A., 2017. The pathology of failed McKee-Farra implants: correlation with modern metal-on-metal-implant failure. J. Mater. Sci. Mater. Med. 28, 66. https://doi.org/10.1007/s10856-017-5882-y.

Murr, L.E., Quinones, S.A., Gaytan, S.M., Lopez, M.I., Rodela, A., Martinez, E.Y., Hernandez, D.H., Martinez, E., Medina, F., Wicker, R.B., 2009. Microstructure and mechanical behavior of Ti-6Al-4V produced by rapid-layer manufacturing, for biomedical applications. J. Mech. Behav. Biomed. Mater. 2 (1), 20–32. https://doi.org/10.1016/j.jmbbm.2008.05.004.

Murr, L.E., Gaytan, S.M., Medina, F., Lope, H., Martinez, E., Machado, B.I., Hernandez, D.H., Martinez, L., Lopez, M.I., Wicker, R.B., Bracke, J., 2010. Next-generation biomedical implants using additive manufacturing of complex, cellular and functional mesh arrays. Phil. Trans. R. Soc. A 368, 1999–2032. https://doi.org/10.1098/rsta.2010.0010.

Muruatoglu, O.K., Bragdon, C.R., O'Connor, D.O., Jasty, M., Harris, W.H., 2001. 'A novel method of cross-linking ultra-high-molecular-weight polyethylene to improve wear, reduce oxidation, and retain mechanical properties. J. Arthroplasty 16, 149–160. https://doi.org/10.1054/arth.2001.20540.

Nakayama, I., Kobori, M., Kamisato, S., Yoshida, M., Nanba, Y., Doi, K., 2000. Development and clinical results of the adjustable sliding hip screw. Orthop. Surg. 37, 122–126.

Ni, G.X., Chiu, K.Y., Lu, W.W., Wang, Y., Zhang, Y.G., Hao, L.B., Lia, Z.Y., Lama, W.M., Lu, S.B., Luk, K.D.K., 2006. Strontium-containing hydroxyapatite bioactive bone cement in revision hip arthroplasty. Biomaterials 27, 4348–4355. https://doi.org/10.1016/j.biomaterials.2006.03.048.

Niinomi, 2012. Shape memory, superelastic and low Young's modulus alloys. In: Amgrosio, L., Tanner, E. (Eds.), Biomaterias for Spinal Surgery. Woodhead Publishing Limited, pp. 462–490.

Nishiguchi, S., Kato, H., Fujita, H., Oka, M., Kim, H.M., Kokubo, T., Nakamura, T., 2001. Titanium metals form direct bonding to bone after alkali and heat treatments. Biomaterials 22, 2525–2533.

Neut, D., Dijkstra, R.J.B., Thompson, J.I., Van der Mei, H.C., Busscher, H.J., 2011. Antibacterial efficacy of a new gentamicin-coating for cementless prostheses compared to gentamicin-loaded bone cement. J. Orthop. Res. 29, 1654–1661. https://doi.org/10.1002/jor.21433.

Okazaki, Y., Rao, S., Ito, Y., Tateishi, T., 1998. Corrosion resistance, mechanical properties, corrosion fatigue strength and cytocompatibility of new Ti alloys without Al and V. Biomaterials 19, 1197–1215.

Okuzu, Y., Fujibayashi, S., Yamaguchi, S., Yamamoto, K., Shimizu, T., Sono, T., Goto, K., Otsuki, B., Matsushita, T., Kokubo, T., Matsuda, S., 2017. Strontium and magnesium ions released from bioactive titanium metal promote early bone bonding in a rabbit implant model. Acta Biomater. 63, 383–392. https://doi.org/10.1016/j.actbio.

Oonishi, H., Kadoya, Y., Masuda, S., 2001. Gamma-irradiated cross-linked polyethylene in total hip replacement: Analysis of retrieved sockets after long term implantation. J. Biomed. Mater. Res. B Appl. Biomater. 58, 167–171.

Oral, E., Beckos, C.G., Malhi, A.S., Muratoglu, O.K., 2008a. The effect of high dose irradiation on the cross-linking of vitamin E-blended ultra high molecular weight polyethylene. Biomaterials 29 (26), 3557–3560. https://doi.org/10.1016/j.biomaterials.

Oral, E., Malhi, A.S., Wannomae, K.K., Muratoglu, O.K., 2008b. Highly crosslinked UHMWPE with improved fatigue resistance for total joint arthroplasty. J. Arthroplast. 23 (7), 1037–1044. https://doi.org/10.1016/j.arth.2007.09.027.

Pattanayak, D.K., Fukuda, A., Matsushita, T., Takemoto, M., Fujibayashi, S., Sasaki, K., Nishida, K., Nakamura, T., Kokubo, T., 2011. Bioactive Ti metal analogous to human cancellous bone: fabrication by selective laser melting and chemical treatments. Acta Biomater. 7, 1398–1406. https://doi.org/10.1016/j.actbio.2010.09.034.

Paxton, E.W., Robert, S., Maletis, G.B., Khatod, M., Yue, E.Y., Davies, M., Low Jr., R.B., Wyatt, R.W.B., Inacio, M.C.S., Funahashi, T.T., 2010. A prospective study of 80,000 total joint and 5000 anterior cruciate ligament reconstruction procedures in a community-based registry. J. Bone Joint Surg. Am. 92, 117–132. https://doi.org/10.2106/JBJS.J.00807.

Piconi, C., Santis, V.D., Maccauro, G., 2017. Clinical outcomes of ceramicized ball heads in total hip replacement bearings: aliterature review. J. Appl. Biomater. Func. Mater. 15 (1), e1–e9. https://doi.org/10.5301/jabfm.5000330.

Pilliar, R.M., 1983. Powder metal-made orthopedic implants with porous surface for fixation by tissue ingrowth. Clin. Orthop. Relat. Res. No. 176.

Posada, O.M., Tate, R.J., Meek, R.M.D., Grant, M.H., 2015. In vivo analyses of the toxicity, immunological, and gene expression effects of cobalt-chromium alloy wear debris and co ion derived from metal-on-metal hip implants. Lubricant 3, 539–568. https://doi.org/10.3390/lubricants3030539.

Price, A.J., Rees, J.L., Beard, D., Juszczk, E., Carter, S., White, S., de Steiger, R., Dodd, C.A.F., Gibbons, M., Smith, P.M., Goodfellow, J.W., Murray, D.W., 2003. A mobile- bearing total knee prothesis compared with a fixed-bearing prosthesis. J. Bone Joint Surg. Br. 85-B, 62–67. https://doi.org/10.1302/0301-620X.85B1.13233.

Price, J.S., Tencer, A.F., Arm, D.M., Bohach, G.A., 1996. Controlled release of antibiotics from coated orthopedic implants. J. Biomed. Mater. Res. 30, 281–286.

Ramakrishna, K., Sridhar, I., Sivashanker, S., Khong, K.S., Ghista, D.N., 2004. Design of fracture fixation plate for necessary and sufficient bone stress shielding. JSME Int. J. Ser. C 47 (4), 1086–1094.

Rieker, C., Kottig, P., 2002. *In vivo* tribological performance of 231 metal-on-metal hip articulations. Hip Int. 12 (2), 73–76.

Saikko, V.S., Pavolainen, P.O., Slatis, P., 1993. Wear of the polyethylene acetabular cup—metallic and ceramic heads compared in hip simulator. Acta Orthop. Scand. 64, 391–402.

Sames, W.J., List, F.A., Pannal, S., Dehoff, R.R., Babu, S.S., 2016. The metallurgy and processing science of metal additive manufacturing. Int. Mater. Rev. 1–46. https://doi.org/10.1080/09506608.2015.1116649.

Semlitsh, M., Staub, F., Weber, H., 1985. Titanium–aluminum–niobium alloy, development for biocompatible, high strength surgical implant. Biomed. Tech. 30, 334–339.

Seppanen, M., Karvonen, M., Virolainen, P., Remes, V., Pulkkinen, P., Eskelinen, A., Luikas, A., Makela, K., 2016. Poor 10-year survivorship of hip resurfacing arthroplasty. Acta Orthop. 87 (6), 554–559. https://doi.org/10.1080/17453674.2016.1246316.

Shinzato, S., Nakamura, T., Kitamura, Y., 2001. Bioactive bone cement: effect of filler size on mechanical properties and osteoconductibity. J. Biomed. Mater. Res. 56 (3), 452–458.

Skinner, J.A., Todo, S., Talor, M., Wang, J.S., Pinskerova, V., Scott, A., 2003. Should the cement mantle around the femoral component be thick or thin. J. Bone Joint Surg. Br. 85-B, 45–52.

Smith, A.J., Dieppe, P., Porter, M., Blom, A.W., 2012. Risk of cancer in first seven years after metal-on-metal hip replacement compared with other bearings and general population: Linkages study between the National Joint Registry of England Wales and hospital episode statics. BMJ. 344, e2383. https://doi.org/10.1136/bmj.e2383.

Spector, M., Reis, M.D., Boune, R.B., Sauer, W.S., Long, M., Hunter, G., 2001. Wear performance of ultra-high molecular weight polyethylene on oxidized zirconium total knee femoral components. J. Bone Joint Surg. Am. 83-a (Suppl. 2), 80–86. Part 2.

Spetzger, U., Frasca, M., Konig, S.A., 2016. Surgical planning, manufacturing and implantation of an individualized cervical fusion titanium cage using patient-specific data. Eur. Spine J. 25, 2239–2246. https://doi.org/10.1007/s00586-016-4473-9.

Sprenger, T.R., Doerzbacher, J.F., 2003. Tibial osteotomy for the treatment of varus gonarthrosis: Survival and failure analysis to twenty-two years. J. Bone Joint Surg. Am. 85-A, 469–474.

So, K., Kaneuji, A., Matsumoto, T., Matsuda, S., Akiyama, H., 2013. Is the bone-bonding ability of a cementless total hip prosthesis enhanced by alkaline and heat treatments? Clin. Orthop. Relat. Res. 471 (12), 3847–3855. https://doi.org/10.1007/s11999-013-2945-3.

Steinemann, S.G., 1980. Evaluation of Biomaterials. John Wiley & Sons Ltd.

Sun, S.H., Koizumi, Y., Kurosu, S., Li, Y.P., Matsumoto, H., Chiba, A., 2014. Build-direction dependence of microstructure and high-temperature tensile property of co-Cr-Mo alloy fabricated by electron-beam melting (EBM). Acta Mater. 64, 154–168. https://doi.org/10.1016/j.actamat.2013.10.017.

Takatori, Y., Moro, T., Ishihara, K., Kamogawa, M., Oda, H., Umeyama, T., Kim, Y.T., Ito, H., Kyomoto, M., Tanaka, T., Kawaguchi, H., Tanaka, H., 2015. Clinical and radiographic outcomes of total hip replacement with poly (2-methacryloyloxyethyl phosphorylcholine)-grafted highly cross-linked polyethylene liners: Three-year results of a prospective consecutive series. Mod. Rheumatol. 25 (2), 286–291. https://doi.org/10.3109/14397595.2014.941438.

Takemoto, M., Fujibayashi, S., Neo, M., So, K., Akiyama, N., Matsushita, T., Kokubo, T., Nakamura, T., 2007. A porous bioactive titanium implant for spinal interbody fusion: an experimental study using a canine model. J. Neurosurg. Spine 7 (4), 435–443. https://doi.org/10.3171/SPI-07/10/435.

Tanaka, K., Kamimura, A., Katayama, T., Kinoshita, S., Sakoda, H., Kuramoto, K., 2008. Influence of environmental degradation and vitamin- E (α-tocopherol) addition on the fatigue crack growth property of ultra high molecular weight polyethylene. J. Soc. Mater. Sci. 57 (9), 875–881. https://doi.org/10.2472/jsms.57.875.

Taniguchi, N., Fujibayashi, S., Takemoto, M., Sasaki, K., Otsuki, B., Nakamura, T., Matsushita, T., Kokubo, T., Matsuda, S., 2016. Effect of pore size on bone ingrowth into porous titanium implants fabricated by additive manufacturing: an in vivo experiment. Mater. Sci. Eng. C 59, 690–701. https://doi.org/10.1016/j.msec.2015.10.069.

Teramura, S., Sakoda, H., Terao, T., Endo, M.M., Fujiwara, K., Tomita, N., 2008. Reduction of wear volume from ultrahigh molecular weight polyethylene knee components by the addition of vitamin E. J. Othop. Res. 26, 460–464. https://doi.org/10.1002/jor.20514.

Todd, B., Thomas, T., 2008. Unicompartmental knee arthroplasty. J. Am. Acad. Orthop. Surg. 16 (1), 9–18.

Tomita, N., Kitakura, T., Onmori, N., Ikeda, Y., Aoyama, E., 1999. Prevention of fatigue cracks in UHMWPE joint components by addition of vitamin E. J. Biomed. Mater. Res. Appl. Biomater. 48, 474–478.

Turner, A.C., Sugimoto, T., Uetsuki, K., Hyon, S.H., Tomita, N., 2015. Mechanical and oxidative performance of high-dose electron-beam irradiated, dl-α-tocopherol (vitamin E) blended UHMWPE. J. Biomech. Sci. Eng. Jpn. Soc. Mech. Eng. 10 (1), 1–14. https://doi.org/10.1299/jb.14-00238.

Uhthoff, H.K., Poitras, P., Backman, D.S., 2006. Internal plate fixation of fractures: short history and recent developments. J. Orthop. Sci. 11, 118–126. https://doi.org/10.1007/s00776-005-0984-7.

Wang, D., Wang, Y., Wu, S., Lin, H., Yan, Y., Fan, S., Gu, C., Wang, J., Song, C., 2017. Customized a Ti6Al4V bone plate for complex pelvic fracture by selective laser melting. Materials 10, 35. https://doi.org/10.3390/ma10010035.

Weightman, B., Light, D., 1986. The effects of the surface finish of alumina and stainless steel on the wear rate of UHMW polyethylene. Biomaterials 7, 20–24. https://doi.org/10.1016/0142-9612(86)90083-9.

Wilcox, B., Mobbs, R., Wu, A.M., Phan, K., 2017. Systematic review of 3D printing in spinal surgery: the current state of play. J. Spine Surg. 3 (3), 433–443. https://doi.org/10.21037/jss.2017.09.01.

Whittaker, J.P., Charron, K.D., McCalden, R.W., MacDonald, S.J., Bourne, R.B., 2010. Comparison of steady state femoral head penetration rates between two highly cross-linked polyethylene in total hip arthroplasty. J. Arthroplasty 25 (5), 680–686. https://doi.org/10.1016/j.arth.2009.05.006.

Wittenberg, R.H., Steffen, R., Windhagen, H., Bücking, P., Wilcke, A., 2013. Five-year results of a cementless short-hip-stem prosthesis. Orthop. Rev. 5, e4. https://doi.org/10.4081/or.2013.e4.

Wroblewski, B.M., Siney, P.D., Fleming, P.A., 2001. Triple taper polished cemented stem in total hip arthroplasty. J. Arthroplast. 16 (8 Suppl), 37–41.

Wyatt, M.C., 2015. Custom 3D-printed acetablur implants in hip surgery-innovative breakthrough or expensive bespoke upgrade? Hip Int. 25 (4), 375–379. https://doi.org/10.5301/hipint.5000294.

Yamamoto, K., Tateiwa, T., Takahashi, Y., 2017. Vitamin E-stabilized highly crosslinked polyethylene: the role and effectiveness in total hip arthroplasty. J. Orthop. Sci. 22, 384–390. https://doi.org/10.1016/j.jos.2017.01.012.

Yamamuro, T., Takagi, H., 1991. Bone bonding behaviour of biomaterials with different surface characteristics under load-bearing conditions. In: Davies, J.E. (Ed.), The Bone-Material Interface. University of Toronto, pp. 406–414.

Yamaguchi, S., Nath, S., Matsushita, T., Kokubo, T., 2014. Controlled release of strontium ions from abioactive Ti metal with a ca-enriched surface layer. Acta Biomater. 10 (5), 2282–2289. https://doi.org/10.1016/j.actbio.2014.01.026.

Yamaguchi, S., Nath, S., Sugawara, Y., Divakarla, K., Das, T., Manos, J., Chrzanowski, W., Matsushita, T., Kokubo, T., 2017. Two-in- one biointerfaces-antimicrobial and bioactive nanoporous gallium titanate layers for titanium implants. Nano 7, 229. https://doi.org/10.3390/nano7080229.

Yamasaki, H., Sakai, H., 1992. Osteogenic response to porous hydroxyapatite ceramics under the skin of dogs. Biomaterials 13, 308–312. https://doi.org/10.1016/0142-9612(92)90054-R.

Zhang, B.G.X., Myers, D.E., Wallace, G.G., Brandt, M., Choong, P.F.M., 2014. Bioactive coatings for orthopaedic implants—recent trends in development of implant coatings. Int. J. Mol. Sci. 15, 11878–11921. https://doi.org/10.3390/ijms150711878.

Further reading

McTighe, T., Brazil, D., Clarke, I., Keppler, L., Keggi, J., Tkach, T., McPherson, E., 2015. Metallic modular taper junctions in total hip arthroplasty. JISRF Reconstr. Rev. 5(2) https://doi.org/10.15438/rr.5.2.108.

Sing, S.L., An, J., Yeong, W.Y., Wiria, F.E., 2016. Laser and electron-beam powder-bed additive manufacturing of metallic implants: a review on processes, materials and designs. J. Orthop. Res. 34, 369–385. https://doi.org/10.1002/jor.23075.

Testworth, K., Block, S., Glatt, V., 2017. Putting 3D modelling and 3D printing into practice: Virtual surgery and preoperative planning to reconstruct complex post-traumatic skeletal deformities and defects. SICOT J. 3 (16), 1–10. https://doi.org/10.1051/sicotj/2016043.

Trevisan, F., Calignano, F., Aversa, A., Marchese, G., Lombardi, M., Biamino, S., Ugues, D., Manfred, D., 2018. Additive manufacturing of titanium alloys in the biomedical field: processes, properties and applications. J. Appl. Biomater. Funct. Mater. 16 (2), 57–67. https://doi.org/10.5301/jabfm.5000371.

Advances in clinical applications of metal biomaterials for spinal reconstruction

18

Hiroyuki Hasebe, Manabu Ito
Department of Orthopedic Surgery, National Hospital Organization Hokkaido Medical Center, Sapporo, Japan

18.1 Introduction

Metallic materials have the longest history in the field of orthopedic surgery among numerous biomaterials. The first use of metallic implants for spine fractures dates back to more than 100 years ago. Since then, metallic implants were used routinely for spinal fractures and spinal deformities. The advantages of metals are excellent mechanical stiffness and toughness to provide unstable sites with adequate mechanical stability to lead solid bony union. The common indications of metallic implants for spinal surgery are fixation of spinal fractures and dislocations causing neurological deficits and deformity correction in patients with scoliotic and/or kyphotic deformity.

Although metallic implants are often removed at 1 or 2 years after surgery in the extremities to prevent osteopenia or osteoporosis caused by a stress-shielding effect around the metallic implant, spinal implants are rarely removed even after solid spinal fusion is achieved. A reason for this is that spine surgeries are even more invasive than other orthopedic surgery in the extremities so that multiple surgery for a patient is not desirable. Growing rods are used for juvenile progressive spinal deformities to correct their deformity without spinal fusion (instrumentation without fusion). Many modifications to spinal instrumentation surgery are going on to minimize surgical invasiveness using percutaneous pedicle screws through minimal skin incision. As the elderly population shows a significant increase around the globe, the demands for metallic spinal implants to correct their severe spinal deformities are increasing dramatically in the recent years.

18.2 History of spinal instrumentation

Hadra reported the first application of metallic implant to the spinal column in 1891 (Hadra, 1891). Ag wires were used for the treatment of spinal fracture in the thoracic spine. Other clinically used metals in spine surgery were stainless steel which was invented during the first world, Co-Cr was in the 1920s, and titanium and titanium alloys were in the 1960s. Due to the superior biocompatibility of titanium, most

Metals for Biomedical Devices. https://doi.org/10.1016/B978-0-08-102666-3.00018-3
© 2019 Elsevier Ltd. All rights reserved.

commonly used metal in the present spine surgery is titanium alloys. In 1942, Rogers described the interspinous wiring method used for trauma-induced cervical instability (Rogers, 1942).

The introduction of Harrington instrumentation was in 1962, which was the most important historical event in the spinal reconstruction surgery (Harrington, 1962). The spinal implants of Professor Paul Harrington consisted of hooks and rods made of stainless steel for the treatment of severe spinal deformity and fracture dislocations of the spine (Fig. 18.1). Since the introduction of his device, surgical procedures to correct and stabilize the spine with metallic implants have shown a dramatic improvement. And, the surgeries using metal implants to correct and stabilize the injured spine were named spinal instrumentation surgery. The Harrington instrumentation surgery was modified later by adding additional anchors including sublaminar wires. Luque, M.D. introduced his surgical technique using sublaminar wires at the annual meeting of the Scoliosis Research Society in 1976 (Luque, 1982) (Fig. 18.2). This implant was used for many spinal disorders including adolescent idiopathic scoliosis (AIS) and spinal traumas including fracture dislocations causing neurological deficits. The next historical event was that two French spine surgeons (Professor Cotrel and Professor Dubousset) developed their own spinal implants and correction technique for AIS with combination of multiple hooks and rod rotation maneuvers (Cotrel et al., 1984) (Fig. 18.3). By their surgical

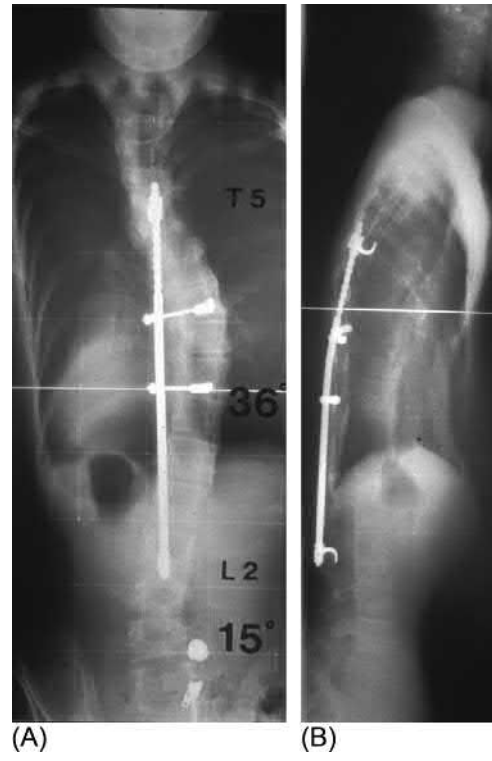


Fig. 18.1 Harrington instrumentation. (A) PA radiograph and (B) lateral radiograph.

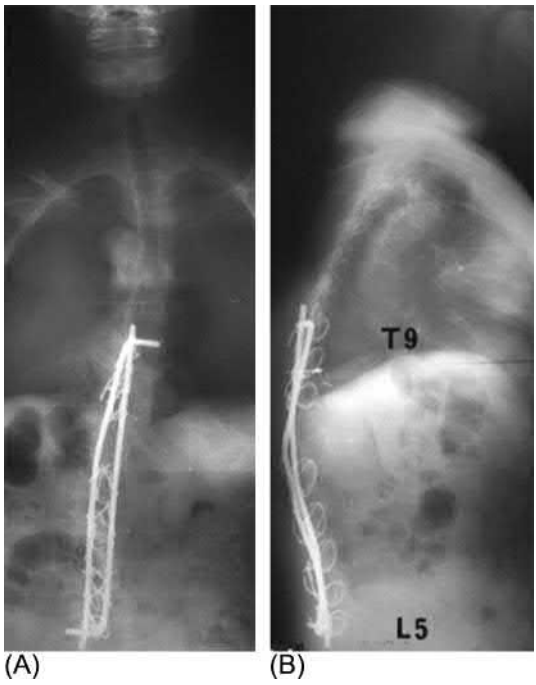


Fig. 18.2 Luque sublaminar wiring. (A) PA radiograph and (B) lateral radiograph.

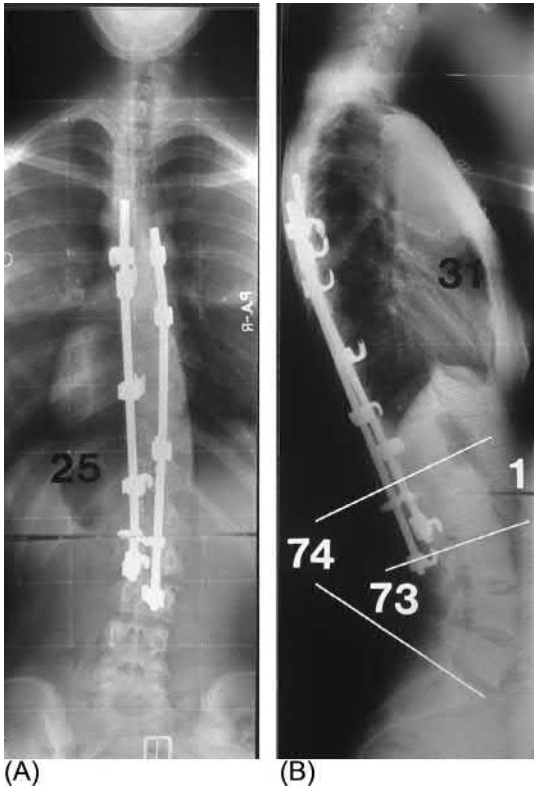


Fig. 18.3 Cotrel-Dubousset (CD) instrumentation. (A) PA radiograph and (B) lateral radiograph.

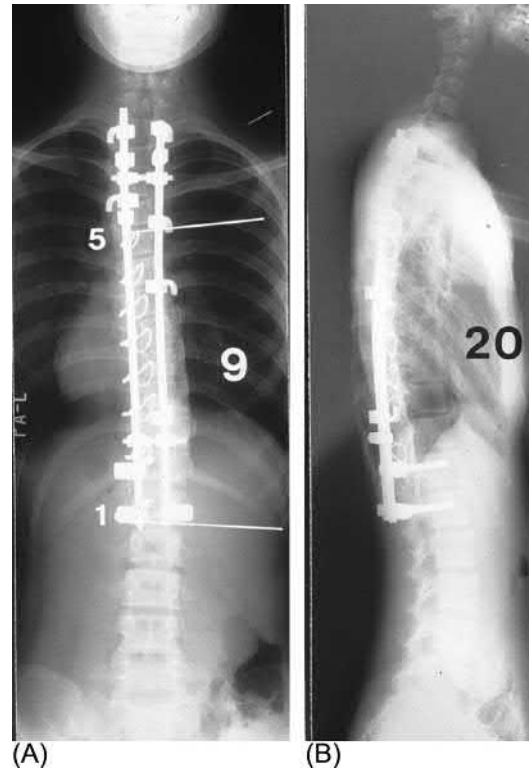


Fig. 18.4 Hybrid instrumentation for adolescent idiopathic scoliosis. (A) PA radiograph and (B) lateral radiograph.

technique, the correction rate of AIS showed a dramatic improvement. In the 1980s, the ISOLA system and TRSH system using a combination of pedicle screws, hooks, and sublaminar wires were introduced for spinal deformity surgery. This system was called a hybrid system using different types of anchors at each vertebra (Fig. 18.4). In the 1990s, only pedicle screw system was introduced by a Korean spine surgeon, Professor Suk. Due to the biomechanical superiority of pedicle screw, pedicle screw system provided the highest correction rate for AIS over 70% (Suk et al., 1995). By the application of pedicle screw system, many deformity correction procedures were reported with excellent three-dimensional (3D) correction of spinal deformity especially in AIS (Fig. 18.5). The spinal implants above were used for posterior spine surgery.

As to anterior spinal instrumentation, Dwyer system was introduced in 1969 (Dwyer et al., 1977) (Fig. 18.6) and Zielke instrumentation was in 1978 (Zielke, 1982). These implants consisted with one vertebral body screw and a rod connecting each screw. An implant with a single screw and rod did not provide satisfactory correction of spinal deformity so that a new system consisting of two vertebral body screws and two rods was developed by Professor Kaneda, a Japanese spine surgeon,



Fig. 18.5 Pedicle screw instrumentation for adolescent idiopathic scoliosis. (A) PA radiograph and (B) lateral radiograph.



Fig. 18.6 Dwyer anterior instrumentation: AP radiograph.



Fig. 18.7 Kaneda anterior instrumentation for lumbar scoliosis: PA radiograph.

in 1984 (Kaneda et al., 1997). His implant was revised several times for the use of correction of AIS and treatment for spinal burst fractures at the thoracolumbar junction (Fig. 18.7).

18.3 Biomechanics of spinal instrumentation

Numerous biomechanical studies have been performed to evaluate the pullout strengths of different types of fixation anchors for the spine. Biomechanically reliable fixation anchors can make shorter segment fusion which make surgery less invasive and provide a better rate of biological fusion.

In the cervical spine, posterior wiring technique is the most traditional instrumentation technique still widely used for various cervical pathologies. The shortcoming of the posterior interspinous wiring is to stabilize only the posterior tension band construct and provides stability only in flexion instability. It does not provide stability against extension, rotation, or lateral bending. Posterior screw and plate systems provide better stability for all directions (Johnston et al., 2006; Jones et al., 1997).

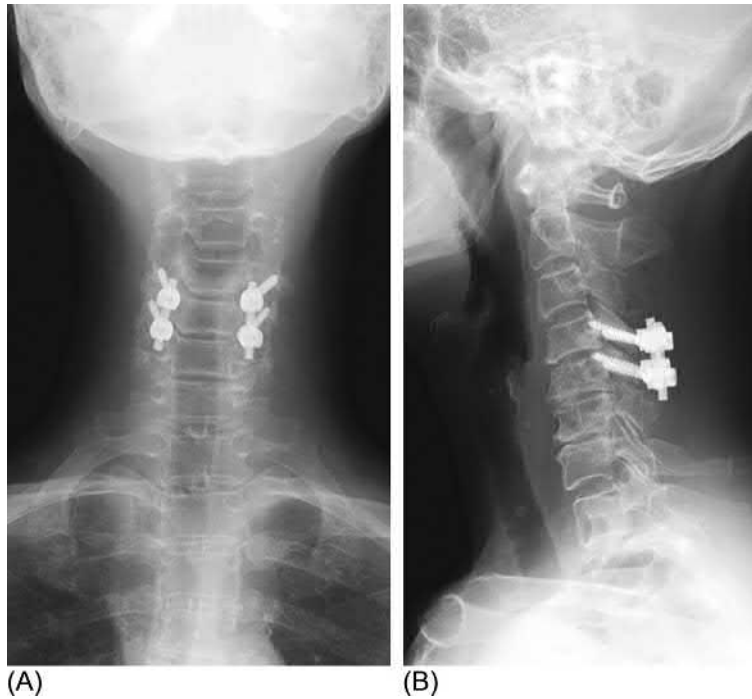


Fig. 18.8 Cervical lateral mass screw system. (A) AP radiograph and (B) lateral radiograph.

Laminar screws have major role in C1-C2 fixation and have lesser biomechanical stability as compared to lateral mass screws (LMS) (Fig. 18.8) and cervical pedicle screws (CPS).

LMS has biomechanical limitations due to small amount of bony purchase and thereby lesser pullout strength especially in the presence of osteoporosis. Pullout strength of LMS is more in the upper-middle cervical spine than in lower cervical spine (Johnston et al., 2006; Jones et al., 1997). In many cases, unstable spines cannot rely only on LMS, and often need an additional anterior procedure to achieve three column stability. Many studies have reported the superior biomechanical stability of CPS over LMS with an advantage of supporting both the anterior and posterior columns, eliminating the need for an additional anterior procedure. CPS offers more stable construct for occipitocervical fusion and cervicothoracic fixation, and the fusion rates in the subaxial cervical spine were better than those of LMS. Many biomechanical studies proved greater pullout strength of CPS compared to LMS and the failure in CPS is rather due to fracture at the pedicle than screw loosening which is frequently seen in LMS.

Other biomechanical studies of spinal instrumentation have focused on the forces on the spinal implants during correction procedures of spinal deformity. Salmingo et al. investigated on the force on pedicle screws and rods during rod rotation

procedures for correction of AIS (Salmingo et al., 2012). They reported the highest pullout force was around 170 N at the apex of scoliosis curve and the total amount of force on the concave side rod was about 1400 N in a patient with 70-degree single curve treated with pedicle screws placed at all spinal levels within a curve. If the curve was much larger and the number of pedicle screws was reduced, the pull-out force of a pedicle screw would increase significantly so that the chances of screw pullout may become much higher. Screw pullout is a serious surgery-related complication needing an additional surgery which may have tremendous negative impacts on patients.

Biomechanical evaluations of spinal implants are indispensable to seek best treatment methods and develop a new spinal implant before its clinical application for its safety.

18.4 Clinical application of spinal implant

18.4.1 Pedicle screw system

The most popular spinal instrumentation system at the present is a pedicle screw system. This system consists of two screws placed at the bilateral pedicles, which are linked to other cranially and caudally placed screws with a metal rod or a plate. This system has the highest mechanical stability among numerous spinal fixation systems (Johnston et al., 2006; Jones et al., 1997). This system can be applied to the whole spine from the occiput to the sacrum to correct 3D deformity of the spine (Abumi et al., 1994). Due to the anatomical limitations in the size of the pedicle, pedicle screw placement is not always possible if the pedicle diameter is less than 3 mm. The middle cervical spine in patients with rheumatoid arthritis and the upper to middle thoracic spine in those with severe spinal deformity are the areas where pedicle screws are difficult to place accurately. Preoperative planning of measuring the size of the pedicles are important to determine whether pedicle screws can be placed or not. The locations of other important organs such as the vertebral arteries in the cervical spine and the aorta in the thoracic spine should be carefully checked before surgery. Any damage to these important vessels by pedicle screws may lead serious complications including brain infarction or massive bleeding from the aorta which is a fatal complication if occurred. For the cervical spine, LMS are often used if pedicle screw insertion is not safe or impossible.

To adjust large personal variations in the 3D alignment of the spine, spine surgeons frequently bend rods or plates to fit the individual spinal alignment of the spine during operation. Titanium alloys are most commonly used in spinal surgeries due to their easiness to bend during surgery by surgeons' hands. Bending a metallic rod or plate at multiple times during surgery may lead the metallic material to plastic deformation which makes them weaker in the mechanical stiffness and often ends with implant failures (Demura et al., 2015). Spine surgeons should know the mechanical

characteristics and limitations of each material and be aware of the risks of excessive manual bending of the rods or plates.

Under the presence of osteoporosis, pedicle screws are easy to loosen because the fixation between screw and bone is very weak. To strengthen pedicle screws in osteoporotic spine, polymethylmethacrylate (PMMA) or small hydroxyapatite blocks are often inserted at the pedicle holes together with screws to reinforce their pullout force. Another surgical technique to make pedicle screw fixation stiffer is to make changes to the screw direction. Traditional pedicle screw is placed along with the pedicle axis which is parallel to the vertebral endplates targeting the middle of the vertebral body. In osteoporotic spine, the middle of the pedicle and vertebral body becomes vacant because these areas are mainly consisting of cancellous bone which is seriously affected by osteoporosis. Alternative screw placement method is called cortical bone trajectory (CBT) in which pedicle screws should be inserted from the inferior-medial aspect of the pedicle targeting the lateral upward direction to catch the upper part of the pedicle with thick cortical bone (Santoni et al., 2009) (Fig. 18.9). Cortical bone is hard and is not severely affected by osteoporosis. Biomechanical studies showed CBT screws provided better stability especially in the lumbar spine.



Fig. 18.9 Cortical bone trajectory and intervertebral cage in lumbar degenerative disorders with osteoporosis.

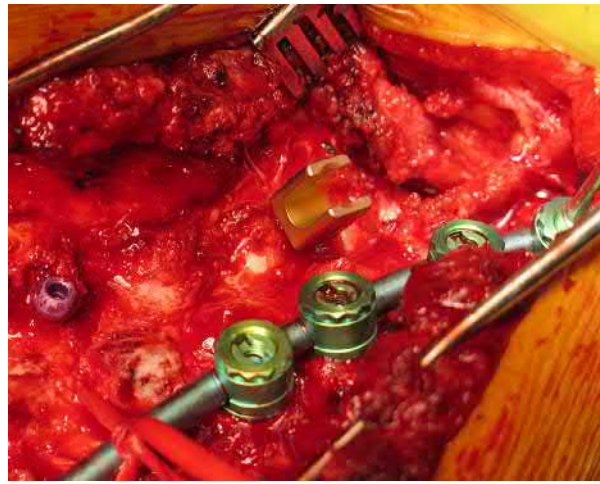


Fig. 18.10 Placement of transverse hook. A golden implant is a transverse hook.

18.4.2 Hooks

Hooks are often used at the thoracic spine for patients with spinal deformity such as AIS and adult spinal deformity (Fig. 18.10). The anatomical sites for hook placement are the transverse process, lamina and pedicle. In many patients, pedicle size in the upper thoracic spine is small for screw placement so that hook placement is a common alternative technique as a strong anchor to the spine. A single hook cannot provide reliable biomechanical stiffness unlike a pedicle screw. Hooks should be placed at least two sites at the cephalad and caudal side of the fixation area. Claw setting by two hooks is often used to provide better stability. A common claw setting is a combination of a transverse hook and pedicle hook at the same vertebra. And another claw setting is an intersegmental claw using the same combination of hooks between two neighboring vertebrae. Hook placement at the laminae needs special attention not to push the spinal cord. Hook placement from cephalad at the central part of the laminae has a high risk for the hook to push the spinal cord due to the thickness and shape of the laminae. For safe placement of a lamina hook from cephalad to caudal direction, it is better to remove and make thinner the cephalad portion of the lamina and chose a hook with a short neck to prevent the tip of hook from getting into the spinal canal. Hooks are often used for osteoporotic spine if pedicle screws are unreliable mechanically. Also, for a long spinal fixation in adult patients, hooks are placed at the most cephalad-instrumented vertebra. The reason for this is that hooks allow some motions to the spine in the sagittal plane even after the spinal implants are properly placed. Due to this mechanical effect of hooks, the risk of proximal junctional vertebral fractures just above the spinal implant may decrease to some extent compared with all pedicle screw construct.

18.4.3 Sublaminar wires and tapes

Sublaminar wires had been popular to stabilize the spine before pedicle screws came into the clinical field. Same as hooks placed at the laminae, sublaminar wires have a risk to push the spinal cord when passing wires under the laminae. The metallic material of sublaminar wires was used to be stainless steel, but it has changed to titanium alloys.

Due to the potential risk of sublaminar wires to the spinal cord, the use of metallic sublaminar wires is decreasing and is replaced by high molecular polyethylene tapes (Takahata et al., 2007). The tapes are 3 mm or 5 mm in width which is wider than sublaminar wires. This width has a benefit especially for patients with severe osteoporosis. Thin metallic sublaminar wires may cut the osteoporotic fragile laminae. Woven soft tapes with wider contact surface of may have a lesser risk of cutting the osteoporotic laminae. One of the problems of using sublaminar tapes is that these tapes are invisible on postoperative radiographs. It is difficult for surgeons to check and monitor the postoperative conditions of these tapes on radiographs. Also, the tightening strength needs special attention during surgery not to break the fragile laminae. The tightening strength is around 25 pounds for a normal spine and for osteoporotic spines less than 20 pounds is recommended.

18.4.4 Rods

Metallic rods are placed between pedicle screws, sublaminar wires, or tapes to correct spinal deformity and stabilize the spinal column. Rods play the most important role to correct the deformed spine and maintain the corrected spine alignment until solid spinal fusion is obtained. Even after bony fusion is complete, placed rods are still carrying mechanical loads during daily activities. The diameter of rods ranges from 3 to 6 mm according to the area of the spine. The rods for the cervical spine do not need significant stiffness because the mechanical loads in the cervical spine are much smaller than those in the thoracic and lumbar spine. For patients with large and rigid spinal deformity, 6 mm rods made of titanium or Co-Cr are commonly used for correction of the curves and its maintenance.

The human spine has its own physiological curves in the sagittal plane. The cervical spine has a lordotic curve, the thoracic spine has kyphosis and the lumbar spine has lordosis. The magnitude of each sagittal curve has personal difference and there are significant changes in different ages. During surgery, surgeons cut a rod into an appropriate length to fit each patient and bend it to fit the sagittal curve in each patient. Intraoperative rod bending reduces the stiffness of the metal significantly and multiple rod bending may lead to rod breakage after surgery. Although there are differences in the values of elongation at break of different metals, all metallic rods have the same behavior that the stiffness of any metallic rod decreases significantly after multiple rod bending. All spine surgeons should be aware of this mechanical behavior of metals.

18.4.5 Vertebral cages and intervertebral cages

As well as pedicle screws, rods, and plates, intervertebral cages or spacers are utilized after resection of intervertebral discs in degenerative spinal disorders with spinal instability. There are many different shapes or sizes in intervertebral spacers clinically available in the recent years (Fig. 18.9). Due to a growing demand of intervertebral cages for the surgical treatment of adult spine deformity, there are different cages which are placed through three different surgical approaches such as posterior access, transforaminal access (posterolateral access), or lateral access. A recent trend is that some medical device companies are selling titanium-coated polyetheretherketone (PEEK) cages or titanium-alloy cages with porous structures to make better and faster biological bondage between cages and the surrounding vertebral bodies.

Vertebral cages are used after resection of one or two vertebral bodies in patients with severe vertebral body fractures and spinal tumors (Fig. 18.11). In most clinical situations, the cages are filled with autogenous, allogenic, or synthetic bone grafts to obtain solid biological fusion to the adjacent vertebrae. Another benefit of using spinal cages is reduction of the need of structural bone grafts taken from the patient' iliac bone or fibula, because the bone graft harvest sites often cause persisting pain which is still one of the major problems to be solved in the field of spinal surgery.

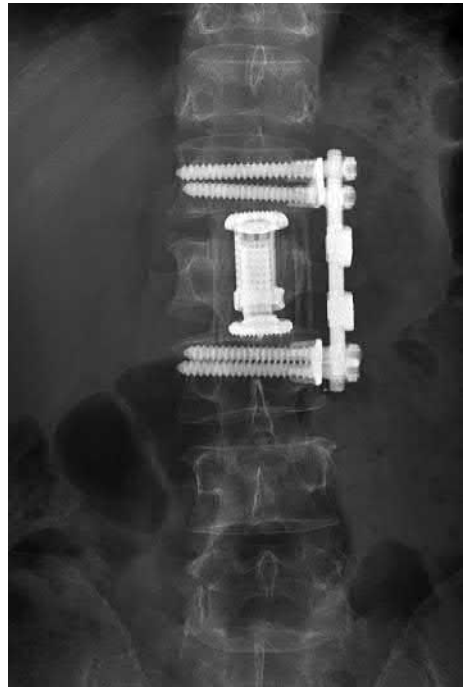


Fig. 18.11 Vertebral cage. A vertebral cage is placed at the fractured vertebral body.

18.4.6 Growth friendly spinal instrumentation surgery

Most metallic spinal implants are used for spinal arthrodesis for adult or adolescent patients whose body-height growth has almost finished. For child patients under growth with progressive severe spinal deformity, growth friendly spinal implants are used to correct their spinal deformities (Akbarnia et al., 2005). Due to the size of the vertebral bodies in children, pedicle screws can be placed from the age around 5 or 6 years. If juvenile patients have progressive severe spinal deformity, spinal implants allowing spinal growth in parallel to a patient's body height growth are indicated. Solid anchor points should be created at the cephalad and caudal end vertebra of the curve by using hooks or pedicle screws. For the upper thoracic spine, a combination of hooks is commonly used due the size limitation for pedicle screws in small children. For the lumbar spine, pedicle screws are used for the distal anchors. The first surgery is done to place both cephalad and caudal anchors with metallic implants and posterior spinal fusion is conducted at the anchor points. At 3 or 4 months after the first surgery, making sure of solid posterior spinal fusion at the two anchor points, the second surgery is performed to start deformity correction with distraction force between the two anchor points (Fig. 18.12). Two metal rods are placed from the cephalad anchor point and the other two metal rod are from the caudal anchor point. These four rods are connected at the middle of the curve and start to put a distraction force between the cephalad and caudal anchor points. End-to-end or side-to-side rod connectors are used to maintain the force for correction of the curve. Additional surgery will be followed at a 6-month interval to elongate the spine to catchup the trunk growth of a juvenile patient. Since this treatment requires multiple surgery, there are many surgery-related complications reported (Watanabe et al., 2013). Reported complication rates were around 60% including rod breakage, hook dislodgement, skin breakdown, and surgical site infection. In the recent years, magnetic controlled growing rod system was introduced to minimize multiple time surgery (Cheung et al., 2014). However, the long-term clinical results of this new growing rod system are not available today.

18.4.7 Motion preservation technology

The main purpose to use spinal implants is to obtain solid bony fusion at the area where spinal implants are placed. By achieving solid spinal arthrodesis, we are sacrificing one of the biological functions of the spine; that is, spinal mobility or flexibility. One solution not to sacrifice the mobility of the spine is to use total disc replacement (TDR) for degenerative pathologies in the lumbar and cervical spine. TDR has been used in the lumbar spine since 1980s, and more recently in the cervical spine. Although the biomechanical concepts are the same and both are inserted through an anterior approach, lumbar TDR is conventionally indicated for chronic low back pain, whereas cervical TDR is used for soft disc hernia causing neurological deficits and severe radiating pain to the upper extremities. There are numerous basic and clinical studies, including prospective randomized comparative trials, have demonstrated non-inferiority to conventional spinal fusion surgery (Vital and Boissière, 2014; Radcliff et al., 2016; Fan et al., 2017).



Fig. 18.12 Growing rod system for early-onset scoliosis. (A) PA radiograph and (B) lateral radiograph.

The clinical use of TDR has been decreasing significantly in the lumbar spine during the last decade due to a high rate of loosening and dislodgement of the implants in the lumbar spine and revision surgeries for lumbar TDR are technically difficult and risky due to the adhesion to the great vessels and the abdominal organs. On the contrary, TDR for the cervical spine has become a standard surgical technique for simple disc herniation or degenerative radiculomyelopathy at one or two spinal segments in young healthy patients without osteoporosis.

18.4.8 Metallic wear debris in spinal instrumentation

Metallic wear debris is one of the major clinical concerns if young patients should have spinal implants for many years (Hallab et al., 2003). Metallic wear commonly occurs at the junctions between rods and screw heads or sublaminar metallic wires due to micromotion at the junctions by trunk motions in daily living. Special attention should be made for spinal deformity patients in children who undergo spinal correction and fusion with metallic spinal implants. In most child patients surgically treated

with metallic implants for their severe spinal deformity, spinal implants are not removed after surgery to avoid multiple invasive surgery. There are controversies with regards to the benefits and demerits of removing spinal implants used in child patients. Most metallic implants for bone fractures in the extremities are commonly removed once bony union is complete. Removal of implant may enhance bone remodeling at the fracture site to make the bone union mature and stiffer. Based on this concept, some spine surgeons remove spinal implants routinely at postoperative 1 and 2 years after the completion of bony union. There are, however, some child patients who show a progression of their scoliotic curves after removal of the spinal implants. Previous studies regarding accumulation of metal wear debris in child patients with spinal instrumentation showed that there were little adverse effects of metallic debris on the human body even if patients had metallic spinal implants for two or three decades (Zielinski et al., 2014).

18.4.9 Artifacts on magnetic resonance images

One of the demerits of using metallic implants for spine surgery is a formation of artifacts around the metallic implants on magnetic resonance (MR) images, which disturb clinical assessment of the surrounding tissues (Fig. 18.13) (Hargreaves et al., 2011). When metal implants are placed in the spine, device-related artifacts interfere clinicians with assessing neural disorders next to the implants. Another concern is that

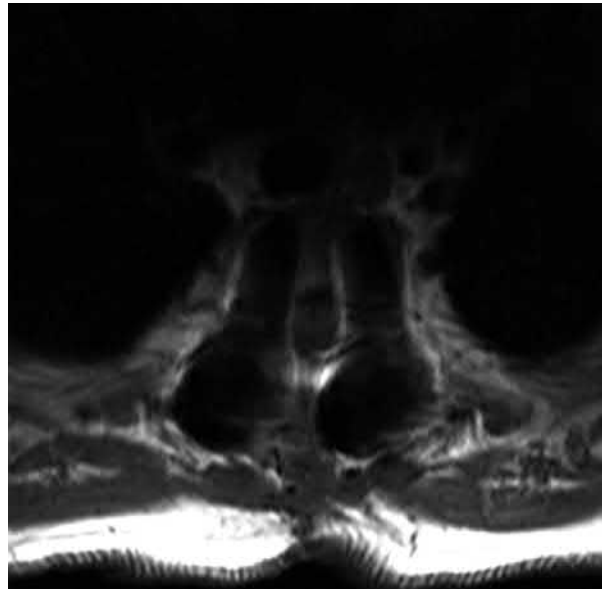


Fig. 18.13 Metal-related artifacts on MR image. Axial plane of T1-weighted MR image.

metallic implants may impart heat to the surrounding tissues while taking MR images. Titanium alloys are the most popular material for recent spinal implants due to their biocompatibility and fewer metal-related artifacts in MR images. Even though titanium alloys produce least artifacts in MR images, the spinal cord and nerve roots are not be able to assess due to the artifacts caused by the presence of metallic spinal implants in magnetic resonance imaging (MRI). The use of spinal implants made of Co-Cr is increasing in the recent years for correction of rigid spinal deformities due to their superior mechanical stiffness to obtain better correction and maintain the spinal stability after surgery. The MR artifacts of Co-Cr metallic implants, however, are much stronger than those of titanium alloys so that postoperative assessment around the Co-Cr spinal implant are impossible.

18.4.10 Spine surgery for adults and the elderly

One of the social problems in the developed countries is a rapid increase in the elderly population. The chances to surgically manage osteoporotic spinal fractures and following rigid kyphotic deformity in the elderly population show a steady rise. Osteoporotic spinal fractures are associated with significant morbidity and an increased risk of mortality (Lau et al., 2008). These fractures often cause a notable amount of pain and therefore are associated with functional disability and a decreased quality of life (QOL). The treatment of osteoporotic spinal fracture is predominately nonsurgical, but patients who fail to improve with nonsurgical management are indicated for surgical intervention. Cement augmentation of painful osteoporotic vertebral body fractures consists of percutaneous stabilization of the vertebral bodies with PMMA. Vertebroplasty is characterized by the insertion of PMMA into the fractured vertebra; Kyphoplasty uses an inflatable balloon to create vertebral body expansion before the injection of cement (Long et al., 2012). Calcium phosphate cement (CPC) is also used for cement augmentation for osteoporotic spinal fracture (Gumpert et al., 2014). In many severe osteoporotic patients, injected PMMA or CPC will move around after surgery due to the mechanical weakness of the surrounding vertebral bodies. In these cases, posterior additional spinal instrumentation is added to prevent cement loosening and to stabilize the spinal column. During postoperative follow-up, adjacent vertebral fractures are commonly seen after spinal fixation surgery in patients with osteoporosis. Medication for osteoporosis such as parathyroid hormone or bisphosphonates should be delivered for a long-term after spinal instrumentation surgery in these patients.

In the recent years, based on the progress of medical treatment, more and more adult patients with spinal deformity including scoliosis, kyphosis, or both undergo spinal deformity surgery with metallic implants. Global trunk imbalance makes the life expectancy of the elderly shorter. Despite the growing needs for the elderly patients, this type of surgery for the elderly has a high rate of surgery-related complications (Lenke et al., 2016). Minimization of surgical invasiveness and strict patients' selection is needed for adult spinal deformity surgery.



Fig. 18.14 Minimally invasive spinal stabilization: (A) AP radiograph after percutaneous pedicle screw placement and (B) multiple small skin incisions for screw insertion.

18.4.11 Minimally invasive spinal stabilization surgery

Conventional open spine surgery with metallic implants is an invasive surgery with long operative time and considerable blood loss. There is a new movement of making spine reconstruction surgery less invasive by reducing damage to the soft tissues. This type of surgery is called minimally invasive spinal stabilization (MISt) to use small skin incisions and some special soft tissue retractors for pedicle screw insertion (Fig. 18.14). Instead of making a long midline skin incision in the back, small incisions are made just at the sites of pedicle screw insertion. All surgical procedures are done under radiological imaging guidance or 3D navigation systems. By using this surgical technique, intraoperative blood loss has decreased dramatically, which is beneficial for patients to return early to their normal life. This technology is getting popular in the field of spine surgery in the recent years. One of the problems of this technique is a large amount to radiation exposure for surgeons and clinical staff during surgery. Another shortcoming of this technique is that adequate bone grafting is difficult through very small skin incisions. MISt surgery is effective especially for aged patients with metastatic spine tumors and some types of spinal traumas because their general conditions are not good for invasive conventional spine surgery (Miscusi et al., 2015).

18.5 Conclusions

This chapter describes the history of metallic spinal implants and their trends in the present spine surgery. For more than 100 years, metallic spinal implants have been playing a major role in spinal reconstruction surgery treating spinal deformity, trauma, tumor, and many other degenerative diseases. There are many different biomaterials clinically available in the recent years, such as hydroxyapatite and different types of polymers. Due to the weakness of their mechanical toughness and strain properties, metals are not replaced by other materials in the field of spinal surgery. Reducing artifacts in MR images to disturb clinical evaluations adjacent to metallic spinal implants is one of the issues to be solved in the future. Also, considering the growing demands of metallic spinal implants for severe spinal deformities in all age groups, there are expectations for metals to meet the new clinical needs even after a long history of their use in spine surgery.

References

Abumi, K., et al., 1994. Transpedicular screw fixation for traumatic lesions of the middle and lower cervical spine. Description of the techniques and preliminary report. J. Spinal Disord. 7, 19–28.

Akbarnia, B.A., et al., 2005. Dual growing rod technique for the treatment of progressive early-onset scoliosis: a multicenter study. Spine 30 (17 Suppl), 46–57.

Cheung, J.P., et al., 2014. A novel approach to gradual correction of severe spinal deformity in a pediatric patient using the magnetically-controlled growing rod. Spine J. 14 (7), e7–13.

Cotrel, Y., et al., 1984. Nouvelle technique d'ostheosynthèse rachidienne sègmentaire par voie postèrieure. Rev. Chir. Orthop. Reparatrice Appar. Mot. 70, 489–495.

Demura, S., et al., 2015. Influence of rod contouring on rod strength and stiffness in spine surgery. Orthopedics 38 (6), e520–e523.

Dwyer, A.P., et al., 1977. The late complications after the Dwyer anterior spinal instrumentation for scoliosis (abstr). J. Bone Joint Surg. Br. 59, 117.

Fan, D., et al., 2017. Total disc replacement versus fusion for lumbar degenerative disc disease: a systematic review of overlapping meta-analyses. Eur. Spine J. 26, 806–815.

Gumpert, R., et al., 2014. Demineralization after balloon kyphoplasty with calcium phosphate cement: a histological evaluation in ten patients. Eur. Spine J. 23 (6), 1361–1368.

Hadra, B.E., 1891. Wiring of the vertebrae as a means of immobilization in fracture and Pott's disease. In: The Times and Register. Medical Press, Philadelphia, PA, pp. 1–8.

Hallab, N.J., et al., 2003. Spinal implant debris-induced osteolysis. Spine 28 (20), S125–S138.

Hargreaves, B.A., et al., 2011. Metal-induced artifacts in MRI. Am. J. Roentgenol. 197, 547–555.

Harrington, P.R., 1962. Treatment of scoliosis correction and internal fixation by spinal instrumentation. J. Bone Joint Surg. Am. 44, 591.

Johnston, T.L., et al., 2006. Cervical pedicle screws vs. lateral mass screws: uniplanar fatigue analysis and residual pullout strengths. Spine J. 6 (6), 667–672.

Jones, E.L., et al., 1997. Cervical pedicle screws versus lateral mass screws. Spine 22 (9), 977–982.

Kaneda, K., et al., 1997. Anterior correction of thoracic scoliosis with Kaneda anterior spinal system: a preliminary report. Spine 22 (12), 1358–1368.

Lau, E., et al., 2008. Mortality following the diagnosis of a vertebral compression fracture in the Medicare population. J. Bone Joint Surg. Am. 90 (7), 1479–1486.
Lenke, L.G., et al., 2016. Neurologic outcomes of complex adult spinal deformity surgery: results of the prospective, multicenter Scoli-Risk-1 study. Spine 41 (3), 204–212.
Long, S.S., et al., 2012. Vertebroplasty and kyphoplasty in the United States: provider distribution and guidance method, 2001-2010. AJR Am. J. Roentgenol. 199 (6), 1358–1364.
Luque, E.R., 1982. Segmental spinal instrumentation for correction of scoliosis. Clin. Orthop. Relat. Res. 163, 192–198.
Miscusi, M., et al., 2015. Comparison of minimally invasive surgery with standard open surgery for vertebral thoracic metastases causing acute myelopathy in patients with short- or mid-term life expectancy: surgical technique and early clinical results. J. Neurosurg. Spine 22 (5), 518–525.
Radcliff, K., et al., 2016. Five-year clinical results of cervical total disc replacement compared with anterior discectomy and fusion for treatment of 2-level symptomatic degenerative disc disease: a prospective, randomized, controlled, multicenter investigational device exemption clinical trial. J. Neurosurg. Spine 25 (2), 213–224.
Rogers, W.A., 1942. Treatment of fracture-dislocation of the cervical spine. J. Bone Joint Surg. Am. 24, 245–258.
Salmingo, R., et al., 2012. Corrective force analysis for scoliosis from implant rod deformation. Clin. Biomech. 27, 545–550.
Santoni, B.G., et al., 2009. Cortical bone trajectory for lumbar pedicle screws. Spine J. 9 (5), 366–373.
Suk, S.I., et al., 1995. Segmental pedicle screw fixation in the treatment of thoracic idiopathic scoliosis. Spine 20, 1399–1405.
Takahata, M., et al., 2007. Comparison of novel ultra-high molecular weight polyethylene tape versus conventional metal wire for sublaminar segmental fixation in the treatment of adolescent idiopathic scoliosis. J. Spinal Disord. Tech. 20, 449–455.
Vital, J.M., Boissière, L., 2014. Total disc replacement. Orthop. Traumatol. Surg. Res. 100 (1 Suppl), S1–14.
Watanabe, K., et al., 2013. Risk factors for complications associated with growing-rod surgery for early-onset scoliosis. Spine 38 (8), E464–E468.
Zielinski, J., et al., 2014. Carbon coated implants as a new solution for metal allergy in early-onset scoliosis: a case report and review of the literature. Spine Deform. 2 (1), 76–80.
Zielke, K., 1982. Ventral derotation spondylolisthesis. Results of treatment of cases of idiopathic lumbar scoliosis. Z. Orthop. 120, 320–329.

Further reading

Stradiotti, P., et al., 2009. Metal-related artifacts in instrumented spine. techniques for reducing artifacts in CT and MRI: state of the art. Eur. Spine J. 18 (Suppl. 1), 102–108.

New-generation metallic biomaterials

19

T. Narushima
Department of Materials Processing, Tohoku University, Sendai, Japan

19.1 Introduction

The number of elderly people is rapidly increasing in both the developed and developing countries. Moreover, it is predicted that the number of individuals suffering from injuries sustained during falls and deterioration of bodily functions will increase in this increasingly aging society. To improve the quality of life (QOL) of these individuals, medical and dental technologies have to further improve for reconstruction of functions of the human body. Highly functional and safe biomaterials can contribute to the development of medical and dental technologies and tissue engineering. Because of the mechanical strength and ductility of metallic biomaterials, they could replace damaged hard tissue (Niinomi, 2002). It is known that 70%–80% of implants are fabricated using metallic biomaterials such as stainless steels, cobalt (Co)-chromium (Cr) alloys, and titanium (Ti) and its alloys (Niinomi et al., 2012).

The primary materials used in orthopedics are Co-Cr and Ti alloys (Narushima, 2005), because biomaterials exhibiting high mechanical strength and excellent ductility are required in this field. Metallic biomaterials have been widely used as implants in the medical and dental fields, and their mechanical properties are superior to those of ceramic or polymer biomaterials. Fig. 19.1 illustrates the amount of wrought Ti and its alloys shipped for medical use in Japan (Japan Titanium Society, 2018). Recently, a steady increase in the demand for Ti and its alloys, which are primary metallic biomaterials, has been observed.

Most metals are thermodynamically unstable under biological conditions. The corrosion of metallic biomaterials cannot be avoided, and oxide films form as a corrosion product under biological conditions (Blackwood, 2003). Oxide films, such as Cr and Ti oxides, are uniform and dense and act as protective passive films with excellent adherence to metallic biomaterials.

As medical and dental technologies and tissue engineering advance, biomaterials exhibiting low elastic moduli, shape memory effect/superelasticity, wear resistance, superplasticity, appropriate magnetic susceptibility, biodegradability, and hot/cold workability become increasingly desirable. These properties have to be achieved in practical devices of various shapes under a range of biological and economic conditions.

In this chapter, the current status of metallic biomaterials and the research and development of new-generation metallic biomaterials and their processing are discussed.

Metals for Biomedical Devices. https://doi.org/10.1016/B978-0-08-102666-3.00019-5
© 2019 Elsevier Ltd. All rights reserved.

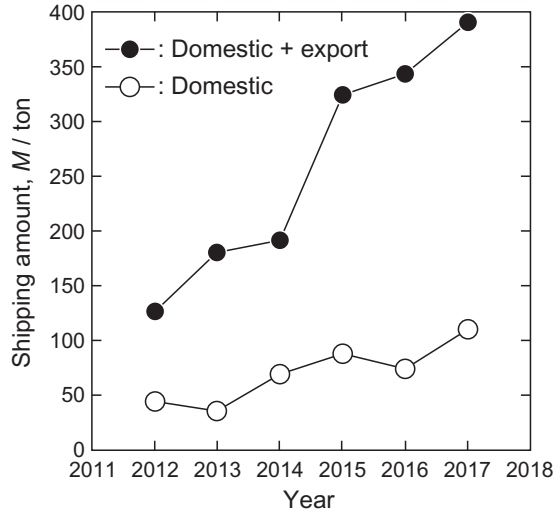


Fig. 19.1 Amount of wrought Ti and its alloys shipped for medical use in Japan (Japan Titanium Society, 2018).

19.2 Brief overview of traditional metallic biomaterials

Table 19.1 presents the chemical compositions of the stainless steels, Co-Cr alloys, and Ti and its alloys, which are registered in the American Society of Testing and Materials (ASTM) standards for surgical implant applications. The contents of alloying elements will hereafter be expressed as mass percentages and the "mass %" notation will be omitted unless otherwise noted. These metallic biomaterials are used as substitutes for hard-tissue replacements, including total hip and knee joint replacements, fracture healing aids, spinal fixation devices, stents, catheter guide wires, dental implants, orthodontic dental archwires, and cochlear implants, because of their excellent mechanical and functional properties (Hanawa, 2012). Fig. 19.2 summarizes the minimum tensile strength and total elongation requirements for metallic biomaterials according to the ASTM. Stainless steels exhibit excellent hot/cold workability and are relatively low-cost biomaterials. Co-Cr alloys typically exhibit superior mechanical strength and excellent wear resistance, but their hot/cold workability is low unless nickel (Ni) is added. Although the ductility and wear resistance of Ti and its alloys are inferior to those of stainless steels and Co-Cr alloys, their corrosion resistance and biocompatibility are exceptional.

19.2.1 Stainless steels

Austenitic stainless steels are registered in the ASTM standards for surgical implant applications, as presented in Table 19.1. The primary alloying elements for these steels are Cr, Ni, molybdenum (Mo), manganese (Mn), and nitrogen (N). The Cr accelerates passivation and improves corrosion resistance in oxidizing acid solutions and pitting corrosion resistance in chloride solutions, but it is a ferrite-stabilizing element. Ni stabilizes the austenitic phase and improves corrosion resistance in

Table 19.1 Chemical compositions of metallic biomaterials registered in the ASTM standards (mass%)

Stainless steels	Co-Cr alloys	Ti and its alloys
Fe-18Cr-14Ni-2.5Mo (C < 0.03) F138-13, wrought (bar and wire) F139-12, wrought (sheet and strip) F1350-08, wrought (wire) F2257-09, wrought (tube)	Co-28Cr-6Mo F75-12, castings	CP Ti, α type F67-13 Grade 1 Grade 2 Grade 3 Grade 4
Fe-22Cr-13Ni-5Mn-2.5Mo (C < 0.03, 0.2 < *N* < 0.4) F1314-13, wrought (bar and wire)	Co-28Cr-6Mo F1537-11, wrought F799-11, wrought (forgings)	Ti-6Al-4V, α + β type F1108-04, castings F1472-08, wrought
Fe-21Cr-10Ni-3Mn-2.5Mo (0.25 < *N* < 0.5) F1586-13, wrought (bar)	Co-20Cr-15W-10Ni F90-09, wrought F1091-12, wrought (wire)	Ti-6Al-4V ELI[a], α + β type F136-12a, wrought
Fe-23Mn-21Cr-1Mo (0.85 < *N* < 1.10) F2229-12, wrought (bar and wire)	Co-35Ni-20Cr-10Mo F562-13, wrought F688-10, wrought (plate, sheet, and foil) F961-08, wrought (forgings)	Ti-6Al-7Nb, α + β type F1295-11, wrought
Fe-11Mn-17Cr-3Mo (0.45 < *N* < 0.55) F2581-12, wrought (bar and wire)	40Co-20Cr-16Fe-15Ni-7Mo F1058-08, wrought (wire and strip)	Ti-3Al-2.5 V, α + β type F2146-13, wrought (seamless tube)
		Ti-13Nb-13Zr, near β type F1713-08, wrought
		Ti-12Mo-6Zr-2Fe, β type F1813-13, wrought
		Ti-15Mo, β type F2066-11, wrought
		NiTi, intermetallics F2063-12, wrought

[a]*ELI*, Extra low interstitial.

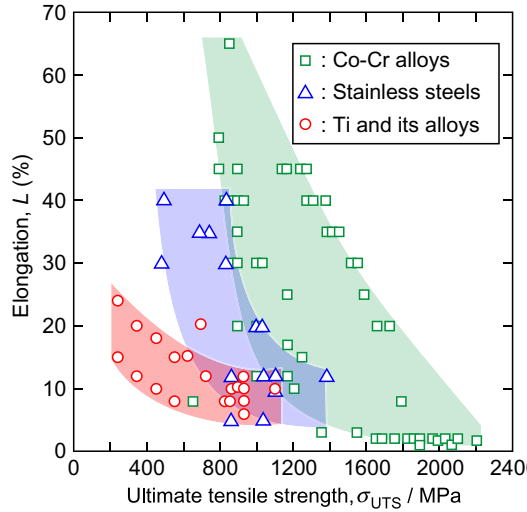


Fig. 19.2 Tensile strength and elongation of stainless steels, Co-Cr alloys, and Ti and its alloys registered in the ASTM standards.

nonoxidizing acid solutions by stabilizing the passive film. However, Ni has been highly associated with metal allergies and toxicity when Ni ions elute from the implants into the human body. Mo contributes to the stability of passive films and improves corrosion resistance in chloride solutions. Mn stabilizes the austenitic phase, increases the solubility of N, and decreases the magnetic susceptibility; however, it also decreases corrosion resistance. Increasing the content of N is preferred for stabilizing the austenitic phase, strengthening, and improving corrosion resistance. However, Cr_2N could precipitate during heat treatment when the N content of the steel is higher than its solubility at the heat treatment temperature. The precipitation of Cr_2N results in decreased ductility and corrosion resistance. Therefore, the maximum N content in biomedical stainless steels is limited to 1 mass%. Adding Cr and Mn is known to increase the solubility of N in stainless steels.

Wrought stainless steels are low carbon (C) iron (Fe)-Ni-Cr-Mo (type 316 L), high-N Fe-Cr-Ni-Mn-Mo, and Ni-free high-N Fe-Cr-Mn-Mo alloys. Type 316 L stainless steel has been primarily used in implants. Decreasing the C content to <0.03 mass% minimizes sensitization caused by the formation of a Cr-depleted zone because of the grain-boundary precipitation of $Cr_{23}C_6$, thus, lowering corrosion resistance.

19.2.2 Co-Cr alloys

It has been known since the 1900s that Co-based alloys exhibit excellent wear resistance. In the 1930s, cast Co-Cr-Mo alloy (Vitallium) was developed for dental applications. Cast and wrought Co-Cr-Mo alloys have been recognized as the most suitable biomaterials for sliding parts in artificial joints because of their excellent wear resistance compared to stainless steels and Ti alloys.

The ASTM F75 and F799 Co-28Cr-6Mo alloys have been used to fabricate stems, balls, and cups of artificial hip joints of both metal-on-ultrahigh molecular weight polyethylene (UHMWPE) and metal-on-metal types, and sliding components for artificial knee joints. Co-Cr-Mo alloys typically contain C and N to avoid the formation of the σ-phase (Co(Cr,Mo)). C and N form carbonitride precipitates in Co-Cr-Mo alloys during solidification and heat-treatment processes. Numerous types of precipitates have been reported to occur in Co-Cr-Mo alloys (Narushima et al., 2013), such as the σ, $M_{23}X_6$-type, η (M_6X-$M_{12}X$-type), π (M_2T_3X-type) (Mineta et al., 2010; Ueki et al., 2016a), χ (Sugawara et al., 2015), M_7X_3-type, and M_2X-type phases (where M and T represent metallic elements, and X represents C and/or N). The σ and χ-phases are intermetallic compounds, and the other phases are carbonitrides. Because of the formation of precipitates, the forging temperature has to be strictly maintained above 1273 K (Lee et al., 2006).

Co-Cr alloys in Co-20Cr-15 tungsten (W)-10Ni (ASTM F90), Co-35Ni-20Cr-10Mo (ASTM F562), and Co-20Cr-16Fe-15Ni-7Mo (ASTM F1058) systems that contain Ni as alloying element are used as wrought materials. Since they exhibit excellent hot/cold workability and can be strengthened by cold working, they have been used for manufacturing coronary stents, intracranial aneurysm clips, orthodontic dental archwires, and fracture healing aids such as bone plates and wires. The workability of these Co-Cr alloys is superior to that of Co-Cr-Mo alloy without added Ni.

19.2.3 Ti and its alloys

Ti and its alloys are lightweight and nonmagnetic materials, which exhibit excellent corrosion resistance, low elastic moduli, and exceptional specific strength. They also exhibit superior biocompatibility, causing few allergic reactions. In addition, Ti possesses a unique property, known as osseointegration (Brånemark et al., 1977), which refers to the direct bonding between Ti and bone at optical microscopic level. Because of this property, Ti and its alloys exhibit excellent biocompatibility with bone and have been widely used to manufacture medical and dental implants for hard-tissue replacements, specifically for parts where long-term contact with bone is expected.

Among Ti and its alloys, α-type commercially pure (CP) Ti and the α + β-type Ti-6 aluminum (Al)-4 vanadium (V) alloy are the most commonly used for biomedical applications. The Ti-6Al-4V alloy possesses higher mechanical strength than CP Ti. Because of concerns on the potential cytotoxicity of V and potential neurotoxicity of Al, studies on the alloy designs of V-free and Al-free α + β-type Ti alloys have been conducted since the 1980s (Okazaki et al., 1998). In the 1990s, finite-element and animal studies analyzed the effectiveness of low elastic modulus biomaterials for hip prostheses (Wang, 1996). The mismatch between the elastic moduli of the biomaterials and that of the surrounding bone was considered to be the primary reason for implant loosening and stress shielding of bone. Developing metallic biomaterials with lower elastic moduli has been conducted for β-type Ti alloys in Ti-niobium (Nb) and Ti-Mo systems.

It is well known that NiTi exhibits shape memory effect and superelasticity and is commonly used for orthodontic dental archwires, catheter guide wires, intracranial aneurysm clips, orthopedic staples, and stents. Recently, Ni-free Ti-based alloys with

shape memory effect and superelasticity have been developed in Ti-Nb and Ti-Mo systems (Chai et al., 2008). Since the reversible and thermoelastic transformation between the β and α″-phases in β-type Ti alloys is associated with the shape memory effect and superelasticity, shape memory, and superelastic Ti-based alloys presenting composition ranges similar to that of the low elastic modulus β-type Ti alloys have been investigated.

19.3 Newer alloys as metallic biomaterials

New alloys as metallic biomaterials and their fabrication processes are discussed here, focusing primarily on stainless steels, Co-Cr alloys, and Ti and its alloys. Other metallic biomaterials, such as magnesium (Mg) alloys, Fe alloys, zinc (Zn) alloys, bulk metallic glasses, zirconium (Zr) alloys, and high-entropy alloys (HEA), are also discussed in this section.

19.3.1 Stainless steels

To avoid possible Ni allergy concerns, the development of Ni-free stainless steels has been studied. Table 19.2 presents the chemical composition, manufacturing process, and mechanical properties of the Ni-free stainless steels developed to date. Numerous Ni-free stainless steels have been developed, including Fe-(15–18)Cr-(10–12)Mn-(3–6)Mo-0.9N (Uggowitzer et al., 1996), Fe-18Cr-18Mn-2Mo-0.9N (Menzel et al., 1996), Fe-(19–23)Cr-(21–24)Mn-(0.5–1.5)Mo-(0.85–1.1)N (Gebeau and Brown, 2001), Fe-24Cr-1N and Fe-24Cr-2Mo-1N (Kuroda et al., 2003), Fe-(16–20)Cr-(12–16)Mn-(2.5–4.2)Mo-(0–0.25)Nb-(0.75–1)N-(0–0.15)C (Koch et al., 2002), and Fe-17Cr-14Mn-2Mo-0.45N (Ren et al., 2004) in an Fe-Cr-Mn-Mo-N system. The alloy design and manufacturing of Ni-free stainless steels for biomedical applications was conducted taking into consideration the stability of the austenitic phase, corrosion resistance, magnetism, and mechanical properties of the alloys. Ni-free stainless steels are typically used for wires, bone screws, and bone plates, which are fabricated using cold working processes. Therefore, stable austenitic phase with a lower magnetic susceptibility for excellent magnetic resonance imaging (MRI) compatibility is required even after the cold working process. During the cold working process, a stress-induced martensitic transformation could occur.

Coronary stents are one of the target applications of Ni-free stainless steels (Yang and Ren, 2010; Katada and Taguchi, 2015). Type 316 L stainless steel, Co-C alloys, and platinum (Pt)-Cr alloys have been used to manufacture coronary stents, where Ni is an alloying element. Animal experiments on the implantation of Ni-free high-N stainless steel stents in pig coronary arteries indicated that they decrease the formation of neointima, in part by avoiding the activation of inflammatory processes (Fujiu et al., 2012).

N appears to be an essential alloying element for Ni-free stainless steels. A cost-effective N-addition process, removal of impurities, and suppression of grain growth are essential for fabricating new-generation Ni-free stainless steels.

Table 19.2 Ni-free stainless steels for biomedical applications

Chemical composition (mass%)	Manufacturing process	Tensile strength (MPa)	Elongation (%)	Ref.
Fe-(15-18)Cr-(10-12)Mn-(3-6)Mo-0.9N	Pressure electroslag remelting and counter pressure casting	981-1110 (Forged and solution annealed)	53-70 (Forged and solution annealed)	Uggowitzer et al. (1996)
Fe-18Cr-18Mn-2Mo-0.9N	Pressure electroslag remelting	(0.2% proof stress) 600 (Annealed) 2100 (50% cold worked)		Menzel et al. (1996)
Fe-(19-23)Cr-(21-24)Mn-(0.5-1.5)Mo-(0.85-1.1)N	Electroslag remelting	931 (Annealed) 2206 (80% cold worked)	49 (Annealed) 3 (80% cold worked)	Gebeau and Brown (2001)
Fe-24Cr-1N	Forming and nitrogen absorption (1473 K, 1 atm, ∽129.6 ks)	800	25	Kuroda et al. (2003)
Fe-24Cr-2Mo-1N	Forming and nitrogen absorption (1473 K, 1 atm, ∽129.6 ks)	1000	45	Kuroda et al. (2003)
Fe-(16-20)Cr-(12-16)Mn-(2.5-4.2)Mo-(0-0.25)Nb-(0.75-1)N-(0–0.15)C	Pressure electroslag remelting	1030 (Solution annealed) (0.2% proof stress) 590 (Solution annealed)	70 (Solution annealed)	Koch et al. (2002)
Fe-17Cr-14Mn-2Mo-0.45N	Vacuum induction melting (N_2 gas alloying and adding nitride ferroalloys)	810 (After solution) (0.2% proof stress) 450 (After solution)	60 (After solution)	Ren et al. (2004)

19.3.2 Co-Cr alloys

Co-Cr-Mo alloys and other Co-Cr alloys containing Ni as alloying element are discussed in this section.

19.3.2.1 Co-Cr-Mo alloys (Narushima et al., 2015)

Adding a small amount of alloying element to Co-Cr-Mo alloys is an effective way of controlling their microstructure. Adding Zr (Lee et al., 2007) or boron (B) (Chiba and Nomura, 2009) to Co-Cr-Mo alloys has been reported to be effective for producing a fine microstructure under as-cast conditions. Adding N is known to be effective for improving the mechanical properties of as-cast Co-Cr-Mo alloys. In addition, N is an effective alloying element for improving the workability of wrought Co-28Cr-6Mo alloys (Mori et al., 2010) as it suppresses the formation of the σ-phase and the γ-to-ε martensitic transformation. It has been reported that N stabilizes the γ-phase in the Co-29Cr-6Mo alloy by increasing the energy barrier for the γ-to-ε transformation and thus decreasing the kinetic rate of the transformation by forming Cr-N short-range order (Li et al., 2012). Adding N to Co-Cr-Mo alloys also increases their mechanical strength (Dempsey et al., 1987; Yamanaka et al., 2014). The strengthening of Co-29Cr-6Mo alloys was a result of the nanosized Cr_2N precipitates in the γ matrix; however, adding >0.1 mass% N content decreased the elongation to failure because of the increasing number of annealing twins that formed (Yamanaka et al., 2014).

It was reported that increasing the Cr content of biomedical Co-Cr-Mo alloys up to 34 mass%, which was greater than the Cr content of ASTM F75 and F799, was effective for increasing the solubility of N and improving the mechanical strength and ductility under as-cast conditions (Lee et al., 2008). Specifically, the Co-33Cr-5Mo-0.3 N alloy was reported to satisfy the type five criteria that involve the highest strength according to the ISO 22764 international standard for dental alloys under as-cast conditions (Yoda et al., 2012). This alloy can be used to produce partial dentures with mesh or clasp using one-piece dental castings. As for corrosion resistance, the amount of metal elution is decreased by increasing the Cr content. It is anticipated that, because of their superior mechanical properties and corrosion resistance, high-Cr and high-N Co-Cr-Mo alloys will be used as future practical dental casting alloys.

19.3.2.2 Co-Cr alloys containing Ni as alloying element

Manufacturing stents for coronary arteries is a significantly expansive market, and wrought Co-Cr alloys such as Co-20Cr-15W-10Ni (ASTM F90, L605), Co-35Ni-20Cr-10Mo (ASTM F562, MP35N), and Co-20Cr-16Fe-15Ni-7Mo (ASTM F1058, Elgiloy) are primary candidates for this. Coronary stents should be manufactured using alloys possessing high ultimate tensile strength (UTS), low 0.2% proof stress (0.2%PS), and high elongation characteristics in the plastic deformation region, as they are used under plastically deformed conditions in coronary arteries. Typically, these characteristics cannot be simultaneously achieved.

Both the tensile strength and ductility of Co-20Cr-15 W-10Ni (ASTM F90, L605) can be improved by subjecting the alloy to low-temperature heat treatment (LTHT) at 673–873 K, as shown in Fig. 19.3 (Ueki et al., 2016b, 2018). It was confirmed that thin ε layers were formed during LTHT. These thin ε layers affected the strain-induced martensitic transformation (SIMT) and suppressed the formation of ε-phase at grain boundaries during plastic deformation to improve the mechanical properties of this

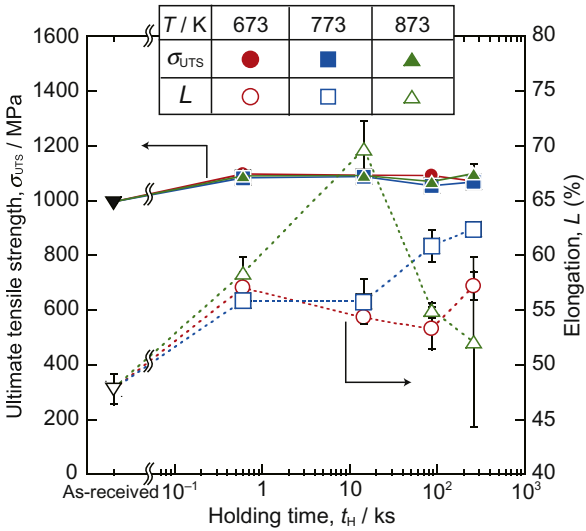


Fig. 19.3 Improvement of strength and elongation of Co-20Cr-15W-10Ni alloys subjected to low-temperature heat treatment (LTHT) at 673-873 K (Ueki et al., 2016b).

alloy. At heat-treatment temperatures of 973–1473 K, which are higher than those of LTHT, carbonitride precipitates such as the $M_{23}X_6$-type and η-phases were formed, which lowered the mechanical properties and corrosion resistance of the alloy. Since no carbonitride precipitates form during LTHT, it would be possible to improve both strength and ductility without impairing the excellent corrosion resistance of the Co-20Cr-15 W-10Ni alloy.

19.3.3 Ti and its alloys

19.3.3.1 β-type Ti alloys

The elastic moduli of stainless steels and Co-Cr alloys are >200 GPa, and α-type CP Ti and α + β-type Ti alloys feature elastic moduli of 90–110 GPa, which are significantly greater than that of cortical bone (10–30 GPa). The β-type Ti alloy is known to exhibit a smaller elastic modulus than the α-type and α + β-type Ti alloys; therefore, the β-type Ti alloy is considered to be the primary candidate for low elastic modulus metallic biomaterials.

Alloy design has been studied for the Ti-Mo, Ti-Nb, Ti-Zr, Ti-Ta, and Ti-Fe systems (Niinomi, 2018). Fig. 19.4 shows the postannealing elastic modulus, UTS, and total elongation of the representative β-type Ti alloys (Narushima, 2005). Elastic moduli of approximately 80 GPa were reported for the Ti-Mo systems, including Ti-12Mo-6Zr-2Fe (Wang et al., 1993), Ti-15Mo-2.8Nb-0.2 silicon (Si)-0.28 oxygen (O) (Fanning, 1996), and Ti-15Mo (Zardiackas et al., 1996), and elastic moduli of 50–60 GPa were achieved for the Ti-Nb systems such as Ti-35.3Nb-5.1Ta-7.1Zr (Ahmed et al., 1996), Ti-29Nb-13Ta-4.6Zr (TNTZ) (Kuroda et al., 1998), and Ti-35Nb-4.0 tin (Sn) (Matsumoto et al., 2005). As can be seen in Fig. 19.4, the β-type

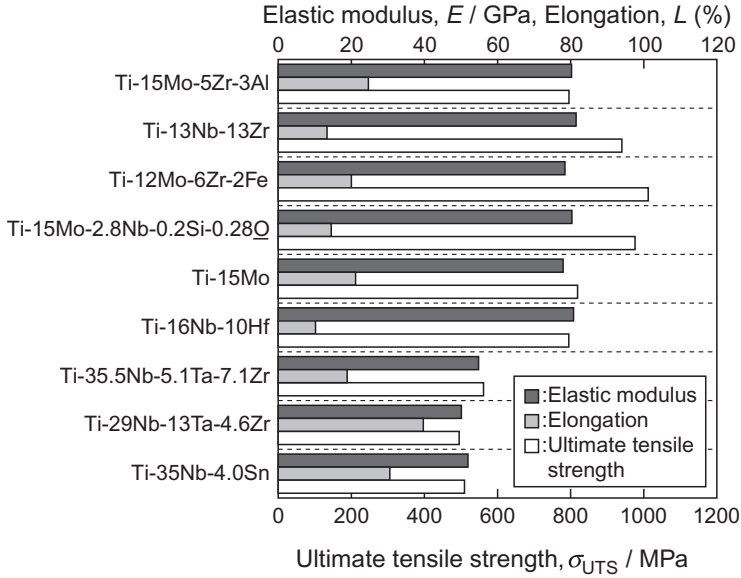


Fig. 19.4 Mechanical properties of low elastic modulus β-type Ti alloys (Narushima, 2005).

Ti alloys with low elastic moduli tend to present lower mechanical strength after annealing. However, both low elastic modulus and high mechanical strength could be achieved after cold rolling of the β-type Ti alloys in the Ti-Nb system (Saito et al., 2003; Matsumoto et al., 2005).

The anisotropy of the elastic modulus of the β-type Ti alloy single crystal has been studied. Fig. 19.5 illustrates the crystallographic anisotropy of the elastic moduli of the β-type Ti-29Nb-13Ta-4.6Zr alloy single crystal (Tane et al., 2008). The elastic modulus of the β-type Ti alloy single crystal is highly dependent on the crystallographic orientation, where the elastic moduli in the ⟨100⟩ and ⟨111⟩ directions were the smallest and largest, respectively, of the elastic moduli associated with all crystallographic orientations. The elastic modulus in the ⟨100⟩ direction is approximately 35 GPa, which is half that in the ⟨111⟩ direction and is similar to that of human cortical bone. These results imply that polycrystals with textures where the crystallographic ⟨100⟩ directions are oriented along the loading direction of human bone, or single crystals presenting ⟨100⟩ directions oriented along the loading direction of human bone, are considered to be promising candidates for biomedical implants, as their elastic moduli are comparable to that of human bone.

19.3.3.2 Ti alloys with shape memory effect and superelasticity

It has been reported that the elastic strain of these alloys was approximately 3%, which is significantly smaller than that of NiTi. Texture control by cold rolling and heat treatment of Ti-22Nb-6Al alloys (Kim et al., 2006), and increasing the critical stress

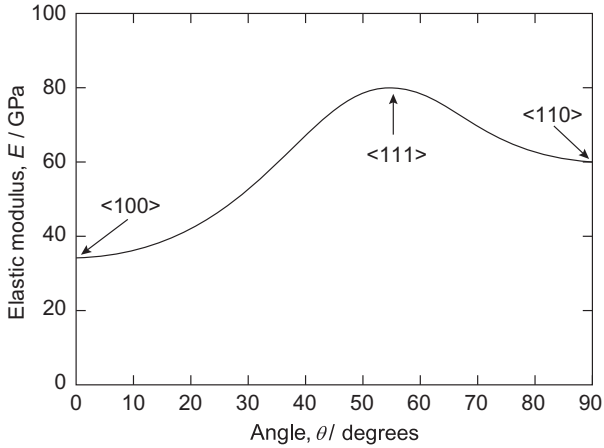


Fig. 19.5 Orientation dependence of elastic moduli of Ti-29Nb-13Ta-4.6Zr single crystal in the directions between ⟨100⟩ and ⟨110⟩ (Tane et al., 2008).

for permanent deformation by adding interstitial solute elements to Ti-22Nb alloys (Kim et al., 2005), were reported to effectively improve the shape memory and superelastic properties of these alloys.

Recently, a new Ti-Zr-Nb-Sn alloy system was developed as an Ni-free biomedical superelastic alloy with exceptional recovery strain and superior biocompatibility (Fu et al., 2015). A superior superelastic recovery strain of 6.0% was reported for the Ti-18Zr-12.5Nb-2Sn, Ti-18Zr-11Nb-3Sn, and Ti-18Zr-9.5Nb-4Sn alloys subjected to cold-rolling and solution treatment (ST) because of the combined effects of a superior transformation strain and strong recrystallization texture. The Ti-18Zr-11Nb-3Sn alloy exhibited excellent cyclic stability with an extremely narrow stress hysteresis of approximately 20 MPa. Moreover, the alloy was cytocompatible.

19.3.3.3 Low-cost Ti alloys

Although not originally developed as biomaterials, the α + β-type Ti-Fe-O-N alloys, represented by the Ti-1Fe-0.35O-0.01N alloy (Fujii, 2003), have been evaluated for dental applications because of their higher strength compared to CP Ti and lower fabrication costs compared to the Ti-6Al-4V alloy (Koike et al., 2005). Their strength and ductility are intermediate between those of CP Ti and Ti-6Al-4V alloy, and their fabrication costs are relatively low because they contain Fe and O, which are the primary impurity elements in Ti sponge produced using the Kroll process.

The effect of interstitial light elements such as O and N on biomedical Ti alloys has been actively studied in order to achieve both functional improvement and cost reduction. The effect of adding O, which is essential for reasonable alloy design, on the microstructural control and phase transformation in the Ti-Nb-O and Ti-Mo-O alloy systems, has been comprehensively studied. It was reported that a nano-sized modulated domain structure was observed for the β-phase of β-type Ti-Nb-O alloy systems (Tahara et al., 2011) and the α″ martensite phase was stabilized by the strain field of

the O atoms (Tahara et al., 2016). The wavelength of modulated structures by spinodal decomposition increased as the O content of the β-type Ti-Mo-O alloy systems increased, resulting in a decrease in the maximum hardness and suppression of the spinodal decomposition because of the increase in elastic energy for decomposition (Saeki et al., 2018). Niinomi et al. studied the effect of the O content on the phase stability and properties of biomedical β-type Ti-29Nb-13Ta-4.6Zr alloys (Niinomi et al., 2016; Homma et al., 2018). The Ti-29Nb-13Ta-4.6Zr-0.1O and Ti-29Nb-13Ta-4.6Zr-0.4O alloys were subjected to single step and two-step annealing heat treatments to promote the formation of ω- and α-phases, respectively. After the two-step annealing, a significant volume fraction of ω precipitate was retained in the Ti-29Nb-13Ta-4.6Zr-0.4O alloy, while the α-phase was primarily observed in the Ti-29Nb-13Ta-4.6Zr-0.1O alloy (Niinomi et al., 2016). It was suggested that adding O stabilized the ω-phase in Ti-29Nb-13Ta-4.6Zr alloys and the dispersion of the ω-phase can be utilized to prevent the growth of the α-phase because of soft impingement. The Ti-V-O and Ti-Nb-O alloy systems are candidates for manufacturing low-cost α + β-type Ti alloy because the alloying elements: V and Nb present high oxygen solubility, similar to that of Ti. Alloy design was conducted for the Ti-V-O alloy system (Ueda et al., 2016). It was reported that the tensile strength and total elongation of the Ti-4V-0.6O alloy were comparable to those of the Ti-6Al-4V alloy, thus indicating that this alloy would be a low-cost α + β-type Ti alloy candidate (Omiya et al., 2017).

Utilizing low-cost common β-stabilizing elements such as Mn, Al, Cr, or Fe is a key issue in the research and development of low-cost β-type Ti alloys with superior mechanical and biological performance. The low-cost β-type Fe-13Cr-1Fe-3Al alloy, with favorable tensile and fatigue properties (Ogawa et al., 2007), was developed for welfare equipment, such as wheelchairs. Ti-Mn alloys have been investigated as future low-cost β-type alloys for biomedical applications (Ikeda et al., 2009; Santos et al., 2015, 2016a). Santos et al. reported the phase stability, mechanical properties, and cytocompatibility of β-type Ti-(6, 9, 13, and 18 mass%)Mn binary alloys subjected to ST at 1173 K for 3.6 ks (Santos et al., 2015). They indicated that the Ti-9Mn alloy exhibited a mechanical and biological performance that was comparable or superior to that of the commonly used Ti-6Al-4V extra low interstitial (ELI) alloy and CP Ti. Adding Mo to a Ti-Mn alloy led to improving its mechanical properties and corrosion resistance (Santos et al., 2016a). The elongation and UTS values of the Ti-5Mn-4Mo and Ti-6Mn-3Mo alloy were 34% and 14%, and 935 and 1220 MPa, respectively. Moreover, adding Mo to the Ti-Mn alloys decreased their corrosion rates. To further reduce their costs, the metal injection molding (MIM) process was studied for Ti-Mn and Ti-Mn-Mo alloy systems (Santos et al., 2016b, 2017), where improving ductility remains a concern.

To suppress the stress shielding effect for patients and springback for surgeons, low and high elastic moduli, respectively, are required for spinal fixation devices. To address these conflicting elastic moduli requirements, the concept of self-tunable elastic modulus was introduced for Ti-Cr alloys, as shown in Fig. 19.6 (Niinomi, 2018).

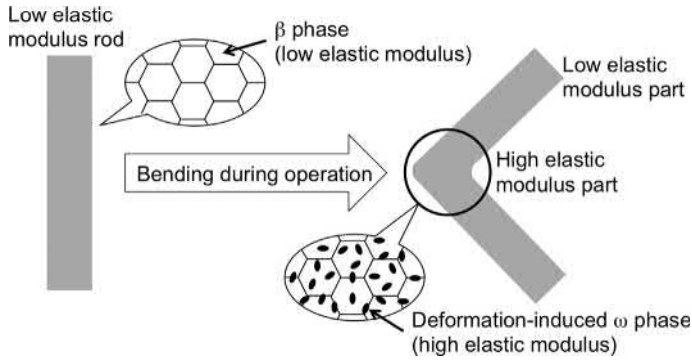


Fig. 19.6 Schematic explanation of concept of spinal fixation rod with self-adjustable elastic modulus concept (Niinomi, 2018).

The self-tunable elastic modulus is based on the formation of the deformation-induced ω-phase and its high elastic modulus (Zhao et al., 2012). It should be noted that Cr is a common alloying element.

19.3.4 Other metallic biomaterials

Recent advances in biodegradable metals, such as Mg alloys, Zn alloys, and Fe alloys are discussed in this section. Bulk metallic glasses, Zr alloys, and HEA designed for biomedical applications are also discussed.

19.3.4.1 Mg alloys

Biodegradable polymer and ceramic materials are widely used for implants, such as plates, screws, pins, and interbody fusion cages. Biodegradable implants eliminate the need for a second surgery for implant removal.

Mg alloys are expected to be candidates for biodegradable metallic biomaterials. The elastic moduli of Mg and its alloys are in the 40–45 GPa range. Mg is essential for human metabolism, it is naturally found in bone tissue, and is harmlessly excreted in urine as a soluble and nontoxic oxide (Staiger et al., 2006). As the corrosion rate of CP Mg in the human body is high and its mechanical properties are inferior to those of other metallic biomaterials, improving its corrosion resistance and mechanical properties through alloying and surface modification should be pursued (Li and Zheng; 2013, Gu et al., 2014; Hornberger et al., 2012). The alloy design details and surface treatment of biomedical Mg and its alloys are described in Chapter 9.

19.3.4.2 Fe alloys

Fe and its alloys have become promising biodegradable metals for temporary cardiovascular and orthopedic implants because of their unique biodegradability, good biocompatibility, and excellent mechanical properties (Wang et al., 2017). In

particular, biodegradable Fe-based alloys exhibit mechanical properties comparable to those of the alloys used in practice for stents, such as type 316 L stainless steel (Mouzou et al., 2016). Biodegradable Fe alloys have been studied in the Fe-Mn alloy systems, such as Fe-Mn-C (Mouzou et al., 2016) and Fe-Mn-Si (Drevet et al., 2018) alloys, because adding Mn to Fe increases the degradability of alloys in chloride solution environment and improves strength-ductility balance through transformation-induced plasticity (TRIP) and the twinning-induced plasticity (TWIP) effects. The effect of the composition of the alloy and biological environments on the degradation rates and corrosion products of Fe-Mn-based alloys has to be clarified for practical applications.

19.3.4.3 Zn alloys

It was reported in 2013 that Zn and its alloys harmlessly and uniformly degrade in the human body (Bowen et al., 2013). Their biodegradation rates, which are intermediate between those of Mg alloys and Fe alloys, appear to be ideal for stent applications. Moreover, Zn alloys need to achieve the superior biocompatibility, degradation, and mechanical properties required for biodegradable stent applications (Bowen et al., 2016). Adding alkaline earth metals to Zn is an effective way to improve its strength and hardness; therefore, the biodegradable properties of Zn-Mg, Zn-Mg-calcium (Ca) (Levy et al., 2017), and Zn-Al-strontium (Sr) (Liu et al., 2018) alloys have been analyzed. Recently, adding lithium (Li) (Zhao et al., 2017) and Zr (Wątroba et al., 2018) to Zn has been investigated, and the biological and mechanical properties of the obtained alloys have been reported. Basic studies are required on the effect of microstructure, including precipitates, on the mechanical and biological properties of Zn alloys.

19.3.4.4 Bulk metallic glasses

Amorphous alloys typically exhibit higher tensile strength and lower elastic moduli than crystalline alloys of the same composition (Inoue, 2000). Amorphous alloys also exhibit higher corrosion resistance than crystalline alloys. Bulk metallic glasses exhibit superior strength and low elastic moduli, making them suitable for biomedical applications. Bulk metallic glasses for biomedical applications have been developed in Ti-, Zr-, Fe-, Mg-, Zn-, Ca-, and Sr-based alloying systems (Li and Zheng, 2016).

Ti-based bulk metallic glasses in Ti-Zr-copper (Cu)-palladium (Pd) (Zhu et al., 2007), and Ti-Zr-Cu-Pd-Nb (Qin et al., 2008) systems have been developed. An elastic modulus of approximately 80 GPa, a tensile strength of 2050 MPa, and a plastic strain of >6.5% were obtained for the $(Ti_{40}Zr_{10}Cu_{36}Pd_{14})_{100\text{-}X}Nb_X$ ($X = 1$ and 3) bulk metallic glass. Mg-based bulk metallic glasses, such as Mg-Zn-Ca and Mg-Cu-yttrium (Y)-Zn alloy systems, have been developed for biodegradable implant materials. The $Mg_{75}Cu_{13.33}Y_{6.6}Zn_5$ bulk metallic glass exhibits a UTS of 1040 MPa, an elastic modulus of 42 MPa, and an elongation of 19% (Dambatta et al., 2015).

Li and Zheng reported that future research directions are aimed at overcoming the brittleness, increasing the glass forming ability to obtain corresponding bulk metallic glasses with larger sizes, removing/reducing toxic elements, and surface modifications (Li and Zheng, 2016).

19.3.4.5 Zr alloys

MRI is widely used as a critical diagnostic tool for the entire body, and specifically for orthopedic and brain surgery. However, MRI diagnosing is inhibited when metals are implanted in the body, because metallic implants, such as stainless steels, Co-Cr alloys, and Ti alloys, become magnetized by the intense magnetic fields of MRI instruments and artifacts could occur on the images. Therefore, materials with low magnetic susceptibility comparable to that of the surrounding tissues are preferable (Nomura et al., 2009). The magnetic susceptibility of Zr is lower than that of Ti and Co-Cr alloys. A number of Zr-based alloys, such as Zr-Ti, Zr-Mo, Zr-Nb, and Zr-ruthenium (Ru) alloys were studied as potential candidates for biomedical applications. In the Zr-Nb systems, the magnitude of the magnetic susceptibility decreases as follows: β-phase > α-phase > ω-phase (Nomura et al., 2009). The effects of phase constitution on magnetic susceptibility and mechanical properties were reported for the Zr-(0–3)Mo (Suyalatu et al., 2011) and Zr-(0 − 20)Nb (Kondo et al., 2011) alloy systems. The formation of the ω-phase is effective for decreasing the magnetic susceptibility, but it also decreases the ductility of Zr alloys.

A combination of low elastic modulus and low magnetic susceptibility is expected for the β-type Zr alloys. The β-type Zr-4Mo-4Sn alloy was reported to exhibit a low elastic modulus of 48 GPa and low magnetic susceptibility of 1.22×10^{-6} cm^3 g^{-1} (Guo et al., 2018).

19.3.4.6 High-entropy alloys

HEA must be single-phase solid solution and contain five or more principal elements, and the concentration of each element should be between 5 and 35 at.% (Miracle and Senkov, 2017).

An equiatomic TiNbTaZrMo HEA containing biocompatible elements was developed as metallic biomaterial, which consisted of two body-centered cubic (bcc) solid solution phases in the as-cast and annealed states (Todai et al., 2017). This HEA exhibited an equiaxed fine dendrite structure in the as-cast state and presented exceptional strength and deformability and superior biocompatibility, comparable to that of CP Ti, indicating the possibility of using HEAs as a new class of metallic biomaterials. For this alloying system, the nonequiatomic $Ti_{2.6}$NbTaZrMo HEA was also proposed as metallic biomaterial, based on the thermodynamic calculations, and its solidification microstructure was reported (Nagase et al., 2018).

Research on HEAs used for biomedical applications has focused on the Ti alloy system. The concept of HEA can be applied to other metallic biomaterial systems, such as Co-Cr alloys and stainless steels.

19.4 Novel processing technologies for metallic biomaterials

Novel processing technologies for fabricating porous metallic biomaterials and grain refining are discussed in this section.

19.4.1 Porous metallic biomaterials

Numerous methods, such as sintering metal powders, space holder methods, combustion synthesis, plasma spraying, decomposition of foaming agents, and additive manufacturing (Ryan et al., 2006), have been proposed for fabricating porous metallic biomaterials. A low elastic modulus is one of the advantages of porous metallic biomaterials. Porous CP Ti (Oh et al., 2003) and the β-type Ti-15Mo-5Zr-3Al alloy (Nomura et al., 2005) exhibit elastic moduli similar to that of cortical bone at a porosity of approximately 25%–30%, as shown in Fig. 19.7. The appropriate balance between the elastic modulus and mechanical strength has to be established in bulk porous biomaterials, as introducing pores into the bulk body decreases the tensile and fatigue strength. Porous Ti has been considered as scaffold for bone regeneration and tissue engineering (Karageorgiou and Kaplan, 2005). Controlling the porosity and size, shape, and distribution of pores in bulk porous Ti is essential for scaffolds with appropriate strength and biocompatibility. In addition, as osteogenesis is known to be affected by the direction of pores in bulk porous materials (Nakano et al., 2006), the direction of pores should be taken into consideration when designing scaffolds.

Additive manufacturing technology has received significant attention for fabricating porous biomaterials. Additive manufacturing can create complex three-dimensional (3D) components from computerized models of the parts using layer-by-layer

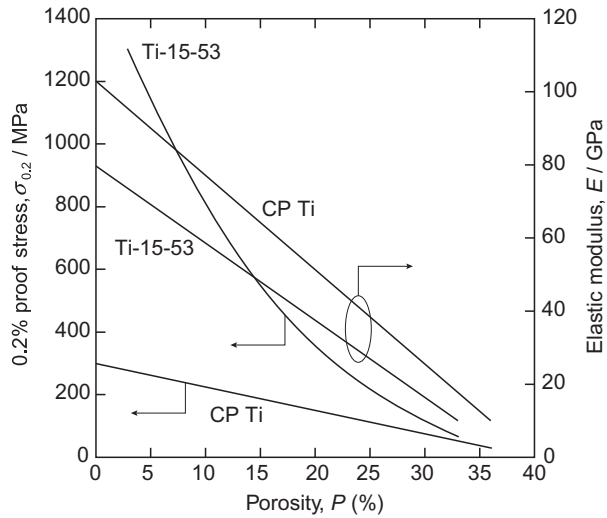


Fig. 19.7 0.2% proof stress in three-point bending tests and elastic modulus of porous CP Ti and Ti-15Mo-5Zr-3Al (Ti-15-53).

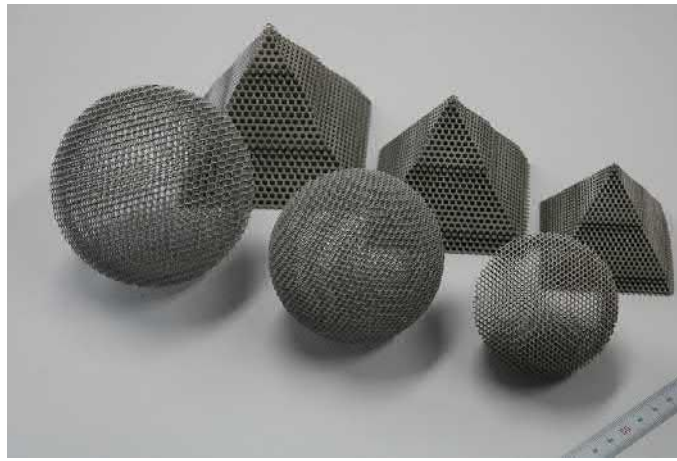


Fig. 19.8 Appearances of porous Ti-6Al-4V alloy products with quadrangular pyramidal and spherical shapes.
Courtesy of Prof. Nakano, Osaka University, Japan.

construction (Ryan et al., 2006), therefore, it could allow to precisely control the porosity and size, shape, distribution, and direction of pores of the parts. Fig. 19.8 illustrates the appearance of porous Ti-6Al-4V alloy products with quadrangular pyramidal and spherical shapes fabricated by additive manufacturing with electron beam melting (Ikeo et al., 2014). Additive manufacturing of metallic biomaterials and their properties are discussed in Chapter 12. The fabrication technologies and properties, including the biomedical applications, of metallic porous materials have been summarized in a review paper (Zhao et al., 2018).

19.4.2 Crystal-grain refinement

Crystal-grain refinement in metallic materials is a common method to improve the balance of strength and ductility. In this section, recent advances in the grain refining of metallic biomaterials are discussed.

19.4.2.1 Severe plastic deformation

Severe plastic deformation techniques, such as high-pressure torsion (HPT), equal-channel angular pressuring (ECAP), and accumulative roll bonding (ARB), have been widely used to prepare submicron-grained materials to improve their mechanical properties. Grain refinement of the α-type CP Ti, α + β and β-type Ti alloys, and Co-Cr-Mo alloys by severe plastic deformation has been studied and improvements in the tensile strength, fatigue properties, and superplastic properties of these materials have been reported.

The effect of severe plastic deformation during ECAP on microstructure was reported for α-type CP Ti (Dyakonov et al., 2015) and the α + β-type Ti-6Al-4V

ELI alloy (Saitova et al., 2009). The effect of combining ECAP and thermomechanical treatment on the mechanical properties of the α + β-type Ti-6Al-4V ELI alloy has been investigated for implant applications. An improvement in the fatigue strength of the alloy was reported, and grains 0.17 μm in size formed.

The HPT processing technique has been applied to a number of metallic systems, such as the α + β-type Ti-6Al-7Nb (Ashida et al., 2015), β-type Ti-29Nb-13Ta-4.9Zr (Yilmazer et al., 2013, 2014), and Co-Cr-Mo (Isik et al., 2016a,b) alloys, to improve their mechanical properties, while focusing on their biomedical applications. An average diameter of approximately 50 nm was obtained after HPT processing the Co-28Cr-6Mo alloy. The ε-phase fraction increased from 0% before HPT to approximately 80% after HPT. A UTS >1600 MPa and an elongation of approximately 2% were achieved through HPT processing (Isik et al., 2016a). After HPT processing, annealing at 1273 K for 0.3 ks increased the elongation to >10%, while UTS was approximately 1500 MPa, the average grain size was 6.5 μm, and the ε-phase fraction was approximately 0% (Isik et al., 2016b).

19.4.2.2 *Reverse transformation treatment (Narushima et al., 2015)*

The grain size of biomedical Co-Cr-Mo can be refined through reverse transformation (RT) treatment without hot or cold plastic transformation. The grain refinement process consists of a two-step heat treatment. The solution-treated alloy is first subjected to isothermal aging at 1073 K to form a lamellar structure comprised of hexagonal close-packed (hcp) ε-phase and precipitates, and then the aged alloy with lamellar microstructure is RT-treated to obtain the face-centered cubic (fcc) γ-phase at a temperature of 1273–1473 K (Kurosu et al., 2010). The temperatures of 1073 and 1273–1473 K are in the stability regions for the ε- and γ-phases, respectively. This process decreased the average grain size from an initial 200 to 20–25 μm for the Co-27Cr-5Mo-0.16 N alloy. Fig. 19.9 shows the stress-strain curves of the

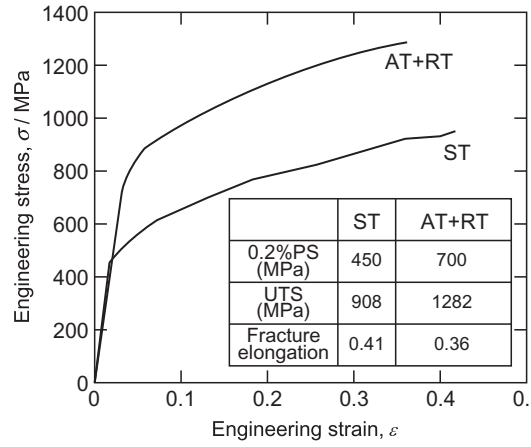


Fig. 19.9 Stress-strain curves of Co-27Cr-5Mo-0.16 N alloys after solution treatment (ST) and aging treatment (AT) followed by reverse transformation (RT) at 1273 K for 300 s (Kurosu et al., 2010).

Co-27Cr-5Mo-0.16 N alloys after ST and aging treatment (AT) followed by RT at 1273 K for 300 s (Kurosu et al., 2010). The tensile strength of the alloy was improved by subjecting it to AT followed by RT, while the ductility remained approximately constant.

During the additive manufacturing process using electron beam melting of Co-Cr-Mo alloys, preheating at approximately 1150 K, which is a temperature where the ε-phase is stable, is required. Therefore, the microstructure, such as the ε-phase fraction, depends on the preheating time, that is, height in built direction. This inhomogeneity in microstructure of additive manufactured Co-Cr-Mo alloy (Sun et al., 2015) can be eliminated using the AT followed by RT treatment (Wei et al., 2017).

19.4.2.3 Microalloying

It is known that adding small amounts, approximately 0.1 mass%, of rare-earth elements such as Y, erbium (Er), cerium (Ce), and lanthanum (La), around 0.1 mass %, into α + β-type Ti alloys effectively suppresses grain growth in the β region. The fine precipitates of rare-earth oxides formed in the alloy suppress β grain growth through pinning. Specifically, Y was found to be the most effective element for suppressing the growth of β grains for the biomedical α + β-type Ti-4.5Al-6Nb-2Fe-2Mo alloy at high temperatures such as 1573 K (Ueda et al., 2013). Adding B was also reported to be effective for refining the β grain of the β-type Ti-29Nb-13Ta-4.9Zr alloy by forming TiB (Song et al., 2011).

19.5 Future trends

The research and development of new-generation metallic biomaterials and novel processing methods to fabricate and modify them will continue. This research is aimed at functionally and economically improving biomedical devices to expand their applications beyond hard-tissue replacement and cardiovascular treatment, to soft-tissue replacement and tissue engineering.

Adding N and Mn could be a critical aspect for designing new Ni-free stainless steels. However, as stated in Section 19.3.4, one of the candidate biodegradable alloys is the Fe-Mn alloy system, and, adding Mn significantly decreases corrosion resistance. Precise alloy design is required. For Co-Cr alloy systems, elucidating the effect of alloying elements and processing parameters on the microstructure is essential to improve their properties such as tensile strength, elongation in the plastic deformation region, corrosion resistance, and radiopaqueness. Accumulating basic data on the thermodynamic properties and phase transformations is required. As for Ti and its alloys, developing the β-type Ti alloys for controlling the elastic modulus and shape memory effect/superelasticity is still considered a critical issue. Low-cost biomedical α, α + β, and β-type Ti alloys need to be developed. Surface modification of Ti and its alloys is essential to improve their compatibility with bone tissue. Biodegradable alloys are required in the cardiovascular and orthopedic fields. Currently, Zn alloys, Fe alloys,

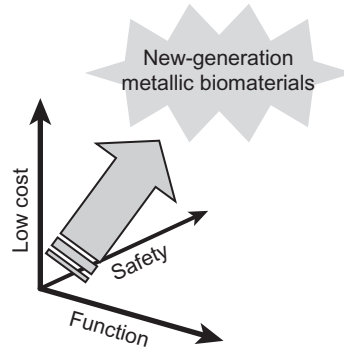


Fig. 19.10 Future trends in fabricating metallic biomaterials.

and bulk metallic glasses, as well as Mg alloys are actively studied as biodegradable alloys, and this trend will continue in the future.

Although biocompatibility is a priority for metallic biomaterials, their production cost is another critical aspect. Low-cost production processes can be achieved by using low-cost alloying elements and reasonable processes for desired texture, grain size, and phases. Common metal elements, such as Cr, Al, Fe, and Mn and interstitial light elements, such as C, N, and O are candidates for low-cost alloying elements. These common metals and interstitial light elements can be expected to contribute to the development of new and improved functionalities of these alloys. Alloy design and processing using these elements need to be investigated and further developed. New-generation metallic biomaterials will be created to achieve a balance between function, safety, and cost (Fig. 19.10).

19.6 Further information sources

Metallic biomaterials

Park J and Lakes RS (2007), *Biomaterials: an introduction*, Springer, New York.

Mayer VA (2013), *2013 Annual book of ASTM standards, section thirteen, medical devices and services, vol.13.01*, West Conshohocken, ASTM International.

Niinomi M, Narushima T and Nakai M (2015), *Advances in metallic biomaterials, Springer series in biomaterials science and engineering, vol. 3 (Tissues, materials and biological reactions) and vol. 4 (Processing and Applications)*, Springer, Berlin.

Co-Cr alloys

Sims CT, Stoloff NS and Hagel WC (1987), *Superalloys II*, Wiley, New York.

Ti and its alloys

Brunette DM, Tengvall P, Textor M and Thomsen P (2001), *Titanium in medicine: material science, surface science, engineering, biological responses and medical applications*, Springer, Berlin.

Leyens C and Peters M (2003), *Titanium and titanium alloys*, Weinheim, Wiley-VCH.

Froes FH (2015), *Titanium-physical metallurgy, processing, and applications*, ASM International, Materials Park.

References

Ahmed, T., Long, M., Silvestri, J., Ruiz, C., Rack, H.J., 1996. A new low modulus, biocompatible titanium alloy. In: Blenkinsop, P.A., Evans, W.J., Flower, H.M. (Eds.), Titanium'95: Science and Technology, Proc. 8th Int. Conf. Titanium. The University Press, London, pp. 1760–1767.

Ashida, M., Chen, P., Doi, H., Tsutsumi, Y., Hanawa, T., Horita, Z., 2015. Superplasticity in the Ti-6Al-7Nb alloy processed by high-pressure torsion. Mater. Sci. Eng. A 640, 449–453.

Blackwood, D.J., 2003. Biomaterials: past successes and future problems. Corros. Rev. 21, 97–124.

Bowen, P.K., Drelich, J., Goldman, J., 2013. Zinc exhibits ideal physiological corrosion behavior for bioabsorbable stents. Adv. Mater. 25, 2577–2582.

Bowen, P.K., Shearier, E.R., Zhao, S., Guillory II, R.J., Zhao, F., Goldman, J., Drelich, J.W., 2016. Biodegradable metals for cardiovascular stents: from clinical concerns to recent Zn-alloys. Adv. Healthcare Mater. 5, 1121–1140.

Brånemark, P.-I., Hansson, B.O., Adell, R., Breine, U., Lindström, J., Hallén, O., Öhman, A., 1977. Osseointegrated implants in the treatment of the edentulous jaw, experience from a 10-year period. Scand. J. Plast. Reconstr. Surg. 11 (Suppl. 16), 1–132.

Chai, Y.W., Kim, H.Y., Hosoda, H., Miyazaki, S., 2008. Interfacial defects in Ti-Nb shape memory alloys. Acta Mater. 56, 3088–3097.

Chiba, A., Nomura, N., 2009. Biomedical Implant Materials. Japan patent, pp. P2008–69394A.

Dambatta, M.S., Izman, S., Yahaya, B., Lim, J.Y., Kurniawan, D., 2015. Mg-based bulk metallic glasses for biodegradable implant materials: a review on glass forming ability, mechanical properties, and biocompatibility. J. Non-Cryst. Solids 426, 110–115.

Dempsey, A.J., Pilliar, R.M., Weatherly, G.C., Kilner, T., 1987. The effects of nitrogen additions to a cobalt-chromium surgical implant alloy. Part 2 mechanical properties. J. Mater. Sci. 22, 575–581.

Drevet, R., Zhukova, Y., Malikova, P., Dubinskiy, S., Korotitskiy, A., Pustov, Y., Prokoshkin, S., 2018. Martensitic transformations and mechanical and corrosion properties of Fe-Mn-Si alloys for biodegradable medical implants. Metall. Mater. Trans. A 49, 1006–1013.

Dyakonov, G.S., Zemtsova, E., Mironov, S., Semenova, I.P., Valiev, R.Z., Semiatin, S.L., 2015. An EBSD investigation of ultrafine-grain titanium for biomedical applications. Mater. Sci. Eng. A 648, 305–310.

Fanning, J.C., 1996. Properties and processing of a new metastable beta titanium alloy for surgical implant applications: TIMETAL 21SRx. In: Blenkinsop, P.A., Evans, W.J., Flower, H.M. (Eds.), Titanium'95: Science and Technology, Proc. 8th Int. Conf. Titanium. The University Press, London, pp. 1800–1807.

Fu, J., Yamamoto, A., Kim, H.Y., Hosoda, H., Miyazaki, S., 2015. Novel Ti-base superelastic alloys with large recovery strain and excellent biocompatibility. Acta Biomater. 17, 56–67.

Fujii, H., 2003. Control of mechanical properties of Ti-Fe-O-N based titanium alloys by thermomechanical processing. Mater. Sci. Forum 426-432, 661–666.

Fujiu, K., Manabe, I., Sasaki, M., Inoue, M., Iwata, H., Hasumi, E., Komuro, I., Katada, Y., Taguchi, T., Nagai, R., 2012. Nickel-free stainless steel avoids neointima formation following coronary stent implantation. Sci. Technol. Adv. Mater. 13, 064218.

Gebeau, R.C., Brown, R.S., 2001. Biomedical implant alloy. Adv. Mater. Process 159, 46–48.

Gu, X.-N., Li, S.-S., Li, X.-M., Fan, Y.-B., 2014. Magnesium based degradable biomaterials: a review. Front. Mater. Sci. 8, 200–218.

Guo, S., Shang, Y., Zhang, J., Zhang, J., Meng, Q., Cheng, X., Zhao, X., 2018. A metastable β-type Zr-4Mo-4Sn alloy with low cost, low Young's modulus and low magnetic susceptibility for biomedical applications. J. Alloys Compd. 754, 232–237.

Hanawa, T., 2012. Research and development of metals for medical devices based on clinical needs. Sci. Technol. Adv. Mater. 13, 064102.

Homma, T., Arafah, A., Haley, D., Nakai, M., Niinomi, M., Moody, M.P., 2018. Effect of alloying elements on microstructural evolution in oxygen content controlled Ti-29Nb-13Ta-4.6Zr (wt%) alloys for biomedical applications during aging. Mater. Sci. Eng. A 709, 312–321.

Hornberger, H., Virtanen, S., Boccaccini, A.R., 2012. Biomedical coatings on magnesium alloys—a review. Acta Biomater. 8, 2442–2455.

Ikeda, M., Ueda, M., Matsunaga, R., Ogawa, M., Niinomi, M., 2009. Isothermal aging behavior of beta titanium-manganese alloys. Mater. Trans. 50, 2737–2743.

Ikeo, N., Ishimoto, T., Serizawa, A., Nakano, T., 2014. Control of mechanical properties of three-dimensional Ti-6Al-4V products fabricated by electron beam melting with unidirectional elongated pores. Metall. Mater. Trans. A 45, 4293–4301.

Inoue, A., 2000. Stabilization of metallic supercooled liquid and bulk amorphous alloys. Acta Mater. 48, 279–306.

Isik, M., Niinomi, M., Cho, K., Nakai, M., Liu, H., Yilmazer, H., Horita, Z., Sato, S., Narushima, T., 2016a. Microstructural evolution and mechanical properties of Co-Cr-Mo alloy subjected to high-pressure torsion. J. Mech. Behav. Biomed. Mater. 59, 226–235.

Isik, M., Niinomi, M., Liu, H., Cho, K., Nakai, M., Horita, Z., Narushima, T., Ueda, K., 2016b. Optimization of microstructure and mechanical properties of Co-Cr-Mo alloys by high-pressure torsion and subsequent short annealing. Mater. Trans. 57, 1887–1896.

Japan Titanium Society, 2018. Statistical Data. (private communication).

Karageorgiou, V., Kaplan, D., 2005. Porosity of 3D biomaterial scaffolds and osteogenesis. Biomaterials 26, 5474–5491.

Katada, Y., Taguchi, T., 2015. Nickel-free high-nitrogen stainless steel. In: Niinomi, M., Narushima, T., Nakai, M. (Eds.), Advances in Metallic Biomaterials: Tissues, Materials and Biological reactions. In: Springer Series in Biomaterials Science and Engineering, vol. 3. Springer, Berlin, pp. 125–156.

Kim, H.Y., Sasaki, T., Okutsu, K., Kim, J.I., Inamura, T., Hosoda, H., Miyazaki, S., 2006. Texture and shape memory behavior of Ti-22Nb-6Ta alloy. Acta Mater. 54, 423–433.

Kim, J.I., Kim, H.Y., Hosoda, H., Miyazaki, S., 2005. Shape memory behavior of Ti-22Nb-(0.5-2.0)O(at%) biomedical alloys. Mater. Trans. 46, 852–857.

Koch, S., Büscher, R., Tikhovski, I., Brauer, H., Runiewicz, A., Dudzinski, W., Fischer, A., 2002. Mechanical, chemical and tribological properties of the nickel-free-nitrogen steel X13CrMnMoN18-14-3 (1.4452). Mater. Werkst. 33, 705–715.

Koike, M., Ohkubo, C., Sato, H., Fujii, H., Okabe, T., 2005. Evaluation of cast Ti-Fe-O-N alloys for dental applications. Mater. Sci. Eng. C 25, 349–356.
Kondo, R., Nomura, N., Suyalatu, T.Y., Doi, H., Hanawa, T., 2011. Microstructure and mechanical properties of as-cast Zr-Nb alloys. Acta Biomater. 7, 4278–4284.
Kuroda, D., Niinomi, M., Norinaga, M., Kato, Y., Yashiro, T., 1998. Design and mechanical properties of new β type titanium alloys for implant materials. Mater. Sci. Eng. A 243, 244–249.
Kuroda, D., Hanawa, T., Hibaru, T., Kuroda, S., Kobayashi, M., Kobayashi, T., 2003. New manufacturing process of nickel-free austenitic stainless steel with nitrogen absorption treatment. Mater. Trans. 44, 414–420.
Kurosu, S., Matsumoto, H., Chiba, A., 2010. Grain refinement of biomedical Co-27Cr-5Mo-0.16N alloy by reverse transformation. Mater. Lett. 64, 49–52.
Lee, S.-H., Takahashi, E., Nomura, N., Chiba, A., 2006. Effect of carbon addition on microstructure and mechanical properties of a wrought Co-Cr-Mo implant alloy. Mater. Trans. 47, 287–290.
Lee, S.-H., Uchikanezaki, T., Nomura, N., Nakamura, M., Chiba, A., 2007. Effects of zirconium addition on microstructures and mechanical properties of Co-29Cr-6Mo Alloy. Mater. Trans. 48, 1084–1088.
Lee, S.-H., Nomura, N., Chiba, A., 2008. Significant improvement in mechanical properties of biomedical Co-Cr-Mo alloys with combination of N addition and Cr-enrichment. Mater. Trans. 49, 260–264.
Levy, G.K., Leon, A., Kafri, A., Ventura, Y., Drelich, J.W., Goldman, J., Vago, R., Aghion, E., 2017. Evaluation of biodegradable Zn-1%Mg and Zn-1%Mg-0.5%Ca alloys for biomedical applications. J. Mater. Sci. Mater. Med. 28, 174.
Li, H.F., Zheng, Y.F., 2016. Recent advances in bulk metallic glasses for biomedical applications. Acta Biomater. 36, 1–20.
Li, N., Zheng, Y., 2013. Novel magnesium alloys developed for biomedical application: a review. J. Mater. Sci. Technol. 29, 489–502.
Li, Y.P., Yu, J.S., Kurosu, S., Koizumi, Y., Matsumoto, H., Chiba, A., 2012. Role of nitrogen addition in stabilizing the γ phase of biomedical Co-29Cr-6Mo alloy. Mater. Chem. Phys. 133, 29–32.
Liu, Y., Yin, Z., Liu, Y., Geng, C., Chen, X., Xu, J., Peng, J., 2018. Study on the in vitro degradation behavior of commercial Zn-4%Al-Sr alloy for biomedical applications. Int. J. Electrochem. Sci. 13, 1640–1655.
Matsumoto, H., Watanabe, S., Hanada, S., 2005. Beta TiNbSn alloys with low Young's modulus and high strength. Mater. Trans. 46, 1070–1078.
Menzel, J., Kirschner, W., Stein, G., 1996. High nitrogen containing Ni-free austenitic steels for medical applications. ISIJ Int. 36, 893–900.
Mineta, S., Namba, S., Yoneda, T., Ueda, K., Narushima, T., 2010. Carbide formation and dissolution in biomedical Co-Cr-Mo alloys with different carbon contents during solution treatment. Metall. Mater. Trans. A 41, 2129–2138.
Miracle, D.B., Senkov, O.N., 2017. A critical review of high entropy alloys and related concepts. Acta Mater. 122, 448–511.
Mori, M., Yamanaka, K., Matsumoto, H., Chiba, A., 2010. Evolution of cold-rolled microstructures of biomedical Co-Cr-Mo alloys with and without N doping. Mater. Sci. Eng. A 528, 614–621.
Mouzou, E., Paternoster, C., Tolouei, R., Purnama, A., Chevallier, P., Dubé, D., Prima, F., Mantovani, D., 2016. In vitro degradation behavior of Fe-20Mn-1.2C alloy in three different pseudo-physiological solutions. Mater. Sci. Eng. C 61, 564–573.

Nagase, T., Todai, M., Hori, T., Nakano, T., 2018. Microstructure of equiatomic and non-equiatomic Ti-Nb-Ta-Zr-Mo high-entropy alloys for metallic biomaterials. J. Alloys Compd. 753, 412–421.

Nakano, T., Kan, T., Ishimoto, T., Ohashi, Y., Fujitani, W., Umakoshi, Y., Hattori, T., Higuchi, Y., Tane, M., Nakajima, H., 2006. Evaluation of bone quality near metallic implants with and without lotus-type pores for optimal biomaterial design. Mater. Trans. 47, 2233–2239.

Narushima, T., 2005. Titanium and its alloys as biomaterials. J. Jpn. Inst. Light Met. 55, 561–565.

Narushima, T., Mineta, S., Kurihara, Y., Ueda, K., 2013. Precipitates in biomedical Co-Cr alloys. JOM 65, 489–504.

Narushima, T., Ueda, K., Alfirano, 2015. Co-Cr alloys as effective metallic biomaterials. In: -Niinomi, M., Narushima, T., Nakai, M. (Eds.), Advances in Metallic Biomaterials: Tissues, Materials and Biological Reactions. In: Springer Series in Biomaterials Science and Engineering, vol. 3. Springer, Berlin, pp. 157–178.

Niinomi, M., 2002. Recent metallic materials for biomedical applications. Metall. Mater. Trans. A 33, 477–486.

Niinomi, M., Nakai, M., Hieda, J., 2012. Development of new metallic alloys for biomedical applications. Acta Biomater. 8, 3888–3903.

Niinomi, M., Nakai, M., Hendrickson, M., Nandwana, P., Alam, T., Choudhuri, D., Banerjee, R., 2016. Influence of oxygen on omega phase stability in the Ti-29Nb-13Ta-4.6Zr alloy. Scr. Mater. 123, 144–148.

Niinomi, M., 2018. Recent progress in research and development of metallic structural biomaterials with mainly focusing on mechanical biocompatibility. Mater. Trans. 59, 1–13.

Nomura, N., Kohama, T., Oh, I.H., Hanada, S., Chiba, A., Kanehira, M., Sasaki, K., 2005. Mechanical properties of porous Ti-15Mo-5Zr-3Al compacts prepared by powder sintering. Mater. Sci. Eng. C 25, 330–335.

Nomura, N., Tanaka, Y., Suyalatu, K.R., Doi, H., Tsutsumi, Y., Hanawa, T., 2009. Effects of phase constitution of Zr-Nb alloys on their magnetic susceptibilities. Mater. Trans. 50, 2466–2472.

Ogawa, M., Shimizu, T., Noda, T., Ikeda, M., 2007. The effect of Al content on tensile and fatigue properties of solution-treated and quenched Ti-13Cr-1Fe alloys. Mater. Trans. 48, 390–394.

Oh, I.-H., Nomura, N., Masahashi, N., Hanada, S., 2003. Mechanical properties of porous titanium compacts prepared by powder sintering. Scr. Mater. 49, 1197–1202.

Okazaki, Y., Rao, S., Ito, Y., Tateishi, T., 1998. Corrosion resistance, mechanical properties, corrosion fatigue strength and cytocompatibility of new Ti alloys without Al and V. Biomaterials 19, 1197–1215.

Omiya, M., Ueda, K., Narushima, T., 2017. Microstructure and mechanical properties of an $\alpha+\beta$ type Ti-4V-0.6O alloy. Mater. Trans. 58, 1250–1256.

Qin, F.X., Wang, X.M., Xie, G.Q., Inoue, A., 2008. Distinct plastic strain of Ni-free Ti-Zr-Cu-Pd-Nb bulk metallic glasses with potential for biomedical applications. Intermetallics 16, 1026–1030.

Ren, Y., Yang, K., Zhang, B., Wang, Y., Liang, Y., 2004. Nickel-free stainless steel for medical applications. J. Mater. Sci. Technol. 20, 571–573.

Ryan, G., Pandit, A., Apatsidis, D.P., 2006. Fabrication methods of porous metals for use in orthopaedic applications. Biomaterials 27, 2651–2670.

Saeki, S., Kobayashi, S., Okano, S., 2018. Effect of oxygen addition on the spinodal decomposition and hardness of Ti-4at%Mo alloy. J. Jpn. Inst. Met. Mater. 82, 197–203.

Saito, T., et al., 2003. Multi functional titanium alloy "GUM METAL" Mater. Sci. Forum 426-432, 681–688.

Saitova, L.R., Höppel, H.W., Göken, M., Semenova, I.P., Raab, G.I., Valiev, R.Z., 2009. Fatigue behavior of ultrafine-grained Ti-6Al-4V 'ELI' alloy for medical applications. Mater. Sci. Eng. A 503, 145–147.

Santos, P.F., Niinomi, M., Cho, K., Nakai, M., Liu, H., Ohtsu, N., Hirano, M., Ikeda, M., Narushima, T., 2015. Microstructures, mechanical properties and cytotoxicity of low cost beta Ti-Mn alloys for biomedical applications. Acta Biomater. 26, 366–376.

Santos, P.F., Niinomi, M., Liu, H., Nakai, M., Cho, K., Trenggono, A., Champagne, S., Hermawan, H., Narushima, T., 2016a. Improvement of microstructure, mechanical and corrosion properties of biomedical Ti-Mn alloys by Mo addition. Mater. Des. 110, 414–424.

Santos, P.F., Niinomi, M., Liu, H., Nakai, M., Cho, K., Itoh, Y., Narushima, T., Ikeda, M., 2016b. Fabrication of low-cost beta-type Ti-Mn alloys for biomedical applications by metal injection molding process and their mechanical properties. J. Mech. Behav. Biomed. Mater. 59, 497–507.

Santos, P.F., Niinomi, M., Cho, K., Liu, H., Nakai, M., Narushima, T., Ueda, K., Itoh, Y., 2017. Effects of Mo addition on the mechanical properties and microstructures of Ti-Mn alloys fabricated by metal injection molding for biomedical applications. Mater. Trans. 58, 271–279.

Song, X., Niinomi, M., Tsutsumi, H., Nakai, M., Wang, L., 2011. Effects of TiB on the mechanical properties of Ti-29Nb-13Ta-4.6Zr alloy for use in biomedical applications. Mater. Sci. Eng. A 528, 5600–5609.

Staiger, M.P., Pietak, A.M., Huadmai, J., Dias, G., 2006. Magnesium and its alloys as orthopedic biomaterials: a review. Biomaterials 27, 1728–1734.

Sugawara, K., Alfirano, M.S., Ueda, K., Narushima, T., 2015. Formation of the χ-phase precipitate in Co-Cr-Mo alloys with additional Si and C. Metall. Mater. Trans. A 46, 4342–4350.

Sun, S.-H., Koizumi, Y., Kurosu, S., Li, Y.-P., Chiba, A., 2015. Phase and grain size inhomogeneity and their influences on creep behavior of Co-Cr-Mo alloy additive manufactured by electron beam melting. Acta Biomater. 86, 305–318.

Suyalatu, K.R., Tsutsumi, Y., Doi, H., Nomura, N., Hanawa, T., 2011. Effects of phase constitution on magnetic susceptibility and mechanical properties of Zr-rich Zr-Mo alloys. Acta Biomater. 7, 4259–4266.

Tahara, M., Kim, H.Y., Inamura, T., Hosoda, H., Miyazaki, S., 2011. Lattice modulation and superelasticity in oxygen-added β-Ti alloys. Acta Mater. 59, 6208–6218.

Tahara, M., Inamura, T., Kim, H.Y., Miyazaki, S., Hosoda, H., 2016. Role of oxygen atoms in α″ martensite of Ti-20 at.% Nb alloy. Scr. Mater. 112, 15–18.

Tane, M., Akita, S., Nakano, T., Hagihara, K., Umakoshi, Y., Niinomi, M., Nakajima, H., 2008. Peculiar elastic behavior of Ti-Nb-Ta-Zr single crystals. Acta Mater. 56, 2856–2863.

Todai, M., Nagase, T., Hori, T., Matsugaki, A., Sekita, A., Nakano, T., 2017. Novel TiNbTaZrMo high-entropy alloys for metallic biomaterials. Scr. Mater. 129, 65–68.

Ueda, K., Nakaoka, S., Narushima, T., 2013. β-grain refinement of α+β type Ti-4.5Al-6Nb-2Fe-2Mo alloy using rare-earth-oxide precipitates. Mater. Trans. 54, 161–168.

Ueda, K., Kobayashi, T., Narushima, T., 2016. Microstructure and mechanical property of α+β type Ti-(0-10)mass%V-(0.5-1)mass%O alloys. J. Jpn. Inst. Met. Mater. 80, 60–65.

Ueki, K., Kurihara, Y., Mineta, S., Alfirano, U.K., Namba, S., Yoneda, T., Narushima, T., 2016a. Changes in microstructure of biomedical Co-Cr-Mo alloys during aging at 973 to 1373 K. Mater. Trans. 57, 2048–2053.

Ueki, K., Ueda, K., Narushima, T., 2016b. Microstructure and mechanical properties of heat treated Co-20Cr-15W-10Ni alloy for biomedical application. Metall. Mater. Trans. A 47, 2773–2782.

Ueki, K., Ueda, K., Nakai, M., Nakano, T., Narushima, T., 2018. Microstructural changes during plastic deformation and corrosion properties of biomedical Co-20Cr-15W-10Ni alloy heat-treated at 873 K. Metall. Mater. Trans. A 49, 2393–2404.

Uggowitzer, P.J., Magdowski, R., Speidel, M.O., 1996. Nickel free high nitrogen austenitic steels. ISIJ Int. 36, 901–908.

Wang, H., Zheng, Y., Liu, J., Jiang, C., Li, Y., 2017. In vitro corrosion properties and cytocompatibility of Fe-Ga alloys as potential biodegradable metallic materials. Mater. Sci. Eng. C 71, 60–66.

Wang, K., Gustavson, L., Dumbleton, J., 1993. Low modulus, high strength, biocompatible titanium alloy for medical implants. In: Froes, F.H., Caplan, I.L. (Eds.), Titanium'92: Science and Technology. TMS, Warrendale, PA, pp. 2697–2704.

Wang, K., 1996. The use of titanium for medical applications in the USA. Mater. Sci. Eng. A 213, 134–137.

Wątroba, M., Bednarczyk, W., Kawałko, J., Bała, P., 2018. Effect of zirconium microaddition on the microstructure and mechanical properties of Zn-Zr alloys. Mater. Charact. 142, 187–194.

Wei, D., Koizumi, Y., Takashima, T., Nagasako, M., Chiba, A., 2017. Fatigue improvement of electron beam melting-fabricated biomedical Co-Cr-Mo alloy by accessible heat treatment. Math. Res. Lett. 6, 93–99.

Yamanaka, K., Mori, M., Chiba, A., 2014. Effects of nitrogen addition on microstructure and mechanical behavior of biomedical Co-Cr-Mo alloys. J. Mech. Behav. Biomed. Mater. 29, 417–426.

Yang, K., Ren, Y., 2010. Nickel-free austenitic stainless steels for medical applications. Sci. Technol. Adv. Mater. 11, 014105.

Yilmazer, H., Niinomi, M., Nakai, M., Cho, K., Hieda, J., Todaka, Y., Miyazaki, T., 2013. Mechanical properties of a medical β-type titanium alloy with specific microstructural evolution through high-pressure torsion. Mater. Sci. Eng. C 33, 2499–2507.

Yilmazer, H., Niinomi, M., Cho, K., Nakai, M., Hieda, J., Sato, S., Todaka, Y., 2014. Microstructural evolution of precipitation-hardened β-type titanium alloy through high-pressure torsion. Acta Mater. 80, 172–182.

Yoda, K., Suyalatu, T.A., Nomura, N., Tsutsumi, Y., Doi, H., Kurosu, S., Chiba, A., Igarashi, Y., Hanawa, T., 2012. Effects of chromium and nitrogen content on the microstructures and mechanical properties of as-cast Co-Cr-Mo alloys for dental applications. Acta Biomater. 8, 2856–2862.

Zardiackas, L.D., Mitchell, D.W., Disegi, J.A., 1996. Characterization of Ti-15Mo beta titanium alloy for orthopaedic implant applications. In: Brown, S.A., Lemons, J.E. (Eds.), Medical Applications of Titanium and Its Alloys. ASTM, West Conshohocken, PA, pp. 60–75.

Zhao, B., Gain, A.K., Ding, W., Zhang, L., Li, X., Fu, Y., 2018. A review on metallic porous materials: pore formation, mechanical properties, and their applications. Int. J. Adv. Manuf. Technol. 95, 2641–2659.

Zhao, S., McNamara, C.T., Bowen, P.K., Verhun, N., Braykovich, J.P., Goldman, J., Drelich, J.W., 2017. Structural characteristics and in vitro biodegradation of a novel Zn-Li alloy prepared by induction melting and hot rolling. Metall. Mater. Trans. A 48, 1204–1215.

Zhao, X.F., Niinomi, M., Nakai, M., Hieda, J., 2012. Optimization of Cr content of metastable β-type Ti-Cr alloys with changeable Young's modulus for spring fixation applications. Acta Biomater. 8, 2392–2400.

Zhu, S.L., Wang, X.M., Qin, F.X., Inoue, A., 2007. A new Ti-based bulk glassy alloy with potential for biomedical application. Mater. Sci. Eng. A 459, 233–237.

Absorbable metals for cardiovascular applications

20

Sergio Loffredo[*,†], *Hendra Hermawan*[‡], *Maurizio Vedani*[†], *Diego Mantovani*[*]
*Department of Mining, Laboratory for Biomaterials and Bioengineering, CRC-I, Metallurgical and Materials Engineering and CHU de Québec research center, Laval University, Quebec City, QC, Canada, †Department of Mechanical Engineering, Politecnico di Milano, Milan, Italy, ‡Department of Mining, Metallurgical and Materials Engineering and CHU de Québec research center, Laval University, Quebec City, QC, Canada

20.1 Introduction

The use of cardiovascular stents for the treatment of atherosclerosis dates back to the 1980s, when the first device, made from stainless steel, was successfully implanted inside a human (Sigwart et al., 1987). A stent is a tubular metallic mesh that is used to reopen a partially occluded blood vessel. This is done by guiding the stent to the diseased site by means of a catheter. Once in position, the stent is expanded with the aid of a balloon, which is then deflated and removed. Most commonly the stents are made from stainless steels, cobalt (Co)-chromium (Cr) alloys, or nickel (Ni)-titanium (Ti) shape memory alloys (Poncin and Proft, 2004).

In order to limit long-term adverse phenomena observed in bare metal stents (BMS), such as restenosis (Virmani and Farb, 1999), current clinical practice uses metallic stents which have been coated with a drug-eluting polymer. Although capable of limiting restenosis, drug-eluting stents (DES) showed a significant incidence of late stent thrombosis (Camenzind et al., 2007). Allergenic reactions due to the release of Ni ions, which are present inside most alloy compositions (Köster et al., 2000), are also a cause for concern. Together with the evidence that artery remodeling takes place between 6 months and 1 year postimplantation (Ormiston and Serruys, 2009), a device that would support artery remodeling, while disappearing after this time, can be envisaged.

The first attempts to produce absorbable stents date from the 1980s (Indolfi et al., 2016), with the development of polymer-based implants. Since then, few devices received approval for commercialization from regulatory agencies. Namely, the Igaki-Tamai stent received approval for coronary artery disease (CAD) treatment in Japan, the Remedy stent for peripheral disease in Japan and Europe, and the Absorb stent in Europe and the United States (Indolfi et al., 2016). All these devices are made from poly-l lactic acid (PLLA) with a drug-eluting coating. While the Remedy stent showed long-term safety in humans up to 10 years (Nishio et al., 2012), the Absorb stent showed higher incidence of late stent thrombosis (Wykrzykowska et al., 2017) and late luminal loss (Serruys et al., 2016) when compared to state-of-the-art DES. The Absorb stent was finally retired from the market in late 2017 (FDA, 2017).

Metals for Biomedical Devices. https://doi.org/10.1016/B978-0-08-102666-3.00020-1
© 2019 Elsevier Ltd. All rights reserved.

In addition to the aforementioned biological concerns, polymers are known to have a much lower strength with respect to metals, which implies that polymeric stents must be significantly bigger in order to withstand the same inflation pressures used for metallic ones.

Metallic absorbable stents were first investigated in 2001 (Peuster et al., 2001), where a pure Fe stent was implanted inside the descending aorta of New Zealand white rabbits. In addition to this, Mg alloys were explored for absorbable stents since 2003 (Heublein et al., 2003). Magnesium (Mg) and iron (Fe)-based alloys are the two most studied metals for this kind of implants. In the recent years, also zinc (Zn) and Zn-based alloys gained attention from the research community (Bowen et al., 2016). The only materials that have been used in clinical trials are Mg-based alloys, dating back from 2005 (Peeters et al., 2005). Today, a drug-eluting Mg-based absorbable stent received approval for commercialization in 2016 following clinical trial success (Haude et al., 2016a, b, 2017).

Nowadays, two main factors still limit the diffusion of absorbable metallic stents in clinical practice:

- The limited mechanical properties of Mg-based stents, which do not allow to manufacture devices as small as those made from Co-Cr alloys.
- The lack of standardized testing procedures for assessing the biological performances of absorbable metals.

20.2 Requirements for absorbable stents

The requirements that a metal must possess in order to be used for an absorbable device are multifold. Such a device must ensure proper support for artery remodeling for a time that spans from 6 to 12 months in most patients (Ormiston and Serruys, 2009). After this need has expired, the material should ideally degrade as quickly as possible in order to avoid long-term complications, as visible from Fig. 20.1. The degradation of the device should be as uniform as possible, so to prevent unexpected failures of the implant.

As discussed earlier, elements that are severely toxic to humans must be avoided. Since, during the absorption process, the elements composing the device are dissolved, the ions that form must be bound by transporters that can excrete them safely. If such ions have a negative interaction with cells, inflammatory reactions may develop, which could lead to extensive cell necrosis.

The detailed requirements concerning the mechanical properties of an absorbable stent can be found in Table 20.1. The elastic modulus must be high in order to minimize the risk of elastic recoil after expansion. Moreover, the tensile yield strength must not be too high, so that the inflation pressure to apply for the stent to expand is not excessive; otherwise artery burst may occur (Poncin and Proft, 2004). Furthermore, the material must possess an ultimate tensile strength as high as possible in order to minimize the risk of failure upon expansion and during its service life. Finally, the elongation to failure must exceed 20%, so that correct placement and inflation of the device is ensured.

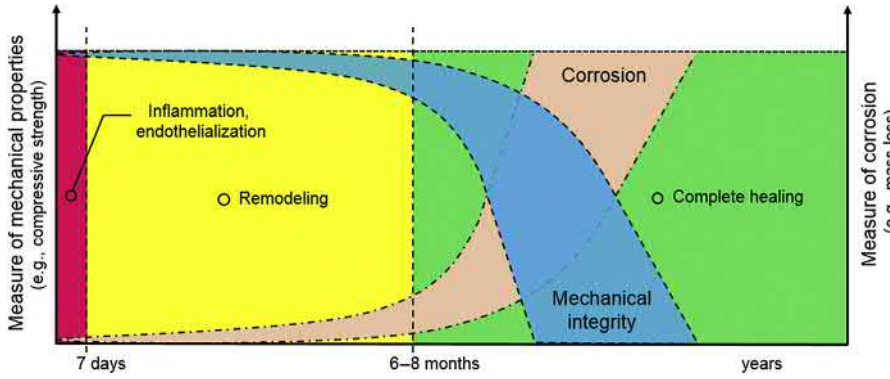


Fig. 20.1 Schematics of the absorption process for an absorbable cardiovascular stent (Hermawan 2018).
Reproduced with permission from Springer.

Table 20.1 Requirements for a metallic material to be used as absorbable stent

Property	Value
0.2% yield strength	>200 MPa. Too high may lead to acute recoil, below this value mechanical resistance is not sufficient
Elastic modulus	As high as possible to prevent recoil. Materials for inert stents have an elastic modulus around 200 GPa
Ultimate tensile strength	>300 MPa, but as high as possible for giving maximal radial strength to the device
Elongation to failure	>30% to withstand expansion
Fatigue life	$>10^7$ cycles, since the required mechanical integrity is of 6 months
Yield strength to elastic modulus ratio	As low as possible to limit acute recoil after expansion
Degradation rate	≥20 μm/year in vivo (assuming a linear degradation process)
Corrosion mechanism	Uniform to limit the risk of sudden failure

Adapted from Bowen, P.K., et al., 2016. Biodegradable metals for cardiovascular stents: from clinical concerns to recent Zn-alloys. Adv. Healthc. Mater. 5(10), 1121–1140.; Poncin, P., Proft, J., 2004. Stent tubing: understanding the desired attributes, in Medical Device Materials: Proceedings of the Materials and Processes for Medical Devices Conference, Materials Park, OH, ASM International, 253–259.

20.3 Development of absorbable metallic stents

20.3.1 Materials

The requirements demanded to a material for being used for producing absorbable metallic stents were described in the previous section. In the last 20 years, three classes of metals have been identified as viable candidates for this aim: Mg-, Fe-, and Zn-based alloys. All of them have a limited resistance to corrosion in physiological

environments. Moreover, they play a role in key functions in the body, such as enzymatic regulation and protein synthesis (Zheng et al., 2014). In addition to this, their cytotoxicity and hemocompatibility is low or negligible, especially when considering the ion release rate during the absorption period (Zheng et al., 2014). While Mg-based stents have succeeded at the clinical stage (Haude et al., 2016a), Fe- and Zn-based devices are still at the animal testing level because of different shortcomings concerning their degradation behavior and mechanical properties, respectively (He et al., 2016; Bowen et al., 2016). An overview of different alloys proposed for absorbable cardiovascular devices is presented in Table 20.2.

Table 20.2 Overview of mechanical properties of selected alloys for absorbable metallic stents, together with the most common alloys used for stents

Material	Prior treatment	Yield strength (MPa)	Ultimate tensile strength (MPa)	Maximum elongation (%)	References
316LVM stainless steel	From ASTM F138 standard	340	670	48	Poncin and Proft (2004)
L605 Co-Cr	From ASTM F90 standard	380–780	820–1200	35–55	Poncin and Proft (2004)
Mg, pure	As cast	20	86	13	Gu and Zheng (2010)
WE43 (Mg-4Y-3REE)	Extruded (no further information)	217	298	22	Gu and Zheng (2010)
JBDM (Mg-Nd-Zn-Zr)	Extruded at 250°C	162	234	26	Zhang et al. (2012)
Fe, pure	Annealed at 550°C	140	205	25.5	Moravej et al. (2010)
Fe-35Mn	Cold rolled + sintered at 1100°C	235	550	31	Hermawan et al. (2008)
Fe-21Mn-0.7C-1Pd	Cold worked + annealed at 700°C	505	1020	48	Schinhammer et al. (2012)
Zn, pure	Hot extruded at 250°C	51	111	60	Mostaed et al. (2016)
Zn-0.5 Mg	Hot extruded at 250°C	159	297	13	Mostaed et al. (2016)
Zn-7Ag	Hot extruded at 250°C	240	290	26	Sikora-Jasinska et al. (2017a, b)

20.3.1.1 Mg-based alloys

Mg, in its pure form, does not comply with the mechanical requirements discussed in Section 20.2. Because of this, several alloy compositions were developed. One of the first examples of Mg-based alloys developed for cardiovascular stents was the WE43 alloy, including 4% of yttrium (Y) and 3% of rare earth elements (REE). Preclinical trials found no signs of toxicity, although the absorption of the device was completed before the remodeling period finished (Di Mario et al., 2004). Together with early absorption, in-stent restenosis has been one of the main obstacles to the application of Mg alloys. Implantation of a bare-metal absorbable stent in pigs showed a decreased lumen area with respect to BMS or DES (Maeng et al., 2009). Similar outcomes were observed in the frame of the INSIGHT and PROGRESS clinical trial (Erbel et al., 2007; Bosiers, 2009).

In order to improve the stenosis and degradation rates, together with mechanical properties, two parallel and complementary strategies were developed: first, to modify the alloy composition and second, to alter the surface of the device by including a coating (Zheng et al., 2014).

The improvement of degradation rate and mechanical properties through alloying encompasses two common concepts. First, to have a fine and homogeneous grain structure inside the alloy through thermomechanical treatments. Second, to avoid the presence of second phases. As far as mechanical properties go, the relationship between the yield strength and grain size is dictated by the Hall-Petch relationship (Hall, 1951): in fact, the yield strength is inversely proportional to the square root of the average grain size, thus implying that, the smaller the grains, the higher the strength of the material. In addition to this, the presence of second phases can create preferential sites for developing cracks inside the material when it is deformed. When discussing about the corrosion behavior, a fine and homogeneous grain structure can lead to a more uniform corrosion (Ge et al., 2013). Moreover, the absence of second-phase particles can prevent the appearance of galvanic corrosion.

For the aforementioned reasons, only some elements can be alloyed with Mg to make materials with the desired properties. Among them, zirconium is a strong grain refiner, with limited effects on human cytocompatibility (Feyerabend et al., 2010). It must although be added in limited quantities, in order not to generate second phases. Other elements that respect the design constraints are certain REE, such as gadolinium (Gd), neodymium (Nd), dysprosium (Dy), and Y. Alloys with other elements commonly found inside the body, such as Zn and calcium (Ca), cannot achieve sufficient ductility for use in cardiovascular stents. They have nevertheless found commercial applicability for absorbable bone fixation prostheses, such as pins or screws (Lee et al., 2016; Plaass et al., 2016). A selection of the most promising Mg-based alloys is found in Table 20.2.

Surface modifications can be used effectively to control the degradation of the device, while limiting the risk of acute and chronic inflammatory reactions at the implantation site (Zheng et al., 2014). The surface of the device can be covered with an inert or a functional coating. In the latter case, a drug can be embedded, in order to limit the occurrence of postimplantation stenosis (Haude et al., 2013).

Combining the two parallel strategies led to positive clinical outcomes, also during long-term follow-up, for a Mg-based absorbable stent with a drug-eluting polymeric coating, which was approved for commercialization by the European Commission in 2016 (Magmaris, Biotronik) (Haude et al., 2016a, b, 2017; Fajadet et al., 2016).

20.3.1.2 Fe-based alloys

Although pure Fe was investigated for absorbable stents before Mg and its alloys, it has not found commercial applications yet. Since the very first in vivo tests, although good biological performances were observed, a very slow degradation rate was reported (Peuster et al., 2001, 2006). Together with this, pure Fe is ferromagnetic, which can make postimplantation follow-up difficult (Hermawan et al., 2008). Its main advantage lies in the mechanical properties, which are closer to those of stainless steel, as visible from Table 20.2. On the other hand, current state-of-the-art stents are mainly made from Co-Cr alloys, which have far superior performances with respect to stainless steel. In order to adjust the degradation rate and to improve the mechanical properties, the same strategies as in the case of Mg-based alloys (alloying and surface modification) can be applied.

Manganese (Mn) is the most explored alloying element for Fe. The reasons for this choice are multifold. First, it can solve the problem of ferromagnetism of Fe, since it stabilizes its paramagnetic form, called austenite. Second, it increases the degradation rate by decreasing the overall corrosion potential (Schinhammer et al., 2010). Third, it improves the mechanical properties by solution strengthening and stabilizing austenite, which is more ductile than pure Fe (Hermawan et al., 2008).

If only Mn is added to Fe, it is necessary to insert a high amount of it in order to obtain a fully austenitic form. On the other hand, high quantities of Mn can raise concerns over its biocompatibility, since it can be neurotoxic and a cofactor for the insurgence of Parkinson's disease (Crossgrove and Zheng, 2004). It must be noted, however, that the main path for the accumulation of Mn inside the brain is via the respiratory system; blood transport plays a minor role (Crossgrove and Zheng, 2004). The degradation of Fe-Mn alloys was observed to be faster with respect to pure Fe in vitro, while the in vivo corrosion occurs rather slowly (Drynda et al., 2015).

Among Mn-containing alloys, twinning-induced plasticity (TWIP) steels are those with the best mechanical performances, being very similar to Co-Cr alloys (Mouzou et al., 2016a, b; Schinhammer et al., 2012). The addition of carbon (C) and Mn modifies their deformation mechanism, which in turn affects significantly their mechanical properties (Bouaziz et al., 2011). Their degradation behavior appears better than pure Fe (Schinhammer et al., 2013). However, the formation of a stable passive film hinders the long-term absorption to occur (Mouzou et al., 2016a).

Because of the aforementioned toxicity concerns, Mn-free alloys were also developed with several elements (Sikora-Jasinska et al., 2017a, b; Liu and Zheng, 2011; Čapek et al., 2016). The main limitation for such alloys stands in their poorer mechanical properties with respect to their Mn-containing counterparts, although the corrosion behavior looks more promising.

As far as surface modification is considered, different treatments can be carried out, among which surface patterning (Huang and Zheng, 2016) and nitriding (Feng et al., 2013; Lin et al. 2015) are worth mentioning. Combining plasma nitriding with a drug-eluting coating allowed to manufacture a pure Fe stent possessing suitable absorption properties in an animal model (Lin et al., 2016).

20.3.1.3 Zn-based alloys

The investigation of Zn-based alloys for cardiovascular stents is more recent than Mg-and Fe-based systems. However, absorption properties of pure Zn in vivo are very interesting, since a slow degradation during artery remodeling, while faster afterwards, was observed (Bowen et al., 2013). The main limitation of pure Zn lies in its poor strength. In addition to this, pure Zn is affected by strain softening, a phenomenon for which its strength decreases under plastic deformation (Edwards et al., 1971). In order to improve the strength of pure Zn without sacrificing its ductility, several alloying elements have been explored, such as Mg, Ca, aluminum (Al), and strontium (Sr) (Mostaed et al., 2016; Li et al., 2015). One of the most interesting alloying elements from a mechanical properties point of view is silver, since it can eliminate strain softening (Sikora-Jasinska et al., 2017a, b; Zhao et al., 2017).

Cytocompatibility studies reveal the absence of adverse reactions for Zn, both in vitro and in vivo (Bowen et al., 2013, 2015; Drelich et al., 2017; Yang et al., 2017).

20.3.2 In vitro testing and standardization

In order to assess the biological performances of absorbable materials, in vitro test are the first step toward validating a given material for use inside humans. Such tests can be grouped into two main categories, which are degradation tests without cell contact and cytocompatibility/hemocompatibility tests.

20.3.2.1 Degradation tests

Degradation tests are used to assess the corrosion behavior of an absorbable material. At present, no ASTM/ISO standards are present to regulate such tests for absorbable metals, although they are under development. Most commonly, generalized corrosion testing methods are used, which can be classified as static immersion tests, electrochemical tests, and dynamic immersion tests:

Static immersion tests

In this type of test, a sample of the material that is investigated is immersed in a defined quantity of a pseudo-physiological solution. The immersion time can vary from few hours to several days. The degradation rate is measured as a function of the mass lost during immersion, as per the ASTM G31 standard (ASTM, 2012). It must be noted, however, that this test is reliable only for generalized and uniform corrosion, and it does not allow to take into account localized corrosion phenomena, such as galvanic coupling or intergranular corrosion (ASTM, 2012). The choice of the

medium is critical for assessing the degradation rate and degradation products that are formed. Some pseudo-physiological media simulate the blood plasma composition better than others, such as Hanks' modified salt solution or the simulated body fluid (Tolouei et al., 2016). In addition to this, the testing atmosphere should be chosen carefully, since it can critically affect the test outcomes (Mouzou et al., 2016b).

Electrochemical tests

Different types of electrochemical tests can be used for assessing the corrosion rate and degradation mechanisms of a material, the two most common being potentiodynamic polarization (PDP) and electrochemical impedance spectroscopy (EIS). In both experiments, a three-electrode cell is used, comprising: the reference electrode, which gives the voltage with respect to which the corrosion potential is measured, the counter electrode, acting as cathode in the electrochemical cell, and the working electrode, which is the sample whose corrosion is investigated. As in the case of static immersion, the cell must be immersed in a suitable aggressive medium. PDP allows to measure the degradation rate by calculating the corrosion current density (ASTM, 2014a). On the other hand, EIS can also give insights on the corrosion mechanism of the material. In this case, after having determined the corrosion potential, small sinusoidal oscillations of potential are applied around its value (ASTM, 1999). The results allow to determine, for example, whether the material has the tendency to passivate during time.

20.3.2.2 Dynamic immersion tests

In this case, similarly to static immersion, a sample is kept in contact with a pseudo-physiological solution for a given time. The fluid contacts the sample in a laminar flow, in order to simulate the shear stress that blood flow imposed on an implanted stent (Lévesque et al., 2008). Having a flowing fluid can significantly affect the outcomes of degradation tests, as reported by several authors (Lévesque et al., 2008; Moravej et al., 2010; Liu and Zheng, 2011). Also, a bioreactor can be used to simulate fluid flow, possibly even using explanted animal arteries (Wang et al., 2017). Schematics of two dynamic immersion setups can be found in Fig. 20.2.

As mentioned in the introduction, one of the main existing limitations for absorbable metallic stents lies in the absence of standardized procedures for evaluating their degradation rate. Both ISO and ASTM are currently developing standards for this purpose. Concerning degradation tests, ASTM is currently developing a specific standard as work item WK52640, which is expected to be published in 2018 (Hermawan, 2018).

20.3.2.3 Biological tests

Biological tests for absorbable metals include cytocompatibility and hemocompatibility tests. Their main aim is to evaluate if the material interacts properly with cells and blood, not favoring adverse events, such as the formation of thrombi or cell necrosis.

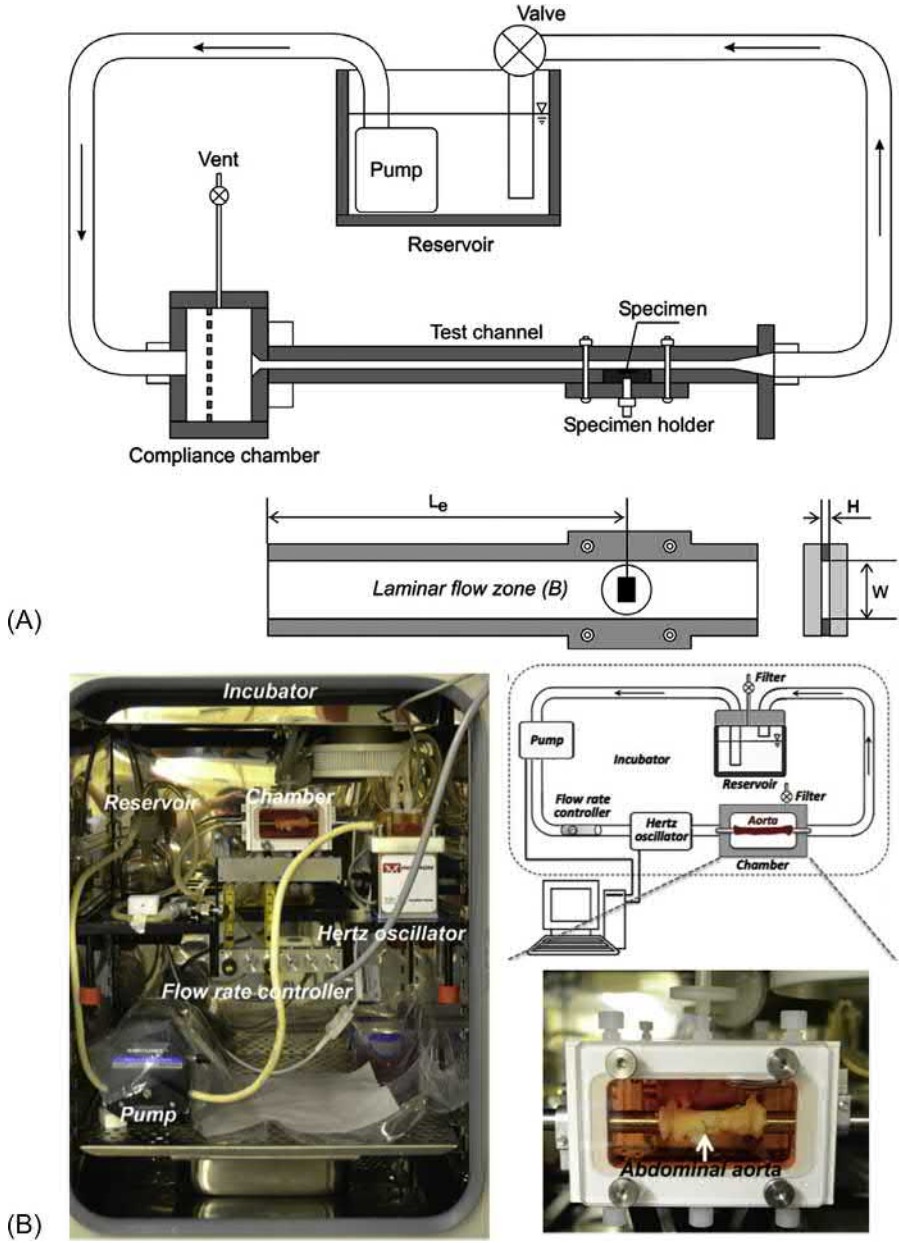


Fig. 20.2 Two different designs for dynamic immersion tests: (A) rigid polymeric test bench (Lévesque et al., 2008) and (B) ex vivo bioreactor (Wang et al., 2017).
Reproduced with permission from Elsevier.

20.3.2.4 Cytocompatibility tests

Several aspects of the reaction of cells in contact with a foreign material can be evaluated by means of cytocompatibility tests, including the ability to proliferate, the metabolic activity, and the immune response. Traditionally, these tests are regulated by the ISO-10993 standards (ISO, 2002). Tests can be performed with the material in direct contact with the cells, or extracting eluates of the metal to be put in contact with the cells. The choice between direct and indirect contact tests can alter significantly the outcomes in terms of cytocompatibility (Hänzi et al., 2010). The latest ISO guidance suggests the use of eluates in the case of absorbable metals (ISO, 2014). It is also important to choose the most suitable cell types for predicting the interactions inside a human artery. A vessel wall is composed by three layers of different types of cells: the innermost layer is made of endothelial cells (ECs), the intermediate layer of smooth muscle cells (SMCs), and the outermost layer of fibroblasts (FBs) (Mitchell and Schoen, 2010). The most relevant cell types for these tests are ECs and SMCs.

20.3.2.5 Hemocompatibility tests

In order to assess the interaction between blood and the material, two aspects are mostly analyzed, that are hemolysis and platelet adhesion. Hemolysis is the breaking of erythrocytes, which causes the release of free hemoglobin inside the blood. According to the ASTM F756 standard, a material can be considered hemocompatible when its hemolysis rate (the ratio between free hemoglobin and total hemoglobin) is below 5% (ASTM, 2014b). Such standard also regulates the testing method for hemolysis. Platelet adhesion, on the other hand, studies the tendency of the material to favor platelets to adhere on its surface, in order to determine the formation of a thrombus is possible.

As mentioned above, contrarily to the case of degradation tests, some specific guidance for absorbable materials has been published by standardization agencies (ISO, 2014).

20.3.3 In vivo testing

Animal tests are usually the second validation step after in vitro tests have provided appropriate results. Ideally, a finished stent should be used for animal studies, since the geometry and the expansion may alter the outcomes for absorption, mechanical integrity, and biological performances (Foin et al., 2014). In most cases, simplified models are used, such as pins or wires (Drynda et al., 2015; Mao et al., 2017; Bowen et al., 2013). In addition to this, different animal models are used for in vivo tests, which may not properly predict the outcomes in humans, since their cardiovascular system can be significantly different. The most used models for in vivo tests for absorbable stents are rats, rabbits, and pigs, as witnessed from several available papers (Wittchow et al., 2013; Bowen et al., 2013; Lin et al., 2017).

Currently, results from animal tests are available from all the three classes of absorbable metals outlined in Section 20.3.1.

20.3.3.1 Mg-based alloys

The first animal tests on Mg-based materials was performed in 2003 on a Mg-Al-REE alloy (AE21) (Heublein et al., 2003). Implantation in porcine arteries showed a too fast degradation rate, since the stent was fully absorbed in 90 days. Successive tests involved the use of the WE43 alloy in porcine arteries (Waksman et al., 2006, 2008; Slottow et al., 2008). Although a lower neointimal area was observed after 3 months, this stent lost mechanical integrity after 28 days, implying that the absorption occurred too fast. However, a similar study (Maeng et al., 2009) observed a significantly reduced lumen area where WE43 stents were implanted, in comparison with stainless steels devices after 3 months. A subsequent test involved the development of a drug-eluting coating on the device surface (Wittchow et al., 2013; Waksman et al., 2017). The outcomes showed that an appropriate coating can produce comparable endothelialization and lumen loss with respect to an inert DES. A comparison of the absorption of this Mg stent with and without drug-eluting coating is visible in Fig. 20.3. A different Mg alloy involves the use of Nd, Zr, and Zn (Yuan et al., 2011). While the in vitro cytocompatibility is good (Mao et al., 2013), an animal trial in rabbits showed the loss of mechanical integrity after 3 months from implantation,

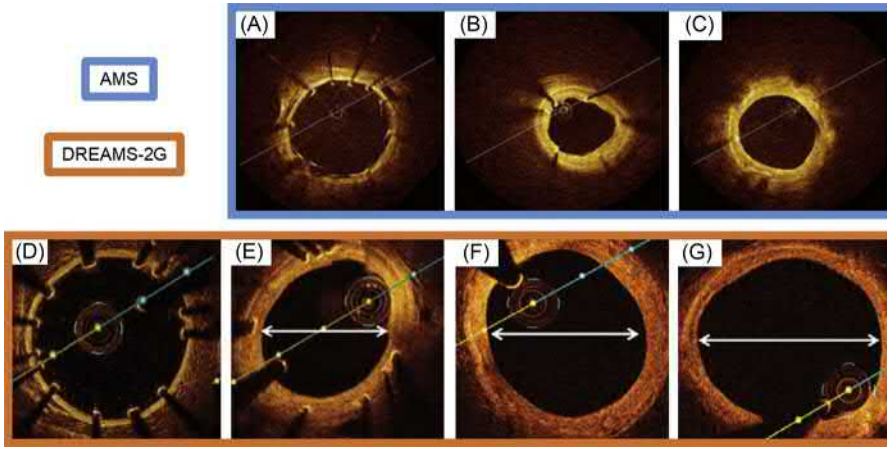


Fig. 20.3 Optical coherence tomography images showing the degradation of Mg stent struts without (AMS, A–C) and with (DREAMS 2G, D–G) a drug-eluting polymeric coating: (A) AMS after implantation, (B) AMS 28 days after implantation, (C) AMS 90 days after implantation, (D) DREAMS-2G after implantation, (E) DREAMS-2G 180 days after implantation, (F) DREAMS-2G 365 days after implantation, and (G) DREAMS-2G 730 days after implantation.
Adapted from Slottow, T.L.P., et al., 2008. 'Optical coherence tomography and intravascular ultrasound imaging of bioabsorbable magnesium stent degradation in porcine coronary arteries'. Cardiovasc. Revasc. Med. 9(4), 248–254.; Waksman, R, et al., 2017. 'Second-generation magnesium scaffold magmaris: device design and preclinical evaluation in a porcine coronary artery model'. EuroIntervention 13(4), 440–449. Reproduced with permission from Elsevier and Europa Digital and Publishing.

together with a reduced lumen diameter (Shi et al., 2017). Using a different coating (PTFE instead of PDLLA) allowed to avoid strut fracture, while increasing the vessel inner diameter (Wang et al., 2016).

20.3.3.2 Fe-based alloys

Among Fe-based alloys, animal tests on finished stents were performed so far only on pure Fe. The earliest outcomes showed that, while pure Fe possesses good short and long-term biocompatibility, the degradation rate is too slow (Peuster et al., 2001, 2006; Waksman et al., 2008). More recent in vivo experiments were carried out on plasma nitrided pure Fe stents. A 120-μm-thick bare stent made from this material, implanted in a porcine model, showed partial device corrosion after 12 months (Feng et al., 2013). If the thickness of the struts is reduced to 70 μm, corrosion occurred more quickly in a rabbit model, while degradation products were not removed after 53 months in a porcine (Lin et al., 2017). Further reducing the strut thickness to 53 μm, while adding a drug-eluting absorbable polymeric coating and a Zn protective barrier, accelerated in vivo degradation in a rabbit model, having 95% of the stent degraded after 13 months (Lin et al., 2016). The long-term non-absorption of the degradation products still suggests that further work has to be done to modify this tendency. Outcomes from the aforementioned tests are shown in Fig. 20.4.

20.3.3.3 Zn-based alloys

While more recently introduced as candidates than the two other classes, Zn-based materials look very promising because of their in vivo behavior. The first outcomes showed that, while corroding slowly in the first 6 months from implantation in a murine model, the absorption accelerated steadily afterwards (Bowen et al., 2013). Other tests confirmed that pure Zn degrades with a linear trend, indicating that a 250 μm wire cross section is reduced by 50% after 20 months from implantation (Drelich et al., 2017). Furthermore, a pure Zn stent implanted in rabbit arteries showed similar results, with a 42% volume reduction after 12 months (Yang et al., 2017). This stent also showed that Zn is progressively depleted from the implantation site, being replaced by Ca and O. Results from such tests are shown in Fig. 20.5.

20.3.4 Clinical trials

Clinical trials are those tests that involve study in humans, and are the final stage before regulatory approval. A stent is considered a high-risk device [FDA and EU class III (Van Norman, 2016b)], so it requires strong clinical evidence before receiving market approval (Van Norman, 2016a). The process starts with first-in-man trials, followed, if successful, by pivotal trials, which use a large pool of subjects (typically above 1000) (Van Norman, 2016a). So far, published results on clinical trials on absorbable metallic stents are limited to Mg-based devices.

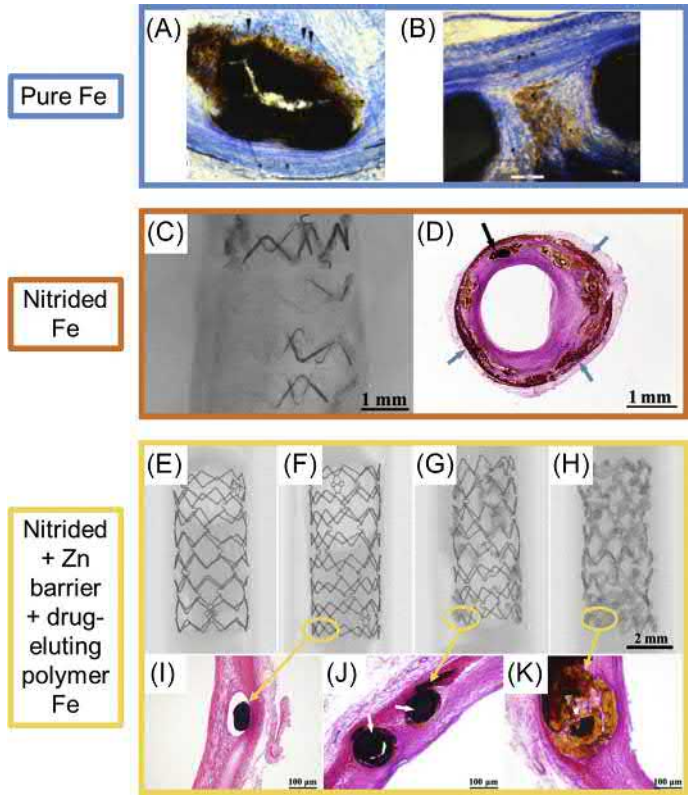


Fig. 20.4 Outcomes from in vivo *tests* on Fe-based stents: histological images of a pure Fe stent in porcine aorta (A) 6 and (B) 18 months postimplantation (Peuster et al., 2001), nitrided Fe stent 53 months after implantation in porcine aorta (Lin et al., 2017): (C) micro-CT and (D) histology showing residual degradation products, nitrided Fe stent with a Zn barrier layer and a drug-eluting polymeric coating implanted in a rabbit aorta (Lin et al., 2016): micro-CT images (E) 3 days, (F) 3 months, (G) 6 months, and (H) 13 months after implantation, and histology around stent struts (I) 3 months, (J) 6 months, and (K) 13 months after implantation, showing residual degradation products.
Reproduced with permission from Elsevier.

The first results on clinical trials date from 2005, for which a stent was implanted in patients with critical limb ischemia (Peeters et al., 2005). Three months after implantation, a significant number of patients had partial or total stenosis around the stent. A successive study (PROGRESS-AMS) showed that the same stent induces no adverse reactions, while its absorption is completed in 4 months, well before artery remodeling was completed (Erbel et al., 2007). Negative outcomes on the AMS device were also observed in the INSIGHT trial, where the stent had a much higher restenosis incidence vs a DES (Bosiers, 2009).

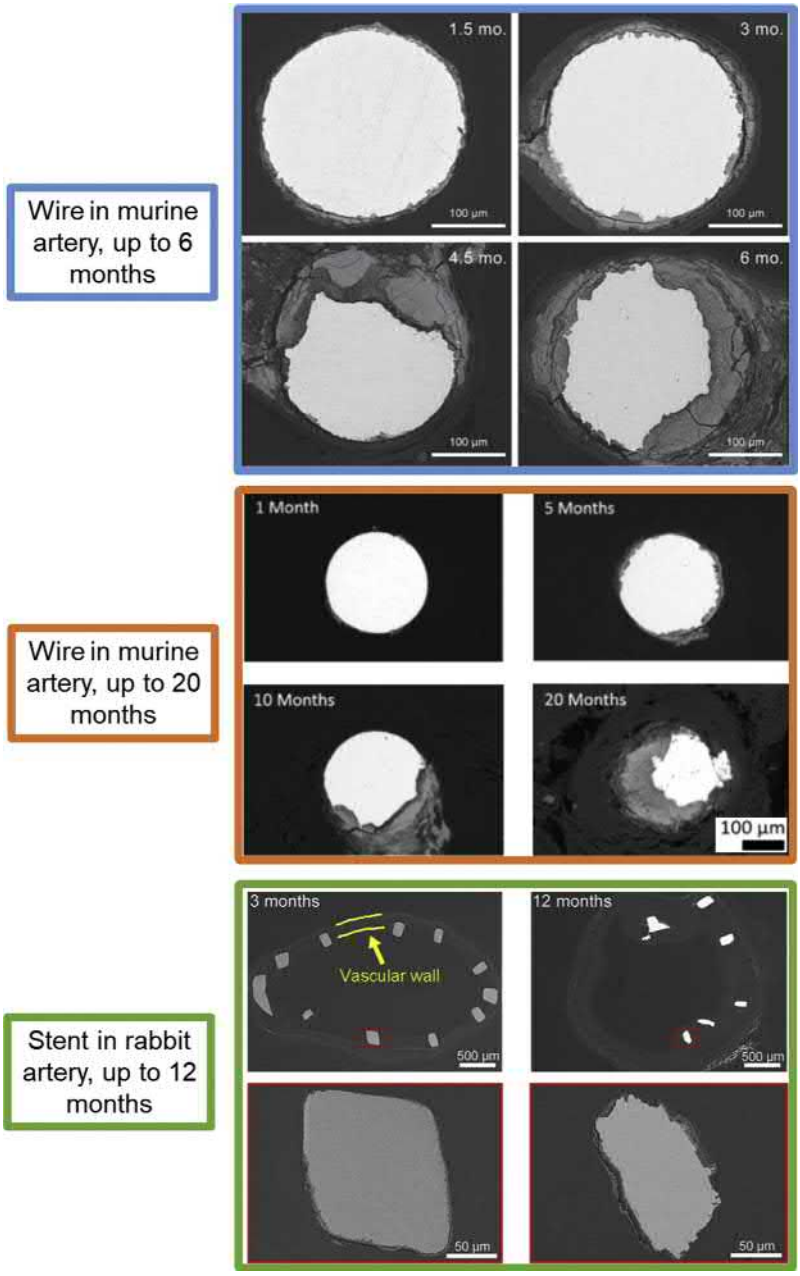


Fig. 20.5 Scanning electron microscopy images of cross sections of pure Zn implants after in vivo tests in different environments (Bowen et al., 2013; Drelich et al. 2017; Yang et al., 2017).
Reproduced with permission of Elsevier and Wiley.

In order to limit restenosis, a drug-eluting degradable coating was added to the device. The first version of this device, named DREAMS, had a PLGA coating on top of the struts, with paclitaxel embedded in the coating as antiproliferative drug. In addition to this, the alloy and strut design were modified (Haude et al., 2013). The clinical trial on this device (BIOSOLVE-I) showed that no scaffold thrombosis or patient death occurs after 12–28 months. However, late lumen loss was higher at 12 and 28 months with respect to state-of-the-art DES (Haude et al., 2013, 2016).

The second iteration of the aforementioned drug-eluting absorbable stent (DREAMS-2G) had a modified coating. In this latter case, sirolimus was embedded in a PLLA matrix (Haude et al., 2016a). This new stent degraded more homogeneously than DREAMS-I, and had reduced late lumen loss at 6 and 12 months (Haude et al., 2016a). Moreover, no thrombosis was observed after 12 and 24 months from implantation (Haude et al., 2016a, b). The stent struts were no longer visible after 6 months from implantation, as visible from Fig. 20.6 (Garcia-Garcia et al., 2018). These results granted approval for commercialization from the EU regulatory agency in 2016, and is currently commercialized as Magmaris (Fajadet et al., 2016).

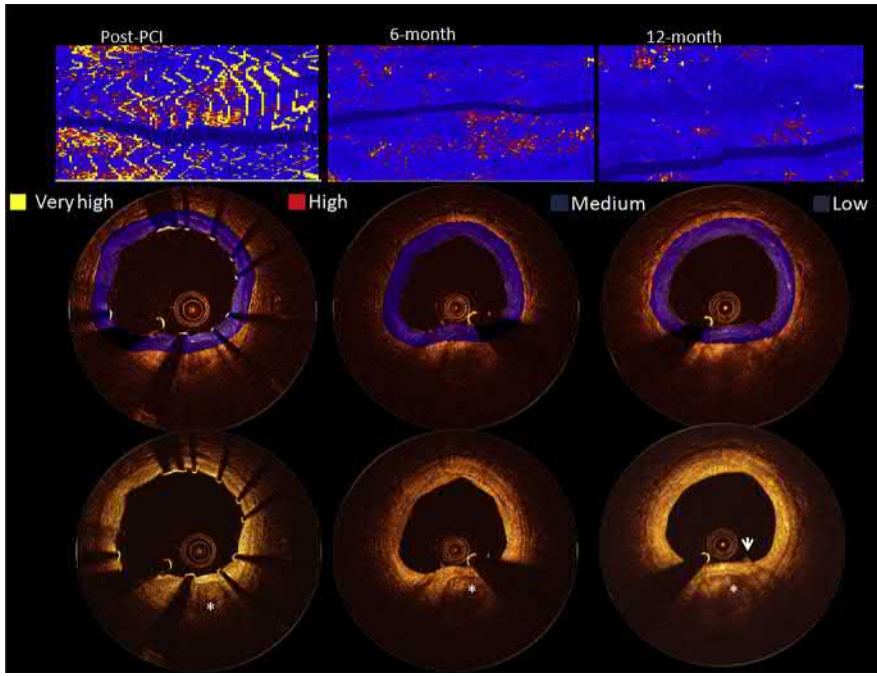


Fig. 20.6 Optical coherence tomography follow-up of a Magmaris stent implanted in human patients after 1, 6, and 12 months from implantation (Garcia-Garcia et al., 2018). Reproduced with permission from Elsevier.

20.4 Current status and outlook

In the last 20 years, the research on absorbable metals for cardiovascular stents produced an important number of successes, culminating in the first commercial device made from an Mg-based alloy. Although clinical practice on absorbable stents is at its embryonal stage, there is the potential of a large-scale revolution in the treatment of cardiovascular diseases.

One of the main challenges to overcome in the next years is to properly correlate the degradation behavior observed in in vitro tests with the animal and human conditions. This is especially true for Fe-based alloys since, although lots of efforts have produced improved corrosion results in vitro, no acceptable corrosion profiles have been seen so far inside animals. Most importantly, it is very difficult to establish a generalized model to correlate the two tests, since different materials, testing environments and conditions, implantation sites, and processing all play a role in influencing the degradation process (Ralston et al., 2010; Sanchez et al., 2015).

Another obstacle to be overcome for the widespread application of absorbable devices is to be able to reproduce the full dimensional scale of devices that is available to surgeons in clinical practice. Currently, the Magmaris stent is available in a limited range of sizes (Fajadet et al., 2016). Because of the aforementioned limitations in the mechanical properties of Mg alloys, such a feat may be surmounted only by optimizing other alloying systems, such as Fe and Zn-based alloys. In addition to this, as shown from the first evidence from clinical trials, it is necessary to tailor the degradation rate of the materials by developing appropriate coatings that may include antiproliferative drugs to limit the proliferation of SMCs in the early stages of endothelialization.

Moreover, the development of standardized procedures for assessing the performances of absorbable metals is needed to have reproducible procedures. Although the same protocols may be applied for testing the inflation behavior of the device, its mechanical properties and the microstructural aspects, this does not hold for the corrosion properties and the biological performances. In fact, the standardizing agencies at the American and global level are currently working on the development of specific standards and guidance on how to apply procedures developed for inert devices.

References

ASTM, 1999. G106: Standard Practice for Verification of Algorithm and Equipment for Electrochemical Impedance Measurements. ASTM International, West Conshohocken, USA.

ASTM, 2012. G31: Standard Guide for Laboratory Immersion Corrosion Testing of Metals. ASTM International, West Conshohocken, USA.

ASTM, 2014a. G59: Standard Test Method for Conducting Potentiodynamic Polarization Resistance Measurements. ASTM International, West Conshohocken, USA.

ASTM, 2014b. F756: Standard Practice for Assessment of Hemolytic Properties of Materials. ASTM International, West Conshohocken, USA.

Bosiers, M., 2009. AMS INSIGHT-absorbable metal stent implantation for treatment of below-the-knee critical limb ischemia: 6-month analysis. Cardiovasc. Intervent. Radiol. 32 (3), 424–435.

Bouaziz, O., et al., 2011. High manganese austenitic twinning induced plasticity steels: a review of the microstructure properties relationships. Curr. Opinion Solid State Mater. Sci. 15 (4), 141–168.

Bowen, P.K., Drelich, J., Goldman, J., 2013. Zinc exhibits ideal physiological corrosion behavior for bioabsorbable stents. Adv. Mater. 25 (18), 2577–2582.

Bowen, P.K., et al., 2015. Metallic zinc exhibits optimal biocompatibility for bioabsorbable endovascular stents. Mater. Sci. Eng. C 56 (1), 467–472.

Bowen, P.K., et al., 2016. Biodegradable metals for cardiovascular stents: from clinical concerns to recent Zn-alloys. Adv. Healthc. Mater. 5 (10), 1121–1140.

Camenzind, E., Steg, P.G., Wijns, W., 2007. Stent thrombosis late after implantation of first-generation drug-eluting stents. Circulation 115 (11), 1440–1455.

Čapek, J., et al., 2016. Microstructure, mechanical and corrosion properties of biodegradable powder metallurgical Fe-2 wt% X (X = Pd, Ag and C) alloys. Mater. Chem. Phys. 181, 501–511.

Crossgrove, J., Zheng, W., 2004. Manganese toxicity upon overexposure. NMR Biomed. 17 (8), 544–553.

Di Mario, C., et al., 2004. Drug-eluting bioabsorbable magnesium stent. J. Interv. Cardiol. 17 (6), 391–395.

Drelich, A.J., et al., 2017. Long-term surveillance of zinc implant in murine artery: surprisingly steady biocorrosion rate. Acta Biomater. 58, 539–549.

Drynda, A., et al., 2015. In vitro and in vivo corrosion properties of new iron-manganese alloys designed for cardiovascular applications. J. Biomed. Mater. Res. B Appl. Biomater. 103 (3), 649–660.

Edwards, G., Shyne, J.C., Sherby, O.D., 1971. Strain softening in powder metallurgy zinc. Metall. Trans. 2 (10), 2955–2958.

Erbel, R., et al., 2007. Temporary scaffolding of coronary arteries with bioabsorbable magnesium stents: a prospective, non-randomised multicentre trial. Lancet 369 (9576), 1869–1875.

Fajadet, J., et al., 2016. Magmaris preliminary recommendation upon commercial launch: a consensus from the expert panel on 14 April 2016. EuroIntervention 12 (7), 828–833.

FDA, 2017. UPDATE on Increased Rate of Major Adverse Cardiac Events Observed in Patients Receiving Abbott Vascular's Absorb GT1 Bioresorbable Vascular Scaffold (BVS)—Letter to Health Care Providers. Available athttps://www.fda.gov/MedicalDevices/Safety/LetterstoHealthCareProviders/ucm582728.htm Accessed June 8, 2018.

Feng, Q., et al., 2013. Characterization and in vivo evaluation of a bio-corrodible nitrided iron stent. J. Mater. Sci. Mater. Med. 24 (3), 713–724.

Feyerabend, F., et al., 2010. Evaluation of short-term effects of rare earth and other elements used in magnesium alloys on primary cells and cell lines. Acta Biomater. 6 (5), 1834–1842.

Foin, N., et al., 2014. Impact of stent strut design in metallic stents and biodegradable scaffolds. Int. J. Cardiol. 177 (3), 800–808.

Garcia-Garcia, H.M., et al., 2018. In vivo serial invasive imaging of the second-generation drug-eluting absorbable metal scaffold (magmaris—DREAMS 2G) in de novo coronary lesions: insights from the BIOSOLVE-II first-in-man trial. Int. J. Cardiol. 255, 22–28.

Ge, Q., et al., 2013. The processing of ultrafine-grained Mg tubes for biodegradable stents. Acta Biomater. 9 (10), 8604–8610.

Gu, X.N., Zheng, Y.F., 2010. A review on magnesium alloys as biodegradable materials. Front. Mater. Sci. China 4, 111–115.
Hall, E.O., 1951. The deformation and ageing of mild steel 3- discussion of results. Proc. Phys. Soc. London, Sect. B 64 (381), 747–753.
Hänzi, A.C., et al., 2010. On the in vitro and in vivo degradation performance and biological response of new biodegradable Mg–Y–Zn alloys. Acta Biomater. 6 (5), 1824–1833.
Haude, M., et al., 2013. Safety and performance of the drug-eluting absorbable metal scaffold (DREAMS) in patients with de-novo coronary lesions: 12 month results of the prospective, multicentre, first-in-man BIOSOLVE-I trial. Lancet 381 (9869), 836–844.
Haude, M., et al., 2016. Safety and performance of the DRug-eluting absorbable metal scaffold (DREAMS) in patients with de novo coronary lesions: 3-year results of the prospective, multicentre, first-in-man BIOSOLVE-I trial. EuroIntervention 12 (2), 160–166.
Haude, M., et al., 2016a. Safety and performance of the second-generation drug-eluting absorbable metal scaffold in patients with de-novo coronary artery lesions (BIOSOLVE-II): 6 month results of a prospective, multicentre, non-randomised, first-in-man trial. Lancet 387 (10013), 31–39.
Haude, M., et al., 2016b. Sustained safety and performance of the second-generation drug-eluting absorbable metal scaffold in patients with de novo coronary lesions: 12-month clinical results and angiographic findings of the BIOSOLVE-II first-in-man trial. Eur. Heart J. 14 (9576), 24492–24500.
Haude, M., et al., 2017. Sustained safety and clinical performance of a drug-eluting absorbable metal scaffold up to 24 months: pooled outcomes of BIOSOLVE-II and BIOSOLVE-III. EuroIntervention 13 (4), 432–439.
He, J., et al., 2016. Advances in Fe-based biodegradable metallic materials. RSC Adv. 6 (114), 112819–112838.
Hermawan, H., 2018. Updates on the research and development of absorbable metals for biomedical applications. Prog. Biomater. 7 (2), 93–110.
Hermawan, H., et al., 2008. Iron–manganese: new class of metallic degradable biomaterials prepared by powder metallurgy. Powder Metall. 51 (1), 38–45.
Heublein, B., et al., 2003. Biocorrosion of magnesium alloys: a new principle in cardiovascular implant technology? Heart 89 (6), 651–656.
Huang, T., Zheng, Y., 2016. Uniform and accelerated degradation of pure iron patterned by Pt disc arrays. Sci. Rep. 6, 23627.
Indolfi, C., De Rosa, S., Colombo, A., 2016. Bioresorbable vascular scaffolds—basic concepts and clinical outcome. Nat. Rev. Cardiol. 13 (12), 719–729.
ISO, 2002. Biological Evaluation of Medical Devices Part 5: Tests for in Vitro Cytotoxicity. ISO, Geneva, Switzerland 10993-5.
ISO, 2014. Cardiovascular Biological Evaluation of Medical Devices—Guidance of Absorbable Implants. ISO, Geneva, Switzerland ISO/DTR 37137.
Köster, R., et al., 2000. Nickel and molybdenum contact allergies in patients with coronary in-stent restenosis. Lancet 356 (9245), 1895–1897.
Lee, J.-W., et al., 2016. Long-term clinical study and multiscale analysis of in vivo. Science 113 (3), 716–721.
Lévesque, J., et al., 2008. Design of a pseudo-physiological test bench specific to the development of biodegradable metallic biomaterials. Acta Biomater. 4 (2), 284–295.
Li, H.F., et al., 2015. Development of biodegradable Zn-1X binary alloys with nutrient alloying elements Mg, Ca and Sr. Sci. Rep. 5, 10719.
Lin, W., et al., 2015. Cytotoxicity and its test methodology for a bioabsorbable nitrided iron stent. J. Biomed. Mater. Res. B Appl. Biomater. 103 (4), 764–776.

Lin, W.-J., et al., 2016. Design and characterization of a novel biocorrodible iron-based drug-eluting coronary scaffold. Mater. Des. 91, 72–79.
Lin, W., et al., 2017. Long-term in vivo corrosion behavior, biocompatibility and bioresorption mechanism of a bioresorbable nitrided iron scaffold. Acta Biomater. 54, 454–468.
Liu, B., Zheng, Y.F., 2011. Effects of alloying elements (Mn, Co, Al, W, Sn, B, C and S) on biodegradability and in vitro biocompatibility of pure iron. Acta Biomater. 7 (3), 1407–1420.
Maeng, M., et al., 2009. Negative vascular remodelling after implantation of bioabsorbable magnesium alloy stents in porcine coronary arteries: a randomised comparison with bare-metal and sirolimus-eluting stents. Heart 95 (3), 241–246.
Mao, L., et al., 2013. Nanophasic biodegradation enhances the durability and biocompatibility of magnesium alloys for the next-generation vascular stents. Nanoscale 5 (20), 9517–9522.
Mao, L., et al., 2017. Enhanced biocompatibility and long-term durability in vivo of Mg-Nd-Zn-Zr alloy for vascular stent application. J. Alloys Compd. 720, 245–253.
Mitchell, R.N., Schoen, F.J., 2010. Blood vessels. In: Kumar, V. et al., (Ed.), Robbins and Cotran Pathologic Basis of Disease. Saunders, Philadelphia, pp. 487–528.
Moravej, M., et al., 2010. Electroformed pure iron as a new biomaterial for degradable stents: in vitro degradation and preliminary cell viability studies. Acta Biomater. 6 (5), 1843–1851.
Mostaed, E., et al., 2016. Novel Zn-based alloys for biodegradable stent applications: design, development and in vitro degradation. J. Mech. Behav. Biomed. Mater. 60, 581–602.
Mouzou, E., et al., 2016a. CO2-rich atmosphere strongly affects the degradation of Fe-21Mn-1C for biodegradable metallic implants. Mater. Lett. 181, 362–366.
Mouzou, E., et al., 2016b. In vitro degradation behavior of Fe-20Mn-1.2C alloy in three different pseudo-physiological solutions. Mater. Sci. Eng. C 61, 564–573.
Nishio, S., et al., 2012. Long-term (>10 years) clinical outcomes of first-in-human biodegradable poly-l-lactic acid coronary stents: Igaki-Tamai stents. Circulation 125 (19), 2343–2353.
Ormiston, J.A., Serruys, P.W.S., 2009. Bioabsorbable coronary stents. Circ. Cardiovasc. Interv. 2 (3), 255–260.
Peeters, P., et al., 2005. Preliminary results after application of absorbable metal stents in patients with critical limb ischemia. J. Endovasc. Ther. 12 (1), 1–5.
Peuster, M., et al., 2001. A novel approach to temporary stenting: degradable cardiovascular stents produced from corrodible metal-results 6-18 months after implantation into New Zealand white rabbits. Heart 86 (5), 563–569.
Peuster, M., et al., 2006. Long-term biocompatibility of a corrodible peripheral iron stent in the porcine descending aorta. Biomaterials 27 (28), 4955–4962.
Plaass, C., et al., 2016. Early results using a biodegradable magnesium screw for modified chevron osteotomies. J. Orthop. Res. 34 (12), 2207–2214.
Poncin, P., Proft, J., 2004. Stent tubing: understanding the desired attributes. In: Medical Device Materials: Proceedings of the Materials and Processes for Medical Devices Conference. ASM International, Materials Park, OH, pp. 253–259.
Ralston, K.D., Birbilis, N., Davies, C.H.J., 2010. Revealing the relationship between grain size and corrosion rate of metals. Scr. Mater. 63 (12), 1201–1204.
Sanchez, A.H.M., et al., 2015. Mg and Mg alloys: how comparable are in vitro and in vivo corrosion rates? A review. Acta Biomater. 13, 16–31.
Schinhammer, M., et al., 2010. Design strategy for biodegradable Fe-based alloys for medical applications. Acta Biomater. 6 (5), 1705–1713.

Schinhammer, M., et al., 2012. Recrystallization behavior, microstructure evolution and mechanical properties of biodegradable Fe–Mn–C(–Pd) TWIP alloys. Acta Mater. 60 (6–7), 2746–2756.
Schinhammer, M., et al., 2013. Degradation performance of biodegradable FeMnC(Pd) alloys. Mater. Sci. Eng. C 33 (4), 1882–1893.
Serruys, P.W., et al., 2016. Comparison of an everolimus-eluting bioresorbable scaffold with an everolimus-eluting metallic stent for the treatment of coronary artery stenosis (ABSORB II): a 3 year, randomised, controlled, single-blind, multicentre clinical trial. Lancet 388 (10059), 2479–2491.
Shi, Y., et al., 2017. In vitro and in vivo degradation of rapamycin-eluting Mg-Nd-Zn-Zr alloy stents in porcine coronary arteries. Mater. Sci. Eng. C 80, 1–6.
Sigwart, U., et al., 1987. Intravascular stents to prevent occlusion and re-stenosis after transluminal angioplasty. N. Engl. J. Med. 316 (12), 701–706.
Sikora-Jasinska, M., et al., 2017a. Fabrication, mechanical properties and in vitro degradation behavior of newly developed Zn-Ag alloys for degradable implant applications. Mater. Sci. Eng. C 77, 1170–1181.
Sikora-Jasinska, M., et al., 2017b. Synthesis, mechanical properties and corrosion behavior of powder metallurgy processed Fe/Mg2Si composites for biodegradable implant applications. Mater. Sci. Eng. C 81, 511–521.
Slottow, T.L.P., et al., 2008. Optical coherence tomography and intravascular ultrasound imaging of bioabsorbable magnesium stent degradation in porcine coronary arteries. Cardiovasc. Revasc. Med. 9 (4), 248–254.
Tolouei, R., et al., 2016. The use of multiple pseudo-physiological solutions to simulate the degradation behavior of pure iron as a metallic resorbable implant: a surface-characterization study. Phys. Chem. Chem. Phys. 18 (29), 19637–19646.
Van Norman, G.A., 2016a. Drugs, devices, and the FDA: part 2: an overview of approval processes: FDA approval of medical devices. JACC Basic Transl. Sci. 1 (4), 277–287.
Van Norman, G.A., 2016b. Drugs and devices: comparison of European and U.S. approval processes. JACC Basic Transl. Sci. 1 (5), 399–412.
Virmani, R., Farb, A., 1999. Pathology of in-stent restenosis. Curr. Opin. Lipidol. 10 (6), 499–506.
Waksman, R., et al., 2006. Safety and efficacy of bioabsorbable magnesium alloy stents in porcine coronary arteries. Catheter. Cardiovasc. Interv. 68 (4), 607–617.
Waksman, R., et al., 2008. Short-term effects of biocorrodible iron stents in porcine coronary arteries. J. Interv. Cardiol. 21 (1), 15–20.
Waksman, R., et al., 2017. Second-generation magnesium scaffold magmaris: device design and preclinical evaluation in a porcine coronary artery model. EuroIntervention 13 (4), 440–449.
Wang, W., et al., 2016. Magnesium alloy covered stent for treatment of a lateral aneurysm model in rabbit common carotid artery: an in vivo study. Sci. Rep. 6, 37401.
Wang, J., et al., 2017. Ex vivo blood vessel bioreactor for analysis of the biodegradation of magnesium stent models with and without vessel wall integration. Acta Biomater. 50, 546–555.
Wittchow, E., et al., 2013. Bioresorbable drug-eluting magnesium-alloy scaffold: design and feasibility in a porcine coronary model. EuroIntervention 8 (12), 1441–1450.
Wykrzykowska, J.J., et al., 2017. Bioresorbable scaffolds versus metallic stents in routine PCI. N. Engl. J. Med. 376, 2319–2328.
Yang, H., et al., 2017. Evolution of the degradation mechanism of pure zinc stent in the one-year study of rabbit abdominal aorta model. Biomaterials 145, 92–105.

Yuan, G., Fu, P., Ding, W., 2011. Magnesium Alloy Used for Degradable Stent Material in Vivo and Preparation Method Thereof. WO Patent 2011160534A1.

Zhang, X., et al., 2012. Effects of extrusion and heat treatment on the mechanical properties and biocorrosion behaviors of a Mg–Nd–Zn–Zr alloy. J. Mech. Behav. Biomed. Mater. 7, 77–86.

Zhao, S., et al., 2017. Structural characteristics and in vitro biodegradation of a novel Zn-Li alloy prepared by induction melting and hot rollin. Metall. Mater. Trans. A 48 (3), 1204–1215.

Zheng, Y.F., Gu, X.N., Witte, F., 2014. Biodegradable metals. Mater. Sci. Eng. R. Rep. 77, 1–34.

Index

Note: Page numbers followed by *f* indicate figures and *t* indicate tables.

A

Absorbable stents
  metals (*see* Metallic absorbable stents)
  polymers, 523–524
  requirements, 524, 525*t*
Absorb stent, 523
Acicular microstructure, 47–49
Additively layered manufactured (ALM) Ti
  chemical composition, 344, 344*t*
  mechanical properties, 344, 345*t*
Additive manufacturing (AM)
  advantages, 336–337
  applications, 337–341
    customized implants, 338–339
    drug delivery, 340–341
    education and training, 339–340
    prosthesis and orthotics, 338
    tools, guides and instruments, 338
  biocompatibility, 343–345
  biological consideration, 342–343
  challenges, 337
  crystallographic anisotropy, 123–125
  design and fabrication process, 331, 332*f*
  dimensional accuracy, 337
  market and statistics, 341–342
  mechanical anisotropy
    AM fabricated product, 122–123, 124*f*
    nominal stress-nominal strain curves, 122, 123*f*
    shape parameters, 122
    Young's modulus and yield stress, 122–123
  Mg alloys, 265–266, 270–272
  orthopedic implants, 431, 456–461
  porous biomaterials, 510–511
  processing methods, test types and findings, 344–345, 346–347*t*
Adolescent idiopathic scoliosis (AIS), 476–482
Adverse local tissue reaction (ALTR), 76–81
Adverse reaction to metal debris (ARMD), 76–81
Aging treatment, 166
Alkali-calcium chloride-heat treatment method, 442
Alumina-zirconia composite (ZTA), 446
AM. *See* Additive manufacturing (AM)
American Society of Testing and Materials (ASTM) standards, 31–33, 496
Ankle joint, 453*f*, 454
Antimicrobial surface modifications, 355
Apatite coatings, 374–375
Arc melting, 311–312
Artificial hip prosthesis, wear properties
  26-mm articular head metal-on-polyethylene bearings, 76–81, 78*f*
  femoral head diameter, 81–82, 81*f*
  γ-radiation dose, 76–81, 79*f*
  hypersensitivity and osteolysis, 76–81
  loading and angle profiles, 76–81, 78*f*
  spherical femoral head penetration, 76–81, 80*f*
  UHMWPE materials, physical properties, 76–81, 77*t*
Artificial joints
  ankle joint, 453*f*, 454
  elbow joint, 453–454, 453*f*
  finger joint, 453*f*, 454
  hip (*see* Total hip replacement)
  knee (*see* Knee replacement)
  shoulder joints, 453–454, 453*f*
  wrist joint, 453–454, 453*f*
Artificial knee prosthesis, wear properties, 82–83
Aseptic lymphocytic vasculitisassociated lesions (ALVALs), 34–36
Atom transfer radical polymerization (ATRP), 392–393
Austenitic-type stainless steels, 7–9
Autoclave. *See* Steam sterilization
AZ91 Mg alloy, 270–272

B

Bare metal stents (BMS), 523, 527
Basic fibroblast growth factor (BFGF), 241–242
Bending strength, 66–69
Biocompatible titanium alloys
  mechanical properties, 322–325
  melting point lowering of, 326–328
Biodegradable alloys, 23
  iron and zinc alloys, 24
  magnesium alloy, 23–24
Biodegradable fixation, 265
Biodegradable metals, 146
Bioinspired reaction, 383–384
Biological apatite (BAp) crystals, 116
  anisotropic ionic crystal, 116–117, 117*f*
  orientation degree of c-axis, 116–118, 118–119*f*
  preferential alignment, 117
Biological bone tissues, metallic biomaterial development
  bone microstructure, anisotropic nature of, 116–118
  mechanical functions improvement, 119–120
  metallic implants with low Young's modulus, 119–120
Biological indicators (BIs), 408
Biological tests, 530–531
Biomechanically reliable fixation anchors, 480
Bisurface knee, 451, 452*f*
Bone cement, 438–439
Bone density, 101
Bone fracture fixation
  CHS and CHY-nail, 455
  materials, 454–455
  plates and screws, 455–456, 456*f*
Bone microstructure, anisotropic nature of, 116–118
Bone mineral content (BMC), 277
Bone mineral density (BMD), 277
Bone quality, 101, 116, 119–120
Boundary element modeling (BEM), 279
Boundary lubrication, 217–218
Breakdown potential, 221
β-type Ti alloys, 369, 503–504
  deformation, 109, 110*f*
  metallic implants with low Young's modulus, 119–120
  phase rule and phase diagram, 113–114
Bulk metallic glasses (BMGs), 268, 508–509
Burgers vector, 105, 107–108

C

Calcium phosphate ceramic coatings
  bioactivity, 369
  coating methods, 369–370
  glass-based materials, 375–377
  thermal spraying, 370–372
  thin film coatings, 372–374
  wet-processing, 374–375
Calcium titanate ($CaTiO_3$) film, 373–374
Cardiovascular stents, 523. *See also* Metallic absorbable stents
Casting, 311
Casting defects, 311
Cathodic protection (CP), 223
Cathodic reaction, 132–134
Cavitation peening, 168–171
CDM. *See* Continuum damage mechanics (CDM)
Cement augmentation, 490
Cementless fixation technique, 369–370, 439–442
Cervical interbody fusion device, 460–461, 461*f*
Cervical lateral mass screws (LMS), 480–481, 481*f*
Cervical pedicle screws (CPS), 480–481
Chemical vapor deposition (CVD), 373
Chlorine dioxide gas (ClO_2) sterilization, 420
Chlorofluorocarbon gas (CFC), 408, 417
Closed-die forging, 296–297, 296*f*
Cobalt-chromium (Co-Cr) alloys, 13
  chemical compositions, 496, 497*t*
  dental casting, 318
  fatigue and fretting fatigue tests, 204–207
  forging, 301–303
  tensile strength and elongation, 496, 498*f*
Co-based alloys
  Ni-free Co-Cr alloys, 15
  properties, 13–15
Co-Cr-Mo alloys, 7, 13–15, 433–434, 438–440, 444–446, 449–451, 453–454, 460, 502

Co-20Cr-15W-10Ni alloys, 502–503, 503*f*
Coefficient of friction, 197–198
Cold and hot forging, 294
Cold crucible levitation melting (CCLM), 311–312, 314*f*
Cold forming, forging, 304–305
Cold rolling (CR), 174, 175*f*
Commercially pure titanium (CP Ti)
  compositions and mechanical properties, 16–17, 16*t*
  fatigue and fretting fatigue tests, 204
Composite strengthening, 111
Compression hip screws (CHS), 455, 455–456*f*
Compression hip Y (CHY)-nails, 455, 455*f*
Computer-aided design (CAD) model, 332–333, 349
Co-Ni-Cr-Mo alloy, 15
Continuum damage mechanics (CDM)
  advantages and disadvantages, 280–282, 281*t*
  AZ31 alloy, 280–282
  calibrated parameters, 280–282, 282*t*
  effective stress, 279–280
  finite element deletion, 279–280
  phenomenological corrosion prediction model, 280–282
  pitting and stress corrosion, 280–282
  steps and variables, 279–280, 280*f*
  tensile test data-set, 280–282
Conventional UHMWPE (CPE), 76–81
Conversion factor, 143
Corrosion
  in aqueous solutions, 131
  behavior, evaluation methods
    corrosion morphology, 146
    electrochemical methods (*see* Electrochemical methods, corrosion)
    immersion tests, 145–146
    tarnish test, 146
  biological environments
    body fluids circulation, 146–147, 149–150
    calcium (Ca) and phosphate ions, proteins, and amino acids, 148
    cells and extracellular matrix, 148–149
    dissolved O_2 concentration, 147–148
    temperature and pH, 147
  corrosion rate, 131–132
  definition, 131
  device design and mechanical loadings, 150
  fatigue
    crack nucleation, 196
    local corrosion, 197
    uniform corrosion, 197
  fretting fatigue, 192, 197
  metal ions release, 131–132
  Mg alloys
    byproducts release, 273–274
    galvanic corrosion, 273–274
    H absorption, 274
    modeling (*see* Corrosion modeling)
    in physiological environment, 274
    pitting corrosion, 276
    Puorbiax diagram, 273–274, 273*f*
    stress corrosion and stress corrosion cracking, 274–276
  morphology, 146
    general/uniform corrosion, 137
    local/nonuniform corrosion, 137–140
  noble metal alloys, 131
  passive surface films, 131
  passivity, 136–137
  process
    cathodic reaction, 132–134
    corrosion current, 135–136
    corrosion potential, 135–136
    electrochemistry, 132
    electrode potential, 132–134
    equilibrium constant, 132–134
    equilibrium potential, 132–135
    free energy change, 132–134
    local cell, 132, 132*f*
    local current, 132
    physical metallurgy, 132
    potential-current (density) curves, 135, 135*f*
    Pourbaix diagram, 134–135
    redox reaction, 132–135
    standard electrode potential, 134, 134*t*
Corrosion current, 135–136
Corrosion modeling
  BEM, 279
  bone fixation hardware, 278–279
  CDM

Corrosion modeling *(Continued)*
advantages and disadvantages, 280–282, 281*t*
AZ31 alloy, 280–282
calibrated parameters, 280–282, 282*t*
effective stress, 279–280
finite element deletion, 279–280
phenomenological corrosion prediction model, 280–282
pitting and stress corrosion, 280–282
steps and variables, 279–280, 280*f*
tensile test data-set, 280–282
finite element analysis (FEA), 278–279
Corrosion potential, 135–136
Cortical bone trajectory (CBT), 483, 483*f*
Corundum blasting, 358
Cotrel-Dubousset (CD) instrumentation, 476–478, 477*f*
Counter electrode (CE), 140, 141*f*, 220
CP Ti. *See* Commercially pure titanium (CP Ti)
Crack nucleation, 196
Crack propagation test, 194–195
Crevice corrosion, 139
Critical resolved shear stress (CRSS), 108–109
Cross slip, 107–108
Crystallographic anisotropy, 123–125
Crystallographic texture, 123–125
Crystals
definition, 99–100
dislocation motion in, 105–109
lattice points, 99–100
Crystal structures
atomic arrangement, 100, 100*f*
body-centered cubic (bcc) structures, 104–105, 105*f*
deformation
dislocation core, 102–103
elastic deformation, 101, 102*f*
grain ripening, 114–115
plastic deformation, 102, 103*f*
recovery, 114–115
recrystallization, 114–115
slip, 103–105
yield stress, 102–103
dislocation and twinning, 98–99
face-centered cubic (fcc) structures, 104–105, 105*f*
hexagonal close-packed (hcp) structures, 104–105, 105*f*
lattice points, 99–100
martensitic transformation, 98–99, 101
non-diffusive transformation, 101
phase transformation, 98–99
superelasticity, 98–99, 101
unit cells and crystal systems, 99–100, 99*f*
von Mises criterion, 100
Custom-made orthopedic implants, 84, 85*t*, 85*f*
Cyclic friction stress, 196
Cyclic shear stress, 198–199
Cytocompatibility tests, 532

D

Decimal reduction time (*D*-value), 407, 407*f*
Deformation-induced transformation, 171
Degradation tests, 529–530
Dental casting alloys, 314–321
Au alloys, 21, 22*t*
Co-Cr alloys, 318
high precious metals, 317
low precious metals, 317–318
Ni-Cr alloys, 321
Ti alloys, 318
Diarthrodial joints, 453, 453*f*
Die chilling, 294–295
Die materials, forging
hot work die steels, 305
selection factors, 305–306
Direct energy deposition (DED), 334, 334*f*
Direct laser deposition (DLD), 334
Dissolution and brittle cracks, 274–276
Dissolved O_2 concentration, 147–148
Drug-eluting absorbable stent (DREAMS), 537
Drug-eluting stents (DES), 523, 527, 533–535, 537
Dry heat sterilization, 416
Duplex calcia coating mold, 314, 316–317*f*
Durability limit. *See* Fatigue limit
Dwyer anterior instrumentation, 478–480, 480*f*
Dynamic immersion tests, 530, 531*f*

E

Edge dislocation, 107–108, 108*f*
Elastic deformation, 101, 102*f*, 103
Elbow joint, 453–454, 453*f*
Electrochemical impedance spectroscopy (EIS), 530

Electrochemically assisted deposition (ECAD) method, 361
Electrochemical methods, corrosion, 146
  anodic polarization tests, 140–141
  corrosion potential, monitoring of, 145
  impedance test, 144–145
  linear polarization resistance method, 143
  Tafel extrapolation method, 141–143
Electrochemical tests, 530
Electron beam lithography (ELB), 359
Electron beam melting (EBM) method, 335, 335*f*, 447–448, 448*f*, 460, 460*f*
Electron beam radiation sterilization, 413–414
Ellingham diagram, 313
Endotoxins, 422
Equal-channel angular pressuring (ECAP), 511–512
Ethylene oxide (EO) gas sterilization, 408, 416–417, 416*f*
EVAHEART, 390
Ex vivo bioreactor, 530, 531*f*

F

Fatigue
  assessment, metallic orthopedic devices, 63
  characteristics, 153
  corrosion
    crack nucleation, 196
    local corrosion, 197
    uniform corrosion, 197
  crack initiation, 192, 193*f*
  crack propagation test, 194–195
  cyclic load, 192–193
  failure, 192
  fatigue life test, 194
  fracture toughness, 194–195
  properties, osteosynthesis devices, 64–70
  strength, pH level, 207
  stress change with time, 192, 193*f*
  tests
    cell culture system, 208–209, 209*f*
    new fatigue test, 208–209
    in simulated body fluid, 197–200
    S-N curve characteristics (*see* S-N curve characteristics)
Fatigue crack propagation
  in air and in vitro
    long fatigue crack propagation, 179–181
    short fatigue crack propagation, 177–178
  catastrophic failure, 176–177
  resistance, 182
Fatigue fracture, 153
Fatigue life, 192–193
Fatigue limit, 194
Fatigue strength
  and bioactive surface modification
    annealed/alumina-sprayed SUS 316L stainless steels, 164, 164*f*
    bioactive ceramics, 163
    biocompatibility, Ti alloys, 163
    fatigue fracture surface, 163–164, 164*f*
    TNTZ, S-N curves, 163–164, 163*f*
  improvement by low Young's modulus
    aging time (AT), 174, 175*f*
    dynamic strength, 174
    ω-phase precipitation, 174
    severe cold rolling, 174, 175*f*
    solution treatment (ST), 174, 175*f*
    static strength, 174
    TNTZ, S-N curves, 174, 175*f*
    TNTZ with TiB_2/Y_2O_3 additions, 174–176, 176*f*
  improvement by treatments
    aging treatment, 166
    cavitation peening, 168–171
    deformation-induced transformation, 171
    heat treatment, 165
    oxygen addition, 171–174
    thermochemical treatment, 168
    thermomechanical treatment, 166–167
  in vitro and in vivo, 156–157
  level
    bending fatigue limit, 154
    bovine bone, fatigue limit of, 154, 155*f*
    elongation at fracture, 154, 156*f*
    Ti alloys, Co alloys, and stainless steels, 154, 155*f*
    Ti-6Al-4V and Ti-6Al-7Nb, fatigue limits of, 154–156
    Young's modulus, 154, 156*f*
  notch-fatigue strength, 158–160
  and surface hardening treatment, 162–163
  of wire, 183–184
Fe-Cr-Ni alloy system, 7–9
Fe-Cr-Ni-Mn alloy system, 7–9
Finger joint, 453*f*, 454
Finite element analysis (FEA), 278–279
Flash-less forging, 296
Flash sterilization, 415

Food and drug administration (FDA), 340–343
Forging
  classification factors, 293–294
  cold and hot forging, 294
  definition, 293
  die materials
    hot work die steels, 305
    selection factors, 305–306
  forgeability properties, 297–298
  hot die and isothermal forging, 294–295
  of metals and alloys
    Co-Cr alloys, 301–303
    cold forming, 304–305
    powder metallurgy forging, 306
    shape memory alloys, 304
    stainless steel, 303
    superplastic forming, 306–307
    Ti and its alloys, 299–301
  microstructural developments and consequence, 298–299
  standards for, 307
  warm forging, 295–297
Fracture toughness, 194–195
Free corrosion potential, 220–221
Free energy change, 132–134
Fretting fatigue, 153
  corrosion, 192, 197
  crack growth rate and crack length, 196, 197*f*
  cyclic friction stress, 196
  definition, 196
  tests
    in simulated body fluid, 197–200
    S-N curve characteristics (*see* S-N curve characteristics)
Friction coefficient, 217, 218*f*
Full film lubrication, 218

G

Galvanic corrosion, 139, 200, 273–274
Gamma radiation sterilization, 411–412, 411*f*
Gaseous hydrogen peroxide, 422
Gas melting, 311
General corrosion, 137
Gold (Au) alloys
  dental casting, 21, 22*t*, 317, 317*t*
  porcelain-fused-to-metal, 21–23, 22*f*, 22*t*
Good laboratory practice (GLP) regulation, 62–63
Grafting from method, 392–393
Grafting to method, 392
Grain refining hardening, 111
Grain ripening, 114–115
Growth friendly spinal instrumentation surgery, 487, 488*f*

H

Hard tissue replacements, Ti and its alloys
  apatite formation, 240–241
  artificial hip joints, 237, 239*f*
  bioinert materials, 240–241
  bone cement fixation, 238–240
  cemented and cementless prostheses, 238–240
  endosseous implants, 238
  human body, hard tissues in, 237, 238*f*
  osseointegration, 238–240
  screw-shaped artificial tooth, 238–240, 239*f*
  subperiosteal implants, 238
  surface modification technology, 238–240
  transosteal implants, 238
Harrington instrumentation, 476–478, 476*f*
Healthcare resterilization, 421
Heat treatment, 165
Hemocompatibility tests, 532
High-entropy alloys (HEA), 509
Highly cross-linked UHMWPE (XLPE), 76–83
High-pressure torsion (HPT) processing technique, 512
High tibial osteotomy (HTO), 449–450
Hip resurfacing arthroplasty (HRA), 445
Hip simulator. *See* Artificial hip prosthesis, wear properties
Hooks, 484
Hot/cold chamber die casting, 269
Hot die and isothermal forging, 294–295
Hot isostatic pressing (HIP), 322
Hydrodynamic lubrication, 217–218
Hydroxyapatite (HA), 249, 440
Hydroxyapatite (HA)/Ti composite coatings, 370
Hydroxycarbonate apatite (HCA), 374

I

Igaki-Tamai stent, 523
Immersion tests, 145–146
Implant metal surface treatment
  biocompatibility, 355
  chemical modifications
    biomimetic approach, 362
    ECAD, 361
    methods, 361
    sol-gel process, 362
  physical modifications
    lithography techniques, 359
    nanotubes, 359–361
    plasma etching techniques, 358
    PVD, 359
    sandblasting techniques, 358
  surface structuring, 356–358
In situ synthesized potassium titanate/Ti alloys
  biological activity, 244
  CaO coating crucible, 243
  in situ dry mixed calcination synthetic method, 243
  SBF solution cultivation, 243–244
  surface micropore Ti, 243–244
Intergranular corrosion, 139
International Organization for Standardization (ISO), 14, 31–33, 32*t*, 39–41, 43–44, 76, 82–83, 147, 423, 446*t*, 502, 532
Intervertebral cages, 486
Iron (Fe) alloys, 24, 507–508
  animal tests, 534
  mechanical properties, 526*t*, 528–529

J

Japanese Industrial Standard (JIS), 31–33
Japanese Orthopedic Association (JOA), 461–462

K

Kaneda anterior instrumentation, 478–480, 480*f*
Knee replacement
  femoral component design, 451–452, 452*f*
  joint bearing surface, 450–451
  materials, 449–450
  types, 448–449, 449*f*
Knee simulator, 82–83
Kyphoplasty, 490

L

Lambda ratio, 217–218
Laser powder bed fusion (LPBF) technique, 333
Lateral mass screws (LMS), 480–482, 481*f*
Lattice points, 99–100
Layer-by-layer (LbL) self-assembly method, 393–394, 395*f*
LEVICAST method, 311–312, 312–313*f*
Linear polarization resistance (LPR) tests, 222
Liquid sterilization, 420–421
Living body environment, 200–201, 208–209
Living cell environment, fatigue tests, 191, 208–209
Local cell, 132, 132*f*
Local corrosion, 197
  crevice corrosion, 139
  galvanic corrosion, 139
  intergranular corrosion, 139
  under mechanical loading, 140
  pitting corrosion, 138–139
Local current, 132
Low-cost Ti alloys, 505–507
Low pressure casting (LPC), 269–270
Low-temperature heat treatment (LTHT), 502–503, 503*f*
Low-temperature hydrogen peroxide gas plasma (LTHPGP) sterilization, 417–419
Low temperature steam and formaldehyde (LTSF) sterilization, 420
Low Young's modulus, fatigue strength
  aging time (AT), 174, 175*f*
  dynamic strength, 174
  ω-phase precipitation, 174
  severe cold rolling, 174, 175*f*
  solution treatment (ST), 174, 175*f*
  static strength, 174
  TNTZ, S-N curves, 174, 175*f*
  TNTZ with TiB_2/Y_2O_3 additions, 174–176, 176*f*
Lubrication
  bovine serum, quality profile of, 219, 219*t*
  joint prostheses application, 219
  lambda ratio, 217–218
  Stribeck diagram, 217, 218*f*

Lumbar interbody fusion device, 460–461, 461*f*
Luque sublaminar wiring, 476–478, 477*f*

M

Magmaris stent, 537, 537*f*
Magnesium (Mg) alloys, 23–24, 507
  advantages, 266
  biocompatibility, 266–267
    bio-safety, 277
    bone mineral content, 277
    bone mineral density, 277
    corrosion properties, 277–278
    cytotoxicity tests, 277
    in vitro and in vivo, 277–278
    pH, 277–278
  biodegradable fixation, 265
  coating, 278
  corrosion
    byproducts release, 273–274
    galvanic corrosion, 273–274
    H absorption, 274
    modeling (*see* Corrosion modeling)
    in physiological environment, 274
    pitting corrosion, 276
    Puorbiax diagram, 273–274, 273*f*
    stress corrosion and stress corrosion cracking, 274–276
  corrosion products, 265–266
  grain refinement, 266
  impurities, 266–267
  macrophages and lymphocytes, 268
  manufacturing, 268–269
    AM, 265–266, 270–272
    casting, 269–270
    machining, 270
  metallic absorbable stents
    animal tests, 533–534
    mechanical properties, 526*t*, 527–528
  Mg-Zn-Ca BMGs, 268
  polymeric biodegradable materials, 265–266
  precipitate hardening, 266
  resorbable and biocompatible bone fixation devices, 268
  solid solution strengthening, 266
  vs. Ti and polymer fixations, 265–266
  Velox CD, 265
Magnetic resonance (MR) artifacts, 489–490
Magnetic resonance imaging (MRI), 25, 241, 489–490, 500, 509
Mandibular reconstruction surgery, 345–349
Martensitic transformation, 98–99
Maximum resolved shear stress plane (MRSSP), 107–108, 109*f*
Mechanical anisotropy, additive manufacturing
  AM fabricated product, 122–123, 124*f*
  nominal stress-nominal strain curves, 122, 123*f*
  shape parameters, 122
  Young's modulus and yield stress, 122–123
Mechanical surface structuring, 358
Metal injection molding (MIM) process, 506
Metallic absorbable stents
  absorption process, schematics of, 524, 525*f*
  clinical trials, 534–537
  Fe-based alloys
    animal tests, 534
    mechanical properties, 526*t*, 528–529
  in vitro testing
    biological tests, 530–531
    cytocompatibility tests, 532
    degradation tests, 529–530
    dynamic immersion tests, 530
    hemocompatibility tests, 532
  in vivo testing, 532–534
  Mg-based alloys
    animal tests, 533–534
    mechanical properties, 526*t*, 527–528
  requirements, 524, 525*t*
  Zn-based alloys
    animal tests, 534
    mechanical properties, 526*t*, 529
Metallic biomaterials, 383, 396
  additive manufacturing technology
    crystallographic anisotropy, 123–125
    mechanical anisotropy, 122–123
  advantages, 97–98
  austenitic stainless steel, 153
  biological bone tissues (*see* Biological bone tissues, metallic biomaterial development)
  coatings (*see* Calcium phosphate ceramic coatings)

Co-Cr alloys, 153
mechanical properties
bone-related implants, 97–98, 98*f*
crystal structure (*see* Crystal structures)
magnetic qualities, 97–98
and microstructure, 115–116
mechanical testing
fatigue (*see* Fatigue)
fretting fatigue (*see* Fretting fatigue)
living body environment, 190–191
metal implants fracture and test methods, 189–190
tensile strength, 191
orthopedic and dental implants, 369
phase rule and phase diagram
binary phase diagram, 111–114, 112*f*
β-phase stabilized elements, 113
β-type Ti alloys, 113–114
equilibrium phases, 111–113
Fe-based alloys, 114
free energy-composition curve, 111–113
meta-stable phase, 111
α-phase stabilized elements, 113
Ti-based two-dimensional phase diagram, 113
strengthening
composite strengthening, 111
grain refining hardening, 111
particle dispersion hardening, 110
precipitation hardening, 110
solution hardening, 110
work hardening, 110
surface modifications, 377–379
Ti alloys, 153
Metallic orthopedic devices, 31
biocompatibility, 33–34
custom-made orthopedic implants, 84, 85*t*, 85*f*
fatigue assessment, 63
highly biocompatible α-β-type Ti alloy
alloying elements, role of, 43–44
biological properties under GLP regulation, 62–63
low-cost manufacturing process, 44–49
manufacturing equivalency, 49–51
metal ions release, 52–53
osteocompatibility, 59–61
in vivo metal release, 61–62
passive film formation, 53–59
mechanical compatibility, 84
metal ion cytotoxicity
ALVALs, 34–36
incubation time, 36–39, 38*f*
J774.1 cells, relative growth ratio, 34–36, 37*f*
L929 and MC3T3-E1 cells, relative growth ratios, 34–36, 36*f*
metal concentration, 36–39, 38*f*
metal ions incorporation in cells, 36–39, 37*f*
metal ion release
immersion test, 39–40, 40*t*
from stainless steels and Co-Cr-Mo alloys, 40–43
performance evaluation
artificial hip prosthesis (*see* Artificial hip prosthesis, wear properties)
artificial knee prosthesis (*see* Artificial knee prosthesis, wear properties)
driving force, 64, 69*f*
four-point bending durability tests, 64, 66–69, 70*f*, 71–73, 73–74*f*
metallic bone screws, 70–71
osteosynthesis devices, mechanical properties of, 64–70
pullout tests, 64, 69*f*
spatial stress distribution analysis, 71–76
static four-point bending and four-point bending fatigue tests, 64, 68*f*
torque *vs*. rotational angle curve, 64, 69*f*
torsional breaking, 64, 69*f*
standardized implantable metals
alloys in orthopedic surgery, 31–33, 33*t*
ASTM, 31–33
fatigue strength, 31–33, 32*f*
ISO, 31–33
JIS, 31–33
optical micrographs and TEM images, 31–33, 34*f*
stainless steel corrosion resistance and biocompatibility, 31–33
testing methods, 31–33, 32*t*
Metallic wear debris, 488–489
Metal-on-metal (MOM) bearings, 396–397, 445
Metal-organic chemical vapor deposition (MOCVD), 373, 374*f*

Metals, in medical devices, 6*t*
biodegradable alloys, 23
iron and zinc alloys, 24
magnesium alloy, 23–24
biological environment, 3–7
biomaterials
advantages, 5–7
toxicity, 7
wear resistance, 7
Co-based alloys
Ni-free Co_Cr alloys, 15
properties, 13–15
in dentistry, 5–7
elements position in periodic table, 7, 9*f*
elongation to fracture and tensile strength, 7, 9*f*
implant metals, properties of, 7, 8*t*
material category and chemical bonding, 5, 5*f*
metallic materials, 5
niobium and tantalum, 25
noble metals and alloys, 21–23
permanent magnetic alloys, 23
shape memory and superelastic alloys, 19–21
stainless steels
definition and category, 7–9
Ni-free austenitic stainless steel, 12–13
type 316L stainless steel, 9–12
titanium
alloys, 18–19
properties, 15–18
Young's modulus, 15
zirconium alloys, 24–25
2-Methacryloyloxyethyl phosphorylcholine (MPC) polymers
antithrombogenicity, 389–390
biocompatibility, 389–390
biomimetic attachment, 390–391
molecular design, 387–388
protein adsorption, 389–390
Ti alloy, 393–396
Ti substrate
grafting from method, 392–393
grafting to method, 392
Microalloying, 513
Micro-arc oxidization (MAO) method, 278, 379
Micro plasma oxidation (MPO), 278
Microwave sterilization, 421
Miller-Bravais indices, 104–105
Minimally invasive spinal stabilization (MISt) surgery, 491, 491*f*
Mixed dislocation, 107–108, 108*f*
Mixed lubrication, 217–218
Mobile knee, 451
Moist and dry heat sterilization, 414–416
Mold materials, 311–314
Motion preservation technology, 487–488

N

Nano-K_2 (Ti_8O_{17})/TiO_2 bioceramic composite coating
anode oxidation, 255
electrochemical method, 254–255
hard tissue repair, 254–255
in situ electrochemical technique, 254, 256–257
SBF cultivation, 258–261
Nano-TiO_2/Ti alloys, fabrication and biocompatibility
annealing treatments, 248–249
Ca/P layer, 247–248
for dental and orthopedic implants, 244–245
EDS, element analysis of, 247–248, 248*f*
HREM image, 245–247, 245*f*
hydrolyzation and aggregation, 246
ion consistency, 246, 246*t*
optimal sintering temperature, 246
phase transformations, 248–249
SBF cultivation, 246
SEM micrograph, 245–247, 245*f*
surface modification, 244–245
surface morphology, 247–248, 247*f*
Ti-2Zr-2Nb alloy ingots, 245
XRD pattern, 246–247, 247*f*
Nernst equation, 132–134
New-generation metallic biomaterials
bulk metallic glasses, 508–509
Fe alloys, 507–508
HEA, 509
Mg alloys, 507
processing technologies
crystal-grain refinement, 511–513
porous biomaterials, fabrication of, 510–511

Zn alloys, 508
Zr alloys, 509
Nickel-chromium (Ni-Cr) alloys, 321
Ni-free austenitic stainless steel, 12–13
Ni-free high-N stainless steel, 202
Niobium, 25
Ni_Ti alloys, 19–21
Nonuniform corrosion. *See* Local corrosion
Notch-fatigue strength, 158–160
Nyquist plot, 144–145

O

Open-circuit potential (OCP), 135–136
Open-die forging, 296, 296*f*
Orthopedic implants. *See also* Metallic orthopedic devices
AM devices
large pelvic defects, 460
lumbar and cervical interbody fusion, 460–461
failures, 461–463, 462*f*, 462*t*
hip (*see* Total hip replacement)
knee (*see* Knee replacement)
Osteocompatibility, Ti alloys, 59–61
Osteoconductivity, 238–240
Osteoinductivity, 238–240
Osteosynthesis devices, 64–70
Overcharge sterilization, 407
Oxidative sterilization techniques, 422
Oxygen addition, 171–174
Ozone sterilization, 420

P

Particle dispersion hardening, 110
Patient-specific bone plates, 338–339, 341–342, 345–349, 348*f*
Pedicle screw instrumentation, 476–478, 479*f*, 482–483
Permanent magnetic alloys, 23
Phospholipid polymers, 384–390
Phosphorylcholine (PC)-modified surfaces, 384–387
Physical vapor deposition (PVD), 359, 372
Pitting corrosion, 138–139, 276
Plasma electrolytic oxidation (PEO), 278
Plasma etching techniques, 358
Plasma spray method, 164
Plastic deformation, 102–104, 103*f*
PMB30, 387–390
Polarization resistance, 143
Poly(methylmethacrylate) (PMMA), 238–240
Poly(MPC-co-methacrylic acid-co-3,4-dihydroxyphenylethyl methacrylamide) (PMDP), 391
Polymer-modified metal substrate, 383–384, 384*f*, 385–386*t*
Poly(ethylene glycol) (PEG)-modified surfaces, 384
Porcelain-fused-to-metal, 21–23, 22*f*, 22*t*
Porous metallic biomaterials, 510–511
Posterior wiring technique, 480–481
Potentiodynamic polarization (PDP), 530
Pourbaix diagram, 134–135
Powder metallurgy (PM) forging, 306
Precipitation hardening, 110
Precision casting method, 311–313, 315*f*
Prions, 421–422
Protein adsorption, 389–390
Pulsed high-intensity light sterilization, 421

R

Radiation sterilization
electron beam, 413–414
gamma rays, 411–412
ultraviolet light, 414
X-rays, 413–414
Radiofrequency magnetron sputtering, 372
Radio-frequency thermal plasma spraying (rf-TPS) method, 370
Recrystallization, 114–115
warm forging, 295–296
Redox reaction, 141–143
equilibrium constant, 132–134
equilibrium potential, 132–135
Reference electrode (RE), 140, 141*f*, 220
Remedy stent, 523
Rest potential, 135–136
Reverse transformation (RT) treatment, 512–513
Rigid polymeric test bench, 530, 531*f*

S

Safety of sterilization, 408
Sandblasting techniques, 358

Saturated calomel electrode (SCE), 140
Scanning probe lithography (SPL), 359
Schaeffler's phase diagram, 12*f*, 15–16
Screw dislocation, 107–108, 108*f*
Security assurance level (SAL), 406–407
Selective laser melting (SLM) method, 270–272, 333–334, 333*f*, 457–461
Self-adjustable elastic modulus concept, 506–507, 507*f*
Self-assembled monolayers (SAMs), 392
Septic loosening, 355
Severe plastic deformation techniques, 511–512
Shape memory alloys, 19–21, 304
Shoulder joints, 453–454, 453*f*
Silver (Ag) alloys, 317–318
Silver-containing calcium phosphate (Ag-CP) coating, 370–372
Simulation body fluid (SBF)
  corrosion fatigue and fretting corrosion fatigue tests, 197–200
  cultivation
    in situ synthesized potassium titanate/Ti alloys, 243–244
    nano-K_2 (Ti_8O_{17})/TiO_2 bioceramic composite coating, 258–261
Slip deformation, 103–105
S-N curve characteristics, 201
  Co-Cr alloy, 204–207
  CP Ti, 204
  316L stainless steel, 202
  Ni-free high-N stainless steel, 202
  Ti-6Al-4V alloy, 203
Sol-gel processing, 362–363
Solution hardening, 110
Spaulding Classification, 406
Spinal implants
  biomechanical studies, 480–482
  clinical application
    elderly population, 490
    growing rod system, 487
    hooks, 484
    magnetic resonance (MR) artifacts, 489–490
    metallic rods, 485
    metallic wear debris, 488–489
    MISt surgery, 491
    motion preservation technology, 487–488
    pedicle screw system, 482–483
    sublaminar wires and tapes, 485
    vertebral cages, 486
Spinal interbody fusion device, 460–461, 461*f*
Stacking fault energy (SFE), 14
Stainless steels, 496–498, 500
  bone fracture fixation, 454–455
  chemical compositions, 496, 497*t*
  definition and category, 7–9
  forging, 303
  Ni-free austenitic stainless steel, 12–13
  type 316L stainless steel, 9–12
Standard electrode potential, 134, 134*t*
Standards development organizations (SDO), 307
Static immersion tests, 529–530
Steam sterilization, 414–415
Stents, 523
Sterilization
  challenges
    endotoxins, 422
    prions, 421–422
  and cleaning, 423
  criterias, 424
  vs. disinfection, 406
  efficiency, 406
  EO gas, 416–417
  LTHPGP, 417–419
  manufacturers, 424
  moist and dry heat, 414–416
  ozone, 420
  parameters, advantages and limitations, 409, 409–410*t*
  radiation
    electron beam, 413–414
    gamma rays, 411–412
    ultraviolet light, 414
    X-rays, 413–414
  regulations and standards, 423
  safety, 408
  validation, 406–408
  VPH, 419–420
SterizoneVP, 420
Stern-Geary equation, 143
Sterrad sterilization. *See* Low-temperature hydrogen peroxide gas plasma (LTHPGP) sterilization
Stiffness-matched mandibular bone fixation plates, 345–349

Strain-hardening exponent, 297
Strain-induced martensitic transformation (SIMT), 502–503
Strain rate sensitivity, 297
Stress corrosion, 274–276
Stress corrosion cracking (SCC), 274–276
Stress-induced transformation, 20–21
Stress shielding, 101
Stress-strain (S-S) curve, 191
Sublaminar wires and tapes, 485
Superelastic alloys, 19–21
Superplastic forming, forging, 306–307
Surface analysis, tribology and tribocorrosion properties
  atomic force microscopy (AFM), 230–231
  chemical properties, 227
  detection limits, 227
  lateral resolution and depth resolution, 227, 227*f*
  mass spectroscopy, 232
  normal air pressure condition, 227
  physical properties, 227
  scanning electron microscopy (SEM), 227–228
  tribofilm, 226–227
  vacuum system, 227
  white light interferometry (WLI), 229
  X-ray photoelectron spectroscopy (XPS), 228–229
Surface cleaning, 423
Surface-initiated atom transfer radical polymerization (SI-ATRP), 392–393
Surface micro-porous Ti
  chemical delaminating, 253–254
  cross-section and element linear distribution diagram, 251, 252*f*
  diffusion reaction, 252–253
  hard-tissue implants, 249
  high magnification SEM images, 251, 252*f*
  hydroxyapatite (HA), 249
  physical delaminating, 253–254
  potassium titanate whisker cladding, 253–254
  pure Ti clad with potassium titanate whiskers, 249
  sample preparation, 250
  surface morphology, 250–251, 251*f*
  titania layers, SEM micrographs, 250–251, 250*f*
  XPS and XRD profiles, peeling layer, 251, 253*f*
Surface structuring, 356–358
Surface treatment, 235, 254–255
Surgical site infection (SSI), 370–371

T

Tantalum, 25
Tarnish test, 146
Tensile stress-strain curve, 191, 192*f*
Tension-to-tension fatigue test, 63, 64*f*
Theoretical strength, 105
Thermal sprayed coatings, 370–372
Thermochemical processing (TCP), 322, 322*f*
Thermochemical treatment, 168
Thermoelastic stress measurement, implant devices, 71–76
Thermomechanical treatment, 166–167
Thin film coatings, 372–374
Three-dimensional (3D) printing. *See* Additive manufacturing (AM)
316L stainless steel, fatigue and fretting fatigue tests, 202
Ti-6Al-7Nb alloy, 18–19
Ti-6Al-4V alloys, 18–19, 34–36, 43–44
  anodic polarization curves, 53–55, 55*f*
  critical current density, 53–55, 56*f*
  fatigue and fretting fatigue tests, 203
  fretting fatigue life, 199–200, 199*f*
  hot forgeability, 49–51
  lyophilized tibia tissue, Ti concentration in, 61–62, 62*f*
  morphometrical parameters, 60–61, 61*f*
  optical micrograph, 63–66
  pH effects, 52–53, 53*f*
  S_N curves, 63, 65*f*
  TEM images, 47–49, 47*f*
  test temperature on maximum strength (α_{max}), 49–51, 50*f*
  volume fraction change, α-phase, 44–47
Ti-29Nb-13Ta-4.6Zr (TNTZ) alloy, 154, 311–314, 318, 324–328, 325–329*f*, 369, 504, 505*f*
TiNbTaZrMo HEA, 509
Titania (TiO_2) nanotubes, 359–360, 360*f*
Titanium (Ti), 311
  alloys (*see* Titanium (Ti) alloys)

Titanium (Ti) *(Continued)*
properties, 15–18
Young's modulus, 15
Titanium (Ti) alloys, 18–19, 311–312
alloying elements, role of, 43–44
atomic number, 235–236
atomic weight, 235–236
biocompatibility, 235
biological properties under GLP regulation, 62–63
biomedical applications and development
cardiac and cardiovascular applications, 241–243
hard tissue replacements, 237–241
bone fracture fixation, 454–455
β-type, 236–237, 369, 503–504
dental casting alloys
dental applications, 318, 321*t*
mechanical properties, 318, 321*t*
sorts and chemical compositions, 318, 319–320*t*
forging, 299–301
in situ synthesized bioceramic coatings
nano-K_2 (Ti_8O_{17})/TiO_2 bioceramic composite coating (*see* Nano-K_2 (Ti_8O_{17})/TiO_2 bioceramic composite coating)
nano-TiO_2/Ti alloys, fabrication and biocompatibility (*see* Nano-TiO_2/Ti alloys, fabrication and biocompatibility)
potassium titanate/Ti alloys, 243–244
surface micro-porous Ti (*see* Surface micro-porous Ti)
in vivo metal release, 61–62
low-cost, 505–507
low-cost manufacturing process
continuous hot-rolling process, 45, 45*f*
forging temperature and forging ratio, 47–49, 48*f*
rolling diameter, 47–49, 49*f*
Ti-15Zr-4Nb-4Ta alloy, 44–45, 44*f*, 47–49, 47*f*
volume fraction changes, α-phase, 45–47, 46*f*
manufacturing equivalency, 49–51
mechanical properties, 235
metal ions release, 52–53
microstructures, 43–44, 43*f*
osteocompatibility, 59–61
passive film formation
ARXPS narrow-range spectra for oxide film, 53–55, 57*f*
Cole–Cole plot, 57–59, 58*f*
critical current density, 53–55, 56*f*
FE-TEM image and EDX analysis, 53–55, 56*f*
Nyquist diagram, 58–59
oxide film role and equivalent circuit, 57–58, 58*f*
R_P *vs.* CPE, 58–59, 59*f*
Ti-6Al-4V and Ti-15Zr-4Nb-4Ta alloys, anodic polarization curves, 53, 55*f*
physical properties, unalloyed Ti, 235–236, 236*t*
shape memory effect and superelasticity, 504–505
spinal surgeries, 482–483
TiNi shape memory alloys, 236–237
Ti-Zr-Nb-Sn alloy system, 505
Ti-15Zr-4Nb-4Ta alloys
anodic polarization curves, 53, 55*f*
ARXPS narrow-range spectra, 53, 57*f*
hot forgeability, 49–51
ingot and 100-mm-square billets, 44–45, 44*f*
lyophilized tibia tissue, Ti concentration in, 61–62, 62*f*
microstructural changes, 44
optical micrographs, 60–61, 60*f*
pH effects, 52–53, 54*f*
room-temperature mechanical properties, 47–49, 49*f*
TEM images, 47–49, 47*f*
test temperature on maximum strength (α_{max}), 49–51, 50*f*
vs. Ti-6Al-4V alloys, 49–51, 51*f*
volume fraction change, α-phase, 45–47, 46*f*
Total disc replacement (TDR), 487–488
Total hip arthroplasty (THA), 445, 448–449
Total hip replacement
cement fixation, 438–439
femoral stem design, 435–438
joint bearing surface, 442–448
materials, 432–435
surface treatments, 439–442
Transverse hook, 484, 484*f*
Tribocorrosion testing
bench tests

anodic polarization scans, 221
cathodic protection, 223
corrosion-related damage quantification, 223
free corrosion potential measurement, 220–221
integrated three-electrode cell, 220, 220*f*
joint simulator tests, 220
linear polarization resistance tests, 222
definition, 219
fretting-corrosion, 219
simulator studies
clinical wear rate, total hip replacements, 223–225, 224*f*
hip joint force, 225, 225*f*
hip/knee prostheses, wear rate, 223
Leeds hip simulator, 225, 226*f*
load profile, 225, 226*f*
running-in state, 223–225
steady state, 223–225
volumetric wear, basic features, 223–225, 224*f*
wear factor, 225
surface analysis (*see* Surface analysis, tribology and tribocorrosion properties)
Tribology testing
definition, 213
Jost Report, 213
surface analysis (*see* Surface analysis, tribology and tribocorrosion properties)
tribological properties
friction, 216–217, 217*t*
lubrication and lubricant, 217–219
wear testing, 214–216
wear types, 214
Twinning-induced plasticity (TWIP) steels, 528
Type I collagen, 116, 117*f*

U

Ultimate tensile strength (UTS), 191
Ultrahigh-molecular-weight polyethylene (UHMWPE), 25, 76–81, 396–397, 434–435, 437, 444–445, 449–451, 453–454
Ultraviolet light radiation sterilization, 414
Unicompartmental knee arthroplasty (UKA), 448–450
Uniform corrosion, 137, 197
United States Occupational Safety and Health Administration (USOSHA), 416–417
United States Pharmacopeia (USP), 422

V

Vanadium-free titanium alloys, 436, 436*f*
Vaporized hydrogen peroxide (VPH) sterilization, 419–420
Velox CD, 265
Ventricular assist device (VAD), 390
Vertebral cages, 486
Vertebroplasty, 490
Vitamin E-diffused UHMWPE (VEPE), 76–81, 434, 450

W

Warm forging, 295–297
Wear debris, 396–397, 434–435, 437, 440, 442, 444–445, 450–451, 488–489
Wear testing methods
coatings, 233
micro- and nano-tribology, 233
modeling, 233
in situ, on line wear testing, 233
specific wear testing, 233
Work hardening, 110
Working electrode (WE), 140, 141*f*, 220
Wrist joint, 453–454, 453*f*
Wrought stainless steels, 498

X

X-ray sterilization, 413–414

Y

Young's modulus, 191
YSTEM 1E Liquid Chemical Sterilant Processing System (Steris), 420–421
Yttria-stablized zirconia (YSZ), 25

Z

Zielke instrumentation, 478–480
Zinc (Zn) alloys, 24, 508
animal tests, 534
mechanical properties, 526*t*, 529
Zirconium (Zr) alloys, 24–25, 509

WOODHEAD PUBLISHING SERIES IN BIOMATERIALS

Despite recent advances in medical devices using other materials, metallic implants are still one of the most commercially significant sectors of the industry. Given the widespread use of metals in medical devices, it is vital that the fundamentals and the behavior of this material are understood. ***Metals for Biomedical Devices, Second Edition,*** has been fully updated and builds upon the success of its first edition, discussing the latest techniques in metal processing methods and the behavior of this important material.

Initial chapters review the current status and selection of metals for biomedical devices. Subsequent chapters cover mechanical behavior, degradation and testing, corrosion, wear testing, and biocompatibility, before discussing the processing of metals for biomedical applications and including topics such as forging metals and alloys, surface treatment, coatings, and sterilization. A new chapter discussing the use of additive manufacturing in the production of medical devices has been added, as well as new material on casting processes. Chapters in the final section discuss the clinical applications of metals, such as orthopedic and new-generation biomaterials.

With its distinguished editor and team of expert contributors, this book is a standard reference for materials scientists, researchers, and engineers working in the medical devices industry and academia.

Dr. Mitsuo Niinomi was a professor in the Department of Biomaterials Science, Institute for Materials Research, Tohoku University, and in the Department of Production Systems Engineering, Toyohashi University of Technology, Japan, and was highly regarded for running the Niinomi Lab which specializes in metallic biomaterials for over 20 years. He has been a professor emeritus of Tohoku University since 2016. He is continuing to teach and study on metallic biomaterials as a specially appointed professor of Osaka University and Meijo University, and a visiting professor of IMR, Tohoku University, and Institute of Materials and Systems for Sustainability, Nagoya University, where his research is focused on designing, development, and evaluation of biological and mechanical biocompatibility of titanium alloys for medical and dental applications.

Technology and Engineering/
Material Science

ISBN 978-0-08-102666-3

9 780081 026663

WP
WOODHEAD
PUBLISHING
An imprint of Elsevier
elsevier.com/books-and-journals

ELSEVIER